SIMULATING DRY SLIDING FRICTION WITH BLOCK-SPRING MODELS

A THESIS SUBMITTED TO
THE GRADUATE SCHOOL OF NATURAL AND APPLIED SCIENCES
OF
MIDDLE EAST TECHNICAL UNIVERSITY

BY

AYDIN AMIREGHBALI

IN PARTIAL FULFILLMENT OF THE REQUIREMENTS
FOR
THE DEGREE OF DOCTOR OF PHILOSOPHY
IN
AEROSPACE ENGINEERING

JANUARY 2023

Approval of the thesis:

SIMULATING DRY SLIDING FRICTION WITH BLOCK-SPRING MODELS

submitted by **AYDIN AMIREGHBALI** in partial fulfillment of the requirements for the degree of **Doctor of Philosophy in Aerospace Engineering Department, Middle East Technical University** by,

Prof. Dr. Halil Kalıpçılar
Dean, Graduate School of **Natural and Applied Sciences** _____

Prof. Dr. Serkan Özgen
Head of Department, **Aerospace Engineering** _____

Prof. Dr. Demirkan Çöker
Supervisor, **Aerospace Engineering Department, METU** _____

Examining Committee Members:

Assist. Prof. Dr. Ali Türker Kutay
Aerospace Engineering Department, METU _____

Prof. Dr. Demirkan Çöker
Aerospace Engineering Department, METU _____

Prof. Dr. Hakan Işık Tarman
Mechanical Engineering Department, METU _____

Prof. Dr. İlker Temizer
Department of Mechanical Engineering, Bilkent University _____

Assist. Prof. Dr. Mehmet Nurullah Balcı
Department of Mechanical Engineering, Hacettepe University _____

Date: 12.01.2023

I hereby declare that all information in this document has been obtained and presented in accordance with academic rules and ethical conduct. I also declare that, as required by these rules and conduct, I have fully cited and referenced all material and results that are not original to this work.

Name, Surname: Aydın Amireghbali

Signature :

ABSTRACT

SIMULATING DRY SLIDING FRICTION WITH BLOCK-SPRING MODELS

Amireghbali, Aydın
Ph.D., Department of Aerospace Engineering
Supervisor: Prof. Dr. Demirkan Çöker

January 2023, 404 pages

Dry sliding friction occurs not only in engineering applications such as jet turbine disk-blade joints, dry friction dampers, and rocket engine gimbals but also along geological faults. In this thesis, dry sliding friction is studied using the Maxwell-slip model and the Burridge-Knopoff model, which consist of block-spring units pulled on a rigid flat by a driver. The initial spring extension, stiffness, and normal load values of the block-spring units are specified by different probabilistic methods. The objective is to investigate the effect of these parameters on the evolution of overall friction and interface slip. The Maxwell-slip model with a single randomized parameter, initial lateral spring extension, can produce a range of frictional behavior from stick-slip to steady-sliding. Two asperity-based approaches, one based on Nayak's probability density functions and the other based on the fractal geometry, are used to characterize the Maxwell-slip model units as well. Both approaches generate random asperity heights and tip curvatures. Stick-slip behavior was not observed using these approaches. Considering the inertial force in the Maxwell-slip model can make friction force oscillate even to negative values at high-enough sliding speeds. The Burridge-Knopoff model with an initial linear lateral force distribution can generate

both stick-slip and steady-sliding regimes. The friction force drops are accompanied by pulse-like propagation of slip zones at the interface. The propagation speed of these slip zones can exceed the longitudinal wave speed under the Coulomb friction law.

Keywords: Friction, Maxwell-slip model, Burridge-Knopoff model, Asperity, Fractal

ÖZ

BLOK YAY MODELLERİYLE KURU KAYMA SÜRTÜNMESİNİN İNCELENMESİ

Amireghbali, Aydın
Doktora, Havacılık ve Uzay Mühendisliği Bölümü
Tez Yöneticisi: Prof. Dr. Demirkan Çöker

Ocak 2023 , 404 sayfa

Kuru kayma sürtünmesi, yalnızca jet türbini disk-kanat bağlantıları, kuru sürtünme sönümleyicileri ve roket motoru yalpa çemberleri gibi mühendislik uygulamalarında değil, aynı zamanda jeolojik fay hatlarında da meydana gelmektedir. Bu tezde, bir sürücü tarafından esnemez bir düzlem üzerinde çekilen blok yay birimlerinden oluşan Maxwell-kayma modeli ve Burridge-Knopoff modeli kullanılarak kuru kayma sürtünmesi incelenmiştir. Blok yay ünitelerinin ilk yanal uzaması, direngenliği ve normal yük değerleri farklı olasılıksal yöntemlerle belirlenmiştir. Amaç, bu parametrelerin toplam sürtünme ve arayüz kaymasının gelişimi üzerindeki etkisini araştırmaktır. Tek rastgele parametresi ilk yanal yay uzaması olan bir Maxwell-kayma modeli, tutma-kaymadan kararlı kaymaya kadar bir dizi sürtünme davranışı gösterebilir. Maxwell-slip model birimlerini karakterize etmek için biri Nayak'ın olasılık yoğunluk fonksiyonlarına, diğeri fraktal geometriye dayanan iki pürüz tabanlı yaklaşım kullanılmıştır. Her iki yaklaşım da rastgele pürüz yükseklikleri ve uç eğrilikleri üretir. Bu yaklaşımlar izlendiğinde tutma-kayma davranışının sergilenmesi gözlemlenmedi. Maxwell kayma modelindeki atalet kuvvetinin hesaba katılması, yeterince yüksek

kayma hızlarında sürtünme kuvvetinin negatif değerlere bile salınmasını sağlayabilir. Başta doğrusal bir yanal kuvvet dağılımı olan bir Burridge-Knopoff modeli, tutma-kayma ve sürekli kayma davranışları üretebilir. Sürtünme kuvveti düşüşlerine arayüzde gözlemlenen kayma bölgelerinin atım şeklinde ilerleyişi eşlik eder. Coulomb sürtünme yasası uygulandığı takdirde, bu atım bölgelerinin ilerleme hızı boyuna dalga hızını aşabilir.

Anahtar Kelimeler: Sürtünme, Maxwell-slip modeli, Burridge-Knopoff modeli, Pürüz, Fraktal

In affectionate memory of my friend, teacher, and grandfather,
Mir Ali Asghar Khan Amireghbali (1925-2018)

ACKNOWLEDGMENTS

I wish to express my gratefulness to Professor Demirkan Çöker, for all he has taught me and all his support. I would like to thank the thesis monitoring committee members, Professor Hakan Işık Tarman and Professor Ali Türker Kutay, for their unwavering support and tolerance. I am thankful to the thesis jury members for contributing key ideas that helped me shape the content of the thesis. I feel a profound gratitude towards Professor Oğuz Uzol, the director of RÜZGEM (METUWIND) Center For Wind Energy Research, who provided me with the opportunity of using the center's office building.

I am immensely grateful to Can Muyan for his friendship through all the years of our doctoral studies under the supervision of Professor Çöker. I appreciate friendly relationship of the current students of Çöker Research Group: Ahmet Çevik, Ilgın Tutku Özcan, Onur Ali Batmaz, Umut Altuntaş, Erdem Dinler, and the graduated students: Miraç Onur Bozkurt, Emine Burçin Özen, Burak Ogün Yavuz, Yezdan Medet Korkmaz, Burcu Taşdemir and Tamer Tahir Ata and also to Fırat Ergin, the group's former floormate and recent officemate. I am thankful to Ömer Ataş for his friendship and help especially during the pandemic, and to Şahin Kürekçi, Amir Jale Forouzan, Reza Shabani, Ferit Sait, and Ramazan Günlü for their good company. I greatly appreciate the many years of friendship provided by Farhad Hassani and Turaç Farsadi.

I thank TÜBİTAK (the scientific and technological research council of Turkey) for the financial support provided during project number 115M585.

Words are inadequate to express my love and gratitude toward my parents, Faezeh Eghbali Namin and Mir Yadollah Amireghbali, my sister, Sahar, and my brother, Sahand.

TABLE OF CONTENTS

ABSTRACT v

ÖZ vii

ACKNOWLEDGMENTS x

TABLE OF CONTENTS xi

LIST OF TABLES xvi

LIST OF FIGURES xvii

LIST OF ABBREVIATIONS xxxv

CHAPTERS

1 INTRODUCTION 1

1.1 Tribology: A historical view 1

1.1.1 A pre-modern history 2

1.1.2 A modern history 4

1.2 The concept of critical distance 9

1.3 The Burridge-Knopoff model 11

1.4 Some friction models of control engineering 12

1.5 A spectrum of research fields 16

1.6 Surface roughness and fractals 28

1.7 Contributions 34

1.8 The outline of the thesis 35

2 QUASI-STATIC MAXWELL-SLIP MODEL WITH RANDOM INITIAL SPRING EXTENSIONS 39

2.1 Introduction 39

2.2 Method 42

2.2.1 The proposed approach to the Maxwell-slip model 43

2.2.2 Constraints on the maximum time step size 46

2.2.3 Initial block positions as roughness 48

2.3 Results 51

2.4 Discussion 56

2.4.1 A claim about the behavior of geological faults 56

2.4.2 Possible effects of the fault frictional properties 59

2.4.3 The onset of periodicity 60

2.4.4 About the steady sliding plateau 61

2.5 Conclusions 62

2.6 Future work 63

3 QUASI-STATIC MAXWELL-SLIP MODEL CHARACTERIZED BY NAYAK PARAMETER 65

3.1 Introduction 65

3.1.1 Normal contact 66

3.1.2 Sliding contact 69

3.2 Method 72

3.3 Results 78

3.3.1 Case 1 ($\boldsymbol{\alpha = 5.15, \sigma = 1\ \mu m}$) 79

3.3.2 Case 2 ($\boldsymbol{\alpha = 11.2, \sigma = 1\ \mu m}$) . . . 101

3.4 Summary . . . 120

3.5 Future work . . . 120

4 QUASI-STATIC MAXWELL-SLIP MODEL CHARACTERIZED BY FRACTAL DIMENSION . . . 123

4.1 Introduction . . . 124

4.2 Method . . . 128

4.2.1 Generation of the surface: Midpoint displacement method . . . 129

4.2.2 Calculation of the second spectral moment . . . 131

4.2.3 Calculation of the summit curvatures . . . 135

4.2.3.1 Circular paraboloid fit to an an elliptic asperity . . . 135

4.2.3.2 Geometric mean curvature of an elliptic asperity . . . 136

4.3 Results . . . 137

4.3.1 Case 1 ($\boldsymbol{H = 0.75, \sigma_0 = 1\ \mu m}$) . . . 137

4.3.2 Case 2 ($\boldsymbol{H = 0.95, \sigma_0 = 1\ \mu m}$) . . . 162

4.4 Summary . . . 183

4.5 Future work . . . 183

5 DYNAMIC MAXWELL-SLIP MODEL WITH LINEAR INITIAL SPRING EXTENSIONS . . . 187

5.1 Introduction . . . 187

5.2 Method . . . 192

5.2.1 Block's motion under Coulomb's friction law . . . 193

5.2.2 A flowchart for the Maxwell-slip model . . . 200

5.3 Results . . . 202

5.4 Discussion . . . 212

5.5 Summary . . . 212

5.6 Future work . . . 213

6 THE BURRIDGE-KNOPOFF MODEL WITH LINEAR INITIAL LATERAL FORCES . . . 215

6.1 Introduction . . . 216

6.2 Method . . . 222

6.2.1 Free boundary conditions . . . 225

6.2.2 Periodic boundary conditions . . . 226

6.2.3 The equations of motion . . . 228

6.2.4 Algorithm . . . 239

6.2.5 Pseudocode . . . 241

6.2.6 Flowchart . . . 245

6.2.7 Block's stopping time and stopping position . . . 254

6.2.8 Time-dependent static friction COF . . . 255

6.2.9 A time step size criterion . . . 256

6.3 Results . . . 259

6.3.1 Case 1 ($\gamma = \mathbf{0.1}$) . . . 261

6.3.2 Case 2 ($\gamma = \mathbf{0.9}$) . . . 296

6.4 Summary . . . 323

6.5 Future work . . . 323

7 DISCUSSION . . . 325

7.1 General remarks . . . 325

7.2 On asperity-based results . . . 329

REFERENCES . . . 335

A FRACTIONAL BROWNIAN MOTION . . . 365

A.1 Definition . . . 365

A.2 Statistical self-affinity . . . 366

A.3 The variance of increments . . . 367

A.3.1 An inappropriate way for generating fBm . . . 369

A.3.2 Self-affine transformation as a function . . . 370

A.4 The covariance of increments . . . 370

B YASTREBOV'S FORMULATIONS . . . 375

B.1 Analytical formulas . . . 375

B.2 Input . . . 378

B.3 Pseudocode . . . 379

C GREENWOOD'S PROBABILITY DISTRIBUTION FUNCTIONS . . . 381

D ACCEPTANCE-REJECTION METHOD . . . 387

E HERTZIAN CONTACT . . . 389

F PLASTICITY INDEX . . . 391

G STICK-SLIP OF THE EQUIVALENT BLOCK-SPRING UNIT . . . 395

H SPRING STIFFNESS IN THE BURRIDGE-KNOPOFF MODEL . . . 399

CURRICULUM VITAE . . . 403

LIST OF TABLES

TABLES

Table 2.1 The static Maxwell-slip model input data 51

Table 5.1 Deceleration and stop time values for the limit cases 199

Table 5.2 The dynamic Maxwell-slip model case studies 202

Table B.1 Nayak parameter, α, against ζ values with $H = \{0.75, 0.85, 0.95\}$ according to Equation (B.7). 378

LIST OF FIGURES

FIGURES

Figure 1.1 A wall painting from the tomb of Tehuti-Hetep 2

Figure 1.2 Leonardo da Vinci's illustrations (1) 3

Figure 1.3 Leonardo da Vinci's illustrations (2) 3

Figure 1.4 Leonardo da Vinci's friction test apparatus recreated 4

Figure 1.5 Coulomb's sketch of the sliding surfaces 5

Figure 1.6 The Prandtle-Tomlinson and Frenkel-Kontorova models 6

Figure 1.7 A sketch of the nominal and real contact areas, and the Greenwood-Williamson model assumptions 8

Figure 1.8 A sketch of Rabinowicz's friction apparatus 9

Figure 1.9 Dieterich's rock test result 10

Figure 1.10 Wear and fretting fatigue life as a function of slip amplitude . . . 10

Figure 1.11 The Burridge-Knoppof model 11

Figure 1.12 Iwan's model and elasto-plastic behavior 12

Figure 1.13 Bristle model 13

Figure 1.14 The empirical dependence of lubricated friction on velocity . . . 14

Figure 1.15 The Maxwell-slip model 15

Figure 1.16 A schematic of some scientific and technological fields and applications that involve dry sliding friction 17

Figure 1.17 Blade-disc firtree joints in turbines 18

Figure 1.18 Frictional damping in turbines 19

Figure 1.19 Fretting damage of a dovetail blade root and surface finishing . . 20

Figure 1.20 The macroslip friction model 22

Figure 1.21 The microslip friction model 22

Figure 1.22 1-DOF system on a frictional belt 23

Figure 1.23 Bifurication diagram 23

Figure 1.24 Falling rod and two-link robotic manipulator contact 24

Figure 1.25 A graphene flake is moved on a graphene substrate. 26

Figure 1.26 The Cascadia subduction zone, and its seismic behavior 27

Figure 1.27 A block-spring-damper model of a geological fault plane 28

Figure 1.28 A surface profile and its roughness 30

Figure 1.29 Exactly self-similar fractals 31

Figure 1.30 Self-similarity of the coast of Britain 32

Figure 1.31 Self-affinity of a fractal profile 33

Figure 1.32 Categorization of the fractals to self-similar and self-affine . . . 34

Figure 2.1 (a) The Burridge-Knopoff model (b) The Maxwell-slip model (c) A rough surface contacts a rigid flat via asperities 41

Figure 2.2 Two types of block position references (a) beneath the stuck block (b) beneath the spring-driver attachment point 44

Figure 2.3 The single block force-drop for the mass-spring unit 45

Figure 2.4 The asperity heights (in percents) and their standard deviation according to the beta PDF for different shape parameters 49

Figure 2.5 An analogy between the effect of (a) asperity height distribution and (b) initial block position distribution, on sliding friction 50

Figure 2.6 Time evolution of the macroscopic COF and the slipped block index numbers for nine shape parameter values 54

Figure 2.7 The macroscopic static COF values against the beta PDF shape parameter 56

Figure 3.1 Maxwell-slip model configuration shown with (a) leaf springs (b) coil springs 71

Figure 3.2 Flowchart of Chapter 2 method 74

Figure 3.3 The normal and tangential contact of a rigid circular paraboloid asperity with the elastic half-space and its block-spring counterpart . . . 77

Figure 3.4 The numerical and analytical (a) real contact area and (b) pressure against compression for Case 1 ($\alpha = 5.15$ and $\sigma = 1\ \mu m$). 89

Figure 3.5 The numerical and analytical relation between real contact area and pressure is superimposed with the theoretical limits proposed by BGT and Persson for Case 1 ($\alpha = 5.15$ and $\sigma = 1\ \mu m$). 90

Figure 3.6 The number of contacting asperities as percentage of the total number of generated asperities against compression for Case 1 ($\alpha = 5.15$ and $\sigma = 1\ \mu m$) according to the numerical results. 91

Figure 3.7 Real contact area against the percentage of the contacting asperities for Case 1 ($\alpha = 5.15$ and $\sigma = 1\ \mu m$) according to the numerical results. 92

Figure 3.8 Plastic contact area against compression for Case 1 ($\alpha = 5.15$ and $\sigma = 1\ \mu m$) according to the numerical and analytical results. 93

Figure 3.9 The numerical results for sliding at $\delta = 1$ for Case 1 ($\alpha = 5.15$ and $\sigma = 1\ \mu m$): (a) COF against the driver position and (b) Block slippage history against the driver position. 94

Figure 3.10 Histograms of (a) normal load (b) tangential stiffness and (c) load to stiffness ratio for Case 1 ($\alpha = 5.15$ and $\sigma = 1\ \mu m$) at $\delta = 1$. . . 95

Figure 3.11 The numerical results for sliding at $\delta = 2$ for Case 1 ($\alpha = 5.15$ and $\sigma = 1\ \mu m$): (a) COF against the driver position and (b) Block slippage history against the driver position. 96

Figure 3.12 Histograms of (a) normal load (b) tangential stiffness and (c) load to stiffness ratio for Case 1 ($\alpha = 5.15$ and $\sigma = 1\ \mu m$) at $\delta = 2$. . . 97

Figure 3.13 The numerical results for sliding at $\delta = 3$ for Case 1 ($\alpha = 5.15$ and $\sigma = 1\ \mu m$): (a) COF against the driver position and (b) Block slippage history against the driver position. 98

Figure 3.14 Histograms of (a) normal load (b) tangential stiffness and (c) load to stiffness ratio for Case 1 ($\alpha = 5.15$ and $\sigma = 1\ \mu m$) at $\delta = 3$. . . 99

Figure 3.15 The numerical results for sliding under different compression values, $\delta = 1, 2, 3$, for Case 1 ($\alpha = 5.15$ and $\sigma = 1\ \mu m$) 100

Figure 3.16 The numerical and analytical (a) real contact area and (b) pressure against compression for Case 2 ($\alpha = 11.2$ and $\sigma = 1\ \mu m$). 108

Figure 3.17 The numerical and analytical relation between real contact area and pressure is superimposed with the theoretical limits proposed by BGT and Persson for Case 2 ($\alpha = 11.2$ and $\sigma = 1\ \mu m$). 109

Figure 3.18 The number of contacting asperities as percentage of the total number of generated asperities against compression for Case 2 ($\alpha = 11.2$ and $\sigma = 1\ \mu m$) according to the numerical results. 110

Figure 3.19 Real contact area against the percentage of the contacting asperities for Case 2 ($\alpha = 11.2$ and $\sigma = 1\ \mu m$) according to the numerical results. 111

Figure 3.20 Plastic contact area against compression for Case 2 ($\alpha = 11.2$ and $\sigma = 1\ \mu m$) according to the numerical and analytical results. 112

Figure 3.21 The numerical results for sliding at $\delta = 1$ for Case 2 ($\alpha = 11.2$ and $\sigma = 1\ \mu m$): (a) COF against the driver position and (b) block slippage history against the driver position. 113

Figure 3.22 Histograms of (a) normal load (b) tangential stiffness and (c) load to stiffness ratio for Case 2 ($\alpha = 11.2$ and $\sigma = 1\ \mu m$) at $\delta = 1$. . . . 114

Figure 3.23 The numerical results for sliding at $\delta = 2$ for Case 2 ($\alpha = 11.2$ and $\sigma = 1\ \mu m$): (a) COF against the driver position and (b) block slippage history against the driver position. 115

Figure 3.24 Histograms of (a) normal load (b) tangential stiffness and (c) load to stiffness ratio for Case 2 ($\alpha = 11.2$ and $\sigma = 1\ \mu m$) at $\delta = 2$. . . . 116

Figure 3.25 The numerical results for sliding at $\delta = 3$ for Case 2 ($\alpha = 11.2$ and $\sigma = 1\ \mu m$): (a) COF against the driver position and (b) block slippage history against the driver position. 117

Figure 3.26 Histograms of (a) normal load (b) tangential stiffness and (c) load to stiffness ratio for Case 2 ($\alpha = 11.2$ and $\sigma = 1\ \mu m$) at $\delta = 3$. . . . 118

Figure 3.27 The numerical results for sliding under different compression values, $\delta = 1, 2, 3$, for Case 2 ($\alpha = 11.2$ and $\sigma = 1\ \mu m$) 119

Figure 4.1 Early stages of grid refinement in the RMD method 129

Figure 4.2 Two "extreme" surface profiles with: (a) maximum and (b) minimum possible zero-crossing density per unit length, D_{zero}. 132

Figure 4.3 The variation of the second spectral moment of Case 1 surface ($H = 0.75$ and $\sigma_0 = 1\ \mu m$) with the number of the finite difference stencil points for both equi-spaced and unequally spaced stencils. 134

Figure 4.4 The variation of the second spectral moment of Case 2 surface ($H = 0.95$ and $\sigma_0 = 1\ \mu m$) with the number of the finite difference stencil points for both equi-spaced and unequally spaced stencils. 134

Figure 4.5 The topography of the rough surface that is generated for Case 1 (with $H = 0.75$ and $\sigma_0 = 1\ \mu m$, but resulted in $\sigma = 0.24\ \mu m$): (a) The isometric view of the generated 3-D fractal surface, (b) The top view of the same surface 146

Figure 4.6 The visualization of the evolution of the real contact area for Case 1 ($H = 0.75$ and $\sigma_0 = 1\ \mu m$) under the compression values $\delta = 0.25, 0.5, 0.75, 1, 1.25$ and 1.5 with the series of frames (a) to (f) . . 147

Figure 4.7 The numerical and analytical (a) real contact area and (b) pressure against compression for Case 1 ($H = 0.75$ and $\sigma_0 = 1\ \mu m$). 150

Figure 4.8 The numerical and analytical relation between real contact area and pressure is superimposed with the theoretical limits proposed by BGT and Persson for Case 1 ($H = 0.75$ and $\sigma_0 = 1\ \mu m$). 151

Figure 4.9 The number of contacting asperities as percentage of the total number of generated asperities against compression for Case 1 ($H = 0.75$ and $\sigma_0 = 1\ \mu m$) according to the numerical results. 152

Figure 4.10 Real contact area against the percentage of the contacting asperities for Case 1 ($H = 0.75$ and $\sigma_0 = 1\ \mu m$) according to the numerical results. 153

Figure 4.11 Plastic contact area against compression for Case 1 ($H = 0.75$ and $\sigma_0 = 1\ \mu m$) according to the numerical and analytical results. . . . 154

Figure 4.12 The numerical results for sliding at $\delta = 0.5$ for Case 1 ($H = 0.75$ and $\sigma_0 = 1\ \mu m$): (a) COF against the driver position and (b) Block slippage history against the driver position. 155

Figure 4.13 Histograms of (a) normal load (b) tangential stiffness and (c) load to stiffness ratio for Case 1 ($H = 0.75$ and $\sigma_0 = 1\ \mu m$) at $\delta = 0.5$. 156

Figure 4.14 The numerical results for sliding at $\delta = 1$ for Case 1 ($H = 0.75$ and $\sigma_0 = 1\ \mu m$): (a) COF against the driver position and (b) Block slippage history against the driver position. 157

Figure 4.15 Histograms of (a) normal load (b) tangential stiffness and (c) load to stiffness ratio for Case 1 ($H = 0.75$ and $\sigma_0 = 1\ \mu m$) at $\delta = 1$. . 158

Figure 4.16 The numerical results for sliding at $\delta = 1.5$ for Case 1 ($H = 0.75$ and $\sigma_0 = 1\ \mu m$): (a) COF against the driver position and (b) Block slippage history against the driver position. 159

Figure 4.17 Histograms of (a) normal load (b) tangential stiffness and (c) load to stiffness ratio for Case 1 ($H = 0.75$ and $\sigma_0 = 1\ \mu m$) at $\delta = 1.5$. 160

Figure 4.18 The numerical results for sliding under different compression values, $\delta = 0.5, 1, 1.5$, for Case 1 ($H = 0.75$ and $\sigma_0 = 1\ \mu m$) 161

Figure 4.19 The topography of the rough surface that is generated for Case 2 (with $H = 0.95$ and $\sigma_0 = 1\ \mu m$, but resulted in $\sigma = 0.23\ \mu m$): (a) The isometric view of the generated 3-D fractal surface, (b) The top view of the same surface 167

Figure 4.20 The visualization of the evolution of the real contact area for Case 2 ($H = 0.95$ and $\sigma_0 = 1\ \mu m$) under the compression values $\delta = 0.25, 0.5, 0.75, 1, 1.25$ and 1.5 with the series of frames (a) to (f) . . 168

Figure 4.21 The numerical and analytical (a) real contact area and (b) pressure against compression for Case 2 ($H = 0.95$ and $\sigma_0 = 1\ \mu m$). 171

Figure 4.22 The numerical and analytical relation between real contact area and pressure is superimposed with the theoretical limits proposed by BGT and Persson for Case 2 ($H = 0.95$ and $\sigma_0 = 1\ \mu m$). 172

Figure 4.23 The number of contacting asperities as percentage of the total number of generated asperities against compression for Case 2 ($H = 0.95$ and $\sigma_0 = 1\ \mu m$) according to the numerical results. 173

Figure 4.24 Real contact area against the percentage of the contacting asperities for Case 2 ($H = 0.95$ and $\sigma_0 = 1\ \mu m$) according to the numerical results. 174

Figure 4.25 Plastic contact area against compression for Case 2 ($H = 0.95$ and $\sigma_0 = 1\ \mu m$) according to the numerical and analytical results. . . . 175

Figure 4.26 The numerical results for sliding at $\delta = 0.5$ for Case 2 ($H = 0.95$ and $\sigma_0 = 1\ \mu m$): (a) COF against the driver position and (b) Block slippage history against the driver position. 176

Figure 4.27 Histograms of (a) normal load (b) tangential stiffness and (c) load to stiffness ratio for Case 2 ($H = 0.95$ and $\sigma_0 = 1\ \mu m$) at $\delta = 0.5$. 177

Figure 4.28 The numerical results for sliding at $\delta = 1$ for Case 2 ($H = 0.95$ and $\sigma_0 = 1\ \mu m$): (a) COF against the driver position and (b) Block slippage history against the driver position. 178

Figure 4.29 Histograms of (a) normal load (b) tangential stiffness and (c) load to stiffness ratio for Case 2 ($H = 0.95$ and $\sigma_0 = 1\ \mu m$) at $\delta = 1$. . 179

Figure 4.30 The numerical results for sliding at $\delta = 1.5$ for Case 2 ($H = 0.95$ and $\sigma_0 = 1\ \mu m$): (a) COF against the driver position and (b) Block slippage history against the driver position. 180

Figure 4.31 Histograms of (a) normal load (b) tangential stiffness and (c) load to stiffness ratio for Case 2 ($H = 0.95$ and $\sigma_0 = 1\ \mu m$) at $\delta = 1.5$. 181

Figure 4.32 The numerical results for sliding under different compression values, $\delta = 0.5, 1, 1.5$, for Case 2 ($H = 0.95$ and $\sigma_0 = 1\ \mu m$) 182

Figure 5.1 Side-driven and top-driven block-spring models 188

Figure 5.2 The Maxwell-slip model with a linear initial spring extension distribution 188

Figure 5.3 The shear impact of adjacent plates 189

Figure 5.4 Finite element model results for the shear impact 190

Figure 5.5 The modes of slip propagation in the shear impact problem . . . 190

Figure 5.6 The block position, velocity and acceleration for three different driver velocities 195

Figure 5.7 The block stop time as x-coordinate of the intersection point. While a and c are assigned one, b values are -1/3, -1/2, -1 and -2 for the black curves from the thinnest to the thickest correspondingly. The stop time is always between $\pi/\sqrt{a}$ and $2\pi/\sqrt{a}$. 196

Figure 5.8 The four possible block state updates due to time increment . . . 198

Figure 5.9 Flowchart for calculation of friction in GMS model 201

Figure 5.10 Case (i): $v_d = 1\ mm/s$ and $x_{max} = 1\text{e}{-13}\ m$ 206

Figure 5.11 Case (ii): $v_d = 1\ mm/s$ and $x_{max} = 1\text{e}{-12}\ m$ 207

Figure 5.12 Case (iii): $v_d = 1\ mm/s$ and $x_{max} = 2.82\text{e}{-11}\ m$ 208

Figure 5.13 Case (iv): $v_d = 10\ mm/s$ and $x_{max} = 1\text{e}{-12}\ m$ 209

Figure 5.14 Case (v): $v_d = 100\ mm/s$ and $x_{max} = 1\text{e}{-12}$ 210

Figure 5.15 The frictional response of models in control literature 211

Figure 5.16 Measured local COF as a function of the interface rupture velocity 213

Figure 6.1 The Burridge-Knopoff model 216

Figure 6.2 The linear slip-weakening friction law 219

Figure 6.3 The experimental and numerical rupture speeds along an interface subjected to shear impact 220

Figure 6.4 Nucleation and acceleration of rupture in the BK model and its different characteristic lengths 221

Figure 6.5 The division of a crack-like nucleation into a pair of pulses that propagate in opposite directions 222

Figure 6.6 The ith block and its immediate neighbors in the BK model . . . 223

Figure 6.7 Periodic boundary condition: assuming that the virtual neighbor of the leftmost (1st) block is the rightmost block; and assuming that the virtual neighbor of the rightmost (M^{th}) block is the leftmost block. . . . 227

Figure 6.8 The external forces exerted on (a) the ith block sliding block and (b) the free body diagram of the ith block sliding block includes the fictitious force, $-ma_i$, in order to apply the principle of d'Alembert. . . 228

Figure 6.9 The block acceleration is assumed to change linearly with time within each time step between the discrete times: the previous time point, $\tau = t$, and the forthcoming time point $\tau = t + \Delta t$. The total grey area beneath $a(\tau)$ is equal to the change in the block velocity within the time step. 229

Figure 6.10 The main flowchart. The outermost loop is called the time-increment loop. The three inner loops are drawn as predefined processes. The corresponding flowcharts of the inner loops are shown in figures 6.11-6.13 250

Figure 6.11 The force criterion loop makes temporary decisions about the status of the blocks. 251

Figure 6.12 The velocity criterion loop deals with the sliding blocks only and determines if they stop or continue sliding. 252

Figure 6.13 The force calculation loop calculates the final spring-exerted force values according the updated block positions. Moreover, the loop records the force overshoot due to neighbor slippages. 253

Figure 6.14 Response of the BK model with exact zero initial block positions and the periodic boundary conditions: (a) friction and the driver traction, (b) the block slippage history, and (c) the percent of the slipping blocks at each time step 267

Figure 6.15 The initial block positions for case one, $\gamma = 0.1$, that assumes a linear spring-force distribution on the blocks in which the leftmost experiences $\gamma\mu_s N$ and the rightmost block experiences $-\gamma\mu_s N$ 268

Figure 6.16 Response of the BK model in case one, linear spring force with $\gamma = 0.1$ with the free boundary conditions: (a) friction and the driver traction, (b) the block slippage history, and (c) the percent of the slipping blocks at each time step 269

Figure 6.17 The zoomed view of zone number 1 (marked in Figure 6.16-(b)) of case one shows a slip pulse propagation on the interface. The threshold (normalization) parameter, t_{th}, is equal to $5714.3\ s$. The total duration of the propagation, t_{prop} is equal to $91.65\ ms$. 270

Figure 6.18 The position of the blocks just before and just after the pulse propagation which is shown in Figure 6.17, i.e. case one, zone number 1. The driver position, x_d is $5.14\ mm$. 271

Figure 6.19 The position and velocity of the blocks during the time interval $(0, 0.009t_{prop})$ for the pulse propagation that is shown in Figure 6.17, i.e. case one, zone number 1. The total duration of the propagation, t_{prop} is equal to $91.65\ ms$. 272

Figure 6.20 A zoomed view of Figure 6.19 273

Figure 6.21 The position and velocity of the blocks during the time interval $(0.01t_{prop},\ 0.09t_{prop})$ for the pulse propagation that is shown in Figure 6.17, i.e. case one, zone number 1. The total duration of the propagation, t_{prop} is equal to $91.65\ ms$ 274

Figure 6.22 A zoomed view of Figure 6.21 275

Figure 6.23 The position and velocity of the blocks during the time interval $(0.1t_{prop},\ t_{prop})$ for the pulse propagation that is shown in Figure 6.17, i.e. case one, zone number 1. The total duration of the propagation, t_{prop} is equal to $91.65\ ms$. 276

Figure 6.24 The pulse velocity and the number of involved (slipping) blocks during the propagation that is shown in Figure 6.17, i.e. case one, zone number 1. The threshold (normalization) parameter, t_{th}, is equal to $5714.3\ s$. The total duration of the propagation, t_{prop} is equal to $91.65\ ms$.277

Figure 6.25 The zoomed view of zone number 2 (marked in Figure 6.16-(b)) of case one shows the tail of the preceding pulse-like event and the onset of a series of sequential and isolated block slippages. The threshold (normalization) parameter, t_{th}, is equal to $5714.3\ s$. 278

Figure 6.26 The zoomed view of zone number 3 (marked in Figure 6.16-(b)) of case one shows the whole series of the sequential and isolated block slippages. The threshold (normalization) parameter, t_{th}, is equal to $5714.3\ s$. The speed of propagation is almost equal to $1\ m/s$. 279

Figure 6.27 The zoomed view of zone number 4 (marked in Figure 6.16-(b)) of case one shows nucleation of a crack that is later divided into two slip pulses that propagate in the opposite directions on the interface. The threshold (normalization) parameter, t_{th}, is equal to $5714.3\ s$. The total duration of the propagation, t_{prop} is equal to $90.26\ ms$. 280

Figure 6.28 The position of the blocks just before and just after the pulse propagation which is shown in Figure 6.27, i.e. case one, zone number 4. The driver position, x_d is $5.98\ mm$. 281

Figure 6.29 The position and velocity of the blocks during the time interval $(0, 0.009t_{prop})$ for the pulse propagation that is shown in Figure 6.27, i.e. case one, zone number 4. The total duration of the propagation, t_{prop} is equal to $90.26\ ms$. 282

Figure 6.30 A zoomed view of Figure 6.29 283

Figure 6.31 The position and velocity of the blocks during the time interval $(0.01t_{prop},\ 0.09t_{prop})$ for the pulse propagation that is shown in Figure 6.27, i.e. case one, zone number 4. The total duration of the propagation, t_{prop} is equal to $90.26\ ms$. 284

Figure 6.32 A zoomed view of Figure 6.31 285

Figure 6.33 The position and velocity of the blocks during the time interval $(0.1t_{prop},\ t_{prop})$ for the pulse propagation that is shown in Figure 6.27, i.e. case one, zone number 4. The total duration of the propagation, t_{prop} is equal to $90.26\ ms$. 286

Figure 6.34 The pulse velocity and the number of involved (slipping) blocks during the propagation that is shown in Figure 6.27, i.e. case one, zone number 4. The threshold (normalization) parameter, t_{th}, is equal to $5714.3\ s$. The total duration of the propagation, t_{prop} is equal to $91.65\ ms$.287

Figure 6.35 The zoomed view of zone number 5 (marked in Figure 6.16-(b)) of case one shows leftward propagation of a slip pulse on the interface. The threshold (normalization) parameter, t_{th}, is equal to $5714.3\ s$. The total duration of the propagation, t_{prop} is equal to $71.01\ ms$. 288

Figure 6.36 The position of the blocks just before and just after the pulse propagation which is shown in Figure 6.27, i.e. case one, zone number 5. The driver position, x_d is $6.65\ mm$. 289

Figure 6.37 The position and velocity of the blocks during the time interval $(0, 0.009t_{prop})$ for the pulse propagation that is shown in Figure 6.35, i.e. case one, zone number 5. The total duration of the propagation, t_{prop} is equal to $71.01\ ms$. 290

Figure 6.38 A zoomed view of Figure 6.37 291

Figure 6.39 The position and velocity of the blocks during the time interval $(0.01t_{prop},\ 0.09t_{prop})$ for the pulse propagation that is shown in Figure 6.35, i.e. case one, zone number 5. The total duration of the propagation, t_{prop} is equal to $71.01\ ms$. 292

Figure 6.40 A zoomed view of Figure 6.39 293

Figure 6.41 The position and velocity of the blocks during the time interval $(0.1t_{prop},\ t_{prop})$ for the pulse propagation that is shown in Figure 6.35, i.e. case one, zone number 5. The total duration of the propagation, t_{prop} is equal to $71.01\ ms$. 294

Figure 6.42 The pulse velocity and the number of involved (slipping) blocks during the propagation that is shown in Figure 6.35, i.e. case one, zone number 5. The threshold (normalization) parameter, t_{th}, is equal to $5714.3\ s$. The total duration of the propagation, t_{prop} is equal to $71.01\ ms$.295

Figure 6.43 The initial block positions for case two, $\gamma = 0.9$, that assumes a linear spring-force distribution on the blocks in which the leftmost experiences $\gamma\mu_s N$ and the rightmost block experiences $-\gamma\mu_s N$ 299

Figure 6.44 Response of the BK model in case two, linear spring force with $\gamma = 0.9$ with the free boundary conditions: (a) friction and the driver traction, (b) the block slippage history, and (c) the percent of the slipping blocks at each time step 300

Figure 6.45 The zoomed view of zone number 1 (marked in Figure 6.44-(b)) of case two shows a slip pulse propagation on the interface. The threshold (normalization) parameter, t_{th}, is equal to $5714.3\ s$. The total duration of the propagation, t_{prop} is equal to $11.6\ ms$. 301

Figure 6.46 The position of the blocks just before and just after the pulse propagation which is shown in Figure 6.45, i.e. case two, zone number 1. The driver position, x_d is $0.57\ mm$. 302

Figure 6.47 A zoomed view of Figure 6.46 303

Figure 6.48 The position and velocity of the blocks during the time interval $(0,\ 0.09t_{prop})$ for the pulse propagation that is shown in Figure 6.45, i.e. case two, zone number 1. The total duration of the propagation, t_{prop} is equal to $11.6\ ms$. 304

Figure 6.49 A zoomed view of Figure 6.48 305

Figure 6.50 The position and velocity of the blocks during the time interval $(0.1t_{prop},\ t_{prop})$ for the pulse propagation that is shown in Figure 6.45, i.e. case two, zone number 1. The total duration of the propagation, t_{prop} is equal to $11.6\ ms$. 306

Figure 6.51 The pulse velocity and the number of involved (slipping) blocks during the propagation that is shown in Figure 6.45, i.e. case two, zone number 1. The threshold (normalization) parameter, t_{th}, is equal to $5714.3\ s$. The total duration of the propagation, t_{prop} is equal to $11.6\ ms$. 307

Figure 6.52 The zoomed view of zone number 2 (marked in Figure 6.44-(b)) of case two shows nucleation of a crack that is later divided into two slip pulses that propagate in the opposite directions on the interface. The threshold (normalization) parameter, t_{th}, is equal to $5714.3\ s$. The total duration of the propagation, t_{prop} is equal to $11.28\ ms$. 308

Figure 6.53 The position of the blocks just before and just after the event which is shown in Figure 6.52, i.e. case two, zone number 2. The driver position, x_d is $1.42\ mm$. 309

Figure 6.54 A zoomed view of Figure 6.53 310

Figure 6.55 The position and velocity of the blocks during the time interval $(0,\ 0.09t_{prop})$ for the pulse propagation that is shown in Figure 6.52, i.e. case two, zone number 2. The total duration of the propagation, t_{prop} is equal to $11.28\ ms$. 311

Figure 6.56 A zoomed view of Figure 6.55 312

Figure 6.57 The position and velocity of the blocks during the time interval $(0.1t_{prop},\ t_{prop})$ for the pulse propagation that is shown in Figure 6.52, i.e. case two, zone number 2. The total duration of the propagation, t_{prop} is equal to $11.28\ ms$. 313

Figure 6.58 The pulse velocity and the number of involved (slipping) blocks during the propagation that is shown in Figure 6.52, i.e. case two, zone number 2. The threshold (normalization) parameter, t_{th}, is equal to $5714.3\ s$. The total duration of the propagation, t_{prop} is equal to $11.28\ ms$. 314

Figure 6.59 The zoomed view of zone number 3 (marked in Figure 6.44-(b)) of case two shows propagation of a slip pulse on the interface. The threshold (normalization) parameter, t_{th}, is equal to $5714.3\ s$. The total duration of the propagation, t_{prop} is equal to $24.88\ ms$. 315

Figure 6.60 The position of the blocks just before and just after the event which is shown in Figure 6.59, i.e. case two, zone number 3. The driver position, x_d is $2.15\ mm$. 316

Figure 6.61 A zoomed view of Figure 6.60 317

Figure 6.62 The position and velocity of the blocks during the time interval $(0,\ 0.09t_{prop})$ for the pulse propagation that is shown in Figure 6.59, i.e. case two, zone number 3. The total duration of the propagation, t_{prop} is equal to $24.88\ ms$. 318

Figure 6.63 A zoomed view of Figure 6.62 319

Figure 6.64 The position and velocity of the blocks during the time interval $(0.1t_{prop},\ t_{prop})$ for the pulse propagation that is shown in Figure 6.59, i.e. case two, zone number 3. The total duration of the propagation, t_{prop} is equal to $24.88\ ms$. 320

Figure 6.65 The pulse velocity and the number of involved (slipping) blocks during the propagation that is shown in Figure 6.59, i.e. case two, zone number 3. The threshold (normalization) parameter, t_{th}, is equal to $5714.3\ s$. The total duration of the propagation, t_{prop} is equal to $24.88\ ms$. 321

Figure 6.66 The zoomed view of zone number 4 (marked in Figure 6.44-(b)) of case two contains what seems to be a set of paralell lines, however, each line is constructed by a series isolated block slippages. The threshold (normalization) parameter, t_{th}, is equal to $5714.3\ s$. The speed of propagation is almost equal to $0.1\ m/s$. 322

Figure 7.1 The numerical results for sliding under different compression values, for Nayak's model with $\alpha = 5.15$ ($H = 0.75$ and $\zeta = 8$) 331

Figure 7.2 The numerical results for sliding under different compression values, for Nayak model with $\alpha = 5.37$ ($H = 0.95$ and $\zeta = 8$) 331

Figure 7.3 The numerical results for sliding under different compression values, for Nayak model with $\alpha = 11.19$ ($H = 0.75$ and $\zeta = 16$) 332

Figure 7.4 The numerical results for sliding under different compression values, for Nayak model with $\alpha = 12.34$ ($H = 0.95$ and $\zeta = 16$) 332

Figure 7.5 The numerical results for sliding under different compression values, for the fractal model with $H = 0.75$ 333

Figure 7.6 The numerical results for sliding under different compression values, for the fractal model with $H = 0.95$ 333

Figure A.1 The anti-persistence and persistence of the fBm 372

Figure B.1 Nayak parameter, α, against $\zeta = \tilde{k}_s/\tilde{k}_l$ for $H = \{0.75, 0.85, 0.95\}$ according to Equation (B.7). 377

Figure C.1 The asperity height probability distribution functions for $\alpha = \{2, 3, 5, 10, 50, 100, 1000\}$ according to Greenwood's simplified elliptic model. 383

Figure C.2 The asperity tip curvature probability distribution functions for $\xi = 1$ and $\alpha = \{2, 3, 5, 10, 50, 100, 1000\}$ according to Greenwood's simplified elliptic model. 384

Figure C.3 The asperity tip curvature probability distribution functions for $\xi = 1.5$ and $\alpha = \{2, 3, 5, 10, 50, 100, 1000\}$ according to Greenwood's simplified elliptic model. 384

Figure C.4 The asperity tip curvature probability distribution functions for $\xi = 2$ and $\alpha = \{2, 3, 5, 10, 50, 100, 1000\}$ according to Greenwood's simplified elliptic model. 385

Figure C.5 The asperity tip curvature probability distribution functions for $\xi = 2.5$ and $\alpha = \{2, 3, 5, 10, 50, 100, 1000\}$ according to Greenwood's simplified elliptic model. 385

Figure C.6 The asperity tip curvature probability distribution functions for $\xi = 3$ and $\alpha = \{2, 3, 5, 10, 50, 100, 1000\}$ according to Greenwood's simplified elliptic model. 386

Figure C.7 Contours of Greenwood's joint PDF for heights and curvatures for $\alpha = 2$ and $\alpha = 10$ 386

Figure E.1 A rigid circular paraboloid is pressed against the elastic half-space. 390

Figure G.1 The stick-slip of the block-spring unit 396

Figure H.1 (a) The isolated unit of the BK model and (b) Two triangular elements that model the unit 400

Figure H.2 Variation of the ratio of the FEM-predicted coil spring stiffness to that which is obtained by simple reasoning, $k_c = ETH/L$, with Poisson ratio for plane stress and plane strain cases 401

LIST OF ABBREVIATIONS

AFM	Atomic force microscope
BC	Boundary condition
BEM	Boundary element method
BGT model	Bush-Gibson-Thomas model
BK model	Burridge-Knopoff model
CDF	Cumulative distribution function
CLA	Center line average
COF	Coefficient of friction
CZM	Cohesive zone model
DFT	Density functional theory
DOF	Degree of freedom
EOM	Equation of motion
ETS	Episodic tremor and slip
FBC	Free boundary condition
fBm	Fractional Brownian Motion
FEM	Finite element method
FFM	Friction force microscope
FFT	Fast Fourier transform
FK model	Frenkel-Kontorova model
GM radius	Geometric mean radius
GW model	Greenwood-Williamson model
HBM	Harmonic balance method
IVP	Initial value problem
LBP	Low plasticity burnishing

LFE	Low frequency earthquakes
LHS	Left-hand side
LSP	Laser shock peening
MEMS	Microelectromechanical systems
MSP	Metallic shot peening
NEMS	Nanoelectromechanical systems
NOP	Noncontact optical profiler
oBm	Ordinary Brownian motion
ODE	Ordinary differential equation
PBC	Periodic boundary condition
PMMA	Polymethylmethacrylate
PSD	Power spectral density
PT model	Prandtle-Tomlinson model
RHS	Right-hand side
RMD method	Random midpoint displacement method
RMS roughness	Root mean square roughness
SP	Stylus profiler
SSE	Slow slip events
2-D	Two-dimensional
3-D	Three-dimensional

CHAPTER 1

INTRODUCTION

The purpose of this chapter is to introduce the broad context within which the thesis places and then to provide an overall picture of the thesis structure and its contributions. Section 1.1 is a brief historical review of the developments in the knowledge of tribology (roughly: the science of friction) from ancient Egypt to the twentieth century. Since the rest of the chapter content cannot be *directly* classified under the title *tribology*, it is structured as independent sections. The chronological order of the developments is preserved as much as possible. In Section 1.2, a key concept in frictional behavior, namely the critical distance, is introduced. The Burridge-Knopoff model, a block-spring model that has been mainly used by earth scientists, is introduced in Section 1.3. A range of friction models that have been used by control engineers (among them the Maxwell-slip model) is introduced in Section 1.4. A broad spectrum of research fields that deal with dry sliding friction (such as vibration, dynamics, and thermodynamics) are addressed in Section 1.5. An introduction to surface roughness and its relation with fractals can be found in Section 1.6. The contributions and outline of the thesis are provided in Sections 1.7 and 1.8, respectively.

1.1 Tribology: A historical view

The term *tribology* is the name of a scientific and technological field of study that involves the friction, lubrication, and wear of contacting surfaces that move relative to each other. Although the term was coined in the twentieth century [1], humankind has dealt with these phenomena since ancient times. The term *tribology* is derived

from Greek *tribein*, which means *to rub*. The term *friction*, which is derived from the Latin root *fricare* means *to rub* as well. In the following subsections a review of the progress of tribology throughout history is provided.

1.1.1 A pre-modern history

Friction is one of the physical phenomena that has challenged the human mind since ancient times [2]. Figure 1.1 shows a wall painting from the tomb of Tehuti-Hetep in Egypt, in which workmen *slide* a colossus fastened on a sled. A workman, who stands on the sled's front end, pours water ahead on the path. According to an empirical study [3], an optimum amount of water can minimize the sliding friction force of sand-sled interface. It seems that the ancient Egyptians (at least around 1880 B.C.) had been well aware of the facilitating role of lubrication as well as the severe difficulties encountered when *sled-rollers* are used on sand [2, 4].

It is astonishing that Leonardo da Vinci (1452–1519) not only explicitly stated the linear dependence of the sliding friction force on the normal load but also discovered that friction is independent of the apparent contact area. In Figure 1.2-(a), Leonardo's illustration of his test apparatus is shown. In Figure 1.2-(b), a block is being pulled on a surface; while the traction force is 1, the weight is 4. One may look at the number 4 in a mirror since it is mirror-written. He wrote: *"friction produces double the amount of effort if the weight be doubled"* [5]. Namely, friction linearly increases with normal

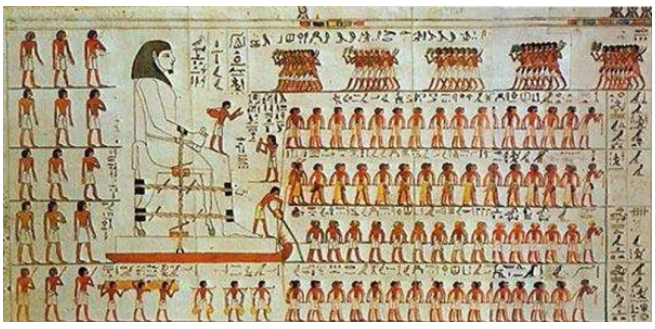

Figure 1.1: A wall painting from the tomb of Tehuti-Hetep shows workmen sliding a colossus on the sand. A workman pours water in from of the sled to reduce its sliding friction [3].

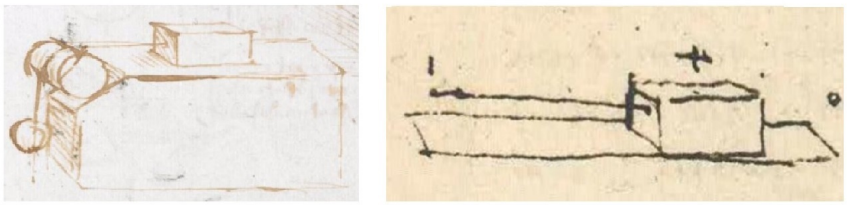

(a) (b)

Figure 1.2: Leonardo da Vinci's illustrations of (a) his friction test apparatus and (b) a block that weighs 4 units (mirror-written) and is pulled by 1 unit of force [5].

load. The conception of coefficient of friction (COF) is widely credited to Leonardo da Vinci [6].

Figure 1.3-(a) shows Leonardo's illustrations of the same 2-D block laid on a surface, once on its greater face and once on its smaller face. In both cases, the hung mass is the same. He wrote: *"friction made by the same weight will be of equal resistance at the beginning of the movement though the contact may be of different breadths or lengths"* [5]. In other words, the static friction force does not depend on the apparent contact area and remains the same despite the configuration change. The weight of the block is visually shown as 5 units. Figure 1.3-(b) shows several different positions at which a 3-D block can be laid and pulled on a surface.

In an experimental study [6], the authors recreated Leonardo's apparatus (Figure 1.4-(a)) and measured the static COF for wooden specimens. They found that roughly-cut specimens that were sullied by hand (intentionally exposed to oily fingerprints and

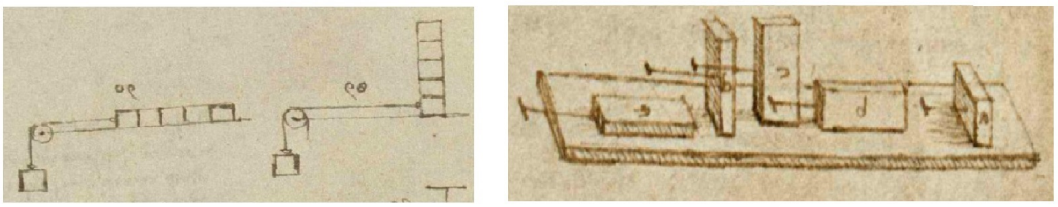

(a) (b)

Figure 1.3: Leonardo da Vinci's illustrations: (a) a 2-D block that is once laid horizontally and once vertically and is pulled by the same hanging mass, and (b) a set of different configurations in which a 3-D block can be placed on a surface and pulled [5].

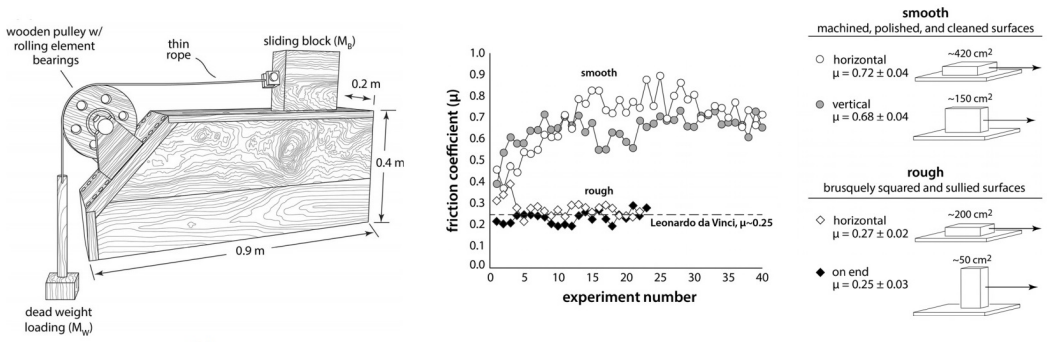

(a) (b) (c)

Figure 1.4: (a) An illustration of the recreation of Leonardo da Vinci's friction test apparatus (his own sketch is shown in Figure 1.2-(a)) (b) The measured static COF values (c) The smooth and rough categories and the considered the apparent contact area case studies [6]

dust) are in good agreement with Leonardo's $\frac{1}{4}$ COF value (Figure 1.2-(b)). Figure 1.4-(b) shows the measured static COF values for (i) rough and sullied (ii) smooth and clean blocks of African coralwood. Both categories have a horizontal (in which the block stands on its largest face) and a vertical (in which the block stands on its smallest face) configuration (1.4-(c)).

Leonardo da Vinci was also aware of the effect of surface roughness on friction and identified roughness as one of the key parameters [7]. He wrote *"... different bodies have different kinds of friction; because if there shall be two bodies with different surfaces, that is that one is delicate and smooth and well-greased or soaped, and it is moved upon a plane of a similar nature, it will move much more easily than one that has been roughened by the use of file or rasp"*.

1.1.2 A modern history

During the modern age, the axioms mentioned above were rediscovered [2, 5] by Guillaume Amontons (1663-1705) and are called Amontons' laws of friction [8]: (1) The friction force depends linearly on the normal applied force, (2) The friction force does not depend on the apparent contact area. Later, Charles-Augustin de Coulomb

(1736-1806), also known for his contributions to the fields of electricity and magnetism (specifically Coulomb's inverse-square law for the electrostatic force between two point charges) performed a set of detailed friction tests. The distinction between kinetic and static COF was substantiated only after the publication of Coulomb's book *Theory of Simple Machines* in 1781 [9]. He investigated the effect of the duration of stationary contact on the static COF and found that the static COF increases with time according to $\mu_s = A + Bt^{\alpha}$ [10]. Coulomb's results can be summarized as:

$$F = \mu N \tag{1.1}$$

where F is the friction force and N the normal load. He found that the COF, μ, is almost independent of the normal load, sliding velocity (provided that it is not too high or too low), the apparent contact area, and the surface roughness [10]. The above equation is called Coulomb's law of friction [9].

Leonhard Euler (1707-1783) proposed a mechanistic, physically based idea for the origin of friction. According to his idea, the friction force results from the interlocking of small angular protrusions on the sliding surfaces. The same idea was developed further by Coulomb, who proposed a simple mathematical model for the interaction of a corrugated surface during sliding. He wrote the equilibrium equation for such a pair of periodically corrugated surfaces by considering the free body diagram. Coulomb's sketch for the configuration is shown in Figure 1.5. His analysis showed that the static COF is a function of the maximum slope of the periodic profile [9, 11, 12].

Nanotribology is a field of study that deals with friction, wear, and adhesion in the atomic (nano-) scale. The field has emerged as a result of technological advances in the development of instruments such as atomic force and friction force microscopes (AFM and FFM). These microscopes can be used to investigate the *single* protrusion

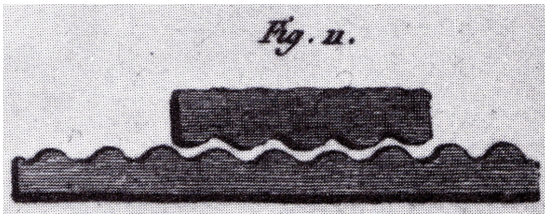

Figure 1.5: Coulomb's sketch of the sliding surfaces [9]

(asperity) contact by sliding a sharp nano-scale diamond tip (scanning probe) on the surface [13].

It is surprising that Euler's idea of the origin of friction (sketched by Coulomb in Figure 1.5) survived into nanotribology via two spring models, namely Prandtle-Tomlinson (PT) and Frenkel-Kontorova (FK) models. The PT and FK models are shown in Figure 1.6. These models were initially used for the investigation of plastic deformation. However, with the development of AFM and FFM, both models have been used widely to study atomic-scale friction in surface physics [14]. The Prandtle-Tomlinson model is composed of a driver that pulls a set of independent atoms on a periodic surface, while the Frenkel-Kontorova model is essentially a chain of interacting atoms that is dragged over a periodic surface. According to Lennard-Jones potential, the interatomic attraction and repultion are a function of interatomic distance. The PT and FK models incorporate these forces by considering external spatially periodic forces [15].

Frank Philip Bowden (1903-1968), a professor of surface physics, set up a research laboratory on friction, lubrication, and bearings (later titled *tribophysics laboratory*) during World War II. Together with David Tabor (who is the author of a book on the metal hardness [16]), he published one of the classical works in tribology, *The friction and lubrication of solids* [12] in 1950. A substantial contribution of Bowden and Tabor's work is emphasizing the critical role of the real contact area in tribological processes. For example, they explained the nature of metallic wear by considering the shearing of the *junctions*, which form only within a small portion of the nominal contact area [12]. Furthermore, Bowden and Tabor considered the maximum static

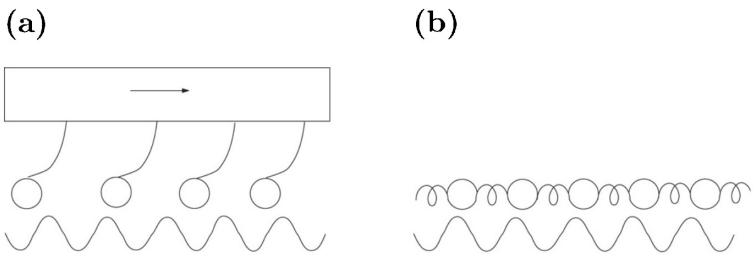

Figure 1.6: The spring models of plasticity and nanotribology: (a) the Prandtle-Tomlinson model and (b) the Frenkel-Kontorova model [14]

friction as function of the material shear strength and the real contact area. They deduced that (since the junctions deform plastically) the real contact area is approximately equal to the normal load ratio to the material's penetration hardness. Then, for non-lubricated metallic pairings, the static COF has to be between $\frac{1}{6}$ and $\frac{1}{5}$ [9]. Note that pure metal pairings can reach much higher static COF values under high compression, and for the elastically deformed interface, the above theory does not work [9].

Bowden and Tabor's conceptualization of the real contact area was mainly a result of their experimental studies on sliding surfaces (specifically the loss of interfacial material due to wear). However, following theoretical studies in the second half of the twentieth century primarily focused on studying the development of real contact area during the normal contact.

No matter how smooth they seem, real surfaces are not flat. The height of an engineering surface fluctuates to some extent. These fluctuations produce local surface maxima, which are called asperities. During normal contact of rough surfaces, the asperities come into contact. Therefore, only a small portion of the apparent (nominal) contact area indeed makes contact as sketched in Figure 1.7-(a). This portion is called the real contact area. In [17], development of the real contact area between glass and plastic samples is imaged.

In 1957, a landmark study by Archard [18] showed that assuming surface roughness as the presence of *protuberances on protuberances on protuberances* results in a linear proportionality between the normal load and the real contact area. Interestingly, the notion of roughness as protuberances on protuberances on protuberances is in accord with the theory of fractals (which was yet to emerge at that time).

During the 1960s and 1970s, Benoit Mandelbrot (1924–2010) developed the basis of fractal geometry. In a *Science* paper published in 1967, he engaged in the problem of measuring the length of the coastline of Britain [19]. He used the concepts of self-similariy and the *fractional* dimension. Later these concepts were extended to surface topology and provided a new approach to modeling and understanding a rough surface as a multi-scale geometry, namely as a *self-affine* fractal [20]. Subsection 1.6 introduces the meaning and categories of fractals. Appendix A contains some math-

ematical explanations about the fractional Brownian motion (fBm), a well-known self-affine fractal that is used in modeling rough surfaces.

In 1966, Greenwood and Williamson developed a multi-asperity model (later called Greenwood-Williamson model) that assumes the asperity height to be a Gaussian random variable and the asperity tip radius to be the same for all of the asperities (Figure 1.7-(b)). The asperities were assumed to be far from each other. Thus, Archard's proposition was not considered. By approximating the tail of the Gaussian PDF with an exponential function, the Greenwood-Williamson (GW) model found a linear relation between the normal load and the real contact area [21]. In 2001, Greenwood criticized the GW model for assuming that the asperities are distant from each other and expressed a need to return to the earlier Archard concept [22].

In 1971, Nayak used the techniques of random process theory to provide a probabilistic model for the heights and curvatures of a rough surface summits (asperities) [24]. A probability density function (PDF) of heights and a joint PDF of heights and curvatures were obtained. He showed that the obtained PDFs are fully determined by a single parameter, later called Nayak parameter (or spectral/spectrum breadth [25]). The parameter is a function of the spectral moments of the surface: the variance of the heights, the variance of the slopes, and the variance of the curvatures.

Further progress of the studies on modeling normal contact of rough surfaces are addressed in Chapters 3 and 4, where the Bush-Gibson-Thomas (BGT) model (based on the random process theory) [26], Greenwood's simplified elliptic model (based on Nayak's PDFs) [27], and Persson's theory (based on the pressure PDF) [28, 29] are introduced.

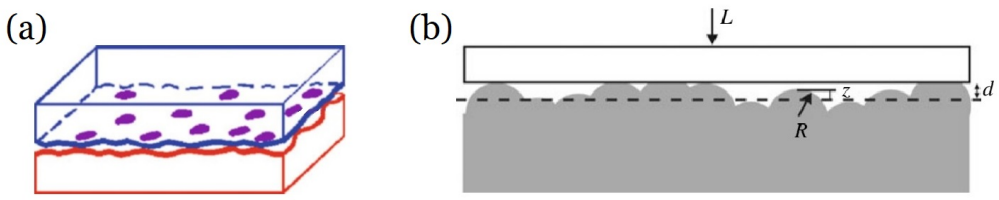

Figure 1.7: A sketch of: (a) The nominal and real contact areas [23], and (b) The Greenwood-Williamson model [1]

1.2 The concept of critical distance

The concept of critical distance was initially proposed in 1958 by Rabinowicz in his experimental study of the stick-slip phenomenon [30] by using the apparatus that is shown in Figure 1.8. He observed that although the slippage length of the rider decreases with increasing the stiffness of the apparatus, it is *not* an ever-decreasing parameter that gradually tends to zero. Instead, a certain (finite) spring stiffness zeros the slippage length abruptly. He concluded that a critical slippage length exists below which the rider cannot stick-slip. In other words, stick-slip is abruptly eliminated when the slippage length reaches a critical value (does not undergo a gradual decay down to zero). He also observed that when a sudden change is applied to the velocity of the belt, the friction force changes gradually and reaches a stable value only after the rider slips a specific length.

Rabinowicz's other observation was that when a slider in stationary contact on a surface is suddenly moved by impact, the friction force does not suddenly drop to its dynamic value. Instead, the static friction force persists until a specific length (of the same order of magnitude as the critical distance) is slid. He concluded that the critical distance is an intrinsic frictional characteristic of the surface, which determines the amplitude of the stick-slip phenomenon (and if it would happen or not). In Rabinowicz's tests, the measured critical length is approximately equal to 10 microns [30].

In the late 1970s, a series of papers were published by Dieterich [31–33] in which, based on rock friction experiments, a framework for constitutive modeling of friction was established. Dieterich changed the sliding velocity of the rock specimens abruptly and (like Rabinowicz) observed [31] that the steady-state friction force appears only after a specific length (critical distance, d_c), is traveled (Figure 1.9). This

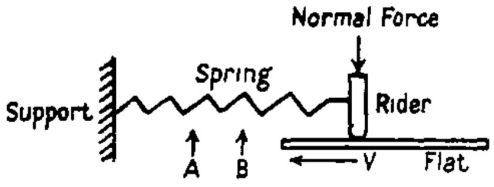

Figure 1.8: A sketch of Rabinowicz's friction apparatus [30]

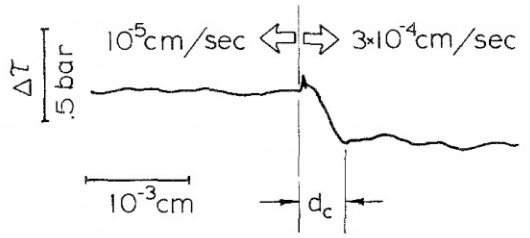

Figure 1.9: Dieterich's rock test result [31] shows the critical displacement, d_c, as the length that has to be traveled for the friction force to become stable after a jump in sliding velocity.

length (distance) was reported to be independent of the normal stress and the sliding velocity while consistently dependent on the surface *roughness*. Dieterich argued that the critical length can be viewed as the distance that has to be traveled by the slider to eliminate the *population of contacts* that corresponds to the previous velocity. He proposed that d_c is related to the average shear strain that is needed to *break contacting asperities* and also to the average dimensions of the *zones* of contact [31].

The concept of critical length has also been proposed in the fretting fatigue literature [35, 36]. Figure 1.10 shows that when the slip amplitude is below the left vertical

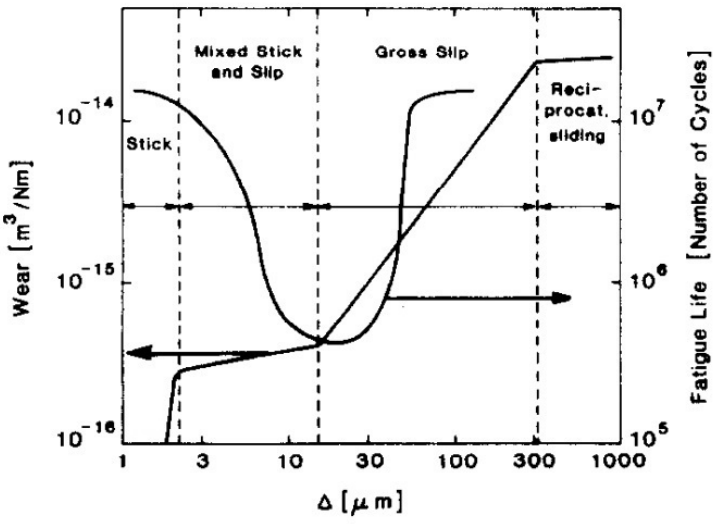

Figure 1.10: Wear and fretting fatigue life as a function of slip amplitude [34]. Wear terminates below a certain slip amplitude.

dashed line, the whole interface is stuck and wear decays the fastest with decrease in the slip amplitude. Furthermore, fretting fatigue life is the longest. However, in the *mixed stick and slip* region, the interface slips partially and fretting cracks become the dominant mode of damage while wear grows the slowest. In the *gross slip* region, wear increases faster (compared to the mixed stick and slip region) and prevents fretting cracks from propagation. In other words, in the gross slip region wear competes fretting fatigue.

1.3 The Burridge-Knopoff model

Geomechanics and geophysics concern with modeling and understanding behavior of the geological faults. A wide-ranging review of the related literature is provided in Chapter 2. In a 1966 *Science* paper, geophysicists proposed the stick-slip of rock as a possible mechanism for earthquakes [37]. A cornerstone study was published in 1968 in which a block-spring model (Figure 1.11) of the geological fault (later called Burridge-Knopoff model) was developed [38]. The study includes numerical and experimental investigations and majorly focuses on the statistics of the shocks (block slippages), after-shocks, and their energies.

Some geophysicists have used the BK model to reproduce the empirical power-law relation between the number and magnitude of earthquakes. The law is called Gutenburg-Richter and states that the number of earthquakes, N, decreases with an increase in the earthquake magnitude, M, according to the power law: $N = 10^{a-bM}$. The constants a and b are different for each geological fault and can be obtained by fitting the power (or scaling) law to the statistical data [39].

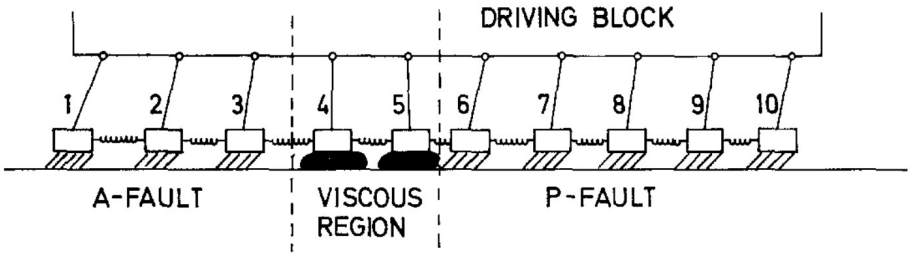

Figure 1.11: The Burridge-Knoppof model as sketched in [38]

1.4 Some friction models of control engineering

In 1966, Iwan proposed a model to study the hysteretic behavior of structures. The model consists of a set of Jenkin's elements that are fixed at one end and are capable of sliding on a driver at the other end (Figure 1.12-(a)). A Jenkin's element consists of a linear spring connected in series to a Coulomb (slip) damper. The element is an elastic perfectly plastic unit (Figure 1.12-(b)); below the Coulomb threshold, the element behaves elastically, and the traction force increases/decreases linearly. Above the threshold, a constant traction is experienced by the driver.

In 1968, Dahl [40] developed a friction simulator that can be used in modeling the dynamics of systems that involve sliding or rolling. The friction simulator is expressed as a *block diagram* and is used to model the hysteresis loops of ball bearing tests.

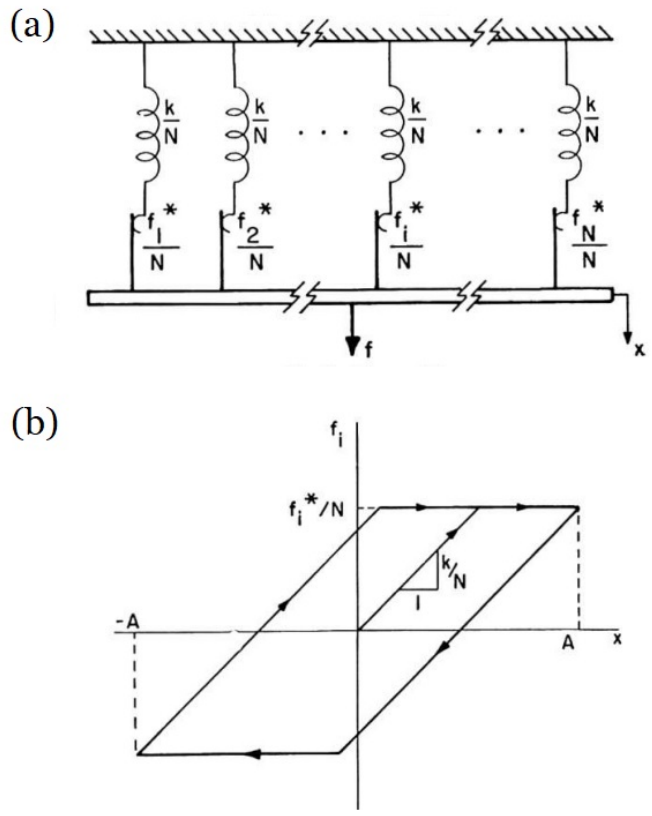

Figure 1.12: (a) Iwan's model is composed of a series of Jenkin's elements that can slip on the pulling driver (b) Elasto-plastic behavior of Jenkin's elements

In 1985, Karnopp proposed a new "stick-slip friction law" to avoid numerical difficulties involved in the sudden sign change in friction when the direction of motion changes [41]. The law assumes zero friction when the velocity is small enough. He investigated the dynamic response of two different mechanical systems which experience friction between their parts by using the *bond graph models* and *block diagrams*. Karnopp and his co-workers have published a book on system dynamics that explains the use of bond graph models and block diagrams in control engineering applications [42].

The bristle model [43], proposed in 1991, assumes surface asperities to be linear leaf springs that interact with the rigid slider (Figure 1.13). The model is used to simulate the friction force of a gimbal (a pivoted support that makes the fixation of an object on a rotating platform possible). The gimbal is acted upon by a *closed loop control system* that takes the gimbal angle as feedback and tries to enforce a commanded angle. Karnopp's stick-slip friction law is also found to be suitable in modeling the gimbal [43].

In 1995, a friction model was proposed [44] by the control community, which was later named LuGre. The term *LuGre* is generated by combining the first parts of the names of the academic institutes with which the authors of the paper were affiliated to: Lund Institute of Technology, in Sweden, and the Polytechnic of Grenoble, in France. The LuGre model is a heuristic model based on the bristle model. In a huris-

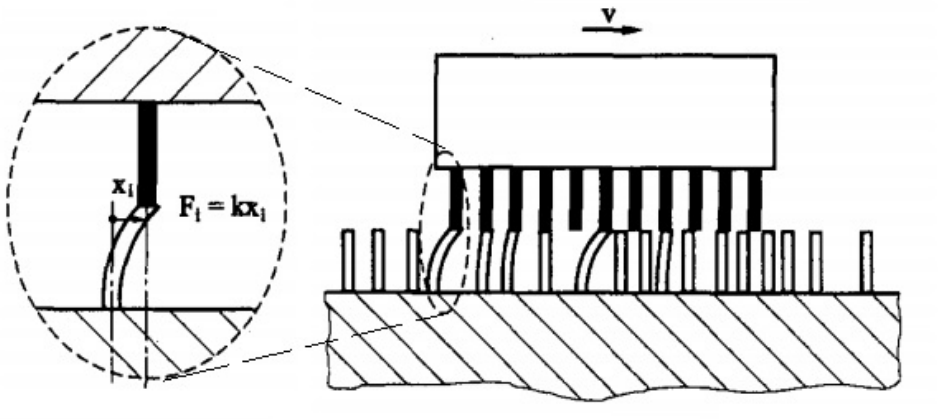

Figure 1.13: Bristle model [2]

tic manner, the model assumes a differential equation for the average deflection of the bristles, which is called the state equation. The friction force is then defined as a function of the state variable. This approach does not deal with the physics of asperity contacts, instead, it tries to guarantee generation of the observed phenomena of lubricated friction, such as Stribeck effect (weakening of friction with velocity) and viscous friction (strengthening of friction with velocity) into the equations (definitions) from the very beginning. A sketch of this empirical velocity dependence of lubricated friction is shown in Figure 1.14. The LuGre model is used to study the dynamics of a block-spring system [45], to investigate the stability of a 1-DOF system with a spring and a damper [46–48], and to design an observer-based compensator for controlling a DC motor [49].

In 2000, a new model of friction was developed [51], which was later called Leuven model after the name of the Catholic University of Leuven, in Belgium. The authors criticize LuGre model and show that it is incapable of fitting a measured torque-angle curve of a robot properly. On the other hand, the Leuven model shows an excellent fit to the pre-sliding hysteresis of the same robotic joint. This success is attributed to the inclusion of a nonlocal memory. The nonlocal memory allows branching of the friction force depending on the whole set of the past extremum hysteresis forces rather than just the last extremum (the local memory). Like the LuGre model, the Leuven model is based on a nonlinear state equation and defines friction as a function of the state variable. Both LuGre and Leuven models are "bristle models".

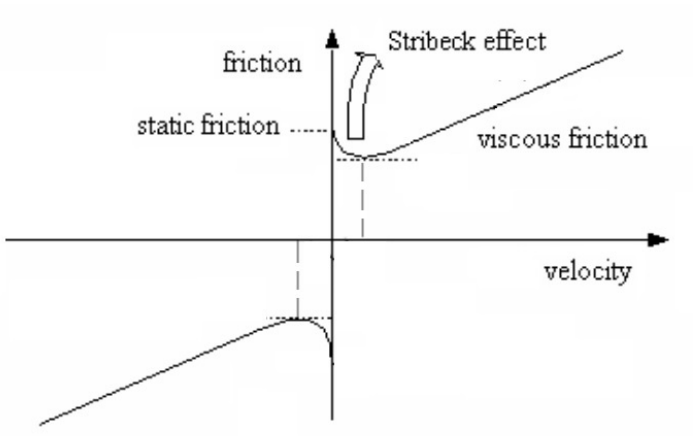

Figure 1.14: The empirical dependence of lubricated friction on velocity [50]

In [52], a set of independent block-spring units that are pulled by a driver on a flat surface (Figure 1.15) are used to model the hysteresis of a piezoelectric actuator. Each block-spring behaves as an elasto-plastic element, i.e., as in Figure 1.12-(b). The model is referred to as *Generalized Maxwell Slip* in accord with the name given in [53]. The normal loads and stiffness values are assigned such that the hysteresis of the piezoelectric actuator is reproduced by the superposition of the spring forces. The Maxwell-slip model (as it is called henceforth) is essentially the same as Iwan's model (compare Figure 1.15 with Figure 1.12).

Frictional (or friction-induced) hysteresis [54, 55] describes the *pre-sliding* (an opposed to *gross sliding*) behavior of frictional interfaces. The Maxwell-slip model is used in the control engineering literature as a tool for friction identification, e.g., for a milling table [56] and for a pneumatic artificial muscle [57]. In [58], a gearbox's friction-induced hysteresis is modeled using the Maxwell-slip, and LuGre models. In [59], along with methods such as neural networks, the Maxwell-slip model is used to reproduce a tribometer's experimental time series of position and force. One can obtain the force-position hysteresis by eliminating time from the position and force data. In [60], the Maxwell-slip model is implemented into the Leuven model to resolve a computational issue: stack overflow.

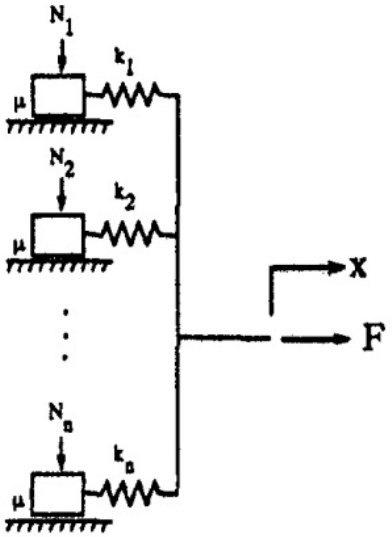

Figure 1.15: The Maxwell-slip model [52]

Alongside the heuristic models such as LuGre [44], there are also physically-based studies in the literature that incorporate surface roughness and asperity contact into the block-spring models. A class of physically-based studies mainly uses the GW model to characterize block-spring models for studying sliding friction (Subsection 3.1.2).

In [61], after providing a long list of friction models, it is claimed that none of them has been capable of simulating dynamic frictional phenomena like the Stribeck effect and friction lag (variation of friction with the excitation frequency). Then, a novel model is proposed with units composed of a single mass connected to the driver with pairs of vertical and horizontal springs and dampers. These elements are moved on a multi-asperity surface. The model is capable of reproducing a range of experimentally observed frictional phenomena qualitatively.

1.5 A spectrum of research fields

Surprisingly, friction is still a subject of extensive research. A schematic of some study fields involving *dry sliding friction* is presented in Figure 1.16. Some of the related applications and keywords are provided for each field of study. Tribology investigates friction, wear, and lubrication directly. A broad range of tribological applications in engineering and science has been investigated in the literature [23]. The field of research is so vast that many hybrid branches such as biotribology (tribology of orthopedic/dental implants) and nanotribology (tribology at nanoscale, e.g., in nanoelectromechanical systems, or NEMS) have emerged.

Fretting damage happens in the contacting bodies that undergo relative repetitive displacements, where the bodies move back and forth against each other [62]. Depending on the amount of normal force and the displacement amplitude, the damage may develop due to wear (fretting wear), cracking of the surface (fretting fatigue), or both (Figure 1.10). In [63] an energy-based criterion for fretting damage is obtained based on experimental results. Fretting damage occurs in many engineering applications, such as lug-bush connections and riveted strap joints, especially when the structure is subjected to high-frequency loading, e.g., in a helicopter fuselage or a gas turbine.

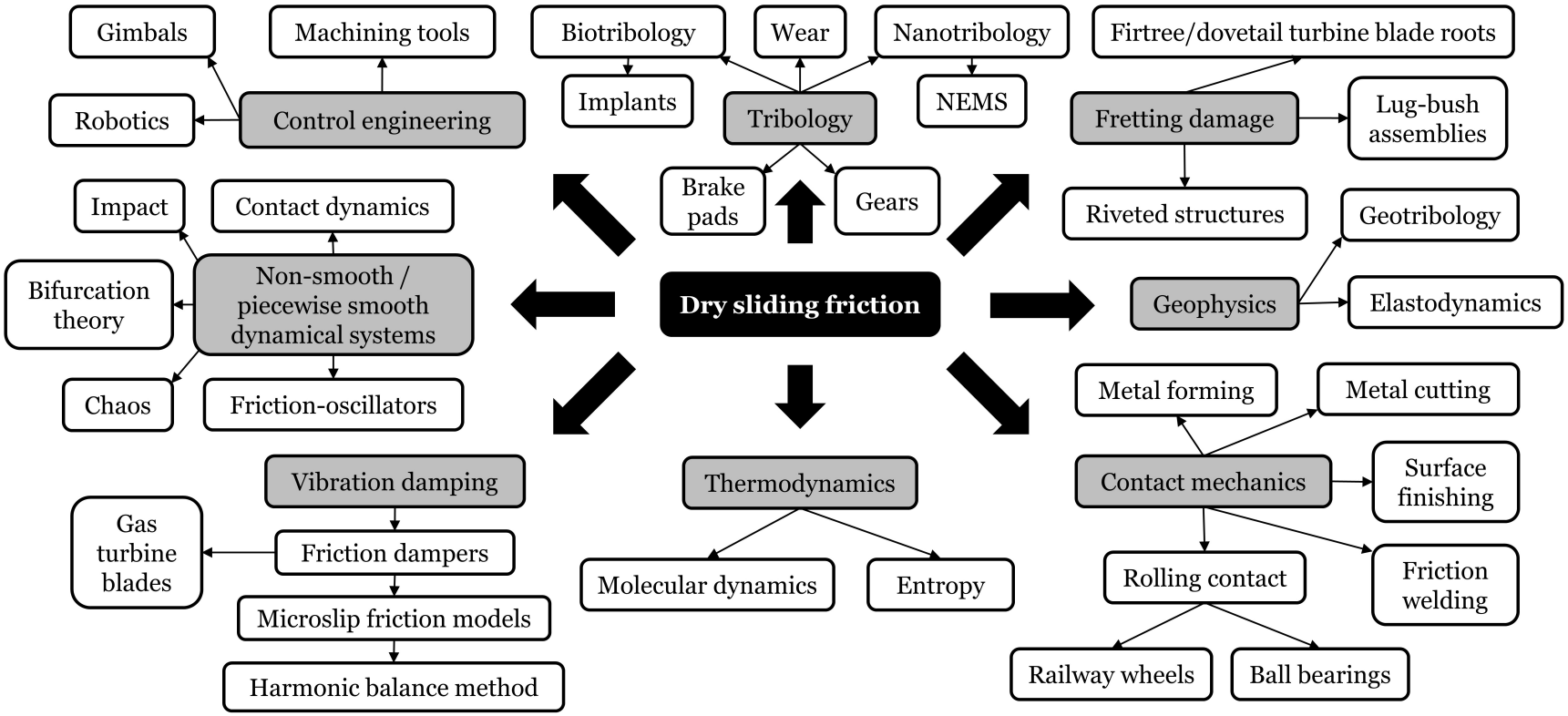

Figure 1.16: A schematic of some scientific and technological fields and applications that involve dry sliding friction

In some gas/steam turbines, the blades and the rotating disk are not manufactured as one piece. Instead, the blades are inserted into the disk slots (Figure 1.17). Two of the most famous blade-disk joints are called firtree and dovetail. These names are due to the shape of the tenon (the blade root). One of the aims of this kind of joint is frictional damping, i.e., dissipation of the blade vibrations via frictional contact between the blade root and the disk slot. In some cases, extra damping is provided by designing contact interfaces between the blade platforms and fixed dampers (Figure 1.18-(a)) or between the blade plateforms and underplatform frictional dampers (Figure 1.18-(b)). When the disc rotates, the dampers are pressed against blade platforms by centrifugal force.

Although the firtree/dovetail joints and dampers dissipate the vibration of the blades, they raise concerns about the stress concentration on the frictional contact areas, as the prospective locations of the fretting crack initiation (Figure 1.19-(a)). Surface finishing processes like metallic shot peening (MSP) and laser shock peening (LSP) have been used in the aerospace industry to improve the surface properties against fretting damage (Figure 1.19-(b)).

Both processes create a field of compressive residual stress on the surface, change the surface roughness and prolong the blade lifetime [65–67]. In [68], low plasticity

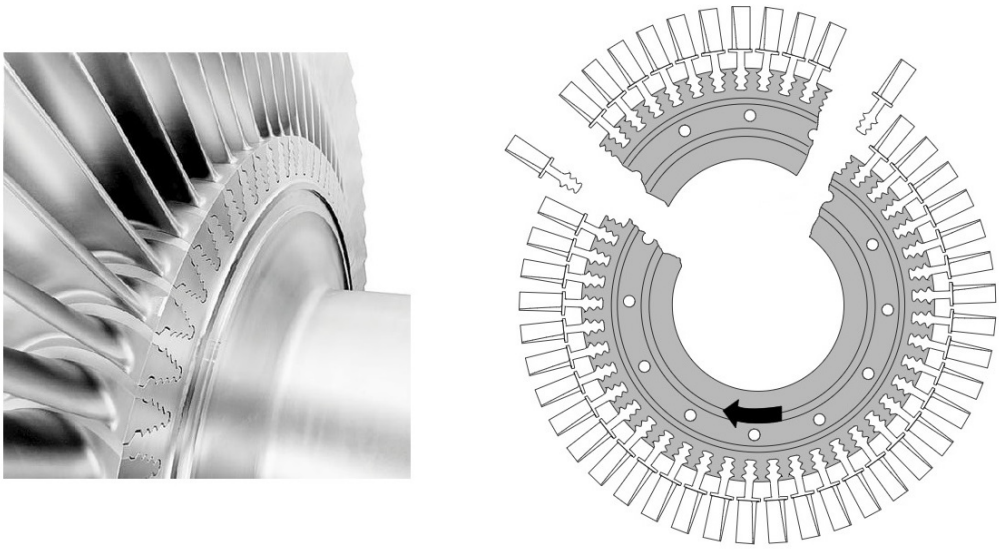

Figure 1.17: Blade-disc firtree joints (fixings) in turbines [64]

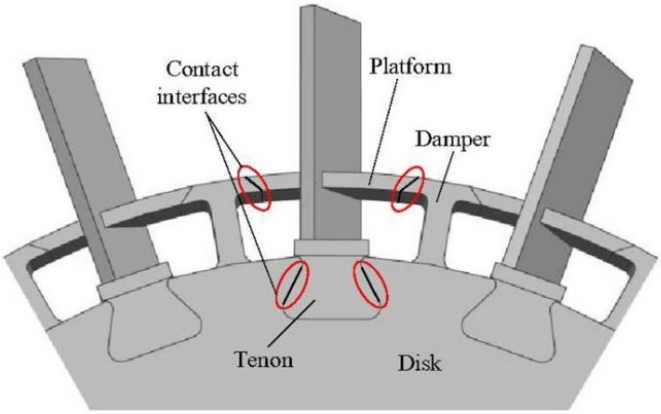

(a)

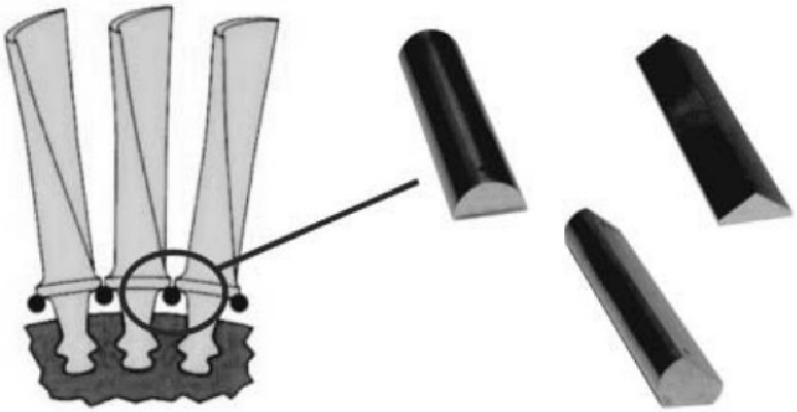

(b)

Figure 1.18: Different configurations of frictional damping in turbines: (a) Frictional interfaces between the blade platforms and T-shaped dampers, and between tenons (blade roots) and disc slots [69] (b) Underplatform frictional damping with symmetrical, unsymmetrical and wedge-shaped dampers [70]

burnishing (LPB) process is investigated as an alternative to the conventional shot peening on a dovetail specimen. Although LBP leads to the formation of a nearly-polished (low-roughness) surface, it does not raise adhesion to the extent that the fretting fatigue life is deteriorated [68].

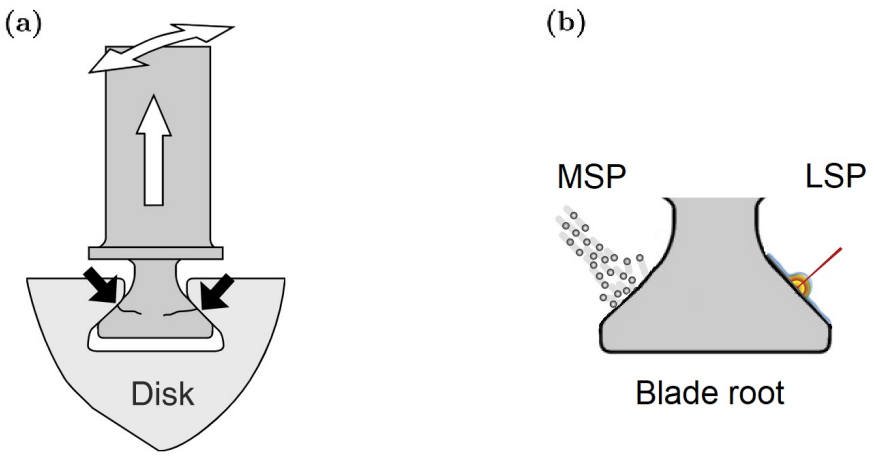

Figure 1.19: (a) Fretting damage of a dovetail blade root under cyclic loading [64], (b) Metallic shot peening (MSP) and laser shock peening (LSP) treatments on the blade root contact surface [66]

In an extensive wiki titled *Aeroengine Safety* [64], Axel Rossmann provides a rich source of illustrations, explanations, and information about different aspects of jet engine mechanics. The reader may find chapters 6 (on fretting damage), 12 (on material behavior), and 16 (on surface finishing) *of the wiki* highly informative.

The geophysics community is interested in the behavior of the geological faults in two major aspects: (i) the earthquake statistics and (ii) the dynamics of the fault rupture. Modeling these aspects needs a proper friction model. Sliding friction of the tectonic plates against each other is studied by elastodynamic analysis [71–73] and also experimental and numerical approaches [74, 75]. Geoscientists have started to notice the similarities between geoscience and tribology. The term *Geotribology* is coined to encourage further scientific cooperation between the fields [76].

Contact mechanics is an enormously rich field of study that started with the development of the Hertzian theory in the nineteenth century. Johnson's *Contact Mechanics* book brings a wide range of approaches and solutions together [77]. Johnson's contributions to the field are summarized in [78]. A rich source of the analytical approaches based on the theory of elasticity can be found in Gladwell's treatise on contact mechanics [79]. Another valuable source of the theoretical approaches to elastic contact problems is published by Hills, Nowell, and Sackfield [80]. For details of

complex analysis and integral equation formulation of the contact problems, one may see [81]. Popov's books provide an encyclopedia of the available solutions [9, 82]. He co-published a book that explains the use of *dimentionality reduction method* for obtaining 3-D contact problem solutions from their available 2-D counterparts [83]. To attain the available analytical and numerical approaches to rolling contact (e.g. in railway-wheel contact and ball bearings) one may find [84] highly beneficial. In a paper published in 1961, Greenwood, Minshall, and Tabor, emphasize the role of hysteresis losses in the contacting viscoelastic bodies (losses within the bulk of the material) which undergo rolling and sliding friction [85].

Alongside these rich sources of analytical approaches, *continuum contact mechanics* is a well-developed theory [86–88] and forms the basis of *computational contact mechanics*. A comprehensive study of *dry sliding friction* [89] reviews a range of issues that includes: (i) observed frictional phenomena, (ii) continuum models and variational formulation of elastodynamics, and (iii) the computational procedures of FEM as well as the dynamic stability of a frictional slider. The finite element models of metal forming/cutting, surface finishing, and friction welding have been widely used in the literature and have successfully modeled the processes. Some recent developments in contact mechanics are addressed in a 2021 paper [90]. For example, the FFT-assisted boundary element method (BEM) [91] is referred to as a standard tool for contact simulations of real surfaces in research and industry [90].

Friction is an irreversible dissipative process and it seems that entropy can be a measure of friction. However, there is no direct way of measuring entropy. Therefore, using thermodynamic methods in tribology is still controversial. In [92], Nosonovsky claims that entropic methods have great potential in the design of new materials (e.g., self-lubricated or self-healing surfaces), MEMS, and green tribology. In [93], a thermodynamic approach rooted in the works of C. F. Gauss and J. W. Gibbs (in the nineteenth century) is applied to the problem of dry sliding friction. The approach is based on the concept of surface energy and considers the formation and disappearance of the real contact areas at the nanoscale. The obtained COF values are shown to agree with those obtained by an AFM.

The vibratory response of systems with frictional contact is investigated by using

two kinds of friction models [94]. In *macroslip friction models*, the contact region is modeled as a single contact point that either sticks or slips (Figure 1.20). In *microslip friction models*, the contact interface is modeled as a beam that can be partly sticking and partly slipping (Figure 1.21). Both models have been used to obtain the forced response of turbine blades which have friction dampers [94, 95]. The steady-state response is usually found by applying the harmonic balance method (HBM), which uses Fourier expansion method [96].

Consider the 1-DOF system on a frictional rolling belt that is shown in Figure 1.22. The block motion can turn into a chaotic stick-slip under certain conditions [97]. Friction oscillators are members of non-smooth (or piecewise-smooth) dynamical

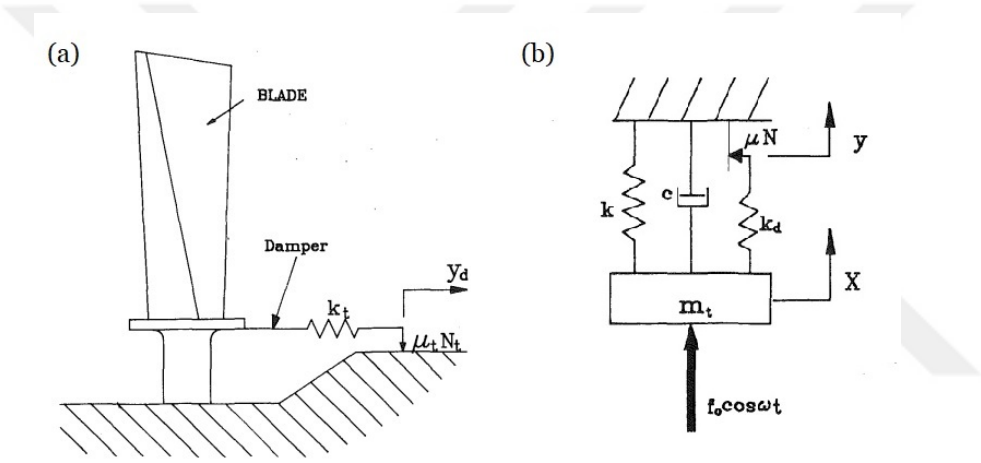

Figure 1.20: (a) Turbine blade with a friction damper (macroslip friction model), and (b) its equivalent 1-DOF vibration system with a frictional point contact [95]

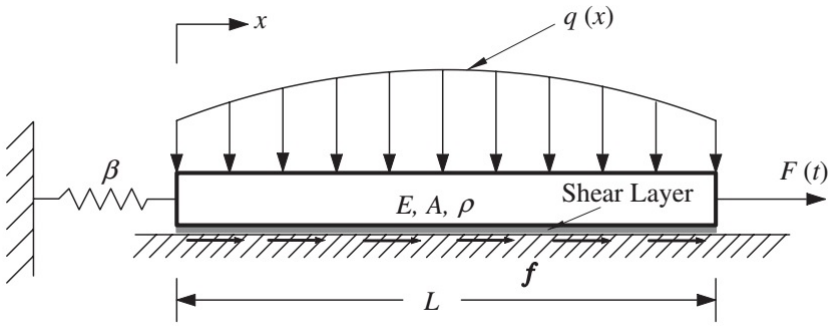

Figure 1.21: A 1-D microslip friction model with convex load distribution [94]

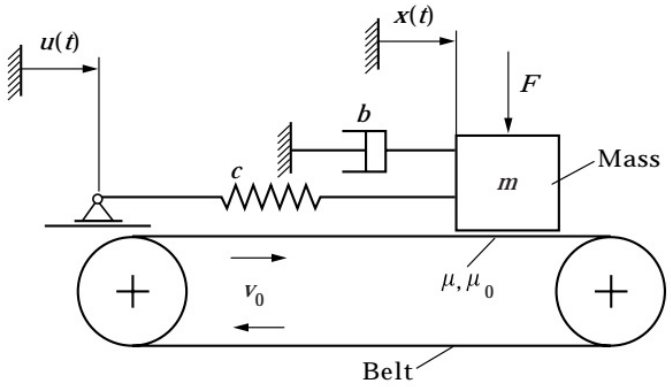

Figure 1.22: 1-DOF system moves on / with a frictional belt [97].

systems [98, 99]. The non-smoothness of these mechanical systems is mainly due to the stick-slip phenomenon, which is the source of discontinuity. These jumps and switches in the state of a frictional oscillator can make its behavior chaotic.

The points at which transition between the sticking and slipping states can occur are usually shown using bifurcation diagrams. The LuGre friction model [44] is used for the 1-DOF friction oscillator that is shown in Figure 1.22 [48]. The bifurcation diagram of the oscillator is shown in Figure 1.23. At low driver speeds, the maximum and minimum spring extensions are nearly the same, i.e., the block stays almost at the same position. By further increase in the driver velocity, the block starts to stick and slip in an orderly manner. At higher driver velocities, the stick-slip behavior becomes chaotic (aperiodic and irregular).

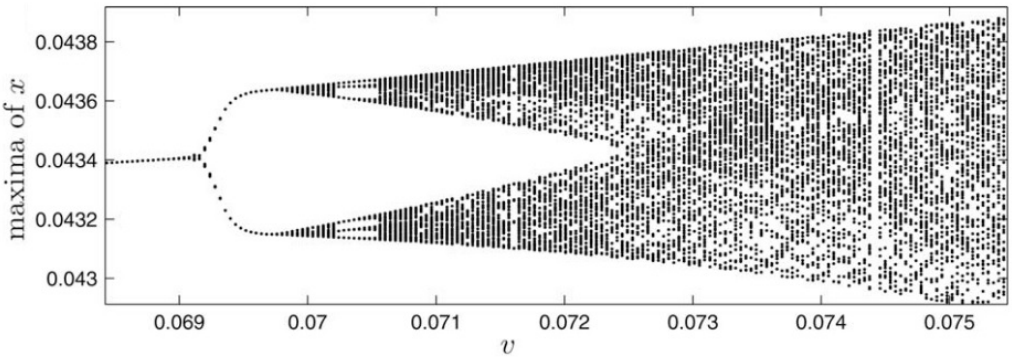

Figure 1.23: Bifurication diagram for the system that is shown in figure 1.22 [48]

High-frequency friction-induced vibration of the brake pad on the disc is called brake squeal [100]. Many researchers believe that the squeal (usually accompanied by brake noise) is due to the instability of the brake-disc vibration amplitudes (flutter). Linear stability analysis of some lumped-parameter models is performed in [100]. Friction-induced vibration of a pin-on-disc test rig and its frictional instability (squeal) is investigated theoretically and experimentally by Butlin and Woodhouse [101]. The stability of a block-spring system under the rate (velocity) and state (time) dependent friction law is studied by Ranjith and Rice [102]. Galvanetto conducted a series of studies on the dynamics and stability of frictional block-spring systems; for the dynamics of a 2-DOF block-spring system one may see [103]. In [104], he has proposed a computational approach to the nonlinear dynamics of the BK model is proposed.

Besides the friction oscillators, (frictional) impact [105] may produce problems that can be treated by the bifurcation theory [106]. The sketches of two of these systems are shown in Figure 1.24. Figure 1.24-(a) shows *the classical Painlevé problem*; the rigid rod motion becomes unpredictable after the impact with the rigid surface under Coulomb's friction law. Figure 1.24-(b) shows a two-link robotic manipulator that contacts a frictional belt; the tip of the link can stick, slip, fly and impact. In addition to these types of problems, non-smooth contact dynamics method has been applied to problems like deep drawing process, and frictional granular flow [107].

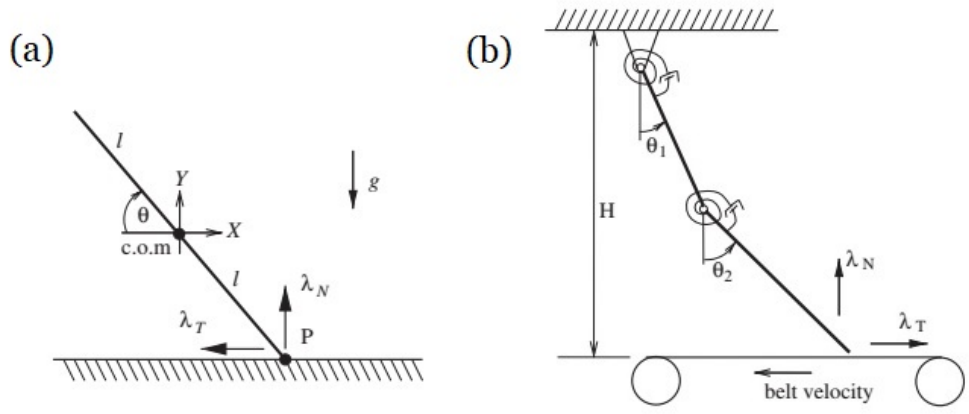

Figure 1.24: (a) A falling rod contacts a frictional surface (b) A two-link robotic manipulator contacts a frictional belt.

A fascinating book on the control of systems with friction and impact [108] brings together the theoretical methods involved in the analysis of the piecewise-smooth mechanical systems and the control engineering. For a broad overview of the approaches that are used in the control engineering to deal with the frictional systems one may find H. Olsson's doctorate thesis, *Control Systems with Friction (1996)*, quite useful [109]. In the thesis, the stability and control of frictional systems that are capable of undergoing unwanted oscillations (such as an inverted pendulum and a servo-mechanism) are investigated, and friction compensators (observer-based controllers) are designed. Furthermore, adaptive control and fuzzy logic can be combined to build an *adaptive fuzzy friction model* which extracts its rules from the measured data [110]. The model is used in controlling a 1-DOF robotic arm.

Friction as a multi-scale physical phenomenon is still subject to extensive scientific research. Sometimes the technological and computational advancements spark gold rushes. A good example is the molecular dynamics simulations of graphene flake. Graphene is an isolated single-layer hexagonal lattice of carbon atoms. The 2010 Nobel Prize in Physics was awarded to A. K. Geim and K. S. Novoselov for extracting graphene from a piece of graphite. Graphene has unique mechanical, thermal, electronic, and optical properties [111, 112]. Under certain conditions, the sliding of graphene flake produces an ultra-low friction force (superlubricity) [113]. These exceptional properties make the graphene a promising choice for use in the NEMS and MEMS [112, 113]. Many studies [112–116] have used spring models to simulate the sliding of a graphene flake (usually on a graphite substrate) as shown in Figure 1.25.

On the other end of the spectrum, in the study of earthquakes, the effect of friction is yet a matter of intensive research, especially with the discovery of long-lasting low-frequency seismic vibration (tremor) in a nonvolcanic region in southwest Japan [117]. The coincidence of the tremor (long duration trains of weak seismic signals) with slip data (from the GPS) was discovered in the Cascadia subduction zone [118], Canada's most active earthquake region (Figure 1.26). The phenomenon is called *Episodic Tremor and Slip (ETS)* and has made earth scientists focus on the involved physical processes [119]. Some closely related (but overlooked) phenomena are *low frequency earthquakes (LFE)* and *slow slip events (SSE)* [120–123].

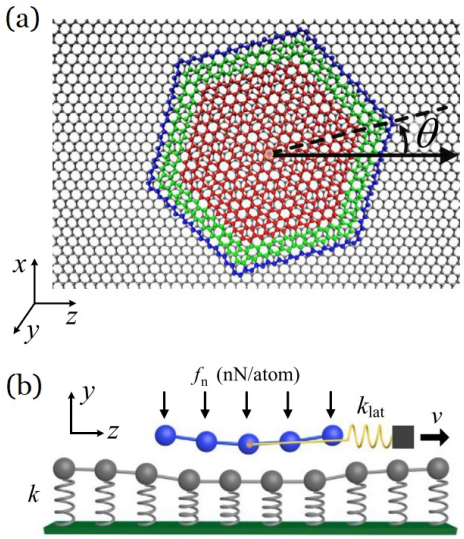

Figure 1.25: A graphene flake is moved on a graphene substrate [112].

The ETS occurs not only in the oceanic subduction zones worldwide, but also in strike-slip faults such as the San Andreas fault in California [124, 125]. The LFE and SSE are sometimes referred to as *slow earthquakes* [120]. In [126], the authors show that if the driving rate of the friction experiments is slowed down to the order of magnitude of oceanic subduction zone speed (centimeters per year), the SSEs can be generated in the laboratory. Machine learning techniques are used to relate acoustic emission of the "labquakes" to their frictional behavior [127, 128].

A fracture mechanics-based equation for rupture speed at a frictional interface is proposed in [129]. The equation can predict the speeds based on the normal stress and the interface properties. The analysis shows that below a critical (crack) length, supershear rupture is impossible. In [130], the existence of a critical length in an infinite elastic-rigid interface is investigated by using FEM. It is shown that the critical length has to be taken into account in the definition of an alternative (regularized) friction law.

Using block-spring models for studying friction is by no means an outdated approach. In a 2020 *Science* article [131], a block-spring model (Figure 1.27) is used to study the effect of elasticity and viscosity of the crust (or the mantle, namely asthenosphere [132]) on its Gutenberg–Richter (power/scaling) law [39]. In [133], the results of a 2-D BK model show that the static COF changes with the model stiffness.

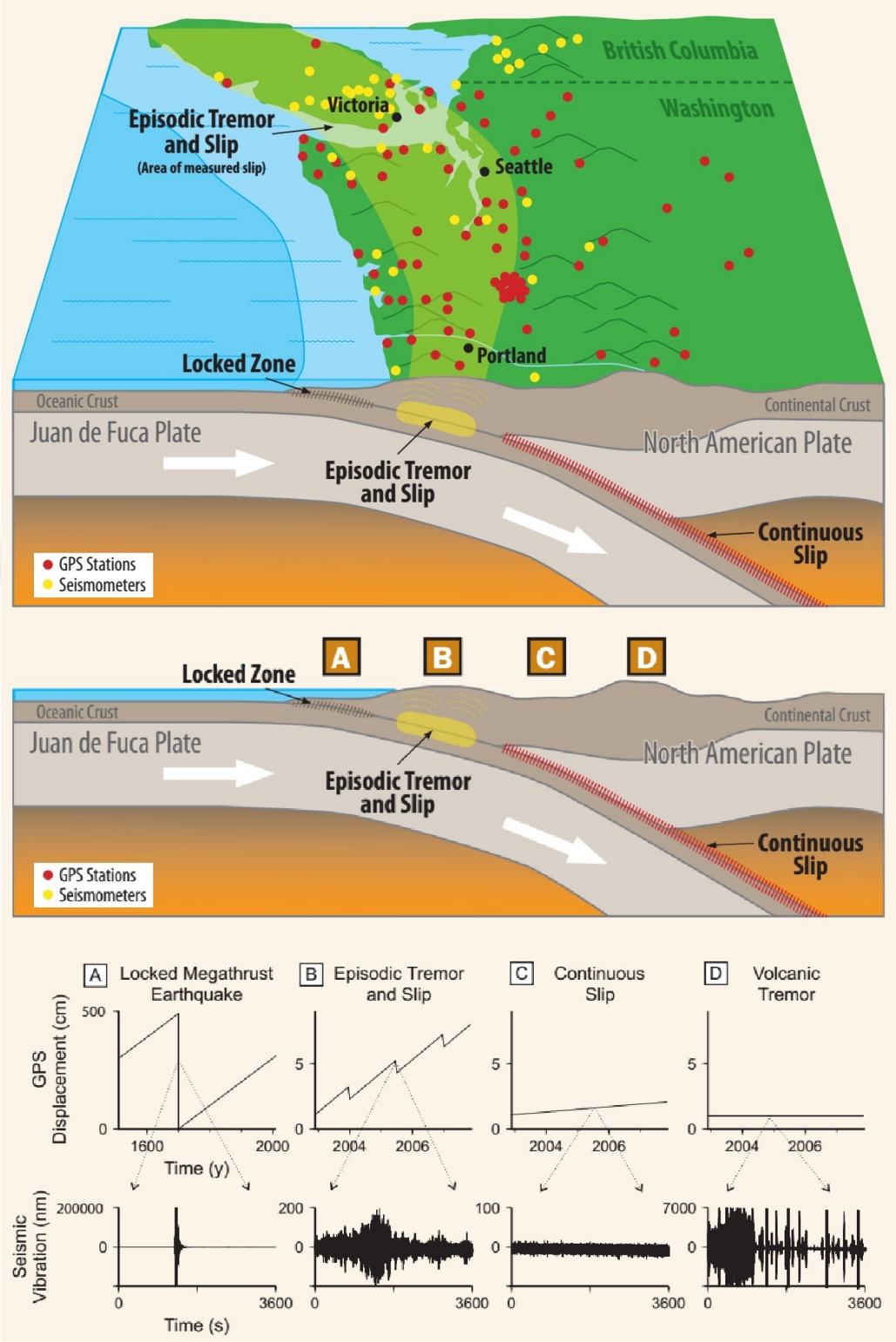

Figure 1.26: A map of the Cascadia subduction zone, its cutaway cross section and the seismic behavior of its parts [119].

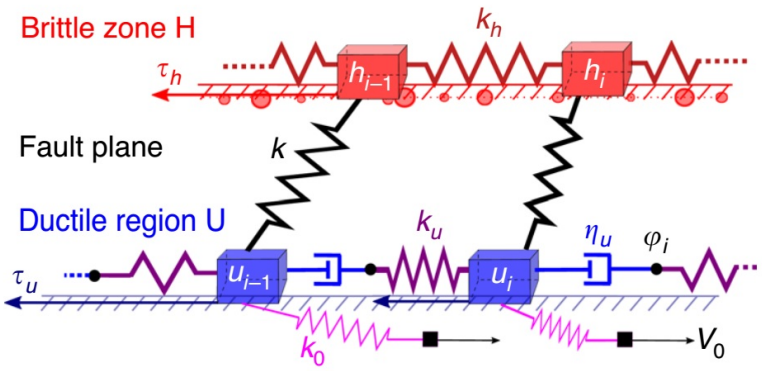

Figure 1.27: A geological fault plane is modeled as a block-spring model (brittle zone) which interacts with a viscoelastic model (ductile region) [131].

Friction force depends on various mechanical, physical, and chemical properties of the sliding surfaces. When insulating materials, e.g., polymeric materials move against each other (or against a metal [134]), charges of opposite polarity can develop an electrostatic attraction force which contributes to friction. Removing electric charge from the sliding polymeric materials such as PMMA and cellulose reduces the dynamic COF and wear significantly. Reducing tribocharging (or triboelectricity) is possible by different methods, such as rinsing the interface with a solvent, corona discharging, or grounding the sliding bodies with a conductive material [135].

What is the origin of macroscopic friction? This question is the title of a 2018 *Science* paper [136] where the molecular origin of friction is probed. The study uses simulations that are based on the density functional theory (DFT) and double-direct shear tests on mica sheets to show that a *quantitative* prediction of friction is possible despite the presence of wear particles. The *potential energy surfaces* of the sliding planes depend on the normal stress and can explain the experimentally observed macroscopic friction of mica.

1.6 Surface roughness and fractals

Two common parameters that are widely used to quantify the roughness of a surface are: average roughness, R_a, and the root mean square (RMS) roughness, R_q. The

average roughness is simply the average value of the sum of the *absolute* value of the heights. Firstly, the profile heights are measured with respect to an arbitrary reference. Also, the average height, μ, is calculated to specify the profile's mean line (or the center-line average, CLA). Note that this average height value contains no information about the profile since it depends on the choice of the reference. The average height value is now subtracted from the previously measured heights (with respect to the arbitrary reference). The result is the profile height with respect to the CLA. Now the *absolute value* of these "shifted" heights can be averaged to find R_a. The definition is concise:

$$R_a = \frac{1}{N} \sum_{i=1}^{N} |z - \mu| \tag{1.2}$$

where N is the number of the measured heights and μ is the average height with respect to an arbitrary reference and determines the position of CLA. The continuous version of the above definition is:

$$R_a = \frac{1}{L} \int_0^L |z - \mu| \, dx \tag{1.3}$$

where L is the length of the measured distance.

The other definition, i.e., RMS roughness, R_q, has an exact statistical meaning. It is the standard deviation of the heights about the CLA and is obtained by:

$$R_q = \sqrt{\frac{1}{N} \sum_{i=1}^{N} (z - \mu)^2} \tag{1.4}$$

where N is the number of measured heights and μ is the average height with respect to an arbitrary reference. The continuous version of the above definition is:

$$R_q = \sqrt{\frac{1}{L} \int_0^L (z - \mu)^2 \, dx} \tag{1.5}$$

where L is the length of the measured distance. Both R_a and R_q are measures of how

far the profile tends to deviate from its CLA (spread of the heights). If the height PDF is Gaussian, $R_q = 1.25R_a$ according to [1, 137].

In Figure 1.28 the profile of the same surface is measured with different methods, and each gives a different value for the standard deviation of the profile heights. Natural/metal surfaces are rough over several length scales. This feature makes fractal geometry the natural choice for the description of the surfaces. Fractal geometry can characterize the profile in a scale-independent manner, i.e., by its fractal dimension.

When people think of fractals, they usually think of shapes like a Sierpinski triangle (Figure 1.29-(a)), or its 3-D counterpart, a Sierpinski tetrahedron (Figure 1.29-(b)), or a visual representation of Mandelbrot set (Figure 1.29-(c)). Serpinsky triangle is an exactly self-similar fractal; any smaller part of the triangle, when scaled up,

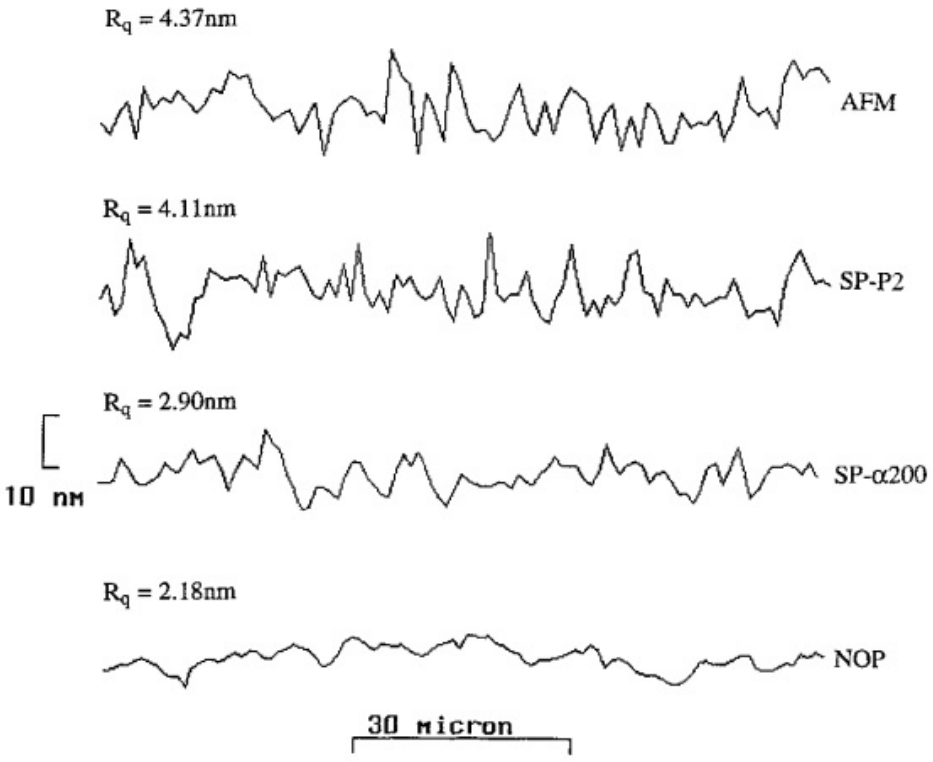

Figure 1.28: The same profile is measured by using an atomic force microscope (AFM), stylus profilers (SP) of different resolutions (stylus tip radii) and a noncontact optical profiler (NOP). Each instrument has a different resolution and provides a different surface RMS roughness.

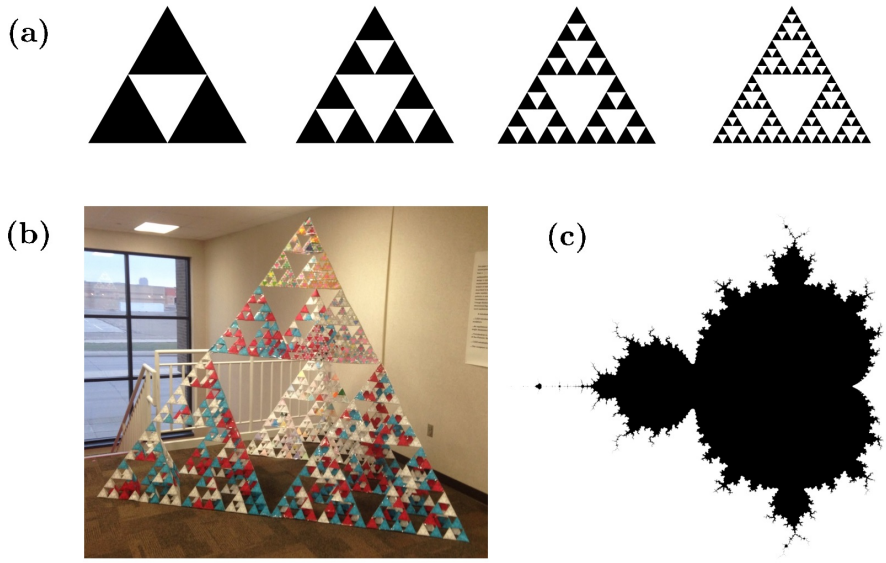

Figure 1.29: Some of the popular *exactly* self-similar fractals: (a) Sierpinski triangle (b) Sierpinski tetrahedron and (c) Mandelbrot set on a complex plane

represents a bigger part *exactly*. The rightmost triangle in Figure 1.29-(a) can be constructed from a re-scaled version of any of the other shown Sierpinski triangles. There are animations that show when a particular region of the Mandelbrot set's graphical representation is zoomed in, similar patterns appear again and again.

However, the fractal geometries encountered in nature are only self-similar in a *statistical* (and not *exact*) sense. A well-known example of statistically self-similar fractals is the seacoast of Britain. The small-scale map of a coastline would look similar (but not exactly similar) to its large-scale map. In his groundbreaking study: *How Long Is the Coast of Britain?* with the second title: *Statistical Self-Similarity and Fractional Dimension*, Mandelbrot showed [19] that the length of different seacoasts around the world, when measured with increased precision (smaller "rulers"), depends on the size of the ruler. In other words, the length is resolution- (or scale-) dependent. The smaller the ruler (yardstick) becomes the longer the measured length of the coastline will be (Figure 1.30). The reason is that when a part of the coastline is zoomed (or scaled up), a statistically similar image of the whole appears which contains more details. The log-log plot of the measured seacoast length against the ruler size is a straight line. The slope of this line is called the fractal dimension of the coastline.

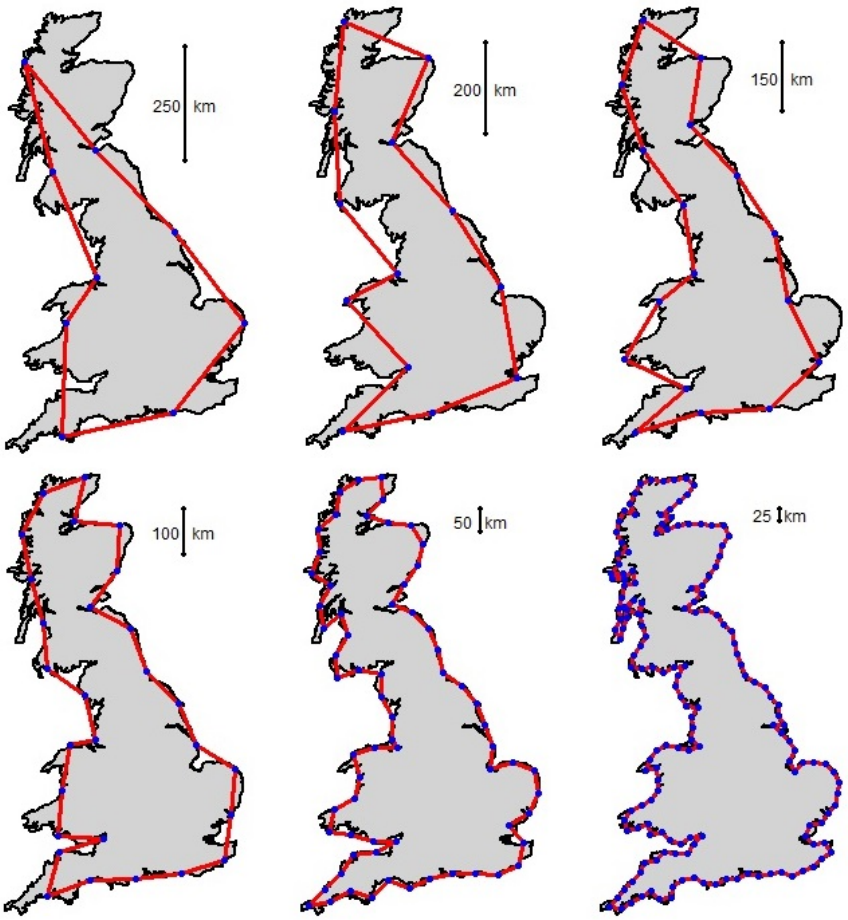

Figure 1.30: The coast of Britain is a *statistically* self-similar fractal and using finer rulers (yardsticks) to measure its length increases the measured length [138].

One should note that a rough terrain or a metal surface are *not* self-similar fractals. When watched on the ground, the landscape height distribution does not seem to statistically represent (or look *similar* to) a widely held view of the same landscape from a helicopter. The self-similarity of a natural landscape can be only present over a finite range of length scales; however, there is an essential difference between the fractal nature of a coastline (a self-similar fractal) and mountainous terrain.

When it is said that a surface is a self-affine fractal, it means that the surface would not remain statistically invariant (would not look *similar*) under an equal magnification (uniform scaling) of the dimensions. To keep a self-affine fractal statistically invariant, the magnification has to be carried out in a specific unequal (non-uniform) manner in different directions. The proper scaling factor of the ordinates has to be

different from that of the abscissas to obtain a similar look. The proper scaling factors are determined by the fractal dimension of the profile. Self-affine fractals have been widely used in the simulation and characterization of rough surfaces [20, 139–141] and their contact [7, 142–147].

Figure 1.31 shows a numerically generated fBm with $H = 0.75$. A fBm is a self-affine fractal. In other words, the generated profile, $X(t)$, preserves its statistical characteristics, e.g., its standard deviation, if transformed according to the following rule: $\lambda^{-H}X(\lambda t)$. For the time being, consider the first ten points as $X(t)$. The process $X(\lambda t)$ is shown with the black-filled markers in the figure for $\lambda = 10$. The ordinates of this set of points, which is more scattered compared to the first ten points, if multiplied with $\lambda^{-H} = 10^{-0.75} = 0.18$, will have a standard deviation that is almost the same as that of $X(t)$, i.e., the set of points from $t = 1$ to $t = 10$.

This rule holds for any value of λ and any part of the process. Suppose one selects points of a self-affine random process apart from each other by a factor of λ. In that case, one has to re-scale the ordinates of the selected points by a factor of λ^{-H} in order to obtain a set that preserves the statistical character of the original random process. This property of the self-affine fractals is explained in detail in Appendix A.

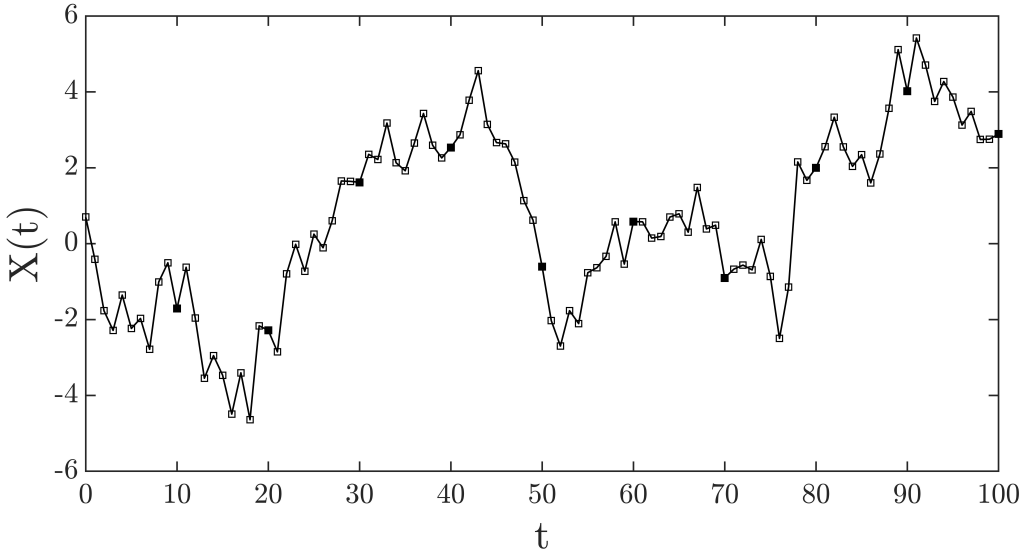

Figure 1.31: Self-affinity of a fractal profile, a fBm with a Hurst exponent equal to 0.75, that is generated numerically

A schematic of the fractal categories is shown in Figure 1.32. The statistically self-similar and statistically self-affine fractals are sometimes called *random fractals* [20, 148] in order to distinguish them from the geometries that are fractal in the exact sense (Figure 1.29).

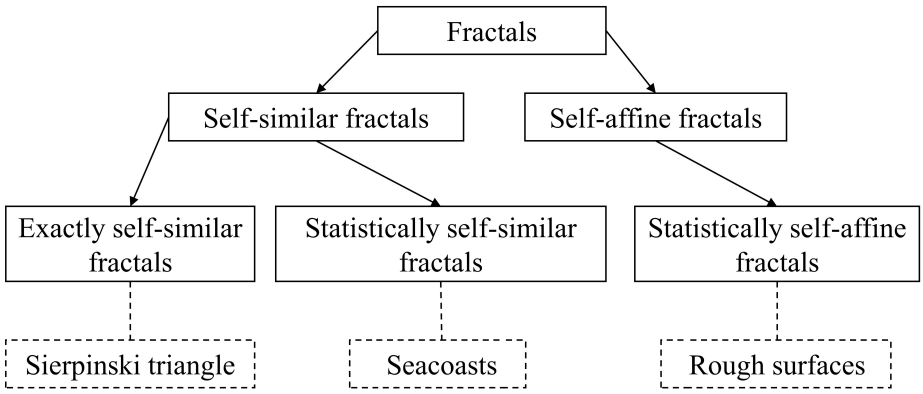

Figure 1.32: Categorization of the fractals to self-similar and self-affine

1.7 Contributions

The dry sliding friction of a rough elastic surface on a rigid flat substrate is simulated by using two different block-spring models: the Maxwell-slip model and the Burridge-Knopoff model. The objective is to investigate the effect of (i) deformation at the interface and (ii) the surface geometry on the frictional behavior under different compression values. Two probabilistic models are used to characterize the Maxwell-slip model: Nayak's PDFs and a fractal model generated by the midpoint displacement method. The frictional behavior of the BK model with linear initial lateral force distribution is studied. For all models, the relation between the frictional behavior and slipping at the interface is investigated.

The first contribution of this thesis is to use three different approaches to incorporate geometrical characteristics of the surface into the Maxwell-slip model. The approaches consist of using:

- Initial spring extensions which are generated with the beta PDF (Chapter 2)

- Asperity heights and curvatures which are generated by using Nayak's PDFs (Chapter 3)
- Asperity heights and curvatures which are obtained from a numerically generated self-affine fractal surface (Chapter 4)

to characterize the Maxwell-slip model. The effects of the surface geometry on the friction force are then studied. The above approaches neglect the inertial force of the block-spring units. The block slippages are assumed to occur in no time. In other words, asperity-based (the micro-scale level) characterization of the Maxwell-slip model is followed by applying a quasi-static assessment of the block-spring dynamics.

The second contribution of the present thesis is to investigate the effect of the inertial force in:

- The Maxwell-slip model (Chapter 5)
- The Burridge-Knopoff model (Chapter 6)

on the friction force and the frictional interface behavior. According to the results, different regimes of frictional sliding (stick-slip and steady sliding) are accompanied by different modes of interfacial behavior (crack-like and pulse-like). Chapters 5 and 6 deal with the sliding of the macro-level continuum in contrast to Chapters 2, 3, and 4.

1.8 The outline of the thesis

In Chapter 1, a brief account of the history of tribology is given. A series of developments in the knowledge of friction that are contributed by the geophysics and control engineering communities is also addressed. The extent of the research fields that face friction one way or the other is explored. A section is devoted to self-affine fractals as a modern mathematical tool that has been successfully used to characterize rough surfaces. The content and contributions of the thesis are stated.

Chapter 2 attempts to model the effect of roughness on the frictional behavior of sliding surfaces by using an indirect, and reductionist approach. The approach assumes that the surface asperities can be modeled as block-spring units with the same stiffness and normal load. The equation of motion for sliding of a single block-spring is solved. The initial lateral extensions of the springs are assumed to be random variables. These values are generated by the beta PDF. An analogy is made between the initial lateral extensions and the surface roughness. The driver is moved horizontally, and the superposition of the spring forces determines the variation of the overall friction for different the beta PDF shape parameters.

In Chapter 3, the heights and the tip curvatures of the asperities are random variables. These random variables are generated by using Nayak's PDFs. The PDFs are derived based on the random process theory and correlate the heights and curvatures by a joint PDF. The standard deviation of the surface heights, slopes, and curvatures are brought together in a single parameter, namely Nayak parameter, and fully specify the PDFs. The set of generated asperities (a set of pairs of asperity height and asperity tip curvature) represents a rigid rough surface and is pressed against an elastic half-space. The real contact area and the normal load of each asperity are calculated by using Hertzian contact formulas. The total contact area and normal load are obtained simply by summing up the asperity contributions. The results are verified with the available analytical solutions. The normal load and tangential stiffness values of the asperities are then transferred to the block-spring units of the Maxwell-slip model and the driver is moved horizontally. The friction and traction forces and the block slippage history are recorded as the driver moves. The results are shown for two Nayak parameters and three compression values. The histograms of the asperity loads, stiffnesses and compressions are provided in each case. In this approach, the spatial data of the asperities, i.e., the coordinates of the asperities on the surface, is absent.

In Chapter 4, a self-affine fractal surface is generated numerically by using the midpoint displacement method. Two numerical schemes to calculate the second spectral moment of the surface (variance of the surface slopes) are introduced. The asperity heights and curvatures are extracted from the generated surface by using two different schemes: (i) fitting paraboloids to the summits (ii) calculating the geometric mean radius by using the finite difference approximation of the derivatives at the summit.

The set of rigid asperities is pressed against an elastic half-space as the compression increases. The results include (i) the normal contact phase in which the real contact area variation with the normal load is checked against the available analytic solution and the histogram of parameters such as asperity load and stiffness are provided and (ii) the sliding phase in which the variation of friction with the movement of the driver is plotted together with the block slippage history. The second procedure is actually the same as that of Chapter 3, i.e., the Maxwell-slip units are characterized by the obtained load and stiffness values. The results are provided for two case studies with different Hurst exponents but the same standard deviation.

In Chapter 5, the Maxwell-slip model is used to study the effect of the inertial forces of the blocks on the friction force and the slip at the interface. The different initial spring extensions are assumed to be linearly distributed. The equation of motion of a single block-spring is solved in to find the duration of the slippage. The results include five case studies with different maximum block positions and driver velocities.

In Chapter 6, the Burridge-Knopoff model is used to investigate the variation of force and the corresponding slip on the interface. The boundary condition of the model can be either free or periodic. The case studies have free boundary conditions. The system of differential equations of motion is reduced to an algebraic system of equations. The algorithm of the method is explained by a pseudocode and a flowchart. Analytical expressions for the exact stopping time and position of a previously sliding block are derived. Inserting a time-dependent static COF into the algorithm is possible. The results include two case studies, both assuming a linear initial tangential force distribution. The variation of friction with the evolution of the slip events at the interface is presented in detail.

In Chapter 7, a qualitative comparison is made among the generated result of the methods applied in Chapters 2-6. The assumptions and limitations of the applied methods are reviewed and the possibility of establishing a quantitative relation among the results, specifically between the results of Chapters 3 and 4, is discussed.

To summarize, Chapter 1 contains a brief account of the context of the thesis and the extent of the ongoing research on dry sliding friction. In Chapter 2, the initial extension of the springs is a random variable and the normal load and stiffness are

assumed the same for the Maxwell-slip model units. In Chapters 3, and 4, the effect of surface geometry on sliding friction is investigated using the Maxwell-slip model. The initial extension of the springs is assumed zero, and the inertial force is neglected. In Chapters 5 and 6, the effect of the inertial force and initial spring extensions on the sliding friction and interfacial slip is investigated using the Maxwell-slip model and the Burridge-Knopoff model. Chapter 7 concludes the thesis by comparing the obtained results.

CHAPTER 2

QUASI-STATIC MAXWELL-SLIP MODEL WITH RANDOM INITIAL SPRING EXTENSIONS

The Maxwell-slip model consists of independent mass-spring units that are slipped by a driver over a rigid, flat, fixed substrate. In this chapter, the model is interpreted as a multi-asperity model and is used to study both the friction force and the mechanisms involved in the sliding of a rough elastic surface. Coulomb friction law is assumed at the single mass-spring level. A beta probability distribution function is used to generate the initial block positions randomly. The standard deviation of the initial lateral position of the blocks is interpreted as the surface roughness. The results show that when the surface is rough enough, the sequential slip of the blocks induces a steady friction force. On the other hand, when the surface is smooth enough, the collective slip of the blocks induces stick-slip. The border between the two regimes of sliding is sharply delineated by a specific roughness value. A tribological implication is that a sufficiently rough surface may bring about steady sliding. A geophysical implication is that a geological fault segment that undergoes aseismic creep may have a rougher surface compared to its locked counterpart.

2.1 Introduction

Friction is ubiquitous in engineering applications and nature; sometimes desirable, e.g., when a driver slams on the brakes, and sometimes disastrous, e.g., when an earthquake occurs. The role of friction in brake dynamics has been investigated by engineers especially because of the possibility of friction-induced oscillations or stick-slip [149]. Such fluctuations in the frictional force can degrade the brake function

and cause brake noise [100]. Preventing stick-slip is also an issue in the control engineering applications, e.g., when precise *motion control* of engineering systems such as robotic manipulators [150], machining tools [56], nanopositioning stages [151] and pneumatic artificial muscles [57] is required. Moreover, geological faults (as frictional interfaces) may undergo stick-slip. The notion of fault stick-slip as a mechanism for earthquakes [37, 152] dates back to Reid's elastic rebound theory that was proposed after the great 1906 San Francisco earthquake [153]. During the *sticking* period, elastic energy is accumulated in the earth's crust along the fault due to deformation. Subsequently, *slipping* causes the release of the stored energy in the form of elastic waves, i.e., the occurrence of an earthquake. However, not all of the fault segments do stick-slip; some of them undergo creep, i.e., slide steadily. A list of some of the well-documented creeping faults is tabulated in [154].

The above-mentioned regimes of frictional sliding, i.e., stick-slip and steady sliding, have been observed in friction tests. In stick-slip regime, friction force successively increases and decreases. Examples of stick-slip can be found e.g., in [155] for brake pads, in [156] for a pair of PMMA specimens, and in [157] for a gold-plated copper slider that moves on a hoop apparatus. On the other hand, in steady sliding regime, the friction force reaches the dynamic friction plateau and becomes steady. Examples of steady sliding can be found in [158] for a rotary apparatus that shears rock specimens, and in [159] for a spherical glass lens that slides on a flat elastomeric surface and again in [157].

The geophysics and engineering communities have separately developed mass-spring models to tackle the problems that involve frictional interface dynamics. Geophysicists have preferred Burridge-Knopoff (BK) model [38] for investigation of the geological fault dynamics and statistics of the earthquakes [160–165]. As shown in Figure 2.1-(a), the BK model has a rigid driver that is connected to a set of blocks with a leaf spring for each of the blocks; each successive pair of blocks is connected by a coil spring. The driver moves horizontally and causes slippage of the blocks on a rigid, flat substrate [38]. On the other hand, engineers have preferred the Maxwell-slip model to the BK model. The Maxwell-slip model is an uncoupled version of the BK model as shown in Figure 2.1-(b). The Maxwell-slip model has been repeatedly used in control engineering literature to provide a friction model to design

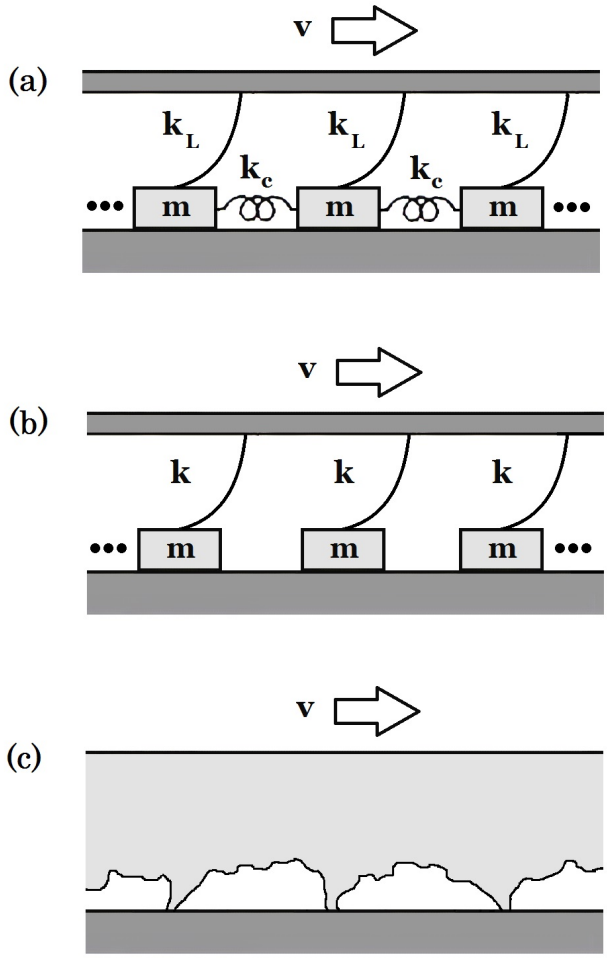

Figure 2.1: (a) The Burridge-Knopoff model (b) The Maxwell-slip model (c) A rough surface contacts a rigid flat via asperities

friction compensators [56, 57, 151, 166–168]. Kligerman and Varenberg [169] used a Maxwell-slip model with massless blocks to study frictional sliding. The model showed that stick-slip regime can be changed to steady sliding regime by increasing the number of the blocks.

Real interfaces are composed of a collection of unconnected contacts [170] (or discrete contact spots [171]) due to the presence of surface asperities as shown in Figure 2.1-(c). A wide range of statistical parameters including the standard deviation and mean value of the surface asperity height distribution can be used as a measure of roughness for metallic and rock surfaces [155, 158, 171]. The lower the standard de-

viation and the mean value, the smoother is the surface [155, 158]. The roughness of the metallic surfaces is traditionally controlled by mechanical surface finishing processes like grinding and polishing [172].

It should point out that the Maxwell-slip and BK models have only tangential stiffness. In other words, the normal stiffness is absent. Consequently, the models have been barely used to study normal contact. In the present approach, the standard deviation of the random distribution of initial *lateral* positions of the blocks is interpreted as the surface roughness, i.e., a measure of asperity height distribution (which is a normal stiffness property). This interpretation provides the opportunity for investigating the effect of surface roughness on the frictional behavior by using the Maxwell-slip model. The details of our interpretation are provided in Subsection 2.3.

In the present approach, a the result of a quasi-static analysis of block motion is applied to the Maxwell-slip model. The model simulates the friction of a rough elastic body that slides on a rigid substrate. The term “quasi-static" indicates that the approach does not take the inertial force of the blocks into account (although the blocks possess mass).

The main suggestion of our results is that while a smooth-enough surface causes collective slip of the asperity tips and gives rise to stick-slip; while, a rough-enough surface prompts sequential slip of the asperity tips and leads to steady sliding. These sliding regimes are sharply delineated by a critical surface roughness value as shown in Section 2.3. The results have fundamental implications in both tribology and geophysics and are discussed in detail in Section 2.4.

2.2 Method

In Subsection 2.2.1, our approach to the Maxwell-slip model for studying frictional sliding is explained and pseudocode of the approach is provided. Subsection 2.2.2 provides four analytical constraints on the maximum size of the time step. In Section 2.2.3, an analogy is drawn between the initial block positions and surface roughness. The analogy is of the utmost importance for making physical interpretations based on the results.

2.2.1 The proposed approach to the Maxwell-slip model

In this subsection, the algorithm of our proposed approach to the Maxwell-slip model is described. The model is composed of a set of independent mass-blocks each attached to a rigid driver via a "leaf spring" (Figure 2-(a)). The driver moves horizontally and triggers slippage of the mass-blocks over a rigid substrate. Each mass-spring unit can be interpreted as an idealized surface asperity which is a cuboid with the length L, width W and height H. Mass of the cuboid is lumped into the block. The leaf spring stiffness, k, is obtained from $k = GLW/H$ where G is the shear modulus of the elastic body. The normal force applied on each block is calculated by $N_b = pLW$, where p is the normal pressure applied on the top of each cuboid. When due to the motion of the driver the spring force exerted on the block exceeds the frictional threshold, $f_{th} = \mu_s N_b$, the block slides forward. According to Coulomb's law of friction, a constant dynamic friction $f_d = \mu_d N_b$, is assumed to act on the block during sliding.

The question is how much traction force, T, should be applied to the driver to move it at a constant velocity? The driver is assumed fixed during the block slippage. Besides, the block is assumed to be transferred to its destination in no time. Consequently, inertial force and variation of the spring force *during* the slippage are ignored. Therefore, the magnitude of the driver traction force is equal to the magnitude of the friction force exerted on the blocks by the substrate. The approach is then called *quasi-static*. The uncoupled character of the Maxwell-slip model makes the approach considerably simple compared to the analogous approach to the BK model [161, 162].

It is found out that the initial position of the blocks has a significant effect on the frictional behavior of the Maxwell-slip model. Thus, the initial block positions are specified by using a probability distribution function. In Subsection 2.2.3, further details about the use of the probability distribution function are explained.

Two different position reference coordinates are used. Position reference 1, shown in Figure 2.2-(a), is just used to derive an analytical expression for the slippage distance of the block. Position reference 1 is fixed to the substrate at the point below the block before its first slippage. Position reference 2, shown in 2.2-(b), is used to assign the

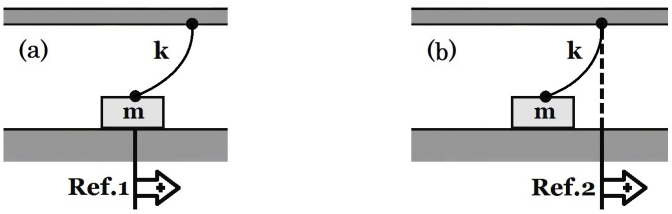

Figure 2.2: Two types of block position references (a) beneath the stuck block (b) beneath the spring-driver attachment point

initial position of the blocks, measure later evolution of the block positions, and also the driver position. Position reference 2 is right below each block's spring-driver attachment point before the driver starts to move, i.e. at $t = 0$. The position of each block is monitored with respect to its exclusive (local) reference 2. Note that the position of the driver in reference coordinate 2 is the same for all of the blocks.

It is assumed that the driver triggers the block slippage, immediately becomes fixed at x_d, and remains there during the slippage of the block. The differential Equation of motion (EOM) for the block in Figure 2.2-(a) with respect to position reference 1 is:

$$m\ddot{x} = f_{spring} - f_d = k(x_d - x) - f_d \tag{2.1}$$

where the initial conditions are $x(0) = 0$ and $\dot{x}(0) = 0$. The sliding time interval can be obtained by solving the EOM and equating the block velocity function to zero. Substituting the answer back into the solution, i.e., $x(t)$, gives an analytical expression for the block slippage distance:

$$\delta x_b = 2\frac{\mu_s - \mu_d}{k} N_b \tag{2.2}$$

The above relation shows that the mass-block would stick-slip under Coulomb friction law. The force-drop in the spring due to exceeding the friction threshold can be obtained from Equation (2.2) as:

$$\delta f = k\delta x_b = 2(\mu_s - \mu_d)N_b \tag{2.3}$$

The force-drop is independent of the spring stiffness. The destination force (as shown graphically in Figure 2.3) is:

$$f_{th} - \delta f = \mu_s N - \delta f = (2\mu_d - \mu_s)N_b \tag{2.4}$$

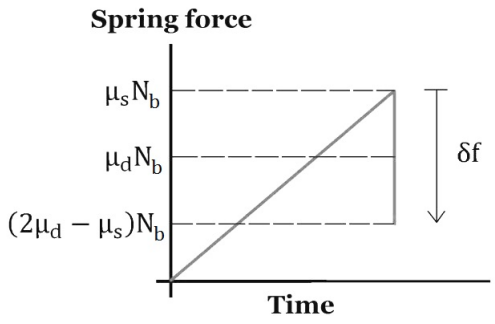

Figure 2.3: The single block force-drop for the mass-spring unit

The above relation is in agreement with [173]. As shown in Figure 2.3, the dynamic friction value is the midpoint between the frictional threshold and the destination force. The other important aspect is that the destination force can be negative if $\mu_d < \mu_s/2$. The negative value indicates that the block has passed the spring-driver attaching point. The above conditional inequality is mentioned in [174], where friction force direction reversal is discussed.

Henceforth, only position reference 2 is used. If the driver moves with a constant velocity, v, the spring force on the ith block is:

$$f_i = k(vt - x_i) \tag{2.5}$$

The sign convention of the position references is positive to the right. As the driver moves, a moment arrives at which the spring force exceeds the static friction threshold, i.e., $f_{th} < f_i$. Then, the block slides forward by δx_b according to Equation (2.2). In each time step, the blocks which exceed the frictional threshold are moved forward. The position of the rest of the blocks is preserved. The traction force, T, is obtained from the summation of the spring forces on all of the blocks. Note that the friction force would be of the same magnitude (but of the opposite sign).

$$T = \sum_{i=1}^{M} f_i \tag{2.6}$$

The overall flow of the algorithm can be summarized in the pseudocode composed of four phases:

1- Specify: the geometrical, mechanical, and frictional characteristics, the shape parameters of the probability distribution function, the time step size, normal pressure, and the final time. Calculate: the spring stiffness, $k = GLW/H$, the normal force on the block, $N_b = pLW$, friction threshold, $f_{th} = \mu_s N_b$ and the slippage distance, δx_b, (according to Equation (2.2)). Generate the initial block positions by using the probability distribution function.

2- Increment time and update the driver position to $v_d t_n$. Calculate all of the spring forces, f_i values, from Equation (2.5) by using the current time and the former block position values. If any of the spring forces exceeds the friction threshold, update the corresponding block position by adding δx_b to its former value. For the spring forces that remain below the threshold, equate the corresponding block position to the former position. These blocks remain stuck in the current time step.

3- Calculate the spring forces, i.e., f_i values, *again* by using the current time but this time with the updated block positions obtained in phase 2. Close the loop by recording time and its corresponding traction force, T, as output. The magnitude of the traction force is equal to the summation of all spring forces obtained in the *present phase* and is calculated by using Equation (2.6).

4- Increment time step counter, n, and time. Check if the final time is reached: If not, execute phase 2; if yes, terminate.

The output is the macroscopic COF (that is traction force divided by the total normal force) as a function of time. The index number of the slipping blocks is also recorded. These outputs are superimposed to study the effect of slippage of the blocks on the traction force.

2.2.2 Constraints on the maximum time step size

The time step size is a crucial factor in determining the history and the number of block slippages. In this subsection, four analytical constraints on the size of the time step are derived.

The first constraint comes forth from assuming a fixed driver during the block slip-

page. This restriction can be interpreted as negligible propagation of the driver during the time step, $\delta x_d = v\Delta t$, compared to the block slippage distance, δx_b, that is obtained from Equation (2.2):

$$\delta x_d \ll \delta x_b \Rightarrow \Delta t \ll 2(\mu_s - \mu_d)\frac{N_b}{kv} \tag{2.7}$$

The second constraint is based on the extent to which the spring force is allowed to surpass the frictional threshold due to the propagation of the driver during the time step, Δt. The force increment has to be a small fraction of the frictional threshold:

$$\Delta f \ll f_{th} \Rightarrow k\delta x_d \ll f_{th} \Rightarrow \Delta t \ll \mu_s \frac{N_b}{kv} \tag{2.8}$$

Two additional constraints for the upper limit of the time increment can be deduced by considering the case of uniform probability distribution, $\alpha = 1$. The third constraint is obtained by considering that when the initial distribution of the blocks is uniformly random, the interval of possible block positions, i.e. $[-d_{max}, d_{max}]$, where $d_{max} = f_{th}/k$, is divided almost equally. In other words, the difference between successive initial block position values (when ordered) is nearly the same and equal to $\overline{x}_0 = 2d_{max}/M$, where M is the number of the blocks. The constraint has to make sliding of two "successive" blocks happen in separate time steps. Restricting the driver displacement to be smaller than $\overline{x}_0$ would guarantee the separation. Ideally, at each time step, Δt, just one block should be triggered by the driver:

$$\delta x_d < \overline{x}_0 \Rightarrow \Delta t < \frac{2\mu_s}{M}\frac{N_b}{kv} \tag{2.9}$$

The fourth constraint is deduced from the nature of steady sliding. The dynamic friction requires that the total amount of increase in the spring forces in *all of the blocks* due to the propagation of the driver within a time step to be equal to the magnitude of spring force reduction due to the slippage of the slipped blocks during the same time step:

$$Mkv\Delta t = N_{slipped} k\delta x_b \tag{2.10}$$

Moreover, consistent with the third constraint, in a uniform distribution it is expected to have just one slipped block if Δt is selected small enough, i.e., $N_{slipped} = 1$. Therefore, by considering Equation (2.2) the fourth constraint can be obtained from

Equation (2.10) as:

$$\Delta t < \frac{\delta x_b}{Mv} \Rightarrow \Delta t < \frac{2(\mu_s - \mu_d)}{M} \frac{N_b}{kv} \tag{2.11}$$

It can be seen that the fourth constraint makes the previous constraints redundant and becomes the single cardinal constraint for determining the time step size. Note that $N_b/kv = pH/Gv$.

2.2.3 Initial block positions as roughness

The standard deviation of the asperity heights is one of the parameters that characterize the surface roughness [155, 158]. Our definition of “rough" and “smooth" is based on the standard deviation of the asperity heights *with the same mean value*. In other words, by the term “rough", a lower concentration (i.e., a higher standard deviation) of the asperity heights around *a specific mean value* is meant. Conversely, by the opposite term, “smooth", a higher concentration (i.e., a lower standard deviation) of the asperity heights about *the same specific mean value* is meant. The order of spatial occurrence of the asperities along the surface neither affects the surface roughness measure nor our results.

In Figure 2.4, the difference between rough and smooth surfaces is illustrated. The ordinate shows the number of asperities of the same height per unit length. To generate a set of random asperity heights, beta probability distribution function is used. To keep the set symmetric about the mean value, the shape parameters are assumed equal, i.e., $\alpha = \beta$. In other words, skewness is zero. Henceforth, only the shape parameter α will be stated. The thinnest line, generated with $\alpha = 1000$, shows the highest concentration of asperity heights around the mean value among the shown cases. Then, the surface represented by the thinnest line is *the least random* (*the smoothest*) surface among the others. As the shape parameter decreases from $\alpha = 1000$ to $\alpha = 1$, the range of the asperity heights widens and finally the concentration disappears. The dashed line, generated with $\alpha = 1$, represents a surface with an equal number of asperities for each existing height. Thus, the *most random* (*the roughest possible*) surface is generated by $\alpha = 1$, i.e., the *uniformly random distribution*.

Let us state the intention behind specifying random initial positions to the blocks ex-

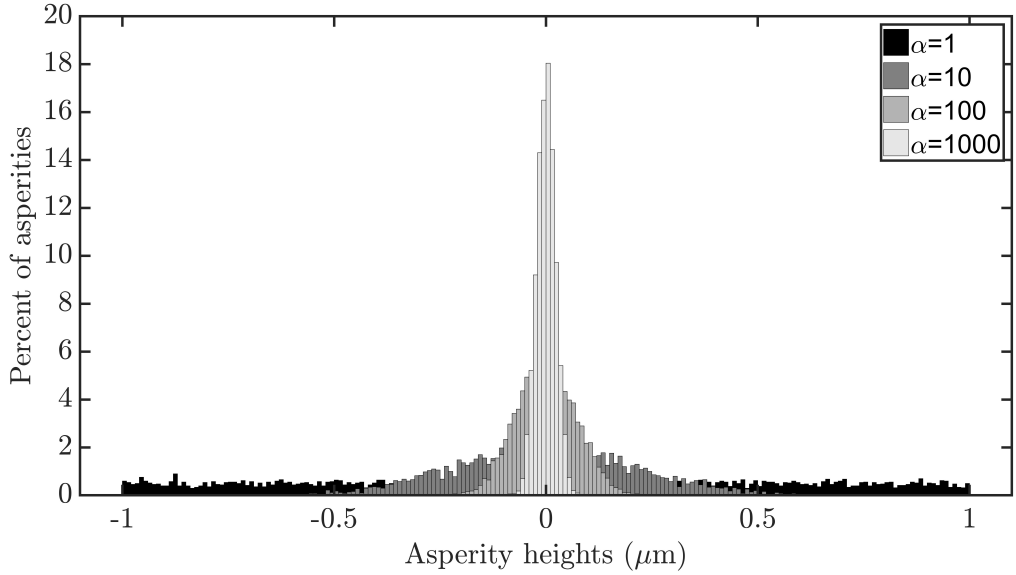

Figure 2.4: The asperity heights (in percents) and their standard deviation according to the beta PDF for different shape parameters

plicitly. An analogy is drawn between the effect of (a) roughness, i.e., asperity height standard deviation, and (b) initial block position distribution, on the required traction force (and consequently on the friction). The analogy of the effects can be explained by considering two distinct scenarios. In the first scenario, the random-height mass-spring units with no lateral displacement are pressed by a flat rigid substrate that has moved upward as shown in Figure 2.5-(a). The mass-spring units on the upper surface represent asperities. The multi-asperity surface has random-height asperities. Therefore, the amount of normal pressure experienced by each of the asperities would be a random quantity. Consequently, the frictional threshold would be a random quantity. In the second scenario, the same-height mass-spring units have blocks with random initial positions as shown in Figure 2.5-(b). In both scenarios, at the onset of motion of the driver, the blocks would slide at randomly different times. This analogous outcome of the two scenarios provides a link between the surface roughness and the block initial positions. The outcome suggests that, at least qualitatively, a random initial block position distribution mimics a random asperity height distribution i.e., the surface roughness. In the first scenario, *asperity heights* randomize the frictional threshold values and govern the sequence of the block slippages. In the second sce-

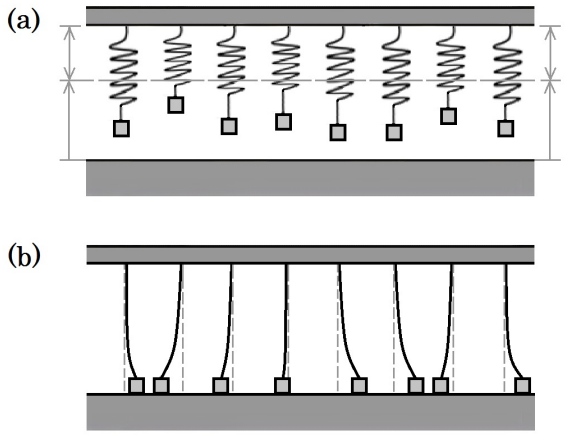

Figure 2.5: An analogy between the effect of (a) asperity height distribution and (b) initial block position distribution, on sliding friction

nario, the randomized variable is the *initial block positions*. These two scenarios correlate and lead to a qualitatively equivalent frictional behavior. In summary, it is claimed that the surface roughness can be modeled *indirectly* by specifying random initial positions to mechanically identical Maxwell-slip unit blocks. Then, a rough surface can be modeled by specifying a high standard deviation to the lateral initial block position distribution; on the other hand, a smooth surface can be modeled by specifying a low standard deviation to the lateral initial block position distribution.

The random set of *initial block positions* is generated by using a beta probability distribution. Each of the values in the set specifies local position of a block with respect to its corresponding position reference as illustrated in Figure 2.2-(b). The beta probability distribution is preferred because it generates random sets within the finite interval $[0\ 1]$ in contrast to Gaussian probability distribution which generates random sets within $(-\infty\ \infty)$. The mean value is equal to 0.5. The set is then subtracted by -0.5 to make the mean value zero by shifting the interval to $[-0.5\ 0.5]$. The whole set is then multiplied by $2d_{max}$ where $d_{max} = f_{th}/k$ is the maximum lateral displacement a block can experience without violating the frictional threshold. The result is a random set of initial block position values with zero as its mean value and d_{max} as its maximum value. The standard deviation of the resulted random set can be shown to be $\sigma = d_{max}(2\alpha + 1)^{-\frac{1}{2}}$.

2.3 Results

In Table 2.1, the model input data are given. The normal pressure value is assumed to be fixed at $200\ MPa$ (which is less than the reported uniaxial compressive strength of Westerly granite [175]). The idealized cuboid asperity dimensions are specified with a geological application in mind. The length, L, height, H, and width, W, of all of the cuboids are assumed equal to 1 meter, and thus the leaf spring stiffness, $k = GLW/H$, and the amount of normal force applied to the block, $N_b = pLW$, is the same for all of the blocks. It can be shown that when the number of the blocks is above 100, the traction force values converge. In order to generate smoother curves, the number of the blocks is considered to be 500. The time increment is selected by considering the constraint stated in inequality (11) which imposes an upper limit of $0.029\ s$. The time step size is selected to be $0.01\ s$.

The initial block positions are sets of random values that are produced by using beta distribution function. These sets are obtained by the procedure mentioned in Subsection 2.2.3. Beta distribution function shape parameter, α, is a measure of surface roughness as explained in Subsection 2.2.3.

The total traction force applied on the driver, T, is calculated from Equation (2.6).

Table 2.1: The static Maxwell-slip model input data

Shear modulus	$G = 28\ GPa$
Normal pressure	$p = 200\ MPa$
Driver velocity	$v = 0.1\ mm/s$
Time step size	$\Delta t = 0.01\ s$
Number of blocks	$M = 500$
Block dimensions	$L = 1\ m$
	$H = 1\ m$
	$W = 1\ m$
Frictional properties	$\mu_s = 0.8$
	$\mu_d = 0.7$

The overall normal force, N, is given by $N = MN_b$ which is the multiplication of a single block normal load, $N_b = pLW$, by the total number of the blocks, M. In all of the plots, the three horizontal lines of μ_s, μ_d and $2\mu_d - \mu_s$ (corresponding to single block force-drop, as shown in Figure 2.3) are also superimposed to monitor the relation between the macroscopic (overall) and the microscopic (block-level) frictional properties. The “microscopic static COF" is the user-specified value for the block-level static COF. The “macroscopic static COF" is the maximum value reached by the *macroscopic COF*, T/N.

In Figure 2.6, the macroscopic COF is plotted as a black line against time. Plots for nine different random initial position distributions, which are specified by α (the shape parameter of the beta probability distribution function) are shown in Figures 2.6-(a) to 2.6-(i). A smaller shape parameter, α, brings about a higher standard deviation for the generated initial block position set and makes it more random as explained in Subsection 2.3. The right ordinate shows the identities of the blocks. At each time step, the index numbers of the slipped blocks are marked with cyan dots while the index numbers of the stuck blocks are left unmarked. A complete lack of markers within a time interval indicates an all-stuck situation. In this manner the history of sliding events is represented and is superimposed on the macroscopic COF plots.

In one extreme, Figure 2.6-(a) has the largest shape parameter, $\alpha = 100,000$, i.e., the least random set of initial block positions. When the time starts to elapse, all of the blocks are stuck and the macroscopic COF rises linearly up to μ_s. There are no cyan dots in this time interval, signifying no occurrence of local slippage at all. When the macroscopic static COF is reached, a sudden drop in force due to the collective slippage of all blocks happens. All of the cyan dots are placed in the narrow time interval (during which the force-drop occurs) and form a vertical “line”, representing an almost-simultaneous slippage of all of the blocks. The macroscopic COF suddenly drops from μ_s to $2\mu_d - \mu_s$ (as expected from Equation (2.4) and shown in Figure 2.3). Afterward, all of the blocks stick anew and the macroscopic COF starts to rise again. The process repeats periodically as the driver continues to advance. This process is called collective stick-slip or *collective interfacial slip* [176].

On the other extreme, Figure 2.6-(i), has the smallest shape parameter, $\alpha = 1$, i.e., the

most random set of initial block positions. In this case, the initial block positions have a uniform probability distribution. Two distinct intervals can be observed. In the first interval, the macroscopic COF initially rises nonlinearly and approaches the plateau of μ_d from below without overshooting. In the second interval, the macroscopic COF stays steady about μ_d fluctuating with a negligible amplitude. The plateau represents the state of steady sliding. In the nonlinear-rise interval, the number of the cyan dots increases monotonically. Beyond a specific time (that is the beginning of the plateau interval) the number of the cyan dots remains approximately the same and the pattern of the cyan dots becomes periodic. The periodicity was expected because every mass-spring unit repeats its slippage periodically. Then, both overall behavior and pattern become periodic after a specific time (subsection 2.4.3). In contrast to Figure 2.6-(a), in which the cyan dots are clustered, in Figure 2.6-(i) the cyan dots are scattered temporally. As opposed to *collective* slippage in Figure 2.6-(a), this asynchronous slippage history is called *sequential interfacial slip* [176].

Figure 2.6 illustrates the overall process of transition from stick-slip (in the first and second columns) to steady sliding (in the third column). As α decreases from Figure 2.6-(a) to 2.6-(f), the amplitude of the macroscopic COF oscillations decreases and the block slippages occur in broader time intervals. By further decrease in α, in Figures 6-(g) to 6-(i), the macroscopic COF oscillations are eliminated and the block slippages occur uniformly with the onset of the dynamic friction (or steady-state) plateau. Furthermore, as the α decreases, the macroscopic static COF, that is the peak of the macroscopic COF, decreases. The extremums of the macroscopic COF, which in Figure 6-(a) are at μ_s and $2\mu_d - \mu_s$, approach μ_d. In other words, the amplitude of stick-slip oscillation about μ_d narrows as α decreases from Figure 2.6-(a) to Figure 2.6-(f). However, below a specific α value the amplitude shrinks almost to zero. In the third column of Figure 2.6, i.e., in Figures 2.6-(g) to 2.6-(i) the macroscopic COF hardly leaves the immediate vicinity of μ_d.

Initially, the slope of the macroscopic COF curve in Figure 2.6 is the same for all of the cases. In Figures 2.6-(a) to 2.6-(h), the rise of the curve is (at least partially) linear up to some point. Within these linear-rise intervals all of the blocks are stuck (no cyan dot exists). The curve starts to deviate from linear behavior with the occurrence of the block slippage events. Note that in Figure 2.6-(i), the linear interval is absent since

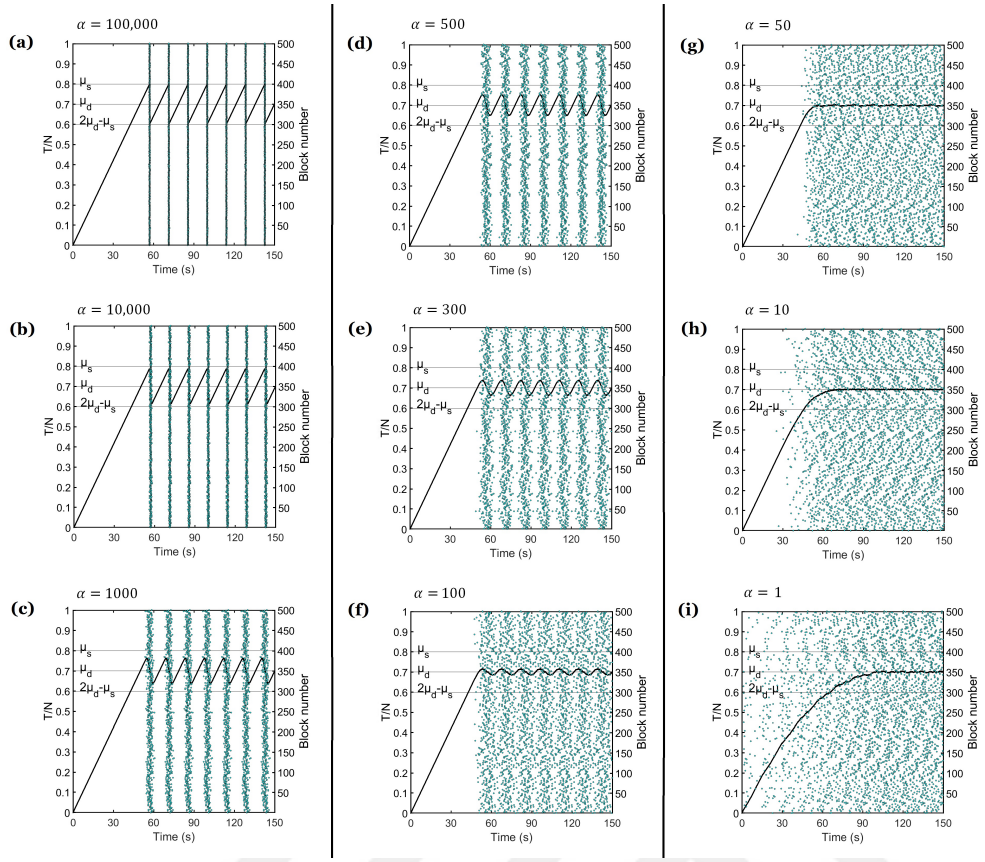

Figure 2.6: Time evolution of the macroscopic COF (the black line) and the slipped block index numbers (the cyan dots) for nine shape parameter values

the slip events occur from the very beginning. In Figure 2.6-(i), the slope of tangent to macroscopic COF is lower than that of the other cases at any specific time step and a longer time is needed for macroscopic COF to reach the plateau in Figure 2.6-(i). The nonlinear-rise interval of Figure 2.6-(i) can be interpreted as a continuous “loss of stiffness" as a result of the *increasing* number of the block slippages.

For all of the cases shown in Figure 2.6, a pattern of repeating cyan dots is built with time as new block slippage events are added to the events that have begun formerly. The onset of the periodicity and the period of the model are expressed analytically in subsection 2.4.3. In Figures 2.6-(g) to 2.6-(i), the onset of the dynamic friction plateau is the onset of the model periodicity. As α decreases, the onset of the plateau is delayed further. The periodic pattern of the cyan dots is completed at the onset of the plateau and henceforth the number of the block slippages within a time window

of the same size becomes almost constant. This almost constant number of slipping blocks depends on the size of the time window within which the block slippages are counted. In subsection 2.4.4, these observations are justified analytically.

In Figure 2.7, the macroscopic static COF is plotted against beta distribution function shape parameter, α, in a logarithmic scale. Each cluster of the black square markers shows the values obtained from 100 runs for each considered α. The blue line is a curve fit to the mean value of the clusters. Although constant microscopic (block-level) coefficients of friction are assumed, the macroscopic (overall) static COF is a function of α. The dashed line plotted at $\alpha = 50$ delineates a border between the two regimes of sliding. The macroscopic static COF values that are extracted from the third column of Figure 2.6 are among the markers to the left of $\alpha = 50$ in Figure 2.7. The macroscopic static COF values that are extracted from the first and second columns of Figure 2.6 are among the markers to the right of $\alpha = 50$ in Figure 2.7. As the value of the shape parameter increases from $\alpha = 1$ (for uniformly random distribution) to $\alpha = 50$ (for a less random distribution), the mean macroscopic static COF remains constant and approximately equal to the value of microscopic dynamic COF. However, beyond $\alpha = 50$, the value of mean macroscopic static COF asymptotically approaches the microscopic static COF with $\log(\alpha)$. Within the interval $1 \leq \alpha \leq 50$ the surface is rough enough to eliminate stick-slip. On the other hand, within the interval $50 < \alpha$, as the surface becomes smoother, stick-slip emerges and intensifies. The transition from steady sliding regime to stick-slip regime occurs very sharply at $\alpha = 50$.

There are some experimental evidence that justify a rougher surface favors smaller stick-slip amplitude and “stiffness". The brake test results performed on commercial low-steel type brake pads with rough and smooth surfaces show that while rough pad surfaces lead to low-amplitude stick-slip, smooth pad surfaces cause pronounced stick-slip [155]. This also means that a rough surface has a lower *macroscopic* COF compared to a smooth surface. Furthermore, the results obtained from shearing Westerly granite specimens with a rotary apparatus [158] show nonlinear frictional behavior before reaching the dynamic friction plateau. Steady sliding seems to be the dominant regime for a wide range of rock surface roughness values [158]. The smoother rock specimens have a higher “stiffness" (i.e. reach to the dynamic friction plateau

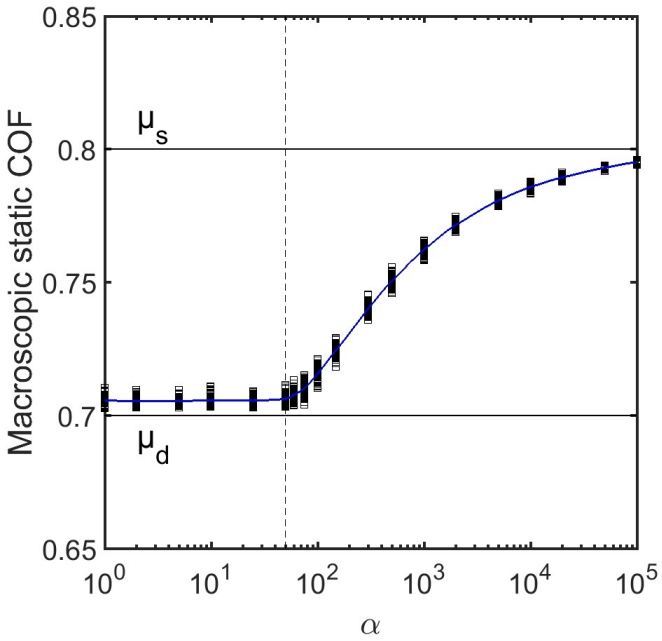

Figure 2.7: The macroscopic static COF values against the beta PDF shape parameter

faster) compared to their rougher counterparts [158].

2.4 Discussion

In the first part of this section, our results are discussed in light of some empirical observations from geophysics literature. The results suggest that a smooth elastic surface that slides on a rigid flat substrate has a higher tendency to stick-slip compared to its rough counterpart. In the second part of this section, some suggestions of our results that concern the effect of the frictional properties on the sliding regime are discussed.

2.4.1 A claim about the behavior of geological faults

Based on the results and the interpretation of the block positions as a measure of roughness, it is anticipated that *fault surface roughness* is a crucial factor in determining its sliding regime. It can be claimed that a sufficiently smooth fault surface

encourages earthquake generation while a sufficiently rough fault tends to be earthquake deficit.

The claim is supported by several empirical studies conducted on oceanic subduction zones. A study based on a newly developed roughness database for the oceanic plates *prior to* subduction clearly shows that for *seismic coupling coefficient* of a zone (a measure of seismicity as defined in [177]) to exceed a specific limit, its seafloor has to be smooth enough [178]. Conversely, for rough enough subduction zones it is not possible to have a seismic coupling coefficient beyond the specific limit [178]. A companion study that considers natural data extracted from an earthquake database besides the previously mentioned seafloor roughness database, emphasizes that great to giant megathrust earthquakes evidently prefer smooth subducting seafloors [179]. Moreover, a review article that investigates seismic and geodetic data related to several subduction zones concludes that highly rugged subducting seafloors undergo aseismic creep and host just small and medium-sized earthquakes [180]. A similar conclusion is drawn by a numerical study in which fault roughness is assumed fractally self-similar [181]. The numerical study shows that seismic moment is a decreasing function of fault roughness [181]. The possible negative/positive effect of fault roughness on seismogenic potential is still under debate [178–180].

In contrast to oceanic subduction zones, measuring the roughness of a strike-slip fault surface is hardly possible. In the following paragraphs an extra body of geophysical literature related to strike-slip faults and their fault surface roughness is addressed. Some recent studies have investigated *the effect of roughness* on frictional regime [182], rupture nucleation and foreshocks [182–184], crack to pulse transition, and earthquake magnitude [185] in laboratory or by numerical methods.

Geological fault segments can be categorized into *locked* and *creeping* [154]. A locked fault segment remains stuck and eventually undergoes a sudden sliding causing an earthquake (or is expected to do so). This stick-slip behavior was proposed as a mechanism for earthquakes in 1966 [37]. As an example, the central part of the Main Marmara Fault (an extension of the North Anatolian Fault offshore Istanbul) is thought to be a locked fault segment [186–188]. The segment experiences a lower level of seismic activity compared to its neighbors [187] and represents an *earthquake*

gap [188]. This fact indicates that the segment is sticking and accumulates strain energy [187]. Therefore, the occurrence of a major earthquake is expected [188].

On the other hand, a creeping fault segment undergoes aseismic slip (or *creep*). The central segment of the San Andreas Fault in California is a famous example. A map of the San Andreas Fault and its historical ruptures at 1857 and 1906 is given in [189]. In 1960, one of the first indications of creep on the central segment was documented as a series of slow and progressive fractures and displacements along a single straight line in the buildings of a winery [190]. The winery was located about 24 kilometers southeast of San Juan Bautista [190]. In [191], a map of the San Andreas Fault that is superimposed upon the location of moderate-large earthquakes makes the central segment *indirectly* highlighted as the aseismic part of the fault between San Juan Bautista and Parkfield. In-depth geodetic observations of the creeping segment as well as rupture contours of 1989 and 2004 earthquakes at the ends of the segment are provided in [192]. Interestingly, slipping *locally and regularly* (and consequently emanating small quantities of seismic energy by degrees) is reported along the central segment of the San Andreas Fault; the creep builds up during these *spasms* of slip [190] and not continually. Measuring displacement of floor slabs in the previously mentioned winery has shown that these spasms of slip are separated by relatively long intervals of little or no slip [190]. Moreover, some other creep records from the San Andreas fault, south of Hollister [193] and Melendy ranch [194] confirm the episodic character of the creep incidence. Further information about the creeping faults around the world can be found in [154]. The debate on whether or not certain fault segments are locked or creeping continues [195, 196].

It can be conjectured that a locked fault may have a smooth surface. The results of our model in Figure 2.6-(a) show that the smoothest surface produces a distinct sawtooth pattern in friction which consists of a set of successive pairs of linear rise (all-sticking) intervals and sudden drop (all-sliding) moments. This force pattern is the fingerprint of stick-slip. During the all-sticking intervals the cyan dots are absent and the load is accumulated. The absence of cyan dots is analog of the low level of seismic activity reported for locked fault segments, e.g. in [187, 188]. On the other hand, the simultaneous presence of all cyan dots at the all-sliding moments is an analog for the occurrence of rupture along the entire fault during which the force

drops. This collective interfacial slip would cause a sudden release of large seismic energy and may generate a massive earthquake.

Furthermore, it can be conjecture that a creeping fault may have a rough surface. In the third column of Figure 2.6, the sufficiently rough surfaces cause a steady-state friction. The absence of stick-slip is analog to the absence of earthquakes. In these cases, local sticking and slipping events happen all the time and involve only a fraction of the blocks, as manifested in the fairly even distribution of the cyan dots. This *asynchronous local stick-slip* (or sequential interfacial slip [176]) of the blocks is an analog for the spasms of slip (reported in the literature as mentioned previously) and can be proposed as a mechanism of aseismic creep.

2.4.2 Possible effects of the fault frictional properties

According to the results shown in Figures 2.6 and 2.7, two key parameters that have a great impact on the macroscopic static COF are the roughness and the dynamic COF. This finding indicates that the static COF obtained from testing fault rock samples, can hardly reveal the nature of the sliding regime of the fault *as long as the microscopic dynamic COF and fault surface roughness are disregarded*. A low microscopic *static* COF can *only* be considered as a cause for fault creep if $\mu_s \approx \mu_d$. This condition ensures a reduction of the force-drop according to Equation (2.3). Imagine that in Figure 2.6-(a), $\mu_s \rightarrow \mu_d$. Then, the horizontal lines for μ_s and $2\mu_d - \mu_s$ approach that of μ_d and would inevitably lead to the elimination of the stick-slip sawtooth. Note that although aseismic creep becomes inevitable if $\mu_s \approx \mu_d$, i.e., in the case of “low" static COF, the condition is not the only possible way for the occurrence of aseismic creep. Based on our results in Figure 2.6, fault surface *roughness* is one of the significant factors that decide the sliding regime of a fault. As shown in Figure 2.7, a sufficiently high roughness can make the macroscopic static COF roughly equal to the dynamic COF. In other words, the surface roughness can override the role of a high microscopic $\mu_s - \mu_d$ value. As a result, a fault segment may undergo aseismic creep due to its sufficiently high surface roughness and despite its “high" *microscopic* static COF [197]. On the other hand, a “low" value of microscopic dynamic COF *per se* does not necessitate creeping behavior of a fault segment. Neither μ_d nor μ_s

by themselves can negate the dominant role of roughness in determining the sliding *regime*.

When a surface is rough enough to induce steady sliding, as in the third column of Figure 2.6, the macroscopic COF plateau hardly deviates from μ_d. It is intriguing that selection of μ_d by the plateau happens despite a small fraction of blocks slide within a time step. As stated in Section 2.2, the majority of the blocks are stuck and ideally, just one block should slide within a time step! Nonetheless, μ_d (and not μ_s) is the parameter that together with normal load would dictate the friction force in steady sliding regime. This idea is supported by [198, 199] in which the role of *dynamic friction* is emphasized to investigate *the expected and surprisingly absent* frictional heat flow along the creeping faults. Moreover, the magnitude of *sliding friction coefficient* is reported to be not sufficiently low to explain the expected low friction along the central segment of the San Andreas Fault [200].

According to [198], the static friction of a fault is expected to be much lower than its rock sample static friction laboratory results due to *random* flaws and local stress concentrations along the fault. This thesis is consistent with the results shown in Figure 2.7, in which the macroscopic COF is in all of the cases smaller than the microscopic static COF. In [156], it is analytically shown that the macroscopic static COF (called “apparent" static COF in [156]) is less than or equal to the microscopic static COF (called “real" static COF in [156]) *for a side-driven mass-spring model*. The *macroscopic* static COF is not a material constant [170, 176, 201]; it is affected by the surface roughness.

2.4.3 The onset of periodicity

It is worthwhile to mention analytical expressions for the onset of the periodicity and the period of the model. The stick-slip of every single mass-spring unit is periodic. Then, the periodic behavior of the Maxwell-slip model starts just after the incident of the *first* slippage of the block with maximum *initial* position, $max\{x_0\}$. The slippage happens when the driver covers the sum of $max\{x_0\}$ and the distance required to reach the frictional threshold in the spring. Thus, the onset of the periodicity occurs

at:

$$t_{op} = (max\{x_0\} + f_{th}/k)/v \tag{2.12}$$

Note that the period of the single mass-spring unit, i.e., f_{th}/kv, is not the period of the model! The period of the model can be found by considering that a triggered block moves forward by the specific distance, δx_b, given by Equation (2.2). It can be shown that the next slippage of such a block would be triggered when *the driver* moves forward by δx_b. Therefore, the period of the model is:

$$t_p = \delta x_b/v \tag{2.13}$$

2.4.4 About the steady sliding plateau

The steady state of friction (observed e.g., in Figures 2.6-(g) to 2.6-(i)) can be explained by proposing that within the plateau the amount of force-rise in *all* of the springs due to proceeding of the driver within a time window is equal to the absolute value of the amount of force-drop in the springs of the *slipped* blocks within the same time window. In other words, after the onset of the model periodicity, within small-enough time intervals, the increase in spring forces is practically eliminated by the slippage of slipped blocks such that the plateau is retained. The proposed steady sliding mechanism requires Equation (2.10). It is interesting that although substantial majority of the blocks are *stuck* (when a sufficiently small time window is considered) the plateau somehow prefers (or is preserved at) *dynamic* COF.

Here, by starting from Equation (2.10) it is shown why during steady state of the friction, the number of slipped blocks within equal time windows remains the same and depends only on the size of the time window. Note that according to the previous section, the period of the model is $\delta x_b/v$. Then, the time window can be defined as a fraction of the period $\Delta T_w = \delta x_b/Dv$ where D is the number of divisions of the period. Now, by substituting $\Delta T = \Delta T_w$ in Equation (2.10) and simplifying:

$$\frac{N_{slipped}}{M}(\%) = \frac{100}{D} \tag{2.14}$$

This window-size dependence of the slipped block percentage was expected for the

reason that when a uniformly dotted plane is evenly divided, the number of dots within each interval is almost the same and decrease with further divisions.

2.5 Conclusions

In this study, a quasi-static approach to the Maxwell-slip model is proposed to investigate frictional sliding of a rough elastic slider on a flat, rigid substrate. Furthermore, the randomness of the initial block positions is interpreted as a measure of the roughness of the elastic surface. Uniform normal pressure distribution is applied, and Coulomb friction law is adopted. Evolution of the macroscopic COF and slippage of the blocks with time is used to investigate the relation between the surface roughness, the mode of interfacial slip and the regime of frictional sliding. The main results are summarized as follows:

1. Below a specific roughness value, *sequential interfacial slip* [176] occurs and brings about steady sliding. Although at each time-step the majority of the blocks are stuck, the plateau of the macroscopic COF prefers the microscopic dynamic COF.

2. Above the specific roughness value, *collective interfacial slip* [176] occurs and brings about stick-slip. The smoother the surface, the higher would be its stick-slip amplitude. When the surface is perfectly smooth, the macroscopic static COF reaches its maximum which is microscopic static COF.

3. The border between steady sliding and stick-slip regimes is distinctly delineated by a specific roughness value.

4. The magnitude of either the microscopic (block-level) static COF or the microscopic dynamic COF *by themselves* play a subordinate role in affecting the sliding regime compared to the surface roughness. However, if the microscopic static and dynamic COF magnitudes are almost equal, steady sliding regime is observed irrespective of the roughness value.

A tribological implication of our results is that a sufficiently rough (or randomly textured) elastic surface would have a lower macroscopic static friction, and a weaker

stick-slip tendency compared to a sufficiently smooth (or regularly patterned) counterpart. The experimental evidence related to the brake pads made of low-steel friction material in [155] supports this implication.

A geophysical implication of our results is that the rougher a geological fault surface is, the less would be its potential to produce earthquakes, and the greater would be its tendency to undergo aseismic creep. Fault surface roughness is one of the parameters that affects the regime of sliding of the faults. A number of empirical studies related to oceanic subduction zones [178–180] support the proposed implication.

2.6 Future work

A direct approach to model roughness is possible. The heights can be assigned according to a random distribution. Then, the asperities can be pressed on a rigid flat surface. In this case the normal loads on the asperities will be the random variable. This is an alternative and straightforward approach when compared to the initial lateral spring extension analogy in the current chapter. Further explanations are provided in section 7.1.

CHAPTER 3

QUASI-STATIC MAXWELL-SLIP MODEL CHARACTERIZED BY NAYAK PARAMETER

In this chapter, normal contact and sliding of a rough surface are investigated by a statistical multi-asperity model. The model is based on Nayak's theory which uses random process theory to analyze the 2-D isotropic Gaussian rough surfaces. Firstly, a set of random asperities is generated. The set is generated using a probabilistic approach proposed by Greenwood [27] and is composed of asperities with different heights and tip radii. Each asperity is assumed to be a rigid paraboloid. Greenwood's PDFs are fully specified by the Nayak parameter, a combination of the spectral moments of the surface PSD. In the normal contact phase, the set of asperities is pressed against an elastic half-space. The normal load and contact area of the asperities are calculated by Hertzian theory. The evolution of the total (real) contact area and total normal load with compression are compared against the existing analytical solutions. Since the analysis is elastic, the plastic deformation limit is also monitored. In the sliding contact phase, the tangential stiffness of each asperity contact area is determined and assigned to a Maxwell-slip model unit. The driver of the Maxwell-slip model is then moved horizontally, and the variation of COF and the slippage history of the blocks with the driver position are recorded and presented.

3.1 Introduction

The body of literature that was found related to (and some inspired) the present study is separated into two parts. In Subsection 3.1.1, those references that deal with the normal contact are reviewed. In Subsection 3.1.2, mainly the block-spring models

that are used for simulating sliding contact are presented.

3.1.1 Normal contact

Using the approach which Longuet-Higgins first proposed in 1957 for modeling ocean surfaces [202, 203], Nayak [24] interpreted the topography of a solid rough surface as a random process. The surface heights are considered a 2-D random variable on a Cartesian grid in which x and y are independent. The tools and techniques of the random process theory are then utilized to characterize and analyze the surface topology. The autocorrelation function of the process, a measure of the similarity of a surface to itself, is then decomposed by the Fourier transform to give the surface's power spectral density (PSD). The moments of the PSD, namely, the zeroth moment, m_0, the second moment, m_2, and the fourth moment, m_4, are indeed the variance of the heights, the variance of the slopes, and the variance of the curvatures of the surface:

$$m_0 = \sigma^2 = \mathrm{E}\Big\{ z^2 \Big\} \tag{3.1}$$

$$m_2 = {\sigma_m}^2 = \mathrm{E}\Big\{ \Big(\frac{\mathrm{d}z}{\mathrm{d}x} \Big)^2 \Big\} \tag{3.2}$$

$$m_4 = {\sigma_\kappa}^2 = \mathrm{E}\Big\{ \Big(\frac{\mathrm{d}^2 z}{\mathrm{d}x^2} \Big)^2 \Big\} \tag{3.3}$$

The central limit theorem states that the joint PDF of n independent random variable is an n-dimensional Gaussian probability distribution as shown in [24, 202]. Nayak [24] defines six random parameters; one of them is the height the rest are the derivatives of the surface height with respect x and y. Then, a 6-dimensional joint PDF is obtained according to the central limit theory. Finally, the PDF of the summit heights and then the joint PDF of the summit heights and curvatures are derived. The derivation is done by ensuring zero slope, and negative curvature at the summits (asperity tips) [24]. The derived PDFs are functions of a parameter called roughness spectral breadth [25] or Nayak parameter [27] and is defined as:

$$\alpha = \frac{m_0 m_4}{m_2^2} \tag{3.4}$$

In 1975, Bush, Gibson, and Thomas proposed a model (BGT model henceforth) which uses elliptic paraboloids to represent (approximate) the asperities (summits) of the surface [26]. The surface is modeled using a random process model similar to the work of Nayak. A joint PDF of the asperity heights and curvature represents the surface. The heights and the principal curvatures of the approximating elliptical paraboloids are equal to those of the surface. Closed-form expressions for the normal load and the real contact area are derived. Furthermore, a closed-form relation between the normal force and the real contact area is obtained. When the separation between the contacting surfaces is high enough (a criterion is provided: $h \gg \sigma\sqrt{\alpha}$), it is shown [26] that asymptotic evolution of the real contact area with the nominal pressure is as follows:

$$\frac{A_r}{A_0} = \kappa \frac{1}{\sqrt{2m_2}} \frac{\sigma_0}{E^*} = \kappa p' \tag{3.5}$$

Where the constant of proportionality, κ, proposed by the BGT model is equal to $\sqrt{2\pi}$, σ_0 is the nominal pressure, i.e., total normal load divided by the nominal contact area and E^* is the composite Young modulus. For a rigid-elastic contact, $E^* = E/(1-\nu^2)$. The above relation is one of the benchmark solutions of the asperity-based models and has been widely used to verify the numerical results [7, 25, 145, 146, 204].

The probabilistic approach proposed by Greenwood and Williamson in 1966 [21] is a cornerstone of the asperity-based models. The surface asperities are assumed to be circular paraboloids of the same curvature. The approach does not suggest a procedure to specify the asperity tip radius (the radius of the osculating sphere of the paraboloids). The asperities are pressed against an elastic half-space. The PDF of heights to find a closed-form relation between the load and evolution of the (total) real contact area and load. The height distribution is assumed to be Gaussian. By approximating the Gaussian tail with an exponential function, a closed-form liner relation between the load and real area is derived.

In 2006, Greenwood proposed a joint PDF of heights and curvatures [27] based by assuming that the asperities are only mildly elliptic. He approximated the elliptical paraboloidal asperity curvatures with an equivalent geometric mean curvature. His approach, which is based on the models proposed in [26] and [24], takes the surface properties into account and therefore is capable of assigning proper asperity radii. The

model is shown to be successful in reproducing the results of the BGT model [27].

Greenwood's 2006 paper [27] provides both the PDF of the asperity (summit) height (with respect to the surface mean) and the joint PDF of the asperity heights and their tip curvatures. These PDFs are completely characterized by the surface's zeroth, second, and fourth spectral moments. In other words, if the variance of the heights, slopes, and curvatures of the points of a rough surface, is known sets of random pairs (of asperity height, asperity tip curvature) representing the character of the rough surface can be generated by the PDFs.

Yastrebov [25, 146] developed an analytical approach for calculating the spectral moment formulas using the power spectarl denrity (PSD) function of the surface. To obtain the moments, the PSD function coefficeint, Hurst exponent, and the cut-off wavenumbers must be specified. This spectral-based approach is discretization-independent and more accurate than the numerical methods that calculate the moments by using the finite-different approximations to the derivatives of *generated* fractal surfaces [25]. In other words, the analytical approach does not need a *generated* surface to *measure* the moments. Rather, the moments are directly determined as a function of the above input values. This approach is explained in detail in Appendix B.

Investigating the tire-road contact, Persson developed a mathematically rigorous theory [205] that can predict the PDF of normal stress (or pressure) on an arbitrarily rough surface. Suppose that a rigid rough half-space is pressed on a flat elastic half-space. If one looks with naked eyes at the interface, it seems that the normal stress is the same over the whole interface. Then, the PDF of the pressure is a Dirac delta function at that specific nominal pressure. However, if the original frame is magnified (say ten times by a microscope), it will turn out that the elastic half-space is pressed only at some asperity tips, and some points do not contact at all. By further magnification (say another ten times), it would be observed that even the former asperity tips do not contact fully but have smaller asperities on top that are in contact with the elastic half-space. Persson shows that (Appendix B of [205]) the PDF of pressure for such a contact problem is a function of the pressure and magnification. The PDF is governed by a partial differential equation resembling the 1-D diffusion (or heat)

equation. The "diffiusion coefficient" of the PDF is a function of the rough surface PSD function. Differentiation of the pressure PDF with respect to the pressure itself and with respect to the magnification.

Persson extends his derivation (Appendix C of [205]) to real contact area, and takes plastic deformation and curved profiles into account. Note that his proposed partial differential equation is derived by using the elastic half-space field solutions (Section IV of [205]) and intrinsically takes the long-range elastic interaction into account. Therefore, the contacting points affect the contact of their neighbors as they press and deform the elastic half-space. This is in sharp contrast to the asperity-based methods like [21, 26, 27] in which the asperities are assumed too far to affect each other. In [206], Persson compares his theoretically found slope for the load-area relation with that of [26] and argues that it has to be due to neglecting interaction of the contacting areas by the BGT model that the slope is smaller than that of BGT model by a factor of $2/\pi$. Thus, the constant of proportionality, κ, in Equation (3.5) is equal to $\sqrt{8/\pi}$ according to Persson's model. Persson's approach does not use Hertzian contact formulas. Therefore, it predicts a broader range of linear variation of the real area with the normal load (up to contact of nearly 30% of the nominal area), which brings about a better agreement with Coulomb friction law in higher normal loads. Explanations and discussions of Manners and Greenwood [29] can be found helpful for a better understanding of Persson's model and derivations. For an extensive review of the approach and related topics, one may see [207].

3.1.2 Sliding contact

Some studies have used asperity-based models to study the sliding behavior. A Gaussian height distribution is assumed in [208], and the asperities are modeled as linear springs. In [209], a closed-form formula for friction is obtained by assuming a Gaussian distribution for the asperity heights. Similar to [21], the asperity tip radius is a constant in both [208] and [209]. Furthermore, the sticking/slipping state of an asperity is determined by the asperity compression. Those asperities that are pressed more are stuck, and the less-compressed asperities slide. Eriten, Polycarpou, and Bergman [210, 211] improved the model proposed in [208] by considering

plasticity, which eliminates the need to specify a COF at the asperity level. The physical-based model in [210] needs only the material and geometrical properties to give the frictional response. It is also shown [210] that during tangential unloading, asperity sliding is history-dependent. The model is used to study the response (hysteresis) of a single DOF dynamical system subjected to different excitation functions [210] and a bolted joint under fretting loading [211]. Vibration of a rough bolted joint is also studies using the BEM [212]. Another study [213] that equips the Maxwell-slip model with statistics of the asperities has been successful in generating experimentally-observed phenomena like frictional lag (dependence of friction on the speed and excitation frequency).

In [214] a closed-form formula for the overall tangential stiffness of the surface at the onset of tangential loading is derived. Additionally, the effect of asperity-spacing (and consequently elastic interaction) is investigated. Furthermore, a numerical approach is used to model the contact of a rough elastic surface with a flat rigid indenter (punch) with rounded edges. In [215] total tangential stiffness of the rough surfaces is investigated by considering elastic energy. In [216], asperity-level friction is studied experimentally and numerically, and the effect of adhesion force is discussed. A discussion about the effects of the adhesion force and plasticity on static friction can be found in [217].

Mass-spring systems have been widely used in the literature for modeling sliding friction. In general, these systems can be divided into two broad categories: (i) the coupled systems in which the blocks are connected to their neighbors by springs, and therefore the motion of each block affects the others, and (ii) the uncoupled systems in which no coupling spring exists between the block and the motions are completely independent. While the first class is preferred by geophysicists to simulate geological fault dynamics, the second class is generally used by the control community, especially in order to model the function of mechanical systems that are subjected to friction.

The coupled models category has two widely-known examples: (i) the Burridge-Knopoff model, which is mainly used by seismologists to investigate earthquake mechanisms [38], and (ii) the Frenkel-Kontorova model, which is exploited by theo-

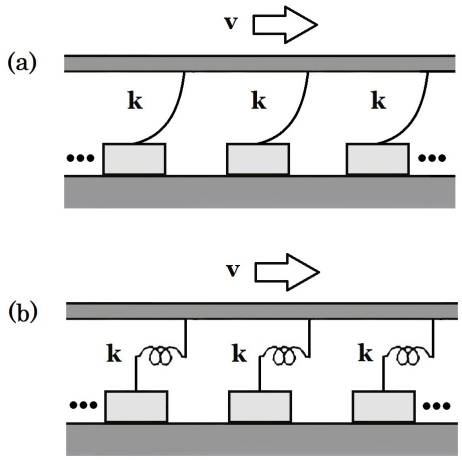

Figure 3.1: Maxwell-slip model configuration shown with (a) leaf springs (b) coil springs

retical physicists, especially to investigate atomic-level behavior of the solids in general and nanotribology specifically [218]. On the other hand, the most known examples of the uncoupled models are (i) the Maxwell-slip model [52], (ii) the Prandtle-Tomlinson model, which has been used to understand the experimental results of atomic force microscopes [15], and the bristle models.

Two equivalent schematics of the model configuration are shown in Figure 3.1. The rigid driver pulls the blocks that are connected to it by leaf springs (Figure 3.1-(a)) or coil springs (Figure 3.1-(b)). Both schematics emphasize that normal stiffness is not considered in the Maxwell-slip model. In some studies, e.g., [52], the blocks are ordered vertically; however, this difference in representation does not mean a change in the configuration essentially.

The Maxwell-slip model has been widely used in the literature for simulating frictional behavior. The model is applied to a diverse range of applications, e.g., pneumatic artificial muscle [57], machining tools [56], positioning systems [151, 168], and servomotors [219]. Generally, the model parameters are tuned such that the response fits a specific set of experimental data. To the author's best knowledge, only a few studies characterize a block-spring system based on the surface geometry or quantities like normal load or stiffness of the surface asperities. In [220], the tangen-

tial stiffness values of Maxwell-slip units are assigned according to an elastic-plastic model, which is proposed by Kogut and Etsion [221]. In [222], the parametric model proposed in [220] is fitted to hysteresis data obtained from a tribometer. In [213], the Maxwell-slip model is used together with GW model, but it needs to be clarified how the stiffness of the springs is determined.

Three comprehensive surveys of the friction models used by the control community are [223–225]. One of the most known examples of the bristle models is the LuGre model [44], which is known for its ability to capture experimentally observed frictional phenomena. The formulation is heuristic because the state equation is not based on physical laws but on the consistency of its results with the experiments. The state is indeed the average deflection of the bristles. The formulation is based on this "virtual" parameter. The LuGre model is known for generating the Stribeck effect (an experimental phenomenon observed in lubricated contact: increase in friction at high-enough sliding velocities) [223].

Al-Bender and co-workers [167] have developed a heuristic approach to the Maxwell-slip model, which, similar to the LuGre model, is based on a state equation. The state represents the average displacement of the bristles (massless asperities). The state equation expresses the rate of spring elongation as a function of the block position. The differentiated form of the state equation is analog to the equation of motion of a mass-damper (with no springs and with a damping coefficient that is a function of the driver velocity) that is moved on a frictionless surface. Despite this, a set of spring stiffness values and constant damping coefficients are later used in [167] to calculate the friction force (by applying the superposition principle). This “heuristic” approach reproduces the hysteresis and rate-dependent frictional behavior and has been successfully used in a control engineering application [226].

3.2 Method

The method is composed of three main parts: (i) generation of a set of random asperities, (ii) normal contact of the set with a rigid flat surface, and (iii) using the asperity load and stiffness values to characterize Maxwell-slip model to study the sliding con-

tact.

A schematic of the flow of the method is shown in Figure 3.2. The algorithm has three main phases: (i) the generation of a set of random asperities, (ii) the *normal contact* phase in which the set of rigid asperities are pressed against an elastic half-space, and the asperity stiffnesses and loads are obtained from Hertzian contact formulas for paraboloids, and (iii) the *sliding contact* phase in which the asperity (tangential) stiffness values and normal loads are transferred to the Maxwell-slip model. The asperities are modeled as (replaced with) mass-spring units with proper properties. Maxwell-slip model driver is then moved horizontally and pulls the units. The summation of the spring forces gives the friction force. The block slippage history is also recorded.

Greenwood's PDFs are used to generate the set of asperities, namely the height PDF and the height-curvature PDF. Appendix C gives a detailed description of these PDFs. The PDFs are fully specified by the zeroth, second, and fourth spectral moments of the "surface" (represented by the set of asperities). As shown by Equations (3.1)-(3.3), the moments are the variances of heights, slopes, and curvatures of such a surface. A combination of these moments, the Nayak parameter, characterizes the PDFs. The definition of Nayak parameter, α, is given in Equation (3.4).

To specify the value of the Nayak parameter such that it represents the geometrical properties of a specific surface, the analytic approach proposed by Yastrebov [25] is used. The approach is based on the PSD of the surface and is explained in Appendix B. The PSD of the surface is the Fourier transform of the surface autocorrelation function [141]. In [25, 227] the PSD is assumed to be a power function of the magnitude of the wave vector, i.e., a straight line in the log-log plot which has a lower and upper (wavenumber) cutoffs as expressed in Equation (B.1). He obtained a closed-form expression for the spectral moments by integration (Equation (B.2)).

The standard deviation of heights, σ, and Hurst exponent, H, are assumed to be known. Note that the zeroth spectral moment of the surface is $m_0 = \sigma^2$. Hurst exponent for 3-D surfaces is defined as $H = 3 - D$, where D is the fractal dimension. For real surfaces it is shown [139] that $2 < D < 3$, then $0.7 < H < 1$.

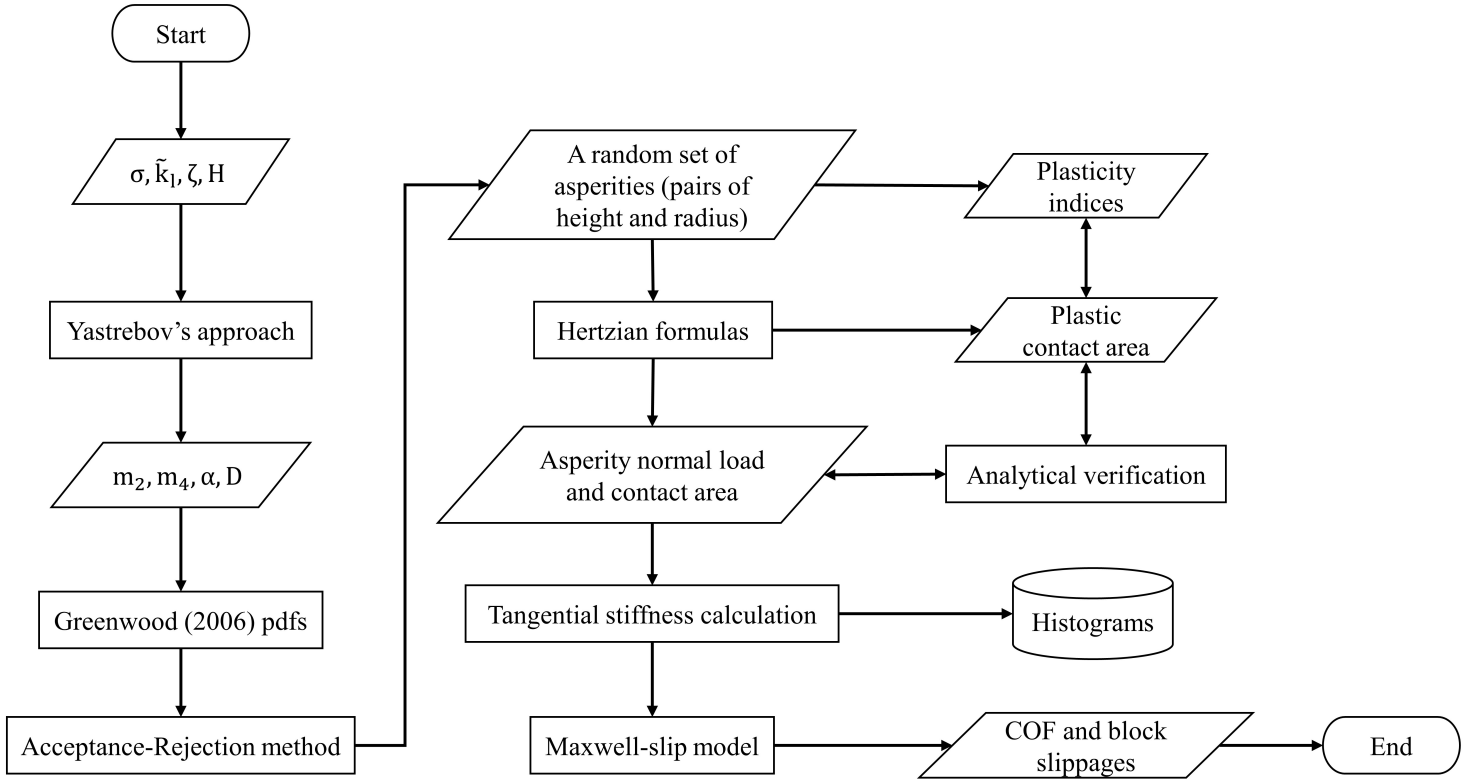

Figure 3.2: Flowchart of Chapter 2 method

By substituting $m_0 = \sigma^2$ into Equation (B.2), the scaling factor of the PSD, ϕ_0 can be obtained. Now, Equation (B.2) can be used to calculate the second and fourth spectral moments, m_2 and m_4. Finally, it is possible to use Equation (3.4).

Now that the PDFs are fully specified, the acceptance-rejection method, a common way of generating random variables from the known PDFs, can be used to obtain a set of pairs of random height and curvature (Appendix D). Firstly, the height values are obtained by using the PDF of heights as given in Appendix in Equation (C.2). Then, the obtained random heights are substituted in Equation (C.2) to find a random curvature corresponding to every one of the already generated heights. Figure C.7 shows that lower height values tend to generate a smaller mean curvature value (a larger radius) for small Nayak parameters. In comparison, higher height values tend to produce sharper tips. For a large enough Nayak parameter, however, the height would not affect the mean curvature value of the asperities much. The number of asperities on the surface, D, is also required. D is given by a formula (Equation (B.8) that is based on Nayak's theoretical approach [24,27]. The number of asperities can be very high in some cases (over millions). Thus, only a fraction of the number is used as the number of generated asperities. In the end, the results are scaled up accordingly.

A numerical procedure is started after the asperity heights and curvatures are generated. The procedure assumes that the asperities are rigid circular paraboloids that are pressed against an elastic half-space. In the beginning, the elastic half-space is in contact with the highest asperity. As compression continues, the other asperities get into contact. Hertzian contact formulas (as shown in Appendix E) are used to obtain the normal load and the contact area of the contacting asperities. Initiation of plastic deformation can be monitored by checking the maximum normal stress and hardness as explained in Appendix F. Furthermore, the "surface" plasticity index, given in [21,27], can be calculated using the generated asperities' average radius (Appendix F). The variation of the total normal load and the total real area with compression is derived in [27]. However, the expressions contain misprints. The corrected form of the expressions (Equations (C.3) and (C.4)) are used to verify the numerical results. An analytical approach to calculate the plastically deformed area is given in [21].

The question of equivalence between a contacting asperity and the Maxwell-slip block-spring unit (Figure 3.3) is considered here. The tangential stiffness of a circular paraboloid asperity can be approximated by using the analytical solution provided in [83] and the Hertzian contact formulas (Appendix E). When a rigid paraboloid is pressed upon an elastic half-space, the contact zone is composed of a sticking central zone with an annular slipping region at its periphery. These are concentric circular regions. When a lateral displacement, u, is applied to the paraboloid, the central sticking circle starts to shrink, and the sliding zone enlarges. This phase is called *partial slip* or *pre-sliding*. At the limit, no sticking zone remains, and *gross sliding* phase starts, i.e., at the onset of sliding, the sticking zone is shrunk to zero.

In [83], a closed-form expression for the lateral displacement is derived. The *maximum* lateral displacement can be obtained by putting the term for stick zone radius equal to zero. If a linear relationship between friction and the lateral displacement is assumed, the tangential stiffness, k_t, of the pair in contact becomes a function of the shear modulus, G, Poisson ratio, ν, and the asperity contact radius, a:

$$k_t = \frac{F_{th}}{u_{max}} = \frac{16}{3}\frac{G}{2-\nu}a = \frac{16}{3}\frac{G}{2-\nu}\sqrt{Rw} \tag{3.6}$$

where R is the paraboloid osculating sphere radius and w is the compression of the asperity or indentation of the half-space by the asperity (Figure 3.3). The above closed-form expression for the asperity's tangential stiffness offers some insight into the dynamics of the block-spring unit, which are discussed in Appendix G.

The asperity heights and radii tips are random variables, and so are the contacting asperities' normal load and tangential stiffness values. These variables would have their own distributions. These distributions change as the compression progresses. In order to have a sense of these distributions, histograms of the asperity normal loads and tangential stiffness values, as well as their ratio, are outputted at some compression values. The normal load and its ratio to the stiffness are also important because these would affect the sliding behavior of the set.

The normal load and stiffness values of the asperities are known and so are those of the block-spring units of the Maxwell-slip model. In other words, every asperity is

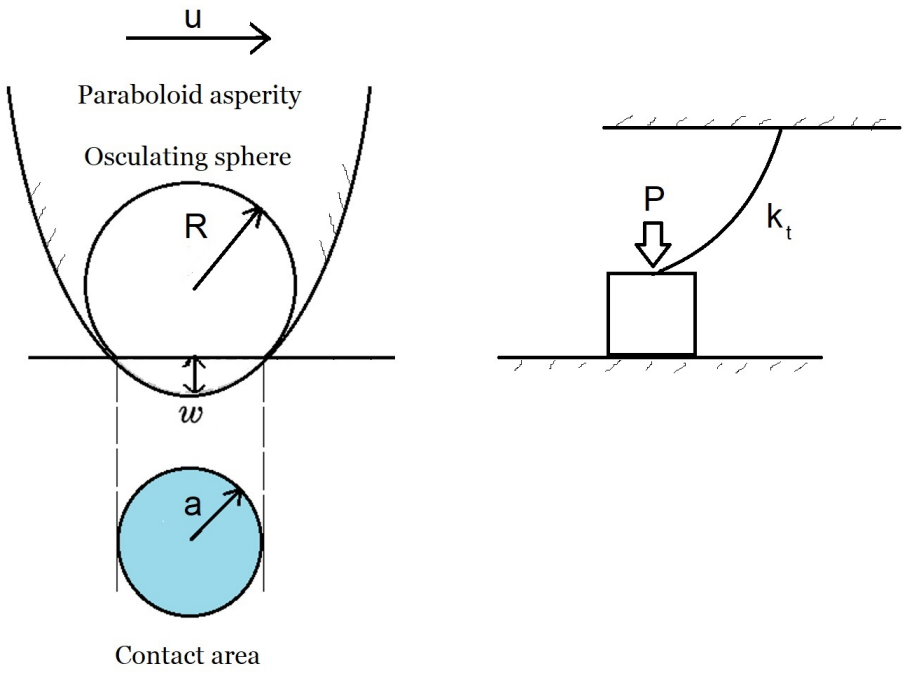

Figure 3.3: The normal and tangential contact of a rigid circular paraboloid asperity with the elastic half-space and its block-spring counterpart

replaced with a block-spring with corresponding load and stiffness. The dynamics of a single block-spring is investigated in Appendix G. In this chapter, it is assumed that when the driver reaches the point at which the block sliding is triggered, the block moves to its destination in no time, i.e., the driver remains fixed during the sliding of the block. The variation of the spring force during its sliding period is not considered. Consequently, the inertial force is ignored. Therefore, the method can be called *quasi-static* in a loose sense. This name is chosen to remark the difference with the *dynamic* approach (used in Chapter 5). Note that the equation of motion is solved in the present approach; however, only the slippage length is used.

Appendix G shows how the frictional behavior of the block-spring unit (its stick-slip) is related to the mechanical and geometrical characteristics of the contacting asperity. From Appendix G it is known that while the normal load on the block determines the maximum force and the force drop, the length of slippage (and therefore the required driver displacement to trigger block sliding) depends on the ratio of the normal load and the tangential stiffness. As shown in Appendix G, the normal load is a function

of both asperity compression and tip radius. On the other hand, the ratio of the normal load and the tangential stiffness is a function of the asperity compression (and not its tip radius). Then, it can be claimed that those block-springs that slide more easily (with less driver motion) and therefore slide more frequently correspond to the asperities that are less pressed.

It is assumed that all the blocks are just beneath their spring-driver attachment point at the beginning. In other words, the initial extension of all of the springs is zero. Since the load and stiffness of every unit are known, the spring force that is experienced by every spring is a known function of the driver position. By noticing this fact, one would not need an algorithm that incrementally moves the driver and checks the spring forces to see whether or which blocks have violated the static friction threshold to decide to move them or not. Instead, the behavior of each block is known in a closed-form, and the total friction force can be calculated simply by superposition. More details about the algorithm of such an alternative approach are available in Appendix G. The friction force is then divided by the total normal force to calculate COF. The variation of COF with the driver position along with the history of the block slippage events describe the overall sliding behavior of Maxwell-slip model as a representative of the set of asperities.

3.3 Results

In this section, the results of the normal and sliding contact of two sets of asperities which are generated by using Nayak parameters $\alpha = 5.15$ and 11.2 are presented. The standard deviation of heights is assumed to be $1\ \mu m$. The normal contact results include the variation of (1) real contact area and normal load with normal compression, (2) real contact area with normal load, (3) percentage of the contacting asperities with compression, (4) real contact area with compression and (5) plastic contact area with compression. The plots of (1), (2) and (5) are superimposed with the existing closed-form solutions for the purpose of validation. The sliding contact results include: (1) the variation of COF with the driver position and its corresponding block slippage history under three different normal compression values and (2) Histograms of the normal load, tangential stiffness, and their ratio for the three different normal

compression values.

In all case studies, the elastic body is assumed to be made of Aluminum with Young modulus of $72\ GPa$ and a Poisson ratio of 0.33. Hardness is $1.52\ GPa$. The nominal contact area is assumed to be a square with edges of $1\ m$ length.

3.3.1 Case 1 ($\alpha = 5.15, \sigma = 1\ \mu m$)

The results presented in Figures 3.4-3.15 are related to Case 1, for which the model parameters are assumed as expressed in the following sentences. The standard deviation, σ, is assumed to be 1 micron. Hurst exponent is equal to 0.75. The dimensionless lower cut-off wavenumber, $\tilde{k}_l$, is assumed to be 256. The cut-off wavenumber ratio, ζ, equals 8. For the above inputs, the Nayak parameter is calculated $\alpha = 5.15$. The spectral moments are $m_0 = 1e-12, m_2 = 7.42e-6, m_4 = 284$. Theoretically, the number of asperities has to be $1,170,336$ according to Equation (B.8). The number of generated asperities is 1000.

In the semi-log plot in Figure 3.4-(a), the ordinates show the variation of contacting real area to the nominal area, A_{real}/A_{nom}, (as a percentage) against the normalized compression, $\delta = d/\sigma$, for Case 1. The nominal area is assumed to be a square with sides of $1m$ in length. Then, the normalized real contact area equals the real contact area. As the rigid rough surface is pressed by the elastic half-space, the real contact area increases.

The solid black line in Figure 3.4-(a) shows the numerical result obtained by summing up the contact area of the members of the set of the generated paraboloid asperities that contact the half-space. These asperities are all generated using the PDFs proposed in Greenwood's work [27]. Hertzian formula (Equation E.1) is used to calculate the contact area for each contacting asperity. The numerical values are obtained by generating only a fraction of the theoretically required number of the asperities (in $1m^2$), which is $1,170,336$ according to Equation (B.8). The results are then scaled up by a factor of $D_{sum}/N_{tot.}$.

The dashed black line in Figure 3.4-(a) represents the closed-form formula for the variation of real contact area with compression. The formula in [27] has a misprint (a

missing multiplier equal to $1/\sqrt{3} = 0.58$) which is corrected in Equation (C.3). The lower limit of the integral on the heights is the position of the half-space, and the upper limit is specified by the height of the highest asperity. The lower and upper limits of the integral on the curvatures are specified by the smallest the largest curvatures of the generated asperities, respectively.

At very small compression values ($\delta < 0.2$), the numerical results agree with the analytical solution even though the number of contacting asperities is not enough for a proper representation of the statistical distribution. For higher compression values ($0.2 < \delta < 2$), the numerical results underestimate the analytical real area by a factor of 2 at worst. Finally, when the compression exceeds a specific limit, here $\delta = 3$, the numerical and analytical results agree reasonably. It should be noted here that for some of the generated sets of asperities, the numerical and analytical results can be far from close. But, even for such cases, when compression is high enough, the results are in good agreement. Increasing the number of generated asperities does not help a better agreement.

In the semi-log plot in Figure 3.4-(b), the ordinates show the variation of normalized nominal normal pressure, $p' = p_{nom}/(E^*\sqrt{2m_2})$, against the normalized compression, $\delta = d/\sigma$, for the same case (Nayak parameter $\alpha = 5.15$, and the height standard deviation, $\sigma = 1\ \mu m$). The nominal area is always assumed to be a square with sides of 1 m in length, then the nominal pressure, p_{nom}, is equal to the normal load. As the rigid rough surface is pressed by the elastic half-space, the normalized nominal pressure increases.

The solid black line in Figure 3.4-(b) shows the numerical result obtained by summing up the normal loads, which are calculated by Hertzian theory for the members of the set of the generated paraboloid asperities that contact the elastic half-space. As explained before, the results are scaled up to account for the theoretical number of the asperities.

The dashed black line in Figure 3.4-(b) represents the closed-form formula for the variation of total normal load with compression. Similar to the analytical formula for real area, the formula that is given for the normal load in [27] has a misprint which is corrected in Equation (C.4). The lower and upper limits of the double integral are

assigned as mentioned for the real area formula. The general trend of increase, Figure 3.4-(b) resembles Figure 3.4-(a).

In Figure 3.5, the variation of real area, A_{real}, (as percent of the nominal area, A_{nom}) with normalized nominal pressure, $p' = p_{nom}/(E^*\sqrt{2m_2})$, is plotted for Case 1 (Nayak parameter $\alpha = 5.15$, and the height standard deviation, $\sigma = 1\ \mu m$). The nominal area is always assumed to be a square with sides of 1 meter in length, then the ratio A_{real}/A_{nom}, is equal to the real area and the nominal pressure, p_{nom}, is equal to the normal load. An increase in the pressure causes an increase in the real contact area.

Indeed, Figure 3.5 enables us to see the relation between the real area and the normal load by eliminating the compression parameter from Figures 3.4-(a) and 3.4-(b). In other words, Figure 3.5 fuses the real area and the normal load into a single graphic and provides the opportunity to compare the results with the theoretical relations proposed in the literature.

The dashed line shows the theoretical relation between the normal load and the real contact area as proposed by the BGT model [26]; the slope equals $\sqrt{2\pi} = 2.5$. On the other hand, the dotted line is the theoretical relation given by Persson's theory, according to which the slope is $\sqrt{8/\pi} = 1.3$ [28, 205]. These theoretical results are used in the literature to verify the numerical results of the normal contact for the asperity-based models [7, 25, 145]. The results are assessed as reasonable if the slope remain between that of BGT and Persson for low pressure values, i.e., for $0 < p' < 0.06$ [25]. A range of theoretical methods predicts a linear relationship between the normal load and real area under small loads [228].

The solid black line shows the numerical result obtained from the set of the generated paraboloid asperities. The ordinate represents the total contact area, and the abscissa shows the total normal load experienced by the asperities in contact with the elastic half-space. When the normal load is low enough, the slope of the curve is nearly the same as that of the BGT model. As the normal load increases, the slope of the curve drops gradually and tends to the slope proposed by Persson's theory.

The solid grey line represents the results of the analytical formulas, which are derived

for the real contact area and the normal load. Although the formulas in [27] have a missed factor (Appendix C), it would not affect the load-area curve because the forgotten part is the same multiplier, $1/\sqrt{3} = 0.58$, for both the load and area. The lower limit of the integral on the heights is the position of the elastic half-space surface, and the upper limit is specified by the height of the highest asperity. The lower and upper limits of the integral on the curvatures are specified by the smallest the largest curvatures of the generated asperities, respectively. At low normal loads, the grey curve coincides with BGT and the numerical results. As the load increases, the grey curve diverges from the numerical values, but its slope is still above Persson's proposed slope. Although for different sets of generated asperities, the black and grey lines change to some extent, their slopes remain persistently between the theoretical bounds.

In Figure 3.6, the increase of the number of contacting asperities (as a percentage of the total number of the asperities, which is a thousand) with the normalized compression, δ, is plotted for set of generated asperities in Case 1 (Nayak parameter $\alpha = 5.15$, and the height standard deviation, $\sigma = 1\ \mu m$). The curve resembles Gaussian cumulative PDF, which was expected since the probability of the asperities above a certain height is proportional to the number of the contacting asperities.

The blue line in Figure 3.6 rises very slowly after contact with the highest asperity. Up to one standard deviation of compression, i.e., $\delta = 1$, only 5.7% of the asperities have gotten into contact and pressed. After $\delta = 1$, the rate of increase of the number of asperities that contact the elastic half-space becomes higher and higher such that at two standard deviation of compression, i.e., $\delta = 2$, the percentage of the contacting asperities is 44.4%. After $\delta = 2$, the rate of increase in contacting asperities with compression remains almost contact. The slope of the linear rise within $2 < \delta < 3$ is nearly equal to 60% per unit δ. At $\delta = 3.05$, all of the thousand asperities have made contact, and higher compressions will not increase the percentage of the contacting asperities. Therefore, the curve reaches a plateau. It may seem unreasonable to have all of the generated asperities in contact at $\delta = 3$. However, note that as shown in Figure C.1, for low Nayak parameters, the PDF of heights is non-Gaussian, and the generated heights are within a tighter interval compared to Gaussian distribution (for which the interval extends over six standard deviations).

In Figure 3.7, the increase of the real contact area with the number of contacting asperities (as a percentage) is plotted for the set of generated asperities in Case 1 (Nayak parameter $\alpha = 5.15$, and the height standard deviation, $\sigma = 1\ \mu m$). Up to a point with an abscissa of 40%, the curve can be assumed linear with a good approximation. The point corresponds to $\delta = 2$ as can be read from Figure 3.6. For the higher percentages of the contacting asperities, which correspond to $2 < \delta < 3$, the rate of increase in the real contact increases. It seems that a parabola can be fitted to the points with an abscissa higher than 40%.

In Figure 3.8, it is shown that according to both numerical and analytical results, up to $\delta = 6$ no plastic deformation initiates in Case 1 (Nayak parameter $\alpha = 5.15$, and the height standard deviation, $\sigma = 1\ \mu m$). In other words, all members of the set of contacting asperities deform elastically even when the compression reaches six standard deviations according to the numerical and analytical approaches. The numerically calculated plastic area is shown in black and lays just under the analytical records, shown in cyan, at zero.

These results are in agreement with the plasticity indices calculated by using Equations (F.5) and (F.8) as proposed in [21] and [27], respectively. Note that the average radius of all asperities, which is equal to $5.23\ cm$ for the set of generated asperities, is used to calculate the plasticity indices. The calculated plasticity indices are 0.23 and 0.14, both are well below 0.5 and therefore no plasticity is expected theoretically.

In Figure 3.9-(a), the variation of COF with the normalized driver position is shown for a subset of generated asperities in Case 1 (Nayak parameter $\alpha = 5.15$, and the height standard deviation, $\sigma = 1\ \mu m$) that is pressed one standard deviation of the set heights down, i.e., $\delta = 1$. The number of contacting asperities (the members of the subset) is 57 at $\delta = 1$. The contacting asperities are modeled as mass-spring units of the Maxwell-slip model, as explained previously. The COF curve is almost linear at the onset of the movement of the driver. Later, small force drops appear on the curve, and the slope (one may say total stiffness) decreases, i.e., the curve does not continue to rise as fast as it began. After reaching the dynamic COF, the curve fluctuates about μ_d. The curve is not tangent to the horizontal line of μ_d.

In Figure 3.9-(b), the point at which slippage of each contacting asperity is triggered

is marked with a red dot for the set of mass-spring blocks that correspond to Case 1 (Nayak parameter $\alpha = 5.15$, and the height standard deviation, $\sigma = 1\ \mu m$) at $\delta = 1$. The abscissas show the normalized position of the driver (as in Figure 3.9-(a)). The ordinates show the block number (the mass-spring unit identifiers). As the driver starts to move 5 blocks slide immediately. This is implied by the red horizontal "lines" that correspond to the block numbers 18, 25, 29, 37 and 39. These are the most frequently sliding blocks. Further movement of the driver causes slippage of the blocks that are harder to trigger, i.e., those block whose corresponding asperities are pressed less. For such blocks, the distance between the red dots is longer. To summarize, the asperities that are pressed more slide later and wait more for their next slippage, e.g., block number 42. Conversely, the asperities that are pressed less slide sooner and wait less for the next slippage, e.g., block number 39.

The slippages of the frequently sliding blocks do not affect the COF curve in Figure 3.9-(a) much since the curve keeps rising linearly despite these frequent slippages. It can be claimed that the load drops due to the slippage of the infrequently-sliding blocks make the COF curve nonlinear after $\delta = 0.5$.

The histograms of the normal loads, tangential stiffness, and the load-to-stiffness ratio for the set of generated asperities of Case 1 (Nayak parameter $\alpha = 5.15$, and the height standard deviation, $\sigma = 1\ \mu m$) that are in contact when $\delta = 1$ are shown in Figures 3.10-(a), 3.10-(b) and 3.10-(c). The number of contacting asperities (the members of the subset) is 57 at $\delta = 1$. Since the number of contacting asperities is small compared to the total number of the generated asperities (only 5.7%), the histograms are coarse and represent the distributions only roughly. In Figure 3.10-(a), 70% of the contacting asperities, i.e., 40 of them, experience the lowest amount of normal load. The remaining percentage is distributed among the higher load-value bins. These bins have quite a smaller number of asperities (6 and below). In Figure 3.10-(b), the percent of asperities with a certain stiffness is relatively low, then rises sharply and later falls steeply, remaining below 5% for the upper half of the stiffness range. Figure 3.10-(c) shows that over 55% of contacting asperities have the lowest load-to-stiffness ratio. Equation (G.5) shows that the load to stiffness ratio is a product of a constant multiplier and the single asperity compression (the multiplicand). Then, the distribution of the ratio is expected to resemble the tail of the height distribution.

In Figure 3.11-(a), the variation of COF with the normalized driver position is shown for a subset of generated asperities in Case 1 (Nayak parameter $\alpha = 5.15$, and the height standard deviation, $\sigma = 1\ \mu m$) that is pressed two standard deviation of the set heights down, i.e., $\delta = 2$. The number of contacting asperities (the members of the subset) is 444 at $\delta = 2$. As explained previously, the contacting asperities are modeled as mass-spring units of the Maxwell-slip model.

The COF curve is almost linear at the onset of the movement of the driver. Later, COF diverges from its linear trend, and the curve does not continue to rise as fast as the linear part. Total stiffness decreases. The curve approaches the horizontal line of μ_d smoothly, becomes its tangent, and continues constructing a plateau. Before and after reaching the dynamic COF, the curve fluctuates a little.

In Figure 3.11-(b), every red dot marks the driver position at which the slippage of each contacting asperity is triggered for the set of mass-spring blocks that correspond to Case 1 (Nayak parameter $\alpha = 5.15$, and the height standard deviation, $\sigma = 1\ \mu m$) at $\delta = 2$. The abscissas show the normalized position of the driver (as in Figure 3.11-(a)). The ordinates show the block number (the mass-spring unit identifiers).

Many blocks remain stuck at the beginning of the driver's movement. No red dot is put for these blocks, e.g., block numbers 60-90. These blocks take more "time" to be triggered. It can be said that the corresponding asperities of these blocks are pressed relatively more than others. Furthermore, these blocks have distant red dots. On the other hand, the frequently sliding blocks seem like red lines, e.g., block number 151. These mass-spring units correspond to the asperities, which are compressed less than the others (Appendix G).

The slippages of the frequently sliding blocks do not affect the COF curve in Figure 3.11-(a) much since, initially, the curve keeps rising linearly despite these frequent slippages. It can be claimed that the load drops due to the slippage of the infrequently-sliding blocks make the COF curve nonlinear after $\delta = 0.25$.

The histograms of the normal loads, tangential stiffness, and the load-to-stiffness ratio for the set of generated asperities of Case 1 (Nayak parameter $\alpha = 5.15$, and the height standard deviation, $\sigma = 1\ \mu m$) that are in contact when $\delta = 2$ are shown

in Figures 3.12-(a), 3.12-(b) and 3.12-(c). The number of contacting asperities (the members of the subset) is 444 at $\delta = 2$. The number of contacting asperities is 44.4% of the generated asperities. In Figure 3.12-(a), 48% of the contacting asperities, i.e. 213 out of 444, experience the lowest normal load. The higher load bins have smaller percentages asperities (below 20%). In Figure 3.12-(b), the percentage of asperities that have a certain stiffness is firstly relatively low (below 5%), then rises gradually to over 20% and later falls firstly slowly and then steeply to 5% and below for the stiffness values higher than $20\ kN/mm$. Some bins of higher stiffness do not have any members. Figure 3.12-(c) shows a general trend of decrease when the load-to-stiffness ratio increases and constructs a Gaussian-like tail (and "half" of the bell) as expected.

In Figure 3.13-(a), the variation of COF with the normalized driver position is shown for a subset of generated asperities in Case 1 (Nayak parameter $\alpha = 5.15$, and the height standard deviation, $\sigma = 1\ \mu m$) that is pressed three standard deviation of the set heights down, i.e. $\delta = 3$. The number of contacting asperities (the members of the subset) is 998 at $\delta = 3$. The contacting asperities are modeled as mass-spring units of the Maxwell-slip model as explained previously. The COF curve is almost linear at the onset of the driver's movement and later diverges from its linear trend, falling to rise at the same rate. One may say total stiffness decreases. The curve approaches the horizontal line of μ_d gradually and becomes tangent to it, and forms a plateau. The fluctuations of the curve are quite small.

In Figure 3.13-(b), the red dots mark the driver positions at which the slippage of each contacting asperity is triggered for the set of mass-spring blocks that correspond to the contacting asperities which are generated for Case 1 (Nayak parameter $\alpha = 5.15$, and the height standard deviation, $\sigma = 1\ \mu m$) at $\delta = 3$. The abscissas show the normalized position of the driver (as in Figure 3.13-(a)). The ordinates show the block number (the mass-spring unit identifiers). Most of the blocks remain stuck at the beginning of the driver's movement. No red dot is put for these blocks, e.g., the block numbers 200-400 and 800-900. These blocks take more time than others for their first slippage and wait more for their subsequent slippages. The corresponding asperities of these blocks are pressed relatively more than others. On the other hand, the frequently sliding blocks seem as red lines, e.g., block numbers 20 and 42. These

mass-spring units correspond to the asperities that are compressed less than the others. The slippages of the frequently sliding blocks do not affect the COF curve in Figure 3.13-(a) much since, initially, the curve keeps rising linearly in spite of these frequent slippages. It can be claimed that the load drops due to the slippage of the infrequently-sliding blocks, e.g., block number 46, make the COF curve nonlinear after $\delta = 0.75$.

The histograms of the normal loads, tangential stiffness, and the load-to-stiffness ratio for the set of generated asperities of Case 1 (Nayak parameter $\alpha = 5.15$, and the height standard deviation, $\sigma = 1\ \mu m$) that are in contact when $\delta = 3$ are shown in Figures 3.14-(a), 3.14-(b) and 3.14-(c). The number of contacting asperities (the members of the subset) is 998 at $\delta = 3$. The number of contacting asperities is 99.8% of the generated asperities.

In Figure 11-(a), about 50% of the contacting asperities, i.e., 220 out of 444, experience the lowest amount of normal load (below $20\ N$) in the first two bins. The percentages of the asperities drop abruptly for the bins above $50\ N$. In Figure 3.14-(b), the percentage of asperities that have a certain stiffness is firstly very low (below 5%), then rises fastly to over 15% and later falls again below 5%, forming a fat tail. Some bins of higher stiffness are empty. Figure 3.14-(c) shows a non-Gaussian distribution for the load-to-stiffness ratio similar to that of the height distribution as expected.

Figure 3.15 shows Figure 3.9-(a), 3.11-(a) and 3.13-(a) superimposed. The variation of COF with the normalized driver position is shown for subsets of generated asperities in Case 1 (Nayak parameter $\alpha = 5.15$, and the height standard deviation, $\sigma = 1\ \mu m$) that are pressed by three different compression values, $\delta = 1, 2, 3$. The number of contacting asperities (the members of the subset) is 57, 444, and 998, respectively. All of the curves are almost linear at the onset of the driver's movement and later diverge from the linear trend, falling to rise at the same rate. One may say that for all of the compression values, total stiffness decreases as the driver moves forward. The curves reach a plateau at μ_d. The fluctuations of the curves become smaller with the increase in compression. A lower compression, δ, leads to a faster rise to the plateau. This seems reasonable because when a set of asperities is pressed less, by intuition, a shorter movement of the driver is enough to end the pre-sliding behavior. In other words, the driver needs less "time" under lower compression values

to reach the plateau of dynamic friction. Conversely, for a set that is pressed more, the driver has to “try” more to trigger slippage of all of the mass-spring units, and the curve rises slower.

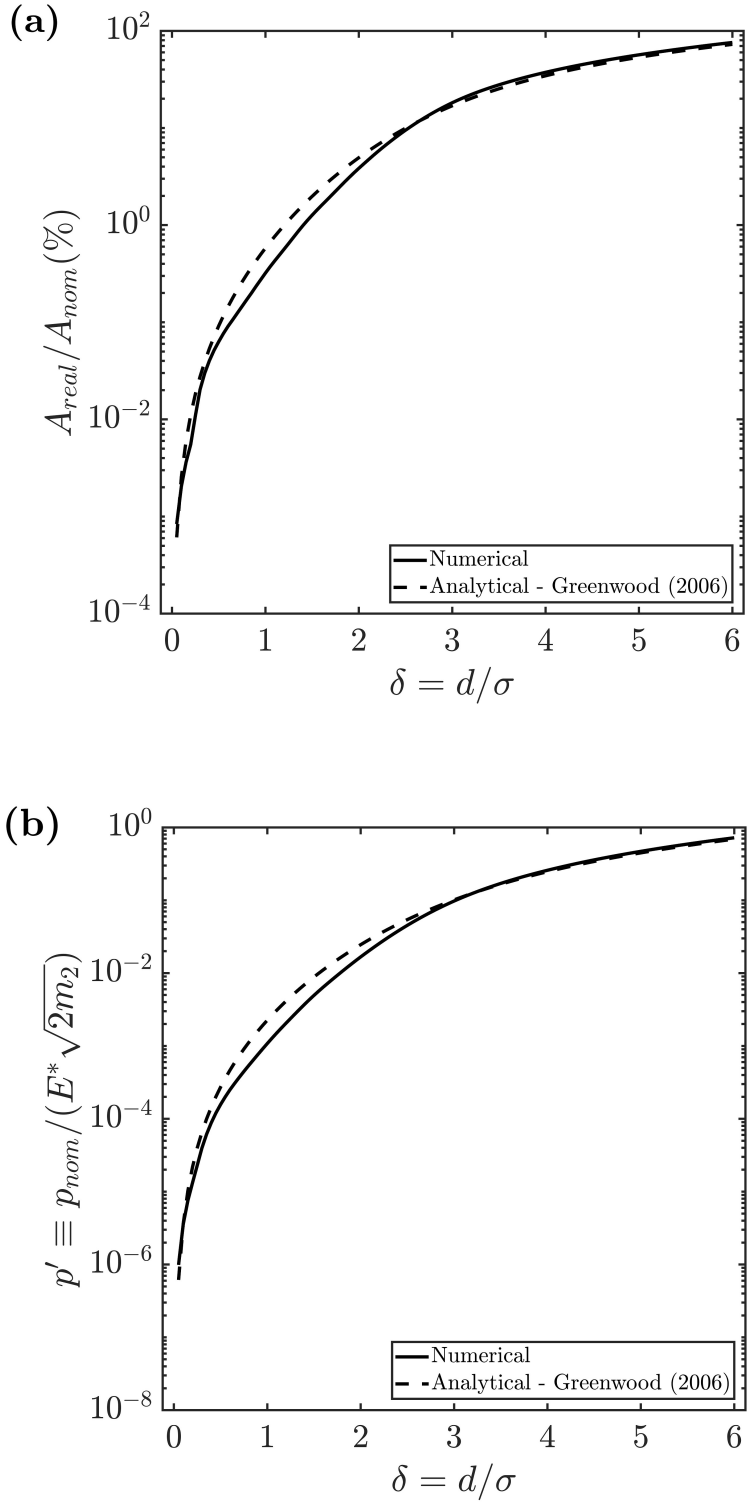

Figure 3.4: The numerical and analytical (a) real contact area and (b) pressure against compression for Case 1 ($\alpha = 5.15$ and $\sigma = 1\ \mu m$).

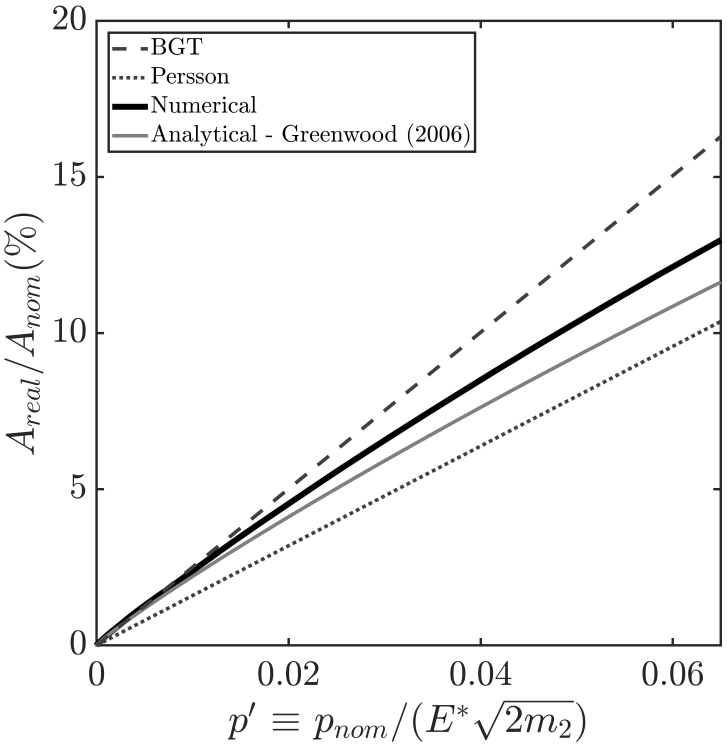

Figure 3.5: The numerical and analytical relation between real contact area and pressure is superimposed with the theoretical limits proposed by BGT and Persson for Case 1 ($\alpha = 5.15$ and $\sigma = 1\ \mu m$).

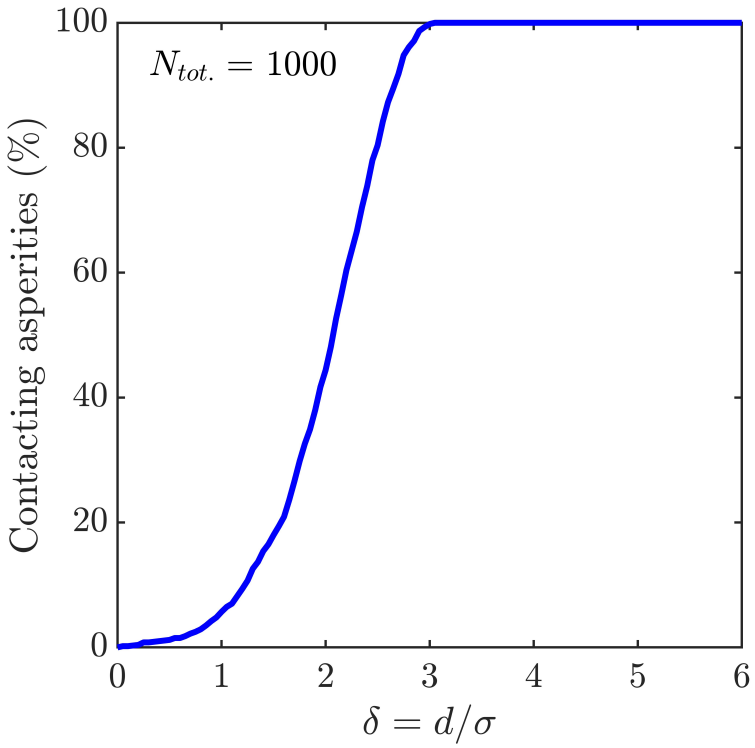

Figure 3.6: The number of contacting asperities as percentage of the total number of generated asperities against compression for Case 1 ($\alpha = 5.15$ and $\sigma = 1\ \mu m$) according to the numerical results.

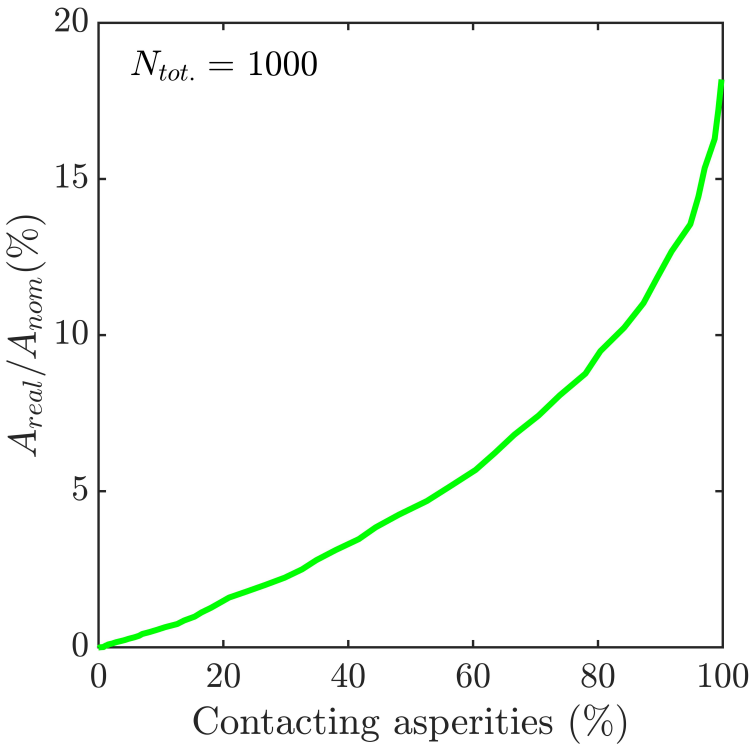

Figure 3.7: Real contact area against the percentage of the contacting asperities for Case 1 ($\alpha = 5.15$ and $\sigma = 1\ \mu m$) according to the numerical results.

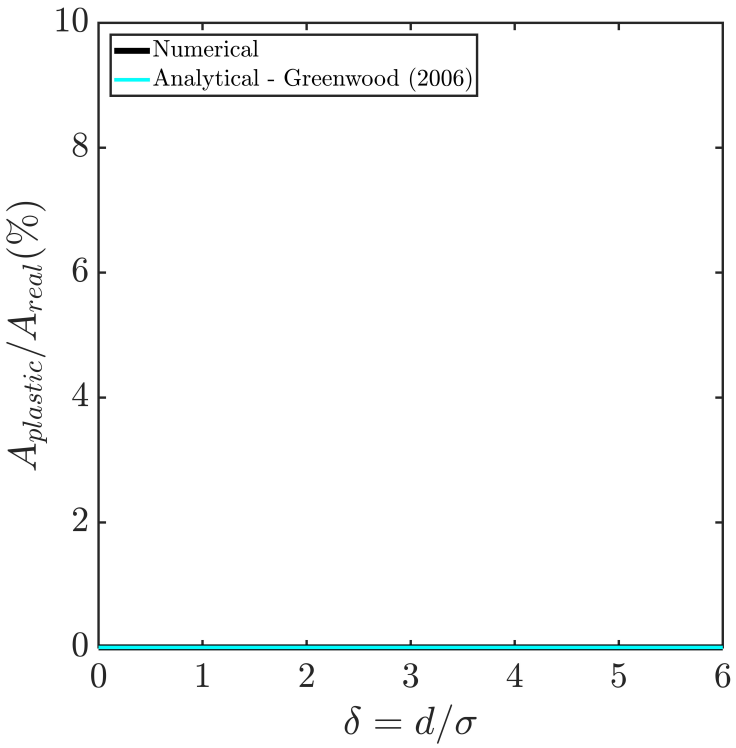

Figure 3.8: Plastic contact area against compression for Case 1 ($\alpha = 5.15$ and $\sigma = 1\ \mu m$) according to the numerical and analytical results.

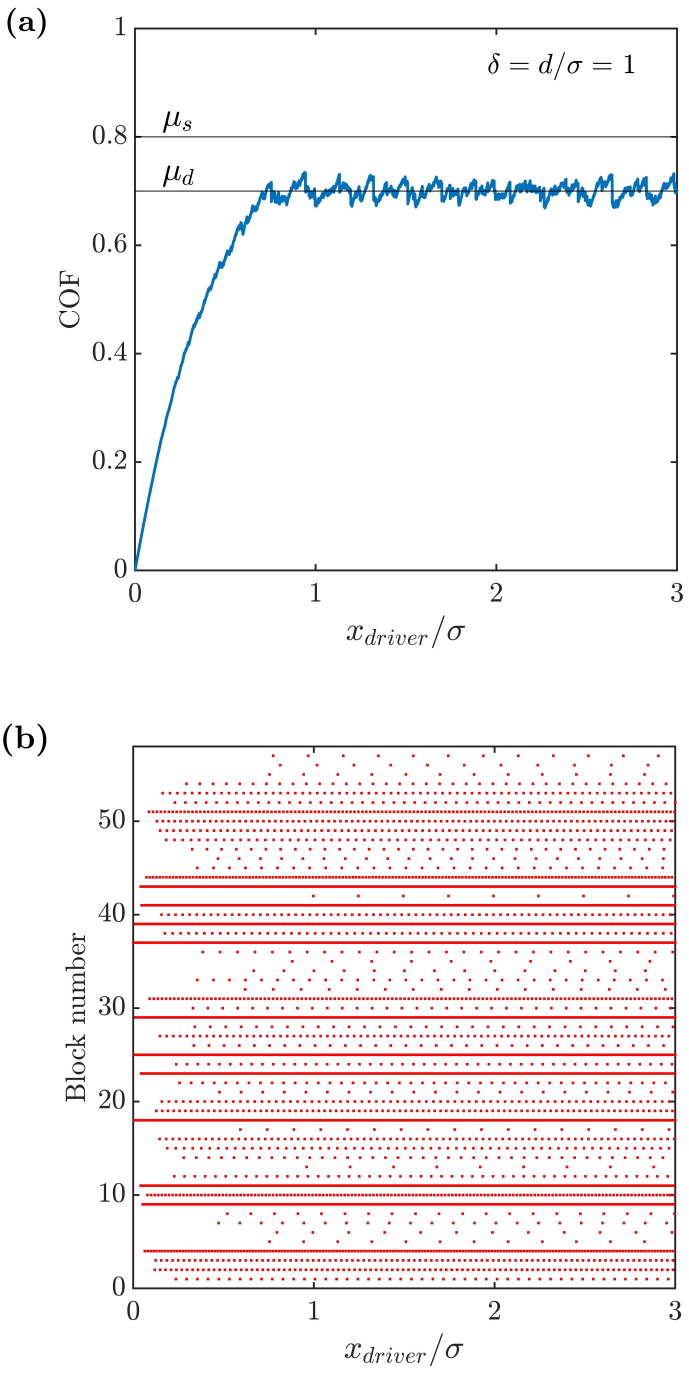

Figure 3.9: The numerical results for sliding at $\delta = 1$ for Case 1 ($\alpha = 5.15$ and $\sigma = 1\ \mu m$): (a) COF against the driver position and (b) Block slippage history against the driver position.

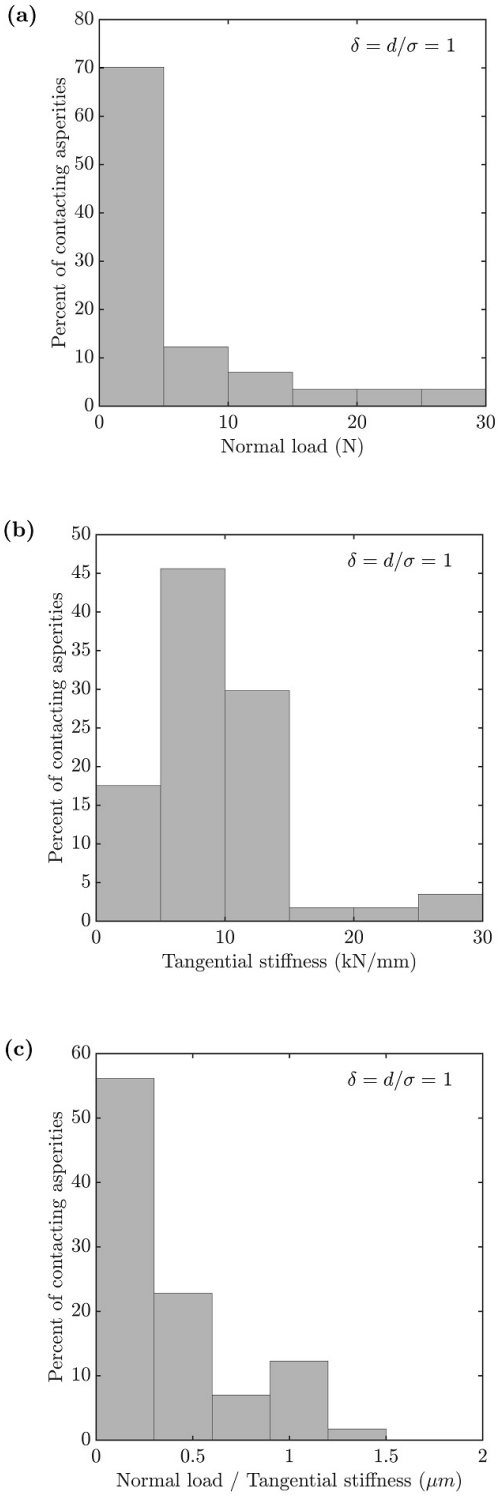

Figure 3.10: Histograms of (a) normal load (b) tangential stiffness and (c) load to stiffness ratio for Case 1 ($\alpha = 5.15$ and $\sigma = 1\ \mu m$) at $\delta = 1$.

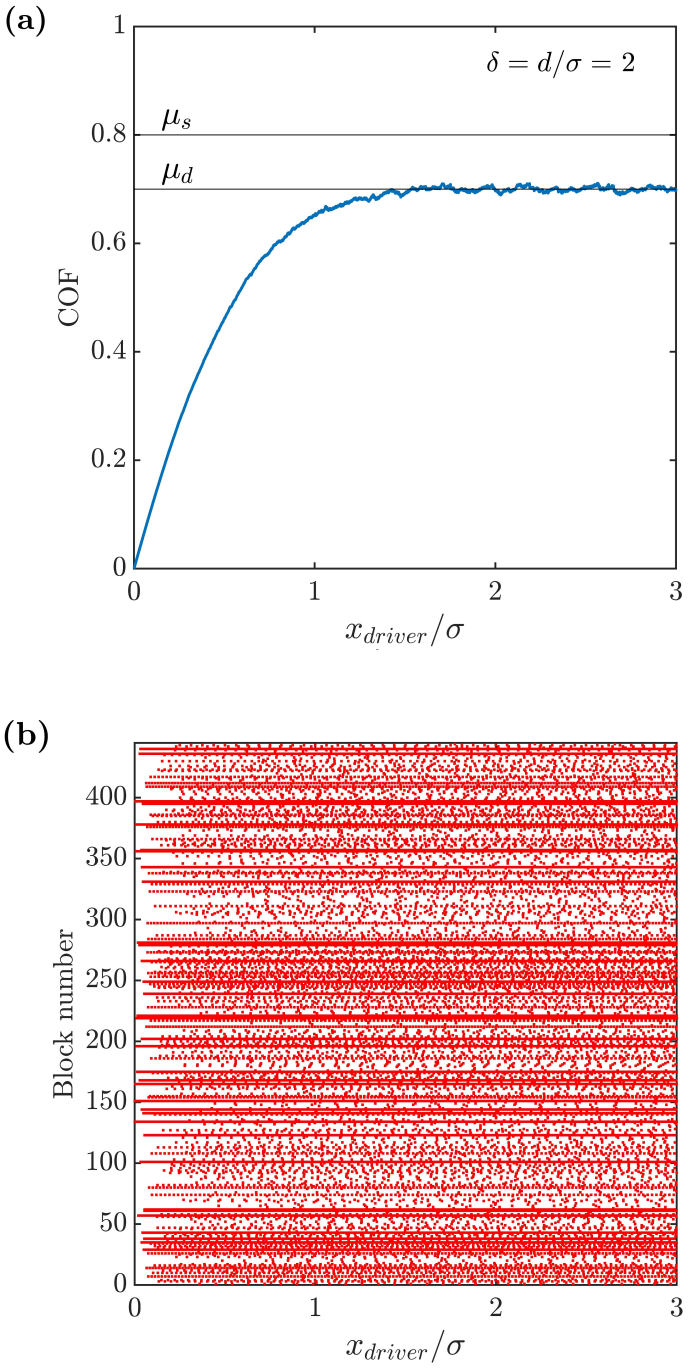

Figure 3.11: The numerical results for sliding at $\delta = 2$ for Case 1 ($\alpha = 5.15$ and $\sigma = 1\ \mu m$): (a) COF against the driver position and (b) Block slippage history against the driver position.

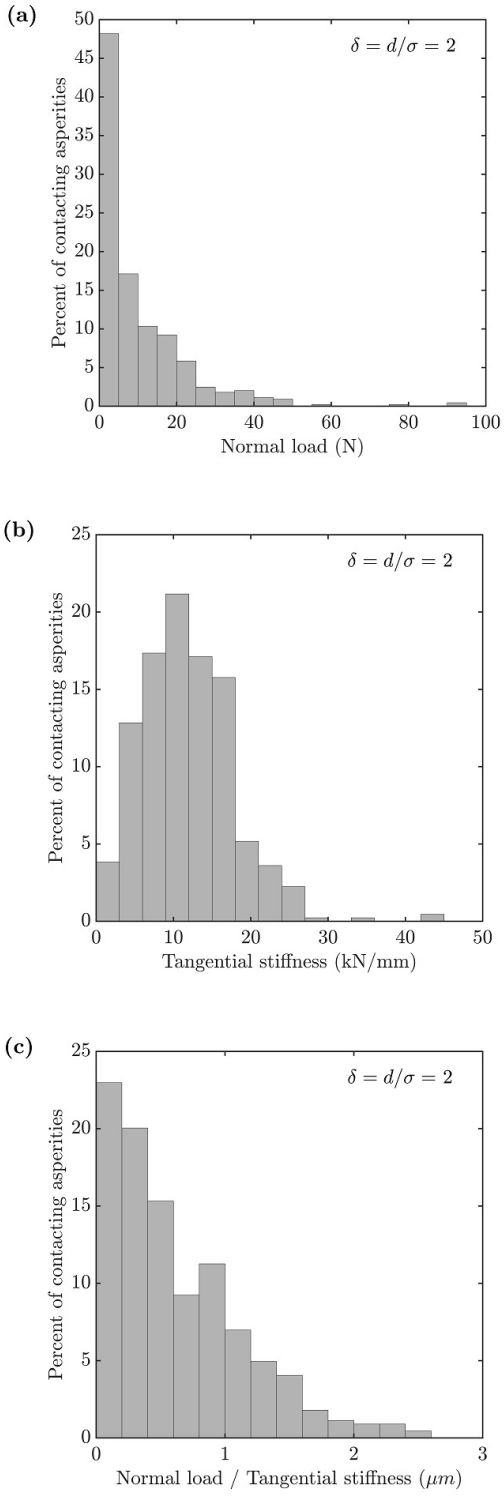

Figure 3.12: Histograms of (a) normal load (b) tangential stiffness and (c) load to stiffness ratio for Case 1 ($\alpha = 5.15$ and $\sigma = 1\ \mu m$) at $\delta = 2$.

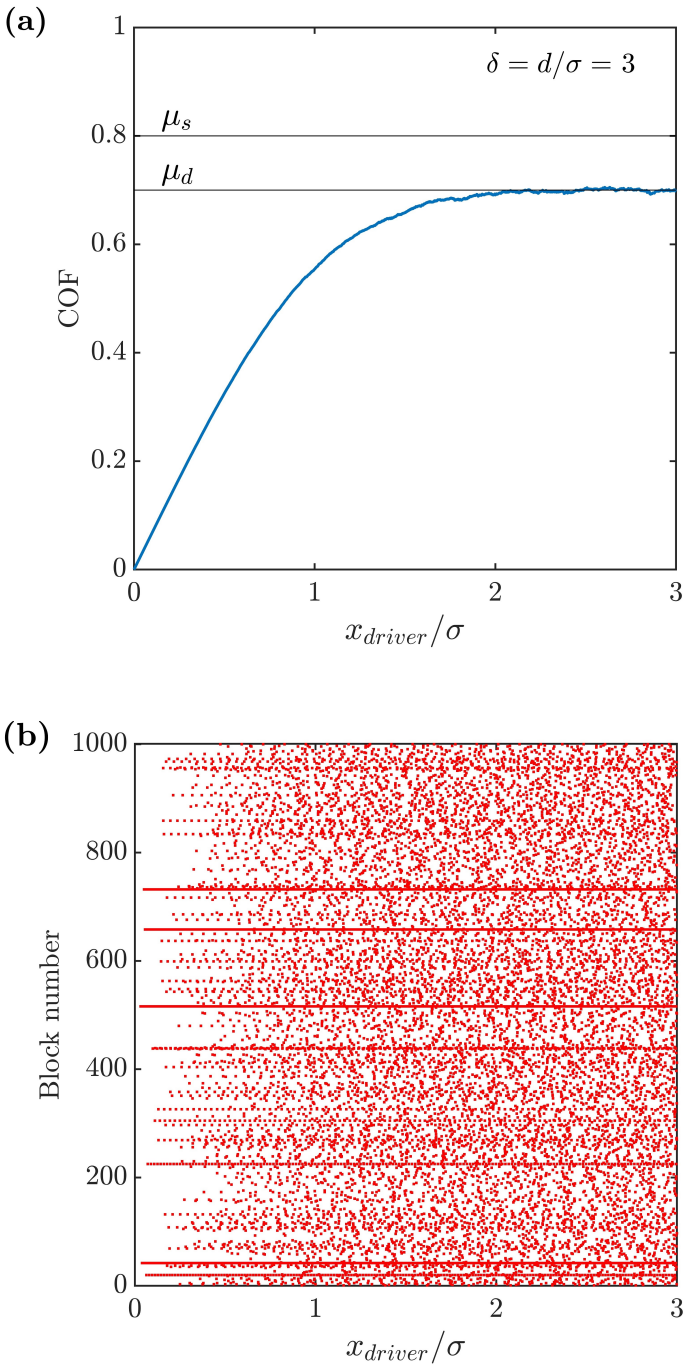

Figure 3.13: The numerical results for sliding at $\delta = 3$ for Case 1 ($\alpha = 5.15$ and $\sigma = 1\ \mu m$): (a) COF against the driver position and (b) Block slippage history against the driver position.

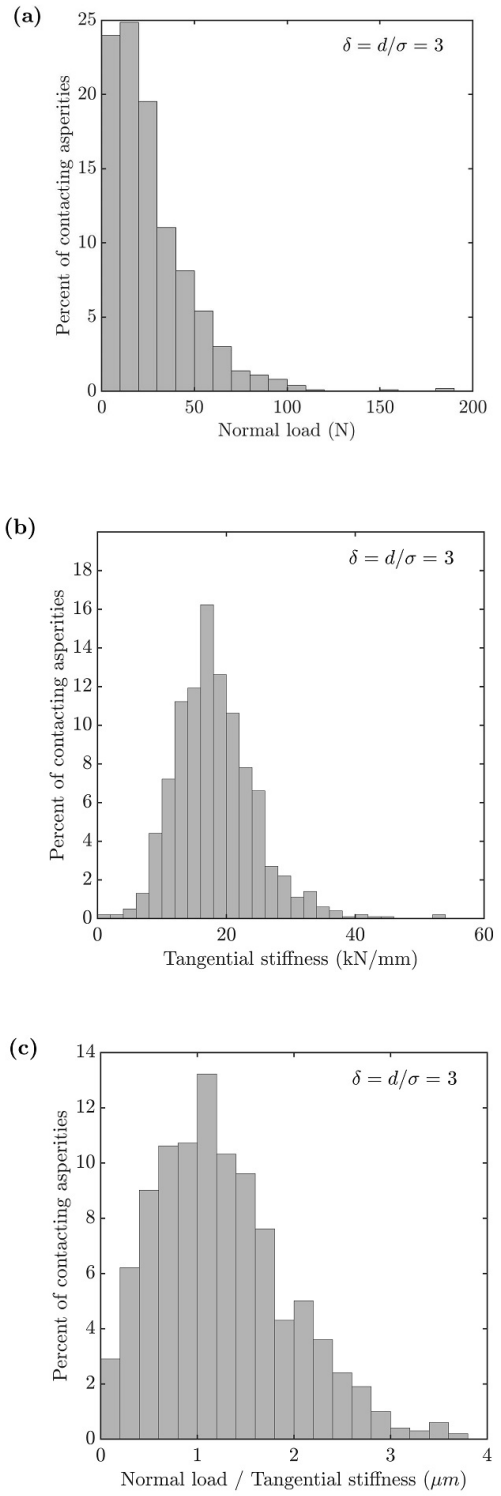

Figure 3.14: Histograms of (a) normal load (b) tangential stiffness and (c) load to stiffness ratio for Case 1 ($\alpha = 5.15$ and $\sigma = 1\ \mu m$) at $\delta = 3$.

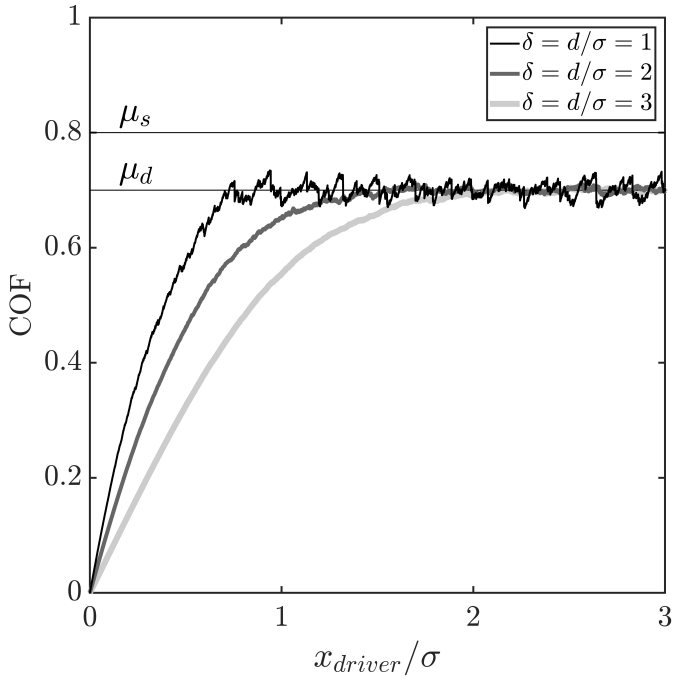

Figure 3.15: The numerical results for sliding under different compression values, $\delta = 1, 2, 3$, for Case 1 ($\alpha = 5.15$ and $\sigma = 1\ \mu m$)

3.3.2 Case 2 ($\alpha = 11.2, \sigma = 1\ \mu m$)

The series of results that are presented in Figures 3.16-3.27 are related to Case 2, for which the input parameters are as follows. The standard deviation, σ, is assumed to be 1 micron. Hurst exponent is equal to 0.75. The dimentionless lower cut-off wavenumber, $\tilde{k}_l$, is assumed to be 256. The cut-off wavenumber ratio, ζ, is assumed 16. For the above inputs Nayak parameter is calculated $\alpha = 11.2$. The spectral moments are: $m_0 = 1e-12, m_2 = 1.18e-5, m_4 = 1570$. Theoretically, the number of asperities has to be $4,053,438$ according to Equation (B.8). The number of generated asperities is 1000.

In the semi-log plot in Figure 3.16-(a), the ordinates show the variation of contacting real area to the nominal area, A_{real}/A_{nom}, (as a percentage) against the normalized compression, $\delta = d/\sigma$, for Case 2. The nominal area is assumed to be a square with sides of 1 meter length. Then, the normalized real contact area is equal to the real contact area. As the rigid rough surface is pressed by the elastic half-space, the real contact area increases.

The black solid line in Figure 3.16-(a) shows the numerical result obtained by summing up the contact area of the members of the set of the generated paraboloids asperities as explained in Case 1. The numerical values are obtained by generating only a fraction of the theoretically required number of the asperities (in 1 m^2), which is 4,053,438 according to Equation (B.8). The results are then scaled up by a factor of $D_{sum}/N_{tot.}$.

The dashed black line in Figure 3.16-(a) represents the corrected version of the closed-form formula for variation of real contact area with compression according to Equation (C.3). The limits of double the integral are specified as in Case 1. In contrast to the results of Case 1 (in Figure 3.4-(a)), Case 2 is capable of generating numerical results that agree with the closed-form solution over the whole range of compression values up to $\delta = 6$ (except very low compressions). It should be noted that for some of the generated sets of asperities the numerical and analytical results can be far from close. Increasing the number of generated asperities does not prevent such disagreements.

In the semi-log plot in Figure 3.16-(b), the ordinates show the variation of normalized nominal normal pressure, $p' = p_{nom}/(E^*\sqrt{2m_2})$, against the normalized compression, $\delta = d/\sigma$, for Case 2 (Nayak parameter $\alpha = 11.2$, and the height standard deviation, $\sigma = 1\ \mu m$). The nominal area is always assumed to be an square with sides of 1 meter length, then the nominal pressure, p_{nom}, is equal to the normal load. As the rigid rough surface is pressed by the elastic half-space, the normalized nominal pressure increases.

The black solid line in Figure 3.16-(b) shows the numerical results obtained by summing up the normal loads for the generated asperities. The results are scaled up to account for the theoretical number of the asperities as explained before. The dashed black line represents the closed-form solution as mentioned for Case 1. The numerical and analytical results agree to a great extent for the whole range of compression. The trend of increase in Figure 3.16-(b) resembles that in Figure 3.16-(a).

In Figure 3.17, the variation of real area, A_{real}, (as percent of the nominal area, A_{nom}) with normalized nominal pressure, $p' = p_{nom}/(E^*\sqrt{2m_2})$, is plotted for Case 2 (Nayak parameter $\alpha = 11.2$, and the height standard deviation, $\sigma = 1\ \mu m$). The nominal area is always assumed to be an square with sides of 1 meter length, then the ratio A_{real}/A_{nom}, is equal to the real area and the nominal pressure, p_{nom}, is equal to the normal load. Increase in the pressure causes increase in the real contact area.

The dashed line in Figure 3.17 shows the theoretical relation between the normal load and the real contact area as proposed by the BGT model [26]. On the other hand, the dotted line is the theoretical relation that is given by Persson's theory [28, 205].

The black solid line in Figure 3.17 shows the numerical result which are obtained from the set of the generated asperities. The ordinates represent the total contact area and the abscissas show the sum of normal load that is experienced by the contacting asperities. At low normal loads the slope of the curve is almost the same as that of BGT model. As the normal load increases the slope of the curve decreases gradually from BGT slope and tends to the slope proposed by Persson's theory.

The grey solid line in Figure 3.17 is obtained using the corrected form of the analytical formulas that are derived for the real contact area and the normal load in Equations

(C.3) and (C.4), respectively. At low normal loads the grey curve coincides with BGT and the numerical results. When p' passes 0.01, the grey curve begins to diverge from that of BGT model but its slope remains above Persson's proposed slope.

In Figure 3.18, increase of the number of contacting asperities (as percent of the total number of the asperities, which is a thousand) with the normalized compression, δ, is plotted for set of generated asperities in Case 2 (Nayak parameter $\alpha = 11.2$, and the height standard deviation, $\sigma = 1\ \mu m$). The increase curve resembles Gaussian cumulative.

The blue line in Figure 3.18 starts to rise very slowly after contact of the highest asperity. Up to one standard deviation of compression, i.e., $\delta = 1$, only 3.2% of the asperities have gotten into contact and pressed. After $\delta = 1$, the rate of increase of the number of asperities that contact the elastic half-space increases. At two standard deviation of compression, i.e., $\delta = 2$, the percentage of the contacting asperities is 27.7% and at $\delta = 3$, it increases to 83.6%. within $2 < \delta < 3$ the rate of increase in the number of contacting asperities remains almost the same. The slope of the linear rise is nearly equal to 56% per unit δ. At $\delta = 3.6$, all of the thousand asperities are in contact and higher compression values will not increase the percentage of the contacting asperities. Therefore, the curve reaches a plateau.

In Figure 3.19, increase of the real contact area with the number of contacting asperities (as a percentage) is plotted for the set of generated asperities in Case 2 (Nayak parameter $\alpha = 11.2$, and the height standard deviation, $\sigma = 1\ \mu m$). Up to the point (42%, 5.7%), the curve can be assumed linear with a good approximation. The point corresponds to $\delta = 1.22$ as can be read from Figure 3.18. For the higher percentages of the contacting asperities, the rate of increase in the real contact is higher.

Figure 3.20 shows the evolution of the normalized plastic area, $A_{plastic}/A_{real}$, (expressed in percent) with compression according to both numerical and analytical results for Case 2 (Nayak parameter $\alpha = 11.2$, and the height standard deviation, $\sigma = 1\ \mu m$). The black line corresponds to the numerical results and predicts initiation of plasticity at $\delta = 3.7$. The numerical $A_{plastic}/A_{real}$ seems to remain constant just after the initiation (and even decrease slightly). This is because the real contact area (the denominator) increases at the same rate (or slightly faster). After $\delta = 4.3$,

the black line pursues a distinct trend of increasing which reaches the critical percent of plastic area, 2%, that is proposed by [21] at $\delta = 5.4$. The limit is marked with the vertical red line. On the other hand, the cyan line represents the analytical result for the evolution of plastic area and predicts no initiation of the contact area up to $\delta = 6$. Note that in the analytical formula the average radius of the asperities, which is equal to $5.23\ cm$ for the set of generated asperities, is used. This value is also used to calculate the plasticity indices by using Equations (F.5) and (F.8) as proposed in [21] and [27], respectively. The calculated plasticity indices are 0.35 and 0.18, which are below 0.5 and therefore theoretically no plasticity is expected. The plasticity in the numerical results can be related to using the variable radii of the asperities in contrast to using the average in the analytical method and the calculation of the plasticity indices.

Figure 3.21-(a) shows the variation of COF with the normalized driver position for a subset of generated asperities in Case 2 (Nayak parameter $\alpha = 11.2$, and the height standard deviation, $\sigma = 1\ \mu m$) that is pressed one standard deviation of the set heights down, i.e. $\delta = 1$. The number of contacting asperities (the members of the subset) is 32 at $\delta = 1$. The contacting asperities are modeled as mass-spring units of the Maxwell-slip model as explained previously. The COF curve is almost linear at the onset of movement of the driver. Later, small force drops appear on the curve and the slope (one may say total stiffness) decreases. The curve becomes tangent to the horizontal line of μ_d and fluctuates about it.

In Figure 3.21-(b), the red dots mark slippage of the mass-spring units that correspond to the set of asperities generated in Case 2 (Nayak parameter $\alpha = 11.2$, and the height standard deviation, $\sigma = 1\ \mu m$) and are in contact at $\delta = 1$. The abscissas show the normalized position of the driver (as in Figure 3.21-(a)). The ordinates show the block number (the mass-spring unit identifiers). At the onset of movement of the driver no block slides (no red dots appear when the driver position is small enough). Then some the red horizontal "lines" appear. These lines correspond to the most frequently sliding blocks. Further movement of the driver causes slippage of the blocks that are harder to trigger (the distance between the red dots are longer). These blocks correspond to the asperities that are pressed less. The slippages of the frequently sliding blocks do not affect the COF curve in Figure 3.21-(a) much since the curve

keeps rising linearly in spite of these frequent slippages. Later, the slippage of the infrequently-sliding blocks makes the COF curve nonlinear by decreasing the total stiffness.

The histograms of the normal loads, tangential stiffness and the load to stiffness ratio for the set of generated asperities of Case 2 (Nayak parameter $\alpha = 11.2$, and the height standard deviation, $\sigma = 1\ \mu m$) that are in contact when $\delta = 1$ are shown in Figures 3.22-(a), 3.22-(b) and 3.22-(c). The number of contacting asperities (the members of the subset) is 32 at $\delta = 1$. Since the number of contacting asperities is small compared to the total number of the generated asperities (only 3.2%), the histograms are coarse and represent the distributions only roughly.

In Figure 3.22-(a), over 55% of the contacting asperities, i.e. about 18 of them, experience the lowest amount of normal load. In Figure 3.22-(b), the percentage of asperities that have a certain stiffness is firstly relatively low (6%), then rises sharply to above 40% and finally falls. Figure 3.22-(c) shows that over 75% of contacting asperities have the lowest load to stiffness ratios.

In Figure 3.23-(a), the variation of COF with the normalized driver position is shown for a subset of generated asperities in Case 2 (Nayak parameter $\alpha = 11.2$, and the height standard deviation, $\sigma = 1\ \mu m$) when the set is pressed two standard deviation of its heights down, i.e. $\delta = 2$. The number of contacting asperities (the members of the subset) is 270 at $\delta = 2$. The contacting asperities are modeled as mass-spring units of the Maxwell-slip model as explained previously. The curve COF diverges from its initial linear trend. One may say total stiffness decreases. The curve approaches the horizontal line of μ_d smoothly, and becomes its tangent. Then, a plateau is formed about the dynamic COF.

In Figure 3.23-(b), every red dot marks the driver position at which the slippage of each mass-spring block happens in Case 1 (Nayak parameter $\alpha = 11.2$, and the height standard deviation, $\sigma = 1\ \mu m$) when $\delta = 2$. The abscissas show the normalized position of the driver (as in Figure 3.23-(a)). The ordinates show the block number (the mass-spring unit identifiers). The slippages of the frequently sliding blocks appear as red lines. These are the less-pressed blocks. The blocks that are pressed more are those that have distant dots.

The histograms of the normal loads, tangential stiffness and the load to stiffness ratio for the set of generated asperities of Case 2 (Nayak parameter $\alpha = 11.2$, and the height standard deviation, $\sigma = 1\ \mu m$) that are in contact when $\delta = 2$ are shown in Figures 3.24-(a), 3.24-(b) and 3.24-(c). The number of contacting asperities (the members of the subset) is 277 at $\delta = 2$. The number of contacting asperities is 27.7% of the generated asperities. In Figure 3.24-(a), about 80% of the contacting asperities, i.e. about 220 out of 277, lay in the two lowest bins of normal load (below 10 N). The higher load bins have quite smaller percentages asperities (below 10%). Some bins of higher stiffness are empty. In Figure 3.24-(b), the percentage of asperities that have a certain stiffness is firstly relatively low (below 5%), then rises gradually to over 20% and later falls steeply to 5% and below for the stiffness values higher than $10\ kN/mm$. Figure 3.24-(c) shows a general trend of decrease when the load to stiffness ratio increases, and constructs a Gaussian-like tail (and "half" of the bell) as expected.

In Figure 3.25-(a), the variation of COF with the normalized driver position is shown for a subset of generated asperities in Case 2 (Nayak parameter $\alpha = 11.2$, and the height standard deviation, $\sigma = 1\ \mu m$) that is pressed three standard deviation of the set heights down, i.e. $\delta = 3$. The number of contacting asperities (the members of the subset) is 836 at $\delta = 3$. The contacting asperities are modeled as mass-spring units of the Maxwell-slip model as explained previously. The COF curve diverges from its initially linear trend, falling to rise at the same rate. One may say total stiffness decreases. The curve approaches the horizontal line of μ_d gradually and becomes tangent to it and forms a plateau. The fluctuations of the curve are quite small.

In Figure 3.25-(b), the red dots mark the driver positions which trigger slippage of the set of mass-spring blocks that correspond to the contacting asperities which are generated for Case 2 (Nayak parameter $\alpha = 11.2$, and the height standard deviation, $\sigma = 1\ \mu m$) at $\delta = 3$. The abscissas show the normalized position of the driver (as in Figure 3.25-(a)). The ordinates show the block number (the mass-spring unit identifiers). The majority of the blocks remain initially stuck. For these blocks not red dot is put. These blocks not only need more "time" to slide but also wait more for their subsequent slippages. The corresponding asperities of these blocks are pressed relatively more than others. On the other hand, the frequently sliding blocks seem as

red lines. These mass-spring units correspond to the asperities that are compresses less than the others.

The histograms of the normal loads, tangential stiffness and the load to stiffness ratio for the set of generated asperities of Case 2 (Nayak parameter $\alpha = 11.2$, and the height standard deviation, $\sigma = 1\ \mu m$) that are in contact when $\delta = 3$ are shown in Figures 3.26-(a), 3.26-(b) and 3.26-(c). The number of contacting asperities (the members of the subset) is 836 at $\delta = 3$. The number of contacting asperities is 83.6% of the generated asperities. In Figure 3.26-(a), above 50

Figure 3.27 shows Figure 3.21-(a), 3.23-(a) and 3.25-(a) superimposed. The variation of COF with the normalized driver position is shown for three subsets of generated asperities in Case 2 (Nayak parameter $\alpha = 11.2$, and the height standard deviation, $\sigma = 1\ \mu m$) that correspond to three different compression values, $\delta = 1, 2, 3$. The number of contacting asperities (the members of the subset) is 32, 270 and 836, respectively. Similar to Case 1 results that are superimposed in Figure (3.15), for $\delta = 1$ the COF curve fluctuates more compared to the other compression values and rises to the plateau of dynamic friction faster.

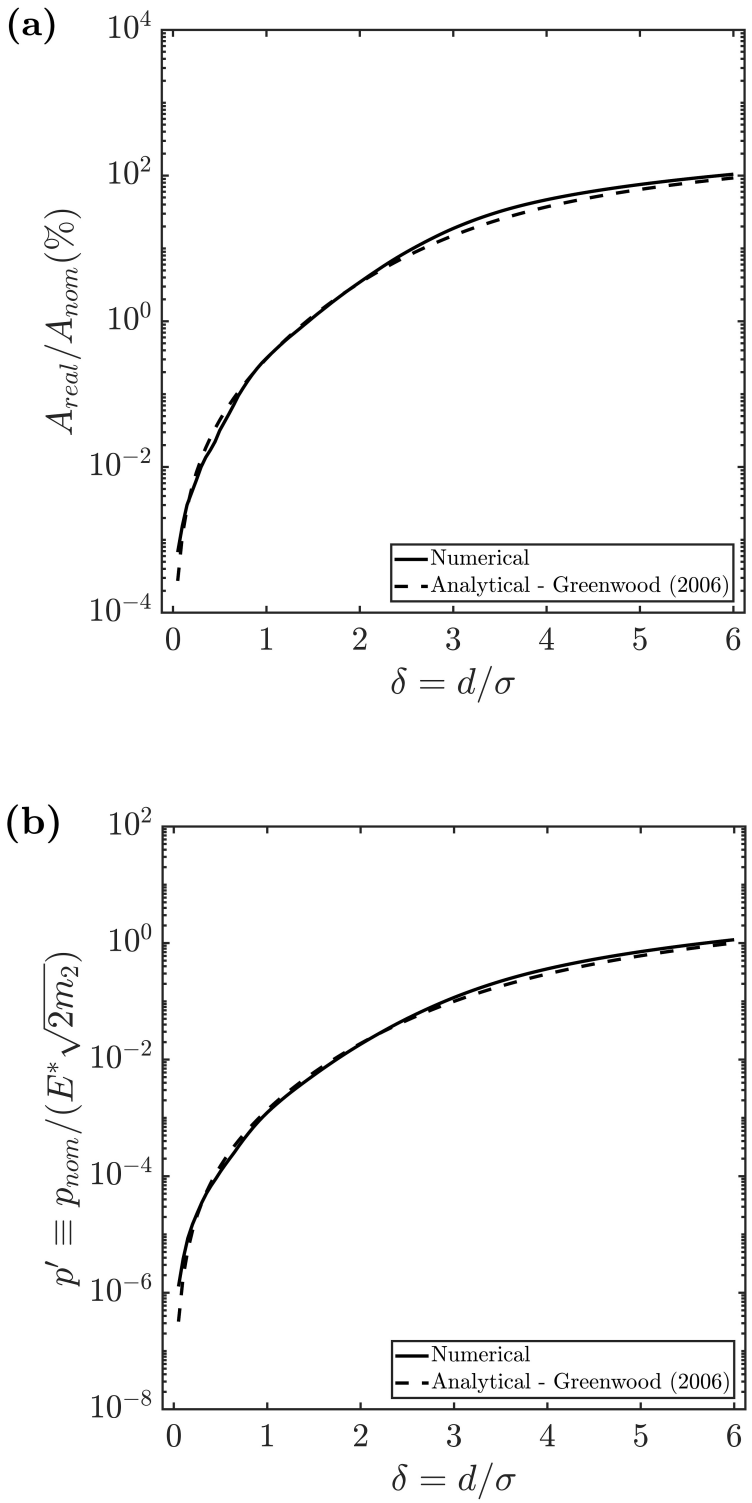

Figure 3.16: The numerical and analytical (a) real contact area and (b) pressure against compression for Case 2 ($\alpha = 11.2$ and $\sigma = 1\ \mu m$).

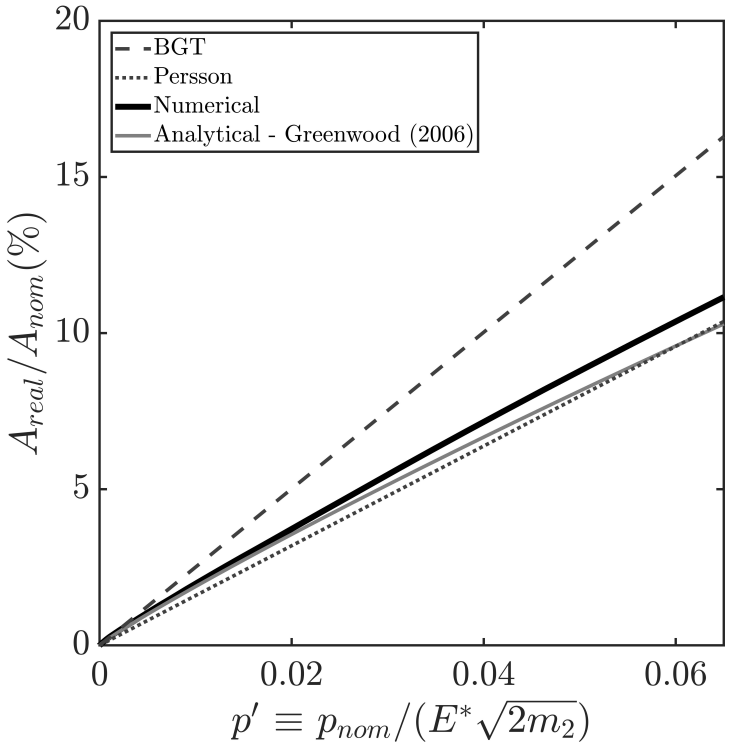

Figure 3.17: The numerical and analytical relation between real contact area and pressure is superimposed with the theoretical limits proposed by BGT and Persson for Case 2 ($\alpha = 11.2$ and $\sigma = 1\ \mu m$).

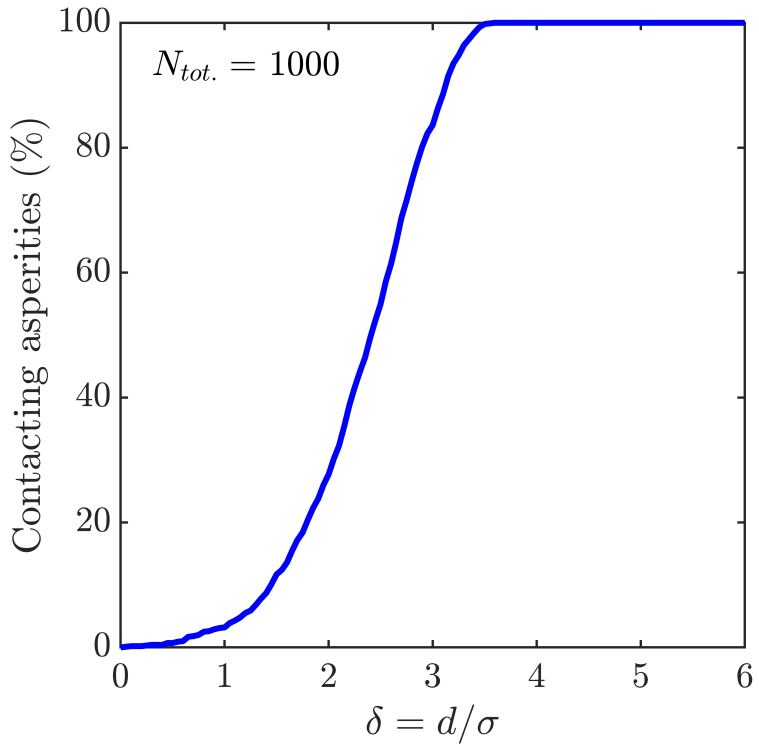

Figure 3.18: The number of contacting asperities as percentage of the total number of generated asperities against compression for Case 2 ($\alpha = 11.2$ and $\sigma = 1\ \mu m$) according to the numerical results.

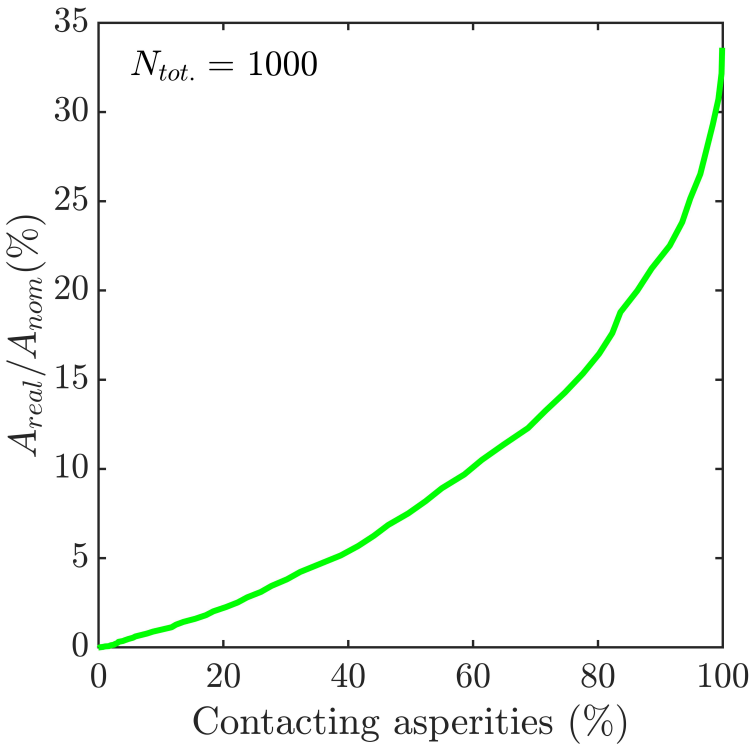

Figure 3.19: Real contact area against the percentage of the contacting asperities for Case 2 ($\alpha = 11.2$ and $\sigma = 1\ \mu m$) according to the numerical results.

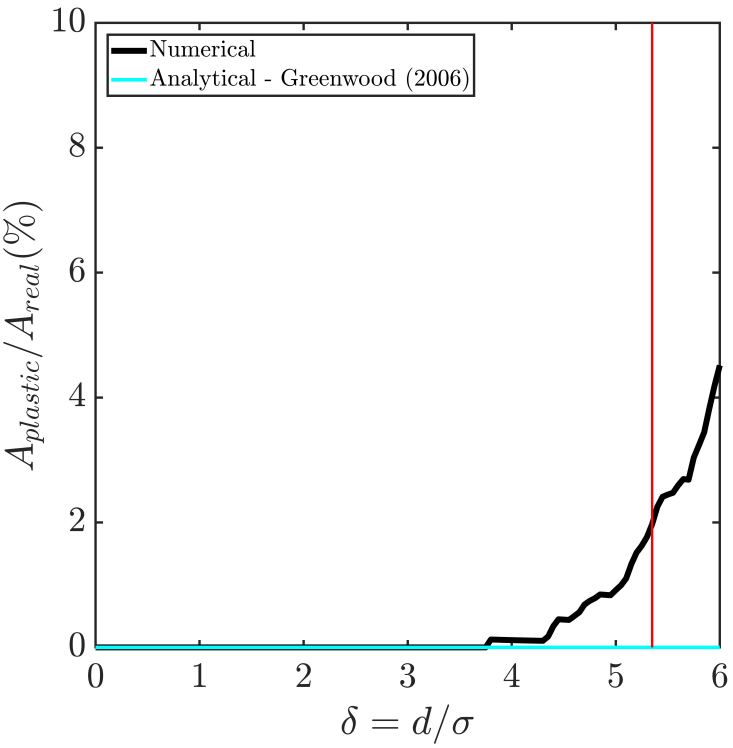

Figure 3.20: Plastic contact area against compression for Case 2 ($\alpha = 11.2$ and $\sigma = 1\ \mu m$) according to the numerical and analytical results.

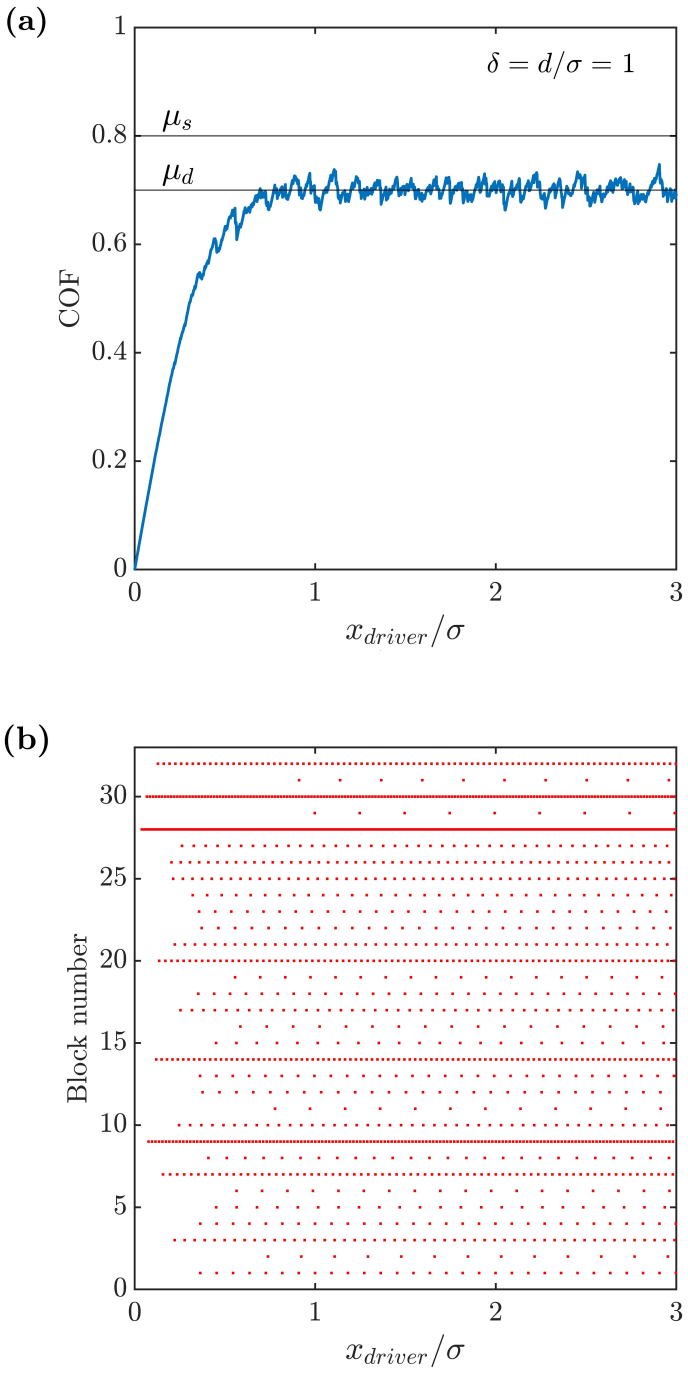

Figure 3.21: The numerical results for sliding at $\delta = 1$ for Case 2 ($\alpha = 11.2$ and $\sigma = 1\ \mu m$): (a) COF against the driver position and (b) block slippage history against the driver position.

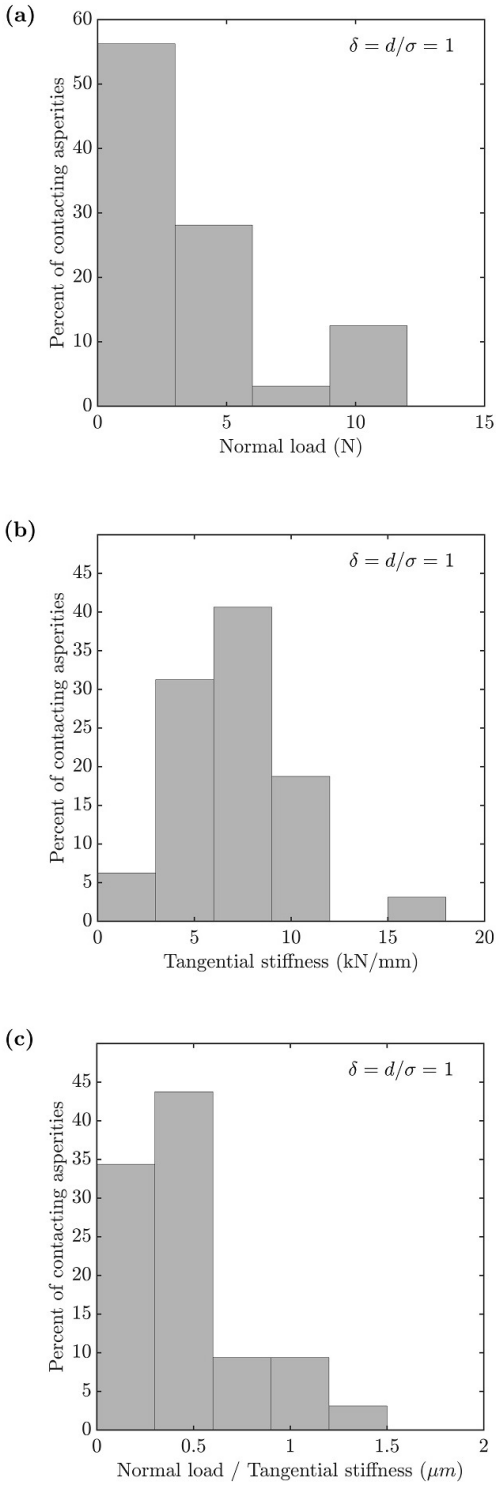

Figure 3.22: Histograms of (a) normal load (b) tangential stiffness and (c) load to stiffness ratio for Case 2 ($\alpha = 11.2$ and $\sigma = 1\ \mu m$) at $\delta = 1$.

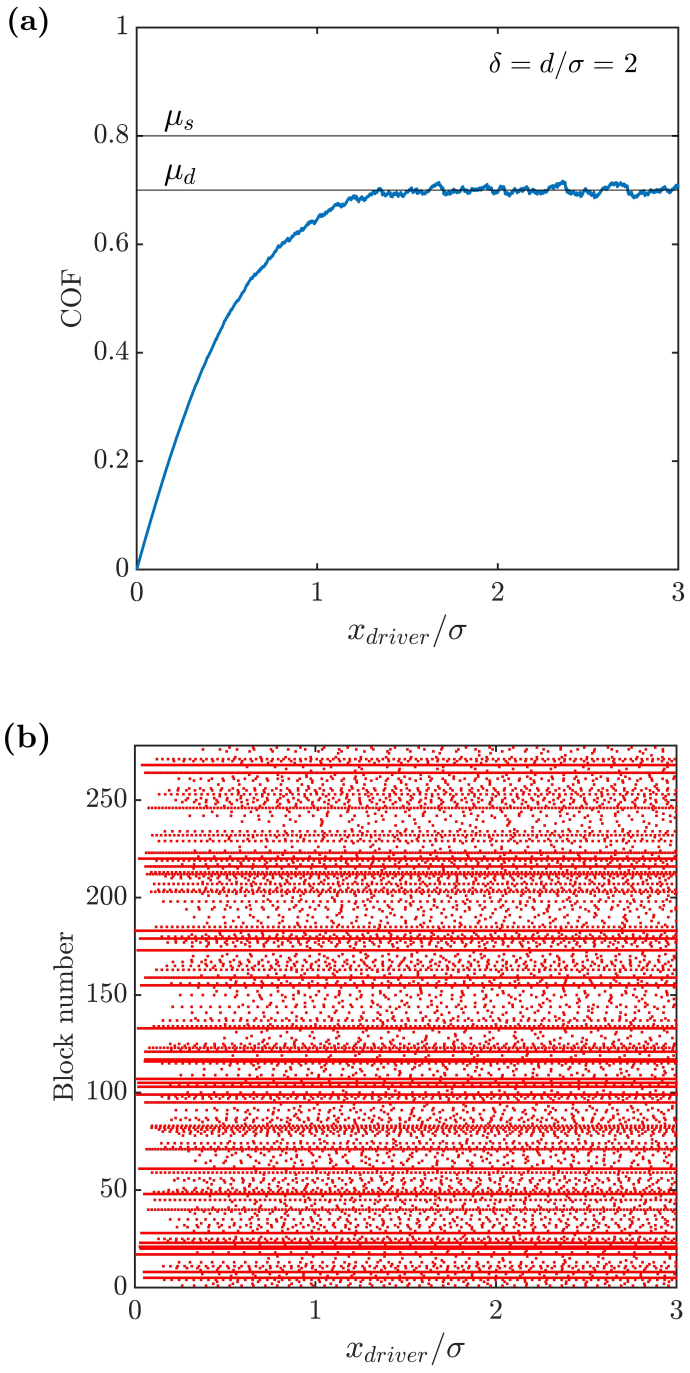

Figure 3.23: The numerical results for sliding at $\delta = 2$ for Case 2 ($\alpha = 11.2$ and $\sigma = 1\ \mu m$): (a) COF against the driver position and (b) block slippage history against the driver position.

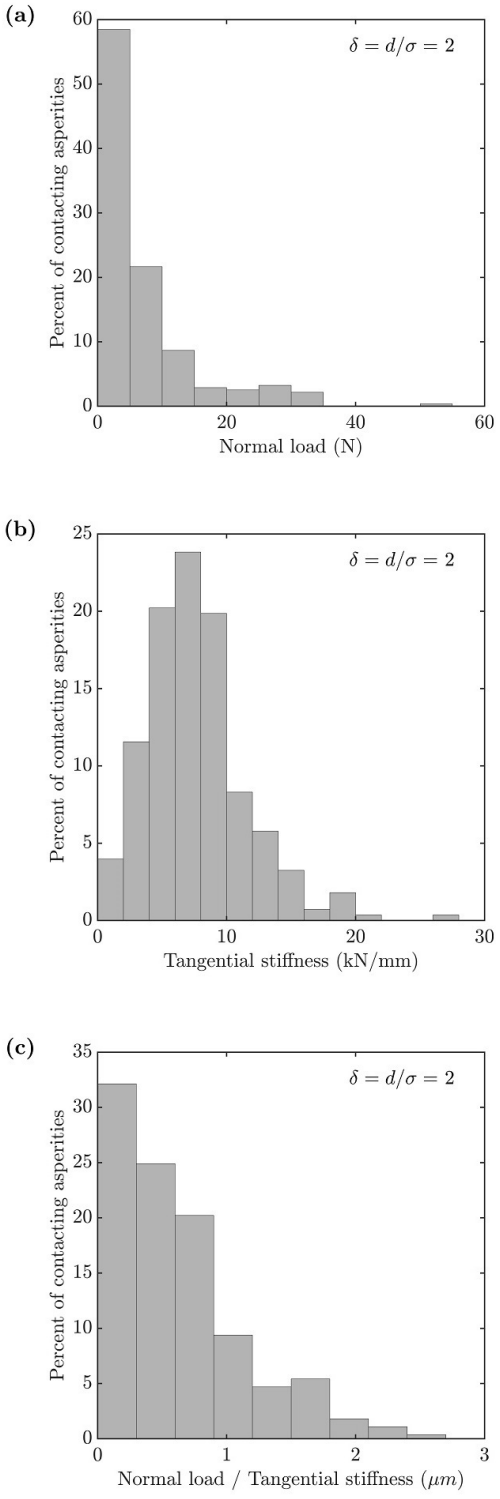

Figure 3.24: Histograms of (a) normal load (b) tangential stiffness and (c) load to stiffness ratio for Case 2 ($\alpha = 11.2$ and $\sigma = 1\ \mu m$) at $\delta = 2$.

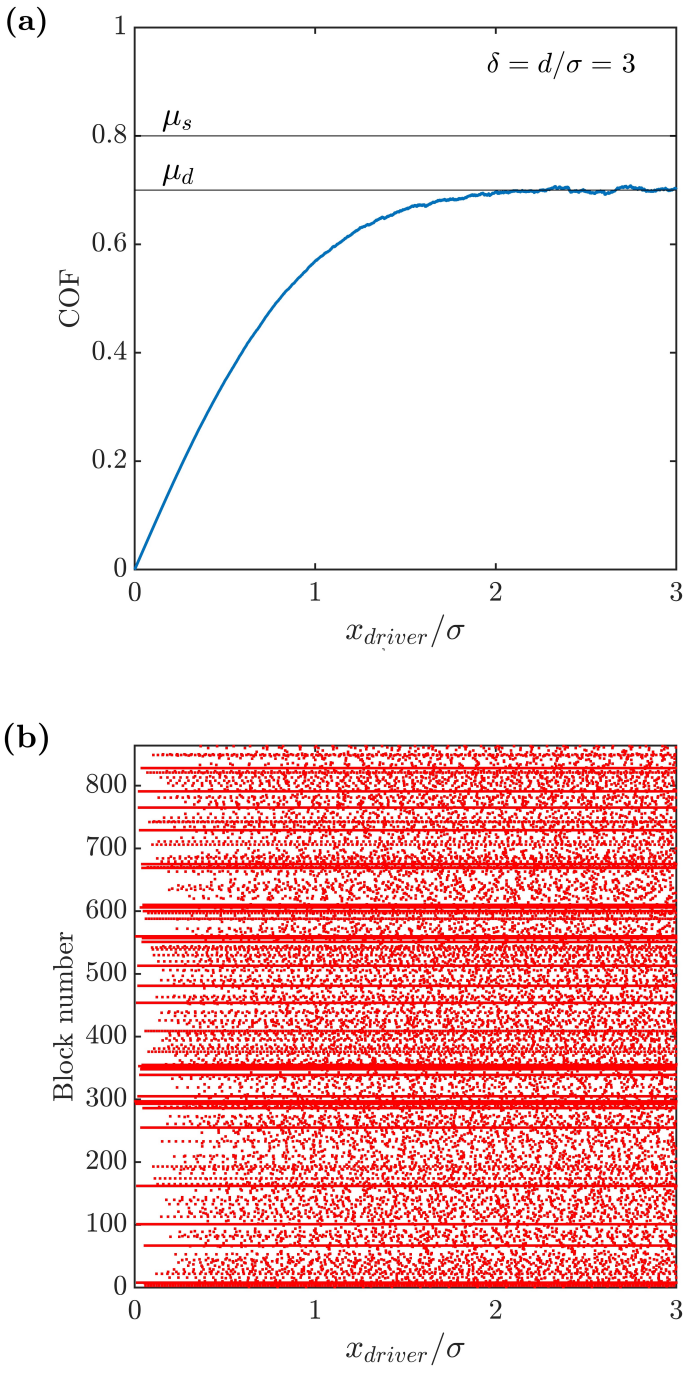

Figure 3.25: The numerical results for sliding at $\delta = 3$ for Case 2 ($\alpha = 11.2$ and $\sigma = 1\ \mu m$): (a) COF against the driver position and (b) block slippage history against the driver position.

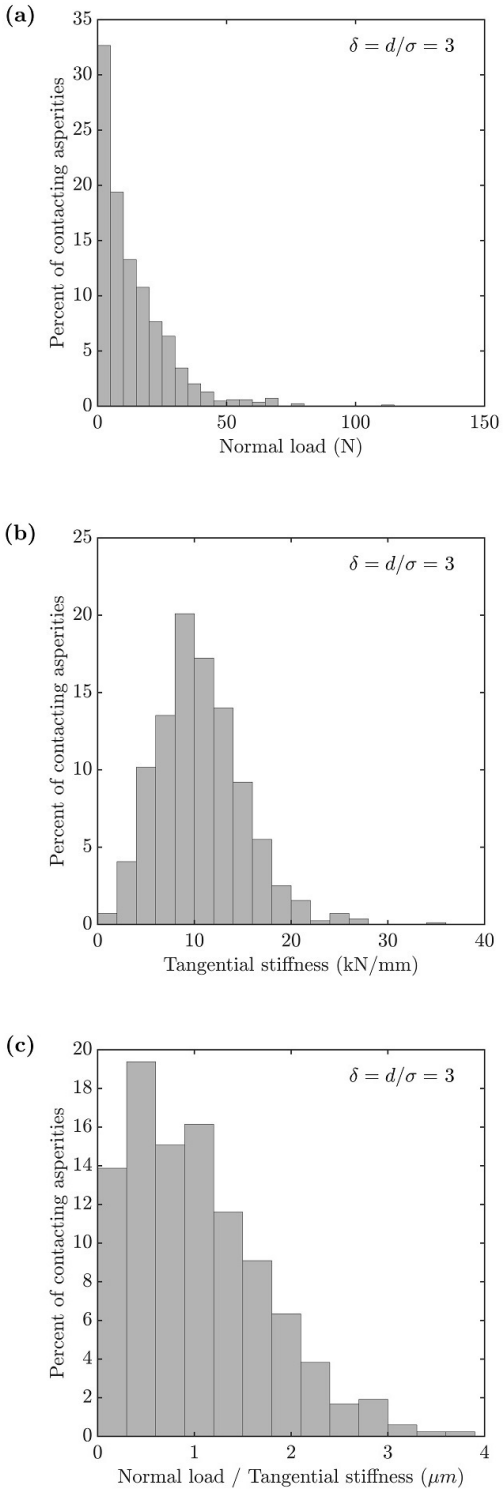

Figure 3.26: Histograms of (a) normal load (b) tangential stiffness and (c) load to stiffness ratio for Case 2 ($\alpha = 11.2$ and $\sigma = 1\ \mu m$) at $\delta = 3$.

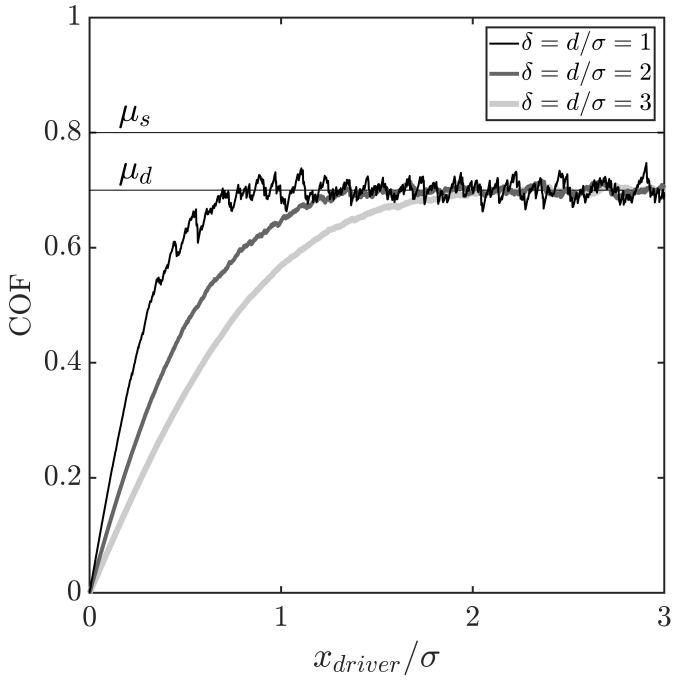

Figure 3.27: The numerical results for sliding under different compression values, $\delta = 1, 2, 3$, for Case 2 ($\alpha = 11.2$ and $\sigma = 1\ \mu m$)

3.4 Summary

In this study, the asperity-based model proposed by Greenwood (2006) is used to characterize the Maxwell-slip model to study the sliding contact of rough surfaces. Greenwood's probability distribution functions (PDFs) are employed to generate random height and curvature values for the surface asperities. The PDFs are fully specified by the surface spectral moments, which can be calculated by an analytical method. Analytical solutions of the contact of circular paraboloids are applied to obtain each asperity's tangential stiffness and the normal load. The generated rigid asperities are progressively pressed against an elastic half-space in the normal contact phase. The evolution of the real contact area with compression is checked with existing analytical solutions. The tangential stiffness and normal load of each contact area are assigned to a Maxwell-slip model mass-spring unit. Then, in the sliding contact phase, the friction force is calculated by the superposition of the spring forces as the units are moved horizontally on the rigid flat substrate. The frictional behavior of the model is studied for a range of surface representations and compression values.

3.5 Future work

- In the normal contact phase, how would Nayak parameter (and RMS roughness) affect the real contact area for a certain load value? Does a rougher surface have a larger real contact area than a smoother surface at the same load?
- Why does the variation of the real area and normal load with compression resemble?
- The sliding phase results are to be generated for a range of standard deviation values.
- Fitting linear and exponential functions to the nonlinear part of COF to conduct a quantitative investigation
- The hysteresis behavior of the system and calculation of the energy dissipation
- The relation between the lower cut-off wavenumber and the mean radius of

curvature (and the plasticity indices) to be studied. The measured mean radius values reported in [21] lay within 10 to 500 microns range.

CHAPTER 4

QUASI-STATIC MAXWELL-SLIP MODEL CHARACTERIZED BY FRACTAL DIMENSION

In this chapter, normal contact and sliding of a self-affine fractal surface are investigated. The fractal surface is generated using the midpoint displacement method on a Cartesian grid. The surface is a 2-D fractional Brownian motion (Appendix A). The asperities are assumed to be circular paraboloids with various osculating spheres. The asperity radii and the tip heights are obtained by fitting the paraboloids to the summits of the generated fractal surface. The main difference between this approach and the previous chapter is that here the position of the asperities is known. In contrast to the GW model [21], the asperity radii are known and non-identical. The radii are obtained from the generated surface by two numerical schemes. The set of rigid asperities is pressed against an elastic half-space. Analytical solutions are used to calculate the normal load, contact area, and tangential stiffness of each asperity. These data are then used to characterize the block-spring units of the Maxwell-slip model. The effect of the surface fractal dimension on the variation of the total normal load and the total real contact area with compression is investigated. The results show that a high fractal dimension causes the formation of small scattered contact zones, while a low fractal dimension causes the formation of large clustered contact zones. The evolution of the real contact area and total load with compression during normal contact is compared against that of the GW model [21]. The sliding behavior of the surface is studied by exploring the variation of COF and block slippages with the driver's position under different compression values.

4.1 Introduction

This section aims to present a body of literature that justifies the selection of a fractal model for studying the normal and sliding contact of rough surfaces. The studies related to the normal contact of multi-asperity models and sliding of block spring models are mentioned only briefly since these were previously presented in Subsections 3.1.1 and 3.1.2, respectively. Thus, the main focus is the importance of a particular class of fractals, namely statistically self-affine fractals (Appendix A), which has been widely used in the literature to model rough surfaces after the seminal work of Mandelbrot [229] at 1968. The two-volume book *Fractals for the classroom* provides a general introduction [230, 231].

Studying the evolution of the real contact area of the rough surfaces under normal load is necessary in understanding mechanical aspects like frictional behavior, sealing, wear and lubrication as well as non-mechanical aspects like heat transfer and electrical conductivity [143]. Yet, according to a recent review article [171], quantification of the real contact area remains a challenge.

The statistical character of the height distribution of the surface specifies the surface roughness. The surface profile can be considered a random process with specific statistical characteristics. However, surface profiling shows that most surfaces are rough over several length scales [143]. Consequently, statistical description using parameters like standard deviation, slope, and curvature of the profile will produce resolution-dependent results [142, 144, 232].

Fractals are known for their scale-invariant property, i.e., their fractal dimension [19, 142]. Resolution-dependence of the conventional surface roughness parameters makes fractal dimension a natural choice for describing surface geometry [144].

Deterministic fractals [20] like Sierpinski triangle or Koch curve (or Koch snowflake) [142] possess exact self-similarity. On the other hand, random fractals like coastlines are statistically self-similar [20]. Both categories, when magnified, remain (exactly or statistically) similar. A second category of random fractals remains statistically the same if the magnification is done *in a specific way*. Suppose that $X(t)$ is a random process that generates the surface height profile. Then, if the factor λ magnifies the

abscissa, then the ordinate has to be scaled with the factor λ^{-H} to preserve statistical "affinity". In other words, the process $\lambda^{-H}X(\lambda t)$ would have the same statistical character as $X(t)$. A process with such a property is called a fractional Brownian motion (fBm) with the Hurst exponent $H \in (0, 1)$ [233]. The fractal dimension of a 2-D self-affine process, i.e., its scale-invariant parameter, is given by $D = 3 - H$. An fBm is a statistically self-affine fractal [20]. Appendix A provides a detailed mathematical description for this class of fractals.

In Appendix A it is shown that the standard deviation of the increments of fBm is a function of the time interval and the Hurst exponent: $\sigma[X(t_j) - X(t_i)] = (t_j - t_i)^H$. When $H \in (0, 0.5)$, the fBm tends to immediately compensate for its increase or decrease. This behavior is called counter-persistence and means that the process fluctuates frequently. On the other hand, when $H \in (0.5, 1)$, the fBm tends to either increase or decrease and rarely changes its trend. This behavior is called persistence and means that the process fluctuates less [234].

Real surface profiles and landscapes are shown to be statistically self-affine fractals [20] (and not self-similar [143]). Persson [139] argues that for most surfaces, whether natural or prepared by surface finishing processes, $2 < D < 2.3$ (or $0.7 < H < 1$) because above $D = 2.3$ (i.e., below $H = 0.7$) the asperities become extremely sharp which would cause them to break away soon as a result of mechanical contact.

The fractional Brownian motion (fBm) [229, 233] is a one-dimensional self-affine random process. The Hurst exponent (or equally the fractal dimension) of the fBm uniquely determines the statistical character of the fBm. An fBm can be extended to 2-D fBm, which is used in modeling rough surfaces and natural landscapes [20]. Two well-known algorithms for the generation of a 2-D fBm are: (i) Random midpoint displacement method [7, 20, 235–237] and (ii) Spectral synthesis method [7, 20, 25, 238–240]. The second method is also known as the Fourier filtering method; however, [140] points to a difference. Appendix A provides a categorization of the available methods for the generation of fBm. For a comprehensive overview of the methods, one may be referred to [241,242]. Using fractals to characterize the surface roughness is not an ultimate solution for the problem of resolution-dependence since cut-offs are not well-defined [7, 171, 232].

Classical contact theories do not consider the roughness of the surface. A large body of literature is devoted to the smooth contact problems [171]. Archard's celebrated model [18] (proposed in 1957) can be considered one of the first attempts at formulating the contact mechanics of rough surfaces, which assumes roughness to be a hierarchical system of spheres placed on top of each other.

Rough surfaces have a set of protuberances that are locally higher with respect to their neighbor points. These local maxima are called asperities. Greenwood proposed a seminal multi-asperity model and Williamson [21] in 1966 for studying the relation between the normal load and the real contact area. The model assumed the asperities to be circular paraboloids whose osculating sphere has the same radius. In other words, the asperities were represented by the same paraboloid. The height of these paraboloids was determined by the Gaussian probability distribution function. The paraboloids were assumed distant enough to the extent that neither their contact area overlaps (no coalescence occurs) nor their penetration of the elastic half-space affects their neighbor asperities (no elastic interaction occurs). The other assumption was that contact occurs via the asperities only. The role of the other points of the surface were assumed to be represented by the contacting paraboloid asperities (which have ever increasing contact areas as load increases).

These implicit assumptions of the GW model [21] were harshly criticized by Greenwood himself in 2001. He argued [22] that a real surface is not properly represented by a set of scattered "local peaks" but by clusters of merging "asperities" which enlarge as the compression proceeds. These merged contact regions are also called contact patches [147, 243], contact zones, clusters, or simply contact areas or "contacts" and are observed in the experiments performed by Dieterich and Kilgore [17, 244] as well as the molecular dynamics model developed by Campañá [245]. Yastrebov [146] uses the perimeter of the contact clusters (patches) to compensate for the discretization errors in calculating the real contact area. Greenwood's criticism [22] is in line with Archard's ideas [18]: (i) Roughness is the existence of protuberances on protuberances on protuberances and (2) Contact points are initially elastic and then become plastic.

GW model predicted a linear relationship between the real area and normal load when

the tail of height Gaussian distribution is approximated with an exponential function [21, 246, 247]. Predicting the development of the real area with normal load has been of special interest, an aim and a tool for evaluating the results of the multi-asperity models [7, 25, 145, 227, 232, 235]. A comparison of the linearity of the area-load relation for the asperity-based models is made in [228].

Two studies provide theoretical proportionality constants, κ, for the development of the real area with normal load: (i) BGT model [26] and (ii) Persson's theory [205]. The BGT model considers a rough surface as a 2-D random process model. The summits of the process are approximated by elliptical paraboloids as surface asperities. In contrast to [21], in the BGT model, the asperities have different radii, which depend on the surface topology. According to BGT model, in Equation (3.5), $\kappa = \sqrt{2\pi} \approx 2.5$ when normal load is low enough. BGT model uses Hertzian contact formulas. Persson developed a theory capable of modeling contact of a fractal surface and considers the long-range elastic interaction of asperities (the effect of deformation of asperity on its neighborhood). According to Persson's model, in Equation (3.5), $\kappa = \sqrt{8/\pi} \approx 1.6$ when real contact area is below 10% of the nominal area [228]. Persson's model does not use Hertzian contact formulas. More information about (i) and (ii) can be found in the previous chapter in Subsection 3.1.1.

In [145], a multi-asperity model is proposed that includes the effects of (i) long-range elastic interaction (the lateral interaction among the asperities) and (ii) coalescence of the asperities. The model uses a self-affine fractal surface that is generated by using a spectral method that was proposed in [239]. The fractal surface is assumed rigid and is pressed on an elastic half-space. The geometric mean curvature (square root of Gauss curvature) at the local maxima of the surface gives the asperity radii. The curvature is calculated using finite difference approximation of the derivatives at the local maxima. Hertzian contact formulas are used to find the asperity normal loads and contact areas. At each compression level, the elasicity solution for deformation of the elastic half-space due to circular Hertzian contact takes the long-range asperity interactions into account by a numerical iterative procedure. Furthermore, those pairs of the asperities that their contact areas overlap are merged (coalesced) to single equivalent asperities.

4.2 Method

A brief overview of the subjects of this section is provided below, and the corresponding subsections are addressed. The scope of the explanations is limited to issues not present in the previous chapter. Note that the final part of the numerical procedure in the current chapter, i.e., pressing the rigid asperities against the elastic half-space, is the same as that of the previous chapter. What is different here is the generation of the whole surface topography and then extracting data from it instead of using PDFs to generate the summits (as in Chapter 3).

An asperity-based Maxwell-slip model is constructed to study a rough surface's normal and sliding contact. The model is characterized by the topography of a generated self-affine fractal. The surface, a 2-D fBm, is generated by the random midpoint displacement (RMD) method. The result is a set of height values on a 2-D Cartesian grid obtained by considering an intrinsic property of self-affine fractals as expressed in Equation (A.6). The algorithm of the method is explained in Subsection 4.2.1. Some existing techniques for calculating the second spectral moment of the surface are presented in Section 4.2.2.

The summits of the surface are replaced by circular paraboloids. The radii of the osculating spheres of the paraboloids are calculated by two distinct approaches. In the first approach, the paraboloid that fits the best to the summit and its eight neighbors is found numerically. The osculating sphere radius of such a paraboloid is used as the radius of the summit. In the second approach, the finite difference derivatives at the point of the summit are used to calculate the geometric mean radius. The details of these procedures can be found in Subsection 4.2.3.

The heights and the radii of the set of summits are known and the set is pressed against the elastic half-space. Hertzian contact formulas (Appendix E) are used to calculate the normal load and contact area of each summit (or asperity). The normal contact analysis gives the total load and the real contact area of the surface as the compression progresses. Neither the long-range elastic interaction nor the coalescence of the asperities is considered. The sliding contact analysis is performed by transferring the normal load and tangential stiffness values of the asperities to the Maxwell-slip

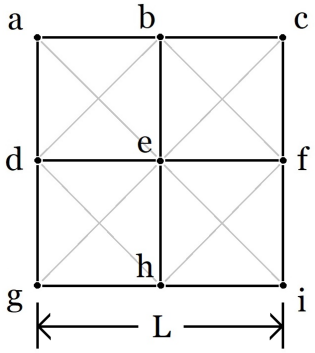

Figure 4.1: Early stages of grid refinement in the RMD method

model. In other words, the asperities are converted to corresponding block-spring units that can be pulled by a driver on the rigid flat surface. The reasoning is the same as that of Subsection 3.2, and the tangential stiffness is calculated by using Equation (3.6). Then, under every compression, the overall COF can be obtained using the fast algorithm proposed in Appendix G. The above procedures are essentially the same as those explained in Chapter 3 and will not be dealt with further in this chapter.

4.2.1 Generation of the surface: Midpoint displacement method

The RMD method is a numerical technique (recursive procedure) used in the literature [7, 20, 235–237] to generate fBm. Assume that you want to generate an fBm with a certain Hurst exponent on a 2-D Cartesian grid with a particular nodal spacing (grid size). The purpose is to assign heights to the grid nodes such that the values obey Equation (A.6), the intrinsic property of fBm. As the name "RMD" implies, the new points (heights) of the process (surface) are generated by adding a random vertical displacement of the average height of the already-existing neighbors.

The Cartesian grid that is shown in Figure 4.1 has a side length of L. The RMD method starts with generating the vertex height values, namely the nodes a, c, g, and i. The vertex heights are specified by a Gaussian variable with a given standard deviation called the initial standard deviation, σ_0. The height of the central node, e, is then calculated by adding a Gaussian variable with a standard deviation equal to $(1/\sqrt{2})^H \sigma_0$, to the average height of the vertexes. Now the heights of the nodes: b,

d, f, and h are obtained by using the heights of their corresponding three neighbors. For instance, for node b, the neighbors are a, e, and c. Again the average height of the neighbors is *displaced* by a Gaussian random variable. However, this time the variable's standard deviation is $(1/2)^H \sigma_0$.

This re-scaling of the standard deviation is done by considering the size of the grid on which the points are generated and *tries* to enforce Equation (A.6). The distance between the central node and the vertexes is $L\sqrt{2}$. However, the distance of the nodes: b, d, f, and h with their corresponding neighbors is $L/2$. Therefore, the scaling ratio, λ, in Equation (A.6) is $1/\sqrt{2}$ for the central node while it is $1/2$ for b, d, f and h. In other words, the standard deviation of the added Gaussian variable is determined by the distance between the node and its corresponding neighbors.

The next stage of refining the grid begins at the intersection points of the grey diagonal lines in Figure 4.1. The intersection points of these lines give the position of a new set of nodes. The corresponding neighbors of these nodes are the four nearest neighboring diagonal nodes. Thus, the scaling ratio for the new nodes with respect to the original grid is $(1/\sqrt{2})^3$. The refining procedure continues till the desired resolution is provided. The grid is always refined such that the next grid size is $1/\sqrt{2}$ times smaller than the previous one. Therefore, at the nth stage of the refinement, the standard deviation of the Gaussian variable has to be set to $\sigma_0(1/\sqrt{2})^{nH}$. As the grid is refined further, the Gaussian variable is made smaller and smaller according to Equation (A.6).

The required input parameters of the RMD method are the Hurst exponent, initial standard deviation, and grid size. The method is time-efficient, however, the output is only an approximation of the fBm [20], and the surface is stationary only when $H = 0.5$ [20]. In [248], Mandelbrot discusses *the nonstationarity of the midpoint displacement curves* and suggests avoiding the RMD method (and *rejoicing too hard* at its robustness), specifically if the Hurst exponent is *nearly* 1. The statistical characteristics of a non-stationary process change with "time", i.e., different parts of the generated surface would have different standard deviations or mean values. Decreasing the grid size does not help, and the problem is amplified as the Hurst exponent approaches one [20]. Large variation of the RMS roughness with sample length [235]

and an undesired surface waviness are reported in [236]. The waviness can be a manifestation of the persistence property of fBm when the Hurst exponent is above 0.5 (see Appendix A) rather than an artifact of the RMD method.

4.2.2 Calculation of the second spectral moment

In this subsection, some methods used in the literature to calculate m_2 are brought forward. The second spectral moment of the surface PSD function, m_2, is an important parameter affecting the slope of the real area normal load of the numerical results as seen in Equation (3.5). The second spectral moment of a surface generated by the RMD method is prone to large fluctuations. This instability of m_2 not only shows up in different realizations of the surface (executions of the RMD method with the same set of the input parameters) [235] but also manifests when different numerical schemes of the finite difference method (forward/central) are used for calculating the surface slope values [7]. In [25], a remedy for the problem is proposed that is based on the PSD function of the surface instead of trying to find m_2 from the discretized geometry in the real space (the detail are provided in Appendix B).

A straightforward way of calculating m_2 from discrete surface data is to use the definition of the parameter, which is the variance of the slopes, i.e., by using Equation (3.2). This means calculating the slopes between every pair of successive heights on the grid and then finding the variance of the slopes would be enough. Since the surface produced by the RMD method is isotropic, i.e., its statistical properties are the same in every direction, the slopes (obtained from different profiles) can be collected in a single set. The variance of the set would be equal to m_2. However, as stated in [235], the value of m_2 can fluctuate largely because the generated surface is not stationary, i.e., its statistical properties change with "time" (at different parts of the grid). Furthermore, the calculation method can be an additional source for numerical fluctuation.

Nayak [24] firstly emphasizes that m_2 is the second spectral moment of the surface PSD and the natural way of calculating m_2 is to use the definition that is based on the

PSD function, $\Phi(k_x, k_y)$:

$$m_2 = \int_{-\infty}^{+\infty} \int_{-\infty}^{+\infty} \Phi(k_x, k_y) k_x^2 k_y^2 dk_x dk_y \tag{4.1}$$

where the PSD is the Fourier transform of the autocorrelation function of the surface, he then proposes two additional methods [24]. Based on a formula from [202], Nayak claims that m_2 is related to the "density" of zero-crossings of the surface profiles, D_{zero}, i.e., the percentage of the zero-crossings with respect to the number of nodes per unit length on the surface profiles:

$$m_2 = \pi^2 \sigma^2 D_{zero}^2 \tag{4.2}$$

The above relation is in agreement with the fact that m_2 is the variance of the slopes (the "mean-square slope" [24]) of the surface, as stated in Equation (3.2). This agreement can be explained intuitively by considering a 2-D profile with the maximum possible D_{zero}. Such a profile has to cross its mean line once in every pair of successive points and thus constructs a regular triangular saw-tooth as shown in Figure 4.2-(a). The saw-tooth profile would have zero average slope since it is composed of successive rises and falls with extremum slopes s_{max} and $-s_{max}$. For this profile, the difference in the slopes is the maximum possible (compared to the profiles with the same standard deviation and the same number of sampling points). Therefore, the variance of slopes, m_2, is the maximum for such a profile is maximum. In brief, the frequent crossing of the mean line, i.e., a large D_{zero}, means a large m_2. On the

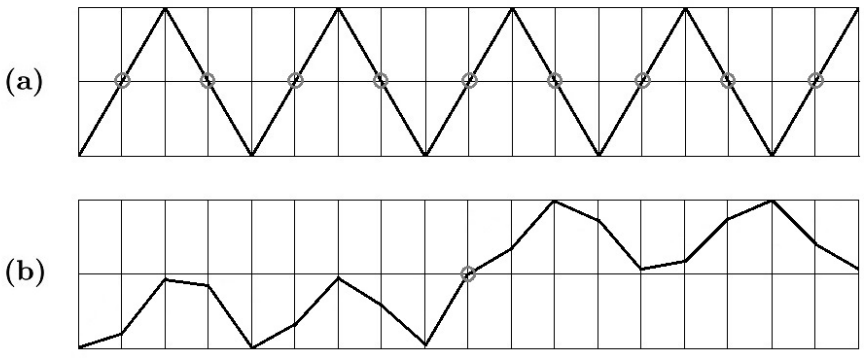

Figure 4.2: Two "extreme" surface profiles with: (a) maximum and (b) minimum possible zero-crossing density per unit length, D_{zero}.

other hand, for a profile with a very small D_{zero}, the *spread* of the slopes (variance of slopes, m_2) is expected to be low too. The reason is that such a profile should avoid its mean line as much as possible, as shown in Figure 4.2-(b). A small absolute value of the slopes (small compared to s_{max}) would ensure the avoidance. This means that a smaller D_{zero} (a profile that avoids crossing its mean line more) requires a smaller m_2. Based on the above considerations, one may claim that a profile with a larger m_2 would be "jerkier" than a profile with a smaller m_2 and consequently sharper tips (smaller radii of curvature) generally.

The relation of σ and m_2 can also be explained by intuition. Imagine that the heights of the profiles, which are shown in Figure 4.2, are doubled. This means a doubled standard deviation of the slopes. Note that m_2 is the standard deviation of the slopes squared. Thus, the standard deviation of the slopes is expected to be directly proportional to σ and D_{zero} as can be seen by taking the square root of the sides of Equation (4.2).

Another method for calculation of m_2 (proposed in the discussion section of [24]) relates m_2 to the second derivative of the autocorrelation function, $R(r)$, at the origin:

$$m_2 = -\left(\frac{\mathrm{d}^2 R}{\mathrm{d}r^2}\right)_{r=0} \tag{4.3}$$

In [249] the discrete form of the autocorrelation function for a 3-D surface is given:

$$R(\tau_x, \tau_y) = \frac{1}{(m-\tau_x)(n-\tau_y)} \sum_{i=1}^{m-\tau_x} \sum_{j=1}^{n-\tau_y} z(i,j) z(i+\tau_x, j+\tau_y) \tag{4.4}$$

where m and n are the numbers of the grid points on a horizontal and a vertical edge, and τ_x and τ_y are shift lengths in x and y directions, respectively. A shift length is the product of an integer and the nodal spacing. By evaluating the function for different $r = \sqrt{\tau_x^2 + \tau_y^2}$, finite difference formulas (stencils) of different orders (depending on the number of considered points) can be used for approximating the second derivative of the autocorrelation function at $r = 0$. If it is assumed that $\tau_x = \tau_y$ and equal to the product of an integer and the grid size (the nodal spacing), then the r values would be equi-spaced. Otherwise, (if $\tau_x \neq \tau_y$) the r values would be unequally-spaced spaced. In the present study, both the equi-spaced and unequally spaced stencils are used. The number of the considered stencil points are 3, 5, 7, 9 and 11.

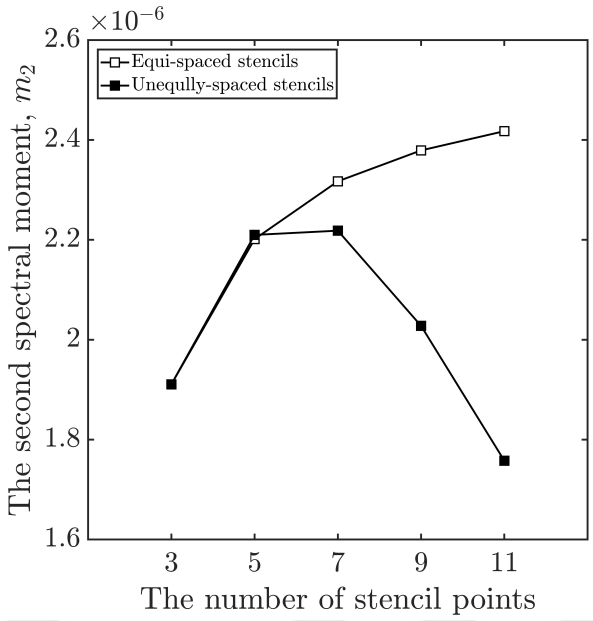

Figure 4.3: The variation of the second spectral moment of Case 1 surface ($H = 0.75$ and $\sigma_0 = 1\ \mu m$) with the number of the finite difference stencil points for both equi-spaced and unequally spaced stencils.

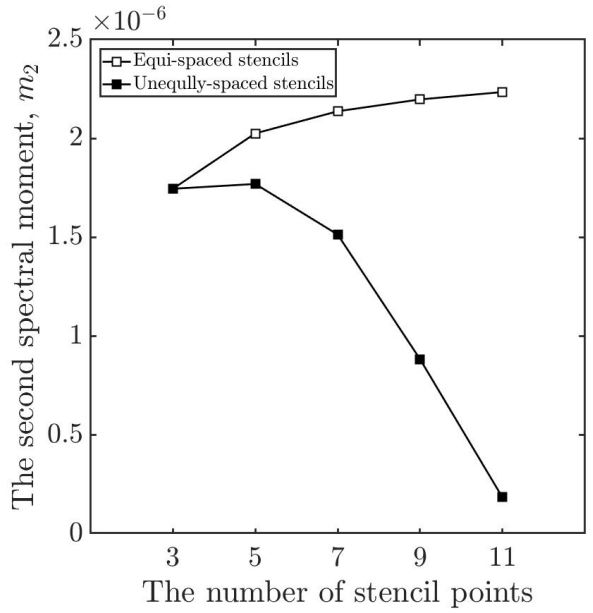

Figure 4.4: The variation of the second spectral moment of Case 2 surface ($H = 0.95$ and $\sigma_0 = 1\ \mu m$) with the number of the finite difference stencil points for both equi-spaced and unequally spaced stencils.

The variation of m_2 with the number of stencil points for the pair of surfaces generated by the Hurst exponents $H = 0.75$ and $H = 0.95$ are shown in Figures 4.3 and 4.4, respectively. The corresponding surfaces, shown in Figures 4.5 and 4.19, are used in Section 4.3 to investigate the normal and sliding behavior as Case 1 and Case 2. The equi-spaced and the unequally spaced stencil results are presented in Figures 4.3 and 4.4. While the equi-spaced stencils produce a rising trend of m_2 values and have a potential of converging to a plateau), the unequally-spaced stencils produce a rise that is followed by a fall in both cases.

4.2.3 Calculation of the summit curvatures

4.2.3.1 Circular paraboloid fit to an an elliptic asperity

To determine the radius of curvature at a summit node, one can fit parabolas to the summit node. Assume that the central point, e, on the grid shown in Figure 4.1 is a summit. Four vertical planes pass through every set of the three nodes (triad), which have the central node in the middle, two axial: b-e-h and d-e-f and two diagonal: a-e-i and c-e-g. One can fit a series of parabolas to the triad on each plane. The vertex of the parabolas is on the central node to guarantee a summit there. This condition requires zero derivatives (a level tangent line to the parabola) at node e. The equation of such a parabola is $z = \alpha t^2$. Firstly, in each vertical plane, a pair of parabolas are fitted to the triad such that at least one of the peripheral node heights lies exactly on the curve. Afterward, the whole range of α values between the extermums of the calculated α values is divided into fine steps, $(\alpha_{max} - \alpha_{min})/1000$. The parabola that corresponds to each of the steps is revolved around the axis that connects the central node to the summit to produce a circular paraboloid. These paraboloids are compared with each other in terms of the summation of the difference between the surface heights and the paraboloid heights on the peripheral nodes. Finally, the paraboloid with the least error (the minimum sum of the height differences) is chosen as the best fit for the summit. Note that the parabola's curvature (the second derivative) is 2α. Therefore, the radius of the osculating sphere of the paraboloid (the radius of the summit), R_{Fit}, is equal to $1/(2\alpha_{Fit})$, where α_{Fit} is the leading coefficient of the best paraboloid fit. These values are used in the numerical scheme. The average value of the osculating sphere

radii of all of the summits is used in the analytical formulas of the GW model.

4.2.3.2 Geometric mean curvature of an elliptic asperity

Assume that the central point, e, on the grid shown in Figure 4.1 is a summit. The finite difference formulas for calculating derivatives can be used to find the radius of curvature at the summit. Let us rename the central node as (i, j) where i refers to the row and j to the column number. The peripheral nodes can be renamed accordingly, e.g., node a becomes $(i-1, j-1)$. Then, the second order derivatives at (i, j) can be approximated [145] by:

$$\kappa_x = \frac{\partial^2 z}{\partial x^2} \approx \frac{z_{i-1,j} - 2z_{i,j} + z_{i+1,j}}{(L/2)^2} \tag{4.5}$$

$$\kappa_y = \frac{\partial^2 z}{\partial y^2} \approx \frac{z_{i,j-1} - 2z_{i,j} + z_{i,j+1}}{(L/2)^2} \tag{4.6}$$

$$\kappa_{xy} = \frac{\partial^2 z}{\partial x \partial y} \approx \frac{(z_{i+1,j+1} + z_{i-1,j-1}) - (z_{i-1,j+1} + z_{i+1,j-1})}{L^2} \tag{4.7}$$

The summit curvature can be defined as the geometric mean of the *principal* curvatures, κ_1 and κ_2:

$$\kappa_{GM} = \sqrt{\kappa_1 \kappa_2} \tag{4.8}$$

The principal curvatures are the eigenvalues of the Hessian matrix:

$$\mathbf{H} = \begin{bmatrix} \kappa_x & \kappa_{xy} \\ \kappa_{xy} & \kappa_y \end{bmatrix} \tag{4.9}$$

The product of the principal curvatures, $\kappa_1 \kappa_2$, is called Gaussian curvature and can be found by calculating the determinant of the Hessian matrix. Therefore, 4.8 can be rewritten as:

$$\kappa_{GM} = \sqrt{\det(\mathbf{H})} = \sqrt{\kappa_x \kappa_y - \kappa_{xy}^2} \tag{4.10}$$

Then, the geometric mean radius of the summit, R_{GM}, is equal to $1/\kappa_{GM}$. These values are used in the numerical scheme. The average value of all of the summit geometric mean radii is used in the analytical formulas of the GW model.

4.3 Results

In this section, the results of the normal and sliding contact of two sets of asperities are presented. The asperities are obtained by considering the topography of fractal surfaces, which are generated using the Random Midpoint Displacement (RMD) method by assuming the Hurst exponent to be $H = 0.75$ and 0.95. The standard deviation of heights is assumed to be $1\ \mu m$. The normal contact results include the variation of: (1) real contact area and normal load with normal compression, (2) real contact area with normal load, (3) percentage of the contacting asperities with compression, (4) real contact area with compression and (5) plastic contact area with compression. The plots of (1), (2) and (5) are superimposed with the existing closed-form solutions for the purpose of validation. The sliding contact results include: (1) the variation of COF with the driver position and its corresponding block slippage history under three different normal compression values and (2) Histograms of the normal load, tangential stiffness, and their ratio for the three different normal compression values.

In all case studies, the elastic body is assumed to be made of Aluminum with Young modulus of $72\ GPa$ and a Poisson ratio of 0.33. Hardness is $1.52\ GPa$. The nominal contact area is a square with edges of $0.01\ m$ length. The initial standard deviation, σ_0, is assumed to be 1 micron. The number of nodes on each edge is $2^{10} = 1024$ because 10 stages of grid refinement are applied. Then, the total number of surface points is $1,048,576$, and the nodal spacing is 10 micron. Note that in the process of generating the surface (Subsection 4.2.1), the standard deviation of the distribution from which the point heights are obtained changes at each stage. Thus, there is no direct control over the standard deviation of the generated surface.

4.3.1 Case 1 ($H = 0.75, \sigma_0 = 1\ \mu m$)

The series of results that are presented in Figures 4.7-4.18 are related to Case 1, for which the Hurst exponent, H, is equal to 0.75 and the initial standard deviation, σ_0, is assigned $1\ \mu m$. The second spectral moment of the PSD, m_2, is obtained by the 11-point equi-spaced finite difference stencil as $m_2 = 2.42e-6$. The values of m_2, calculated for Case 1 by the other stencils, are also present in Figure 4.3. The number

of counted summits (asperities) is $47,499$. Thus, roughly 4.5% of the surface points are summits. Although the initial standard deviation, σ_0, is assumed to be $1\ \mu m$, the final standard surface of all surface points is $\sigma = 0.24\ \mu m$.

In Figure 4.5 the surface that is generated by the RMD for Case 1 is represented. Figure 4.5-(a) shows the 3D topology of the generated surface. The reference (zero) is set to the surface mean (average height), and the heights are measured with respect to it. Figure 4.5-(b) shows the 2-D top view of the same surface. The shown surface topology is used to extract the heights and radii of the set of asperities and, consequently, all of the results that are presented below for Case 1.

In Figures 4.6-(a)-(f), the visualization of the evolution of the real contact area is presented as the compression increases from $d = 0.25$ to $d = 1.5$ in six steps for Case 1 with fitted radii, R_{Fit}. The white frame shows the nominal contact area; the black regions are the real contact areas. The black regions are composed of the smaller circular contact areas of the asperities. These small areas may overlap. Thus, if the black region area is somehow measured, it would be lower than the summation of the circular contact areas. The corresponding numerical real contact area for Figures 4.6-(a)-(f) are: $0.05\%, 0.58\%, 2.4\%, 6\%, 12.25\%$ and 22%. As the compression increases, separate clusters of contact regions form and then unite to create ever greater patches. The shape of the contact region is strongly affected by the topography of the generated surface that is shown in Figure 4.5-(b).

The semi-log plot in Figure 4.7-(a) shows the variation of contacting real area as a percentage of the nominal area, with the normalized compression, $\delta = d/\sigma$ for Case 1. The real contact area increases as the set of rigid asperities are pressed against the elastic half-space. The solid lines represent the numerical results. The solid black line is obtained by using the fitted paraboloid radii value. The solid grey line is the result of using the geometric mean radii values (which are obtained by using finite difference approximation of the surface derivatives at the summit tips). Hertzian formula (Equation E.1) is used to calculate the contact area for each contacting asperity. The dashed lines show the analytical results (according to Equations (C.3) and (C.4)), which are obtained by using the average asperity radius. The lower limit of the integral on the heights is the position of the elastic half-space, and the upper limit is

specified by the height of the highest asperity. The lower and upper limits of the integral on the curvatures are specified by the smallest and the largest curvatures of the numerically generated asperities, respectively.

When the amount of compression is below one standard deviation ($\delta = d/\sigma < 1$), the numerical results do not agree with the analytical solution. However, over $\delta = 1$, when A_{real}/A_{nom} reaches 5%, a good agreement between the numerical and the analytical results starts and continues up to $\delta = 6$. The initial disagreement can be an effect of using average radius values in the analytical real area formula. Note that the average radii are the average radii of all surface asperities (and not just the contacting asperities). In addition, the real area is quite small (below 5%) in the mismatch region. Therefore, another reason can be the effect of the finite nature of the surface and incomplete probabilistic representation of the surface when compression is small. It should be noted here that, in contrast to the previous chapter, the numerical and analytical results are similar in different surface realizations (executions) with the same input.

The semi-log plot in Figure 4.7-(b), shows the variation of normalized nominal normal pressure, $p' = p_{nom}/(E^*\sqrt{2m_2})$, with the normalized compression, $\delta = d/\sigma$, for Case 1. As the rigid rough surface is pressed by the elastic half-space, the normalized nominal pressure increases. The trend of disagreement and agreement between the numerical and the analytical results is similar to that of the real area (4.7).

In Figure 4.8, the variation of real area, A_{real}, (as percent of the nominal area, A_{nom}) with normalized nominal pressure, $p' = p_{nom}/(E^*\sqrt{2m_2})$, is plotted for Case 1 and shows the increase of the pressure with an increase of the real contact area. The solid black line shows the numerical result which are obtained from the set of the generated paraboloid asperities. The ordinate represents the total contact area, and the abscissa shows the total normal load experienced by all the asperities in contact with the elastic half-space. When the normal load is low enough, the slope of the curve is nearly the same as that of the BGT model. As the normal load increases, the slope of the curve drops gradually and tends to the slope proposed by Persson's theory. The solid grey line represents the results of the analytical formulas, which are derived for the real contact area and the normal load, i.e., Equations (C.3) and

(C.4). The lower limit of the integral on the heights is the position of the elastic half-space, and the upper limit is specified by the height of the highest asperity. The lower and upper limits of the integral on the curvatures are specified by the smallest the largest curvatures of the generated asperities, respectively. The grey curve coincides with BGT and the numerical results at low normal loads. As the load increases, the grey curve diverges from the numerical values, but its slope is still above Persson's proposed slope. Although for different sets of generated asperities the black and grey lines change to some extent, their slopes remain persistently between the theoretical bounds.

Figure 4.8 is a combination of Figures 4.7-(a) and 4.7-(b) with the elimination of the compression and provides the opportunity of comparing the results with the theoretical relations that are proposed in the literature. The dashed line shows the theoretical relation between the normal load and the real contact area as proposed by the BGT model [26]. The slope is equal to $\sqrt{2\pi} = 2.5$. On the other hand, the dotted line is the theoretical relation that is given by Persson's theory [28, 205], according to which the slope is $\sqrt{8/\pi} = 1.3$ (Section 3.1.1). These theoretical results are used in the literature in order to verify the numerical results of the normal contact for the asperity-based models [7, 25, 145]. The results are assessed as reasonable if the slope remains between that of BGT and Persson for low pressure values, i.e., for $0 < p' < 0.06$ [25]. In Figure 3.5, only the slope of the curves that are obtained with fitted paraboloid radii is within the theoretical limits (nearly the same as Persson's at least up to $p' = 0.01$). These curves are tangent to the BGT bound at very low pressures $p' = 0.001$. The slope of the curves that are obtained with geometric mean radii are lower than Persson's and lay outside the theoretically predicted region. This disagreement is observed in [25] for high Nayak parameters when Greenwood's simplified elliptic model [27] (Appendix C) is used. Note that the result changes slightly at different code executions and depends on the nodal spacing.

In Figure 4.9, the increase of the number of contacting asperities (as a percentage of the total number of the asperities, which is $47,499$) with the normalized compression, δ, is plotted for the set of generated asperities in Case 1. The curve resembles Gaussian cumulative PDF, and it was expected since the probability of the asperities above a certain height is proportional to the number of the contacting asperities. The method

of calculation of the radii does not affect this curve. Up to one standard deviation of compression, i.e., $\delta = 1$, only about 5% of the asperities have been contacted. Within $1 < \delta < 2$, the rate of increase in the number of asperities grows faster and faster. Within $2 < \delta < 3$, the increase becomes almost linear and after $\delta = 4$ slows down.

In Figure 4.10, the increase of the real contact area with the number of contacting asperities (as a percentage) is plotted for the set of generated asperities in Case 1. The thick line belongs to the numerical model with the fitted paraboloid radii. It rises faster compared to the narrow line in the numerical model with the geometric mean radii. This is reasonable since for Case 1, $\bar{R}_{Fit} = 8.25\ mm$ while $\bar{R}_{GM} = 5.73\ mm$, i.e., the fitted radii are generally larger than the geometric mean radii.

In Case 1, the inception of the plastic deformation for the numerical results with the geometric mean radii happens earlier than those with the fitted radii (Figure 4.11). The numerically obtained plastic area with R_{GM} exceeds 2% of the real contact area only when δ passes 5.5. On the other hand, with R_{Fit}, the numerically obtained plastic area remains below 2%. The analytical results (which are obtained with the average radius values of *all*, $\bar{R}_{Fit}$, and $\bar{R}_{GM}$) predict no inception of the plasticity. These results are in agreement with the plasticity indices calculated by using Equations (F.5) and (F.8) as proposed in [21] and [27], respectively. The calculated plasticity indices are 0.29 and 0.34 when $\bar{R}_{Fit}$ and $\bar{R}_{GM}$ are used in Equation (F.5) respectively. The plasticity index is 0.08 when Equation (F.8) is used with $m_2 = 2.42e-6$. All index values are below 0.5, so plasticity is not expected theoretically.

In Figure 4.12-(a), the variation of COF with the normalized driver position is shown for Case 1 subjected to half standard deviation compression, $\delta = 0.5$. The number of contacting asperities is 712 when $\delta = 0.5$. The contacting asperities are modeled as block-spring units of the Maxwell-slip model as explained in Appendix G. At the onset of the driver's movement, the COF curve is almost linear and then becomes nonlinear as it approaches its plateau at μ_d.

In Figure 4.12-(b), each block slippage is marked with a dot for Case 1 at $\delta = 0.5$. The abscissas show the normalized position of the driver (as in Figure 4.12-(a)). The ordinates show the slipped block number. According to Appendix G, the intervals between the successive slippages of the block spring are the function of the com-

pression of its corresponding asperity only (the interval length is independent of the asperity radius). Therefore, this figure would be exactly the same for both R_{Fit} and R_{GM}. The horizontal "lines" belong to the block-spring units whose corresponding asperity is most pressed. On the other hand, the "dotted horizontal lines" belong to the block-springs, which their corresponding asperities are pressed the least. The "lines" do not affect the COF curve much in Figure 3.9-(a) as the curve remains almost linear in spite of these frequent slippages. The COF curve nonlinearity starts after some block-spring units corresponding to the most pressed asperities (e.g., those with block numbers just below 100) begin to slide when the driver passes 0.2σ.

It should be noted that the choice of either R_{Fit} or R_{GM} would have no effect on the history of the block slippages. The intervals between the successive slippages as well as the interval of the first slippage of the block-spring units, are independent of the radius of their corresponding asperity as shown in Appendix G.

The histograms of the normal loads, tangential stiffness, and the load-to-stiffness ratio for the set of asperities of Case 1 under a compression of $\delta = 1$ are shown in Figures 4.13-(a-c). The number of contacting asperities when $\delta = 0.5$ is 712. The number of contacting asperities is small compared to the total number of generated asperities (only 1.5%). The histograms are coarse and roughly represent the distributions.

In Figure 4.13-(a), nearly 40% of the contacting asperities experience the lowest normal load. The bins seem to be exponentially distributed among the load values. In Figure 4.13-(b), the stiffness bins are firstly low-populated, then rise and fall steeply. This resembles Rayleigh distribution. Figure 4.13-(c) shows a rather monotonous decrease in the load-to-stiffness ratio bin population. Equation (G.5) shows that the load to stiffness ratio is a product of a constant multiplier and the compression of asperity (the multiplicand). Then, the distribution of the ratio is expected to resemble the tail of the height distribution.

In Figure 4.14-(a), the variation of COF with the normalized driver position is shown for Case 1 under one standard deviation of compression, $\delta = d/\sigma = 1$. The number of contacting asperities when $\delta = 1$ is equal to $3,173$, which is 6.68% of the total number of asperities. The contacting asperities are modeled as mass-spring units of the Maxwell-slip model (Appendix G). At the onset of the movement of the driver,

the COF curve rises almost linearly. Then, as the movement continues, COF slowly diverges from its linear trend, and the rise of the curve "slows down". In other words, total stiffness starts to decrease with further movement of the driver. The curve approaches the horizontal line of μ_d smoothly and construct a plateau there. The curve slightly fluctuates about the plateau.

In Figure 4.14-(b), every slippage of a block-spring unit in Case 1 with $\delta = 1$ is marked with a dot. The dot abscissa shows the normalized position of the driver at which the block is slipped (as in Figure 4.14-(a)). The dot ordinates show the block number. Many of the blocks remain stuck at the beginning of the movement of the driver. For these blocks, no dot is put, e.g., the block numbers 900-1000. These blocks wait more to be triggered. The corresponding asperities of these block-spring units are pressed relatively more than others. Furthermore, the successive dots that correspond to these units have wider clearances. On the other hand, some units slide in such a frequent manner that their corresponding dots appear as lines, e.g., the block numbers 1500-1510. These block-spring units correspond to the asperities that are compressed less compared to the others (Appendix G).

By considering Figure 4.14-(a) and -(b) at the same time, it can be seen that the slippages (and consequently the force-drops) of the frequently sliding blocks affect the COF curve only slightly. These slippages cause little nonlinearity in the COF curve in spite of their large number. Only when the load drops due to the slippage of the infrequently-sliding blocks (like blocks 90-100) start happening (when the driver has traveled 0.2σ) does the COF curve show a notable nonlinearity.

The histograms of the normal loads, tangential stiffness, and the load-to-stiffness ratio for Case 1 under a one standard deviation compression are shown in Figures 4.15-(a)-(b)-(c). The number of contacting asperities is $3,173$, which is 6.68% of the total number at $\delta = 1$. In Figure 3.12-(a), nearly $1/4$ of the contacting asperities experience the lowest normal load. The bins of higher loads contain relatively smaller percentages of asperities. The distribution seems to be an exponential decay. In Figure 3.12-(b), the percentage of the block-spring units that have a specific stiffness is firstly low (below 1%) and then rises, passes 9% and later falls below 1% again. The shape of the histogram resembles that of Rayleigh PDF. Figure 4.15-(c) shows a gen-

eral decrease trend when the load-to-stiffness ratio increases and can be interpreted as a Gaussian-like tail or linear function.

In Figure 4.16-(a), the variation of COF with the normalized driver position is shown for Case 1 under one and a half standard deviation of compression, i.e., $\delta = 1.5$. The number of contacting asperities is $7,790$ when $\delta = 1.5$. As explained previously, the contacting asperities are modeled as mass-spring units of the Maxwell-slip model. The COF curve diverges from its linear trend when the driver has traveled 0.25σ. The curve falls to rise at the same rate; one may say total stiffness decreases with the progression of the driver. The curve gradually approaches the horizontal line of μ_d and becomes tangent to it, forming a plateau. The fluctuations of the curve are quite small.

In Figure 4.16-(b), the red dots mark the driver positions at which the slippage of each contacting asperity is triggered for the set of mass-spring blocks that correspond to the contacting asperities which are generated for Case 1 when $\delta = 1.5$. Some blocks remain stuck at the beginning of the driver's movement, while others frequently slide from the beginning. The slippages of the frequently sliding blocks do not affect the COF curve in Figure 4.16-(a) much since the load drops due to the slippage of these blocks are small, even cumulatively.

The histograms of the normal loads, tangential stiffness, and the load-to-stiffness ratio for Case 1 with $\delta = 1.5$ are shown in Figures 4.17-(a)-(b)-(c). The number of contacting asperities is $7,790$ when $\delta = 1.5$. The number of contacting asperities is 16.4% of the generated asperities. In Figure 4.17-(a), above $1/4$ of the contacting asperities experience the lowest normal load. The percentages of the asperities drop abruptly for the bins of higher loads. In Figure 4.17-(b), the bin populations first increase from below 1% to over 7% and then drops below 1%. Figure 4.17-(c) can be interpreted as a Gaussian or linear distribution. All of the histograms resemble their counterparts with lower compression values.

Figure 4.18 superimposes the COF curves which were already shown in Figures 4.12-(a), 4.14-(a) and 4.16-(a). The variation of COF with the normalized driver position is shown for Case 1 with three different compression values, $\delta = 0.5, 1, 1.5$. The number of contacting asperities (and consequently the block-spring units) is $712, 3173$,

and 7790, respectively. The curves are almost linear firstly and later diverge, falling to rise at the same rate. For all compression values, total stiffness decreases as the driver moves forward. All of the curves reach a plateau at mu_d. The fluctuations of the curves become smaller with the increase in compression.

A lower compression, δ, leads to a faster rise to the plateau. This seems reasonable because when a set of asperities is pressed less, by intuition, a shorter movement of the driver is enough to end the pre-sliding behavior. In other words, the driver needs less “time” under lower compression values to reach the plateau of dynamic friction. Conversely, for a set that is pressed more, the driver has to “try” more in order to trigger slippage of all of the mass-spring units and the curve rises slower consequently.

It should be noted that if the ordinates show *friction force* instead of the COF, the curve that corresponds to $\delta = 1.5$ would still reach the plateau "later" than those corresponding to lower compression values. The multiplication of the normal load to COF scales the ordinates only and would not affect the abscissas. Therefore, the plateau is reached by the friction force curves at the same driver positions as for COF curves. The tangent stiffness values can be extracted and compared from the friction curves. The hysteresis behavior of the surface can also be studied. The dissipated energy would be equal to the area below the friction force curve (and not the COF curve).

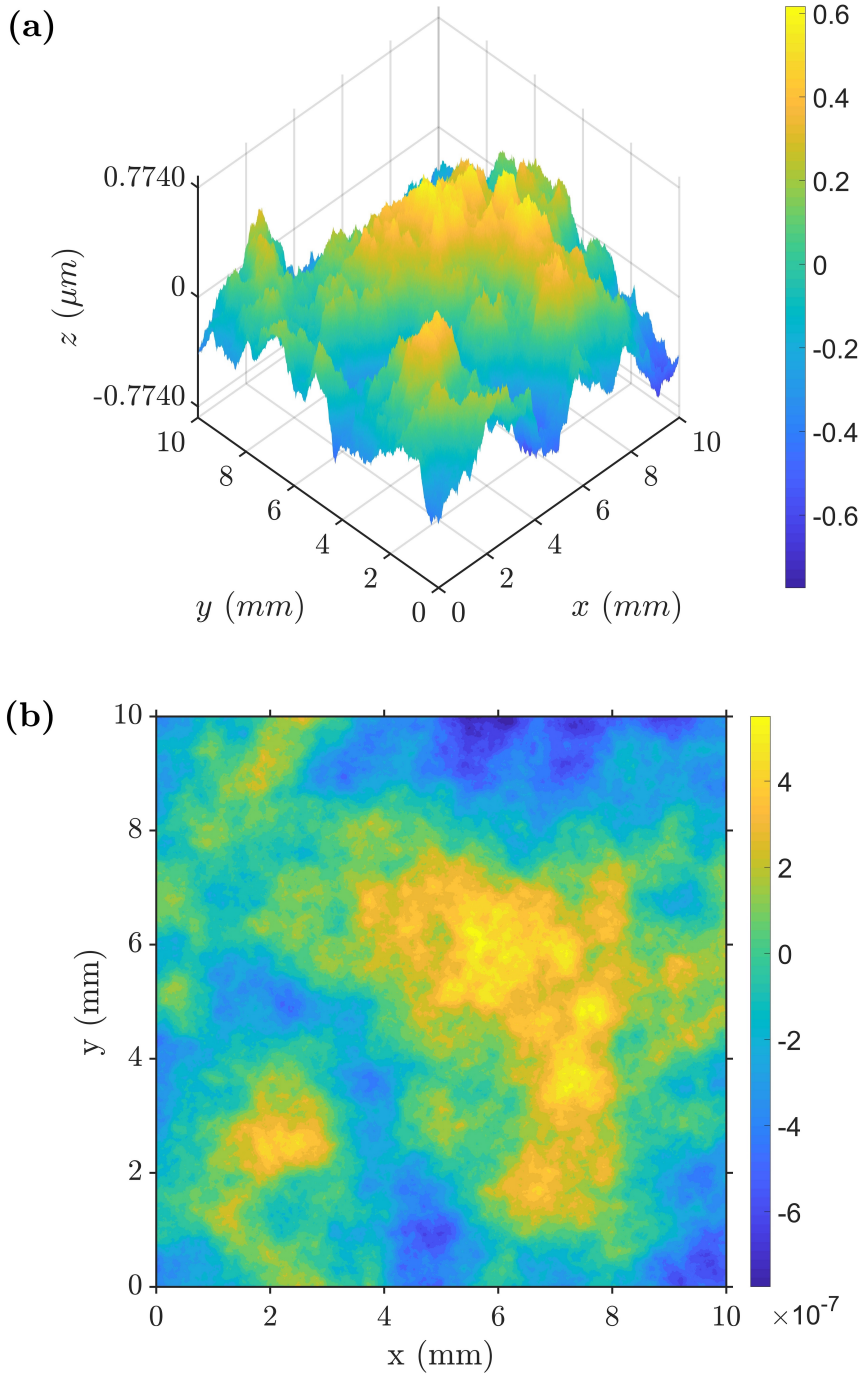

Figure 4.5: The topography of the rough surface that is generated for Case 1 (with $H = 0.75$ and $\sigma_0 = 1\ \mu m$, but resulted in $\sigma = 0.24\ \mu m$): (a) The isometric view of the generated 3-D fractal surface, (b) The top view of the same surface

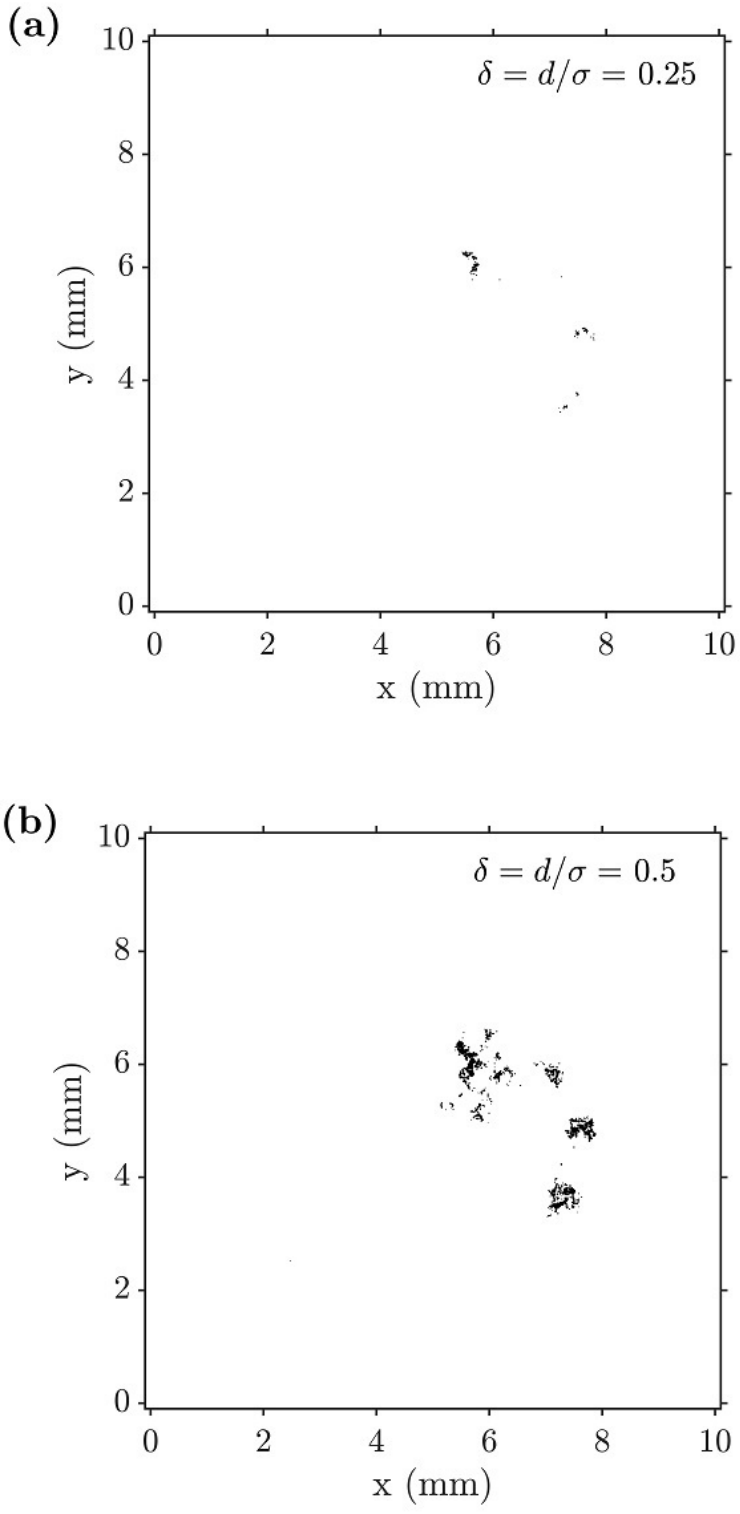

Figure 4.6: The visualization of the evolution of the real contact area for Case 1 ($H = 0.75$ and $\sigma_0 = 1\ \mu m$) under the compression values $\delta = 0.25, 0.5, 0.75, 1, 1.25$ and 1.5 with the series of frames (a) to (f)

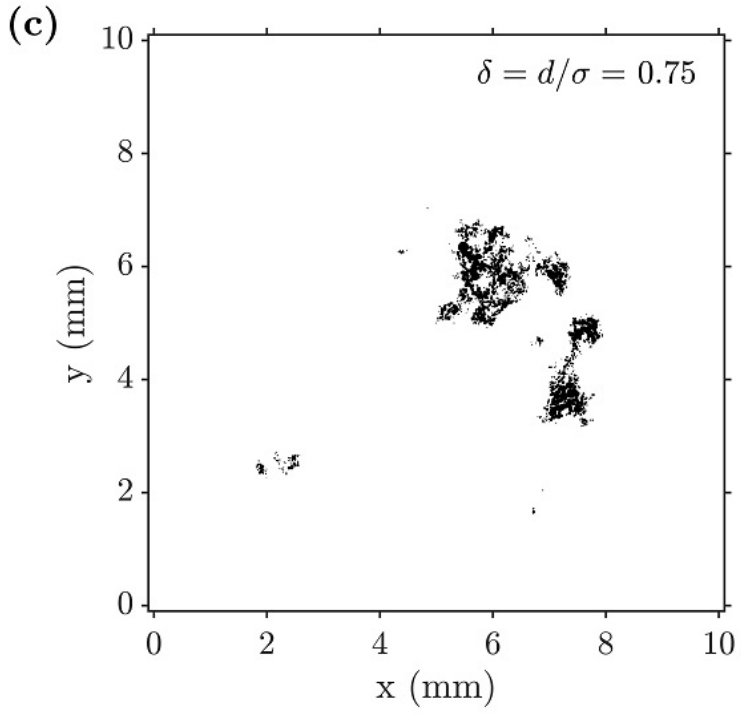

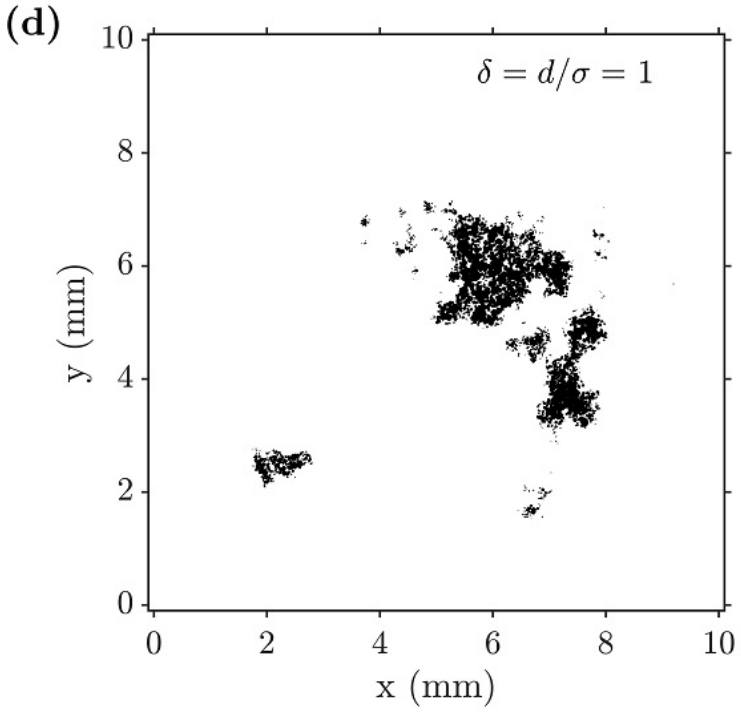

Figure 4.6 continues

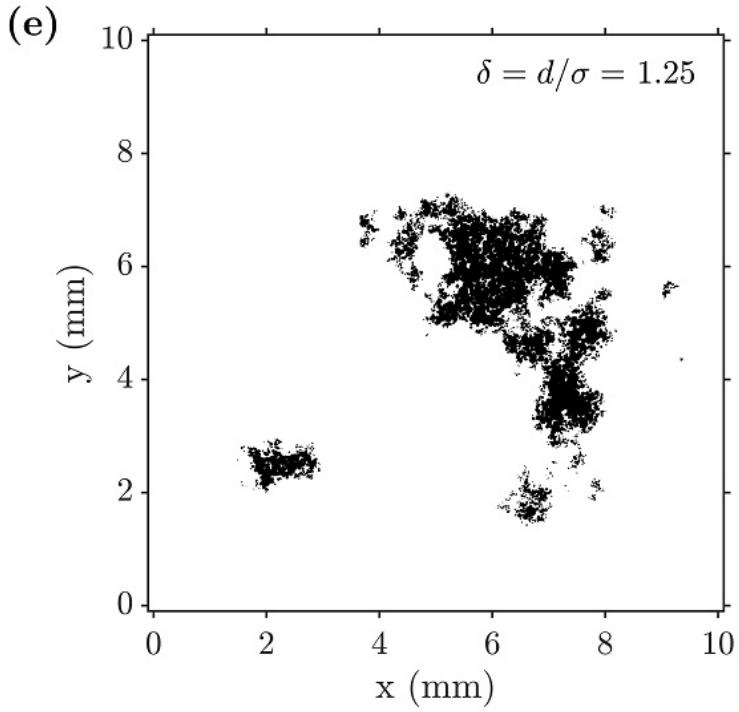

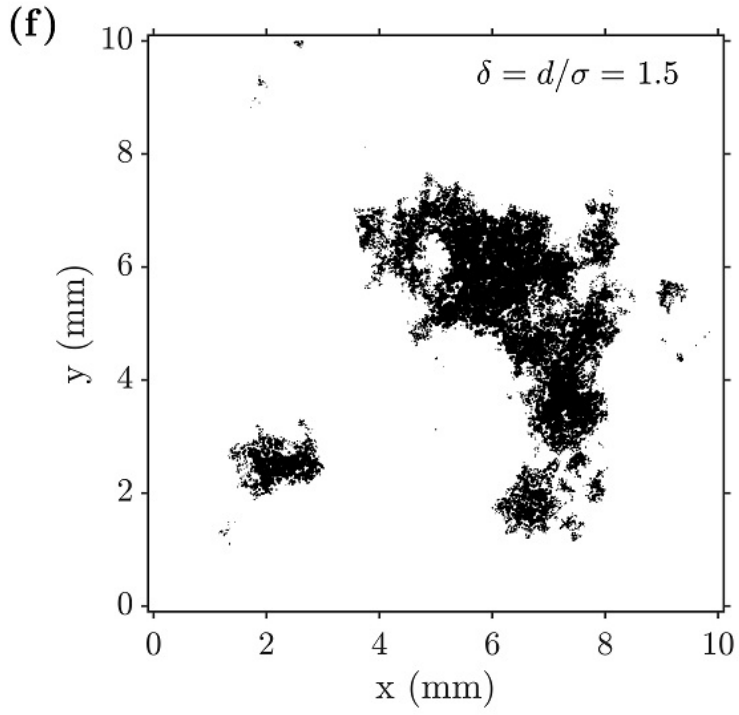

Figure 4.6 continues

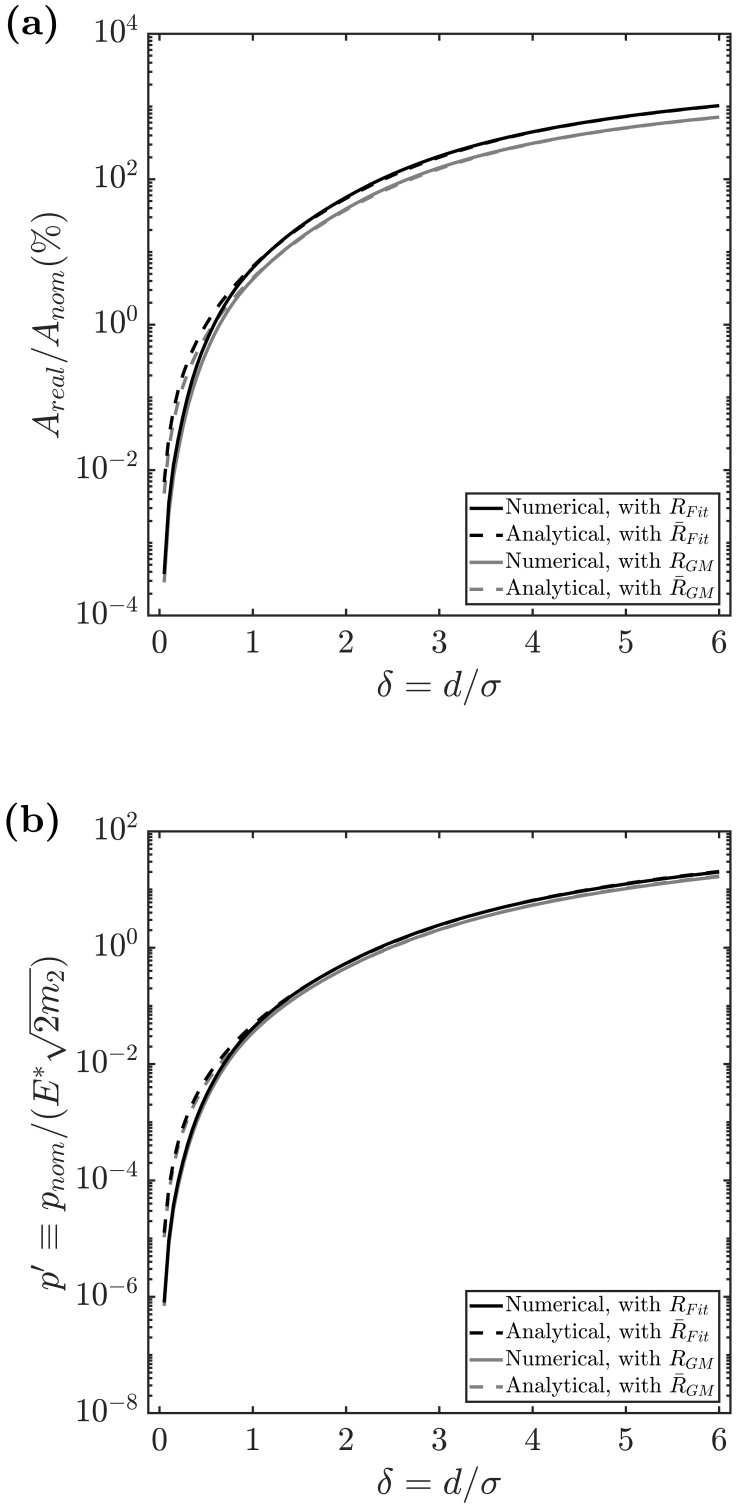

Figure 4.7: The numerical and analytical (a) real contact area and (b) pressure against compression for Case 1 ($H = 0.75$ and $\sigma_0 = 1\ \mu m$).

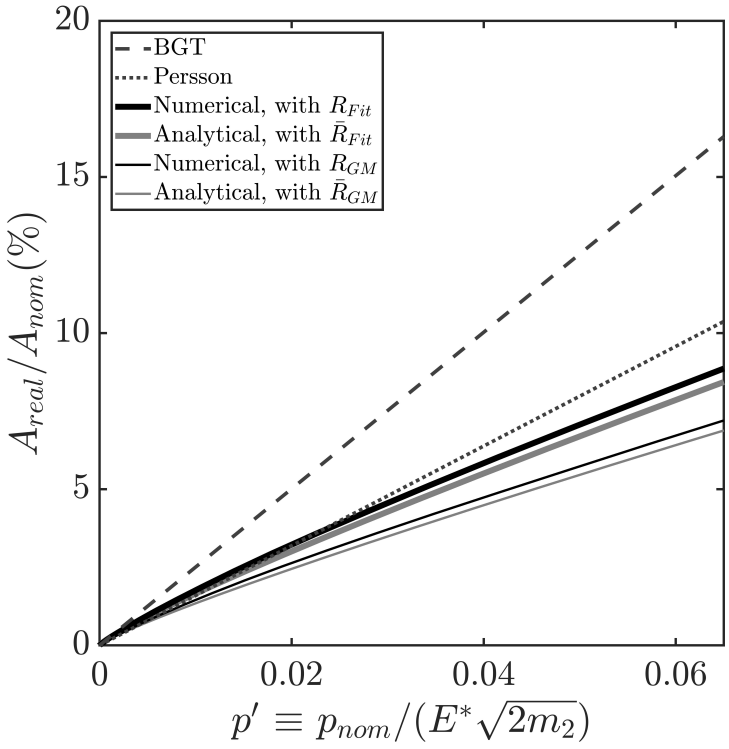

Figure 4.8: The numerical and analytical relation between real contact area and pressure is superimposed with the theoretical limits proposed by BGT and Persson for Case 1 ($H = 0.75$ and $\sigma_0 = 1\ \mu m$).

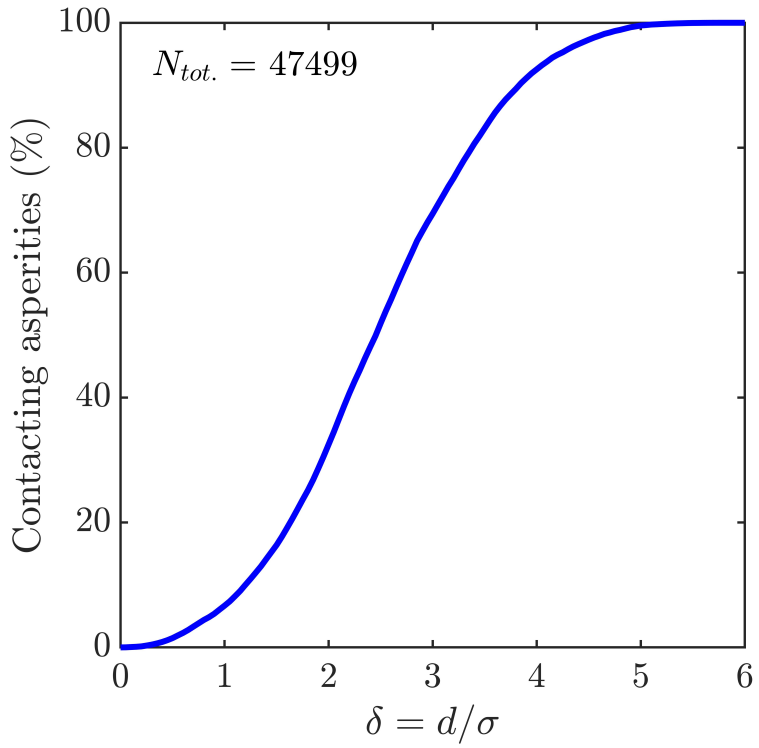

Figure 4.9: The number of contacting asperities as percentage of the total number of generated asperities against compression for Case 1 ($H = 0.75$ and $\sigma_0 = 1\ \mu m$) according to the numerical results.

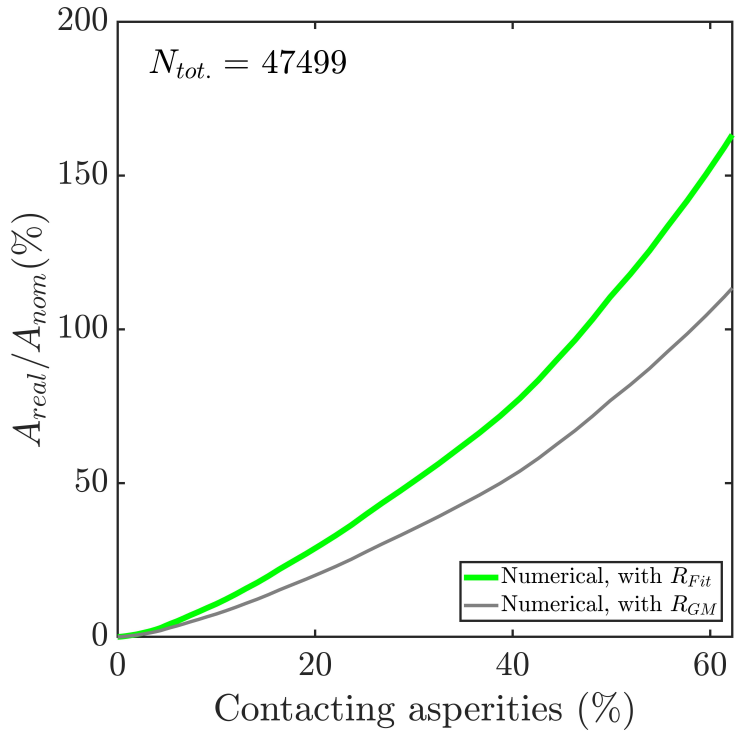

Figure 4.10: Real contact area against the percentage of the contacting asperities for Case 1 ($H = 0.75$ and $\sigma_0 = 1\ \mu m$) according to the numerical results.

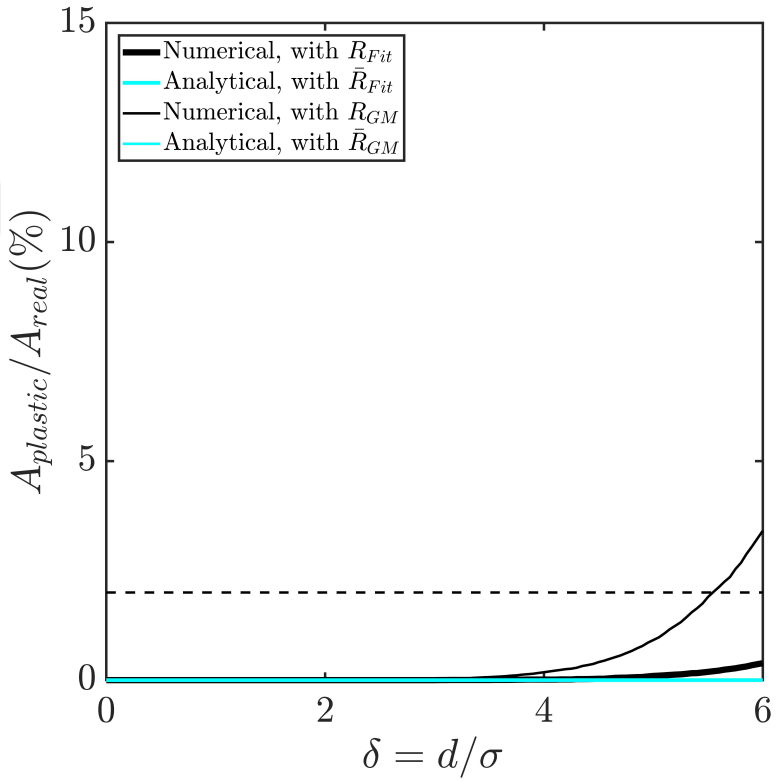

Figure 4.11: Plastic contact area against compression for Case 1 ($H = 0.75$ and $\sigma_0 = 1\ \mu m$) according to the numerical and analytical results.

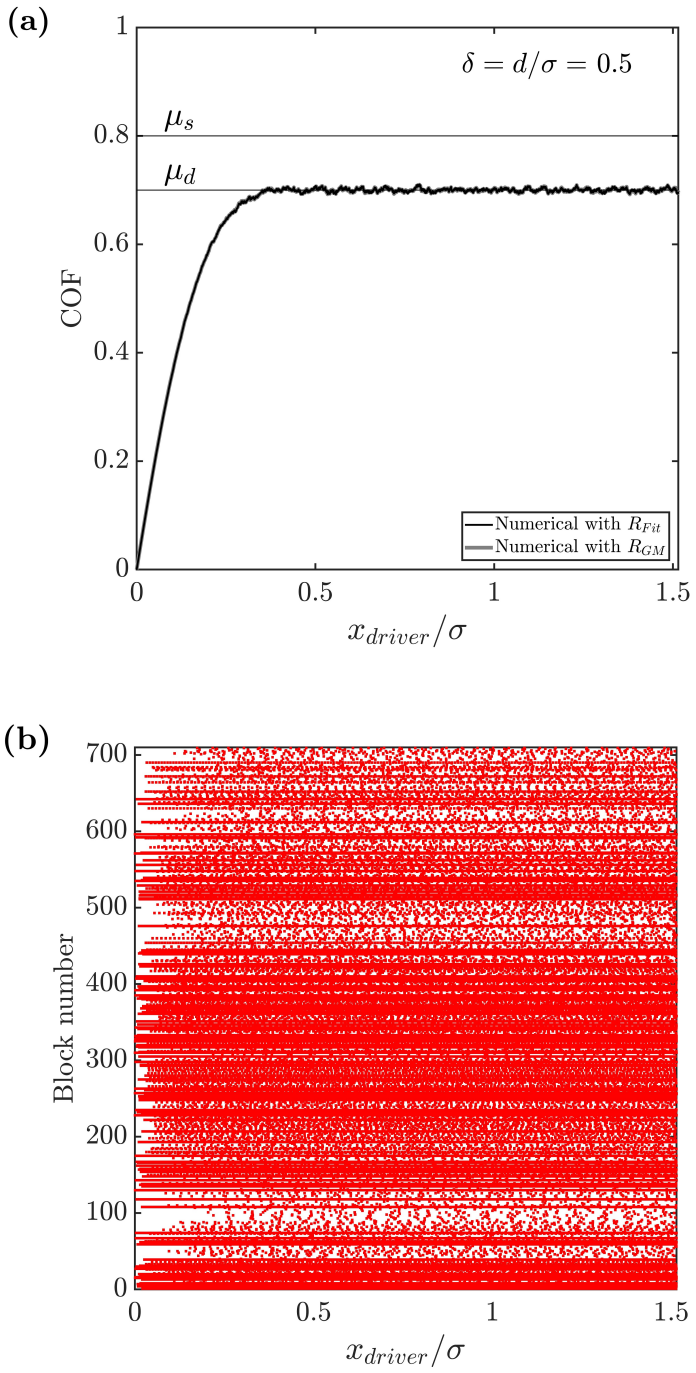

Figure 4.12: The numerical results for sliding at $\delta = 0.5$ for Case 1 ($H = 0.75$ and $\sigma_0 = 1\ \mu m$): (a) COF against the driver position and (b) Block slippage history against the driver position.

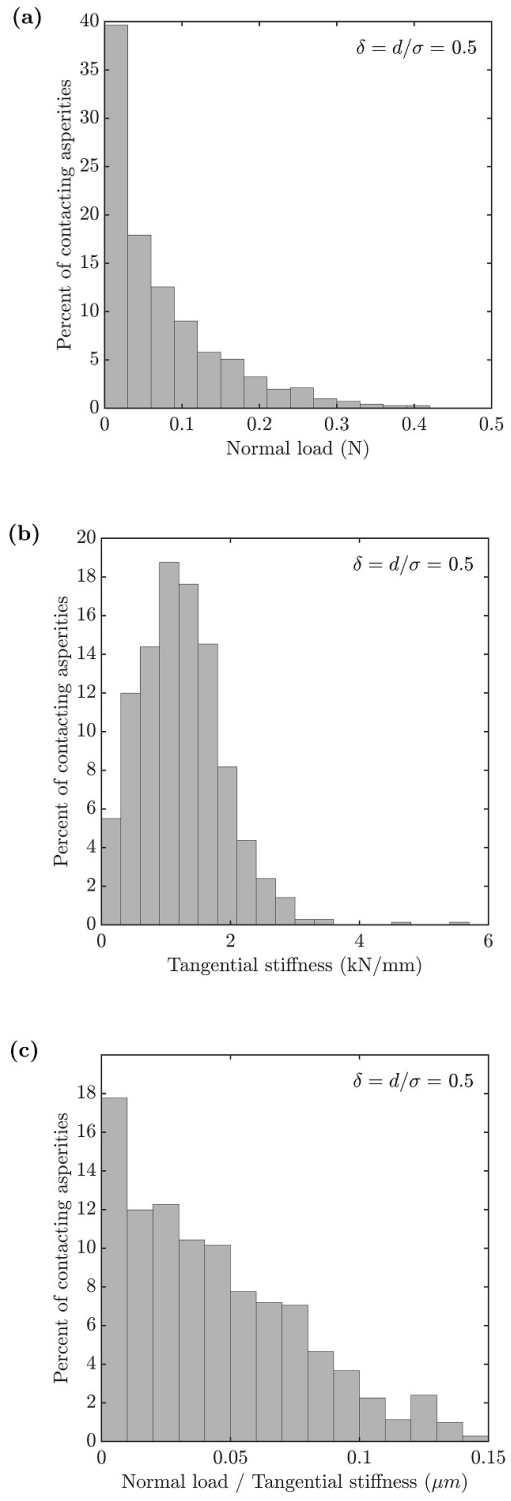

Figure 4.13: Histograms of (a) normal load (b) tangential stiffness and (c) load to stiffness ratio for Case 1 ($H = 0.75$ and $\sigma_0 = 1\ \mu m$) at $\delta = 0.5$.

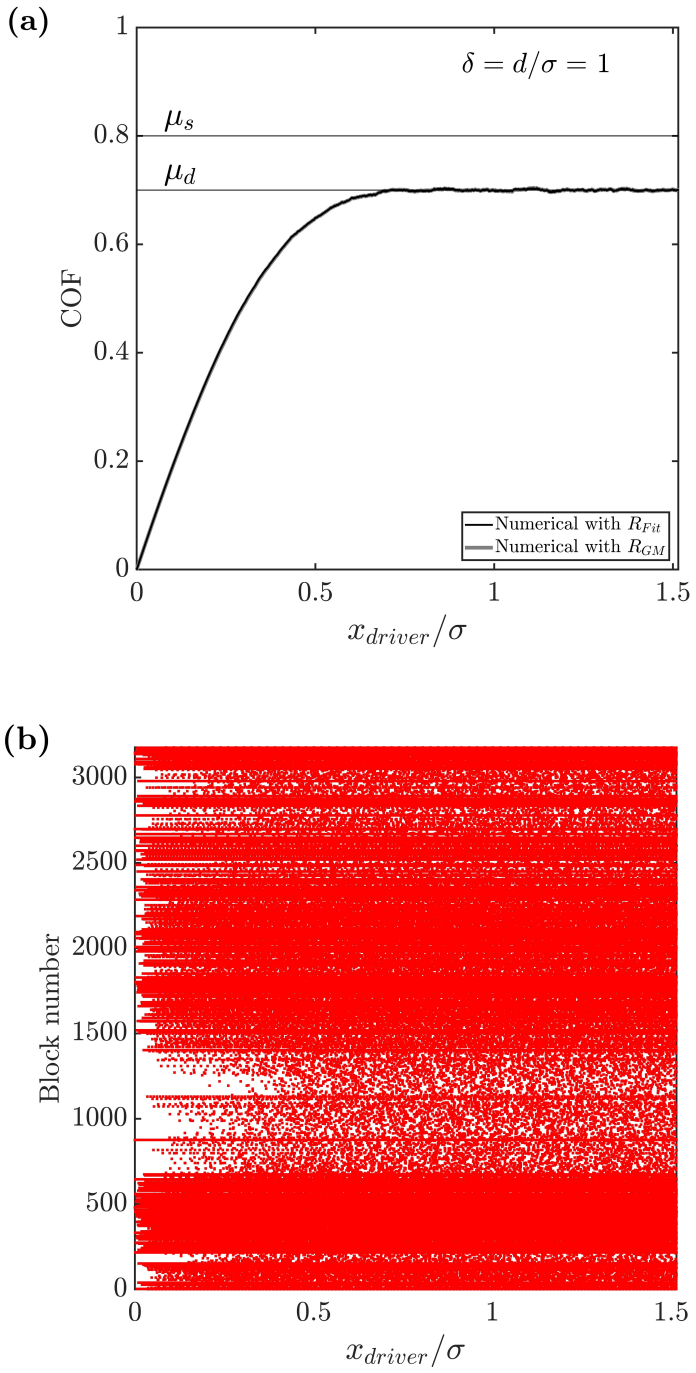

Figure 4.14: The numerical results for sliding at $\delta = 1$ for Case 1 ($H = 0.75$ and $\sigma_0 = 1\ \mu m$): (a) COF against the driver position and (b) Block slippage history against the driver position.

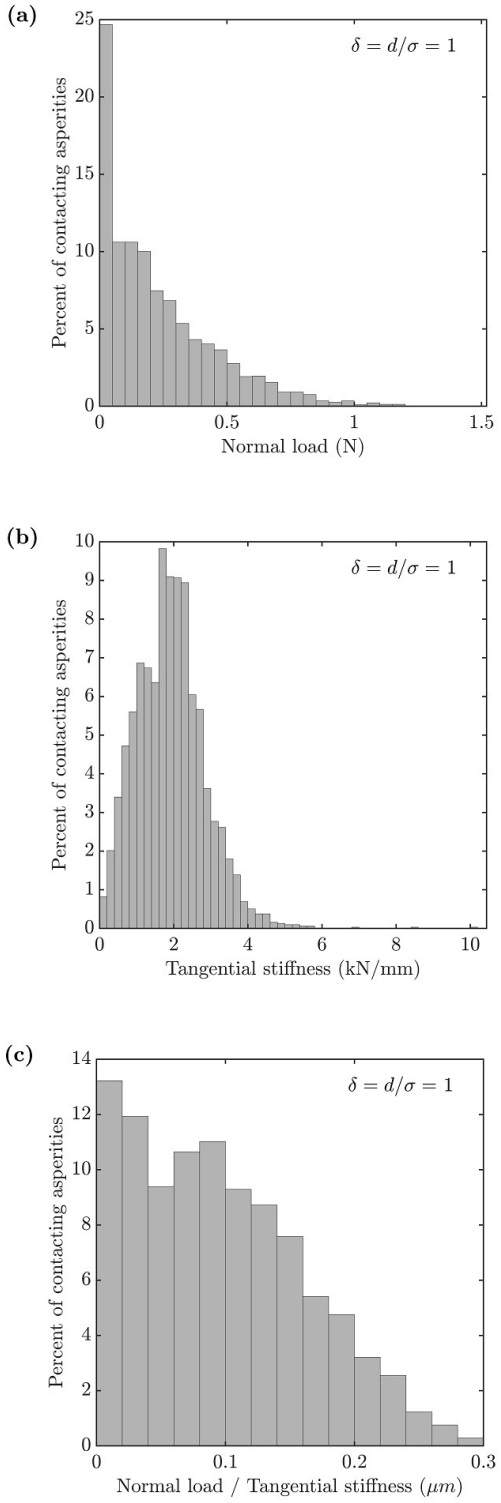

Figure 4.15: Histograms of (a) normal load (b) tangential stiffness and (c) load to stiffness ratio for Case 1 ($H = 0.75$ and $\sigma_0 = 1\ \mu m$) at $\delta = 1$.

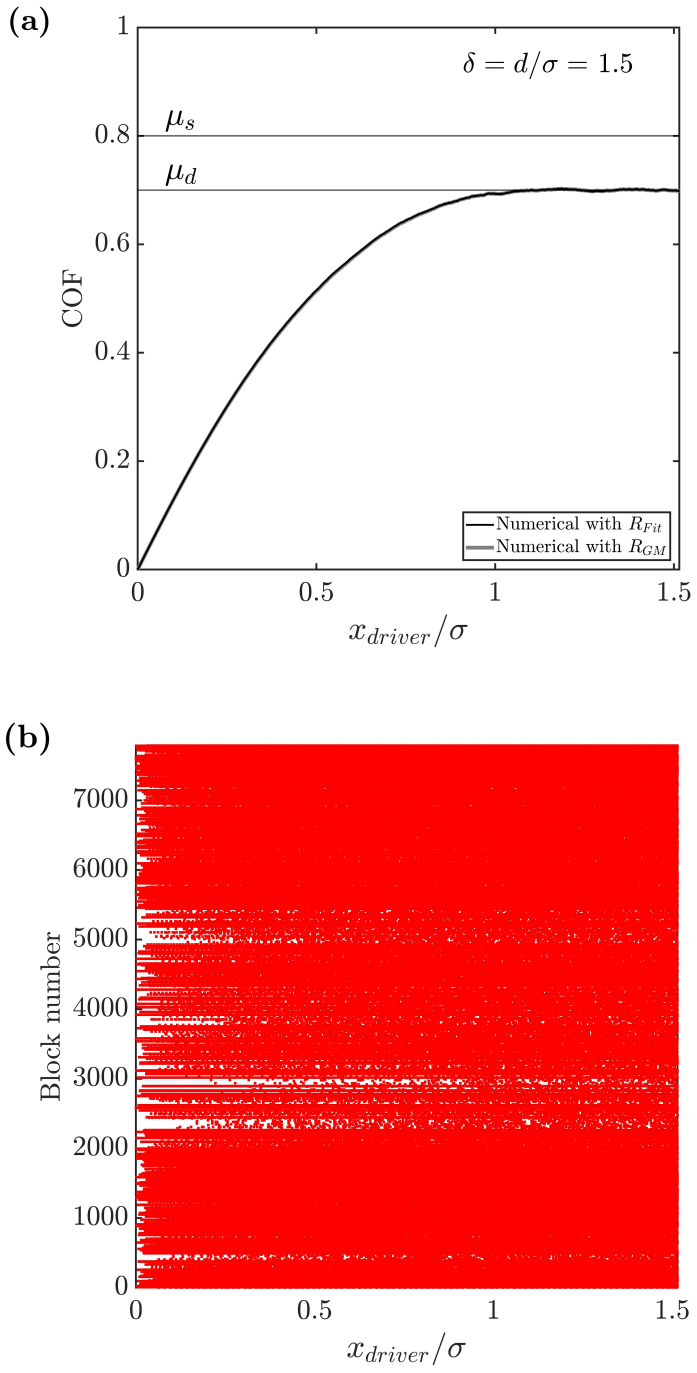

Figure 4.16: The numerical results for sliding at $\delta = 1.5$ for Case 1 ($H = 0.75$ and $\sigma_0 = 1\ \mu m$): (a) COF against the driver position and (b) Block slippage history against the driver position.

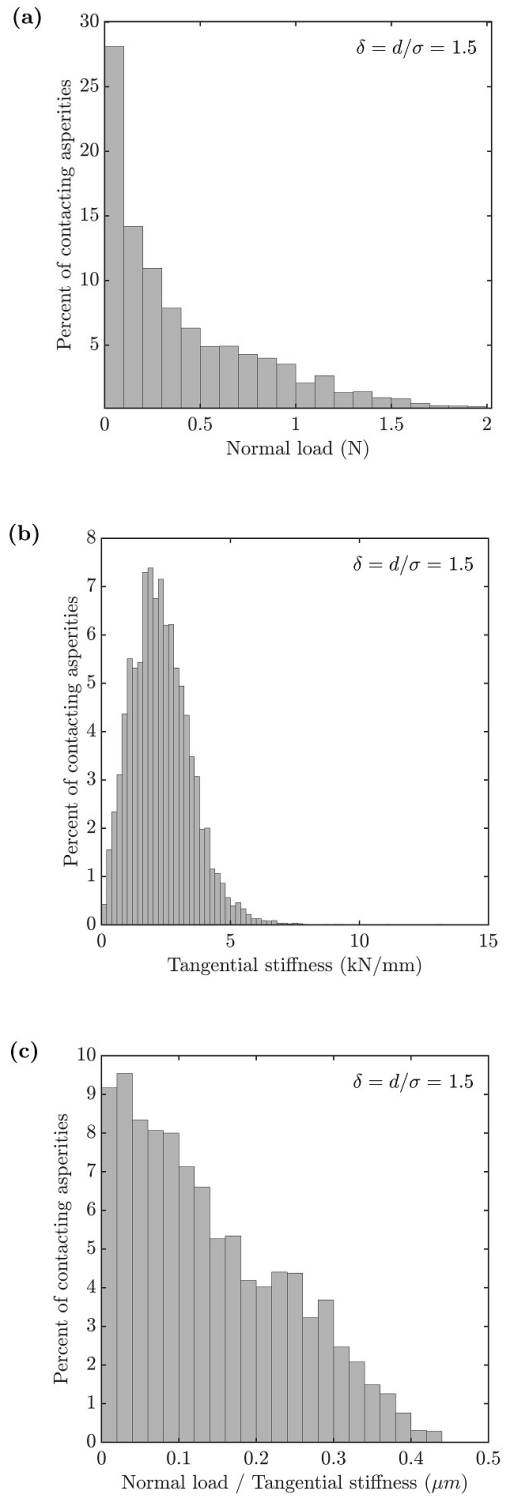

Figure 4.17: Histograms of (a) normal load (b) tangential stiffness and (c) load to stiffness ratio for Case 1 ($H = 0.75$ and $\sigma_0 = 1\ \mu m$) at $\delta = 1.5$.

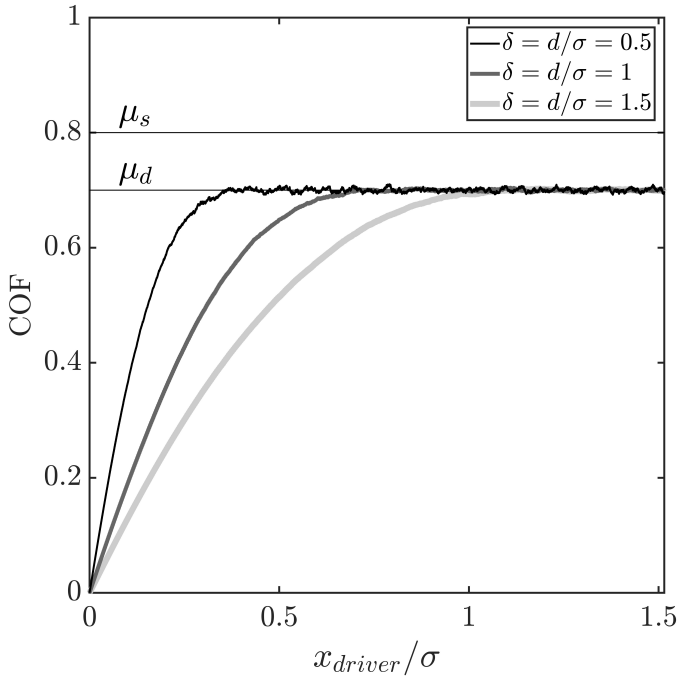

Figure 4.18: The numerical results for sliding under different compression values, $\delta = 0.5, 1, 1.5$, for Case 1 ($H = 0.75$ and $\sigma_0 = 1\ \mu m$)

4.3.2 Case 2 ($H = 0.95, \sigma_0 = 1\ \mu m$)

The series of results that are presented in Figures 4.19-4.32 are related to the normal and sliding contact of Case 2 for which Hurst exponent, H, is equal to 0.75 and the initial standard deviation, σ_0, is assigned a value of one micron. The second spectral moment of the PSD, m_2, is obtained by the 11-point equi-spaced finite difference stencil as $m_2 = 2.23e-6$. The values of m_2, calculated for Case 1 by the other stencils, are also present in Figure 4.4. The number of counted summits (asperities) is $26,373$. Roughly 2.5% of the surface points are summits. Although the initial standard deviation, σ_0, is assumed to be $1\ \mu m$, the final standard surface of all surface points is $\sigma = 0.23\ \mu m$.

In Figure 4.19 the surface that is generated by the RMD for Case 2 is represented in both 3-D and 2-D. Figures 4.20-(a)-(f) visualize the evolution of the real contact area with increasing the compression, $\delta = d/\sigma$, from 0.25 to 1.5 with steps of size 0.25 for Case 2 with fitted radii, R_{Fit}. The corresponding numerical real contact area for the Figures 4.20-(a)-(f) are: $0.1\%, 0.6\%, 1.8\%, 3.9\%, 6.4\%$ and 12% of the nominal contact area.

In the semi-log plot in Figure 4.21-(a), the ordinates show the variation of the numerically and analytically calculated contacting real area to the nominal area ratio, A_{real}/A_{nom}, (as a percentage) against the normalized compression, $\delta = d/\sigma$, for Case 2. While the numerical results are obtained by using the set of obtained fitted paraboloid radii and the geometric mean radii, the analytical results are obtained by the average value of *all* radii of the surface asperities (contacting and not-yet-contacting) in Equations (C.3) and (C.4). Although curves are in a good agreement in vast intervals of the applied compression, the numerical and analytical values depart from each other within $1 < \delta < 2$ temporarily for both types of the radii calculations.

In the semi-log plot in Figure 4.21-(b), the ordinates show the variation of normalized nominal normal pressure, $p' = p_{nom}/(E^*\sqrt{2m_2})$, against the normalized compression, $\delta = d/\sigma$, for Case 2. As the rigid rough surface is pressed by the elastic half-space, the normalized nominal pressure increases and the trend of agreement and disagreement between the numerical and analytical results is similar to that of Figure

4.21-(a).

In Figure 4.22, the variation of real area, A_{real}, (as percent of the nominal area, A_{nom}) with normalized nominal pressure, $p' = p_{nom}/(E^*\sqrt{2m_2})$, is plotted for Case 2. Both of the numerical and analytical results are in good agreement with the theoretical limits of BGT and Persson (Section 3.1.1) as the slopes lay between 1.3 and 2.5 generally.

In Figure 4.23, increase of the number of contacting asperities (as percent of the total number of the asperities, which is a 26.373) with the normalized compression, δ, is plotted for set of generated asperities in Case 2. The increase curve resembles Gaussian cumulative distribution function.

In Figure 4.24, the numerically-obtained real contact area ratio is plotted against the number of contacting asperities (as a percentage) for Case 2 for both the fitted paraboloid radii and the GM radii. The curves seem to be bi-linear. However, it can be a numerical artifact since the counterpart curves in Figure 4.10 rise smoothly.

Figure 4.25 shows the evolution of the ratio of the plastic contact area to the real contact area, $A_{plastic}/A_{real}$, (expressed in percent) with compression according to both numerical and analytical results for Case 2. No inception of the plastic deformation is observed for either of the numerical and analytical results with fitted or geometric mean radii, up to $\delta = 6$. The calculated plasticity indices are 0.15 according to Equation (F.5) with $\bar{R}_{Fit} = 2.7\ cm$ and 0.18 according to the same equation with $\bar{R}_{GM} = 1.9\ cm$ and 0.08 according to Equation (F.8) with $m_2 = 2.23e-6$. All of the calculated plasticity indices are well below 0.5 and therefore lack of plastic behavior is reasonable and theoretically expected.

Figure 4.26-(a) shows the variation of COF with the normalized driver position for Case 2 under half standard deviation of compression, i.e. $\delta = d/\sigma = 0.5$. The number of contacting asperities is 236 at $\delta = 0.5$. The contacting asperities are modeled as mass-spring units of Maxwell-slip model. The COF curve is almost linear at the onset of movement of the driver. Later, the curve changes its slope while still rises linearly. Finally the curve becomes nonlinear before becoming tangent to the horizontal plateau of μ_d. The curve fluctuates about the plateau in a distinct manner.

The effect of the radii (R_{Fit} or R_{GM}) is minimal on the behavior of the curve.

In Figure 4.26-(b), the history of the block slippages are shown for Case 2 under a compression of $\delta = 0.5$. The blocks that are harder to trigger, majority of which have block numbers higher than 200 by chance start to slide only after that the driver had traveled 0.25σ. In addition, there is a class of the block-spring units that are not so-hard-to-trigger and are more populated compared the previous group, e.g., those with block numbers between 70 and 80. It seems that after involvement of these moderate blocks the COF curve starts to show nonlinear behavior after $x_{driver} = 0.1\sigma$ as seen in 4.26-(a). The first group of the units, when involved, make the behavior strongly nonlinear after $x_{driver} = 0.25\sigma$.

The histograms of the normal loads, tangential stiffness and the load to stiffness ratio for Case 2 when $\delta = 0.5$ are shown in Figures 4.27-(a)-(c). The number of contacting asperities (the members of the subset) is 236 at $\delta = 0.5$. Since the number of contacting asperities is small compared to the total number of the generated asperities (only 0.6%), the histograms are coarse.

In Figure 4.27-(a), over 60% of the contacting asperities experience the lowest amount of normal load and the rest are distributed among the higher-load bins which their populations hardly exceed 10%. In Figure 4.27-(b), the percentage of asperities that have a certain stiffness is firstly relatively low (10%), then rises sharply to the maximum (nearly 40%) and then falls. Figure 4.27-(c) shows an irregular trend that does not resemble any known distribution.

In Figure 4.28-(a), the variation of COF with the normalized driver position is shown for a subset of generated asperities in Case 2 when the set of asperities is pressed one standard deviation of its heights down, i.e. $\delta = 1$. The number of contacting asperities (and consequently the number of the block-spring units) is 493 at $\delta = 1$. The COF curve diverges from its linear trend after $x_{driver} = 0.4\sigma$. The curve approaches the horizontal line of μ_d after a shallow drop and fluctuates about the plateau of the dynamic COF.

In Figure 4.28-(b), the history of the block slippages are shown for Case 2 under a compression of $\delta = 1$. The hardest-to-slide blocks majorly have numbers higher than

400 and slide only after that the driver had traveled 0.25σ. On the other hand, the relatively hard to slide blocks (like those between 90 and 110) are greater in number and are triggred after $x_{driver} = 0.25\sigma$. It seems that involvement of this latter group of blocks makes COF curve diverge from linearity while the hardest-to-slide group makes the curve strongly nonlinear as can be seen in 4.28-(a).

The histograms of the normal loads, tangential stiffness and the load to stiffness ratio for Case 2 when $\delta = 1$ are shown in Figures 4.29-(a)-(c). The number of contacting asperities (the members of the subset) is 493 at $\delta = 1$. The number of contacting asperities is 3.9% of the generated asperities. In Figure 4.29-(a), above 30% of the contacting asperities experience the lowest amount of normal load. In Figure 4.29-(b), the percentage of asperities that have a certain stiffness is firstly relatively low, then rises gradually to over 20% and later falls steeply to below 5% for the stiffness values higher than $6\ kN/mm$. Figure 4.29-(c) shows an irregular trend of decrease and increase.

In Figure 4.30-(a), the variation of COF with the normalized driver position is shown for Case 2 with $\delta = 1.5$. The number of contacting asperities (and therefore the block-spring units) is $1,760$ at $\delta = 1.5$. The COF curve diverges from its initially linear trend, falling to rise at the same rate when $x_{driver} = 0.1\sigma$. One may claim that the total stiffness starts to decrease distinctively when the driver passes $x_{driver} = 0.1\sigma$. The curve approaches the horizontal line of μ_d gradually and does not become tangent to it; but continues for a while below and parallel to the μ_d line and then crosses and oscillates about it.

In Figure 4.30-(b), shows the history of slippages of the set of mass-spring blocks that correspond to the contacting asperities of Case 2 surface when $\delta = 1.5$. Similar to the compression values $\delta = 0.5, 1$ the blocks can be categorized as frequently-sliding, moderately-sliding and hard-to-slide. The moderately-sliding blocks, e.g., the blocks $800 - 900$ are larger in number compared to the hard-to-slide blocks and almost all of them are triggered when $x_{driver} = 0.1\sigma$. At the same point the COF curve in Figure 4.30-(a) starts to diverge from its linear rise. It seems that the loss of stiffness happens in a steady manner and the involvement of the hard-to-slide blocks does not affect the constant rate of loss.

The histograms of the normal loads, tangential stiffness and the load to stiffness ratio for Case 2 when $\delta = 1.5$ are shown in Figures 4.31-(a)-(c). The number of contacting asperities (the number of the block-springs) is 836 at $\delta = 1.5$ is 83.6% of the generated asperities. As shown in Figure 4.31-(a), about 45% of the contacting asperities experience a normal load below $0.2\ N$. The population of the higher load bins decreases sharply. In 4.31-(b), the stiffness histogram resembles a Rayleigh PDF. Figure 4.31-(c) shows a fall from 20% to below 5% and then a rise to above 5% and a final drop to zero in the population of the load to stiffness ratio.

In Figure 4.32, the COF curves which are shown in Figures 4.26-(a), 4.28-(a) and 4.30-(a) are superimposed. In other words, the variation of COF with the normalized driver position under three different compression values, $\delta = 0.5, 1, 1.5$ are shown for Case 2. The number of contacting asperities (the number of the block-spring units) are 236, 493 and 1760, respectively. Similar to Case 1 (Figure 4.18), the higher the compression value the "later" the curve reaches the plateau. In contrast to Case 1, the initial slopes of the COF curve for $\delta = 1, 1.5$ are very close.

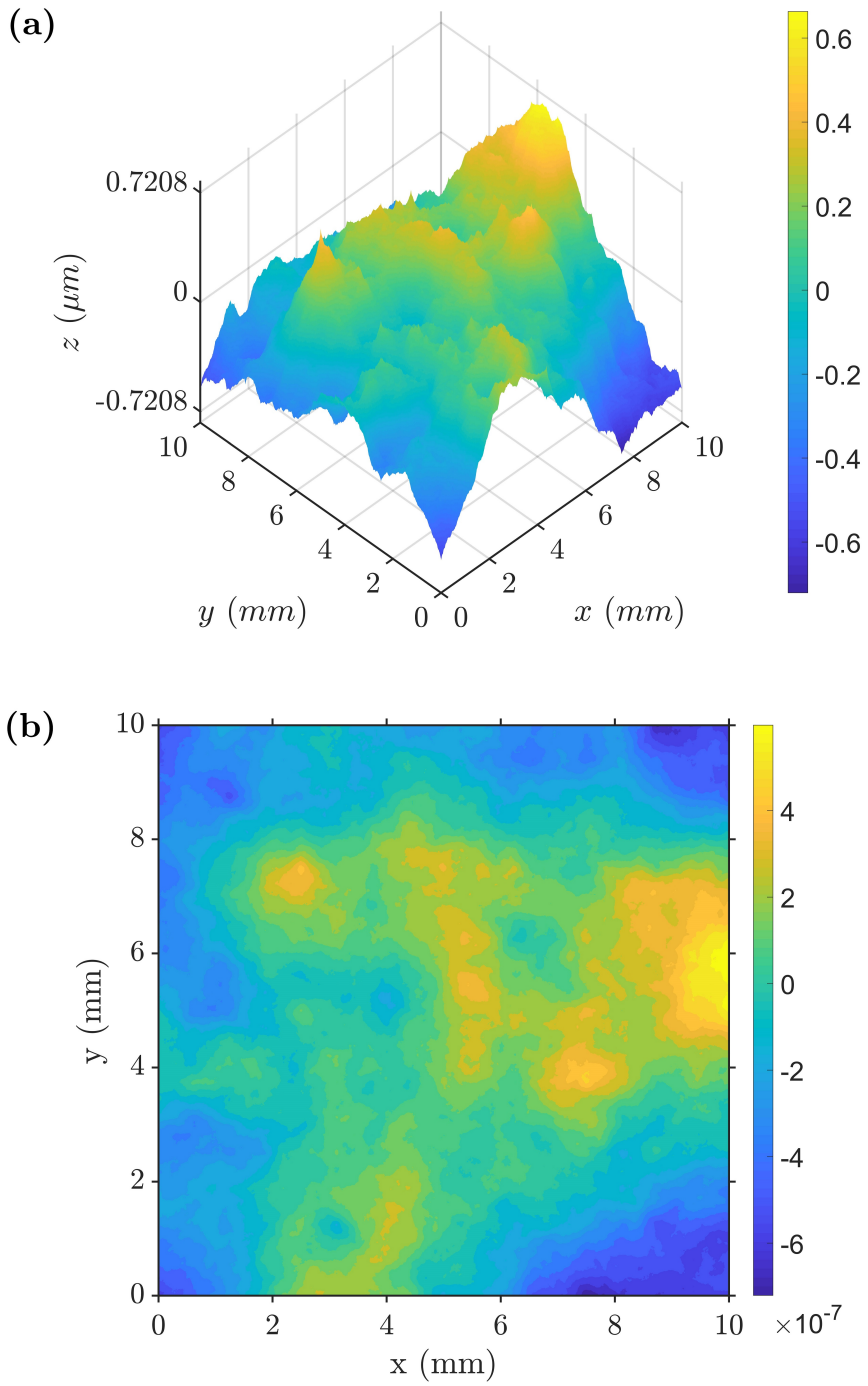

Figure 4.19: The topography of the rough surface that is generated for Case 2 (with $H = 0.95$ and $\sigma_0 = 1\ \mu m$, but resulted in $\sigma = 0.23\ \mu m$): (a) The isometric view of the generated 3-D fractal surface, (b) The top view of the same surface

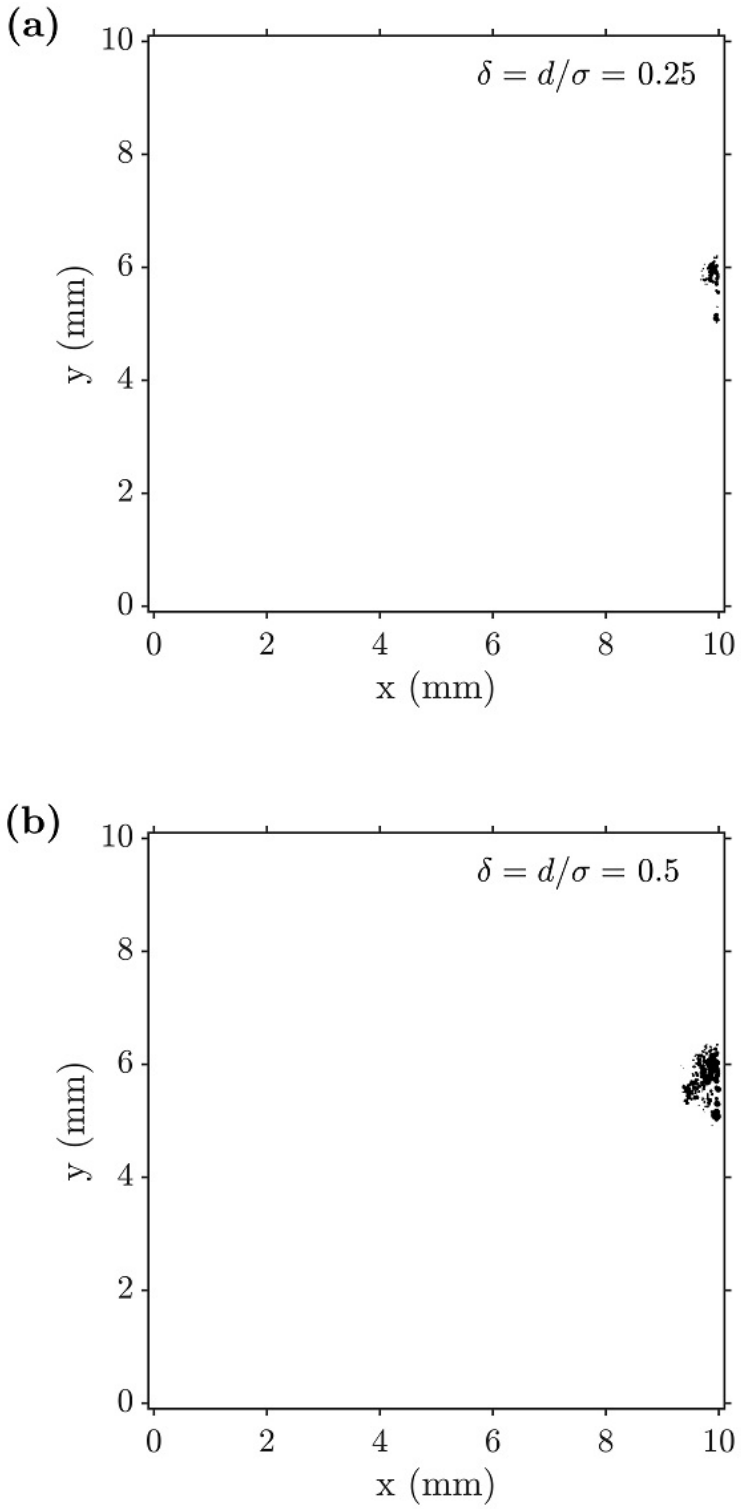

Figure 4.20: The visualization of the evolution of the real contact area for Case 2 ($H = 0.95$ and $\sigma_0 = 1\ \mu m$) under the compression values $\delta = 0.25, 0.5, 0.75, 1, 1.25$ and 1.5 with the series of frames (a) to (f)

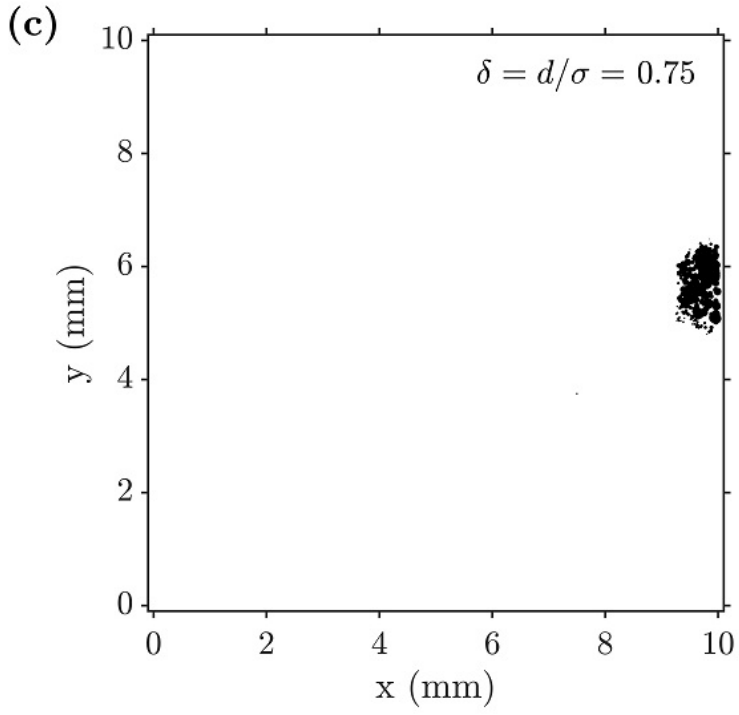

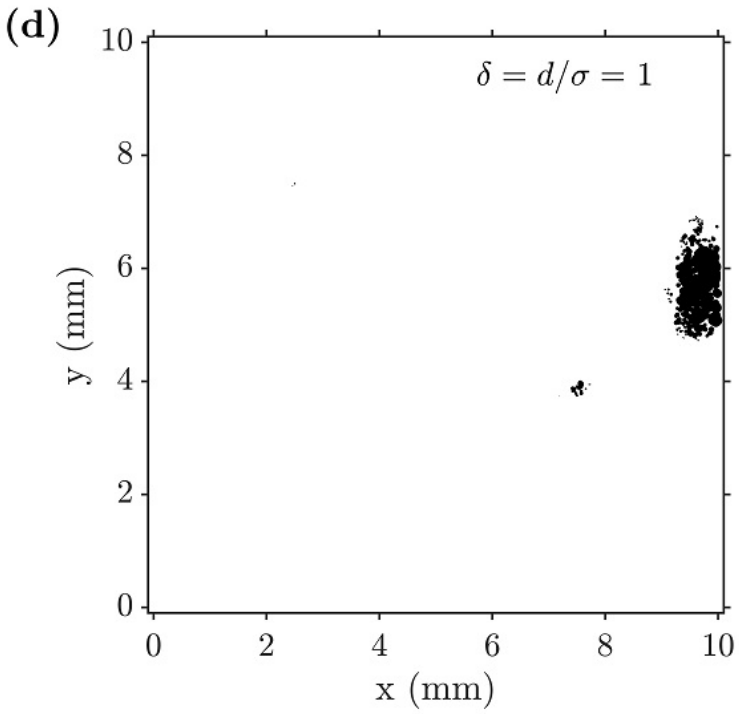

Figure 4.20 continues

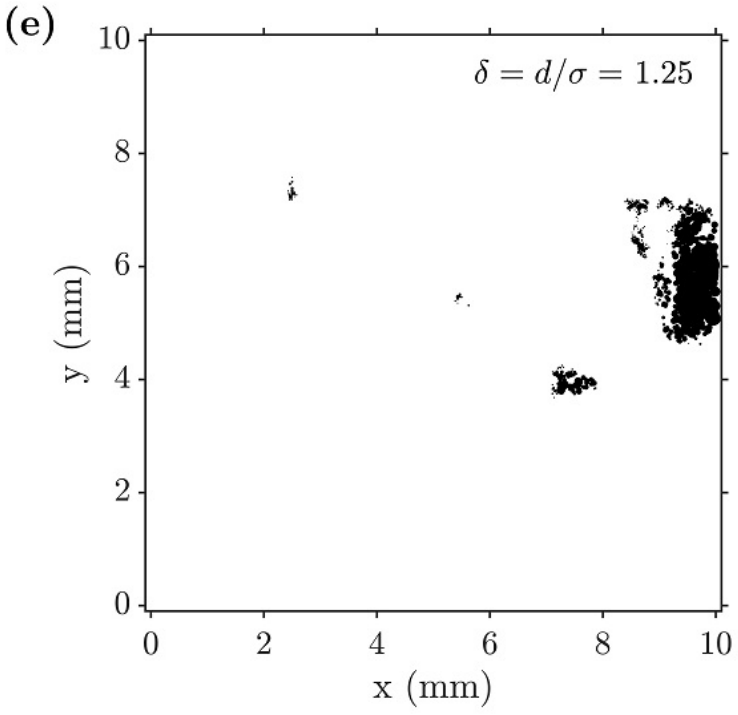

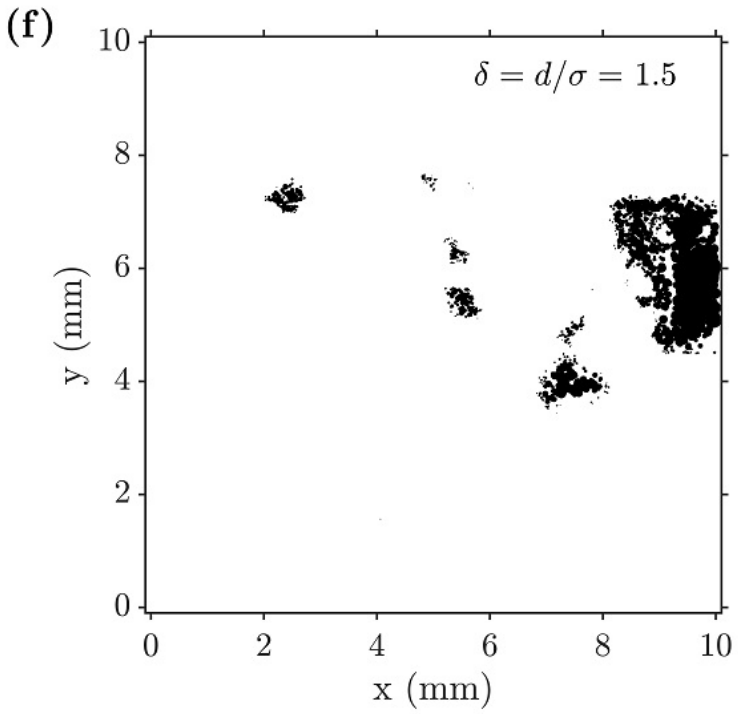

Figure 4.20 continues

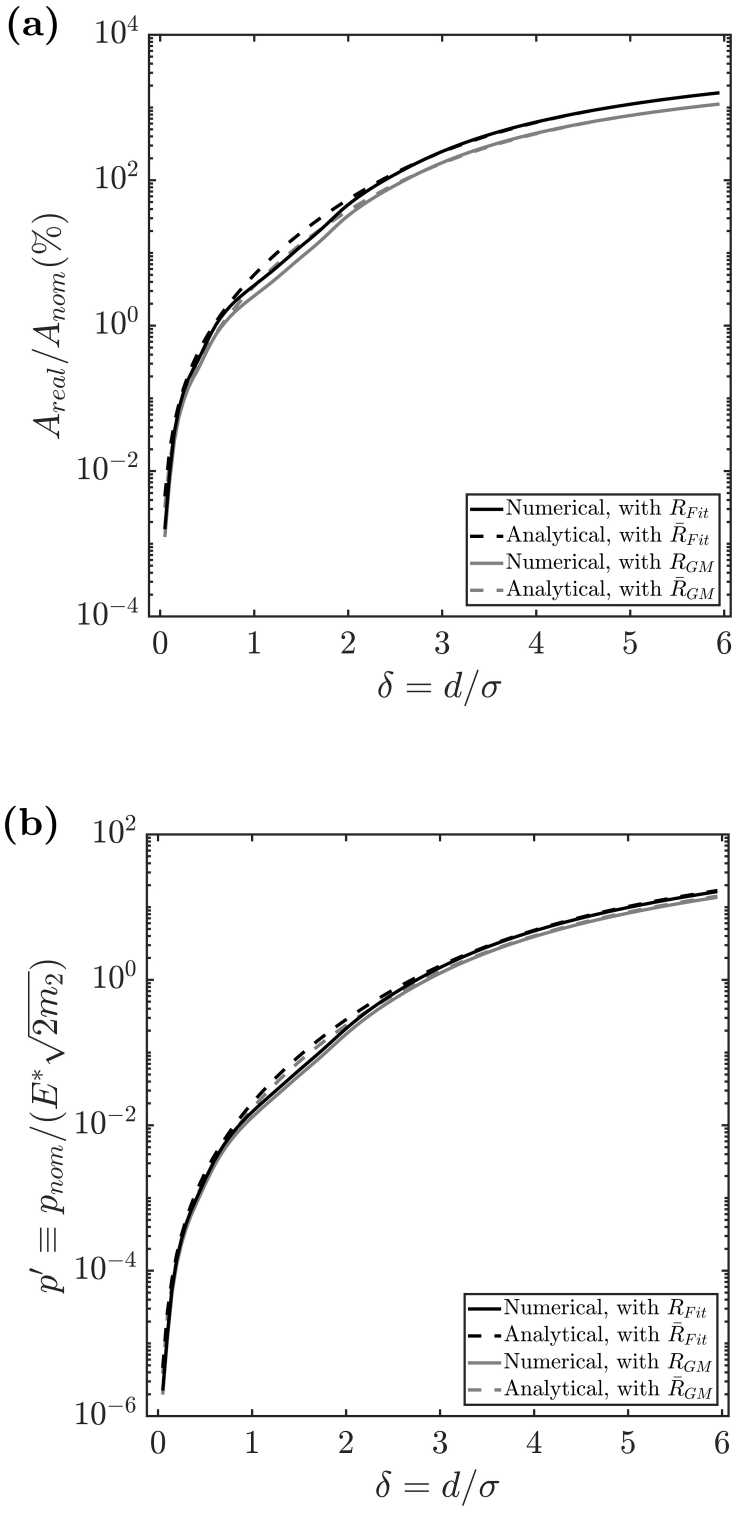

Figure 4.21: The numerical and analytical (a) real contact area and (b) pressure against compression for Case 2 ($H = 0.95$ and $\sigma_0 = 1\ \mu m$).

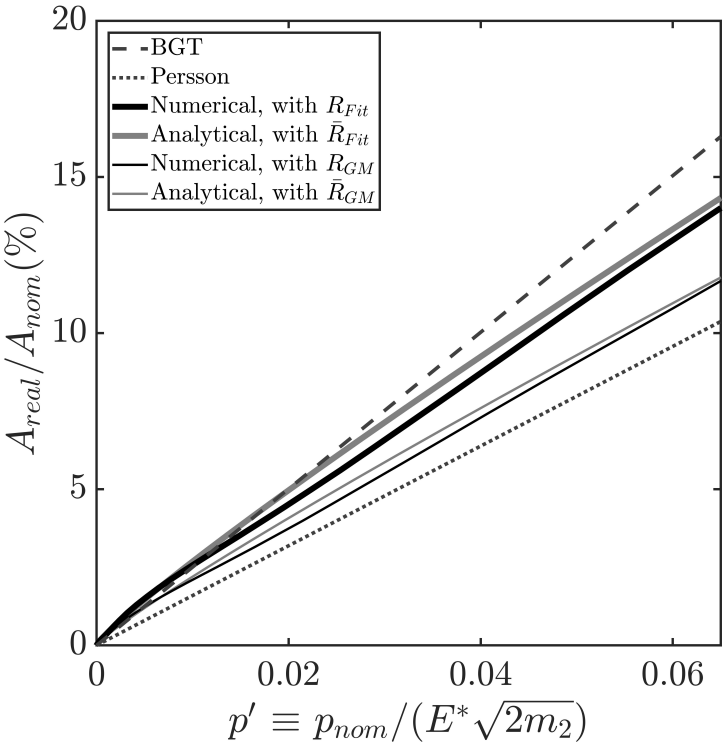

Figure 4.22: The numerical and analytical relation between real contact area and pressure is superimposed with the theoretical limits proposed by BGT and Persson for Case 2 ($H = 0.95$ and $\sigma_0 = 1\ \mu m$).

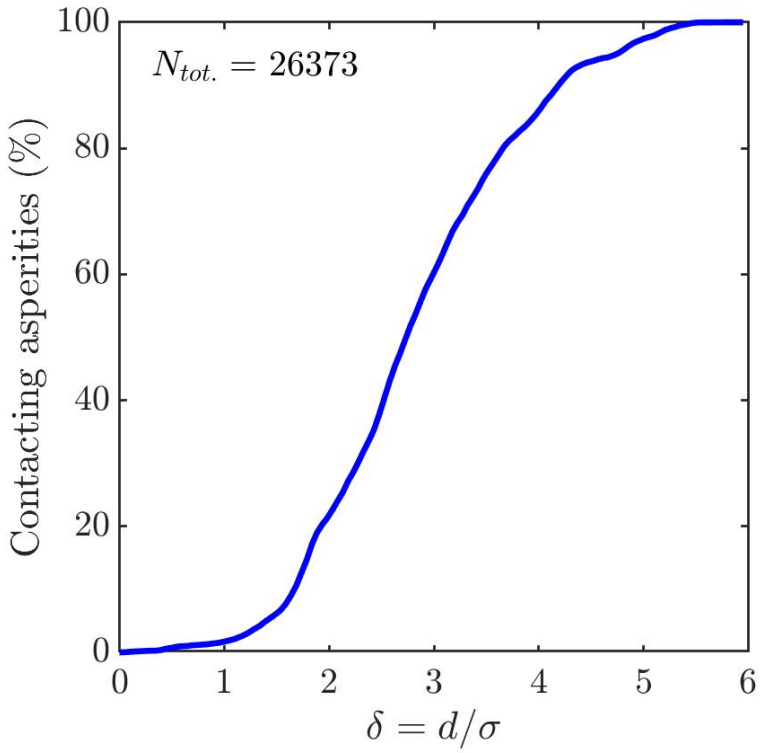

Figure 4.23: The number of contacting asperities as percentage of the total number of generated asperities against compression for Case 2 ($H = 0.95$ and $\sigma_0 = 1\ \mu m$) according to the numerical results.

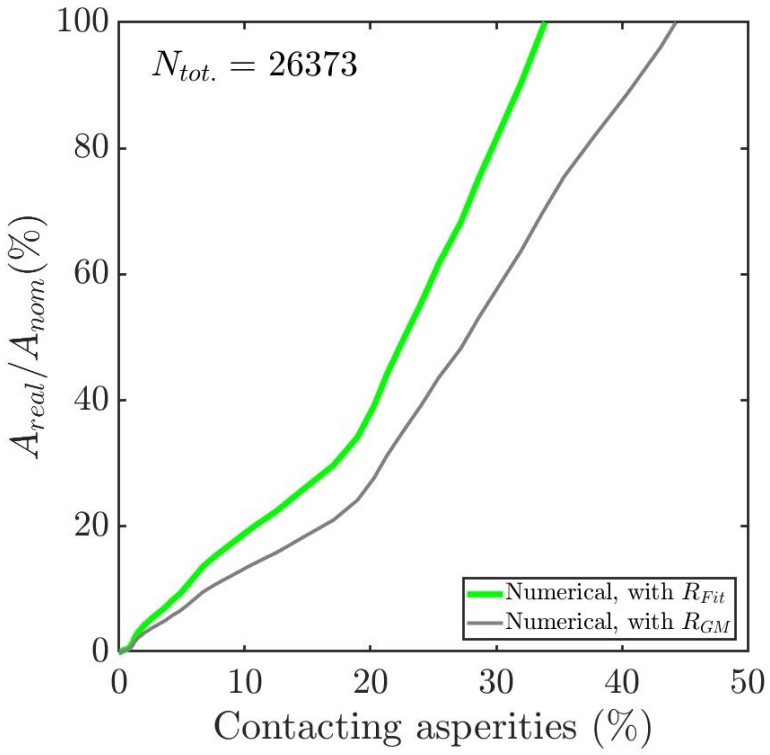

Figure 4.24: Real contact area against the percentage of the contacting asperities for Case 2 ($H = 0.95$ and $\sigma_0 = 1\ \mu m$) according to the numerical results.

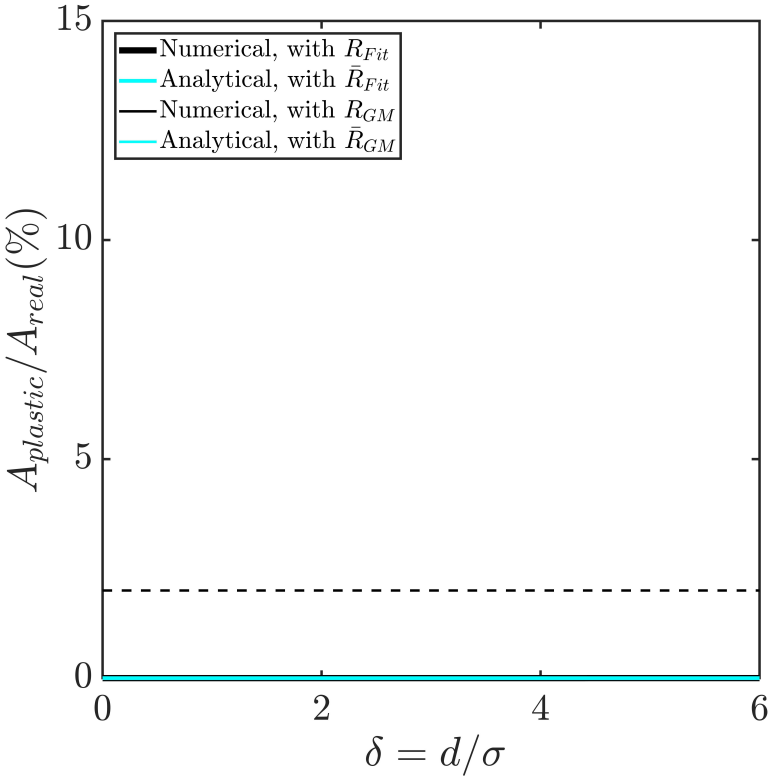

Figure 4.25: Plastic contact area against compression for Case 2 ($H = 0.95$ and $\sigma_0 = 1\ \mu m$) according to the numerical and analytical results.

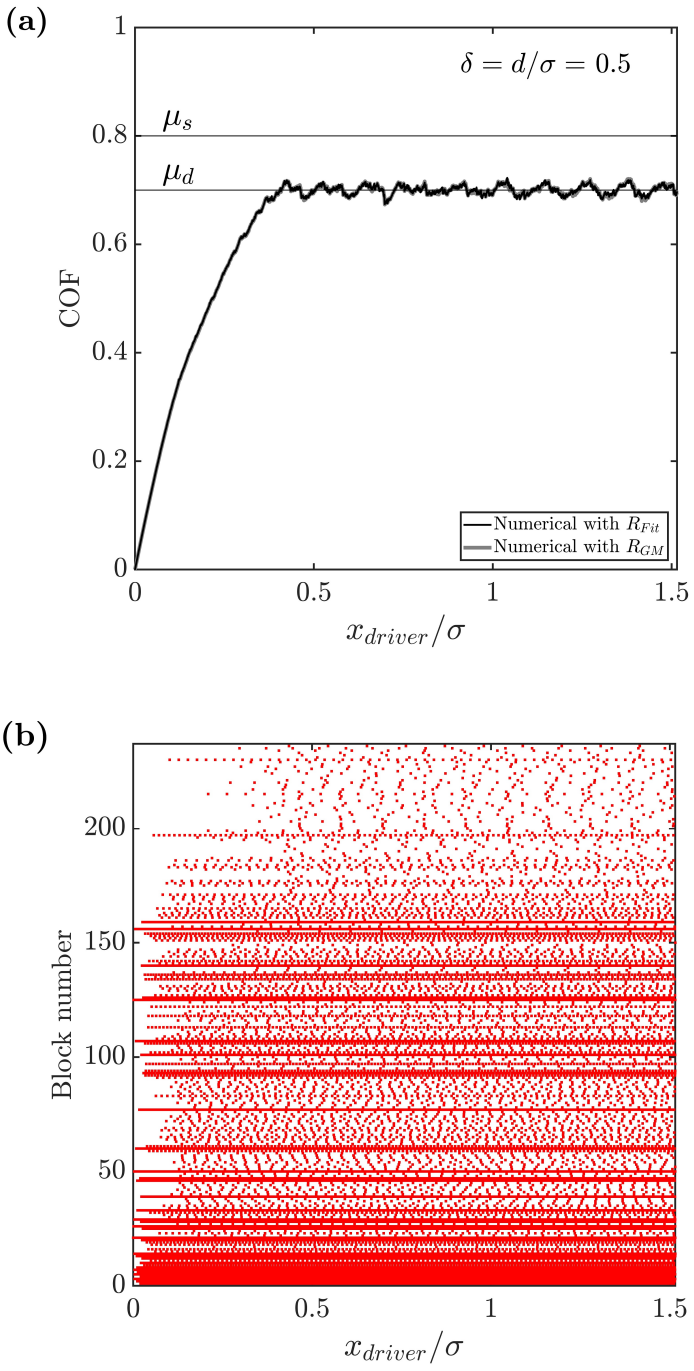

Figure 4.26: The numerical results for sliding at $\delta = 0.5$ for Case 2 ($H = 0.95$ and $\sigma_0 = 1\ \mu m$): (a) COF against the driver position and (b) Block slippage history against the driver position.

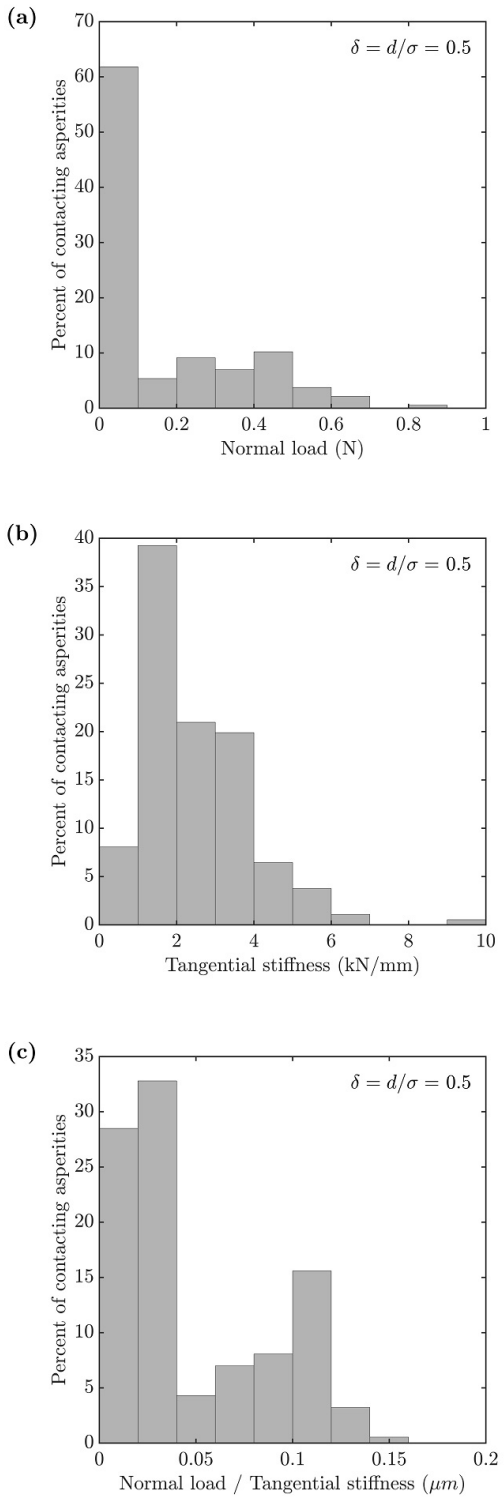

Figure 4.27: Histograms of (a) normal load (b) tangential stiffness and (c) load to stiffness ratio for Case 2 ($H = 0.95$ and $\sigma_0 = 1\ \mu m$) at $\delta = 0.5$.

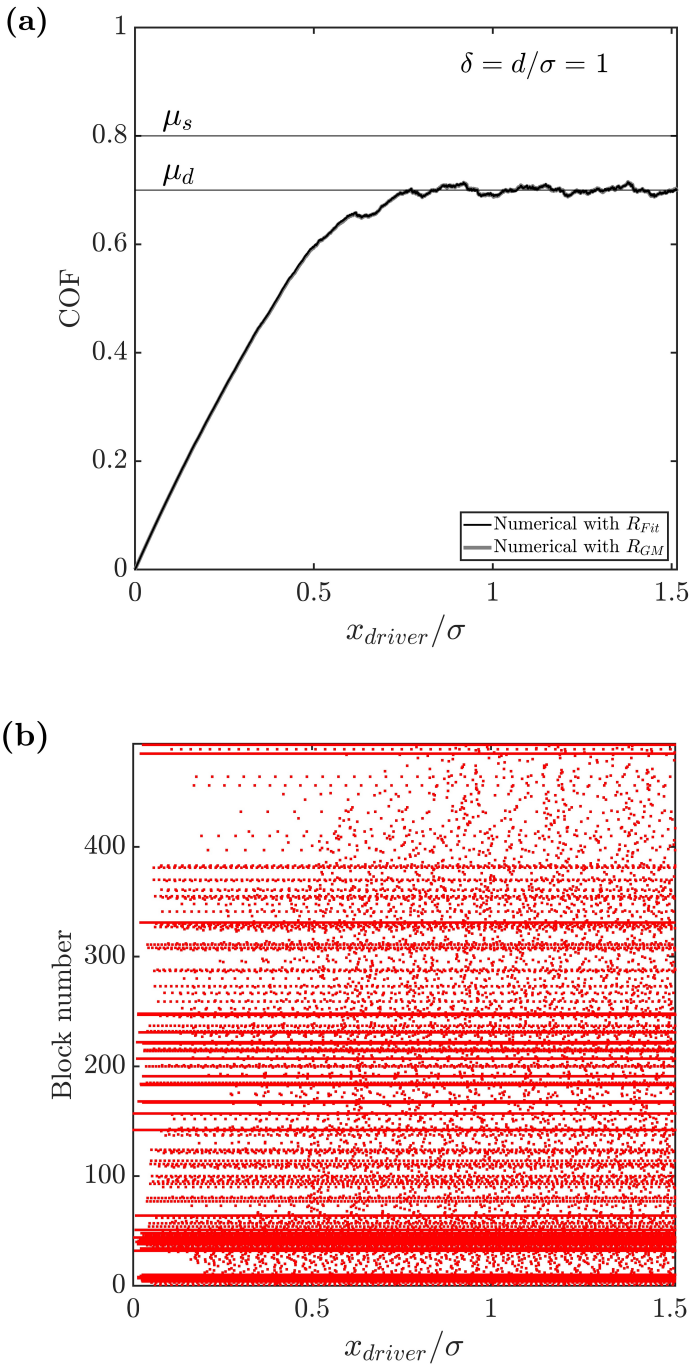

Figure 4.28: The numerical results for sliding at $\delta = 1$ for Case 2 ($H = 0.95$ and $\sigma_0 = 1\ \mu m$): (a) COF against the driver position and (b) Block slippage history against the driver position.

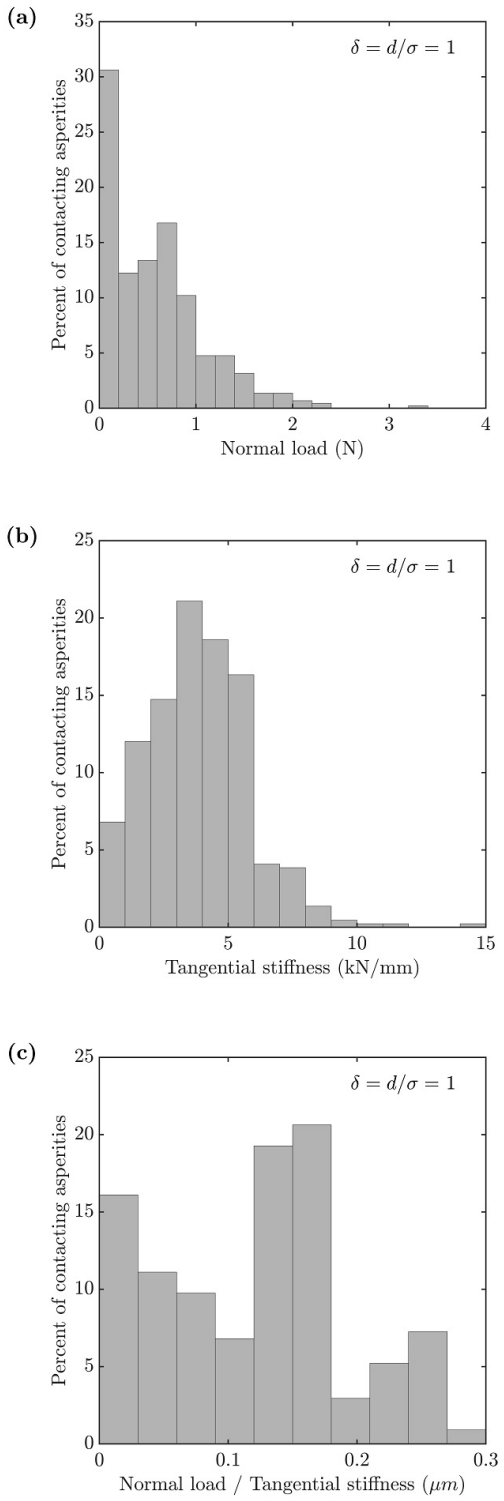

Figure 4.29: Histograms of (a) normal load (b) tangential stiffness and (c) load to stiffness ratio for Case 2 ($H = 0.95$ and $\sigma_0 = 1\ \mu m$) at $\delta = 1$.

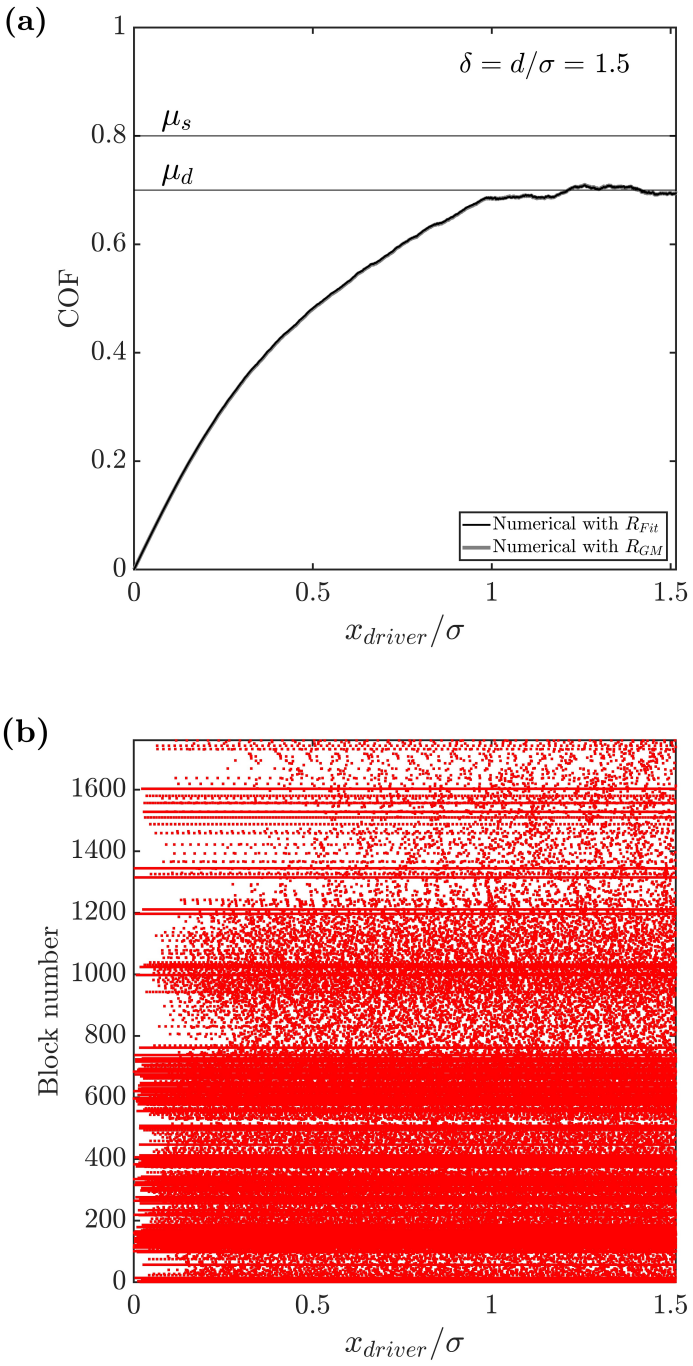

Figure 4.30: The numerical results for sliding at $\delta = 1.5$ for Case 2 ($H = 0.95$ and $\sigma_0 = 1\ \mu m$): (a) COF against the driver position and (b) Block slippage history against the driver position.

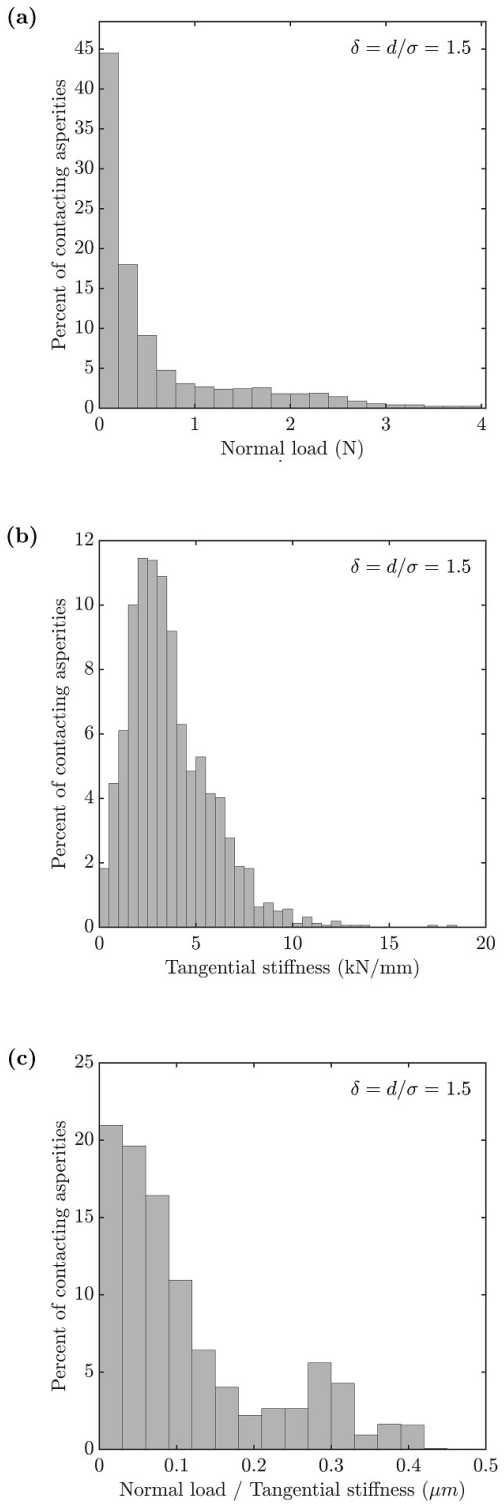

Figure 4.31: Histograms of (a) normal load (b) tangential stiffness and (c) load to stiffness ratio for Case 2 ($H = 0.95$ and $\sigma_0 = 1\ \mu m$) at $\delta = 1.5$.

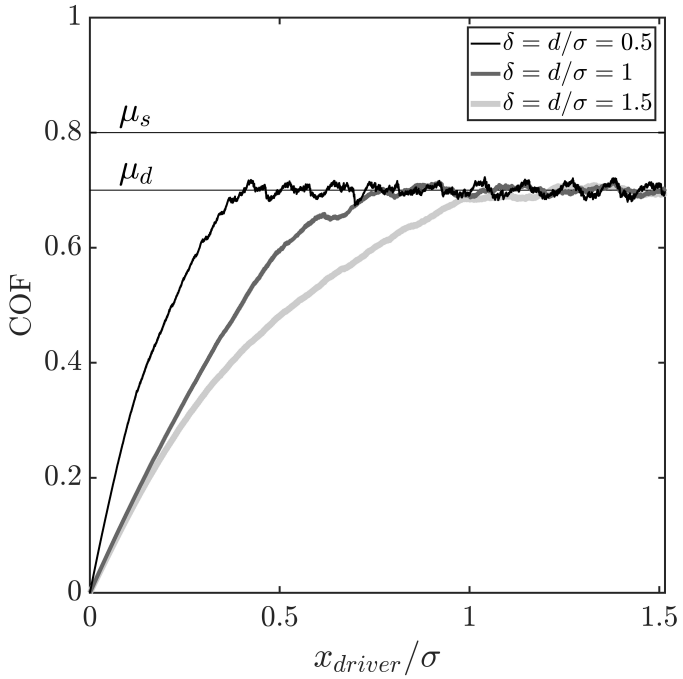

Figure 4.32: The numerical results for sliding under different compression values, $\delta = 0.5, 1, 1.5$, for Case 2 ($H = 0.95$ and $\sigma_0 = 1\ \mu m$)

4.4 Summary

The normal and sliding contact of a computationally generated fractal surface is studied numerically. The normal contact phase is verified by using the analytical formulas of the GW model [21]. Firstly, a 3-D fractal surface is generated by the RMD method. Then, the surface asperity (summit) heights and tip radii are extracted from the numerically generated fractal surface. Two distinct approaches are applied to calculate the asperity tip radii, one by fitting a paraboloid to every asperity tip and the other by using the derivatives of the surface at the asperity tip. The heights and their corresponding radii are assumed to belong to circular paraboloids. These rigid paraboloids are pressed against an elastic half-space by a numerical procedure that uses Hertzian contact formulas to obtain each asperity's normal load and tangential stiffness. The variation of the (overall) real contact area with the normal load is compared against the existing analytical solution proposed by [21]. The load and stiffness of the asperities are then used to characterize the block-spring units of the Maxwell-slip model. These block-spring units are independently attached to a driver that moves horizontally and makes the blocks slide over the rigid flat surface. The variation of COF with the driver position under different amounts of compression is studied alongside the history of the block slippages. The histograms of normal load and tangential stiffness are extracted for different compression values.

4.5 Future work

- To use successive random addition method [20, 237] to generate the surface
- To use spectral synthesis method [25, 238] to generate the surface. In [140] spectral "representation" method is compared with the Fourier filtering method.
- Each pair of the asperities with overlapping contact areas to be coalesced into an equivalent asperity which preserves both the sum of normal load and the sum of contact area of the pair of coalesced asperities. For this purpose, the compression of the equivalent asperity has to be readjusted. By using these assumptions, the radius of the equivalent asperity can be obtained as a function of the sum of normal load on the coalescing pair and the cube of equivalent

asperity contact radius. This scheme would be an alternative to that proposed in [145] in which the radius of the equivalent asperity is assumed to be a function of the radii of the coalescing asperities only. The coalescence would have a crucial effect on the sliding behavior of the Maxwell-slip model since the small number of large contact patches would be modeled as a small number of block-springs in the Maxwell-slip model and would therefore trigger stick-slip. This feature is absent in the present approach. Therefore, even at very high values of compression, steady sliding is still dominant in all of the case studies.

- In [250], the effect of *surface topography* (and *multisclae metrics*) on friction is emphasized. Considering asperity coalescence and the formation of contact patches can help the model show the above effects in a sensible manner.

- Would coalescence, i.e., formation of the contact patches [147] subside the concerns about the occurrence of plasticity? Archard [18] argues that coalescence can make an initially-plastic contact turn elastic!

- Incorporation of the long-range elastic interaction [145, 204] among the asperities

- To compare the normal and sliding contact results against those based on [27] rather than GW model [21].

- Does the fractal surface solve the resolution (scale) dependence problem? Are the results, e.g., area-load relation, independent of the grid resolution? Is it possible to generate the same results by coarsening the surface grid (eliminating points from an existing surface)? Use parallel computing to generate surfaces with higher resolutions and/or greater areas.

- How does the second spectral moment change with the grid size?

- Is it possible to find a closed-form expression for the second spectral moment?

- Is it possible to find the second spectral moment by fitting an exponential function to the values obtained by the finite difference stencils of different sizes? Is the plateau of such a fit a stable m_2 value?

- Variation of the second spectral moment in different runs to be recorded

- The effect of grid size on the summit-to-point ratio to be studied
- What is the relation between the initial standard deviation and the surface standard deviation?
- What is the relation between the initial standard deviation and the standard deviation of the summit heights?
- The effect of the initial standard deviation on the results to be studied
- Calculation of the Nayak parameter by using the definition of the variance to obtain m_0 and m_4. Is it stable? How does it change with the Hurst exponent? According to Yastrebov [25, 227], the Nayak parameter is a function of the Hurst exponent and the cutoff ratio only. Does the calculated Nayak parameter change with the grid size?
- Is there a way to obtain m_4 from the PSD (similar to the way m_2 was obtained)? See the discussion section of [24] and Equation (9.39) in [249].
- The grid size (nodal spacing) is related to the short wavelength cutoff. How does it affect the results?
- How do the nodal spacing and Hurst exponent affect the mean radius obtained by derivatives (geometric mean radius) and the average fitted radius?
- How does setting the heights of the four corners of the surface to zero (as proposed in [236]) affect the results?
- Plot the normal stress distribution function according to the function form that is found analytically in [29]
- Why does the variation of the real area and normal load with compression resemble?
- Hysteresis behavior of the surface to be studied with considering the reciprocal movement of the driver

CHAPTER 5

DYNAMIC MAXWELL-SLIP MODEL WITH LINEAR INITIAL SPRING EXTENSIONS

The sliding of an elastic body on a rigid, flat substrate is investigated by considering the inertial forces using the Maxwell-slip model. The elastic body is modeled as a set of independent mass-spring units that are pulled by a rigid driver. Poisson expansion is introduced by specifying antisymmetric, linear initial block displacement distribution. None of the system parameters is randomized. The normal load on the blocks and the spring stiffnesses are the same for all units. The driver is moved at different velocities. The slippage of each mass-spring unit is governed by deterministic Newtonian mechanics and static/dynamic Coulomb law. Both steady-sliding and stick-slip regimes of friction are reproduced by changing the maximum value of the specified initial block displacement distribution. The steady-sliding regime is accompanied by the propagation of the slip pulses. On the hand, stick-slip is accompanied by crack-like ruptures along the interface. Based on the results, when the driver velocity is high enough local apparent friction coefficient can exceed the static COF due to the inertial effects.

5.1 Introduction

Scientists and engineers have proposed block-spring models to study frictional interfaces. These models can be categorized according to pairwise features like coupled/uncoupled, side-driven/top-driven (Figure 5.1), and discrete/continuum. Each model mirrors the aim of the conducted study. The Maxwell-slip model (Fig. 5.2) is a top-driven system (also called uniformly-loaded system [251]). In this configuration,

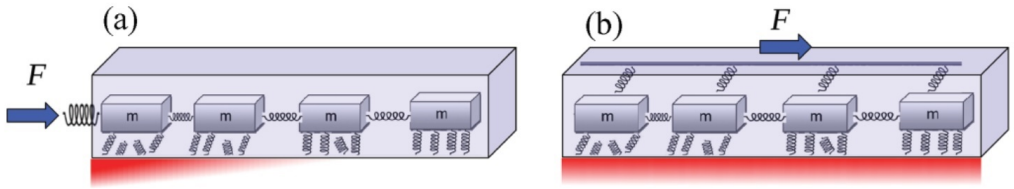

Figure 5.1: (a) Top-driven and (b) side-driven block-spring models [251]

the rigid driver is connected to all units. The other configuration is called side-driven (or edge-loaded [251]), in which the external force is applied to a single unit at one end of the block-spring chain. According to the results of the theoretical models for side-driven systems [156, 251–254], before gross sliding, a multitude of crack-like precursors (ruptures) propagate from the force-applied end (edge) and arrest before reaching the other end. The overall sliding starts when the precursors reach the other end. When this happens, the applied force is about the kinetic friction value, and stays there during the overall sliding (it hardly reaches the static friction value). The interfacial dynamics of the top-driven systems is quite different, as seen in Section 5.3. A range of block-spring models (1-D, 2-D, side-driven, top-driven) is addressed in K. Thøgersen's master thesis [255].

An elastic body under compression expands laterally because of Poisson expansion. Here it is assumed that initially, the elastic body is pressed against a frictionless flat. In other words, the body expands freely. The Maxwell-slip model with an antisymmetric spring extension can be used to model the expansion (Figure 5.2). The model is top-driven.

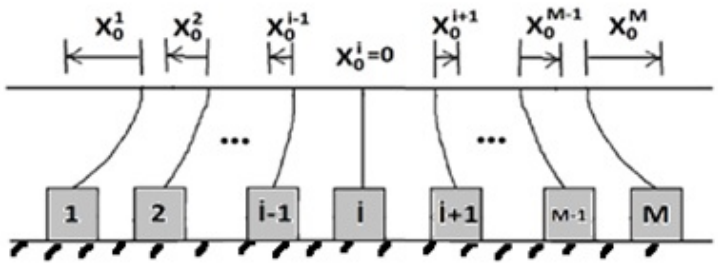

Figure 5.2: The Maxwell-slip model with a linear initial spring extension distribution

In [75], sliding friction between identical adjacent plates under shear impact is studied numerically (using FEM) and experimentally. The boundary conditions are shown in Figure 5.3. The interface is closely monitored. The FEM results that show the crack-like and pulse-like propagation of slip along the interface are given in Figures 5.4-(a) and 5.4-(b), respectively. The contours represent maximum shear variation. The crack-like propagation is accompanied by a steady traction force (Figure 5.4-(a)), while the train of pulses is accompanied by stick-slip (Figure 5.4-(b)). The dependence of the modes of slip propagation on the impact velocity and the normal pressure is shown in Figure 5.5. Both pulse-like and crack-like modes have also been reproduced using the BK model [163].

Experimental study of slip and slip rate at the frictional interface by sliding (PMMA or rock) plates against one another is a quite common practice in the geophysics community [182, 184, 256–258]. The objective is to obtain insight about earthquakes from the laboratory results. Physicists have shown that irregular stick-slip between the PMMA plates can be transformed into a regular stick-slip by adding a small-amplitude oscillating component to the driving force [259]. In an experimental study [260] on a pair of PMMA blocks at the onset of overall sliding, the real contact area is measured by light transmission along the interface. The shear and normal stresses are measured *adjacent* to the interface.

Some studies have reported anomalously high values of local friction coefficient [201,

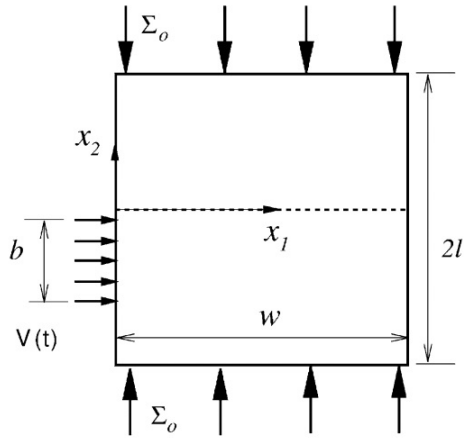

Figure 5.3: Shear impact of the adjacent plates which are pressed together [75].

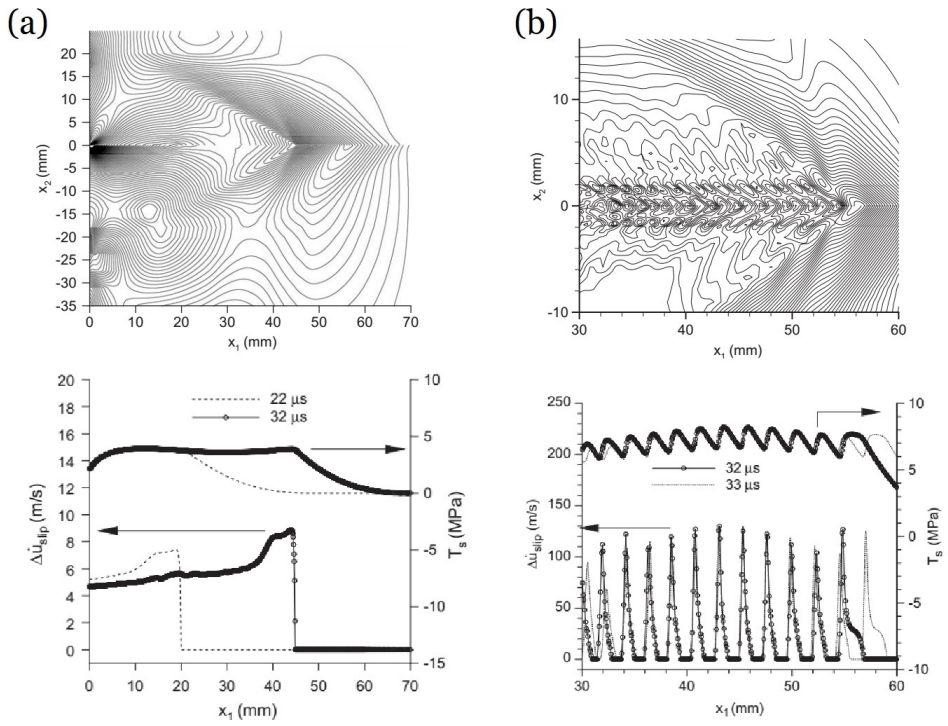

Figure 5.4: FEM results: the maximum shear stress contours and particle velocity along the interface, and traction force for (a) normal pressure of $6\ MPa$ and impact velocity of $2\ m/s$ (b) normal pressure of $10\ MPa$ and impact velocity of $20\ m/s$ [75].

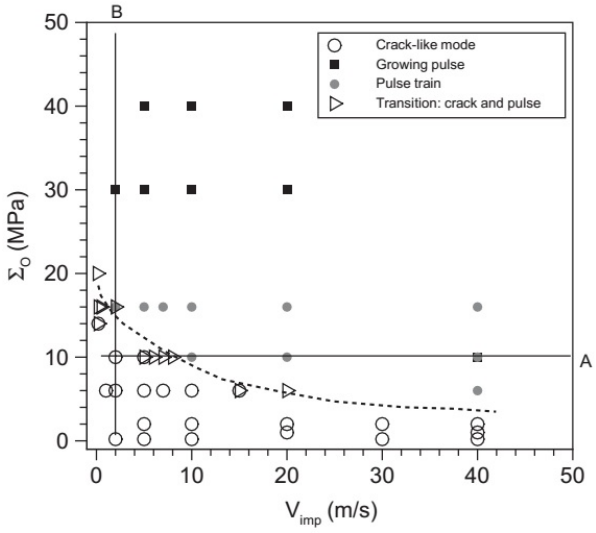

Figure 5.5: The modes of slip propagation as a function of the normal pressure and normal pressure [75].

261]. This unexplained issue emerges from laboratory friction tests in which the local shear-to-normal stress ratio is measured along a PMMA frictional interface. In [261], the maximum value of the ratio of shear stress to normal stress (i.e. apparent COF) is correlated to the velocity of different *rupture fronts* (as they traverse the strain gauges) for edge-loaded (side-driven) and uniformly-loaded (top-driven) systems. The result shows that with an increase in rupture front velocity, the local static COF exceeds static COF by a factor of four without precipitating slip, i.e., before the onset of the gross sliding.

Numerical models have also shown a high local (microscopic) COF [252]. Although apparent COF locally exceeds static COF, the integrated value of the shear stress divided by the integrated value of the normal stress is below static COF. The high values of the local static COF show that the static COF at the micro-level (at the tip of rapid ruptures) is not a material-dependent property [201]. The static COF at the microscopic level (local/ microscopic static COF) can be quite different from its macroscopic counterpart (global/ macroscopic static COF). Fracture mechanics concepts (energy release with crack propagation) are used to explain the relationship between the apparent COF, rupture mode, and microscopic COF [129, 262–264].

In [265], the dynamics of a damped system is investigated numerically by considering the inertia of the contact zone mass. The extracted *stick-slip maps* show how the sliding regime depends on the system parameters such as stiffness, damping, and mass. *Serious errors* in measurement of static COF have been reported due to *tangential contact compliance* [265]. ASTM D1894-14: *Standard Test Method for Static and Kinetic Coefficients of Friction of Plastic Film and Sheeting* reveals that according to an interlaboratory round-robin testing study, both friction coefficient and the regime of sliding are *drastically affected* by the elasticity of the surface.

It has been shown in the literature that when a velocity weakening rate and state friction law is applied, steady sliding would be possible and stable for a single block-spring [266,267]. In this chapter, it is shown that although stick-slip (instability) is the destiny of a single block-spring unit under Coulomb's friction law, when a multitude of blocks are included, the steady sliding of the overall response is possible.

In Subsection 5.4, based on the EOM of a single mass-spring, it is shown analytically

that a large microscopic static COF can be a product of the inertial force. The excess amount for a specific block depends on the normal load on the block and the driver velocity.

5.2 Method

The proposed model, Figure 5.2, consists of independent (uncoupled) equal masses that experience the same normal pressure and are moved with separate springs of the same stiffness over a rigid, flat, and fixed substrate. This configuration is known in the literature as *Maxwell-slip model* [52], *classical Maxwell-slip model* [268] and *Iwan's model* [269]. Randomizing the system parameters(stiffness, mass, and load) is avoided. The static/dynamic Coulomb friction law is assumed.

The approach is based on the EOM of a single mass-spring unit. Each unit is assumed to be of the shape of a rectangular parallelepiped whose mass is lumped at its tip in the form of a block. With every increment in time, the driver advances a step further, and all blocks are monitored to see if a block slips or stops.

Friction is usually defined as the resistance that an object encounters when it moves on another object. The definition becomes ambiguous when the interface's elasticity is considered. Imagine a mass block pulled by a spring on a flat rigid surface. Is friction equal to the force exerted on the driver via the spring? Or is it the force experienced by the blocks (exerted by the flat)? In experiments, what is measured is indeed the force that the driver experiences. Note that the spring force for a single *sliding* mass contains inertial force. According to Newton's second law of motion:

$$f_{spring} = f_d + m\ddot{x} \tag{5.1}$$

where f_d is the dynamic friction. In the case of constant-velocity driver, the pulling force is equal to the sum of spring forces.

In this thesis, the total sum of the spring forces is called traction (pulling force) and the total force exerted *by the substrate* on the blocks is named friction. The contribution of the stuck blocks is the same to both traction and friction forces. However, the

contribution of a sliding block to traction is $f_d + m\ddot{x}$, and its contribution to friction is f_d. The *inertial force* makes friction and traction differ.

An algorithm is developed to decide and record state of each block, and its contribution to overall traction and friction forces at every time step. The driver moves at a constant velocity; therefore, the exerted traction can be obtained from summation of spring forces on the driver. The independent local results are then superposed in a global spatial and temporal frame to simulate the response of the whole contact (a multitude of mass-spring units).

5.2.1 Block's motion under Coulomb's friction law

In this subsection, the EOM of a single mass-spring unit that is pulled on a rigid flat under Coulomb's friction law is investigated. It is shown that for such a block steady sliding state is not possible if the driver keeps moving at a constant velocity. In other words, the block is doomed to stick-slip. The equation of motion for a driver that moves with a constant velocity is solved analytically. In contrast to the convenient assumption of "slow-enough" driver (according to which the driver is supposed to be fixed during slippage of the block), the driver's motion is taken into account. The solution shows that the slippage length of the block is a function of driver velocity (which was not the case for the "slow-enough/fixed" driver). Here the velocity of the driver affects the block's motion, and the block slippage has a duration.

For a single mass, m, that is pulled by a leaf spring, k, with a driver that moves at a constant velocity, v_d, on a surface with the static COF, μ_s, and the dynamic COF, μ_d, the ODE of motion is written as:

$$\ddot{x} + ax + bt + c = 0 \tag{5.2}$$

where,

$$a = \frac{k}{m}, \quad b = -\frac{kv_d}{m}, \quad c = (\mu_d - \mu_s)\frac{N}{m}$$

With the initial conditions:

$$x(0) = 0, \quad \dot{x}(0) = 0$$

The solution of the initial value problem (IVP) is:

$$x(t) = \frac{b}{a^{3/2}} \sin\left(t\sqrt{a}\right) - \frac{bt + c}{a} + c\frac{\cos\left(t\sqrt{a}\right)}{a} \tag{5.3}$$

$$\dot{x}(t) = \frac{b}{a} \cos\left(t\sqrt{a}\right) - \frac{c}{\sqrt{a}} \sin\left(t\sqrt{a}\right) - \frac{b}{a} \tag{5.4}$$

$$\ddot{x}(t) = -\frac{b}{\sqrt{a}} \sin\left(t\sqrt{a}\right) - c.\cos(t\sqrt{a}) \tag{5.5}$$

The closed form solution of the equation of motion for a single block of mass m under Coulomb's friction law, that is pulled with a spring of stiffness k by a driver that moves at a constant velocity v_d, is shown in Equation (5.3). The position of the block is a function of time and is measured with respect to its previous stuck position. The spring stiffness is calculated according to Equation H.1 for the leaf spring.

The plots of block position (with respect to its initial stuck position), velocity and acceleration during its slippage period are shown in Figure 5.6. The nonlinear velocity function shows that the slipping block position with respect to the driver position can never be fixed under Coulomb law. Thus the spring force always varies and cannot be equal to the constant value: $f_d = \mu_d N$.

The stop time is found by equating the velocity function of the block (derivative of the solution) to zero. It leads to the trigonometric equation shown below:

$$\frac{c\sqrt{a}}{b} \sin\left(t_{stop}\sqrt{a}\right) = \cos\left(t_{stop}\sqrt{a}\right) - 1 \tag{5.6}$$

The stop time can be obtained by solving the above trigonometric equation algebraically. By squaring up the sides:

$$t_{stop} = \frac{1}{\sqrt{a}} \left[n\pi + \tan^{-1}\left(\frac{2bc\sqrt{a}}{ac^2 - b^2}\right) \right] \tag{5.7}$$

Note that n has to be selected properly (by considering the sign of the arc tangent term) such that the stop time has the minimum possible value. It leads to a somehow

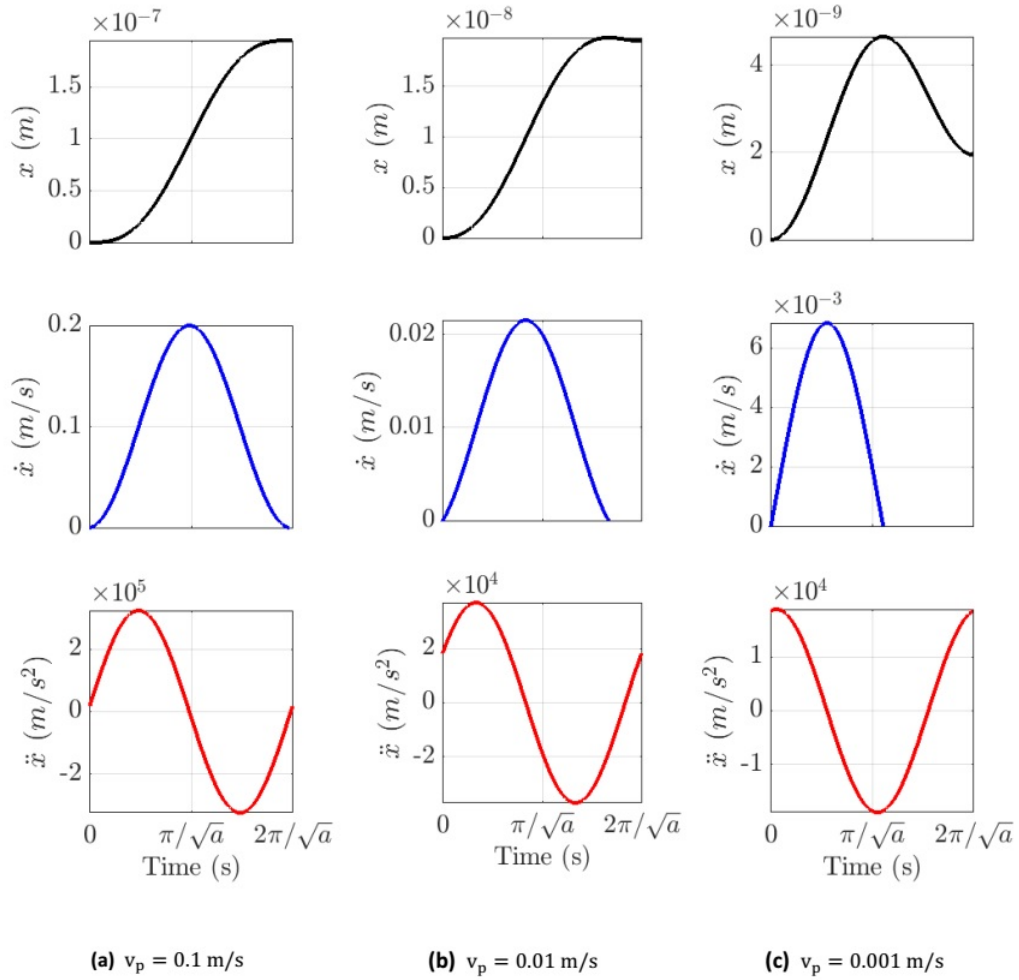

Figure 5.6: The block position, velocity and acceleration for three different driver velocities

vague conditional expression which is triggered by the periodic nature of the trigonometric expression above (selecting n). Furthermore, the argument of the arc tangent in its general form can possess either a positive or a negative value.

The block stop time can also be found by solving Equation (5.6) numerically. A visual approach can also be pursued to solve the trigonometric equation by intersecting left hand side and right hand side of it. This approach provides an insight to the physics of the problem.

The left hand side (LHS) sinusoidal and right hand side (RHS) cosinusoidal expressions of the stop time equation are plotted in Figure 5.7. The effect of the LHS

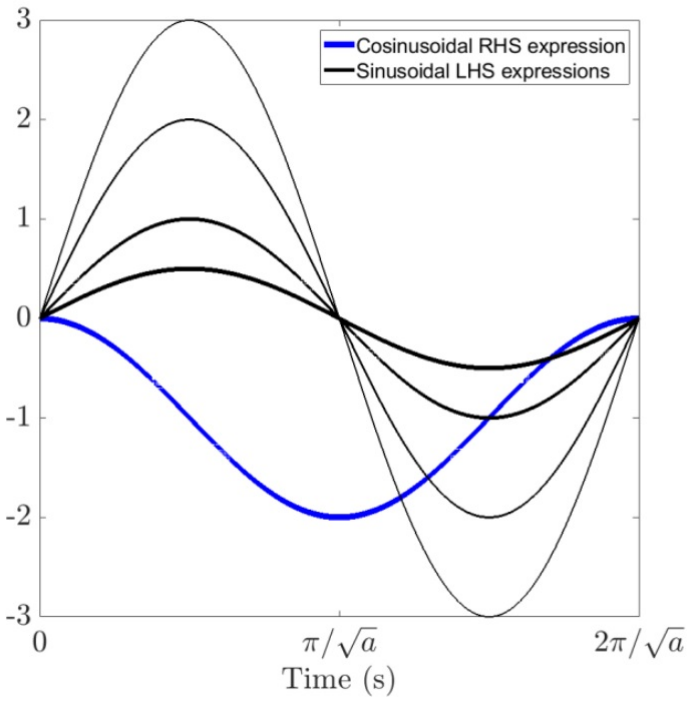

Figure 5.7: The block stop time as x-coordinate of the intersection point. While a and c are assigned one, b values are -1/3, -1/2, -1 and -2 for the black curves from the thinnest to the thickest correspondingly. The stop time is always between $\pi/\sqrt{a}$ and $2\pi/\sqrt{a}$.

expression amplitude, i.e. $c\sqrt{a}/b$, can be expressed in brief as:

$$\lim_{(c\sqrt{a}/b)\to 0} t_{stop} = 2\pi/\sqrt{a} \tag{5.8}$$

$$\lim_{(c\sqrt{a}/b)\to \infty} t_{stop} = \pi/\sqrt{a} \tag{5.9}$$

In Figure 5.7, parameters a and c are assigned the values 1 and -1 respectively. The LHS sinusoidal expression plots (the black curves) are obtained by assigning the values $-1/3,\ -1/2,\ -1,\ \ -2$ and -3 to b parameter. As the absolute value of b (note that it possesses a negative value) is increased (e.g. when driver velocity is increased) the amplitude of the RHS expression decreases (the black lines become thicker). Therefore the x-coordinate of the intersection point (i.e. the stop time) approaches to $2\pi/\sqrt{a}$. In contrary, when b is decreased (e.g. when the driver velocity is decreased), the amplitude of the RHS expression increases (the black curves

become thinner) and the x-coordinate of the intersection point (the stop time) approaches $\pi/\sqrt{a}$. Note that this limit is the stop time for the problem with *no driver motion during the block slippage* assumption.

Figure 5.7 also shows that there is an upper bound for the increase in stop time with increase in the driver velocity, and that is $2\pi/\sqrt{a}$. It depends on the mass and stiffness only. This means that under Coulomb law, sticking is inevitable, independent of the system parameters and then only stick-slip is possible. In other words smooth sliding (steady or unsteady) is impossible. With Coulomb law ruling friction, the latter regime does not come to existence in the first place, thus analyzing its stability makes no sense. No matter how fast the driver pulls, or how much normal force is exerted on it, the block will stick. There is no chance of smooth sliding under Coulomb law, either steady or unsteady. Although the exact value of stop time (or slipping period) is a function of all parameters of the system, its bounds depend only on mass of the block and the spring stiffness (and is independent of the driver speed or the COF values).

The stop time can be used then to find the slipped distance. During the slippage, according to Coulomb law, the constant value of dynamic friction is applied on the block (not on the driver). On the other hand, during sticking period friction is equal to the spring force.

Figure 5.8 shows a diagram of four possible block states and how the decision on the block state is made. The state of a block can be sticking or slipping in the current time step; and it can remain the same or change to the other in the next time step. The criterion to be applied to a currently stuck block is based on force. On the other hand, the criterion to be used in the case of a currently slipping block is based on time. The state changes through arrows 2 and 3 in Figure 5.8.

The flowchart of the algorithm for calculation of the total friction of the Maxwell-slip model (with inertial force taken into account) is shown in Figure 5.9. The model has a multitude of blocks. The initial position of each block is specified and checked in order to prohibit violation of the frictional threshold at $t = 0$. The driver is moved forward within the time increment with a constant velocity. The state of ith block at the time step j is recorded in a matrix as zero for sticking and one for slipping. By

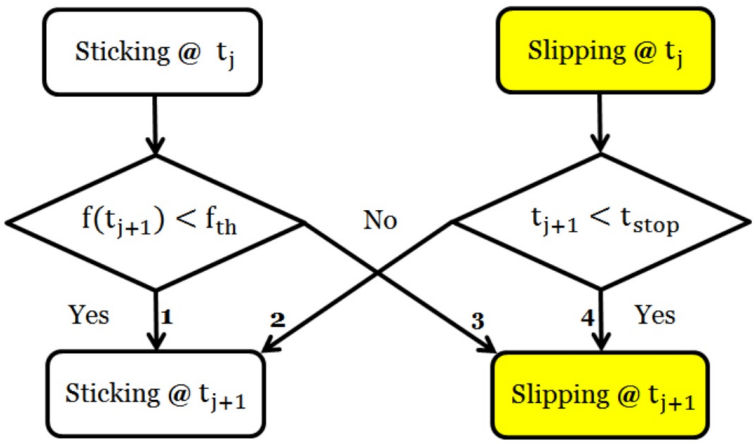

Figure 5.8: The four possible block state updates due to time increment

monitoring the previous state of the block its new state is decided and its force contribution is calculated accordingly. Additional explanations are given in the following subsection.

The simple form of the ODE of motion for a single mass-spring system is:

$$m\ddot{x} = -f_d + f_{spring} \tag{5.10}$$

Since under Coulomb law the block is obliged to stick, the block has to decelerate. Deceleration of the block starts when the right hand side expression becomes negative. This condition is not limited to the cases in which the force exerted by the spring on the block is negative, it can occur whenever:

$$f_{spring} < \mu_d N \tag{5.11}$$

Not only it happens when f_{spring} is backward, but also when f_{spring} is positive but is less than the absolute value of dynamic friction. Note that equating the obtained expression for acceleration to zero is not enough to find the deceleration time. The acceleration has to change sign from positive to negative:

$$\frac{b}{\sqrt{a}} \sin\left(t_{dec.}\sqrt{a}\right) = c.\cos(t_{dec.}\sqrt{a}) \tag{5.12}$$

$$\tan\left(t_{dec.}\sqrt{a}\right) = \frac{c\sqrt{a}}{b} \tag{5.13}$$

Since both b and c are always negative, the right hand side fraction is always positive and the formula for deceleration time is straightforward:

$$t_{dec.} = \frac{1}{\sqrt{a}} \tan^{-1}\left(\frac{c\sqrt{a}}{b}\right) \tag{5.14}$$

Although it seems that when $c\sqrt{a}/b$ tends to zero (e.g. when b goes to infinity), it is physically unacceptable because the block cannot start deceleration right at the beginning of its motion (since it does not move back). Thus, $\tan^{-1}(0)$ has to be interpreted as π rather than zero (the next minimum). Then:

$$\lim_{(c\sqrt{a}/b)\to 0} t_{dec.} = \pi/\sqrt{a} \tag{5.15}$$

The other case of special interest is near-zero driver velocity (i.e. $v_d \simeq 0$ or $b \simeq 0$) in which $c\sqrt{a}/b$ tends to infinity. This is equal to the problem solved with "fixed driver during the block slippage" assumption. Because $\tan^{-1}(\infty)$ is interpreted as $\pi/2$:

$$\lim_{(c\sqrt{a}/b)\to \infty} t_{dec.} = \pi/(2\sqrt{a}) \tag{5.16}$$

To compare the stop time and the deceleration time for the above limit cases, the values are gathered in Table 5.1. Note that both deceleration times happen before their corresponding stop times and the smaller stop time corresponds to the smaller deceleration time and vice versa. The plots of Figure 5.6 are in agreement with these analytical results: it can be seen that as the driver velocity increases (i.e. b increases), the deceleration and stop time values shift from the second row of the Table 5.1 to its first row.

$c\sqrt{a}/b$	$t_{dec.}$	t_{stop}
0	$\pi/\sqrt{a}$	$2\pi/\sqrt{a}$
∞	$\pi/(2\sqrt{a})$	$\pi/\sqrt{a}$

Table 5.1: Deceleration and stop time values for the limit cases

5.2.2 A flowchart for the Maxwell-slip model

Figure 5.9 shows the algorithm for calculation of friction by the Maxwell-slip model as a function of time. The sequence and duration of slicking and slipping events determines evolution of the total friction force. The initial spring extension values is the key parameter that affects the result. These values has a linear and antisymmetric distribution as shown in Figure 5.2. In other words, the initial block position "vector" has a "mirror" at its center. These values are checked to see whether or not the frictional threshold is violated. If any of the blocks violate the maximum friction threshold, the algorithm is terminated. If the number of the blocks is odd, the central block is always at zero. If the number of the blocks is even, then the right-half block positions are the left-half positions with a minus one multiplier.

The initial spring extensions, the normal force on each block, the driver velocity, and mechanical and frictional parameters are given. The spring stiffness and mass is calculated. The closed form solution of the ODE of motion of a single block is used to find the block slippage duration and distance. The state of ith block at j^{th} time step is recorded in the parameter s_{ij}. When the block is stuck, zero is assigned to its state (it is always zero at $t = 0$) and when the block slips, the assigned value changes to one.

Whether stuck or slipping, the force experienced by a block is less than the maximum static friction threshold, f_{th}. To determine the state of a block in the current time step (incremented driver position), its previous state has to be considered. If it was sticking in the previous time step, the force exerted on it in the current time step (after advancement of the driver) is examined. If it is exceeding f_{th}, the block starts slipping. The state changes from sticking, 0, to sliding, 1. In this case, the time and position of violation are recorded in t_{trigg} and x_{trigg} for subsequent use. The frictional contribution of the block becomes equal to $f_d = \mu_d N$.

Note that *the force that is applied to the block* and *the force applied to the driver* (i.e. the spring force) are different from each other. On the other hand, if the block was slipping in the previous time step then a *time-based* criterion (rather than a *force-based* criterion) is used to see if its slippage deadline is reached or not.

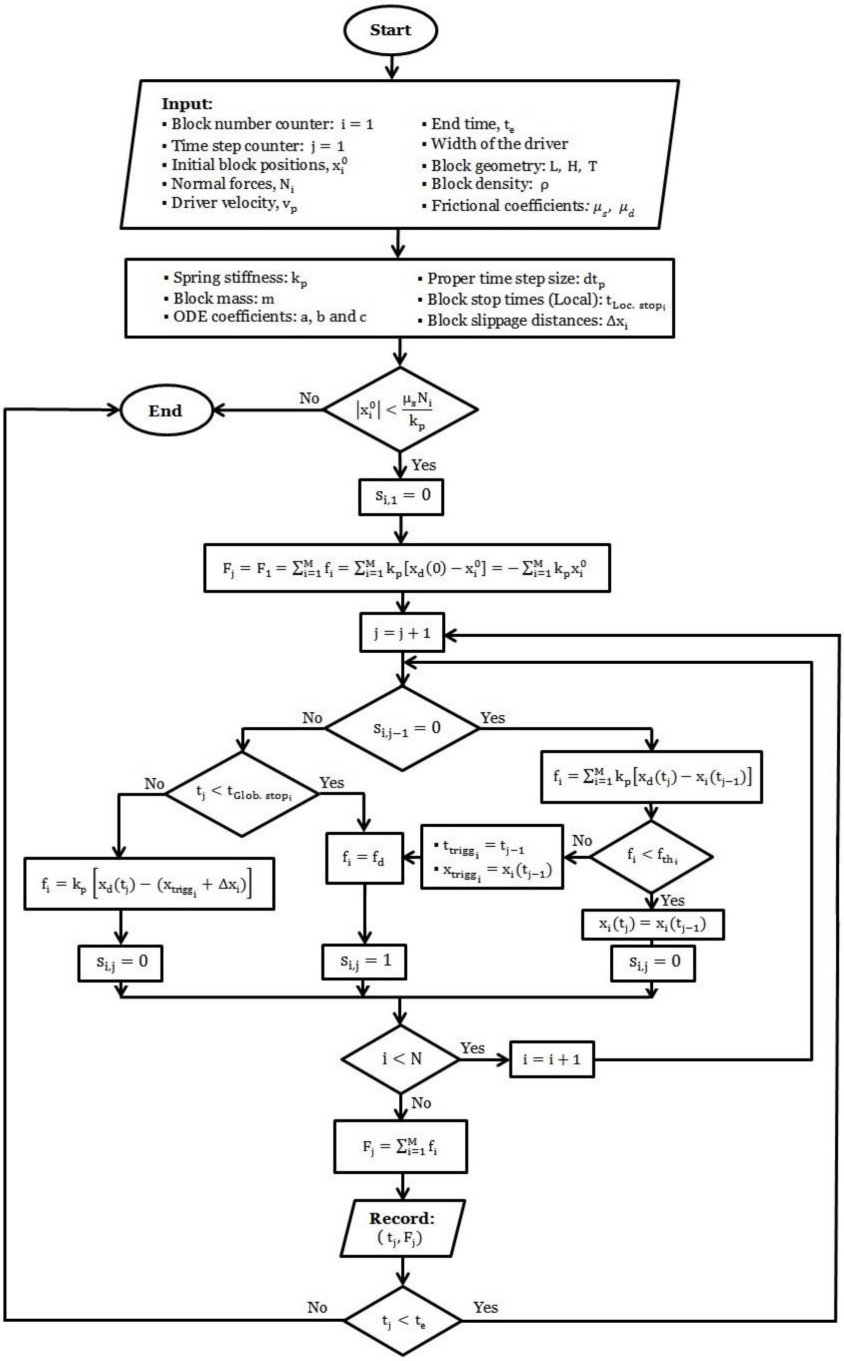

Figure 5.9: Flowchart for calculation of friction in GMS model

After completion of friction contribution loop for all of the blocks, total friction is calculated by summing up the f_i values recorded at the current time, t_j. Then time is incremented. The time loop will continue till the final time.

5.3 Results

The results show that a pulse-like pattern of motion of the masses happens when the initial spring extensions differ enough; the pulse-like pattern transforms to a crack-like pattern for close enough initial mass displacement values.

For all case studies in this chapter, the number of the considered asperities is 500. Each elastic unit is assumed to be cubic with edges of $1\ \mu m$ length. The pressure applied on each unit is assumed to be $1\ MPa$. The slider is supposed to be made of Westerly granite for which Young's modulus is $70\ GPa$, Poisson's ratio is 0.25, and its density is $\rho = 2691\ kg/m^3$.

The shear stiffness of an elastic unit is then equal to $k = GTL/H = 28\ kN/m$, and its mass is $m = \rho TLH = 2.691\text{e}{-15}\ kg$. Thus its sliding duration is between $\pi\sqrt{m/k} = \pi H\sqrt{\rho/G} = 9.74\text{e}{-10}\ s$ and $2\pi\sqrt{m/k} = 2\pi H\sqrt{\rho/G} = 1.95\text{e}{-9}\ s$. The static and kinetic COF values are assumed to be $\mu_s = 0.8$ and $\mu_s = 0.7$.

The maximum possible lateral displacement of a block from its zero-spring-force position can be obtained from $kx_{max} = \mu_s N = \mu_s pTL$. Then $x_{max} = 2.86\text{e}{-11}\ m$. The numbers are too small. Decreasing the stiffness (which currently seems reasonable when compared to [214]) or increasing the normal pressure on the block (which can reach plastic yielding stress according to [176]) can increase the maximum allowed displacement of the block. In spite of the physically unreasonable values, a qualitative agreement exists between the results and some observations.

In this study, initial distribution of the block displacements due to normal load is specified as antisymmetric and linear. Five case studies are considered as shown Table 5.2). Three driver velocities: (1) $v_d = 1\ mm/s$, (2) $v_d = 10\ mm/s$, and (3)

	$x_{max_1} = 10^{-13}$ m	$x_{max_2} = 10^{-12}$ m	$x_{max_3} = 2.82 * 10^{-11}$ m
$v_{d_1} = 1$ mm/s	Case study (i)	Case study (ii)	Case study (iii)
$v_{d_2} = 10$ mm/s	-	Case study (iv)	-
$v_{d_3} = 100$ mm/s	-	Case study (v)	-

Table 5.2: The dynamic Maxwell-slip model case studies

$v_d = 100\ mm/s$ and three maximum initial block displacement values: (1) $x_{max} = 1\text{e}{-13}m$, (2) $x_{max} = 1\text{e}{-12}m$, and $x_{max} = 2.82\text{e}{-11}m$ are investigated.

The results of the cases (i)-(v) in Table 5.2 are displayed in Figures 5.10 to 5.14. Each of these figures consists of four subfigures. Subfigure (a) shows evolution of the ratio of total tangential force to total normal force for both friction and traction forces over time. The contributions of the sliding blocks and the stuck blocks are superimposed. Subfigure (b) shows the index of the block that are at the sliding state with grey dots against time. The percent of the sliding blocks is superimposed (plotted in black). Note that the index number one is assigned to the leftmost block and the driver moves to the right. Subfigure (c) demonstrates particle velocity (i.e. the velocity at which each block moves) along the interface for five different moment. Subfigure (d) shows inertial force distribution $-m\ddot{x} = f_d - f_{spring}$ along the interface at the same five moments.

The case studies (Table 5.2) are separating to two sets. The first set consists of the cases (i), (ii) and (iii) with the same driver velocity of $1\ mm/s$. In Figure 5.10, case study (i) is investigated. Subfigure 5.10-(a) shows that initially the traction force and friction force ratios increase linearly with time up to the static friction coefficient. This interval corresponds to the no-sliding zone in Subfigure 5.10-(b). Afterwards, during a very short time period, while friction ratio becomes equal to kinetic friction, the traction force ratio drops to $2\mu_d - \mu_s$. The same interval in Subfigure 5.10-(b) shows that the whole set of blocks slip almost simultaneously and undergo a *collective interfacial slip* [176]. The stick-slip mode of sliding occurs. In this case study, the initial spring extension values are quite close. The triggering moments are close enough to cause all-slipping periods. All-slipping situations along the interface occur during the force drops as shown in Subfigure 5.10-(c). In Subfigure 5.10-(d), the distribution of the inertial force along the interface is plotted for the same moments. During the all-slipping periods friction and traction remain close. The reason is that the negative and positive parts of $m\ddot{x}$ eliminate each other. The antisymmetric distribution of $m\ddot{x}$ leads to a rapid self-eat-up of the inertial force.

In Figure 5.11, case study (ii) is investigated. A linear increase is observed in traction and friction force ratios which starts to decay linearly before reaching the static COF.

It seems as if the sawtooth shape of Subfigure 5.10-(a) is stretched horizontally. Subfigure 5.11-(b) shows the single pulse that sweeps the interface at different times with all-sticking periods in between. At most 55% of the interface blocks are involved in a pulse (Subfigure 5.11-(b)). Subfigure 5.11-(c) shows the single pulse speed profile as it passes the interface. The self-elimination of the inertial force occurs in this case too (Subfigure 5.11-(d)). therefore, the traction and forces are almost the same (Subfigure 5.11-(a)).

In Figure 5.12, case study (iii) is investigated. By tending x_{max} to its maximum possible value, the traction and friction forces behave nonlinearly Subfigure 5.12-(a). A train of pulses propagates through the interface from the very beginning of the driver motion as shown in Figure 5.12-(b). The blocks undergo a *sequential interfacial slip* regularly [176]. The nonlinear curve does not tend toward static COF. Instead, when the curve reaches the kinetic COF, its value remains almost constant in a plateau. Smooth sliding occurs in this case. In Subfigure 5.12-(c), it is shown that a multitude of pulses are present at the same moment over the interface. The corresponding inertial forces are illustrated in Subfigure 5.12-(d). The friction force (the red curve in 5.12-(a)) resembles that of the Dahl model in Figure 5.15.

Note that up to this point, in all of the demonstrated cases, the pulling force and friction overlay almost exactly and their difference is negligible. The second set of results consists of the cases (ii), (iv) and (v). These case studies have a common maximum block displacement of $x_{max} = 1\mathrm{e}{-12}m$ (Table 5.2). Case study (ii) was mentioned previously.

In Figure 5.13, case study (iv) is investigated. In Subfigure 5.13-(a), the separation of the traction and friction forces is observed and the traction exceeds the static COF periodically. The distinction is due to the inertial force. In contrast to the previous set of case studies, the inertial force does not eliminate itself. The subfigure indicates that at high velocities traction can exceed friction. As can be seen in Subfigure 5.13-(d) the inertial force does not possess an antisymmetric form. Subfigure 5.13-(b) shows a crack-like propagation of rupture at the interface which occurs faster compared to the pulse-like propagation in the previous set of the case studies. Note also that increasing the driver velocity leads to an increase in the duration of sliding of each

block and therefore increases the number of blocks with overlapping sliding period. The friction force (the red curve in 5.13-(a)) resembles that of the classical Karnopp model in Figure 5.15.

In Figure 5.14, case study (v) is investigated. The driver velocity in this case is the greatest among all: $v_d = 100\ mm/s$. Unexpectedly, the traction force ratio becomes negative periodically as shown in Subfigure 5.14-(a). This means that to counteract the total spring forces, it becomes sometimes necessary to apply a force opposite to the direction of motion. This *inversion* of the traction force direction is also observed in finite element simulation of an infinite elastic strip that slides over a rigid flat substrate [174]. The maximum value of the inertial force has increased and has lost its self-eatup character. As shown in Subfigure 5.14-(b), almost all of the blocks slide all the time and the percentage of the sticking blocks drops to zero only in a short time interval. During these short all-sticking intervals the friction and traction overlap as expected.

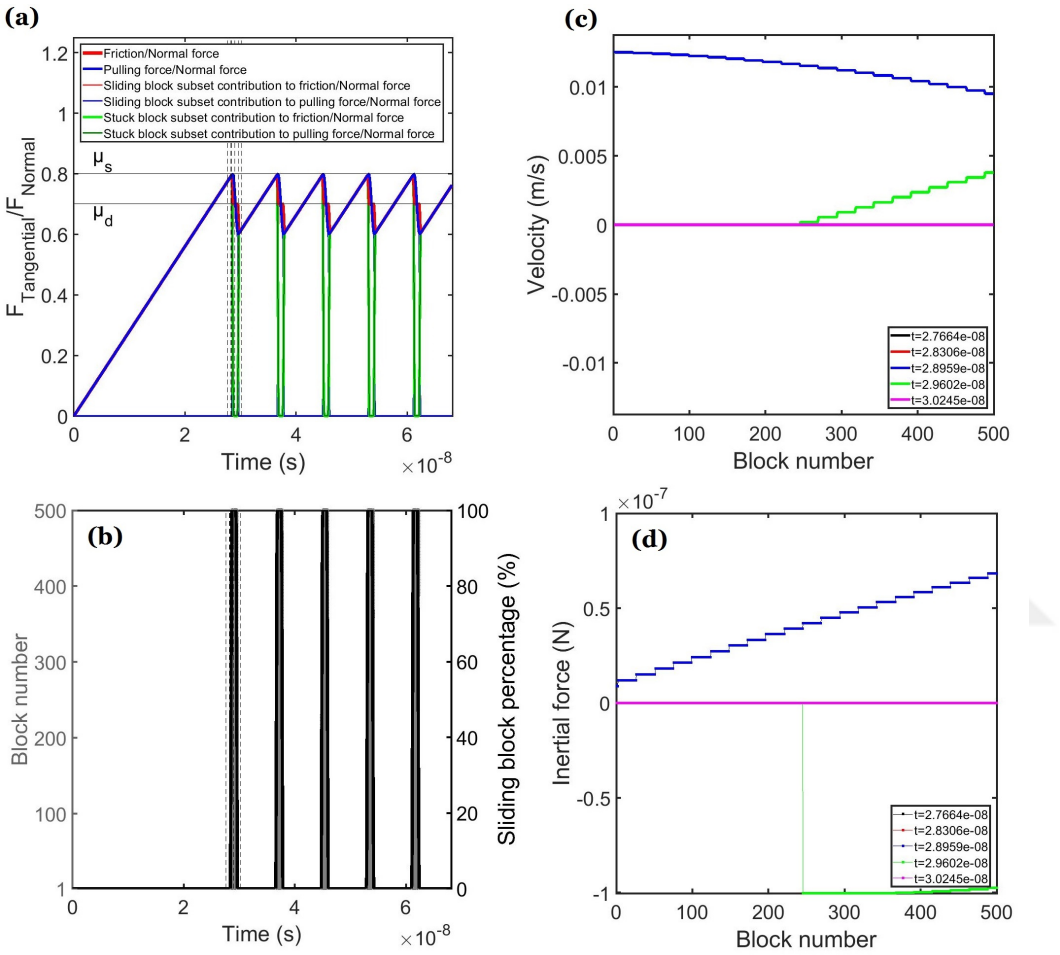

Figure 5.10: Case (i): $v_d = 1\ mm/s$ and $x_{max} = 1\text{e}{-}13\ m$

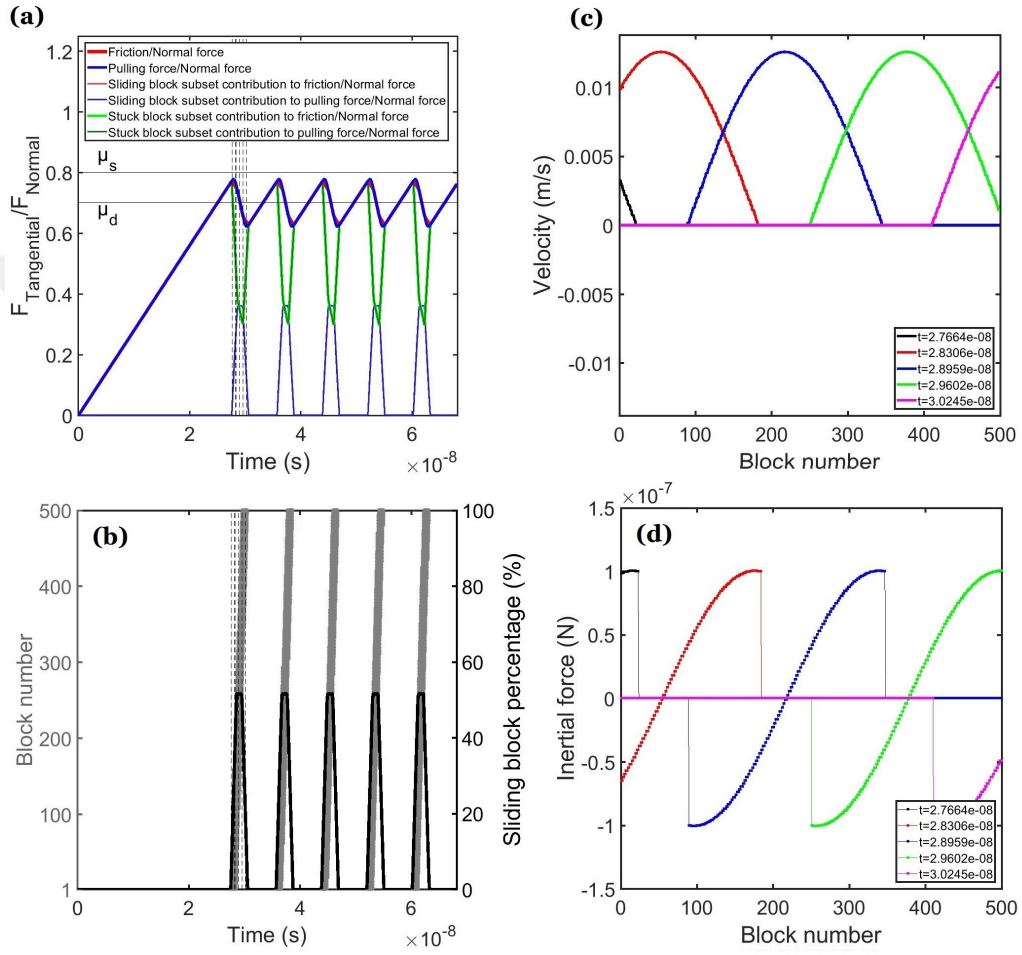

Figure 5.11: Case (ii): $v_d = 1\ mm/s$ and $x_{max} = 1\text{e}{-12}\ m$

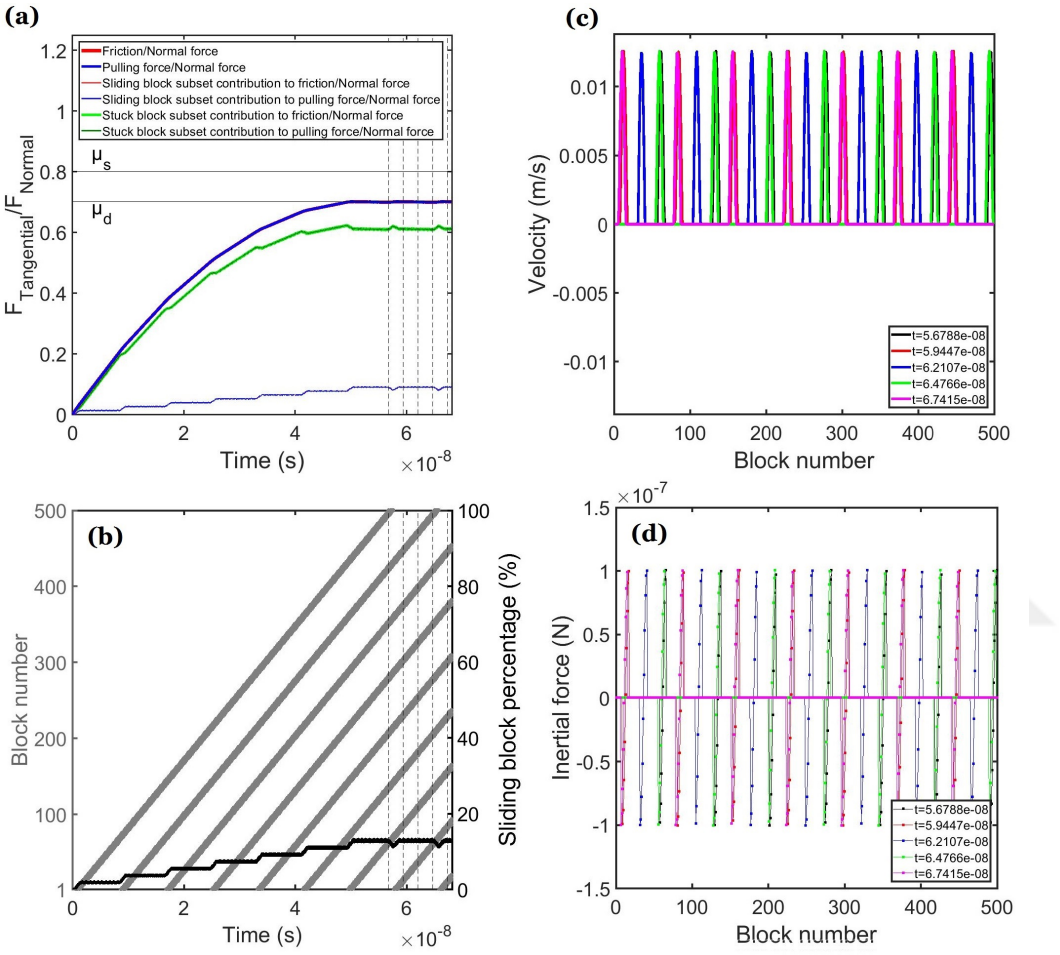

Figure 5.12: Case (iii): $v_d = 1\ mm/s$ and $x_{max} = 2.82\text{e}{-11}\ m$

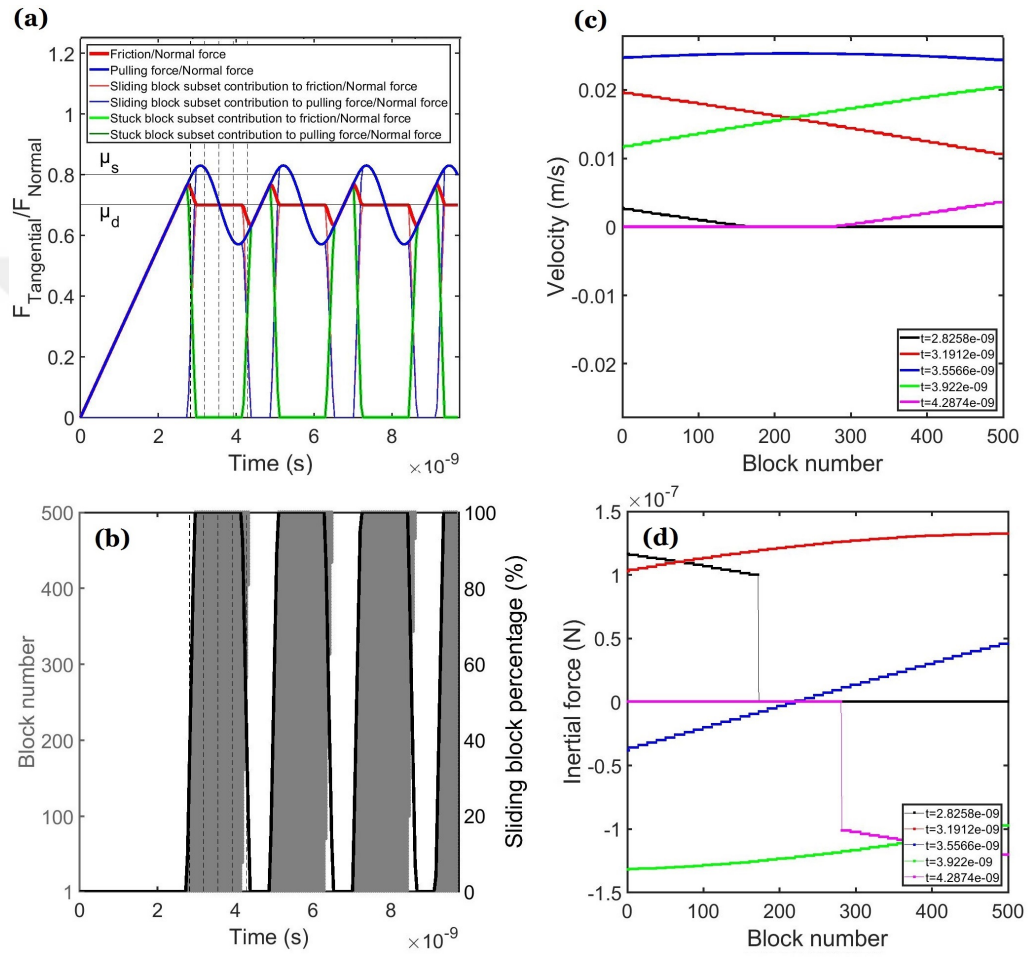

Figure 5.13: Case (iv): $v_d = 10\ mm/s$ and $x_{max} = 1\text{e}{-12}\ m$

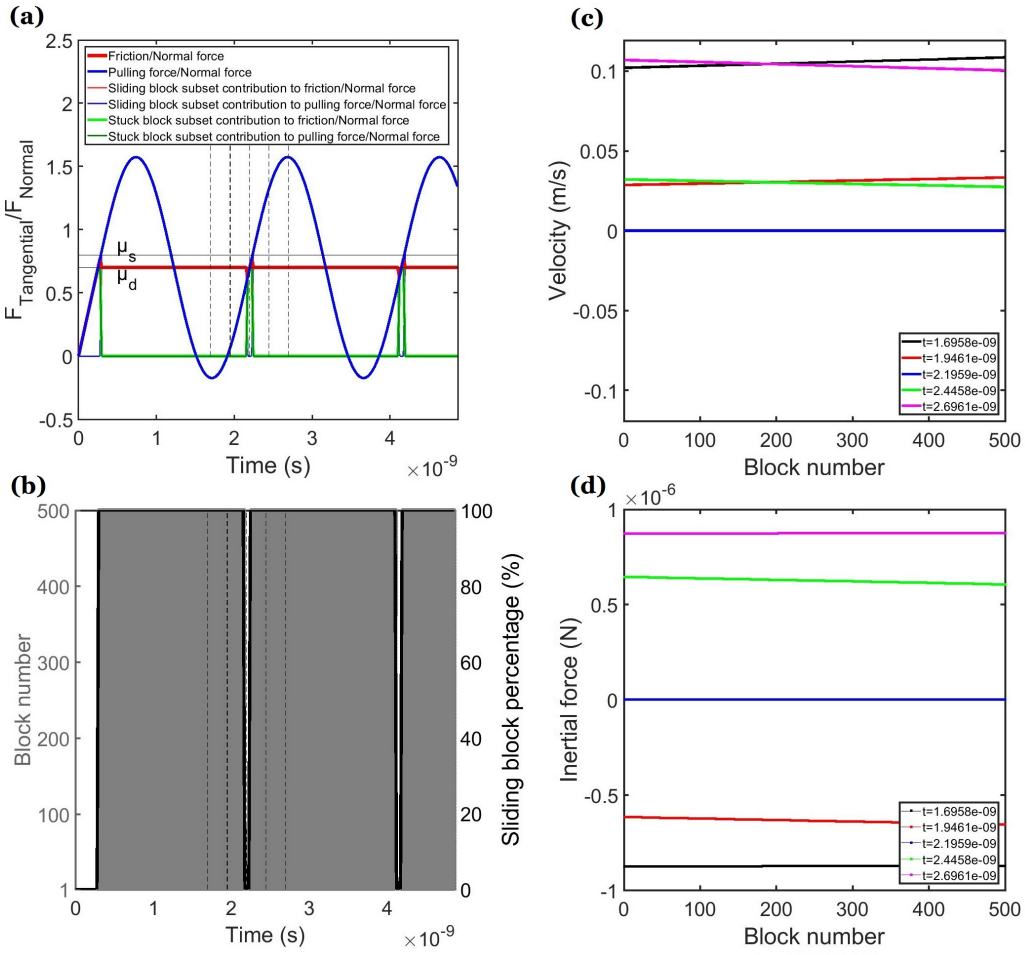

Figure 5.14: Case (v): $v_d = 100\ mm/s$ and $x_{max} = 1\text{e}{-12}$

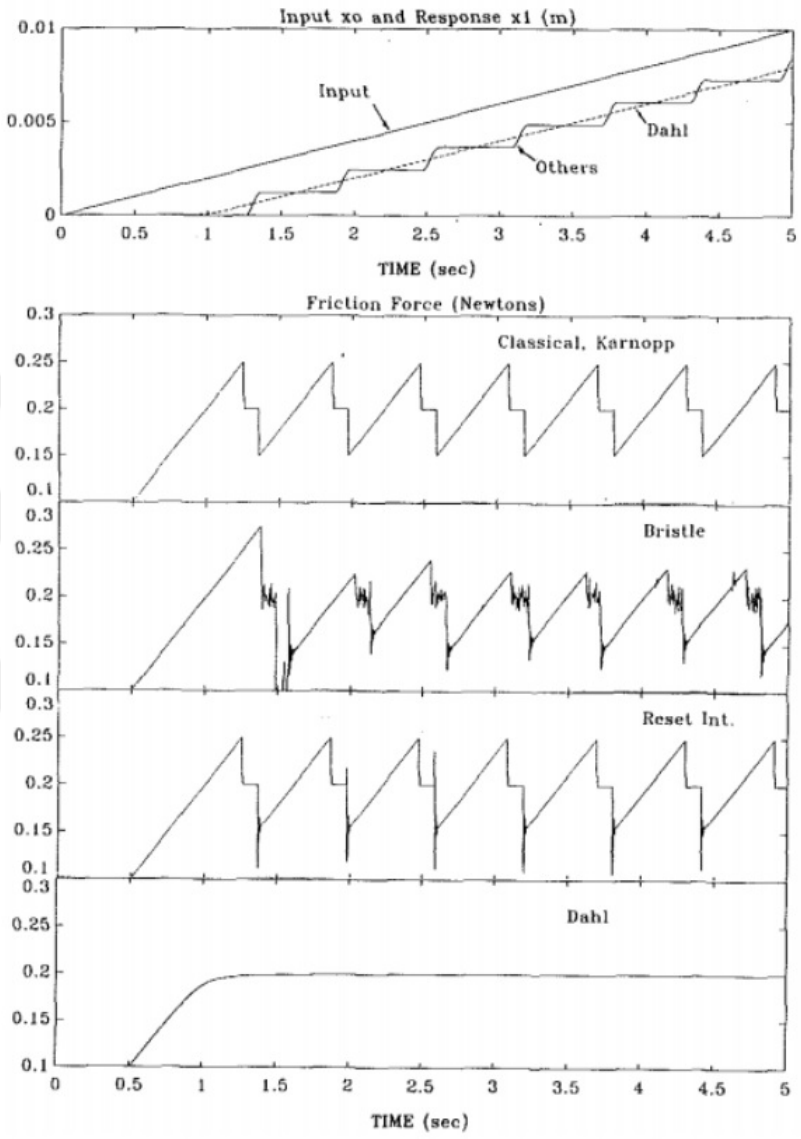

Figure 5.15: The frictional response of the single mass-spring system according to different models in control literature [43]

5.4 Discussion

The solution of the motion for the mass-spring unit is given in Equation (5.3). The spring force (traction) can be found by multiplying the spring extension by the spring stiffness. If the apparent COF is defined as traction force divided by the normal force, for a single mass-spring unit:

$$\mu_{app} = \mu_d + \sqrt{\rho G(\frac{v_d}{p})^2 + (\mu_s - \mu_d)^2}\sin(\omega t + \phi) \tag{5.17a}$$

$$\omega = \frac{1}{H}\sqrt{\frac{G}{\rho}} \tag{5.17b}$$

$$\phi = \arctan(\frac{\mu_s - \mu_d}{\sqrt{\rho G}}\frac{p}{v_d}) \tag{5.17c}$$

where v_d is the driver velocity, p is the pressure applied on the block, ρ is density and μ_s and μ_d are the static and dynamic COF.

The above equation shows that if v_d/p is assumed nearly zero, the maximum apparent COF is the static COF. In this case the apparent COF oscillates about μ_d with an amplitude of $|\mu_s - \mu_d|$. As v_d/p increases, the maximum apparent COF exceeds the static COF. Since the function is sinusoidal, *if the block does not stop* the apparent COF can become negative when v_d/p is high enough.

5.5 Summary

The friction and traction forces and the slip on the interface is studied by using the Maxwell-slip model. In contrast to Chapter 2, the inertial force is considered, and the block slippage has a duration. The driver velocity affects the block slippage length and duration. The initial spring extension distribution is assumed to be linear and antisymmetric. A force-based criterion is used to decide the state of a sticking block. A time-based criterion is used to determine the state of a slipping block. When the maximum spring extension is small, collective interfacial slip occurs, and the slip region propagates as a crack. When the maximum spring extension is large, sequential interfacial slip occurs, and a single pulse (or a train of pulses) propagates along the interface. At low driver velocities, the friction and traction forces are almost the

same. The collective interfacial slip accompanies distinct rises and falls of the forces (stick-slip behavior). The sequential interfacial slip accompanies a nonlinear (creep-like) rise of the friction and traction to the plateau of kinetic friction. At high driver velocities, the traction force differs from the friction due to the block's inertial force. When the driver velocity is high enough, the traction force can become negative. A closed-form expression for the apparent COF is derived. The expression shows that a high driver velocity and a low normal load on a single block can cause anomalously high apparent COF. The expression proposes an explanation for the high local shear to normal stress ratios reported by experimental studies [201, 261].

5.6 Future work

By looking at the experimental results that show a correlation between the rupture speed and the local static COF (Figure 5.16), the question is: can the stress waves [260] that propagate in front of a moving interface crack play the role of a high v_d/p ratio in Equation (5.17)? The inertial force can explain the anomalously high local COF reported in the literature [201, 252, 261].

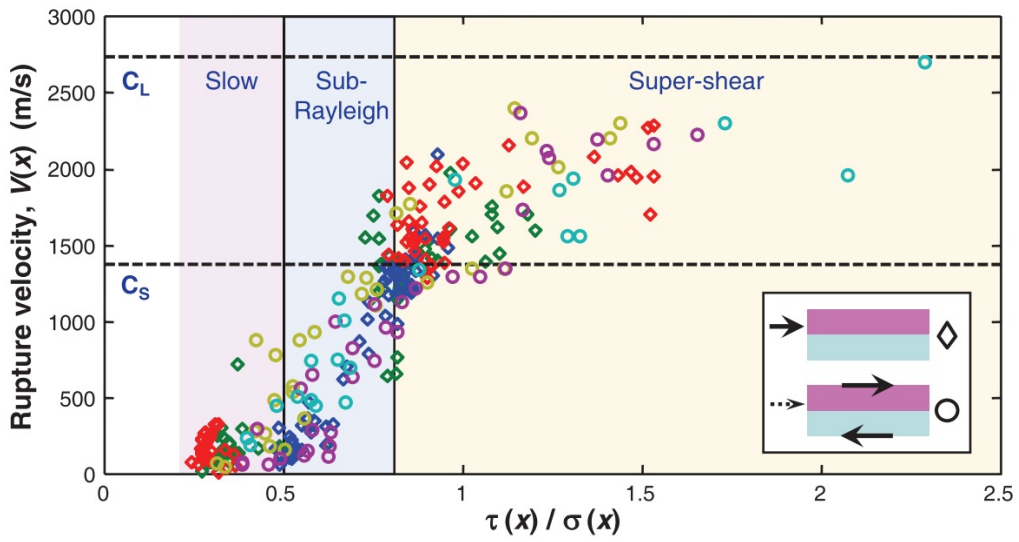

Figure 5.16: Measured local COF as a function of the interface rupture velocity [261]

CHAPTER 6

THE BURRIDGE-KNOPOFF MODEL WITH LINEAR INITIAL LATERAL FORCES

Dieterich [270] proposed a numerical scheme to analyze the Burridge-Knopoff model [38]. This chapter presents the derivation of the equations and explains the algorithm of the scheme. The purpose is to study the effect of different initial block positions and the driver displacement functions on the time evolution of the friction and the driver traction. In Section 6.2, the equation for the resultant spring-exerted force on a block is derived; whether the block is stuck (stationary) or sliding (moving) the resultant is obtained by the same equation. The equation would be used for two main purposes. The first use of the equation is in the force criterion to see if any of the stuck blocks has violated the static friction threshold and therefore has switched its status i.e. has started sliding. The second use of the equation is to calculate the total traction force needed to move the driver. In Section 6.2.3, the equation of motion of the sliding blocks is derived and discretized by assuming that the acceleration of each block is a linear function of time within each time step. A *stepwise forward integration* method [270] is then used to derive block velocity and position at the forthcoming time. The result is an algebraic system of coupled equations of motion which has block accelerations of the forthcoming time as its unknowns. After solving the system for the accelerations, velocity and position of the sliding blocks in the forthcoming time can be calculated. Now, the velocity criterion is used to see if any of the sliding blocks has switched its status i.e. has become stuck. Two errors and one typo are spotted in Dieterich's formulas [270] which are highlighted in yellow. In Section 6.2.4, the algorithm of the method that was proposed in [270] is adapted to calculate the total traction and friction forces. The algorithm is presented by a pseudocode and its corresponding flowchart. The flowchart has a major time increment

loop that includes three minor loops for applying: (i) the force criterion, (ii) the velocity criterion and (iii) final force calculations. Section 6.2.7 proposes an analytical correction to the block stopping time. Section 6.2.8 shows how the algorithm can incorporate a time-dependent aging law for the static frictional threshold. Section 6.2.9 puts forward a criterion about a stable and suitable time step size.

6.1 Introduction

The Burridge-Knopoff (BK) model was proposed in 1967 to study the seismology of the geological faults [38]. As shown in Figure 6.1, the model is composed of a rigid driver that pulls a set of rigid blocks on a rigid flat substrate via leaf springs. Each pair of successive blocks is connected by a coil spring. The force applied by the leaf springs to the blocks has no normal component.

Dieterich [270] used the BK model for numerical simulation of the earthquake aftershocks. Given the position of the driver as a function of time, our purpose is to use the numerical scheme in [270] to study time-variation of: (i) the traction force needed to move the driver, (ii) the friction force that is exerted by the substrate to the blocks and (iii) the sliding/stuck status of the blocks. These variables would be plotted as functions of time for a range of different initial block position distributions. These distributions can be interpreted as the effect (friction-frustrated) Poisson expansion on the interface [251].

The BK model is widely used to study the statistical features of the earthquakes, i.e. the empirical power-law relation between the energy and the number (magnitude

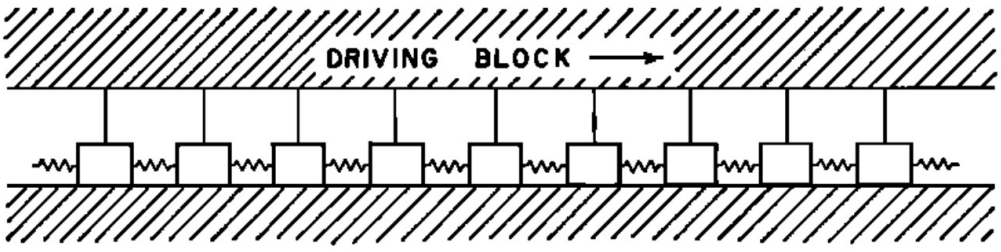

Figure 6.1: The Burridge-Knopoff model as sketched in [270]

versus frequency) of the geological fault ruptures which is known as the Gutenberg-Richter law for earthquakes, especially by physicists [160, 161, 271–275].

In the original paper [38], Burridge and Knopoff assumed that the block-substrate friction is governed by a law that considers the effects of seismic radiation and viscosity and is consequently speed-dependent. The Runge-Kutta method is used to solve the system of differential equations of motion. It is observed that the *steady* solution is unstable in the sense that when perturbed it deviates more and more. This instability and ill-posedness of frictional sliding problems is extensively studied in the literature [72, 276–278].

The other aspect which is studied in [38] is the velocity of sound in the BK model mass-spring system, which is sometimes called the phase velocity. The quantity is related to the velocity of rupture (fracture) propagation on the interface. *By neglecting friction (interface)* a closed-form expression for the velocity of sound for the BK model is found that shows dependency not only on the spring stiffness values, mass and block-spacing but also on the wave number of the harmonic solution. This means that the phase velocity can be infinite even for finite values of the leaf spring stiffness [38].

The issue of supersonic crack propagation velocities in the BK model is addressed later by Knopoff in [279]. He showed that the discretization of the interface continuum causes a violation of the causuality (causing noncausuality) in the sense that it requires blocks to have a foreknowledge of the future events in order to obey the wave equation. The noncausuality is ascribed to the sudden jumps of the inertial coordinate system as the crack tip moves forward. He argues that discretization of the wave PDE causes an *ill-posed* formulation of the fracture criterion and proposes an alternative: a fracture criterion that is based on the dynamic continuum theory. This dynamic correction to the static rule guarantees a rupture velocity below the speed of sound. However, the remedy causes other problems, like lattice oscillations. These undesired consequences (which also cause anomalously high crack propagation velocities) are tackled in [280] where the BK model is equipped with dashpots in order to dissipate the oscillations.

In 1973, Burridge [281] showed that when the static COF is low enough at the in-

terface of two elastic half-spaces, the only admissible speed for propagation of a *slip zone* along the interface (which is governed by Coulomb friction) is the pressure wave speed since lower speeds (Rayleigh and shear wave speeds) are ruled out theoretically. Burridge emphasized that a low-enough static COF is not a necessary condition and propagation with the speed of the pressure wave is always possible.

In 1976, Andrews [282] used a finite different scheme to solve the 1-D wave equation for an interface that is governed by an slip-weakening friction law. Once a point exceeds the static friction the amount of friction that is experienced by it decreases linearly as a function of the amount of slippage. This law (Figure 6.2) is closely related to one of the experimental observations of Rabinowicz [30] which indicates to the existence of a critical distance before which the static friction does not drop to the dynamic friction (already discussed in Subsection 1.1.2). In [283], the critical displacement, the critical energy release rate or the fracture energy (toughness) are used to propose a cohesive zone model (CZM) for dynamic shear faulting which is essentially the same as the slip-weakening friction law. The numerical investigations of Andrews showed that in some cases the crack propagation speed undergoes a sharp transition from sub-Rayleigh speeds to 1.5 times the shear wave speed. These numerical observation was later affirmed by the theoretical investigation of Burridge, Conn and Freund [284] in which the wave equation (governed by a similar cohesive traction law) was turned into an integral equation and solved numerically. According to the results, a stable propagation of the crack is only possible when its speed is $\sqrt{2}c_s$, where c_s is the shear wave speed. The propagation velocities between Raleigh wave speed and the shear wave speed are regarded forbidden since according to the results an increase in the speed of propagation corresponds to a decrease in the driving force of the crack. This makes a stable crack growth within that interval impossible. These results are also confirmed in an analytical investigation of the dynamic crack growth along an *elastic-rigid* interface [285].

Experimental evidence for the supershear crack propagation, $c_s < V$ was provided in [286] in which photoelasticity images of the sliding interface between two Homalite specimen shows that the rupture crack tip travels at speeds near $\sqrt{2}$ times Homalite shear wave speed. Later, intersonic crack propagation speeds, $c_s < V < c_p$, were observed in unidirectional composite plates by using the optical technique of coherent

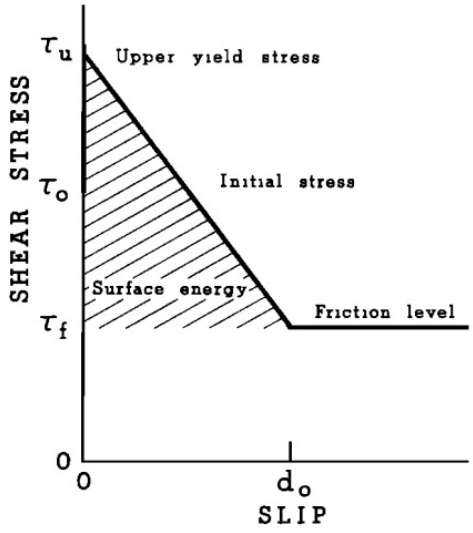

Figure 6.2: The linear slip-weakening friction law [282]

gradient sensing [74]. The existence of supershear ruptures is also supported by the seismic data [287, 288].

Based on ground motion data from seven earthquakes, Heaton [289] proposed *self-healing pulses of slip*, in contract to crack-like propagation, as another possible mechanism for propagation of the interface rupture. In a pulse-like rupture, only a small part of the interface slips and for a short duration (compared to the length and duration of the rupture). The pulse is actually a moving slip zone with locked interface in front of it and healed interface behind. As the pulse moves through the interface it drops the stress and releases energy. This mechanism is an alternative to the crack-like numerical models in which the local slip duration is comparable to the overall duration of rupture. A crack-like rupture requires the slipping points to keep moving till the end of the rupture.

In a numerical simulation of the interface rupture by using the BK model Elbanna and Heaton use a velocity-weakening friction law [290]. The law requires a gradual decay (instead of a sudden drop) from the static friction as a block speeds up from its stuck situation. Firstly, the blocks move slowly and experience high friction and then, as they speed up, the friction decays. In other words as the *velocity* increases the friction *weakens*. In [290] the pulse-like mode involves only $1 - 5\%$ of the total rupture length. Energy balance equation of the pulse provides an opportunity of predicting

the result of rupture given the amount of pre-stress on the blocks. This reduces the computational time drastically and makes investigation of the long-term statistical behavior of the BK model in a shorter time possible. For the details of the derivation one may find Appendix B of Elbanna's doctorate thesis [291] useful. Furthermore, Appendix A of [291] contains a mathematical explanation of the BK model phase velocity under different conditions (with and without velocity-weakening friction), showing the possibility of a supersonic *phase velocity*. However, the *group velocity* is subsonic for both of the fricrional and frictionless cases.

Both the crack-like and pulse-like modes of frictional sliding are observed in experimental and numerical simulations. Coker, Lykotrafitis, Needleman, and Rosakis [75] investigated rupture of the interface between two identical elastic isotropic plates subjected to shear impact by using a photoelastic optical setup and FEM and observed supersonic (with respect to the pressure wave speed) propagation speeds. They used a rate (velocity) and state (time) dependent friction law in the numerical model. Figure 6.3 shows their experimentally and numerically obtained crack tip speeds. They ob-

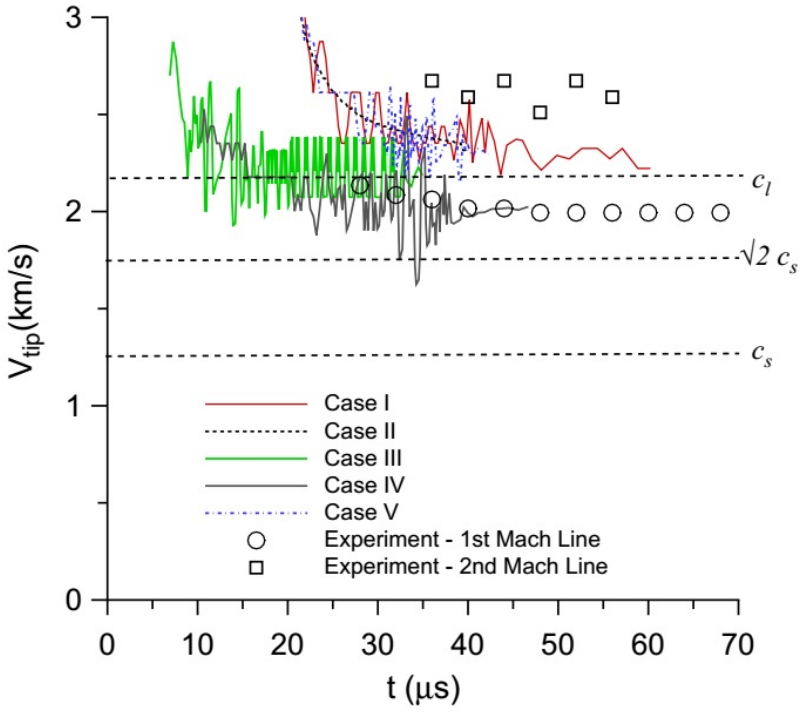

Figure 6.3: The experimentally and numerically obtained rupture speeds along the interface between two identical elastic isotropic plates subjected to shear impact [75]

served that different modes of sliding can occur depending on the amount of the initial compressive stress and the impact velocity. Crack-like mode occurs when the compressive stress and impact velocity are low, otherwise the pulse-like mode becomes dominant.

Another experimental and numerical study was performed by Lu, Lapusta and Rosakis [292]. The laboratory setup is composed of a Homalite plate that has an inclined interface and therefore experiences compression and shear. The rupture is triggered by explosion of a thin wire at the center of the interface. The spectral boundary-integral method is used to simulate the elastodynamic response of the interface and its surrounding. A linear slip-weakening friction law (as in [282]) is assumed. Although the experiments show both the crack-like and pulse-like modes the numerical method has failed to generate a pulse-like response [292]. An experimental investigation of sliding at a frictional bimaterial interface [293] shows that slip-pulses and crack-like ruptures prefer different directions. Strain gauges are used to measure stress and velocity and an optical method is used to measure real contact area.

Some studies have been successful in generating both crack-like and pulse-like modes [294, 295] by using the BK model (Figure 6.4). A recent 1-D continuum model [296] shows that depending on the boundary condition at the top of the interface and the state of the initial stress at the interface, either crack-like or pulse-like propagation

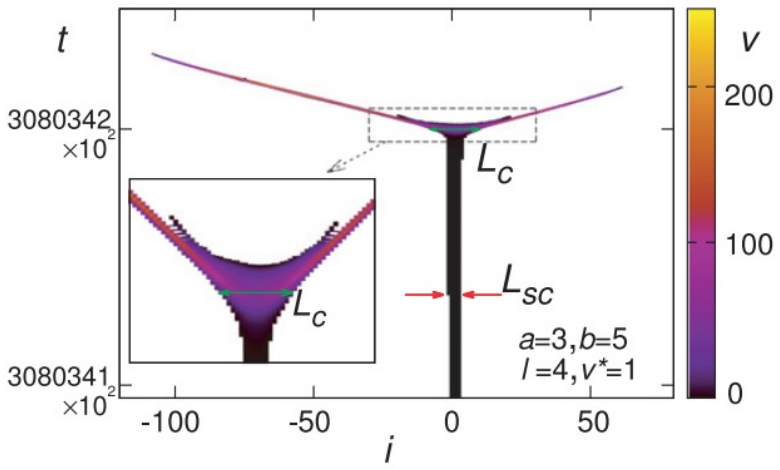

Figure 6.4: Nucleation and acceleration of rupture in the BK model and its different characteristic lengths [294]

can emerge. The transition from the crack-like to pulse-like propagation (Figure 6.5) occurs when the initial shear stress along the interface is symmetric and the displacement BC is applies at the top [296]. The transition is also observed in a complex 3-D model [297].

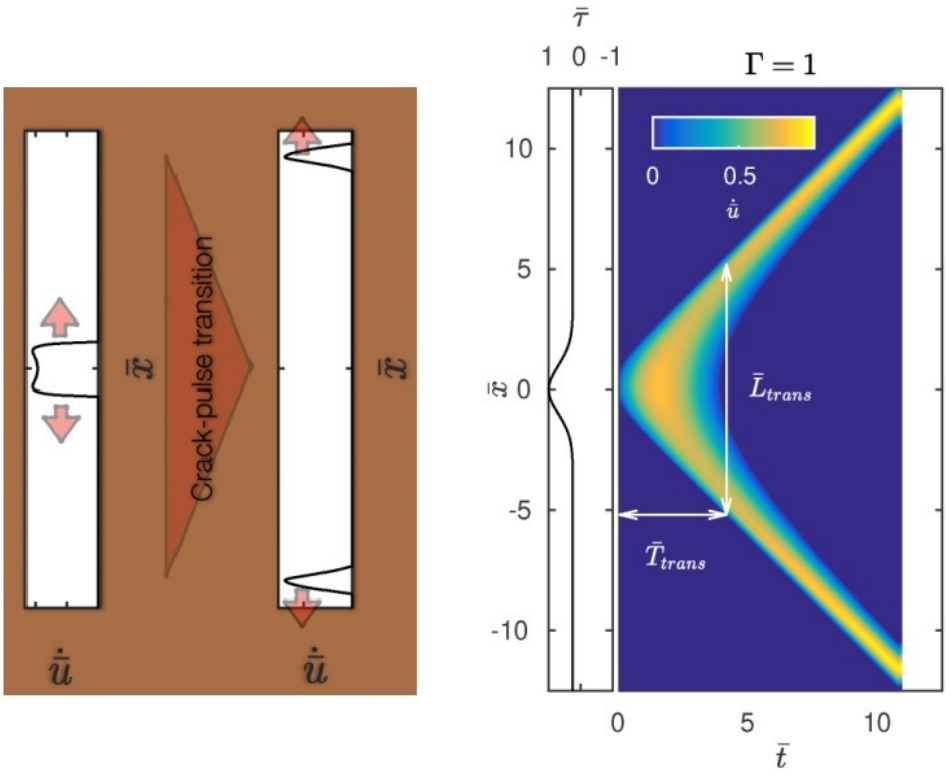

Figure 6.5: The division of a crack-like nucleation into a pair of pulses that propagate in opposite directions [296]

6.2 Method

Consider any of the coil springs in Figure 6.6-(a). The magnitude of the pulling force that the coil spring exerts on one block is equal to the magnitude of the pushing force the same coil spring exerts on the other block. This fact is true for all of the blocks whether stuck or sliding. Thus, summing the resultant spring forces applied on all of the blocks cancels out the counteracting coil spring forces and leaves the sum of the force in the leaf springs only. The latter is equal to the traction force, T, needed to move the driver. On the other hand, the sum of the spring forces on each stuck block is needed to decide whether such a block would remain stuck or would start to slide.

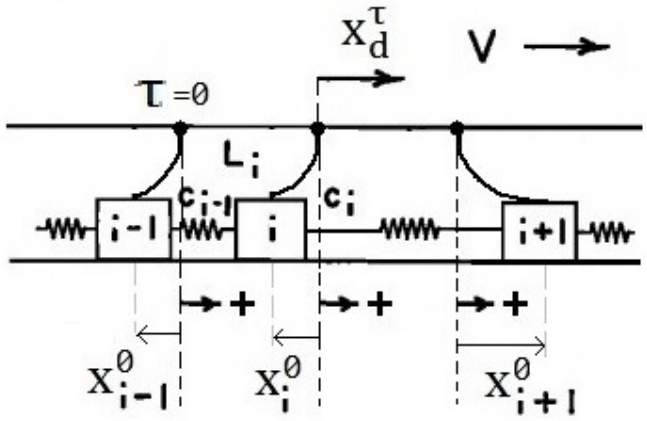

Figure 6.6: The ith block and its immediate neighbors in the BK model

Consider the immediate neighbors of the ith block, i.e. its left neighbor, $(i-1)^{th}$ block, and its right neighbor, $(i+1)^{th}$ block as shown in Figure 6.6. The stiffness of the coil spring to the left of the ith block is named C_{i-1}. The stiffness of the leaf spring that connects the ith block to the driver is named L_i. The stiffness of the coil spring to the right of the ith block is named C_i. "L" stands for "leaf spring" and "C" for "coil spring". A local reference point is assigned for each block to specify its position. The reference point is the projection (the dashed lines) of "the attachment point of the corresponding leaf spring to the driver" (the black dots) on the rigid substrate *before the driver starts to move*, i.e. at $\tau = 0$. Each reference point is fixed to the substrate and is used to specify block and the attachment point positions henceforth. The sign of position is considered to be positive to the right. The initial position of a block can be negative, positive or zero. The driver position is specified as a known function of time.

The resultant spring-exerted force on the ith block is obtained by adding the forces components exerted by the left coil spring, the leaf spring, and the right coil spring on the block:

$$F_i^\tau = C_{i-1}\left(x_{i-1}^\tau - x_i^\tau\right) + L_i(x_d^\tau - x_i^\tau) + C_i(x_{i+1}^\tau - x_i^\tau) \tag{6.1}$$

In the above equation, the multiplier of each spring stiffness value is the amount of change in the corresponding spring's no-force length. It is assumed that if any pair

of successive blocks has the same local position, then the coil spring between them experiences no force. For example, when the leaf springs are vertical (not deformed), i.e., when the blocks are right below their corresponding driver-attachment point, the coil springs are neither compressed nor extended. The negative sign behind x_i^τ can be understood by intuition; the further forward is the position of the ith block, the more backward (negative) force would be exerted by each of the three springs connected to the ith block. A rigorous approach to write the force contributions is to consider the two possible scenarios of compression and extension for each spring which happens due to relative motion of the spring ends. Then, the force contribution expression has to be written such that (no matter which scenario happens) the sign of the force is obtained automatically as expected.

Factoring out x_i^τ in Equation (6.1):

$$F_i^\tau = C_{i-1}x_{i-1}^\tau - (C_{i-1} + L_i + C_i)x_i^\tau + C_i x_{i+1}^\tau + L_i x_d^\tau \tag{6.2}$$

in matrix form:

$$F_i^\tau = \begin{bmatrix} C_{i-1} & -(C_{i-1} + L_i + C_i) & C_i \end{bmatrix} \begin{bmatrix} x_{i-1}^\tau \\ x_i^\tau \\ x_{i+1}^\tau \end{bmatrix} + L_i x_d^\tau \tag{6.3}$$

using the indicial notation:

$$F_i^\tau = K_{ij}x_j^\tau + L_i x_d^\tau, \qquad \{j = i-1,\ \ i,\ \ i+1\} \tag{6.4}$$

where:

$$\begin{cases} K_{i,i-1} = C_{i-1} \\ K_{i,i} = -\left(C_{i-1} + L_i + C_i\right) \\ K_{i,i+1} = C_i \end{cases} \tag{6.5}$$

Note that K is a vector and is expressed with a single free index. The free index, i,

is the block indicator (counter) and specifies the block number for which the relation is written. On the other hand, the summation index, $j = \{i-1,\ \ i,\ \ i+1\}$, helps including the three block positions in a compact format.

Up to this point, the equations are written for the ith block. Now, although a general matrix-format expression can be assembled to calculate the resultant spring-exerted force values for all of the blocks by using Equation (6.4), the expression is superfluous. According to Equation (6.3) the blocks other than those shown in Figure 6.6 do not contribute to the force exerted on the ith block. Then, the non-neighbor block positions would be multiplied by zeros in the assembled stiffness matrix and would contribute nothing. Therefore, constructing an all-inclusive system of equations would be a waste of computational time. Instead of bringing the Equations (6.3) together in a global stiffness matrix (which would be a tridiagonal matrix as claimed in [270]), it is suggested that Equation (6.3) is used on its own for each block by considering $i = \{1,\ 2, \ldots, M-1, M\}$ where M is the number of the blocks.

6.2.1 Free boundary conditions

Assuming free boundary conditions (FBC) means: the left neighbor of the leftmost block and the right neighbor of the rightmost block do not exist. Then, Equation (6.3) for the leftmost and the rightmost blocks has to be written as described below.

For the leftmost block, i.e. the 1st block, no force would be contributed from a left hand side neighbor. Then, when $i = 1$, $C_{i-1} = C_0$ is zero and its corresponding multiplier position, i.e., $x^{\tau}_{i-1} = x^{\tau}_0$ does not exist. Therefore, Equation (6.3) for the leftmost block becomes:

$$F^{\tau}_1 = \begin{bmatrix} 0 & -(L_1 + C_1) & C_1 \end{bmatrix} \begin{bmatrix} x^{\tau}_0 \\ x^{\tau}_1 \\ x^{\tau}_2 \end{bmatrix} + L_1 x^{\tau}_d \tag{6.6}$$

Then:

$$F_1^\tau = \begin{bmatrix} -(L_1 + C_1) & C_1 \end{bmatrix} \begin{bmatrix} x_1^\tau \\ x_2^\tau \end{bmatrix} + L_1 x_d^\tau \tag{6.7}$$

For the rightmost block, i.e. the Mth block, no force would be contributed from a right-hand side neighbor. Then, when $i = M$, $C_i = C_M$ is zero and its corresponding multiplier position, i.e., $x_{i+1}^\tau = x_{M+1}^\tau$ does not exist. Therefore, Equation (6.3) for the rightmost block becomes:

$$F_M^\tau = \begin{bmatrix} C_{M-1} & -(C_{M-1} + L_M) & 0 \end{bmatrix} \begin{bmatrix} x_{M-1}^\tau \\ x_M^\tau \\ x_{M+1}^\tau \end{bmatrix} + L_M x_d^\tau \tag{6.8}$$

Then:

$$F_M^\tau = \begin{bmatrix} C_{M-1} & -(C_{M-1} + L_M) \end{bmatrix} \begin{bmatrix} x_{M-1}^\tau \\ x_M^\tau \end{bmatrix} + L_M x_d^\tau \tag{6.9}$$

6.2.2 Periodic boundary conditions

Assuming the periodic boundary conditions (PBC) means that the left neighbor of the leftmost block is virtually considered to be the rightmost block and in addition the right neighbor of the rightmost block is virtually considered to be the leftmost block. Figure 6.7 shows the PBC. The grey color identifies the blocks that are subjected to the PBC. The dash-lined blocks are the virtual blocks that are used to impose the periodicity. Equation (6.3) for the leftmost and the rightmost blocks has to be written as described below.

For the leftmost block, i.e., the 1st block, shown in grey on the left side of Figure 6.7, the Mth block is assumed as a virtual left hand side neighbor. Thus, when $i = 1$, $C_{i-1} = C_0$ is equal to C_M (is not zero in contrast to the FBC) and the corresponding multiplier position $x_{i-1}^\tau = x_0^\tau$ is equal to x_M^τ. Then, equation (6.3) for the leftmost block becomes:

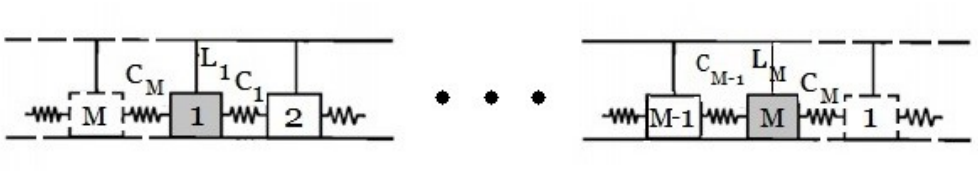

Figure 6.7: Periodic boundary condition: assuming that the virtual neighbor of the leftmost (1st) block is the rightmost block; and assuming that the virtual neighbor of the rightmost (M^{th}) block is the leftmost block.

$$F_1^\tau = \begin{bmatrix} C_M & -(C_M + L_1 + C_1) & C_1 \end{bmatrix} \begin{bmatrix} x_M^\tau \\ x_1^\tau \\ x_2^\tau \end{bmatrix} + L_1 x_d^\tau \tag{6.10}$$

For the rightmost block, i.e., the Mth block, shown in grey on the right side of Figure 6.7, a right neighbor exists which is the 1st block. Therefore, when $i = M$, $C_i = C_M$ is not zero and the corresponding multiplier position $x_{i+1}^\tau = x_{M+1}^\tau \equiv x_1^\tau$. Then, Equation (6.3) for the rightmost block becomes:

$$F_M^\tau = \begin{bmatrix} C_{M-1} & -(C_{M-1} + L_M + C_M) & C_M \end{bmatrix} \begin{bmatrix} x_{M-1}^\tau \\ x_M^\tau \\ x_1^\tau \end{bmatrix} + L_M x_d^\tau \tag{6.11}$$

When all of the components of $\overrightarrow{F}$, i.e., the vector of resultant spring-exerted forces on each block, are obtained the vector would be used in two ways: (i) the sum of all of the components of $\overrightarrow{F}$ together gives the magnitude of the traction force required to be applied to the driver in order to overcome the leaf spring forces, i.e., $T = \sum_{i=1}^{M} F_i$, (ii) those components of $\overrightarrow{F}$ which correspond to the stuck blocks are checked; if any component has exceeded the static friction threshold, its corresponding block is considered as "sliding". To obtain $\overrightarrow{F}$ at the forthcoming time, knowing the block positions at the forthcoming time is necessary. It turns out that knowing the positions requires solution of a system of equations of motion of the sliding blocks!



Figure 6.8: The external forces exerted on (a) the ith block sliding block and (b) the free body diagram of the ith block sliding block includes the fictitious force, $-ma_i$, in order to apply the principle of d'Alembert.

6.2.3 The equations of motion

The external forces that act on the ith block (shown in Figure 6.6) during its sliding interval are shown in Figure 6.8-(a); F_i is the resultant of the spring-exerted forces and k_i is the kinetic friction. Newton's 2nd law of motion for the block gives the EOM:

$$\sum F_{external} = ma \quad \Rightarrow \quad F_i^\tau - k_i = m_i a_i^\tau \tag{6.12}$$

An alternative way to write the EOM is to apply the principle of d'Alembert by assuming that a fictitious (also called inertial) force, $-ma_i$, acts on the block in addition to the spring-exerted and friction forces. The free body diagram is shown in 4-(b). Then, the dynamic problem can be interpreted as a static equilibrium problem. The EOM has to be identical to the equation obtained above:

$$\sum F_{exerted} = 0 \quad \Rightarrow \quad F_i^\tau - k_i - m_i a_i^\tau = 0 \tag{6.13}$$

Dieterich [270] has made a mistake in using the principle of d'Alembert; the direction of the fictitious force is falsely considered reverse. The sign has remained wrong in the posterior equations; thus, the mistake is not a typo.

By substituting the expression found for the resultant spring-exerted force, F_i, in Equation (6.4) into the above EOM:

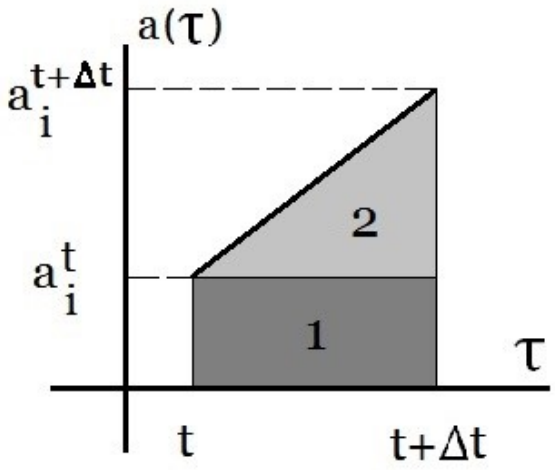

Figure 6.9: The block acceleration is assumed to change linearly with time within each time step between the discrete times: the previous time point, $\tau = t$, and the forthcoming time point $\tau = t + \Delta t$. The total grey area beneath $a(\tau)$ is equal to the change in the block velocity within the time step.

$$k_i = K_{ij}x_j^\tau + L_i x_d^\tau - m_i a_i^\tau, \qquad j = \{i-1,\ i,\ i+1\} \tag{6.14}$$

The EOM of the ith block is obtained in terms of the block positions and accelerations of the ith block and its immediate left and right neighbors. The next step is to discretize the EOM in a time between the previous time, $\tau = t$, and the forthcoming time, $\tau = t + \Delta t$. The aim of the time discretization is to investigate the possibility of obtaining the state of the blocks in the forthcoming time point, $(x_i^{t+\Delta t},\ v_i^{t+\Delta t},\ a_i^{t+\Delta t})$, from the known state of the blocks in the previous time point, $(x_i^t,\ v_i^t,\ a_i^t)$. For this purpose, the block acceleration is assumed to be a linear function of time within each time step, i.e., within $\tau = [t,\ t + \Delta t]$, as shown in Figure 6.9.

The change in the block velocity within the time interval $[t,\ t + \Delta t]$ can be obtained by integrating the proposed linear function for the block acceleration:

$$v_i^\tau|_{\tau=t}^{\tau=t+\Delta t} = v_i^{t+\Delta t} - v_i^t = \int_{\tau=t}^{\tau=t+\Delta t} a_i^\tau d\tau \tag{6.15}$$

which is also equal to sum of the grey areas shown in Figure 6.9:

$$v_i^{t+\Delta t} - v_i^t = A_1 + A_2 = \ \Delta t.a_i^t + \frac{1}{2}\Delta t\left(a_i^{t+\Delta t} - a_i^t\right) \tag{6.16}$$

Then:

$$v_i^{t+\Delta t} = v_i^t + \frac{1}{2}\Delta t\left(a_i^t + a_i^{t+\Delta t}\right) \tag{6.17}$$

Therefore, the only unknown which is required for calculation of the block velocity in the forthcoming time, $v_i^{t+\Delta t}$, is the block acceleration in the forthcoming time, $a_i^{t+\Delta t}$. The above relation can also be verified by algebraic integration. The stepwise acceleration function is the thick black line that is shown in Figure 6.9:

$$a_i^\tau = m\tau + c \tag{6.18}$$

where the slope, m, and y-intercept, c, of the line equation are:

$$\begin{cases} m = (a_i^{t+\Delta t} - a_i^t)/\Delta t \\ c = a_i^t - t.(a_i^{t+\Delta t} - a_i^t)/\Delta t \end{cases} \tag{6.19}$$

Now the integration can be done algebraically:

$$v_i^{t+\Delta t} - v_i^t = \int_{\tau=t}^{\tau=t+\Delta t} (m\tau + c)d\tau = \ (\frac{m}{2}\tau^2 + c\tau)\Big|_{\tau=t}^{\tau=t+\Delta t} \tag{6.20}$$

Therefore:

$$v_i^{t+\Delta t} - v_i^t = \frac{m}{2}(t+\Delta t)^2 + c(t+\Delta t) - \frac{m}{2}t^2 - ct \tag{6.21}$$

By rewriting the above equation:

$$v_i^{t+\Delta t} - v_i^t = m\left[t.\Delta t + \frac{(\Delta t)^2}{2}\right] + c.\Delta t \tag{6.22}$$

Then, by substituting the expressions for the line slope, m, and y-intercept, c, and simplifying, Equation (6.17) is obtained (checked).

The aim is to find $(x_i^{t+\Delta t},\ v_i^{t+\Delta t},\ a_i^{t+\Delta t})$ in terms of $(x_i^t,\ v_i^t,\ a_i^t)$. Pursuing this aim, one is interested in finding an expression for the position of the block in the forthcoming time, $x_i^{t+\Delta t}$. Similar to the procedure adapted above to reach Equation (6.17), integration of the block velocity, v_i^τ, between $\tau = t$ and $\tau = t + \Delta t$ has to be performed. However, firstly an indefinite integral of the block acceleration function, a_i^τ, should be taken in order to determine the velocity function, v_i^τ:

$$v_i^\tau = \int a_i^\tau d\tau = \int (m\tau + c) d\tau = \frac{m}{2}\tau^2 + c\tau + c_0 \tag{6.23}$$

The integration constant, c_0, can be either found by $v_i^\tau = v_i^t$ or $v_i^\tau = v_i^{t+\Delta t}$ (both would yield the same c_0). Using the first condition (i.e., $v_i^\tau = v_i^t$) and substituting the previously known expressions for the slope, m, and y-intercept, c:

$$v_i^t = \frac{m}{2}t^2 + ct + c_0 \quad \Rightarrow \qquad c_0 = v_i^t - a_i^t t + \frac{a_i^{t+\Delta t} - a_i^t}{2\Delta t}t^2 \tag{6.24}$$

Now the definite integral of v_i^τ can be taken by noting that:

$$x_i^\tau \Big|_{\tau=t}^{\tau=t+\Delta t} = x_i^{t+\Delta t} - x_i^t = \int_{\tau=t}^{\tau=t+\Delta t} v_i^\tau d\tau \tag{6.25}$$

which means:

$$x_i^\tau \Big|_{\tau=t}^{\tau=t+\Delta t} = \int_{\tau=t}^{\tau=t+\Delta t} \left(\frac{m}{2}\tau^2 + c\tau + c_0\right) d\tau \tag{6.26}$$

Then:

$$x_i^{t+\Delta t} - x_i^t = \left(\frac{m}{6}\tau^3 + \frac{c}{2}\tau^2 + c_0\tau\right)\Bigg|_{\tau=t}^{\tau=t+\Delta t} \tag{6.27}$$

and therefore:

$$x_i^{t+\Delta t} - x_i^t = \frac{m}{6}[(\Delta t)^3 + 3t(\Delta t)^2 + 3\Delta t.t^2\ ] + \frac{c}{2}\left[2\Delta t.t + (\Delta t)^2\right] + c_0\Delta t \quad (6.28)$$

Finally, by substituting the known expressions for m, c and c_0 and simplifying the expression:

$$x_i^{t+\Delta t} = x_i^t + \Delta t.v_i^t + \frac{(\Delta t)^2}{3}a_i^t + \frac{(\Delta t)^2}{6}a_i^{t+\Delta t} \quad (6.29)$$

The only unknown needed for calculation of the block position in the forthcoming time, $x_i^{t+\Delta t}$, is the block acceleration in the forthcoming time, $a_i^{t+\Delta t}$.

Equation (6.29) differs from that in [270], where instead of $\Delta t.v_i^t$, mistakenly $\Delta t.v_i^{t+\Delta t}$ is typed. The typo does not affect the posterior equations in [270]. The right form of the expression (i.e. the above form) has been substituted into Equation (6.14) in order to derive subsequent equations correctly in [270], e.g., in Equation number 19.

Equations (6.17) and (6.29) reveal that out of the three unknown variables of the forthcoming time state, namely, $x_i^{t+\Delta t}$, $v_i^{t+\Delta t}$ and $a_i^{t+\Delta t}$, the acceleration of the blocks in the forthcoming time is "the great unknown"; because, once the block acceleration is found, its position and velocity could be calculated by using Equations (6.17) and (6.29). Now the question is how to find the block acceleration in the forthcoming time, $a_i^{t+\Delta t}$? The answer lies in the discretized form of the equation of motion. By rewriting Equation (6.14) at $\tau = t + \Delta t$:

$$k_i = K_{ij}x_j^{t+\Delta t} + L_i x_d^{t+\Delta t} - m_i a_i^{t+\Delta t} \quad (6.30)$$

where $j = \{i-1,\ i,\ i+1\}$. Before substituting $x_j^{t+\Delta t}$ from Equation (6.29) into the above equation, the index i has to be renamed to j since the latter is the summation index. In [270], in Equation number 19, replacing i with j is forgotten. After the substitution, the above EOM becomes:

$$k_i = K_{ij}(x_j^t + \Delta t.v_j^t + \frac{(\Delta t)^2}{3}a_j^t + \frac{(\Delta t)^2}{6}a_j^{t+\Delta t}) + L_i x_d^{t+\Delta t} - m_i a_i^{t+\Delta t} \quad (6.31)$$

where $j = \{i-1,\ i,\ i+1\}$. The above equation is different from that which is given in [270] in two respects, namely, the driver position term and the inertial force sign. Finally, the EOM of the ith block is written in terms of the unknown accelerations. It is important to note that due to the summation index, the accelerations of the left and right neighbors in the forthcoming time are also present in the EOM of the ith block. This fact indicates the coupled nature of the motion of the blocks. On the other hand, when a neighbor of the ith block is stuck not only the stuck neighbor but also all of the blocks beyond the stuck neighbor cease to affect the motion of the ith block. In other words, the stuck blocks as separators of clusters of sliding blocks split the system of equations of motion. At every time step, each of the clusters would have its own system of equations and can be solved independent of the other clusters. Note that the exponent of the unknowns in the EOM is one. Then, sliding of the blocks of each of the clusters would be described by a linear coupled system of algebraic equations.

To rewrite the above system of equations of motion in the form of a linear system of algebraic equations, i.e., $\overrightarrow{b} = \mathbf{A}\overrightarrow{x}$, the terms that include the unknown, i.e. $a_i^{t+\Delta t}$, are kept on the right-hand side. The rest of the terms are moved to the left-hand side:

$$k_i - K_{ij}\left(x_j^t + \Delta t.v_j^t + \frac{(\Delta t)^2}{3}a_j^t\right) - L_i x_d^{t+\Delta t} = \frac{(\Delta t)^2}{6}K_{ij}a_j^{t+\Delta t} - m_i a_i^{t+\Delta t}$$

where $j = \{i-1,\ i,\ i+1\}$. The summation on index j can be performed to get rid of j and write the above in terms of index i only. The coupled nature of the equations would become clearer by: (i) Expanding the terms that contain the summation indices on the left-hand side of the EOM:

$$K_{ij}\left(x_j^t + \Delta t.v_j^t + \frac{(\Delta t)^2}{3}a_j^t\right) = K_{i,i-1}\left(x_{i-1}^t + \Delta t.v_{i-1}^t + \frac{(\Delta t)^2}{3}a_{i-1}^t\right) +$$

$$K_{i,i}\left(x_i^t + \Delta t.v_i^t + \frac{(\Delta t)^2}{3}a_i^t\right) +$$

$$K_{i,i+1}\left(x_{i+1}^t + \Delta t.v_{i+1}^t + \frac{(\Delta t)^2}{3}a_{i+1}^t\right)$$

and (ii) Expanding the right-hand side of the EOM:

$$\frac{(\Delta t)^2}{6} K_{ij} a_j^{t+\Delta t} - m_i a_i^{t+\Delta t} = \frac{(\Delta t)^2}{6} K_{i,i-1} a_{i-1}^{t+\Delta t} +$$

$$[\frac{(\Delta t)^2}{6} K_{i,i} - m_i] a_i^{t+\Delta t} +$$

$$\frac{(\Delta t)^2}{6} K_{i,i+1} a_{i+1}^{t+\Delta t}$$

The coupled system of linear algebraic equations of motion can be encapsulated in the indicial form as:

$$b_i = D_{ij} a_j^{t+\Delta t}, \qquad j = \{i-1,\ i,\ i+1\} \tag{6.32}$$

where:

$$b_i = k_i - K_{ij} \left(x_j^t + \Delta t . v_j^t + \frac{(\Delta t)^2}{3} a_j^t \right) - L_i x_d^{t+\Delta t} \tag{6.33}$$

or:

$$b_i = k_i - K_{i,i-1} \left(x_{i-1}^t + \Delta t . v_{i-1}^t + \frac{(\Delta t)^2}{3} a_{i-1}^t \right) + \tag{6.34}$$

$$K_{i,i} \left(x_i^t + \Delta t . v_i^t + \frac{(\Delta t)^2}{3} a_i^t \right) +$$

$$K_{i,i+1} \left(x_{i+1}^t + \Delta t . v_{i+1}^t + \frac{(\Delta t)^2}{3} a_{i+1}^t \right) - L_i x_d^{t+\Delta t}$$

where:

$$\begin{cases} K_{i,i-1} = C_{i-1} \\ K_{i,i} = -\left(C_{i-1} + L_i + C_i \right) \\ K_{i,i+1} = C_i \end{cases} \tag{6.35}$$

and:

$$\begin{cases} D_{i,i-1} = \frac{(\Delta t)^2}{6} K_{i,i-1} \\ D_{i,i} = \frac{(\Delta t)^2}{6} K_{i,i} - m_i \\ D_{i,i+1} = \frac{(\Delta t)^2}{6} K_{i,i+1} \end{cases} \tag{6.36}$$

In [270], left hand side of Equation (6.32) is named C_i, which can cause confusion because a coil spring stiffness is named identically. Here, the notation is then changed from C_i to b_i. Moreover, our derived expression for b_i is of the opposite to its counterpart in [270], i.e. C_i. In brief, $b_i = -C_i$. In addition, there is an inconsistency in the notation of the coefficient matrix in [270], since instead of capital D_{ij}, d_{ij} is used later (which has been used for block position in [270]). The above derivations show that Equations (6.14)-(6.32) are stated wrongly in [270]!

The FBC and PBC alter the form of EOM, Equation (6.32), for the leftmost and the rightmost blocks. Note that all of the terms that involve summation index in Equation (6.32) have originally entered due to substitution of Equation (6.4) into Equation (6.14). As stated in Subsections 6.2.1 and 6.2.2, for both the leftmost and the rightmost blocks and under both the FBC and PBC, the term $L_i x_d^\tau$ in Equation (6.4) remains unaffected in the expression of F_i^τ. Therefore, the only the term in Equation (6.4) that would be affected by the boundary conditions is $K_{ij} x_j^\tau$. In Equation (6.32), all of the terms that involve summation index are derived from $K_{ij} x_j^\tau$ and exist in both b_i and D_{ij}.

Assuming FBC means that:

(I) For $i = 1$, namely the leftmost block, no left neighbor exists. Then:

$$C_{i-1} = C_0 = 0$$

$$K_{i,i-1} = K_{1,0} = 0, \quad K_{i,i} = K_{1,1} = -\left(L_1 + C_1\right), \quad K_{i,i+1} = K_{1,2} = C_1$$

$$x_{i-1}^t = x_0^t, \quad v_{i-1}^t = v_0^t, \quad a_{i-1}^t = a_0^t$$

$$a_{i-1}^{t+\Delta t} = a_0^{t+\Delta t}$$

(II) For $i = M$, namely the rightmost block, no right neighbor exists. Then:

$$C_i = C_M = 0$$

$$K_{i,i-1} = K_{M,M-1} = C_{M-1}$$

$$K_{i,i} = K_{M,M} = -\left(C_{M-1} + L_M\right)$$

$$K_{i,i+1} = K_{M,M+1} = 0$$

$$x_{i+1}^t = x_{M+1}^t, \qquad v_{i+1}^t = v_{M+1}^t, \quad a_{i+1}^t = a_{M+1}^t$$

$$a_{i+1}^{t+\Delta t} = a_{M+1}^{t+\Delta t}$$

Assuming PBC means that:

(I) For $i = 1$, namely the leftmost block, the left neighbor is $i = M$, namely the rightmost block. Then:

$$C_{i-1} = C_0 = C_M$$

$$K_{i,i-1} = K_{1,0} = C_M$$

$$K_{i,i} = K_{1,1} = -\left(C_M + L_1 + C_1\right)$$

$$K_{i,i+1} = K_{1,2} = C_1$$

$$x_{i-1}^t = x_0^t = x_M^t, \qquad v_{i-1}^t = v_0^t = v_M^t, \quad a_{i-1}^t = a_0^t = a_M^t$$

$$a_{i-1}^{t+\Delta t} = a_0^{t+\Delta t} = a_M^{t+\Delta t}$$

(II) For $i = M$, namely the rightmost block, the right neighbor is $i = 1$, namely the leftmost block. Then:

$$C_i = C_M$$

$$K_{i,i-1} = K_{M,M-1} = C_{M-1}$$

$$K_{i,i} = K_{M,M} = -\left(C_{M-1} + L_M + C_M\right)$$

$$K_{i,i+1} = K_{M,M+1} = C_M$$

$$x_{i+1}^t = x_{M+1}^t = x_1^t, \qquad v_{i+1}^t = v_{M+1}^t = v_1^t, \quad a_{i+1}^t = a_{M+1}^t = a_1^t$$

$$a_{i+1}^{t+\Delta t} = a_{M+1}^{t+\Delta t} = a_1^{t+\Delta t}$$

Then, under the FBC:

(I) Equation (6.32) for the leftmost block $(i = 1)$ has to be written by using:

$$b_1 = k_1 - K_{1,1}\left(x_1^t + \Delta t.v_1^t + \frac{(\Delta t)^2}{3}a_1^t\right) + K_{1,2}\left(x_2^t + \Delta t.v_2^t + \frac{(\Delta t)^2}{3}a_2^t\right) - L_1 x_d^{t+\Delta t}$$

$$\Rightarrow b_1 = k_1 + (L_1 + C_1)\left(x_1^t + \Delta t.v_1^t + \frac{(\Delta t)^2}{3}a_1^t\right) - C_1\left(x_2^t + \Delta t.v_2^t + \frac{(\Delta t)^2}{3}a_2^t\right) - L_1 x_d^{t+\Delta t}$$

Note that $D_{1,0} = \frac{(\Delta t)^2}{6}K_{1,0} \Rightarrow D_{1,0} = 0$ and neither the column nor its corresponding acceleration exists.

$$D_{11} = \frac{(\Delta t)^2}{6}K_{1,1} - m_1 \;\Rightarrow\; D_{11} = -\left(L_1 + C_1\right)\frac{(\Delta t)^2}{6} - m_1$$

$$D_{1,2} = \frac{(\Delta t)^2}{6}K_{1,2} \Rightarrow\; D_{1,2} = \frac{(\Delta t)^2}{6}C_1$$

(II) (6.32) for the rightmost block $(i = M)$ block has to be written by using:

$$b_M = k_M - K_{M,M-1}\left(x_{M-1}^t + \Delta t.v_{M-1}^t + \frac{(\Delta t)^2}{3}a_{M-1}^t\right) + K_{M,M}\left(x_M^t + \Delta t.v_M^t + \frac{(\Delta t)^2}{3}a_M^t\right) - L_M x_d^{t+\Delta t}$$

$$\Rightarrow b_M = k_M - C_{M-1}\left(x_{M-1}^t + \Delta t.v_{M-1}^t + \frac{(\Delta t)^2}{3}a_{M-1}^t\right) + \left(C_{M-1} + L_M\right)\left(x_M^t + \Delta t.v_M^t + \frac{(\Delta t)^2}{3}a_M^t\right) - L_M x_d^{t+\Delta t}$$

$$D_{M,M-1} = \frac{(\Delta t)^2}{6}K_{M,M-1} \Rightarrow D_{M,M-1} = \frac{(\Delta t)^2}{6}C_{M-1}$$

$$D_{M,M} = \frac{(\Delta t)^2}{6} K_{M,M} - m_M = -\left(C_{M-1} + L_M\right) \frac{(\Delta t)^2}{6} - m_M$$

Note that $D_{M,M+1} = \frac{(\Delta t)^2}{6} K_{M,M+1} \Rightarrow D_{M,M+1} = 0$ and neither the column nor its corresponding acceleration exists.

On the other hand, under the PBC:

(I) Equation (6.32) for the leftmost block $(i = 1)$ has to be written by using:

$$b_1 = k_1 - K_{1,0}\left(x_0^t + \Delta t.v_0^t + \frac{(\Delta t)^2}{3} a_0^t\right) + K_{1,1}\left(x_1^t + \Delta t.v_1^t + \frac{(\Delta t)^2}{3} a_1^t\right) + K_{1,2}\left(x_2^t + \Delta t.v_2^t + \frac{(\Delta t)^2}{3} a_2^t\right) - L_1 x_d^{t+\Delta t}$$

$$\Rightarrow b_1 = k_1 - C_M\left(x_M^t + \Delta t.v_M^t + \frac{(\Delta t)^2}{3} a_M^t\right) - (C_M + L_1 + C_1)\left(x_1^t + \Delta t.v_1^t + \frac{(\Delta t)^2}{3} a_1^t\right) + C_1\left(x_2^t + \Delta t.v_2^t + \frac{(\Delta t)^2}{3} a_2^t\right) - L_1 x_d^{t+\Delta t}$$

Note that $D_{1,0} = \frac{(\Delta t)^2}{6} K_{1,0} \Rightarrow D_{1,0} = \frac{(\Delta t)^2}{6} C_M$ and its corresponding column is the Mth column since $D_{1,0} \equiv D_{1,M}$.

$$D_{11} = \frac{(\Delta t)^2}{6} K_{1,1} - m_1 \Rightarrow D_{1,1} = -\frac{(\Delta t)^2}{6}\left(C_M + L_1 + C_1\right) - m_1$$

$$D_{1,2} = \frac{(\Delta t)^2}{6} K_{1,2} = \frac{(\Delta t)^2}{6} C_1$$

(II) Equation (6.32) for the rightmost block $(i = M)$ has to be written by using:

$$b_M = k_M - K_{M,M-1}\left(x_{M-1}^t + \Delta t.v_{M-1}^t + \frac{(\Delta t)^2}{3} a_{M-1}^t\right) +$$

$$K_{M,M}\left(x_M^t+\Delta t.v_M^t+\frac{(\Delta t)^2}{3}a_M^t\right)+$$

$$K_{M,M+1}\left(x_{M+1}^t+\Delta t.v_{M+1}^t+\frac{(\Delta t)^2}{3}a_{M+1}^t\right)-L_M x_d^{t+\Delta t}$$

$$\Rightarrow b_M=k_M-C_{M-1}\left(x_{M-1}^t+\Delta t.v_{M-1}^t+\frac{(\Delta t)^2}{3}a_{M-1}^t\right)-$$

$$\left(C_{M-1}+L_M+C_M\right)\left(x_M^t+\Delta t.v_M^t+\frac{(\Delta t)^2}{3}a_M^t\right)+$$

$$C_M\left(x_1^t+\Delta t.v_1^t+\frac{(\Delta t)^2}{3}a_1^t\right)-L_M x_d^{t+\Delta t}$$

$$D_{M,M-1}=\frac{(\Delta t)^2}{6}K_{M,M-1}\Rightarrow D_{M,M-1}=\frac{(\Delta t)^2}{6}C_{M-1}$$

$$D_{M,M}=\frac{(\Delta t)^2}{6}K_{M,M}-m_M=-\left(C_{M-1}+L_M+C_M\right)\frac{(\Delta t)^2}{6}-m_M$$

Note that $D_{M,M+1}=\frac{(\Delta t)^2}{6}K_{M,M+1}\Rightarrow D_{M,M+1}=\frac{(\Delta t)^2}{6}C_M$ and its corresponding column is the 1st column since $D_{M,M+1}\equiv D_{M,1}$.

The EOM of the blocks between the leftmost and the rightmost blocks can be directly obtained by Equation (6.32). However, the EOM of the leftmost and rightmost blocks are affected by the boundary conditions and have to be dealt with in the specific way that is expressed above.

6.2.4 Algorithm

In this section, the algorithm proposed in [270] is adapted to calculate variation of the driver traction and friction with time. The adapted algorithm is presented by a pseudocode and its corresponding flowchart in Subsections 6.2.5 and 6.2.6 respectively. The algorithm includes four iterative loops; the outermost loop increments time and the three inner loops perform operations on the blocks.

The immediate goal of the time increment loop is to compute the unknown values of the state of the blocks in the forthcoming time point, i.e., $(x_i^{t+\Delta t},\ v_i^{t+\Delta t},\ a_i^{t+\Delta t})$ by using the formerly known state of the blocks in the previous time point, i.e., $(x_i^t,\ v_i^t,\ a_i^t)$. However, the procedure is not straightforward. The blocks have to be treated by considering their sliding/stuck status. Moreover, the status of the block may switch within the current time step. In order to assess the status, the force and velocity criteria have to be applied.

The first inner loop is called the force criterion loop. The loop applies the "force criterion" to the stuck blocks in order to detect the stuck blocks that would start sliding. The force criterion loop uses Equation (6.3) to calculate the resultant spring-exerted force on each of the stuck blocks; if the static friction threshold exceeded, the block status is switched to "sliding", and otherwise the status would remain "stuck". The state of the stuck blocks is assigned as $(x_i^{t+\Delta t} = x_i^t,\ v_i^{t+\Delta t} = 0,\ a_i^{t+\Delta t} = 0)$. The previously sliding blocks are assumed "sliding" for now. After the end of the force criterion loop, Equation (6.32) is constructed for the sliding blocks only. The system(s) of EOM is solved for the upcoming time point accelerations. By using Equations (6.17) and (6.17) the state of the sliding blocks is determined subsequently.

The second inner loop is called the velocity criterion loop. The loop applies the "velocity criterion" to the sliding blocks in order to spot the sliding blocks that would stop moving. The velocity criterion monitors the sign of the velocity is monitored in the ends of the time step. A change in the sign means that the block becomes stuck within the time step. The state of the stuck blocks is assigned as $(x_i^{t+\Delta t} = x_i^t,\ v_i^{t+\Delta t} = 0,\ a_i^{t+\Delta t} = 0)$. If the sign is preserved the block would continue sliding. In Section 6.2.7, an analytical expression for the stopping time and the position of the stopping block is derived. In Section 6.2.8, it is shown that considering a time-dependent static COF is possible.

The third inner loop is called the force calculation loop. The loop calculates the resultant spring-exerted force values on all of the blocks by using the updated blocks positions obtained within the current time step. After the end the force calculation loop, the total traction and friction forces at the forthcoming time point are calculated. The outermost loop either increments time or terminates the algorithm.

6.2.5 Pseudocode

In this subsection, a pseudocode of the algorithm that eventually outputs the total traction and friction forces is described in 16 parts. The subparts are executed only if the condition expressed at the beginning of the part is true.

1. Specify the boundary conditions: FBC/PBC.
2. For all of the blocks, assign the initial block position values, $x_i^{(1)}$, such that no block exceeds f_{th_i}. Considering the specified boundary conditions, use (i) Random (ii) Linear and (iii) Hyperbolic tangent [251] initial positions. Set $s_i^{(1)} = 0$.
3. Calculate the time vector, t , that discretizes x_d^{τ} to equal pieces of user-specified length: Δx_d.
4. Set $n = 1$.
5. Calculate $F_i^{(n)}$ by using Equation (6.3) and $T^{(n)} = FR^{(n)} = \sum_{i=1}^{M} F_i^{(n)}$.
6. Increment n by one (The time increment loop starts).
7. Advance the driver to $x_d^{(n)}$.
8. For the blocks for which $s_i^{(n-1)} = 1$, put $s_i^{(n)} = 1$. For the blocks for which $s_i^{(n-1)} = 0$, (The force criterion loop):

   8-1. Calculate the spring exerted force by using Equation (6.3):

$$F_i^{(n)} = \begin{bmatrix} C_{i-1} & -(C_{i-1} + L_i + C_i) & C_i \end{bmatrix} \begin{bmatrix} x_{i-1}^{(n-1)} \\ x_i^{(n-1)} \\ x_{i+1}^{(n-1)} \end{bmatrix} + L_i x_d^{(n)}$$

   Note that: (1) the block position values, $x_j^{(n)}$, are still unknown. Then, this is the precalculation of the resultant spring-exerted force values. (2) The resultant spring-exerted force values for the 1st and the Mth blocks have to be calculated by considering the boundary conditions (FBC/PBC). The specific equations are given in Subsections 6.2.1 and 6.2.2.

8-2. Calculate the current time step block overshoot due to the driver motion for the blocks for which $f_{th_i}^{(n)} < F_i^{(n)}$:

$$\gamma_i^{(n)} = \frac{F_i^{(n)} - f_{th_i}^{(n)}}{f_{th_i}^{(n)}}$$

Note that The measure superscripts belong to the current "time step". However, for the sake of convenience the superscript of the overshoot measure is assigned "n" instead of "n-1".

8-3. Apply the force criterion:

IF $f_{th_i}^{(n)} < F_i^{(n)}$

set $s_i^{(n)} = 1$ (sliding)

ELSE

set $s_i^{(n)} = 0$ (stuck)

set $x_i^{(n)} = x_i^{(n-1)}$ and $v_i^{(n)} = a_i^{(n)} = 0$

END

It is assumed that the blocks that are triggered by the driver within the current time step i.e., the driver-overshot blocks, start to move at t_{n-1}

9. Calculate the average of total overshoot due to the driver motion. The number of the driver-overshot blocks is represented by $c_1^{(n)}$:

$$\Gamma^{(n)} = \frac{1}{c_1^{(n)}} \sum_{j=1}^{c_1^{(n)}} \gamma_j^{(n)}$$

10. For the blocks for which $s_i^{(n)} = 1$ (includes those for which $s_i^{(n-1)} = 1$ since part 8):

10-1. Construct the system(s) of EOM's based on Equation (6.32):

$b_i = D_{ij} a_j^{(n)}$ $j = i-1,\ i,\ i+1$

where:

$$b_i = k_i - K_{ij}\left(x_j^{(n-1)} + \Delta t.v_j^{(n-1)} + \frac{(\Delta t)^2}{3} a_j^{(n-1)}\right) - L_i x_d^{(n)}$$

Note that: (1) For each block only the immediate sliding right and left neighbors take part in Equation (6.32). Thus, instead of a single system of equations for all of the sliding blocks, a number of distinct systems of equations (more than 1 and less than or equal to $M/2+1$) that belong to different sets (clusters) of consecutive sliding blocks may be constructed. (2) In order to apply the boundary conditions (FBC/PBC), the EOM of the 1st and the Mth blocks would have specific expressions for b_1, b_M, $D_{1,j}$ and $D_{M,j}$ as shown at the end of Section 6.2.3.

10-2. Solve the system(s) of EOM's for $a_i^{(n)}$.

10-3. Use Equations (6.17) and (6.29) to find $v_i^{(n)}$ and $x_i^{(n)}$:

$$v_i^{(n)} = v_i^{(n-1)} + \frac{1}{2}\Delta t\left(a_i^{(n-1)} + a_i^{(n)}\right)$$

$$x_i^{(n)} = x_i^{(n-1)} + \Delta t.v_i^{(n-1)} + \frac{(\Delta t)^2}{3}a_i^{(n-1)} + \frac{(\Delta t)^2}{6}a_i^{(n)}$$

11. Apply the velocity criterion to the blocks for which $s_i^{(n)} = 1$: (The velocity criterion loop):

IF $0 \leq v_i^{(n-1)}v_i^{(n)}$ (slides)

save $x_i^{(n)},\ v_i^{(n)},\ a_i^{(n)}$

ELSE (sticks)

set $s_i^{(n)} = 0$

set $x_i^{(n)} = x_i^{\tau_{stop_i}}$ and save $v_i^{(n)} = a_i^{(n)} = 0$

END

It is assumed that a block that stops within the current time step ceases to move at $t_{n-1} < \tau_{stop_i} < t_n$ (instead of stopping at t_{n-1} or t_n) when its position is $x_i^{\tau_{stop_i}}$. The block stopping time and position can be calculated exactly by the formulas derived in Section 6.2.7.

12. For all of the blocks calculate the spring exerted force by using Equation (6.3): (The force calculation loop)

$$F_i^{(n)} = \begin{bmatrix} C_{i-1} & -(C_{i-1} + L_i + C_i) & C_i \end{bmatrix} \begin{bmatrix} x_{i-1}^{(n)} \\ x_i^{(n)} \\ x_{i+1}^{(n)} \end{bmatrix} + L_i x_d^{(n)}$$

Note that: (1) The block position values, $x_j^{(n)}$, are updated. This is the final calculation of the resultant spring-exerted force values, (2) The resultant spring-exerted force values for the 1st and the Mth blocks have to be calculated by considering the boundary conditions (FBC/PBC). The specific equations are given in Subsections 6.2.1 and 6.2.2.

12-1. For the blocks for which $s_i^{(n)} = 0$ and $f_{th_i}^{(n)} < F_i^{(n)}$:

12-1-1. Calculate the block overshoot due to the neighbor motion:

$$\lambda_i^{(n)} = \frac{F_i^{(n)} - f_{th_i}^{(n)}}{f_{th_i}^{(n)}}$$

12-1-2. Set $s_i^{(n)} = 1$.

Note that the overshoot calculated in 12-1-1 is due to the neighbor slippages and can be reduced by time refinement. Switching the status in 12-1-2 improves calculation of the friction force in part 15 by preventing the overshot blocks to contribute as stuck blocks.

13. Calculate the average of total overshoot due to the neighbor motion. The number of the neighbor-overshot blocks is $c_2^{(n)}$:

$$\Lambda^{(n)} = \frac{1}{c_2^{(n)}} \sum_{j=1}^{c_2^{(n)}} \gamma_j^{(n)}$$

14. Calculate the overall driver traction force needed at t_n:

$$T^{(n)} = \sum_{i=1}^{M} F_i^{(n)}$$

15. Calculate the overall friction force at t_n:

$$FR^{(n)} = \sum_{i=1}^{M} [k_i s_i^{(n)} + F_i^{(n)}(1 - s_i^{(n)})]$$

16. If t_n is equal to the last component of the time vector, t_{last}, end the code execution; otherwise, go back to part 6, i.e., continue the execution of the time increment loop.

6.2.6 Flowchart

In this subsection, the grand scheme of the pseudocode (described in Subsection 6.2.5) is discussed by providing the main flowchart of the whole algorithm. The main flowchart uses three distinct subroutines whose flowcharts are also presented and explained in order.

The main flowchart (Figure 6.10) starts with accepting user-specified input which includes: the number and the mass of the blocks, the leaf/coil spring stiffness values, static/dynamic friction COF values, the free/periodic boundary conditions, the random/linear/hyperbolic tangent [251] initial block positions (such that the frictional threshold is not violated), the position of the driver as a function of time, the inverse function of position of the driver (i.e., time as a function of the driver position), the driver position increment, Δx_d, and the final time. The time is discretized to a vector $\overrightarrow{t}$ by using the driver position inverse function such that in each time step the driver traverse the constant length that is specified by the user, Δx_d. Finally, the status of all of the blocks is initialized as "stuck" at $\overrightarrow{t}(1) = 0$, i.e., $s_i^{(1)} = 0$ and the spring force resultant is calculated by using Equation (6.3). Then, the traction and friction forces (which are equal since all of the blocks are stuck) are calculated.

As shown in Figure 6.10, the main flowchart has four iterative for-loops. The outermost loop is named the time-increment loop starts with $n = n + 1$ and includes three inner loops: the force criterion loop, the velocity criterion loop and the force calculation loop. The inner loops are illustrated by the "predefined process" symbols in Figure 6.10. The corresponding flowcharts of the inner loop subroutines are depicted separately in Figures 6.11-6.13.

In Figure 6.10, the time-increment loop starts with increasing the time-step counter by one. The previous time point, t_{n-1}, and forthcoming time point, t_n, are the starting and ending of the current, $(n-1)^{th}$, time step. The driver is placed at its correspond-

ing position at the forthcoming time point, i.e. at $x_d(t_n)$. Then, the counter of the driver-overshot stuck blocks during the current time step, $c_1^{(n)}$, is initialized as zero. Now the force criterion loop has to be executed.

The force criterion loop is shown in Figure 6.11. First of all, the blocks with the sliding status at the previous time point are temporarily assumed to be sliding during the current time-step. Afterwards, the resultant spring-exerted force values on the blocks with the stuck status at the end of previous time step are calculated. In this stage, the block positions at the previous time point are to be used since the block positions at the forthcoming time point are yet to be obtained. Then, the resultant spring-exerted force is indeed "precalculated" here. The final calculation would be made later in the force calculation loop. Now, the force criterion is applied to determine whether or not any of the previously stuck blocks start sliding due to the updated driver position in the current time-step. If the threshold is violated, the block status is identified as "sliding", i.e., $s_i^{(n)} = 1$. The number of such blocks is counted by $c_1^{(n)}$ and for each the driver-exerted overshoot, $\gamma_i^{(n)}$, at the current time step is calculated by:

$$\gamma_i^{(n)} = \frac{F_i^{(n)} - f_{th_i}^{(n)}}{f_{th_i}^{(n)}} \tag{6.37}$$

Otherwise, if the force does not exceed the threshold, the block status is identified as "stuck", i.e., $s_i^{(n)} = 0$, and the block position in the forthcoming time point is equated to the previous block position. For such a block velocity and acceleration are equated to zero. The force criterion loop finishes here. The main flowchart in Figure 6.10 continues the time-increment loop as described below.

After the end of the force criterion loop, the mean value of driver-exerted overshoots is calculated that could be used as a measure to recognize the need for time-step size reduction:

$$\Gamma^{(n)} = \frac{1}{c_1^{(n)}} \sum_{j=1}^{c_1^{(n)}} \gamma_j^{(n)} \tag{6.38}$$

Now that the sliding blocks are identified, the system of equations of motion that was derived in Equation (6.32) can be constructed. The acceleration of the ith sliding

block is coupled with the accelerations of its immediate right and left neighbors only. If either of the neighbors is stuck, their corresponding acceleration would be zero. Therefore, the acceleration of any of the blocks beyond the stuck neighbor would not affect that of the ith block. Consequently, any cluster of the successive neighbor sliding blocks can construct an independent system of equations of motion. By solving these systems of equations, accelerations of the blocks are computed and then velocity and position values can be calculated by using equations (6.17) and (6.29). Now, according to Figure 6.10 the velocity criterion loop has to be executed.

The velocity criterion loop is shown in Figure 6.12. Only the blocks whose status is identified as "sliding" in the force criterion loop are dealt with in the velocity criterion loop. If the sign of the block velocity is preserved, it means that the block continues sliding. Otherwise, the block becomes stuck. The blocks that have *just* switched to the sliding status due to the driver advance (in the force calculation loop of *the present time step*) are excluded from consideration. Because for such blocks always $v_i^{(n-1)} = 0$, then even if $v_i^{(n)} < 0$ the product would yield zero. The required minimum time step size to eliminate the possibility of $v_i^{(n)} < 0$ immediately after $v_i^{(n-1)} = 0$ is discussed in Section 6.2.9.

There is an analytical way to calculate the exact position, $x_i^{\tau_{stop_i}}$, at which such a block would stick. The derivations are given in Section 6.2.7. The velocity criterion loop finishes here. The counter of the neighbor-overshot stuck blocks during the current time step, $c_2^{(n)}$, is initialized as zero. Now, according to Figure 6.10 the force calculation loop has to be executed.

The last inner loop is named the force calculation loop and is shown in Figure 6.13. The loop recalculates the resultant spring-exerted force values on all of the blocks by considering the updated block positions that are computed in the current time step. The neighbor-exerted overshoot, $\lambda_i^{(n)}$, on the stuck blocks is defined and calculated by:

$$\lambda_i^{(n)} = \frac{F_i^{(n)} - f_{th_i}^{(n)}}{f_{th_i}^{(n)}} \tag{6.39}$$

Although the definition of the $\lambda_i^{(n)}$ is the same as $\gamma_i^{(n)}$, the values are calculated at

different stages of the computations in the current time-step. The number of the neighbor-overshot (stuck) blocks is counted by $c_2^{(n)}$. Finally, since nothing more can be done for the neighbor-overshot blocks their status is changed from stuck to sliding in order to modify their contributions to the friction force. The force calculation loop finishes here.

In Figure 6.10, the time-increment loop continues with calculating the mean neighbor-exerted overshoot value in the current time step:

$$\Lambda^{(n)} = \sum_{j=1}^{c_2^{(n)}} \frac{\lambda_j^{(n)}}{c_2^{(n)}} \tag{6.40}$$

This, after $\Gamma^{(n)}$, is the second measure that helps deciding on the time-step size. Effectiveness of reducing the time step size on reducing "high" overshoot measures can be studied by plotting the measures against time. The overshoot measures can also be used to see if "time step split" should be done.

At the end of the time-step, the overall traction and friction forces are calculated by the formulas:

$$T^{(n)} = \sum_{i=1}^{M} F_i^{(n)} \tag{6.41}$$

and:

$$FR^{(n)} = \sum_{i=1}^{M} [k_i s_i^{(n)} + F_i^{(n)}(1 - s_i^{(n)})] \tag{6.42}$$

In the overall traction force formula, the coil spring contributions eliminate each other and the rest is the sum of the leaf spring forces that is equal to the force required to be applied to the driver. In the friction force formula, the block status values are utilized to take into account the sliding blocks contribution (that is dynamic/kinetic friction) and the stuck block contribution (that is the resultant spring-exerted force) separately. The latter is rendered via $1 - s_i^{(n)}$ that switches the zero components in $s_i^{(n)}$ to ones and ones in $s_i^{(n)}$ to zeros, i.e., in $1 - s_i^{(n)}$ the stuck blocks are represented by ones

and the sliding blocks by zeros. Then, the resultant spring-exerted force of the sliding blocks is prevented from contributing to the overall friction force while their kinetic friction contribution is taken into account.

At this point, the time-increment loop has to decide either to execute itself anew or to terminate the algorithm execution. If the forthcoming time point is not the same as the last component of the time vector the loop continues, otherwise the execution is terminated.

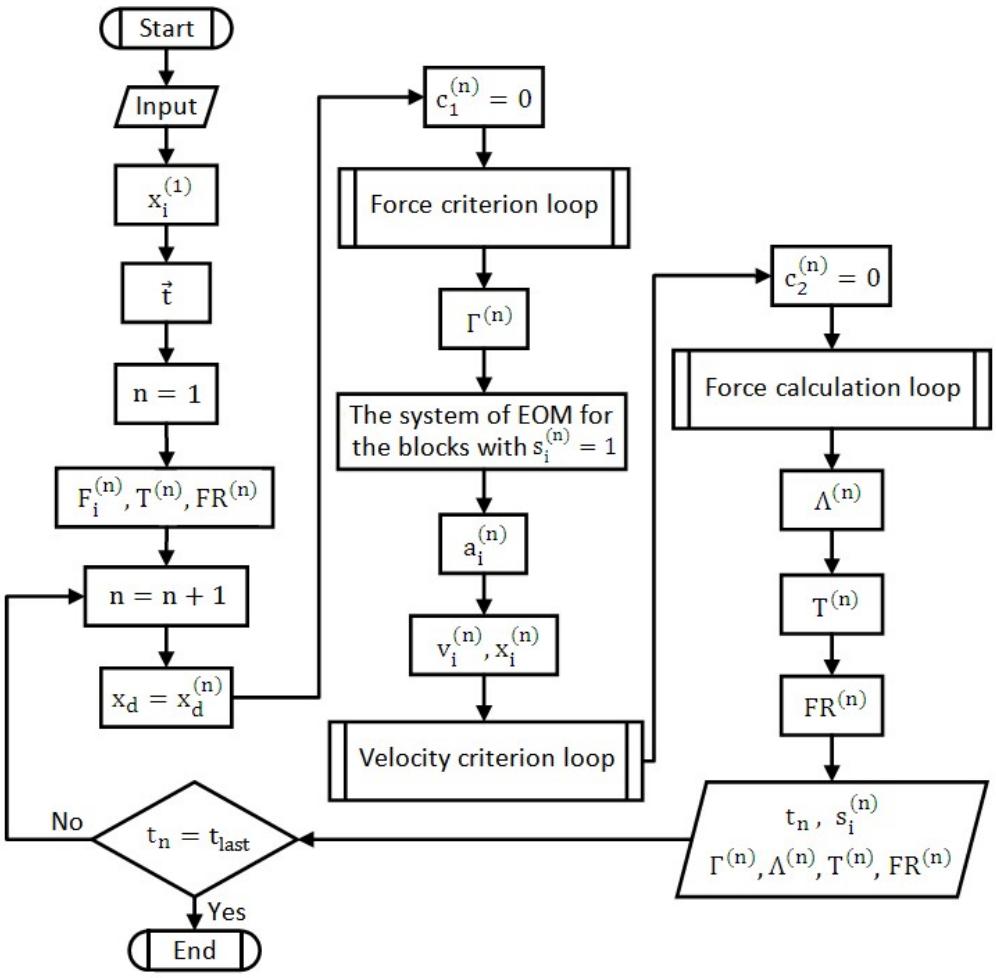

Figure 6.10: The main flowchart. The outermost loop is called the time-increment loop. The three inner loops are drawn as predefined processes. The corresponding flowcharts of the inner loops are shown in figures 6.11-6.13

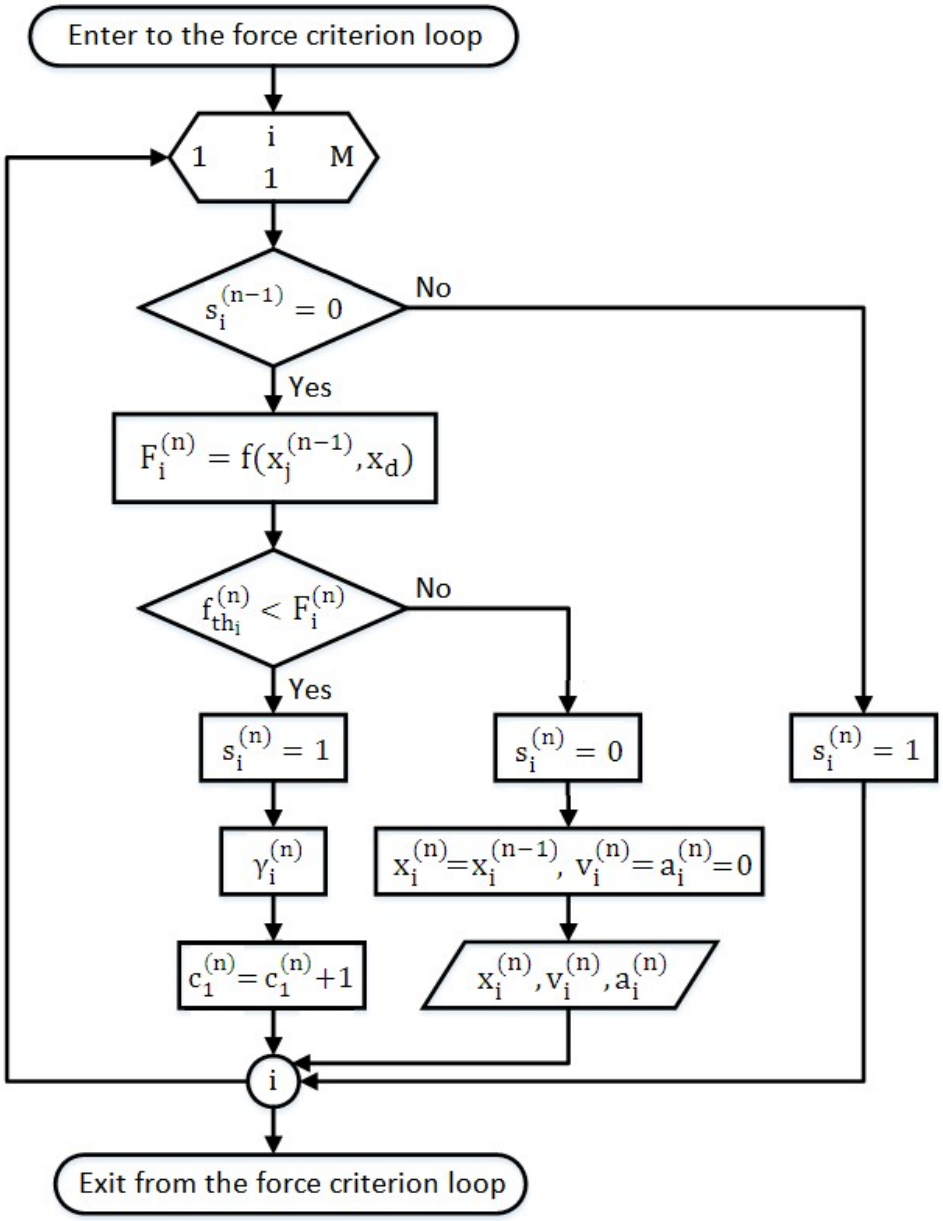

Figure 6.11: The force criterion loop makes temporary decisions about the status of the blocks.

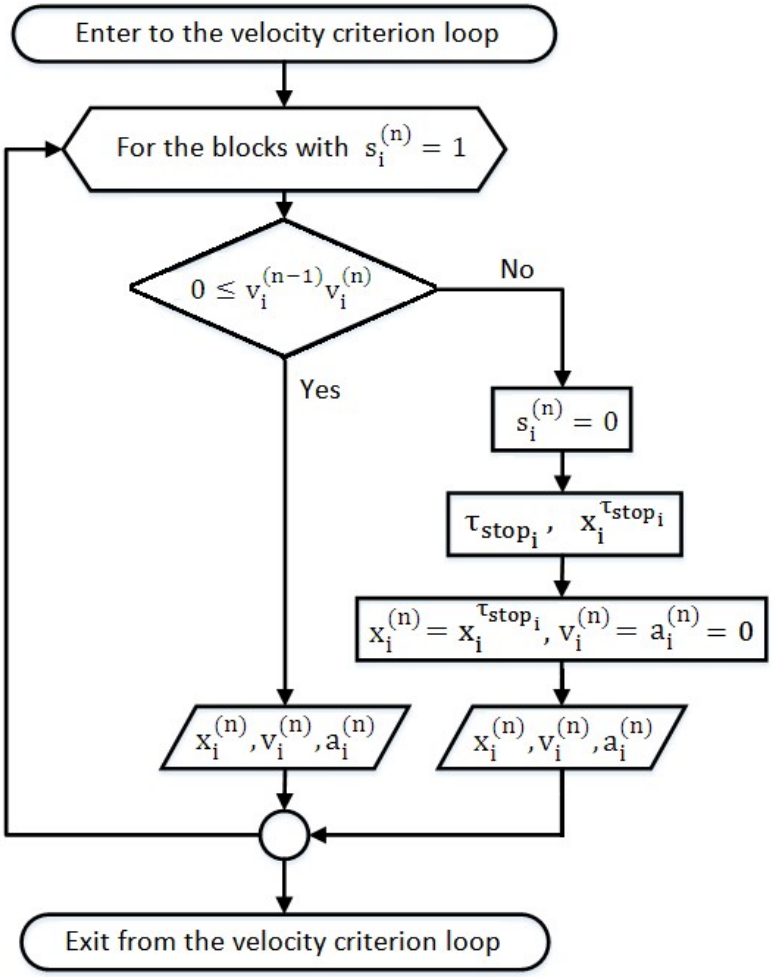

Figure 6.12: The velocity criterion loop deals with the sliding blocks only and determines if they stop or continue sliding.

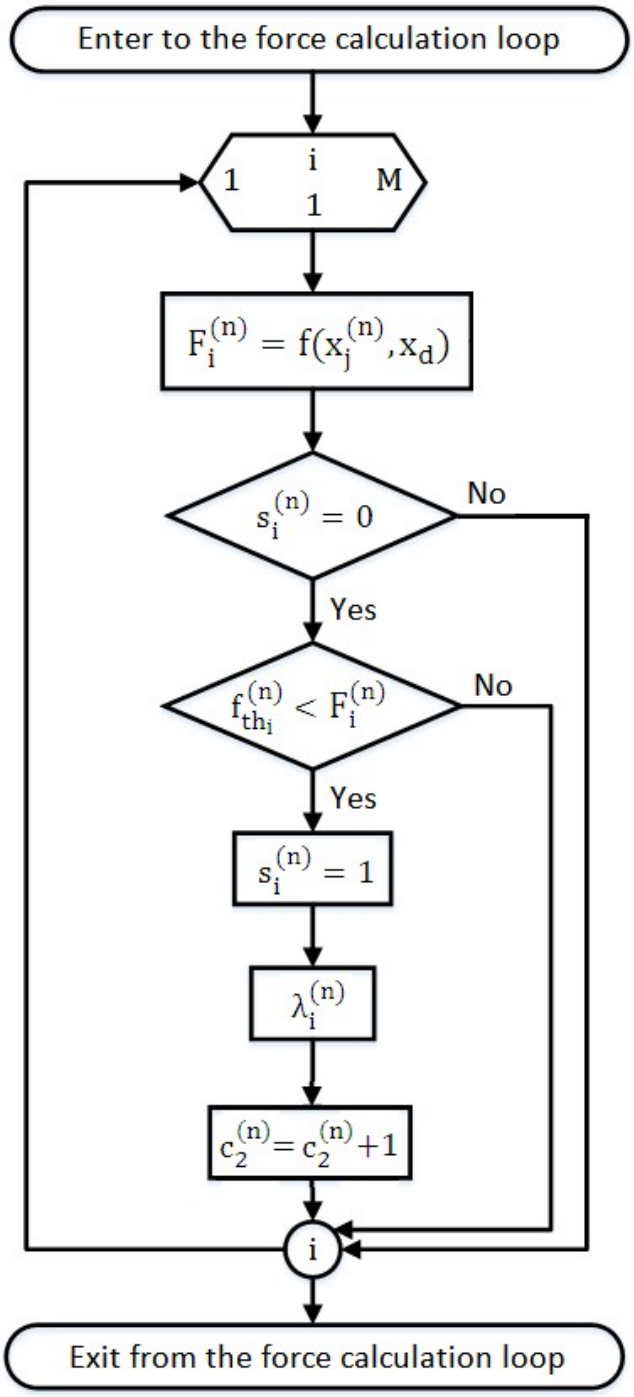

Figure 6.13: The force calculation loop calculates the final spring-exerted force values according the updated block positions. Moreover, the loop records the force overshoot due to neighbor slippages.

6.2.7 Block's stopping time and stopping position

The velocity criterion recognizes if a sliding block stop between the previous time point, τ_1, and the forthcoming time point, τ_2. However, the criterion does not determine exactly when the block stops. Two possible choices are proposed in [270] for the block stopping time are either of the two ends of the current time step and therefore, both cause error.

Alternatively, an analytical expression for the exact stop time, τ_{stop_i}, can be obtained by equating the quadratic expression that was found in Section 6.2.3 for v_i^{τ} with zero:

$$v_i^{\tau_{stop_i}} = \frac{m}{2}\tau_{stop_i}^2 + c\tau_{stop_i} + c_0 = 0 \tag{6.43}$$

Since (1) the block stopping would always happen after the previous time point, i.e. $\tau_1 < \tau_{stop_i}$ and (2) the quadratic velocity function has to be strictly decreasing within the interval $[\tau_1, \tau_2]$, it can be visually seen that the larger root of the second order equation has to be selected:

$$\tau_{stop_i} = \frac{-c + \sqrt{c^2 - 2mc_0}}{m} \tag{6.44}$$

where:

$$m = \frac{a_i^{\tau_2} - a_i^{\tau_1}}{\Delta t} \tag{6.45}$$

$$c = a_i^{\tau_1} - \frac{a_i^{\tau_2} - a_i^{\tau_1}}{\Delta t}\tau_1 \tag{6.46}$$

$$c_0 = v_i^{\tau_1} - a_i^{\tau_1}\tau_1 + \frac{a_i^{\tau_2} - a_i^{\tau_1}}{2\Delta t}\tau_1^2 \tag{6.47}$$

On the other hand, in order to calculate the exact stopping position, the block position function has to be derived by integrating the block velocity function:

$$x_i^\tau = \int v_i^\tau d\tau = \int \left(\frac{m}{2}\tau^2 + c\tau + c_0\right) d\tau = \frac{m}{6}\tau^3 + \frac{c}{2}\tau^2 + c_0\tau + c_1 \tag{6.48}$$

In order to find the integration constant, c_1, the known point $(\tau_1,\ x_i^{\tau_1})$ is substituted:

$$c_1 = x_i^{\tau_1} - \frac{m}{6}\tau_1^3 - \frac{c}{2}\tau_1^2 - c_0\tau_1 \tag{6.49}$$

Substituting back the obtained expression into the block position function:

$$x_i^\tau = \frac{m}{6}(\tau^3 - \tau_1^3) + \frac{c}{2}(\tau^2 - \tau_1^2) + c_0(\tau - \tau_1) + x_i^{\tau_1} \tag{6.50}$$

Therefore:

$$x_i^{\tau_{stop_i}} = \frac{m}{6}(\tau_{stop_i}^3 - \tau_1^3) + \frac{c}{2}(\tau_{stop_i}^2 - \tau_1^2) + c_0(\tau_{stop_i} - \tau_1) + x_i^{\tau_1} \tag{6.51}$$

The above formulae has to be used to calculate the stop position of a sliding block instead of assigning $x_i^{\tau_1}$ or $x_i^{\tau_2}$. The procedure can reduce the error that would be accumulated otherwise.

6.2.8 Time-dependent static friction COF

The present algorithm can be slightly modified to incorporate a sticking (or contact) time-dependent static friction threshold (also called aging law):

$$\mu_s = \mu_0 + A.\log_{10}\left(1 + Bt_{_{stick.}}\right) \tag{6.52}$$

The values of the constants μ_0 and A are given in [298]. The constant B is claimed to be approximately equal to one [298]. However, the above relation is proposed in [31] as an alternative to equation number 1 in [270], that is:

$$\mu_s = \mu_0 + A.\log_{10}\left(t_{_{stick.}}\right) \tag{6.53}$$

Note that the above relation (which is also used in [299]) produces negative values when $t_{stick.}$ is smaller than one second [31]! However, in Equation 6.52, the addition of one prevents calculation of the negative values, whatever the time is.

For the purpose of applying the modified empirical law that has been proposed in [31] into the algorithm, the sticking time, i.e. the amount of time elapsed since the block has ceased moving or has been stationary must be recorded. As explained in Section 6.2.7, the exact stop time, τ_{stop_i}, was being previously calculated in the velocity criterion loop of the present algorithm (Figure 6.12).

The first supplement to the present algorithm is to initialize the τ_{stop_i} for all of the blocks as an all-zero vector. The second supplement is to calculate and update the values of the frictional threshold in the force criterion loop and force calculation loop by using the last available stop time values:

$$f_{th_i}^{\tau_2} = N_i \mu_s^{\tau_2} = N_i[\mu_0 + A.\log_{10}(1 + B(\tau_2 - \tau_{stop_i}))] \tag{6.54}$$

where τ_2 represents the forthcoming time point. Different values of the frictional threshold in the force criterion loop and the force calculation loop would only happen for the blocks that stop; the discrepancy would just happen in the time-step that stopping occurs. However, generally the loop decisions and the overshoot measures γ_i^n and λ_i^n calculations would be evaluated by using the same threshold values within a time-step. All in all, the within-time-step discrepancy of the frictional threshold values would not obstruct implementation of the scheme that is proposed in this section.

6.2.9 A time step size criterion

One of the concerns any numerical discretization scheme is the numerical stability. Since the proposed approach is a "stepwise forward integration" method, the results are expected to be sensitive to the time step size. The question is whether the time step size is small enough for the results *to converge*? Thus, the question can indeed be answered by studying convergence of the results. Does the forces (friction and traction) converge to (or form) certain functions of time by refining the time step?

Or does the response diverge as the time step size is decreased? In the case of divergence the algorithm can be manipulated to catch the exact times at which the block slippages are triggered or stopped. Then, the found values would be inserted into the time vector. The procedure may slow down the execution and can require parallel computing. Measures like driver-exerted overshoot or neighbor-exerted overshoot can also be used as an auxiliary remedy for time-step-specific splitting.

In [270], the time step size is selected to be "one-fifth the time required to propagate a seismic disturbance between adjacent elements". No further explanation is provided. Then, the question has to be asked anew: what is the minimum required time step size? It seems reasonable to first look for the minimum possible block slippage duration, $t_{sliding}^{min.}$. The obtained value should then be divided to further to find the proper time step size that leads to the response convergence. Such a time step size would eliminate the possibility of $v_i^{(n)} < 0$ just after $v_i^{(n-1)} = 0$. Now, the question is which conditions minimize the block sliding duration?

Consider the three blocks shown in Figure 6.7-(b). Assume that either of the left and right neighbors or the diver (or any combination of them) has caused the ith block to start moving. For the block to stick again as soon as possible, the most conservative condition is to assume frozen neighbors and frozen driver. This assumption prevents the neighbors and the driver from helping the ith block to continue sliding. Note that neither of the neighbor nor the driver can move backward. The equation of motion for the block with fixed (frozen) neighbors and driver can be solved solved to find a closed-form expression:

$$t_{sliding}^{min.} = \pi \sqrt{\frac{m}{C_{i-1} + L_i + C_i}} \tag{6.55}$$

Interestingly, the minimum block slippage duration depends only on the total spring stiffness and the mass of the block. In other words, the result is independent of the neighbor or driver positions, the normal force applied on the block or the frictional properties.

By assuming the same coil spring stiffness values and changing the notation:

$$t_{sliding}^{min.} = \pi \sqrt{\frac{m}{k_L + 2k_C}} \tag{6.56}$$

By rewriting the mass and considering the formulas for the stiffness values that are assumed to be:

$$m = \rho LHW, \qquad k_C = E\frac{HW}{L}, \qquad k_L = G\frac{LW}{H}$$

where ρ is the density and L, H, and W are the length, height and width of the lumped cuboid; and E and G represent Young and shear moduli respectively. Appendix H shows that the expressed spring stiffness are reasonable when compared to a simple finite element model of a BK model unit, at least for the plane stress assumption. After substituting:

$$t_{sliding}^{min.} = \pi LH \sqrt{\frac{\rho}{GL^2 + 2EH^2}} \tag{6.57}$$

By limiting ourselves to $L = H = a$, i.e. to cubes only:

$$t_{sliding}^{min.} = \pi a \sqrt{\frac{\rho}{G + 2E}} \tag{6.58}$$

An interface of a specific length, L_0, can be discretized by arbitrary number of cubes. The cube dimension is $a = L_0/M$. Therefore, the time step size can be set according to the criterion:

$$\Delta t \ll \frac{\pi L_0}{M} \sqrt{\frac{\rho}{G + 2E}} \tag{6.59}$$

Therefore, the minimum block slippage duration depends on the mechanical properties of the elastic slider, length of the interface and the number of cubes (discretization). The smaller the cube dimensions the smaller would be the maximum allowable time step size. For example, for Westerly granite: $E = 70\ GPa,\ G = 28\ GPa$ and $\rho = 2,691 kg/m^3$:

$$\Delta t \ll 0.4 * \frac{L_0}{M} \quad (milliseconds) \tag{6.60}$$

Then, by assuming $L_0 = 1000\ m$ and 1000 block, i.e. $L_0/M = L = 1$, which means discretization length in x-direction, L, is $1\ m$, the time step size has to be smaller than $0.4\ ms$. The time step size should be made finer by further divisions. This finer value has to make the Courant number, $C_p \Delta t/L$, smaller than one so that the pressure wave speed cannot skip a block.

6.3 Results

The results of the algorithm for the free boundary condition (FBC) case in which the leftmost has no left hand side neighbor and the rightmost block has no right hand side block are presented. The driver is moved at the constant velocity of $v_d = 1e-6\ m/s$. The force that has to be applied to the driver (traction) and the force that is experienced by the blocks (friction) are superimposed. The corresponding block movements at the interface and their number are also shown such that the relation between the load drop and interfacial events (ruptures) can be investigated. The evolution of rupture is studied by plotting the position and velocity of the blocks during some of the ruptures. Furthermore, the velocity of rupture propagation is calculated for the case studies and compared with the material wave speeds.

The stiffness values of the coil and leaf springs (C and L) are obtained from Equations (H.1) by assuming the block dimensions (length, width and height) to be $1\ m$. Since for Westerly granite Young modulus is $70\ GPa$ and the Poisson ratio is 0.25 (in this case the shear modulus is equal to $28\ GPa$), the spring stiffness values, C and L are proportional to Young and shear moduli, respectively: $L = 7e4\ kN/mm$ and $C = 28e3\ kN/mm$ (note that $1\ kN/mm = 1e6\ N/m$). The normal force on the blocks is assumed constant and is obtained by assuming that the force is such that the compressive strength of Westerly granite (which is reported [175] to be nearly equal to $200\ MPa$) is applied on each block; then, the normal force on each block is $N = 2e8\ N$. The static and dynamic COF are assumed to be 0.8 and 0.7, respectively. Westerly granite density, ρ is $2,691 kg/m^3$ and therefore the pressure wave speed,

$C_p = \sqrt{E/\rho}$ and the shear wave speed, $C_s = \sqrt{G/\rho}$ are calculated to be $5.1\ km/s$ and $2.23\ km/s$, respectively.

The number of blocks is 1000. The initial positions of the blocks are calculated by assigning a linear lateral total spring force on the blocks and solving Equation (6.4). The assigned force distribution starts from a maximum positive (rightward) force on the leftmost block (block 1) which is equal to $\gamma\mu_s N$ and decreases linearly with the block number such that at the rightmost block (block 1000) the spring-exerted force be equal to $-\gamma\mu_s N$. The results are presented for case one, for which $\gamma = 0.1$ and case two, for which $\gamma = 0.9$. The calculated initial block positions for the these cases are shown in Figures 6.15 and 6.43 respectively and are only slightly different from a linear *position* distribution in which the forces on the leftmost and rightmost blocks be $\gamma\mu_s N$ and $-\gamma\mu_s N$.

The results of exact-zero initial position in which no initial lateral displacement of the blocks is presented in Figure 6.14 for the purpose of verification. The boundary condition is assumed periodic to prevent the leftmost and rightmost blocks from ruining the simultaneous stick-slip of the blocks. The time period that is needed to trigger the (simultaneous) slippage of such a system is used for normalizing the time axis values so that making comparison between the different case studies become possible. This period is named threshold time, t_{th}, and is obtained by equating the leaf spring force with the static friction by:

$$t_{th} = \frac{\mu N}{v_d L} \tag{6.61}$$

where L is the leaf spring stiffness. For the set of mechanical and geometrical system parameters that is assumed above, t_{th} is calculated to be 5714.3 seconds. Furthermore, according to the formulation that is given in Subsection 6.2.9, the time step size has to be smaller than $0.4\ ms$. Then, $0.4\ ms$ is divided by 30 such that the Courant number gets smaller that one, i.e. nearly equal to 0.07. The specified time step size for both of the case studies is $13.3\ \mu s$.

Figure 6.14 shows the output of the algorithm for the case of *exact zero initial block positions* with assuming PBC. The purpose is to check if the expected simultaneous

stick-slip of the blocks occurs. Figure 6.14-(a) shows the force periodically increases linearly and drops suddenly. This behavior is exactly the same as stick-slip of a single block. The reason for selecting PBC is that when FBC is chosen, although the first slippage of the blocks occurs simultaneously, this would not continue in a periodic manner. In other words, with assuming FBC, periodicity of the stick-slip would be ruined with time. The reason is that the forces on the leftmost and rightmost blocks become different from the rest of the blocks and gradually diminish the synchronous slippage of the blocks. Figure 6.14-(b) shows the slipped block numbers as time progresses. As expected, in the intervals of linear rise of the force no slippage happens (absence of the markers). On the other hand, at the load drops a concurrent collective slip (which involves all of the blocks) happens on the interface. This can be also seen in Figure 6.14-(c) which shows slippage of 100% of the blocks in sync with the load drops. The fact that the first load drop occurs at $t = t_{th}$ is (as expected) in agreement with the definition of the normalization parameter, Equation (6.61).

6.3.1 Case 1 ($\gamma = 0.1$)

Figure 6.15 shows the initial position of the blocks with respect to their reference coordinates as displayed in Figure 6.6 for case one. The positions are obtained by assuming a linear spring force distribution on the blocks which starts at its maximum (positive rightward force), $F_1 = \gamma\mu_s N$, on the leftmost (1st) block and decreases linearly such that its minimum (negative leftward force), $F_M = -\gamma\mu_s N$, is reached on the leftmost (M^{th}) block. For case one, γ is assumed to be 0.1. This force distribution is then substituted into Equation (6.4) and the obtained system of linear equations is solved to find the initial block positions. Note that at $\tau = 0$ the driver position is zero and therefore the second term on the RHS is absent. The set of obtained initial block positions are only slightly different from a set of directly specified linear initial positions.

Figure 6.16 provides an overall view of the behavior of the BK model in case one. The variation of (a) the fraction and traction forces, (b) the history of the block slippages and (c) the number of the slippages with time is presented in one figure. The time axis is the same for all of the sub-figures so that relating the information becomes possible.

The time is normalized as t/t_{th} in order to ease the comparison of the different case studies. The normalization parameter, t_{th}, is defined in Equation (6.61).

Figure 6.16-(a) shows an initial linear rise of the force (both friction and traction). Before the normalized time reaches 0.9 the normalized force exceeds μ_d and the force suddenly drops below μ_d. The fact that the drop happens before $t/t_{th} = 1$ is reasonable because compared to the case of exact zero positions (shown in Figure 6.14) the slippage of the leftmost block is expected to be triggered earlier because the block experiences a positive spring force at $\tau = 0$. During the load-drop the set of the blocks with numbers 1 (namely the leftmost block) to 525 slip while the rest of the blocks (the RHS of the interface) are stuck as shown in zone number 1 in Figure 6.16-(b). The total number of these slippages does not exceed 2.5% of the total number of the blocks as can be seen in Figure 6.16-(c). This means that the maximum number of the blocks that are involved in the act of sliding is smaller than 25 during the first load-drop. The detail of these block slippages will be investigated later. After the load-drop the force rises again. During this second period of rise, the block numbers 526 to 1000 shift gradually (one by one as can be seen in Figure 6.16-(c)) as shown in zone number 3 of Figure 6.16-(b). The second load-drop occurs after $t/t_{th} = 1$. This load-drop is greater than the first one and is accompanied with sliding of all blocks as shown in zone number 4 of Figure 6.16-(b). However, the sliding of the whole blocks does not happen suddenly since the number of sliding blocks does not exceed 40 during the event as shown in Figure 6.16-(c). After the second load-drop, the force rise is firstly linear but becomes nonlinear with the irregular set of the block slippages which start to occur. The third load-drop is the smallest among the first three and involves the blocks with numbers 661 to 1000 as marked in Figure 6.16-(b) with zone number 5. The maximum number of involved blocks is about 10 as can be read from Figure 6.16-(c).

The zoomed view of zone number 1 in Figure 6.16-(b) is shown in Figure 6.17. The x-axis represents the progress of time while the y-axis represents the interface. The set of block slippages (or the *event*) evolves with time. The event starts with slippage of the leftmost block and immediate participation of its neighbor blocks in the act of sliding. As time goes by, the leftmost block stops sliding but a changing set of sliding blocks constitute a *slipping zone* that moves rightward on the interface. This slipping

zone which seems to move as an entity per se is called a slip pulse in the literature [75, 289, 290, 296]. The slip pulse propagates on the interface for $t_{prop} = 91.65\ ms$.

At the end of the event that is shown in Figure 6.17 the blocks with numbers 1 to 525 are moved from their initial positions as shown in Figure 6.18). The details of the evolution of the block movements with time are presented in these sets of figures: (i) The initiation of the event, when $0.001 \leq t_e/t_{prop} \leq 0.009$, in Figure 6.19 and its zoomed view in Figure 6.20 (ii) The progression of the event, when $0.01 \leq t_e/t_{prop} \leq 0.09$, in Figure 6.21 and its zoomed view in Figure 6.22 and (iii) The overall evolution of the event, when $0.1 \leq t_e/t_{prop} \leq 1$, in Figure 6.23 (which does not need a zoomed view). Each of the specified time intervals for the set of figures (i) and (ii) contains 9 equi-spaced time frames while Figure 6.23 contains 10 equi-spaced time frames.

The first pair of figures, named (i) earlier, provides the opportunity of investigating the interval $t_e = [0.001,\ 0.009]t_{prop}$ or $t_e = [91.65,\ 824.85]\ (\mu s)$ of the event at every 91.65 microseconds. Figures 6.19 and 6.20 show the evolution of the block positions and block velocities in detail. Figure 6.20 shows that the event starts crack-like firstly. Note that the velocity of the leftmost block does not become zero even at the last time frame (the thickest line).

The second pair of figures, named (ii) earlier, investigates the block positions and velocities within the interval $t_e = [0.01,\ 0.09]t_{prop}$ or $t_e = [916.5,\ 8248.5]\ (\mu s)$ of the event at every 916.5 microseconds. Figures 6.21 and 6.22 show the evolution of the block positions and block velocities in detail. Figure 6.22 shows that the event ceases to be crack-like and becomes pulse-like at the second time frame as the leftmost block sticks. The number of the blocks that constitute the pulse deceases with time and the pulse propagation speed also deceases.

Figure 6.23, named (iii) earlier, reveals the details the block positions and velocities within the interval $t_e = [0.1,\ 1]t_{prop}$ or $t_e = [9165,\ 91650]\ (\mu s)$ of the event at every 9165 microseconds. Figure 6.23 shows that the event continues as a single pulse up to the end. The velocity of the involved blocks and the velocity of the pulse decrease as time elapses. At $t_e = 91650\ \mu s$, the event is finished and the absence of the pulse in the last time frame is in agreement with this fact.

Figure 6.24 shows the velocity of the pulse propagation and the number of blocks that are involved in the pulse as time progresses during the event that is shown in Figure 6.17. The propagation velocity is five times grater than the pressure wave speed, however, quickly (in less than $6\ ms$) drops below $2c_p$. The number of involved blocks firstly increases rapidly to above 20 and then drops to only 5 blocks in less than $12\ ms$.

Figure 6.25 shows a zoomed view of zone number 2 in Figure 6.16-(b) and contains the final part of the pulse propagation event that is shown in Figure 6.17 and the beginning part of a series of the individual (isolated) block slippages that appears as an inclined line in zone number 3 in Figure 6.16-(b). A zoomed view of zone number 3 is shown in Figure 6.26. The inclined "line" is indeed composed of dots (block slippages) with no overlap of the time interval. In other words, the blocks with numbers 525 to 1000 slide one by one and there are periods of no block slippage between every pair of the successive isolated slippages. The onset of this block-shifting period is shown in Figure 6.25. The slope of the inclined "line" in Figure 6.26 is nearly equal to $1\ m/s$. This can be interpreted as the speed of propagation of the individual slip events on the interface.

Figure 6.26 shows a zoomed view of zone number 4 in Figure 6.16-(b). The figure shows that the event is actually triggered by block 526. At the beginning, the event nucleates and grows as a crack with two tips that move in opposite direction. Block 526 is the block at which the pulse-like propagation of zone number 1 was ended and the slow-moving individual slippages of zone number 3 were started. Note that the series of isolated slippages of zone 3 have shifted the blocks 525 to 1000 forward to an almost the same extent as can be seen by comparing Figures 6.18 and 6.28. The nucleation and growth of the "inner crack" ends with division of the crack into two slip pulses the move in the opposite directions (Figure 6.26).

Figure 6.28 shows the position of the blocks just before and just after the event the is plotted in Figure 6.26. The details of these displacements are given in the following figures. Figure 6.29 shows evolution of the block positions and velocities within the first 0.009 fraction of the event (propagation) duration at nine equi-distnance time-points (every $0.001t_{prop}$). As mentioned before, the event starts at block number

526. A closer look (Figure 6.30) shows that in this period of the event evolution the inner crack extends both leftward and rightward on the interface and at $0.005t_{prop}$ the process of division into pulses starts to manifest as the velocity of block 526 and its immediate neighborhood begin to decrease towards zero. In spite of the decrease in the central block velocities even more blocks join the crack zone during the interval $[0, 0.009t_{prop}]$.

Figure 6.31 shows evolution of the block positions and velocities within the interval $[0.01t_{prop}, 0.09t_{prop}]$ at nine equi-distnance time-points (every $0.01t_{prop}$). A zoomed view is provided in Figure 6.32. As the event unfolds in this time period, the blocks that have started sliding earlier stop moving. At $0.02t_{prop}$ a new phase of propagation starts with division of the crack into two slip pulses that continue move to the left and right. This is in agreement with Figure 6.26. Figure 6.33 shows that the overall evolution of the event (since $0.1t_{prop}$ till the end of the event at t_{prop}, at every $0.1t_{prop}$) is pulse-like with the pair of single pulses that move to the left (down to block number 1) and right (up to the block number 1000).

Figure 6.42 shows the speed of propagation of the initial nucleation (crack) and the rightward and leftward pulses together with the number of involved blocks as a function of time. The difference between the rightward and leftward pulses is insignificant. If the very early period of nucleation (the initial sharp rise in Figure 6.42-(b)) is neglected, higher propagation speeds are accompanied by a higher the number of the involved blocks.

Figure 6.35 shows a zoomed view of the zone that is numbered 5 in Figure 6.16-(b). The event starts at block 997 and propagates leftward (and shortly rightward to the rightmost block). Note that the block slippages are always rightward, however, a slip pulse as an entity, i.e. a group of neighbor sliding blocks, can "move" both to the right and left. Figure 6.36 shows an initial (and final) block position distribution that is more complex compared to the previous events. The event involves just the block numbers 661 to 1000. Some information about the position and velocity of the blocks during the event are provided in Figures 6.37-6.41. Again the rupture starts in a crack-like manner and splits into pulses. The rightward pulse ends immediately as there is no more blocks on the right. The leftward pulse propagates down to block

number 661. The propagation speed of the leftward pulse is shown as a function of time and is lower when compared to the previous events.

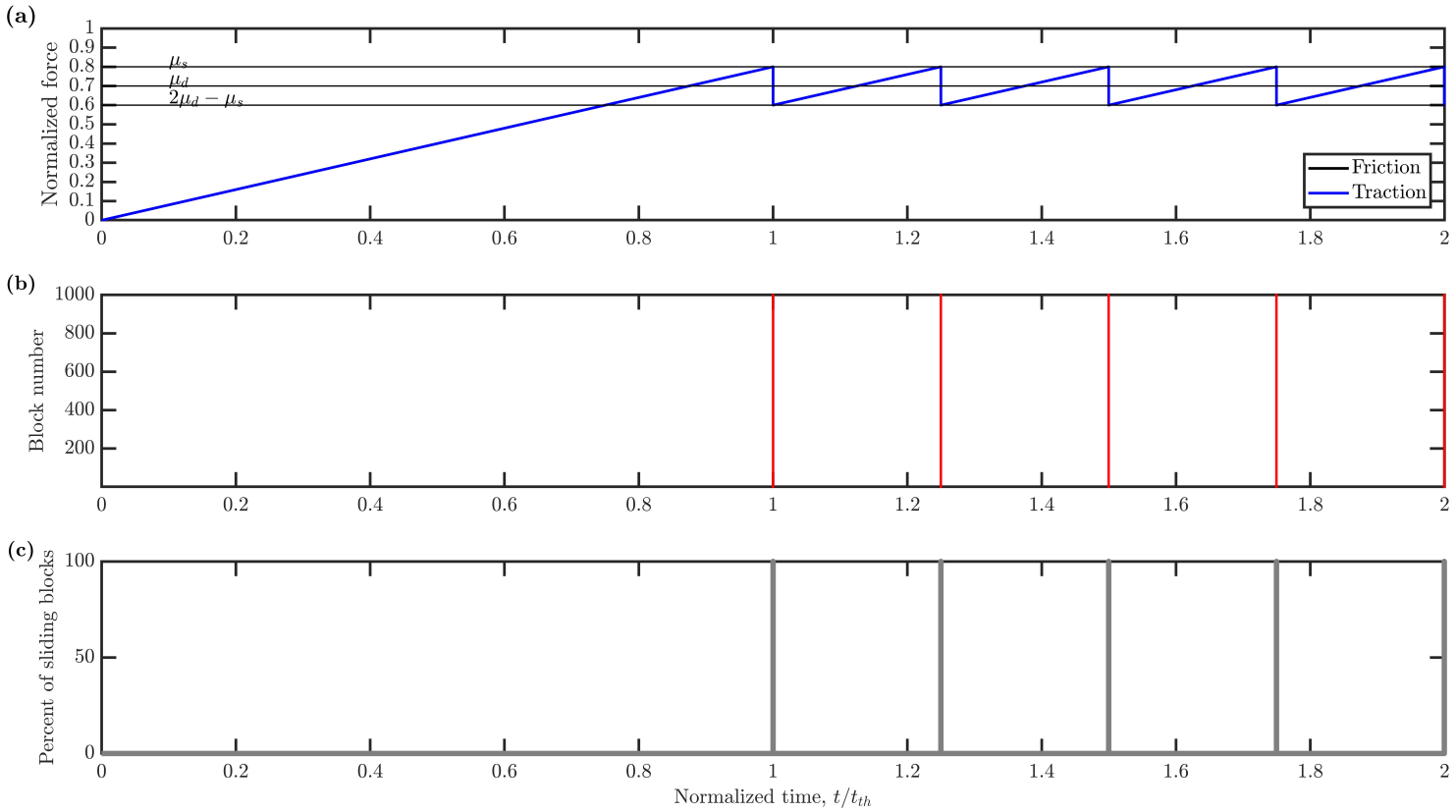

Figure 6.14: Response of the BK model with exact zero initial block positions and the periodic boundary conditions: (a) friction and the driver traction, (b) the block slippage history, and (c) the percent of the slipping blocks at each time step

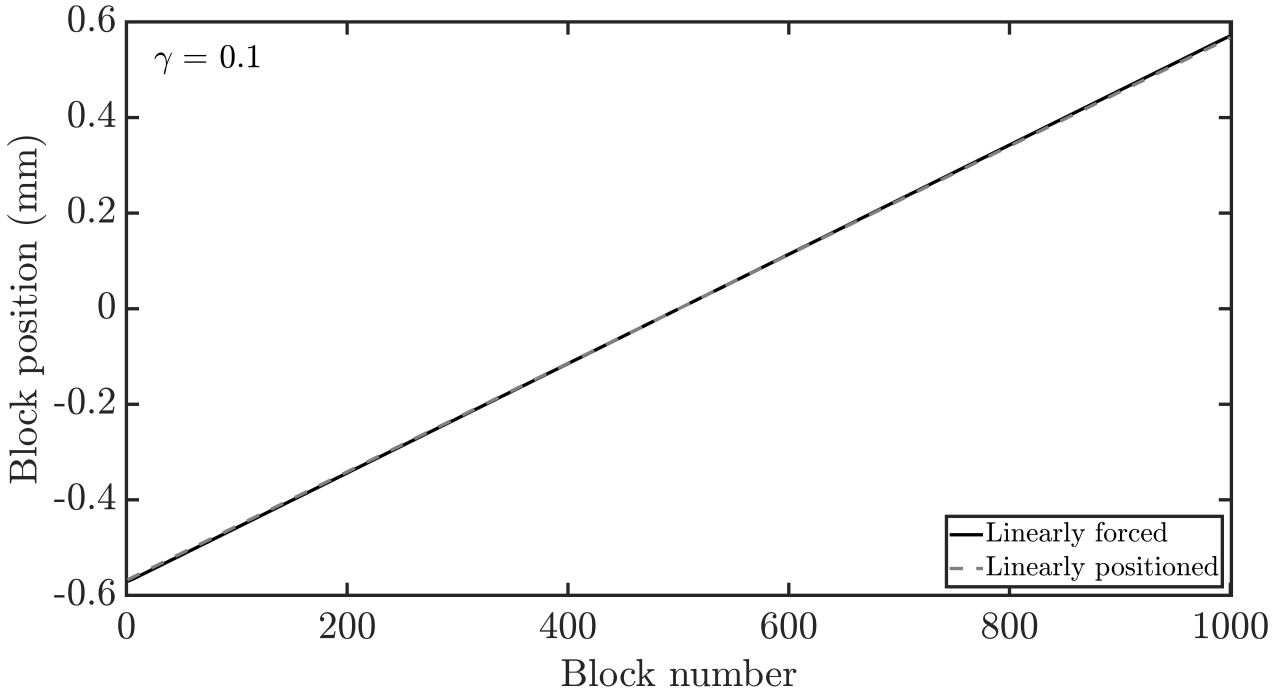

Figure 6.15: The initial block positions for case one, $\gamma = 0.1$, that assumes a linear spring-force distribution on the blocks in which the leftmost experiences $\gamma\mu_s N$ and the rightmost block experiences $-\gamma\mu_s N$

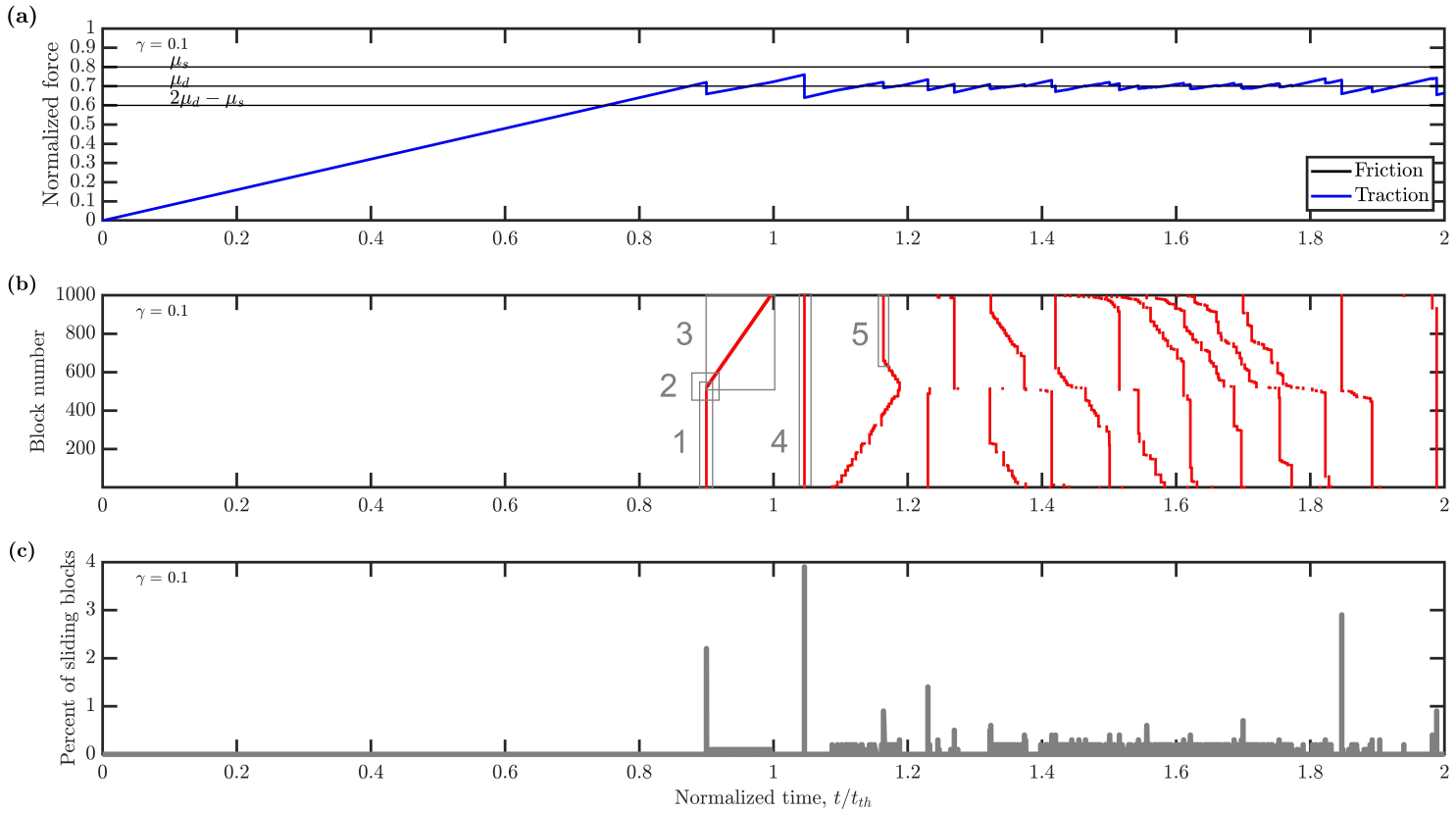

Figure 6.16: Response of the BK model in case one, linear spring force with $\gamma = 0.1$ with the free boundary conditions: (a) friction and the driver traction, (b) the block slippage history, and (c) the percent of the slipping blocks at each time step

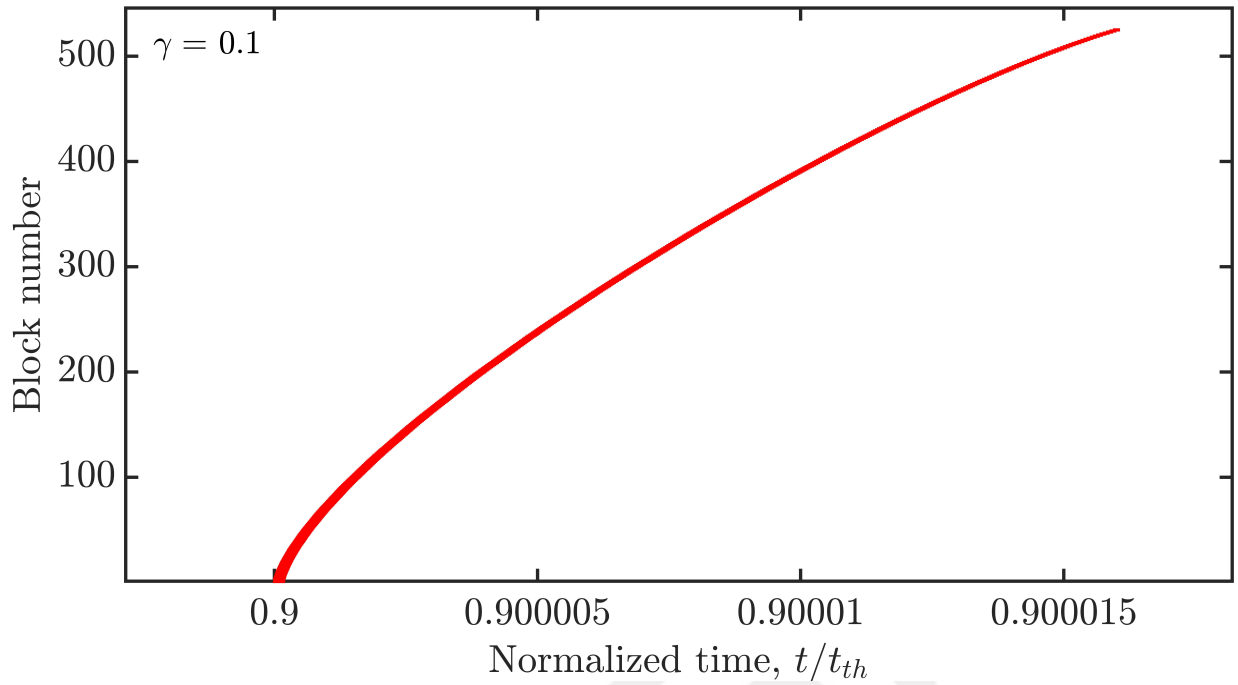

Figure 6.17: The zoomed view of zone number 1 (marked in Figure 6.16-(b)) of case one shows a slip pulse propagation on the interface. The threshold (normalization) parameter, t_{th}, is equal to $5714.3\ s$. The total duration of the propagation, t_{prop} is equal to $91.65\ ms$.

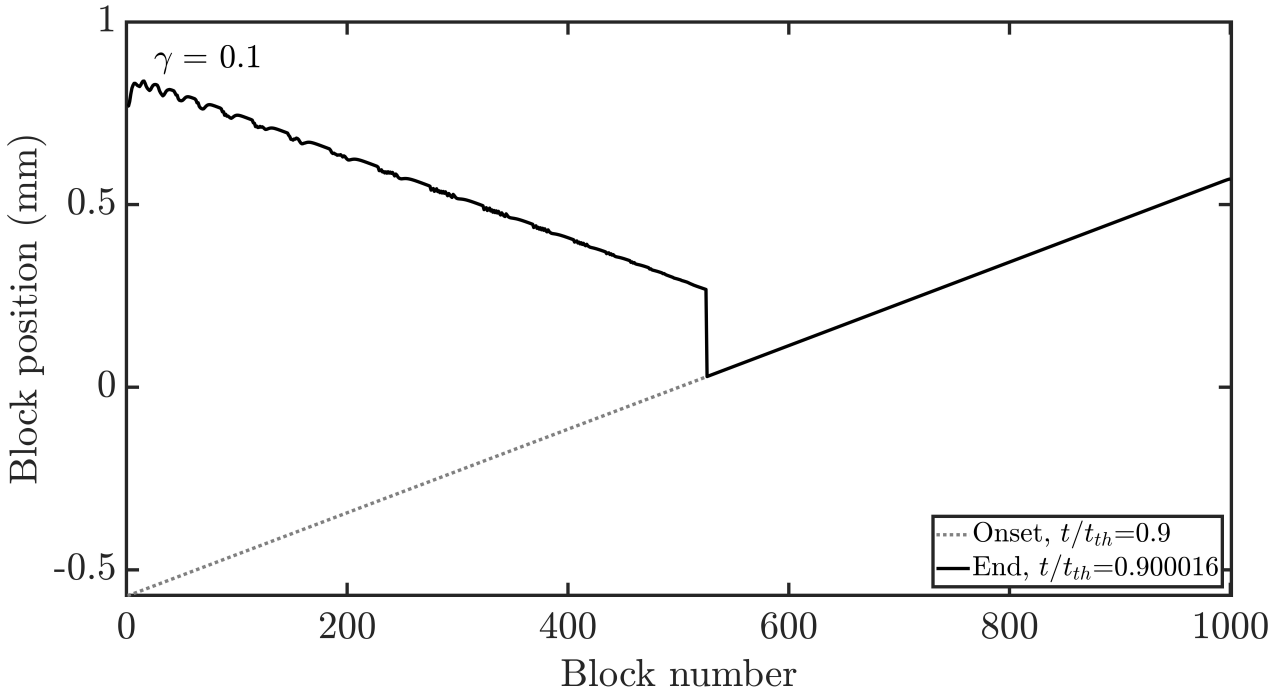

Figure 6.18: The position of the blocks just before and just after the pulse propagation which is shown in Figure 6.17, i.e. case one, zone number 1. The driver position, x_d is 5.14 mm.

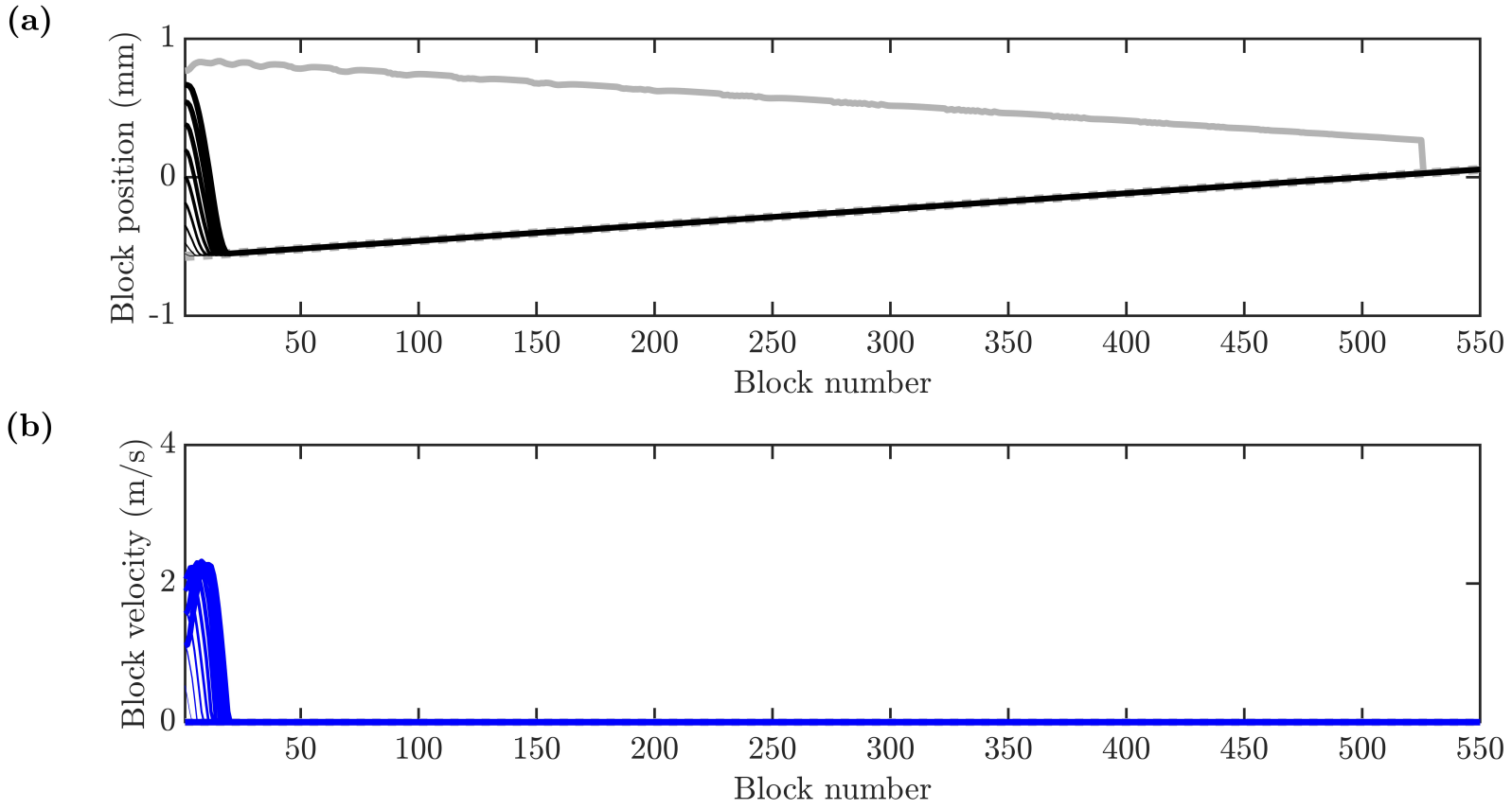

Figure 6.19: The position and velocity of the blocks during the time interval $(0, 0.009t_{prop})$ for the pulse propagation that is shown in Figure 6.17, i.e. case one, zone number 1. The total duration of the propagation, t_{prop} is equal to $91.65\ ms$.

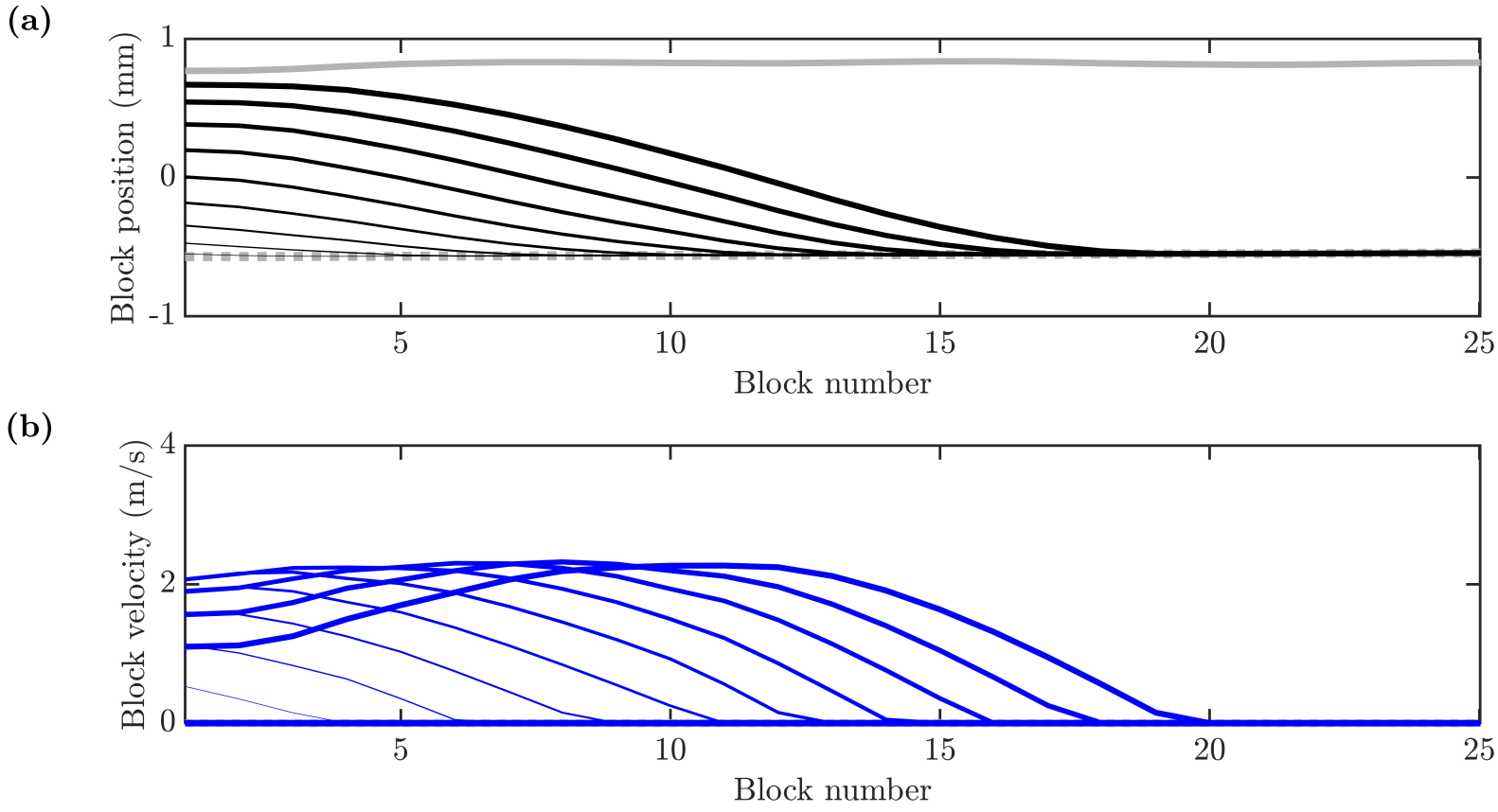

Figure 6.20: A zoomed view of Figure 6.19

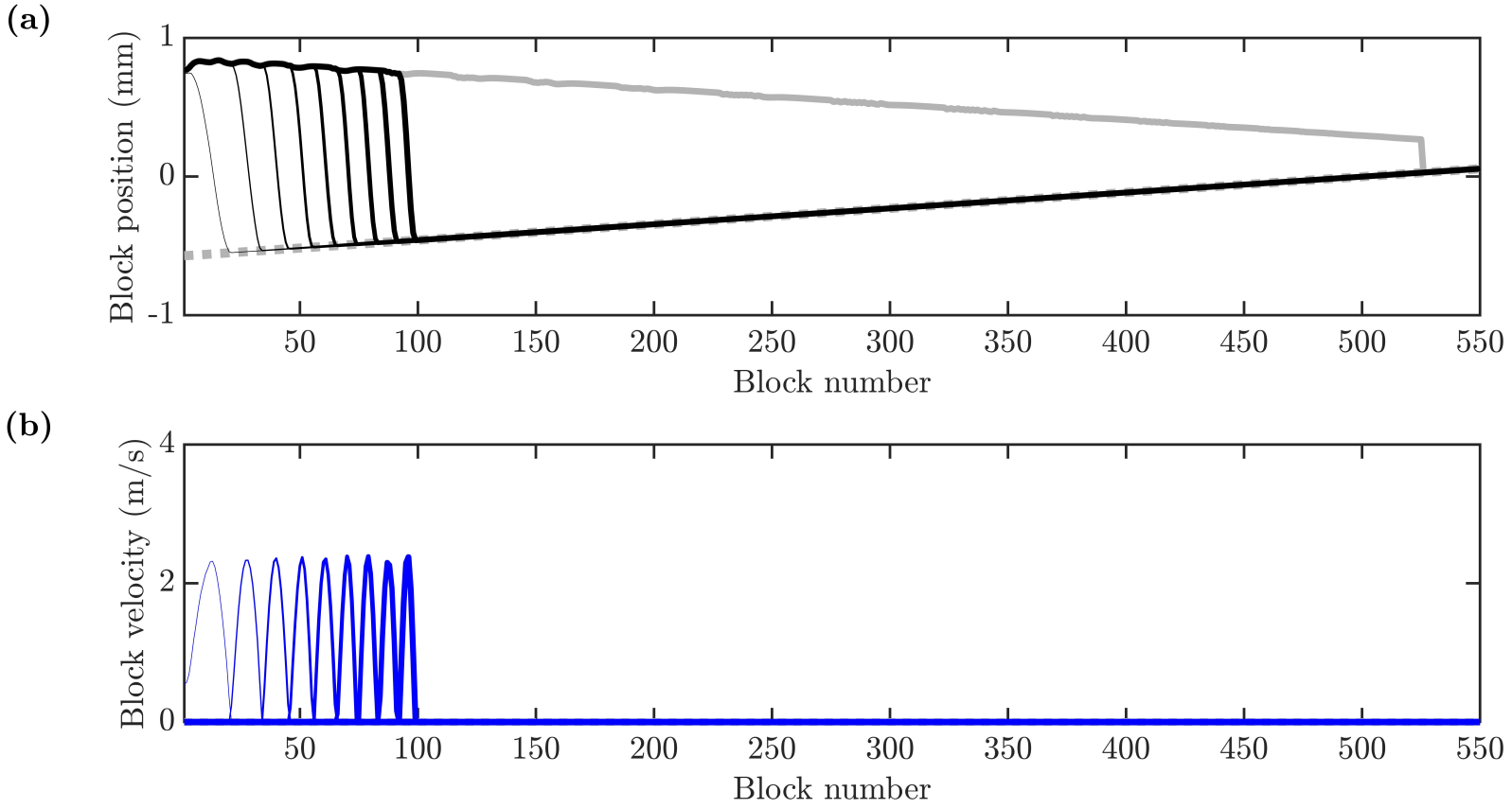

Figure 6.21: The position and velocity of the blocks during the time interval $(0.01t_{prop},\ 0.09t_{prop})$ for the pulse propagation that is shown in Figure 6.17, i.e. case one, zone number 1. The total duration of the propagation, t_{prop} is equal to $91.65\ ms$

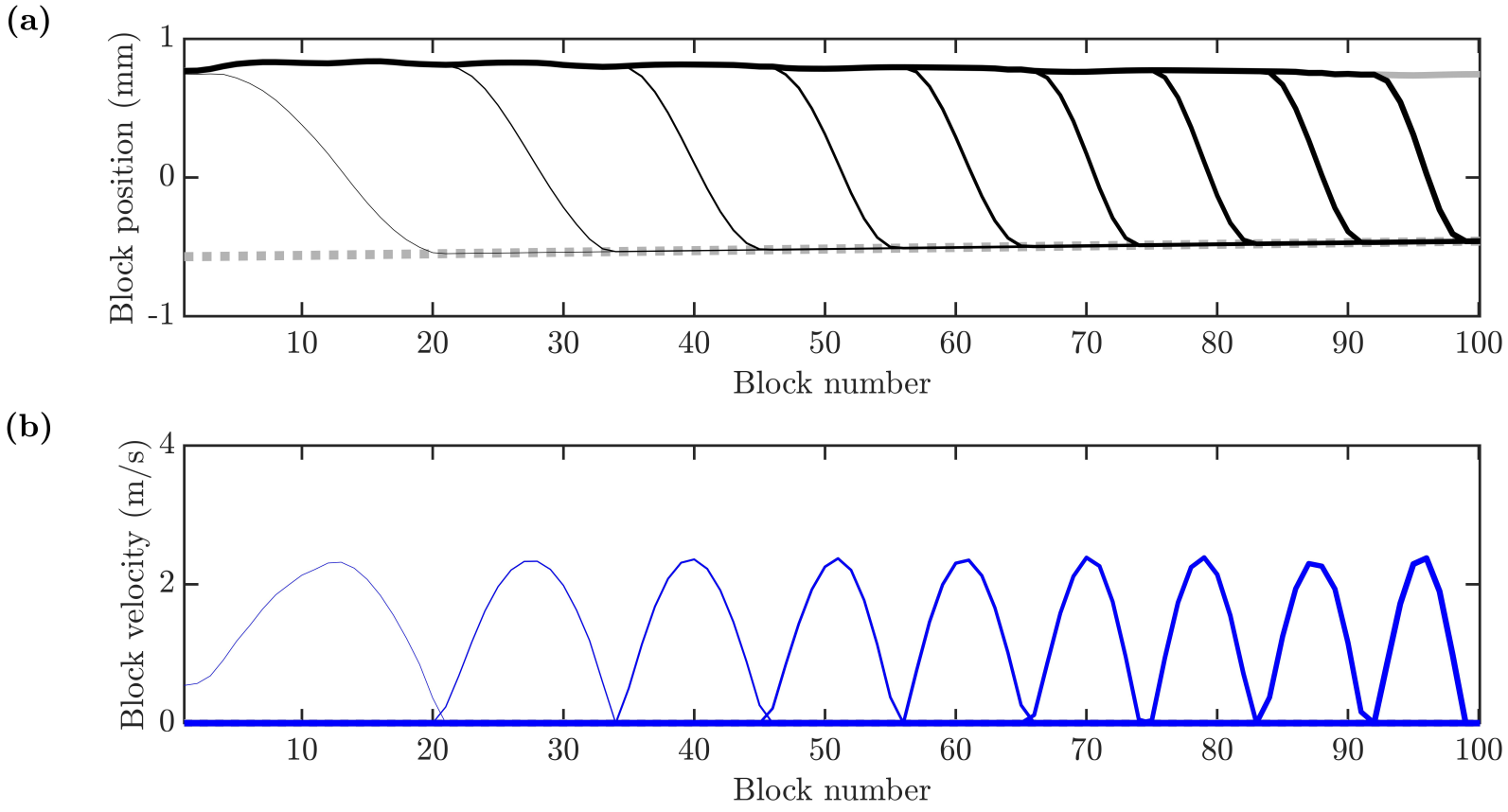

Figure 6.22: A zoomed view of Figure 6.21

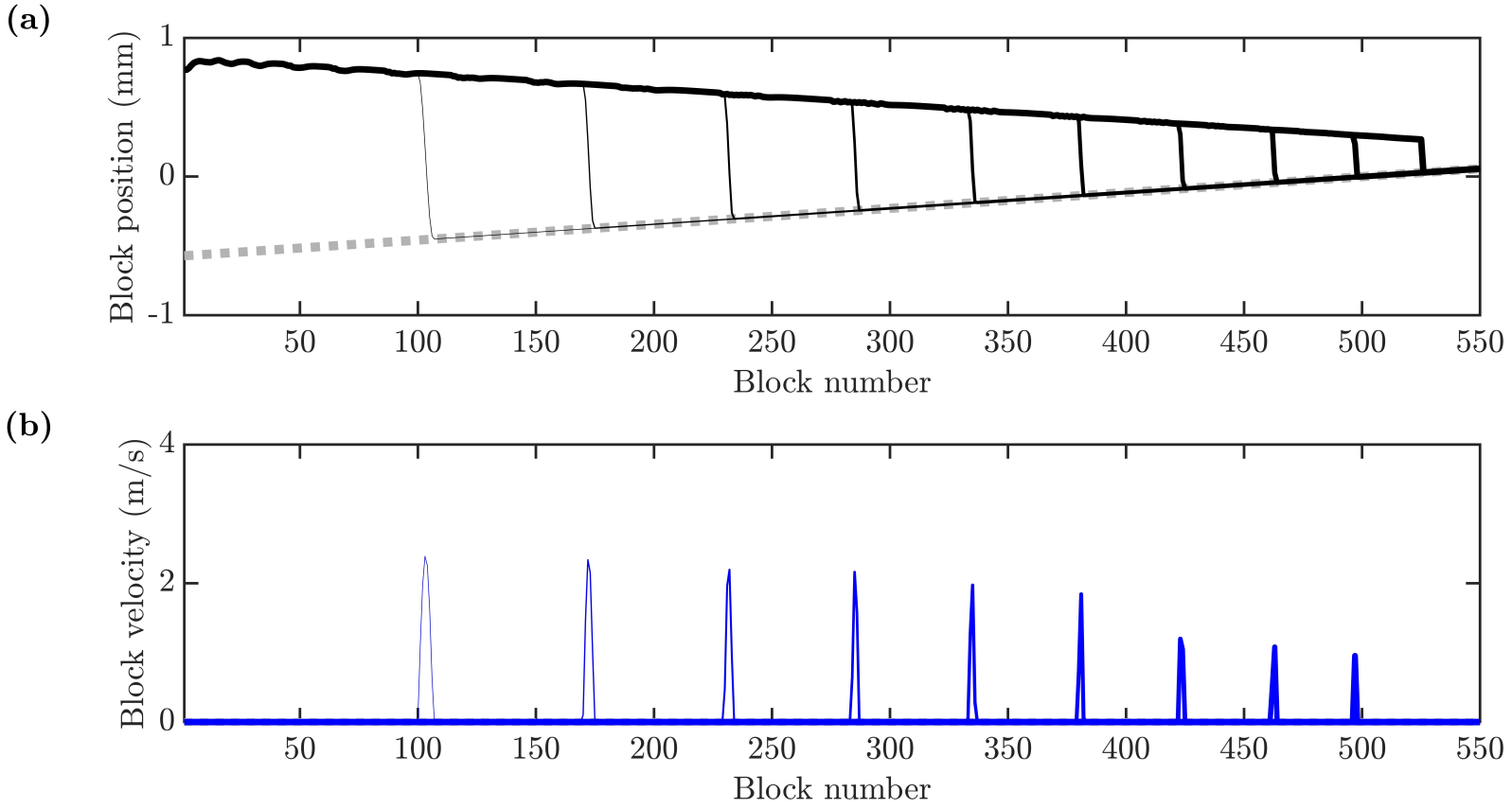

Figure 6.23: The position and velocity of the blocks during the time interval $(0.1t_{prop},\ t_{prop})$ for the pulse propagation that is shown in Figure 6.17, i.e. case one, zone number 1. The total duration of the propagation, t_{prop} is equal to $91.65\ ms$.

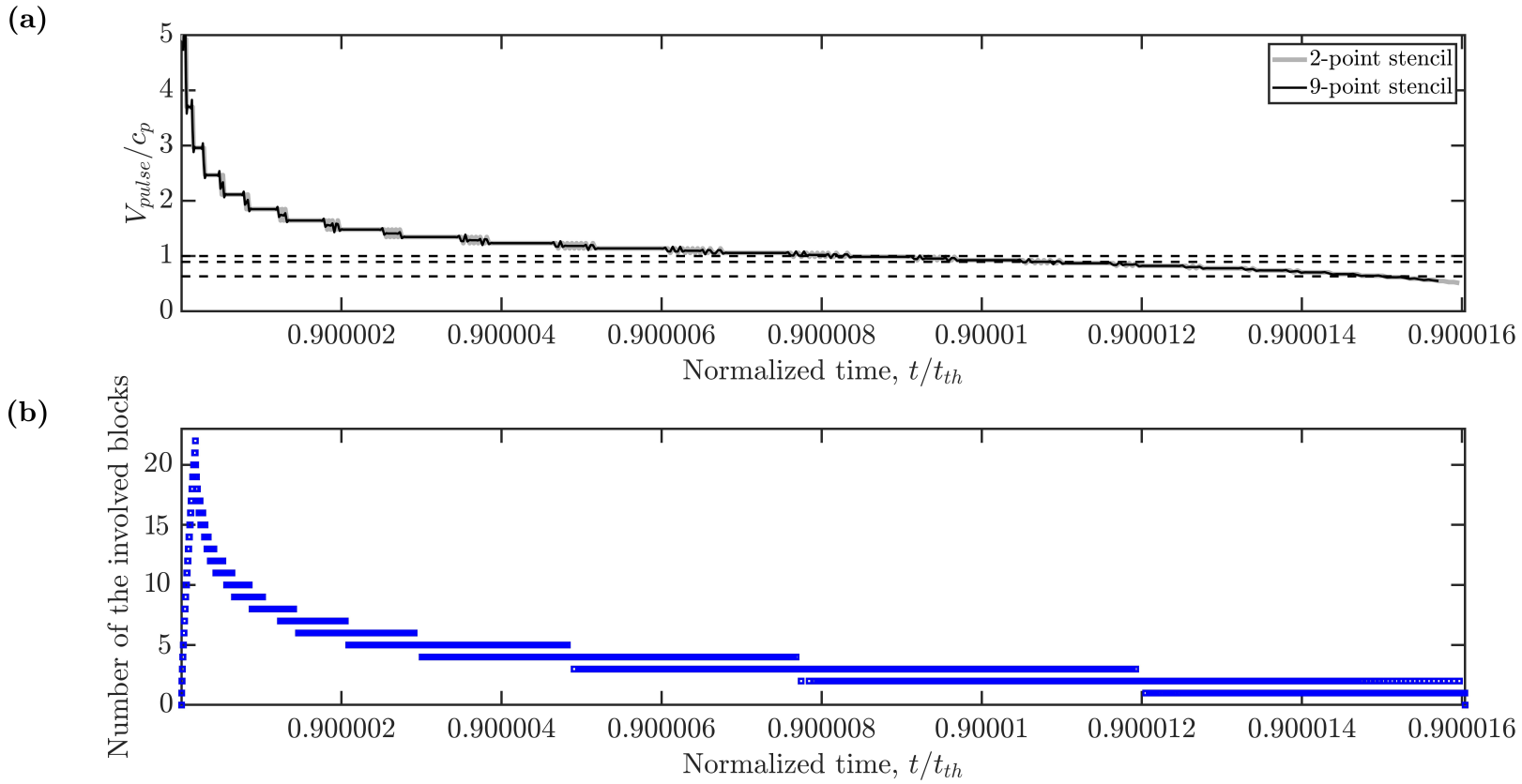

Figure 6.24: The pulse velocity and the number of involved (slipping) blocks during the propagation that is shown in Figure 6.17, i.e. case one, zone number 1. The threshold (normalization) parameter, t_{th}, is equal to 5714.3 s. The total duration of the propagation, t_{prop} is equal to 91.65 ms.

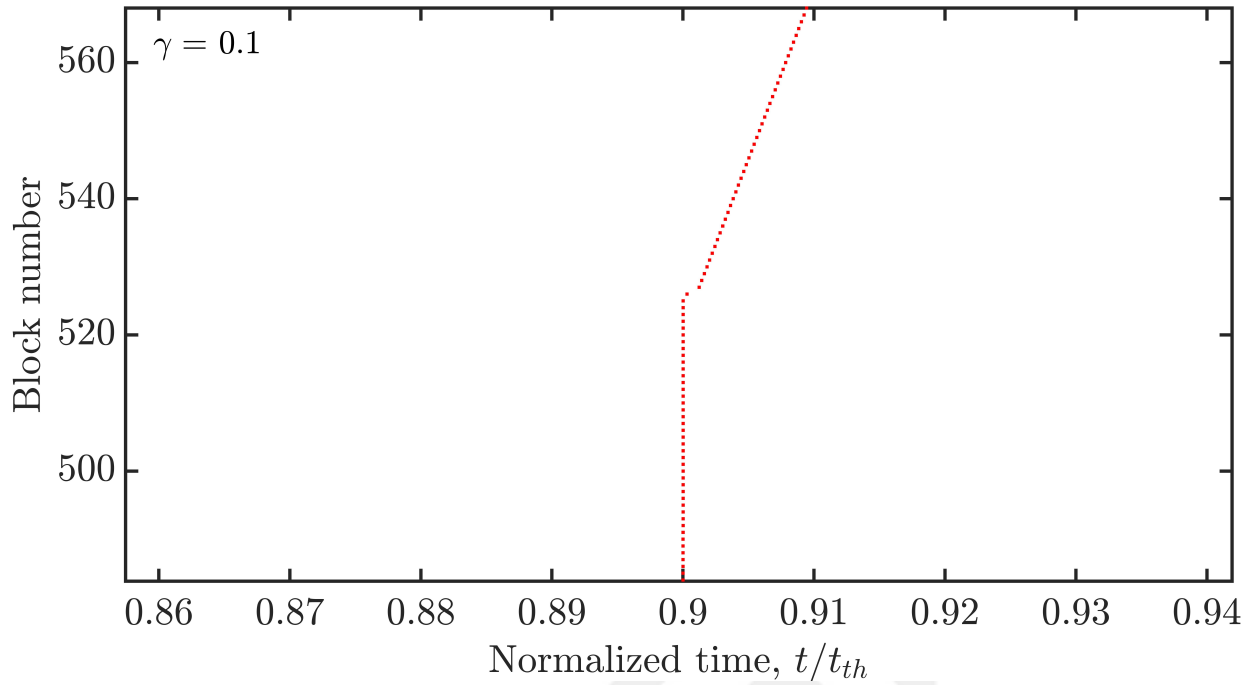

Figure 6.25: The zoomed view of zone number 2 (marked in Figure 6.16-(b)) of case one shows the tail of the preceding pulse-like event and the onset of a series of sequential and isolated block slippages. The threshold (normalization) parameter, t_{th}, is equal to $5714.3\ s$.

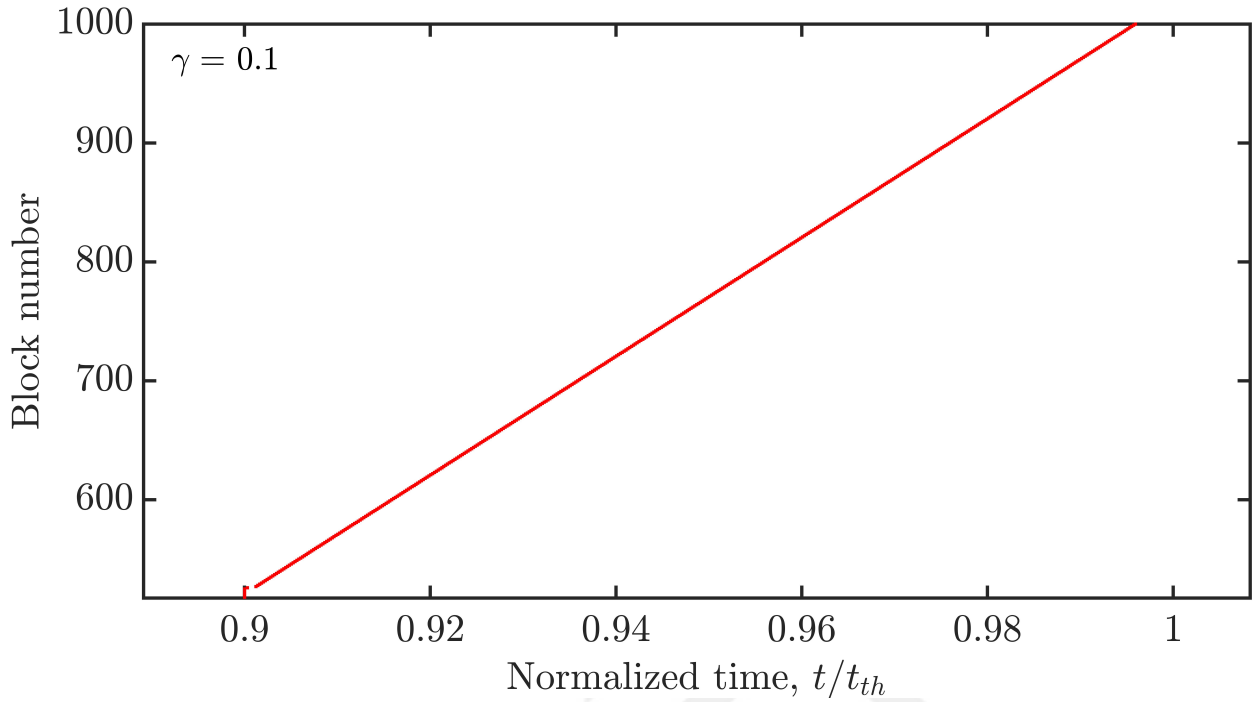

Figure 6.26: The zoomed view of zone number 3 (marked in Figure 6.16-(b)) of case one shows the whole series of the sequential and isolated block slippages. The threshold (normalization) parameter, t_{th}, is equal to $5714.3\ s$. The speed of propagation is almost equal to $1\ m/s$.

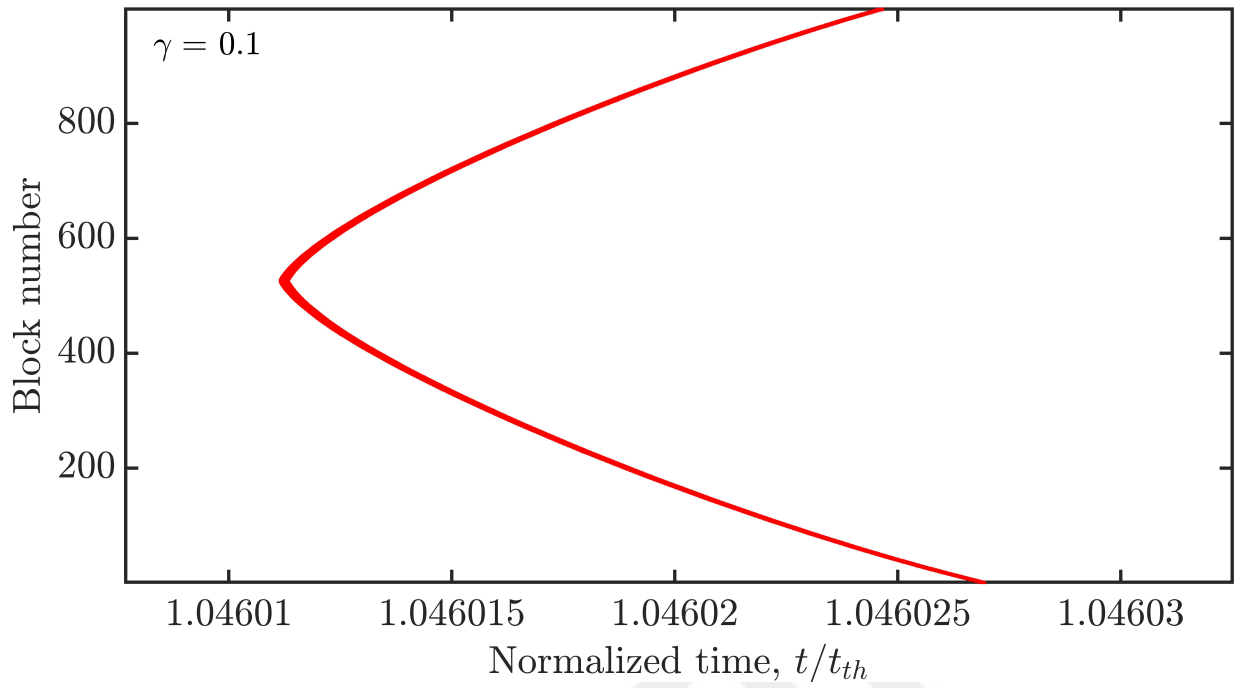

Figure 6.27: The zoomed view of zone number 4 (marked in Figure 6.16-(b)) of case one shows nucleation of a crack that is later divided into two slip pulses that propagate in the opposite directions on the interface. The threshold (normalization) parameter, t_{th}, is equal to $5714.3\ s$. The total duration of the propagation, t_{prop} is equal to $90.26\ ms$.

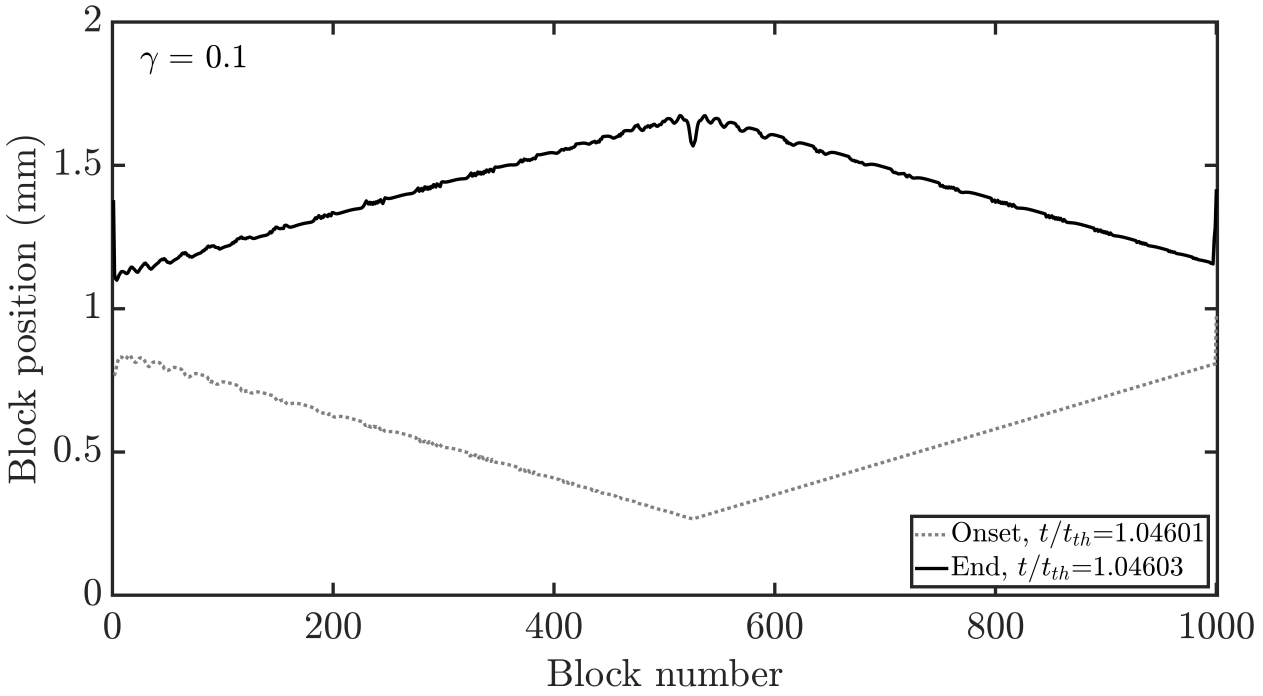

Figure 6.28: The position of the blocks just before and just after the pulse propagation which is shown in Figure 6.27, i.e. case one, zone number 4. The driver position, x_d is 5.98 mm.

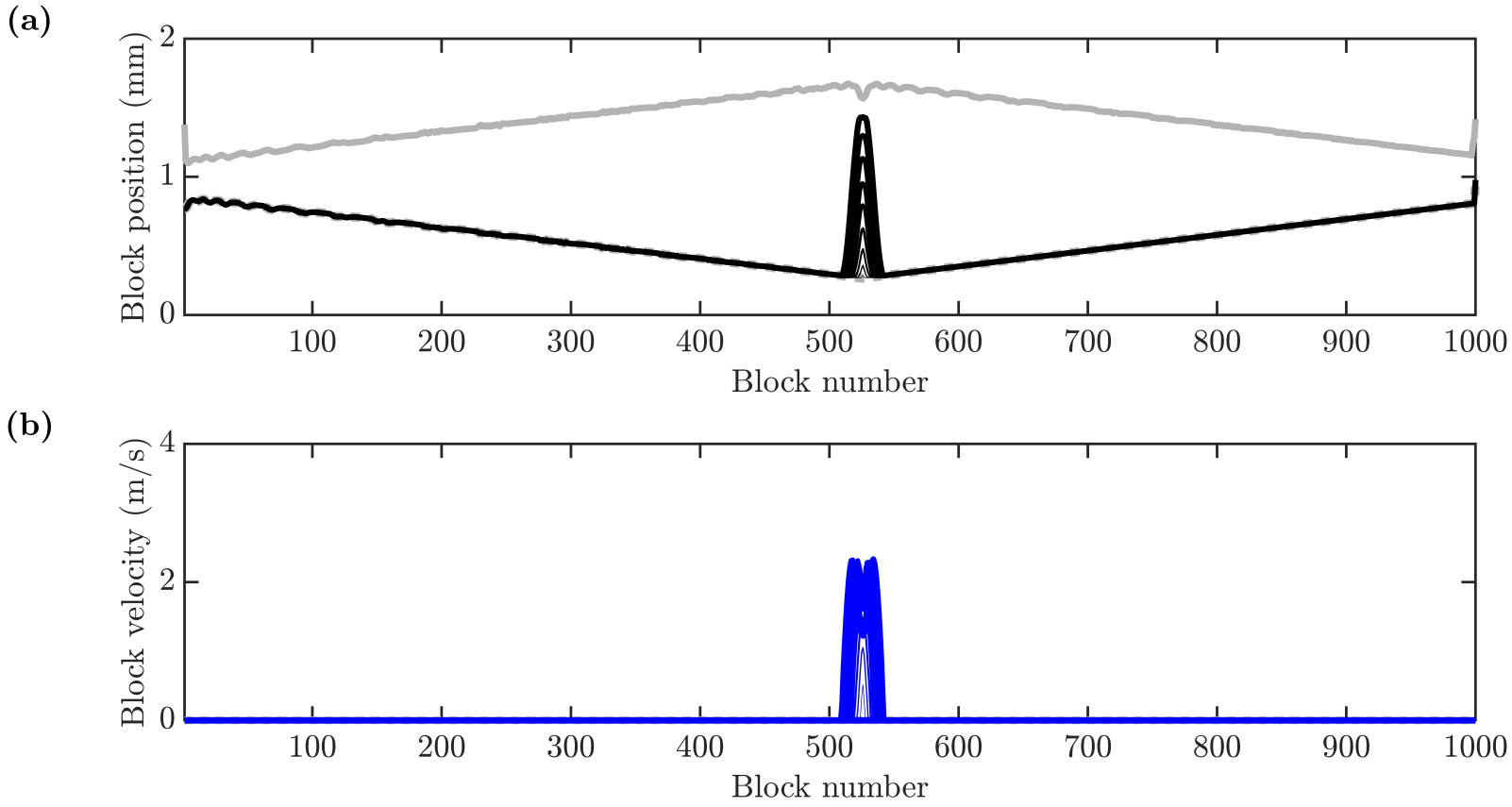

Figure 6.29: The position and velocity of the blocks during the time interval $(0, 0.009t_{prop})$ for the pulse propagation that is shown in Figure 6.27, i.e. case one, zone number 4. The total duration of the propagation, t_{prop} is equal to $90.26\ ms$.

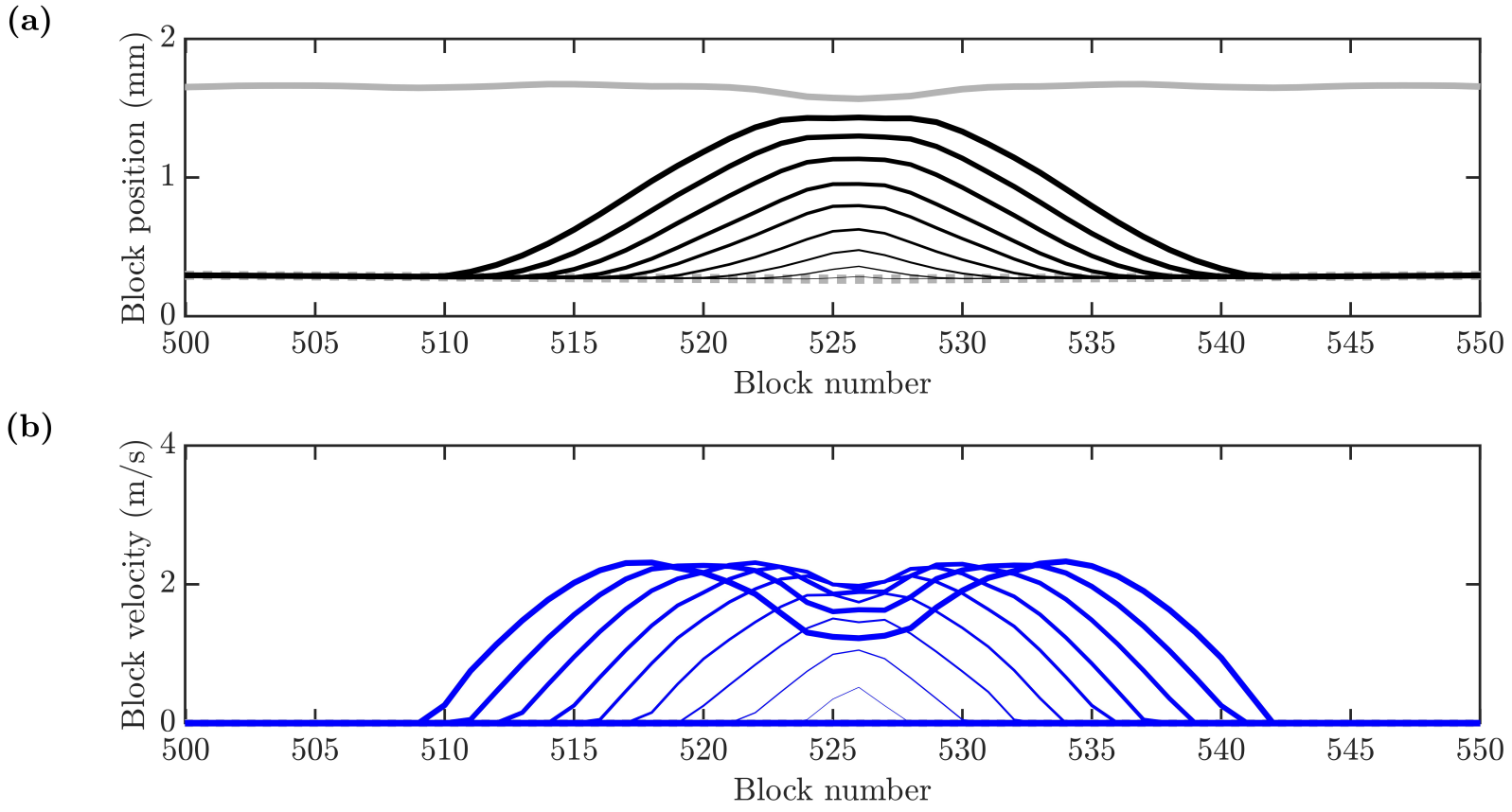

Figure 6.30: A zoomed view of Figure 6.29

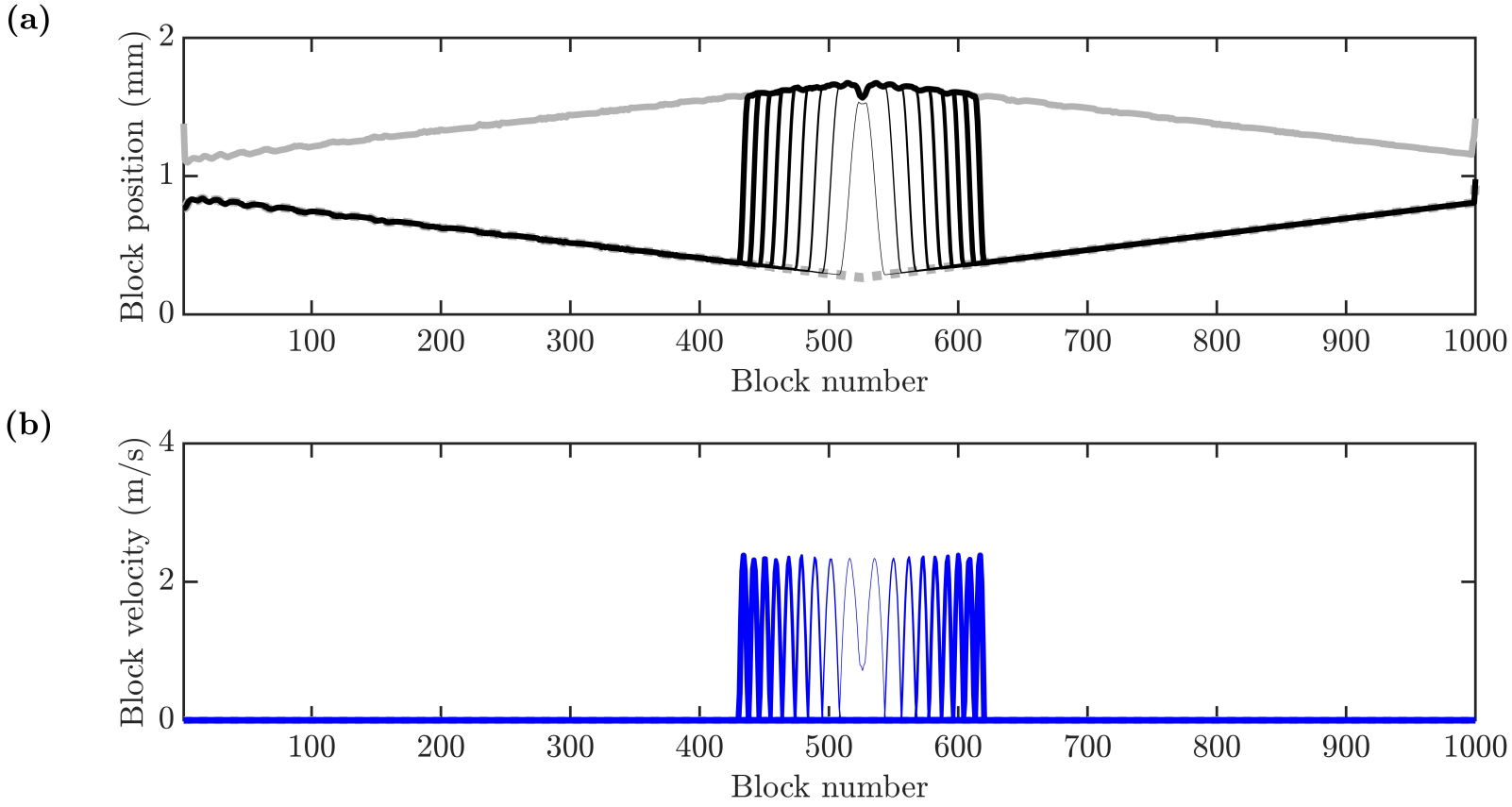

Figure 6.31: The position and velocity of the blocks during the time interval $(0.01t_{prop},\ 0.09t_{prop})$ for the pulse propagation that is shown in Figure 6.27, i.e. case one, zone number 4. The total duration of the propagation, t_{prop} is equal to $90.26\ ms$.

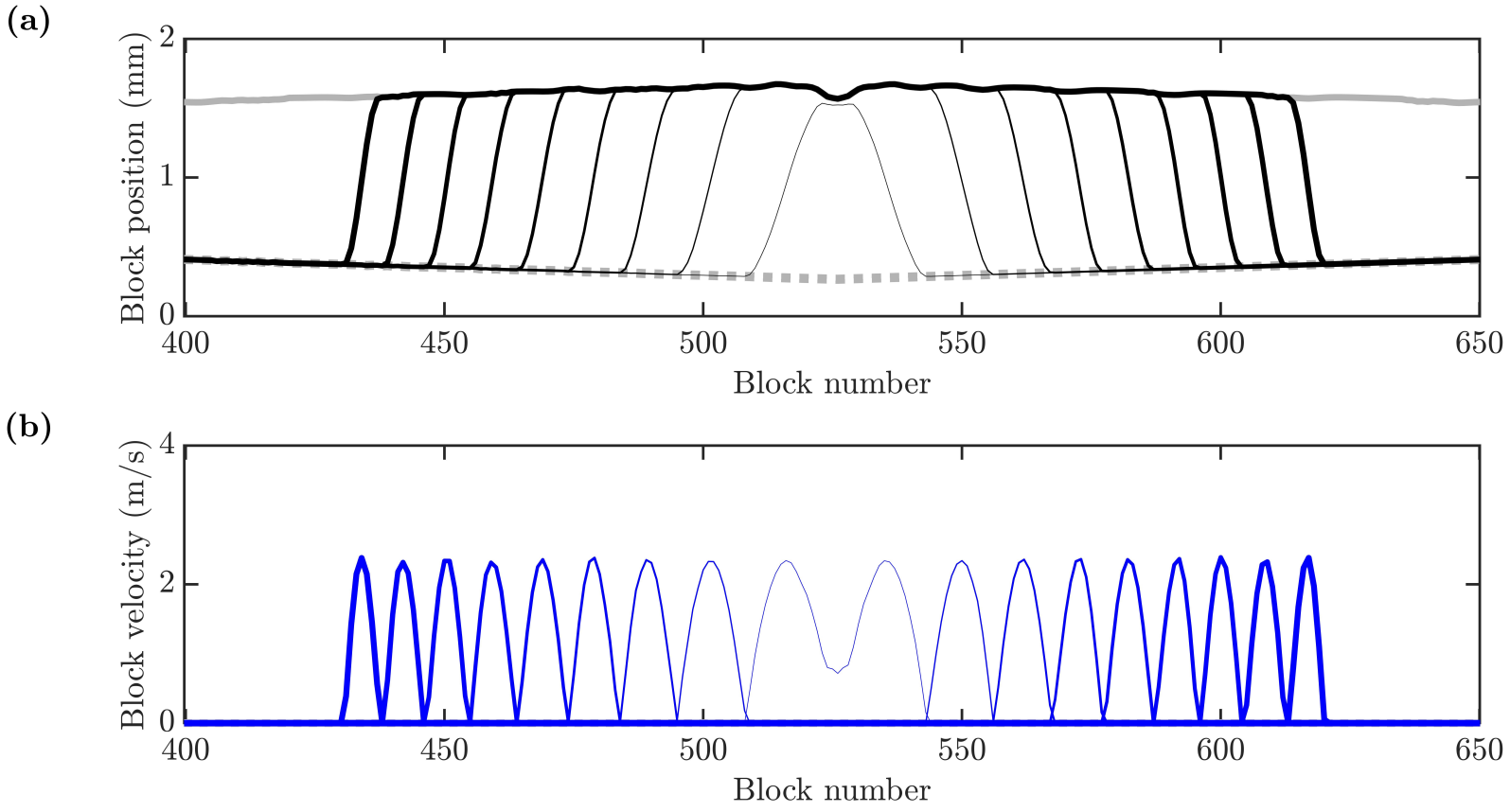

Figure 6.32: A zoomed view of Figure 6.31

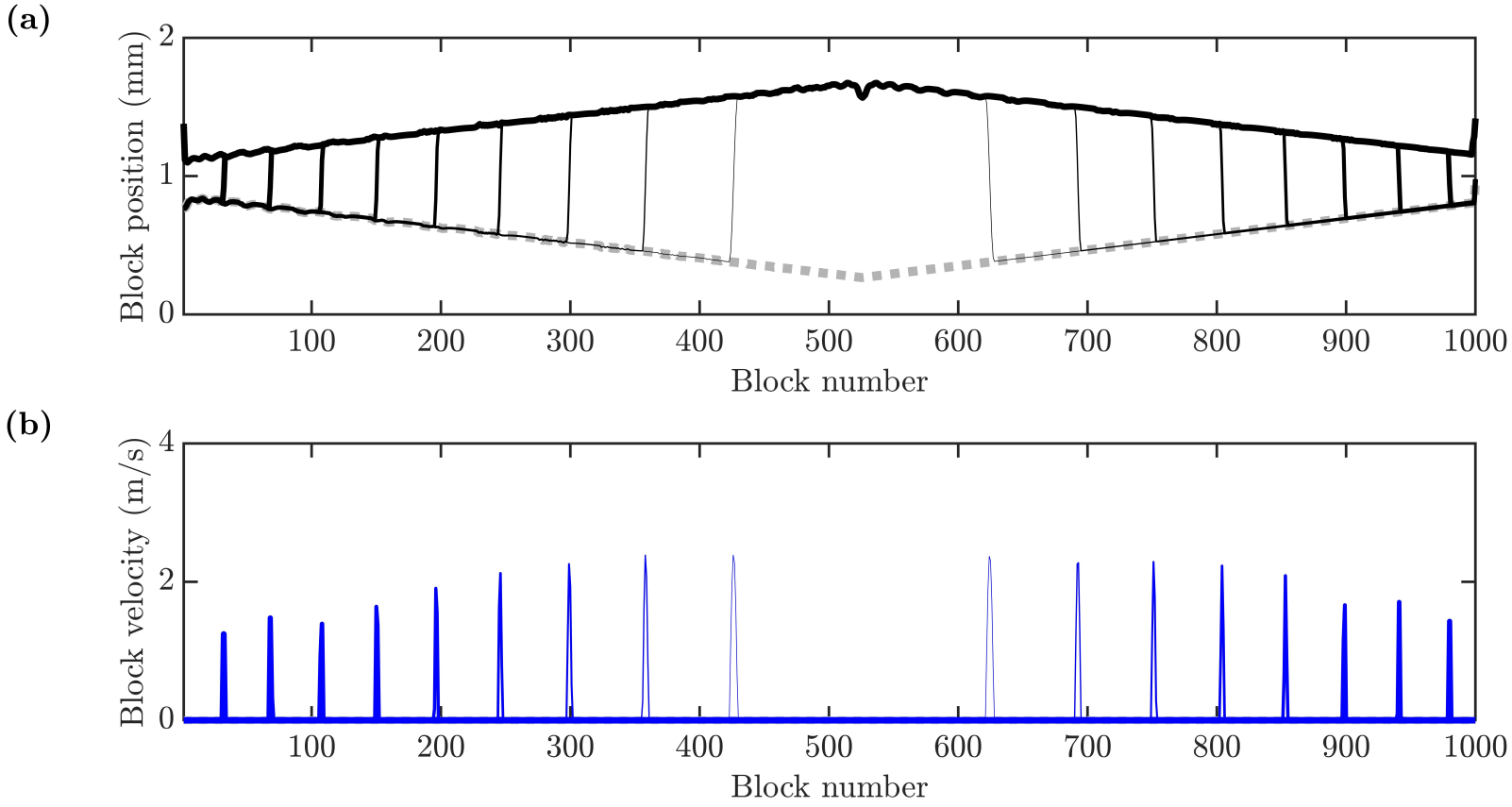

Figure 6.33: The position and velocity of the blocks during the time interval $(0.1t_{prop},\ t_{prop})$ for the pulse propagation that is shown in Figure 6.27, i.e. case one, zone number 4. The total duration of the propagation, t_{prop} is equal to $90.26\ ms$.

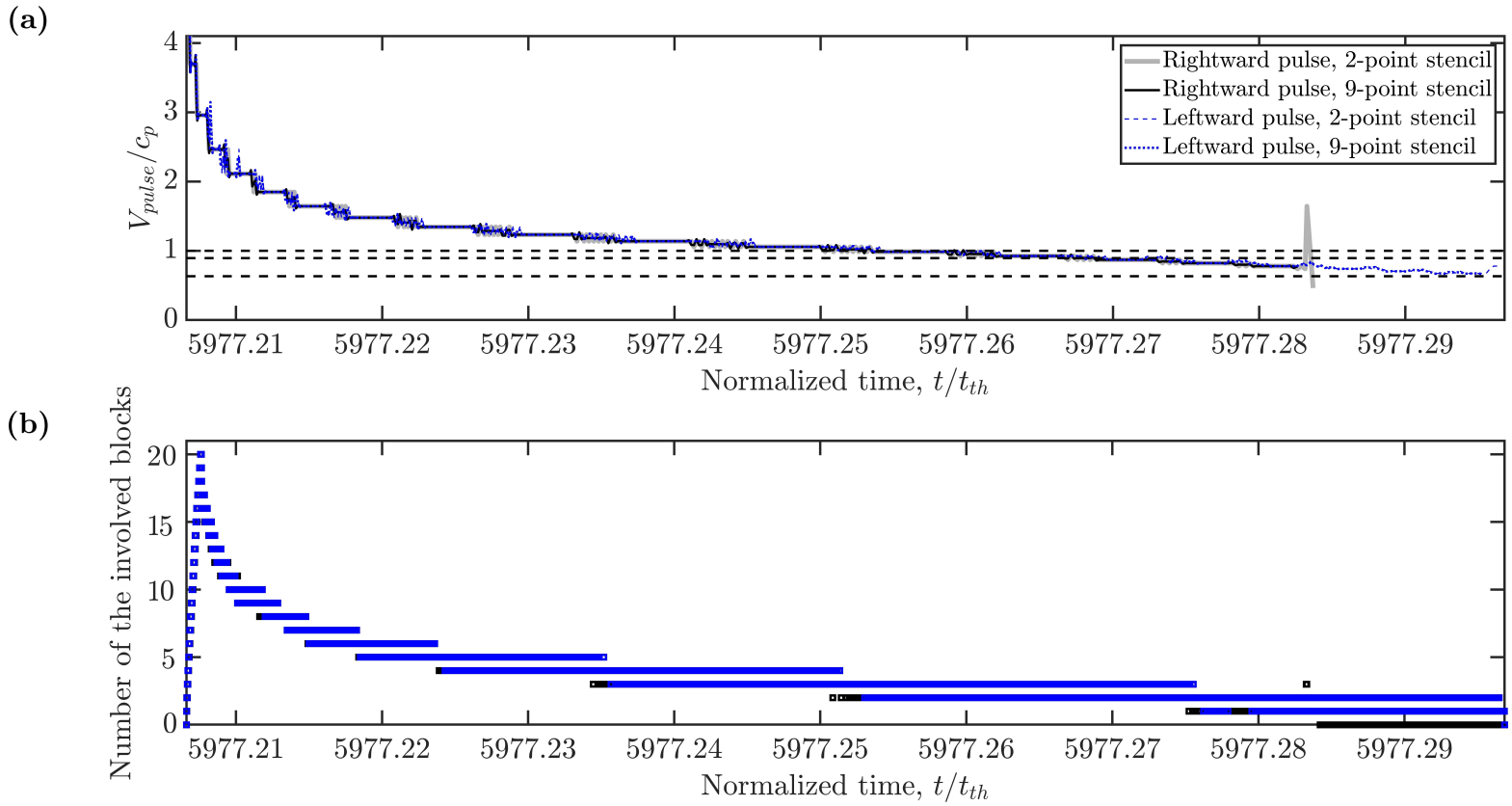

Figure 6.34: The pulse velocity and the number of involved (slipping) blocks during the propagation that is shown in Figure 6.27, i.e. case one, zone number 4. The threshold (normalization) parameter, t_{th}, is equal to 5714.3 s. The total duration of the propagation, t_{prop} is equal to 91.65 ms.

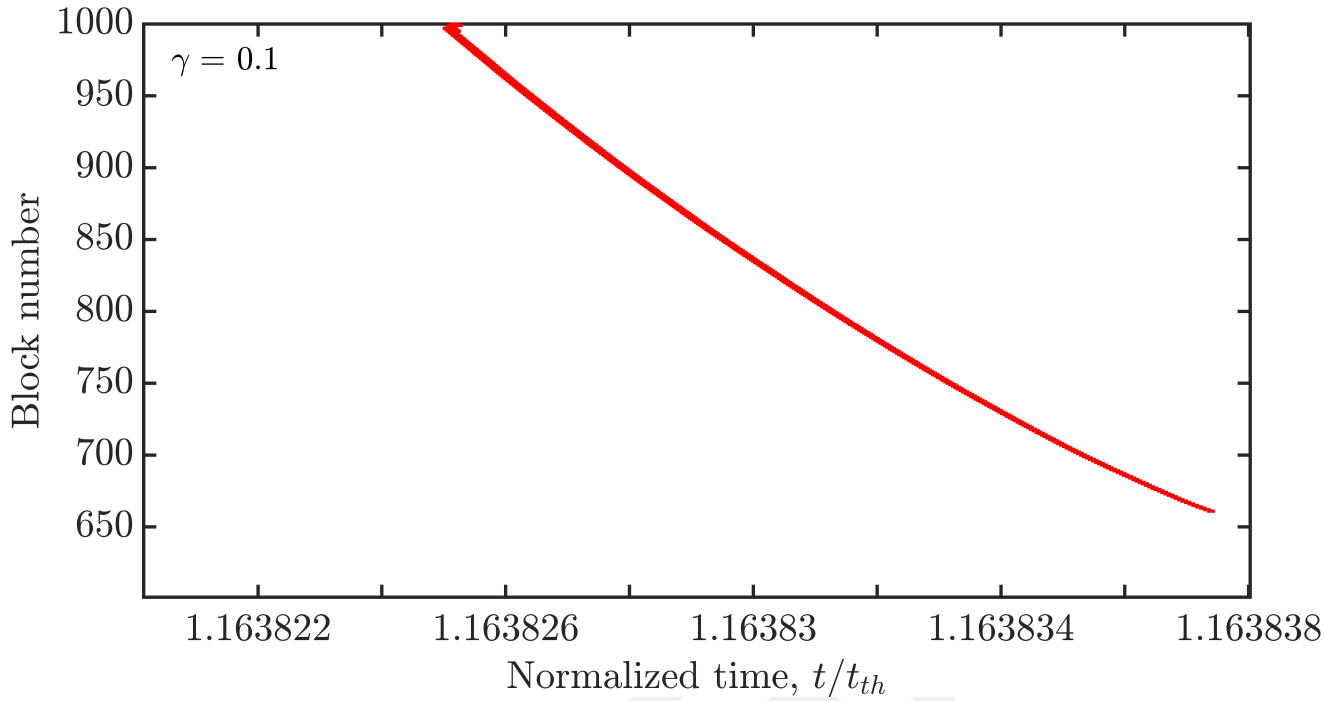

Figure 6.35: The zoomed view of zone number 5 (marked in Figure 6.16-(b)) of case one shows leftward propagation of a slip pulse on the interface. The threshold (normalization) parameter, t_{th}, is equal to $5714.3\ s$. The total duration of the propagation, t_{prop} is equal to $71.01\ ms$.

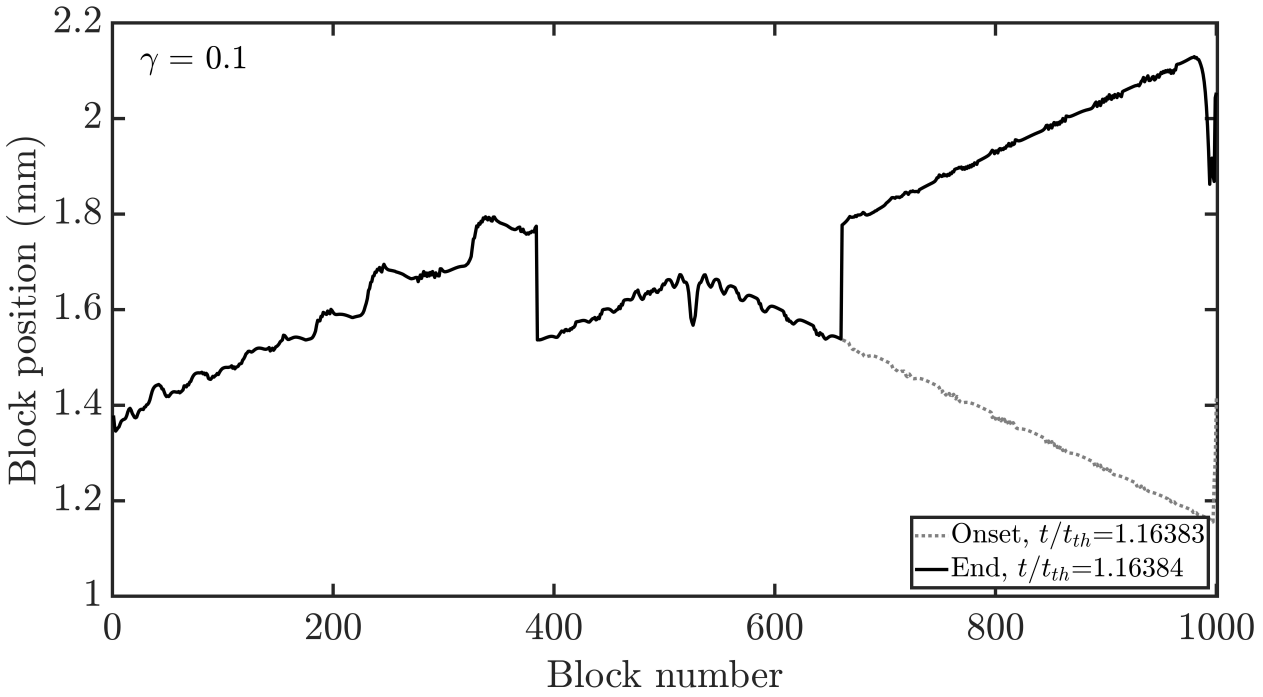

Figure 6.36: The position of the blocks just before and just after the pulse propagation which is shown in Figure 6.27, i.e. case one, zone number 5. The driver position, x_d is 6.65 mm.

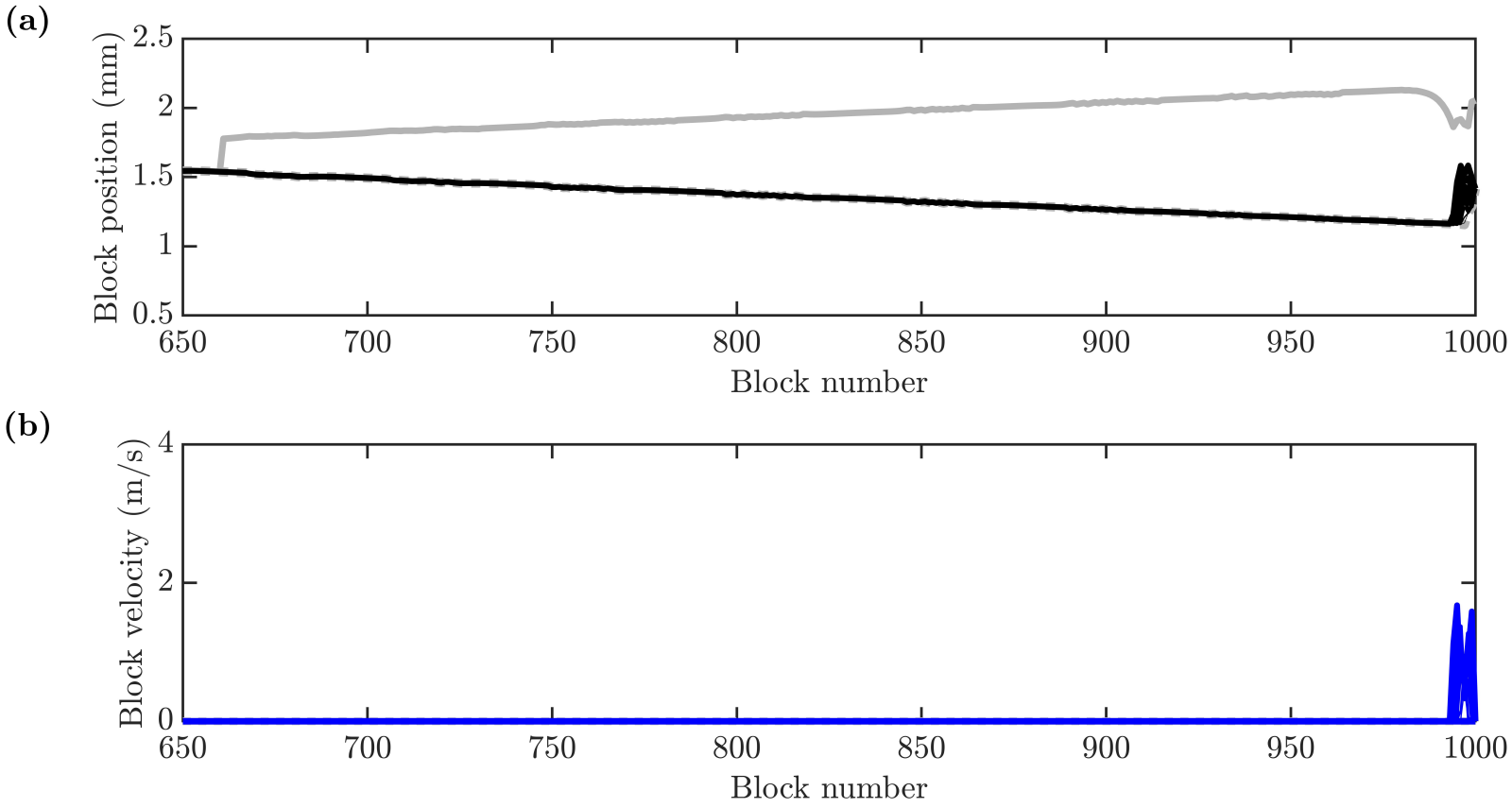

Figure 6.37: The position and velocity of the blocks during the time interval $(0, 0.009t_{prop})$ for the pulse propagation that is shown in Figure 6.35, i.e. case one, zone number 5. The total duration of the propagation, t_{prop} is equal to 71.01 ms.

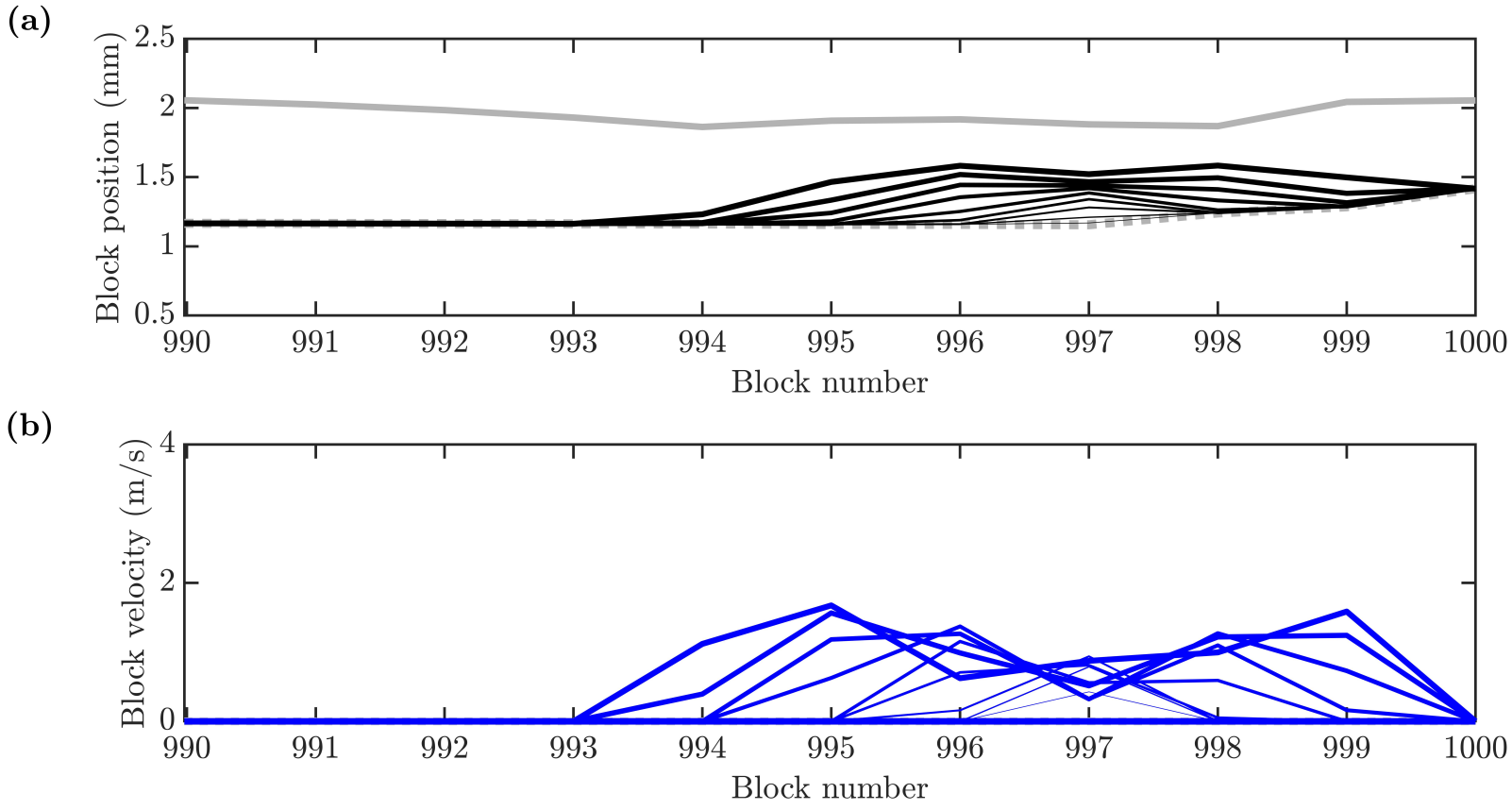

Figure 6.38: A zoomed view of Figure 6.37

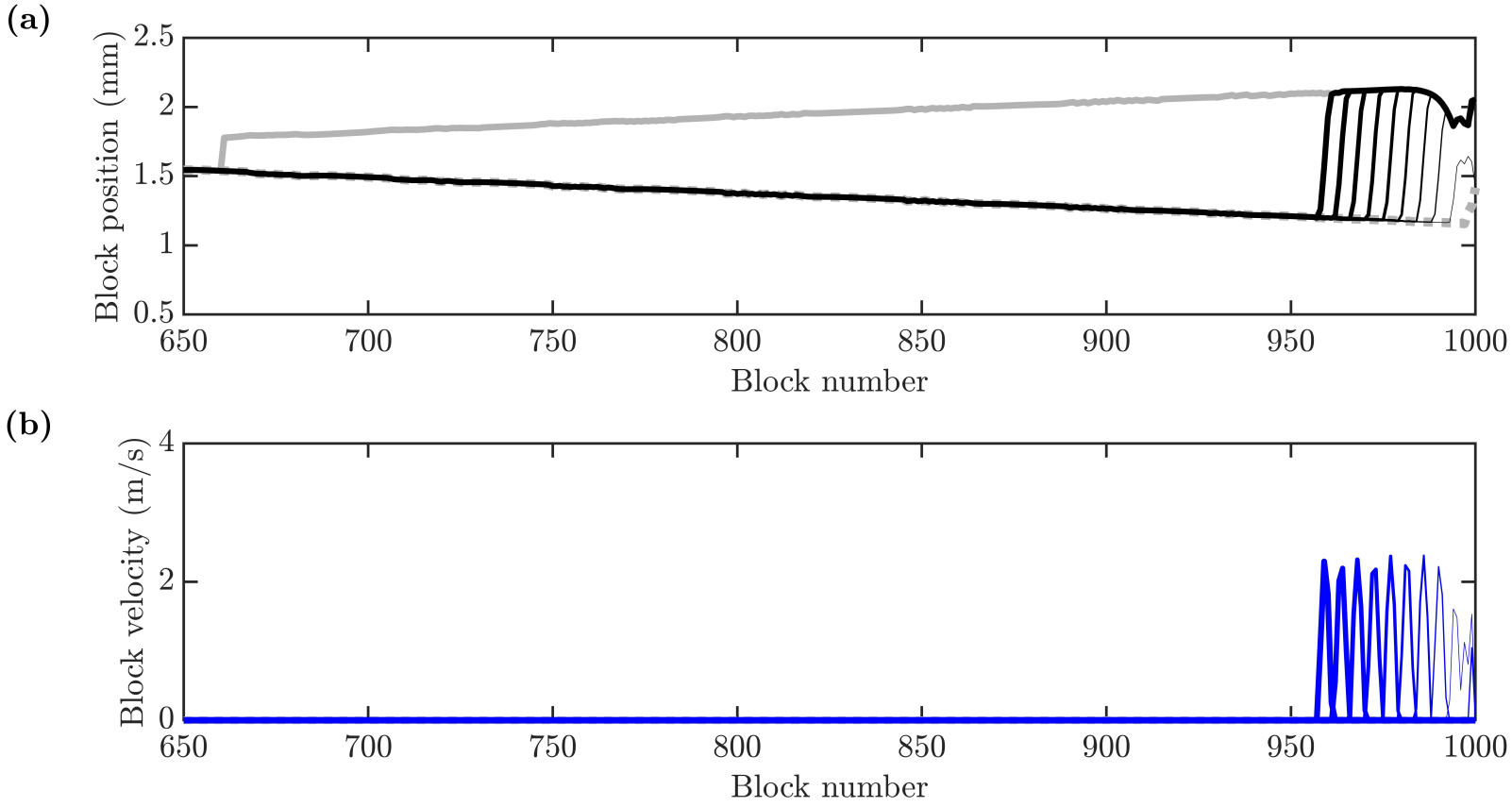

Figure 6.39: The position and velocity of the blocks during the time interval $(0.01t_{prop},\ 0.09t_{prop})$ for the pulse propagation that is shown in Figure 6.35, i.e. case one, zone number 5. The total duration of the propagation, t_{prop} is equal to $71.01\ ms$.

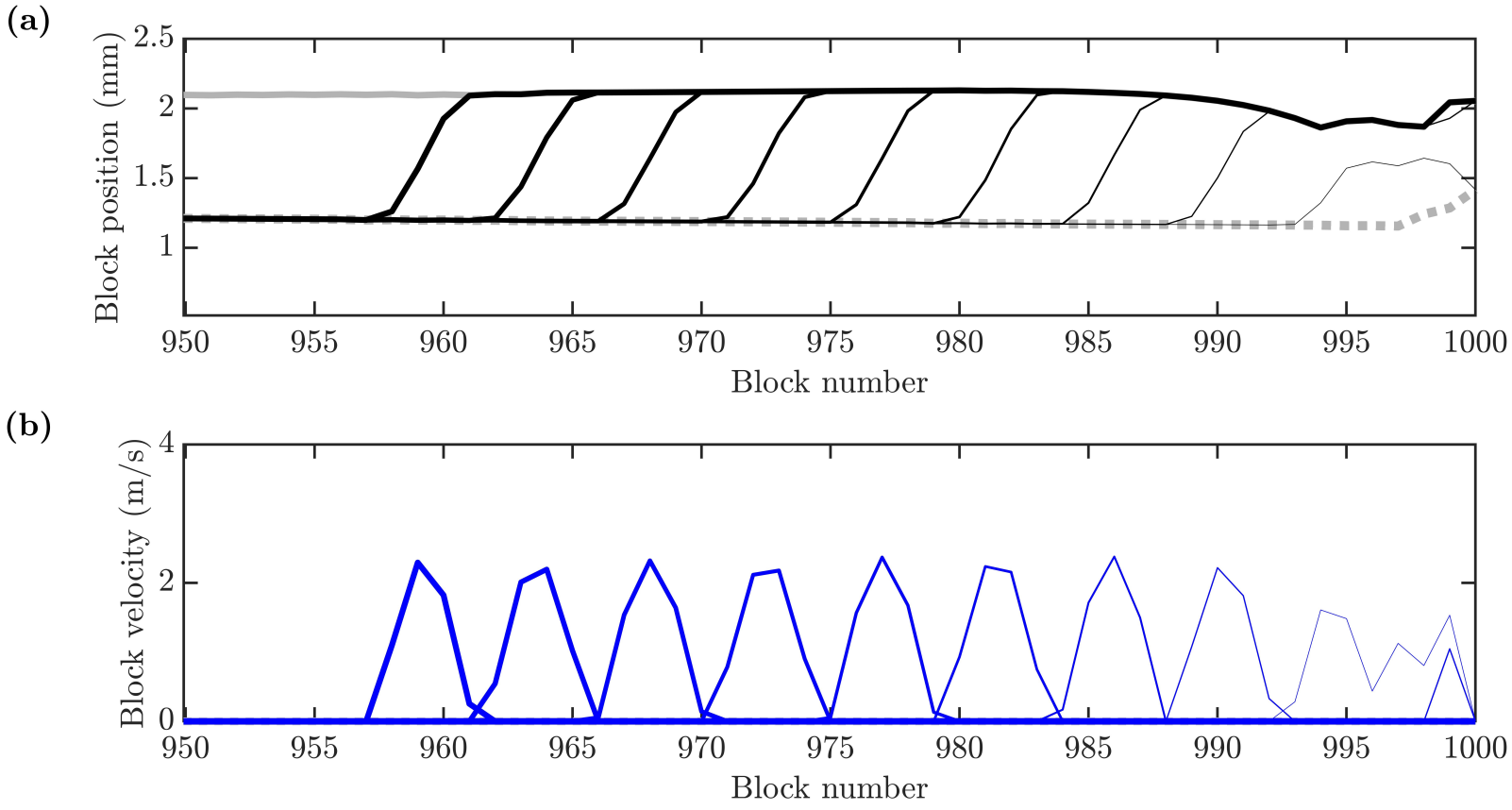

Figure 6.40: A zoomed view of Figure 6.39

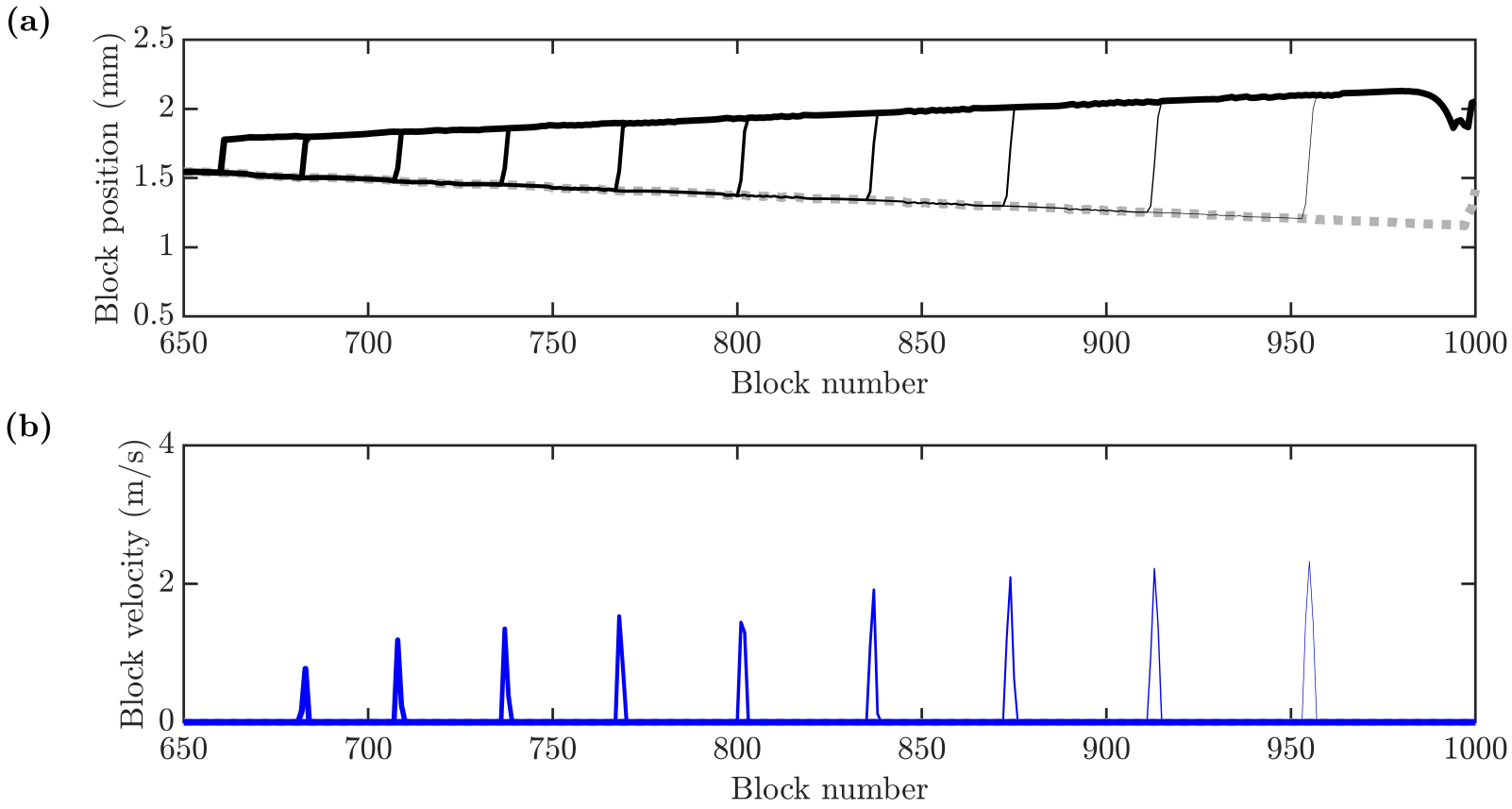

Figure 6.41: The position and velocity of the blocks during the time interval $(0.1t_{prop},\ t_{prop})$ for the pulse propagation that is shown in Figure 6.35, i.e. case one, zone number 5. The total duration of the propagation, t_{prop} is equal to 71.01 ms.

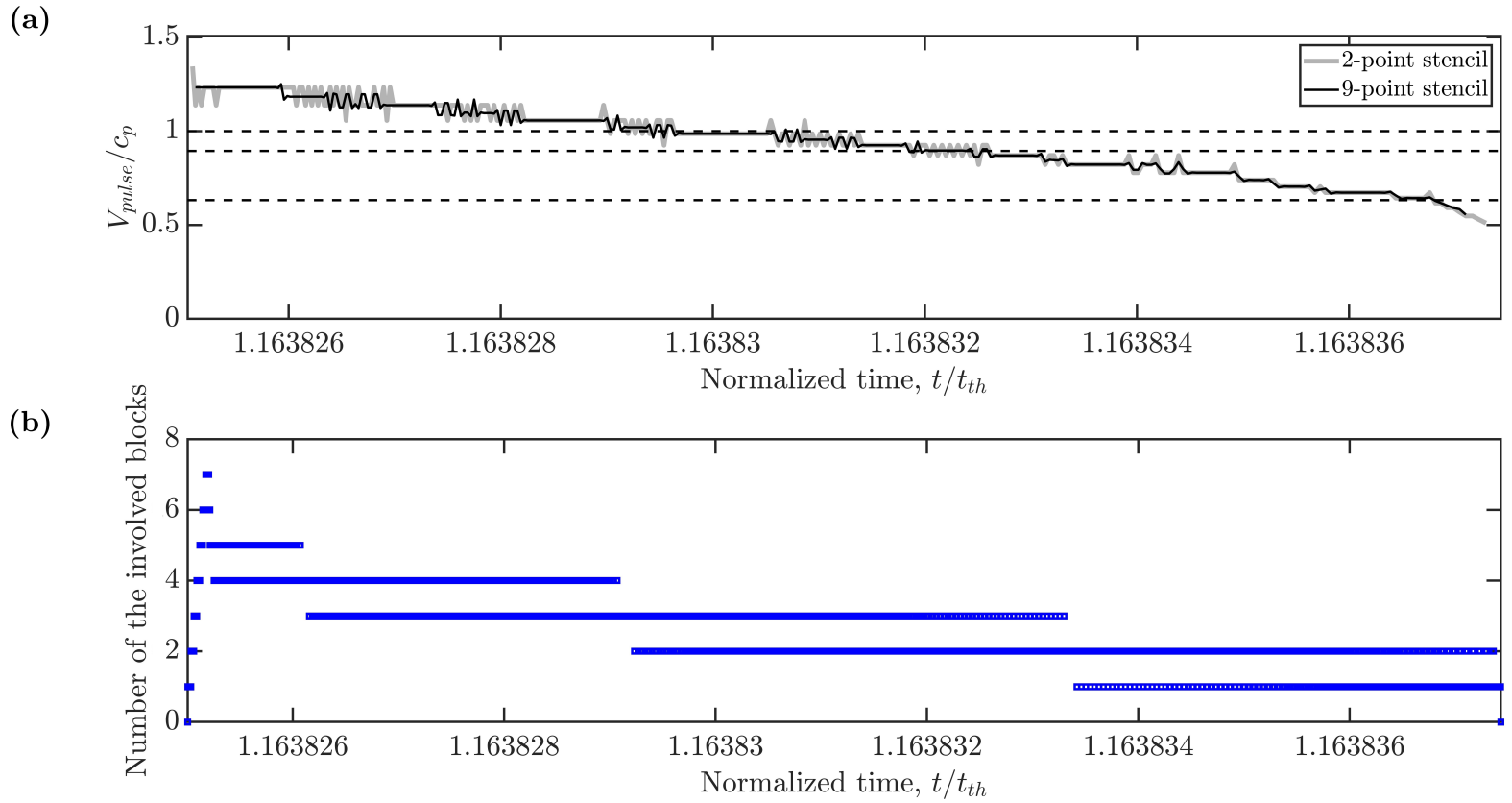

Figure 6.42: The pulse velocity and the number of involved (slipping) blocks during the propagation that is shown in Figure 6.35, i.e. case one, zone number 5. The threshold (normalization) parameter, t_{th}, is equal to 5714.3 s. The total duration of the propagation, t_{prop} is equal to 71.01 ms.

6.3.2 Case 2 ($\gamma = 0.9$)

Figure 6.43 shows the initial position of the blocks when γ is assigned 0.9. Compared with $\gamma = 0.1$ (Figure 6.15) the same blocks are extended more. This was expected as γ determines the amount of the initial spring force on the blocks. The leftmost block is almost $5\ mm$ behind the attachment point of its leaf spring to the driver.The rightmost block is almost $5\ mm$ ahead of the attachment point of its leaf spring to the driver.

Figure 6.44 shows an overall picture of the response of the BK model with $\gamma = 0.9$ (henceforth called case 2) which is composed of: (a) the friction and traction forces, (b) the slippage record of the blocks and (c) the statistics of the sliding blocks as time progresses and the driver moves on. When compared to Figure 6.16-(a), in case 2 the forces rise slower and reach the plateau of dynamic friction later (about $t = 1.5t_{th}$).

There is an essential difference between the slippage records of case 1 and 2 in Figures 6.16-(b) and 6.44-(b). In case 2, up to almost $t = 1.8t_{th}$ still some part of the interface has not undergone any slippage. The ruptures repeatedly occur at the left side of the interface and propagate short distances. A series of isolated slippages start to happen at the termination points of these short ruptures that last for a long time and move in a stable manner to the right end of the interface. Note that the slippage periods of the parallel lines may overlap or not. On the other hand, in case 1, the rupture involve all of the blocks before $t = t_{th}$. Except zone number 3 of Figure 6.16-(b), no series of isolated slippages is observed in case 1 within the investigated time interval. The length of the ruptured parts are generally larger compared to case 2.

The zoomed view of zone number 1 in Figure 6.44-(b) is shown in Figure 6.45. One may cut the figure by vertical lines and project the intersections of the lines and the plot on the y-axis (interface) to study the evolution of the event. The event apparently starts in the form of an "edge crack" which later leaves the edge and becomes a slip pulse that continues to move to the right with a decreasing velocity. The slip pulse propagates on the interface for $t_{prop} = 11.6\ ms$. Figures 6.46 and 6.47 show the block positions just before and just after the propagation of the event. The event starts at block number 1 and ends in block number 63. The more distance is a block from its

zero the more it slides forward. The event starts when the driver is at $x_d = 0.57\ mm$. The crack-like rupture of the event is shown in Figures 6.48 and 6.49 by frames that are provided at $0.01t_{prop} = 116\ \mu s$ intervals. At $t_e = 0.09t_{prop}$ the crack is "healed" at the leftmost block and henceforth becomes a *self-healing pulse* that moves to the right as shown in Figure 6.50 at $0.1t_{prop} = 1.16\ ms$ intervals. The pulse propagation speed is plotted together with the number of the involved blocks against time in Figure 6.51. The propagation velocity is an strictly decreasing function of time and initially possesses an anomalously high value almost equal to $5c_p$. During the crack-like period the number of the involved blocks increases. During the pulse-like period the number of the involved blocks decreases. This can be observed in narrowing of the base of the pulse in Figure 6.50.

The zoomed view of zone number 2 in Figure 6.44-(b) is shown in Figure 6.52. If one draws vertical lines on the figure and project the intersections of the lines and the plot on the y-axis (interface) it can be seen that the event starts as an "inner crack" at block number 63, grows by involving its neighbor blocks on its left and right and later splits into two slip pulse that move to the left (down to block number 1) and to the right (up to block number 122) with a decreasing propagation velocity and a decreasing number of the involved blocks. The duration of the event (which is assumed ended when block number 122 ceases moving) is $t_{prop} = 11.28\ ms$. Figures 6.53 and 6.54 show the effect of the event on the block positions. The event starts when the driver is at $x_d = 1.42\ mm$. The crack-like initiation (nucleation) phase of the event is shown in Figures 6.55 and 6.56 by frames that are provided at $0.01t_{prop} = 112.8\ \mu s$ intervals. At $t_e = 0.09t_{prop}$ the crack is not split yet. As shown in Figure 6.57, at $t_e = 0.1t_{prop} = 1.128\ ms$ the crack does not exist any longer and the pair of generated pulses move in opposite directions till the end of the event. The propagation speeds of the pulses are plotted together with the number of the involved blocks against time in Figure 6.58.

The zoomed view of zone number 3 in Figure 6.44-(b) is shown in Figure 6.59. By pursuing the projection of the sections of the plot on the y-axis it can be observed that the single pulse event starts with a low propagation speed at block number 53, and then experiences two intervals of successive acceleration and deceleration till its end at block number 170. The duration of the event is $t_{prop} = 24.88\ ms$. Figures 6.60 and

6.61 show the change in the block positions due to this event. The event starts when the driver is at $x_d = 2.15\ mm$. In contrast to the previous events the event does not have a crack-like nucleation and is pulse-like from the very beginning as shown in Figures 6.62 and 6.63 by frames that are provided at $0.01t_{prop} = 248.8\ \mu s$ intervals. The pulse propagation continues as shown in Figure 6.57 at $0.1t_{prop} = 2.488\ ms$ intervals. The propagation speeds of the pulses are plotted together with the number of the involved blocks against time in Figure 6.65.

The zoomed view of zone number 4 in Figure 6.44-(b) is shown in Figure 6.66. Each of the inclined paralell "lines" is indeed composed of single block slippage periods that do not overlap. If one looks at the interface at equi-space sections of time these slippage would be seen as a *train of pulses* [75] that slowly travels to the right with a constant velocity. The propagation velocity of this train (obtained from the slope of the "line") is nearly equal to $0.1\ m/s$, i.e. ten times slower than the similar event of case 1 that is present in zone number 3 of Figure 6.16-(b).

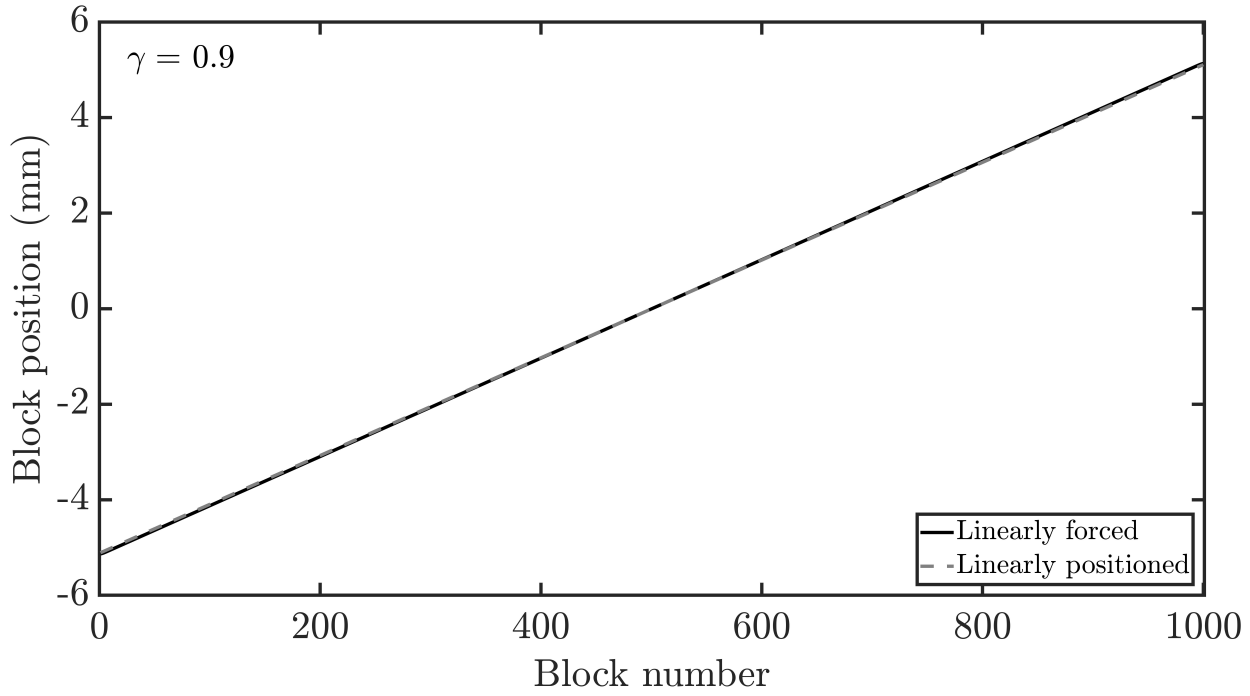

Figure 6.43: The initial block positions for case two, $\gamma = 0.9$, that assumes a linear spring-force distribution on the blocks in which the leftmost experiences $\gamma\mu_s N$ and the rightmost block experiences $-\gamma\mu_s N$

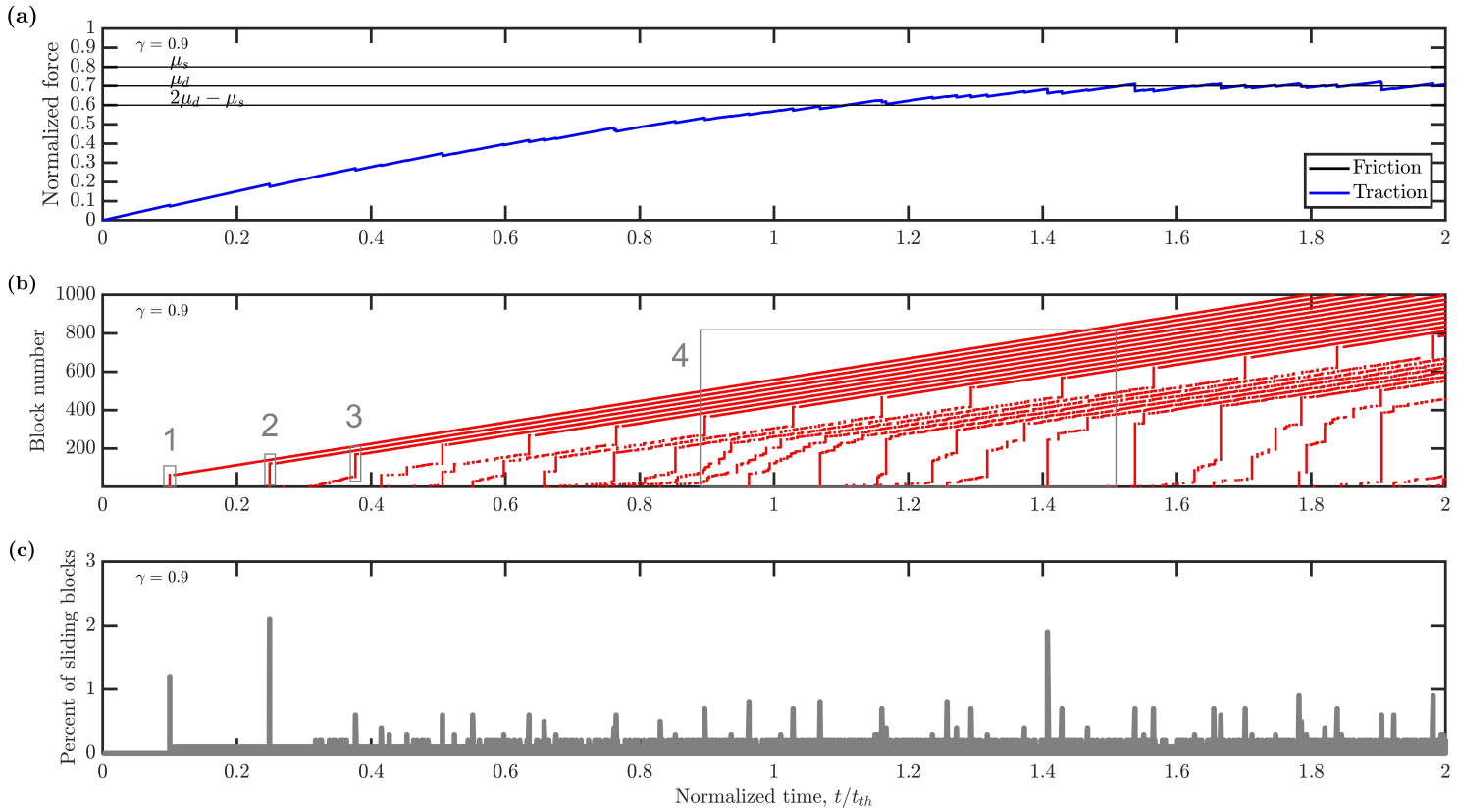

Figure 6.44: Response of the BK model in case two, linear spring force with $\gamma = 0.9$ with the free boundary conditions: (a) friction and the driver traction, (b) the block slippage history, and (c) the percent of the slipping blocks at each time step

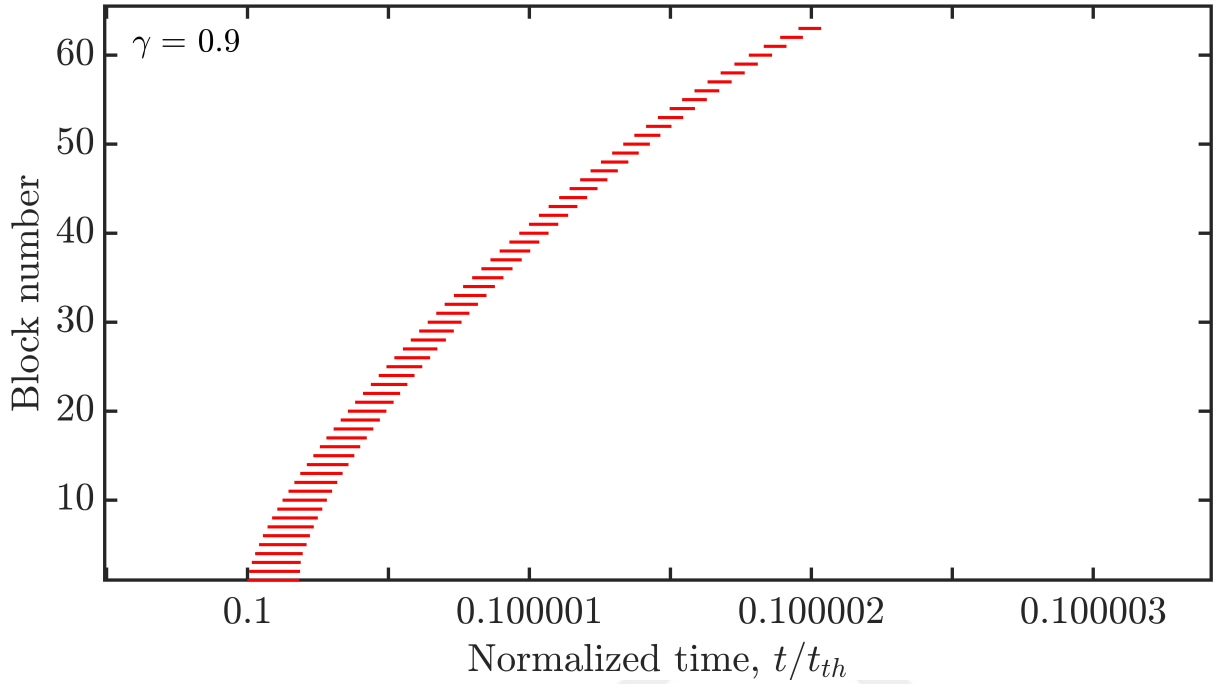

Figure 6.45: The zoomed view of zone number 1 (marked in Figure 6.44-(b)) of case two shows a slip pulse propagation on the interface. The threshold (normalization) parameter, t_{th}, is equal to $5714.3\ s$. The total duration of the propagation, t_{prop} is equal to $11.6\ ms$.

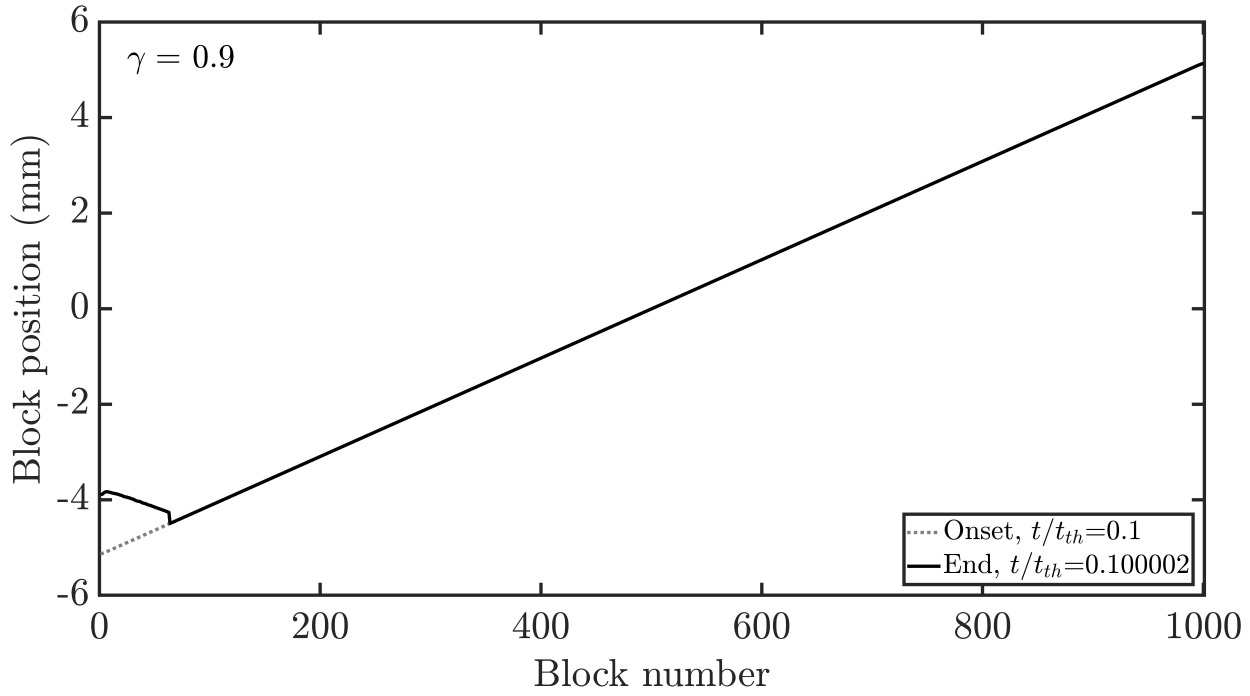

Figure 6.46: The position of the blocks just before and just after the pulse propagation which is shown in Figure 6.45, i.e. case two, zone number 1. The driver position, x_d is $0.57\ mm$.

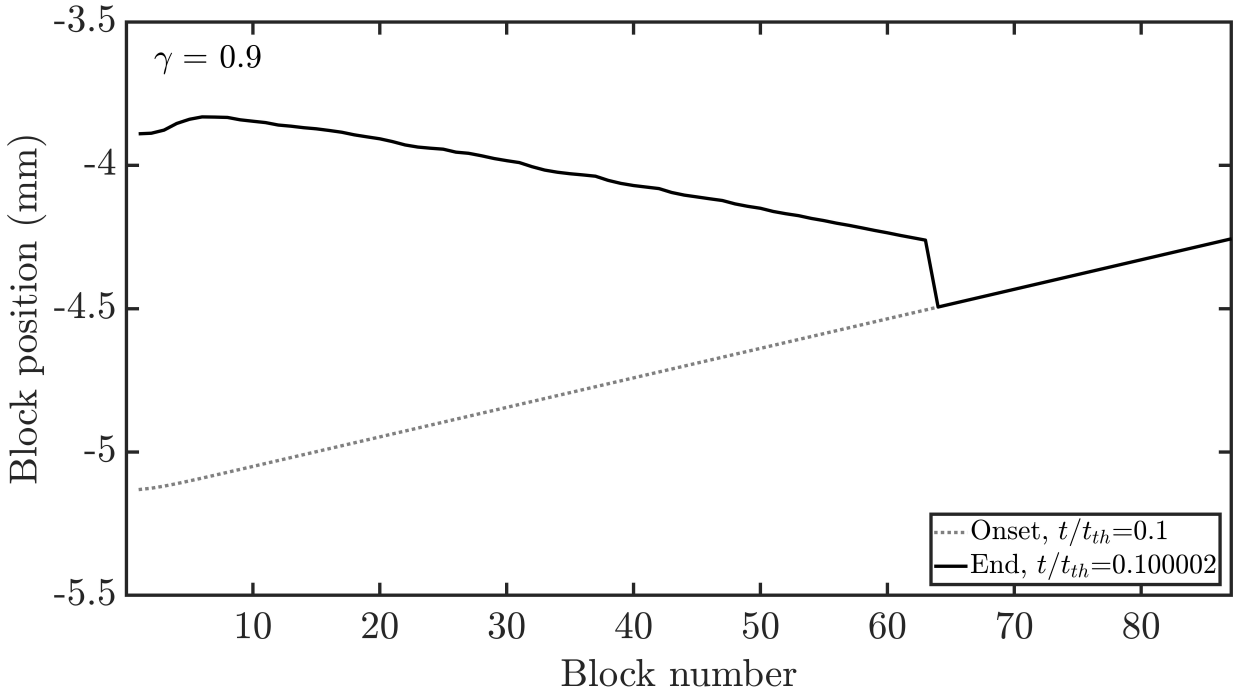

Figure 6.47: A zoomed view of Figure 6.46

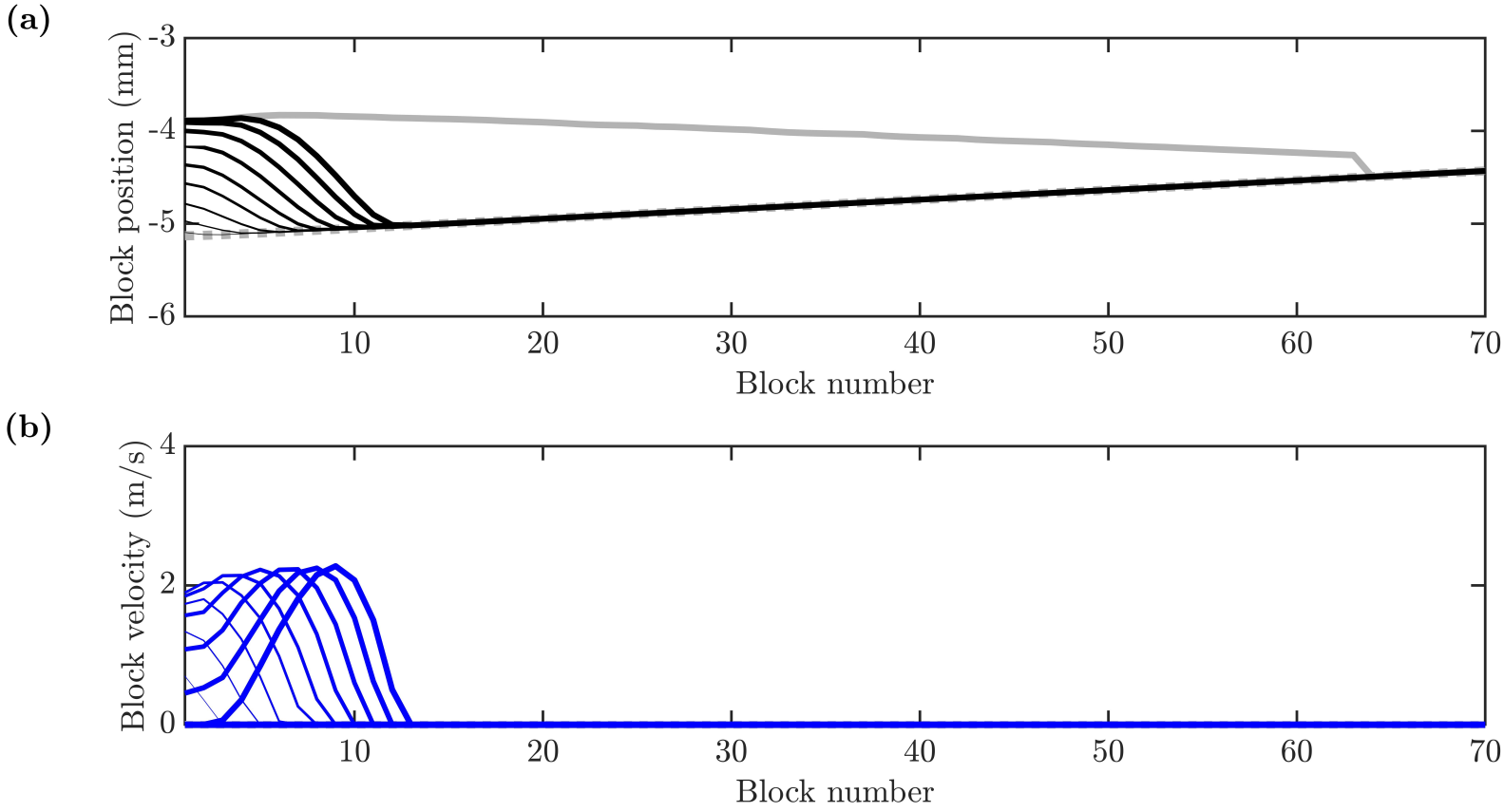

Figure 6.48: The position and velocity of the blocks during the time interval $(0,\ 0.09t_{prop})$ for the pulse propagation that is shown in Figure 6.45, i.e. case two, zone number 1. The total duration of the propagation, t_{prop} is equal to 11.6 ms.

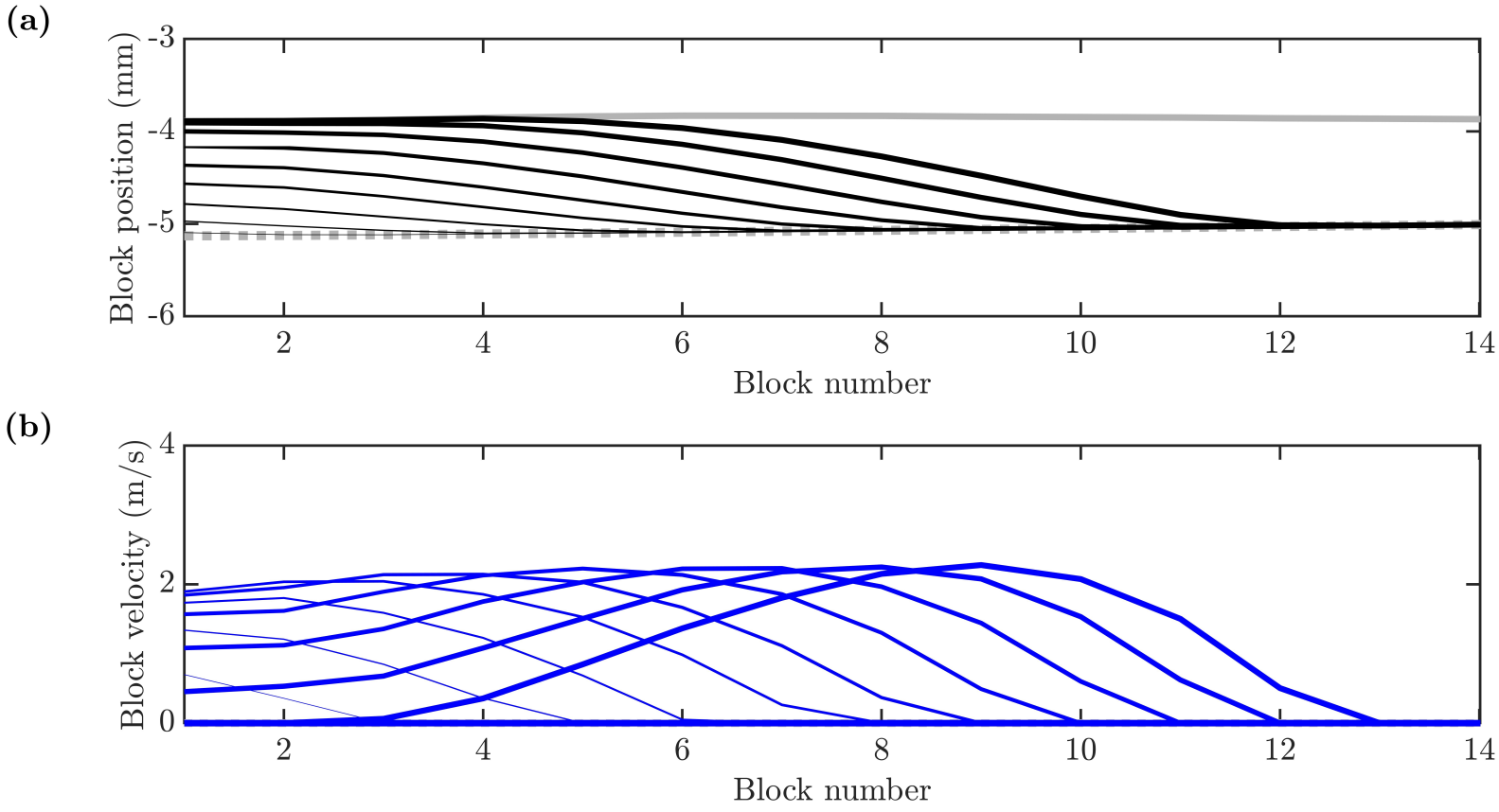

Figure 6.49: A zoomed view of Figure 6.48

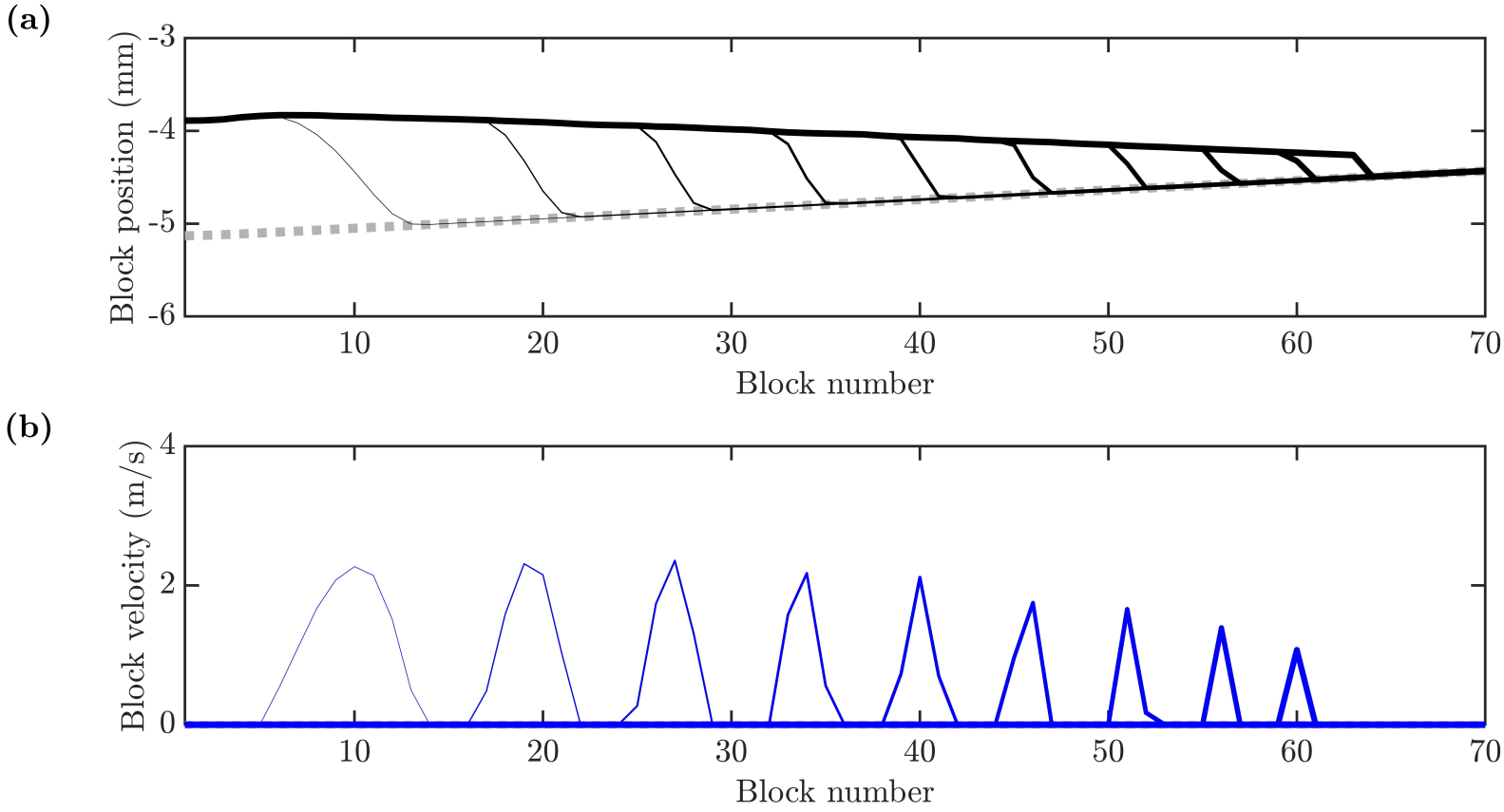

Figure 6.50: The position and velocity of the blocks during the time interval $(0.1t_{prop},\ t_{prop})$ for the pulse propagation that is shown in Figure 6.45, i.e. case two, zone number 1. The total duration of the propagation, t_{prop} is equal to $11.6\ ms$.

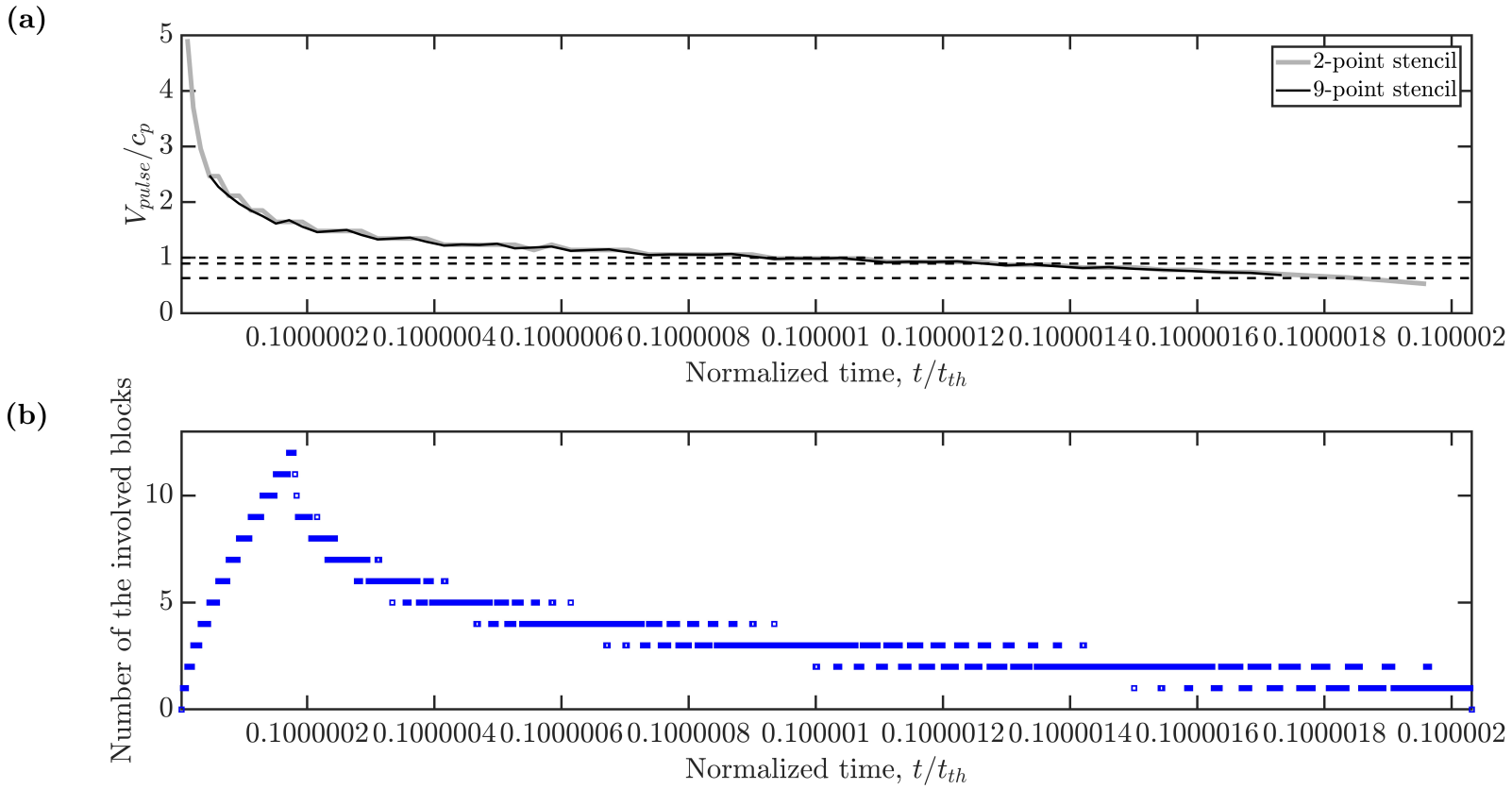

Figure 6.51: The pulse velocity and the number of involved (slipping) blocks during the propagation that is shown in Figure 6.45, i.e. case two, zone number 1. The threshold (normalization) parameter, t_{th}, is equal to $5714.3\ s$. The total duration of the propagation, t_{prop} is equal to $11.6\ ms$.

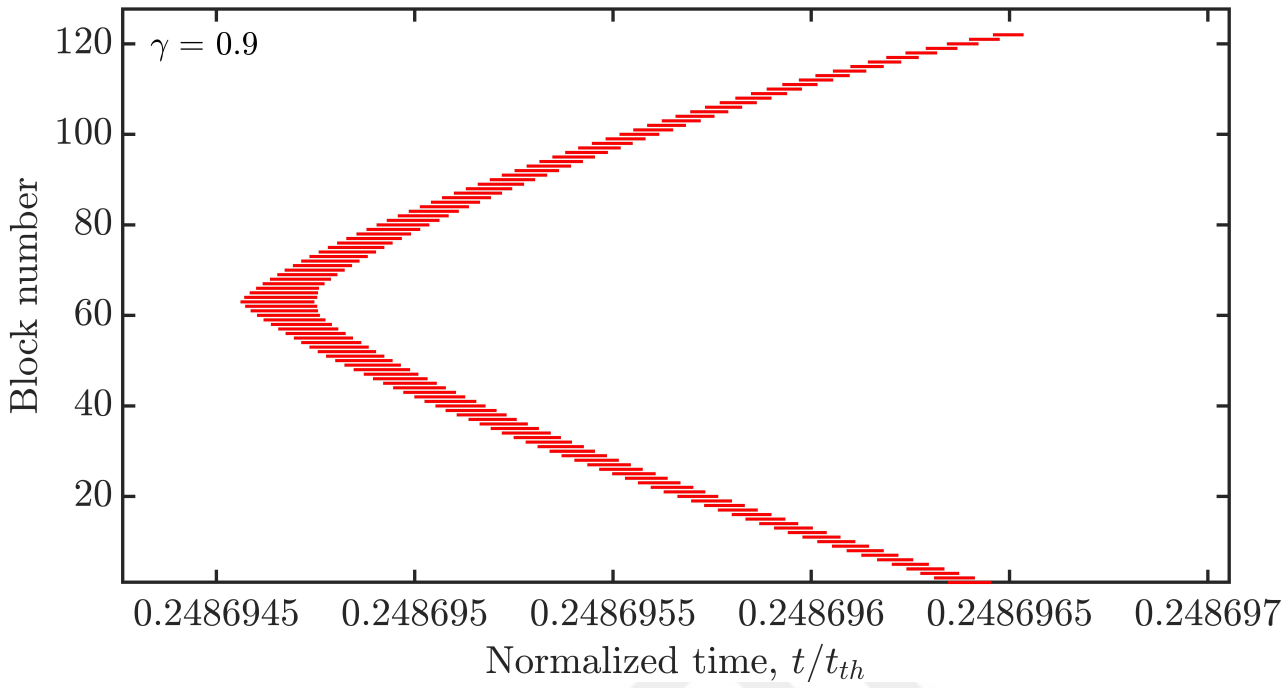

Figure 6.52: The zoomed view of zone number 2 (marked in Figure 6.44-(b)) of case two shows nucleation of a crack that is later divided into two slip pulses that propagate in the opposite directions on the interface. The threshold (normalization) parameter, t_{th}, is equal to $5714.3\ s$. The total duration of the propagation, t_{prop} is equal to $11.28\ ms$.

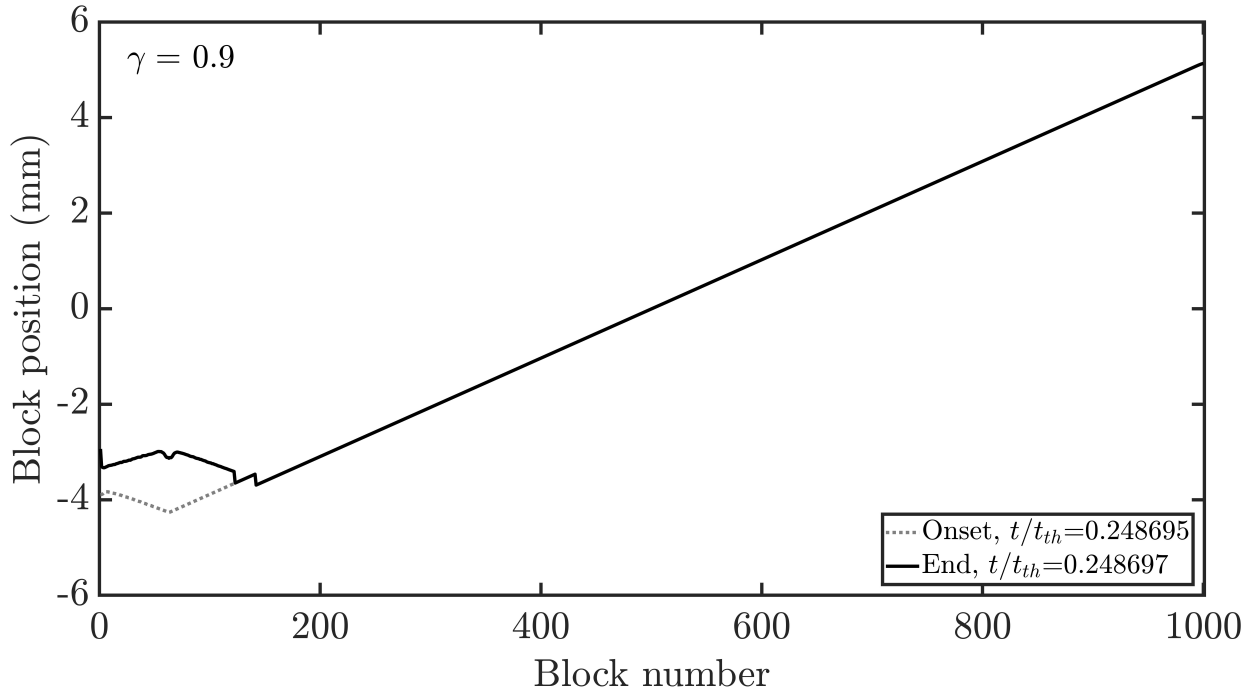

Figure 6.53: The position of the blocks just before and just after the event which is shown in Figure 6.52, i.e. case two, zone number 2. The driver position, x_d is $1.42\ mm$.

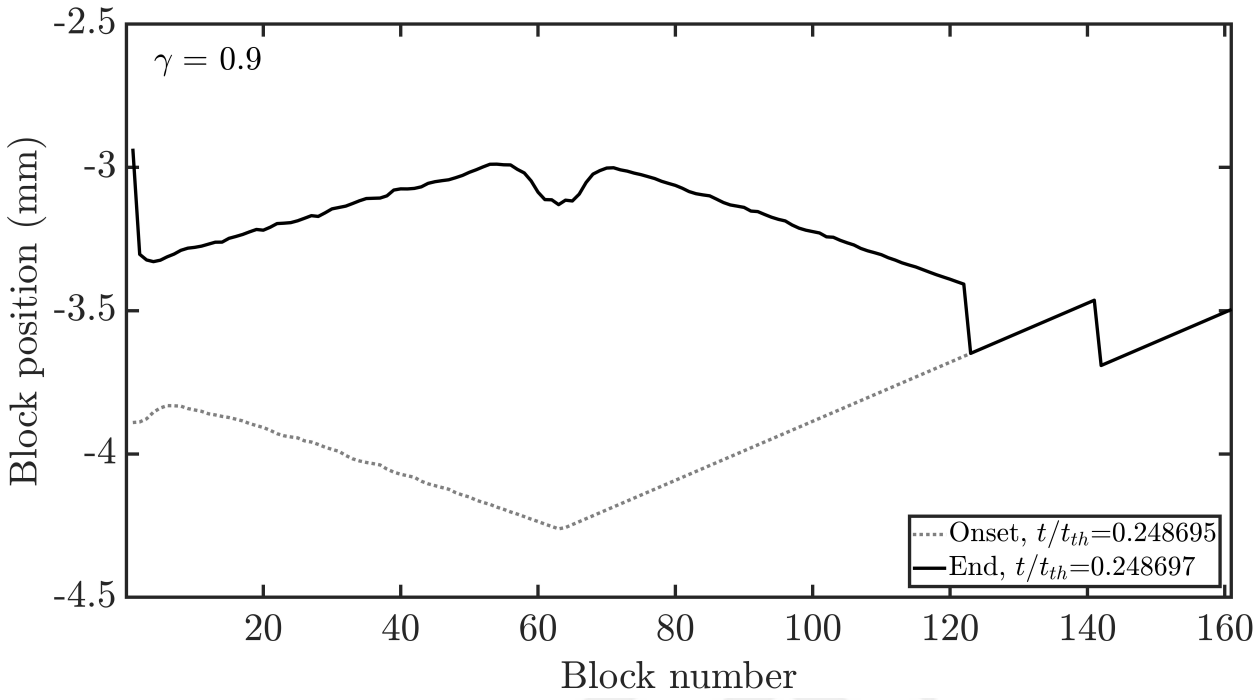

Figure 6.54: A zoomed view of Figure 6.53

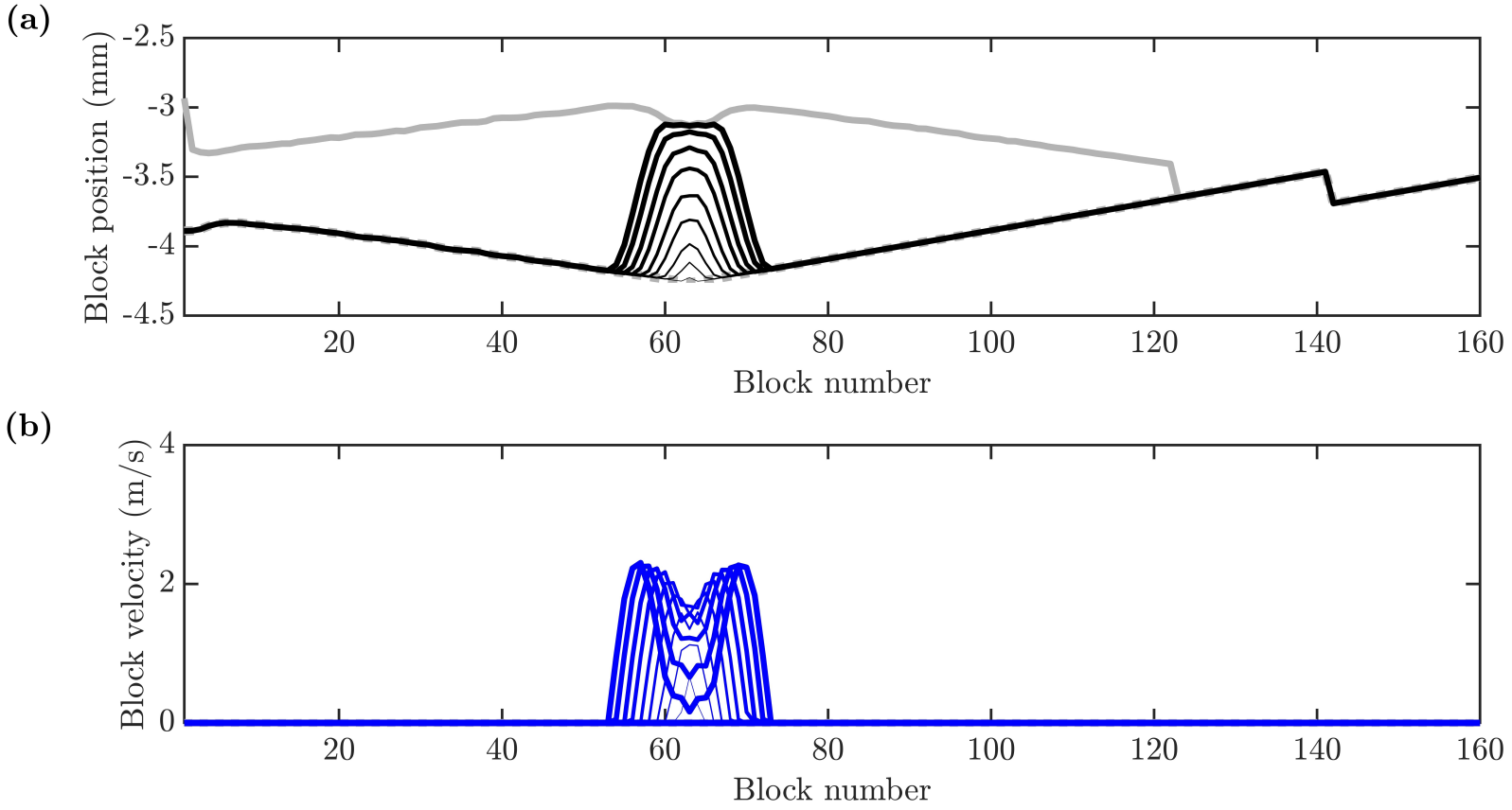

Figure 6.55: The position and velocity of the blocks during the time interval $(0,\ 0.09t_{prop})$ for the pulse propagation that is shown in Figure 6.52, i.e. case two, zone number 2. The total duration of the propagation, t_{prop} is equal to $11.28\ ms$.

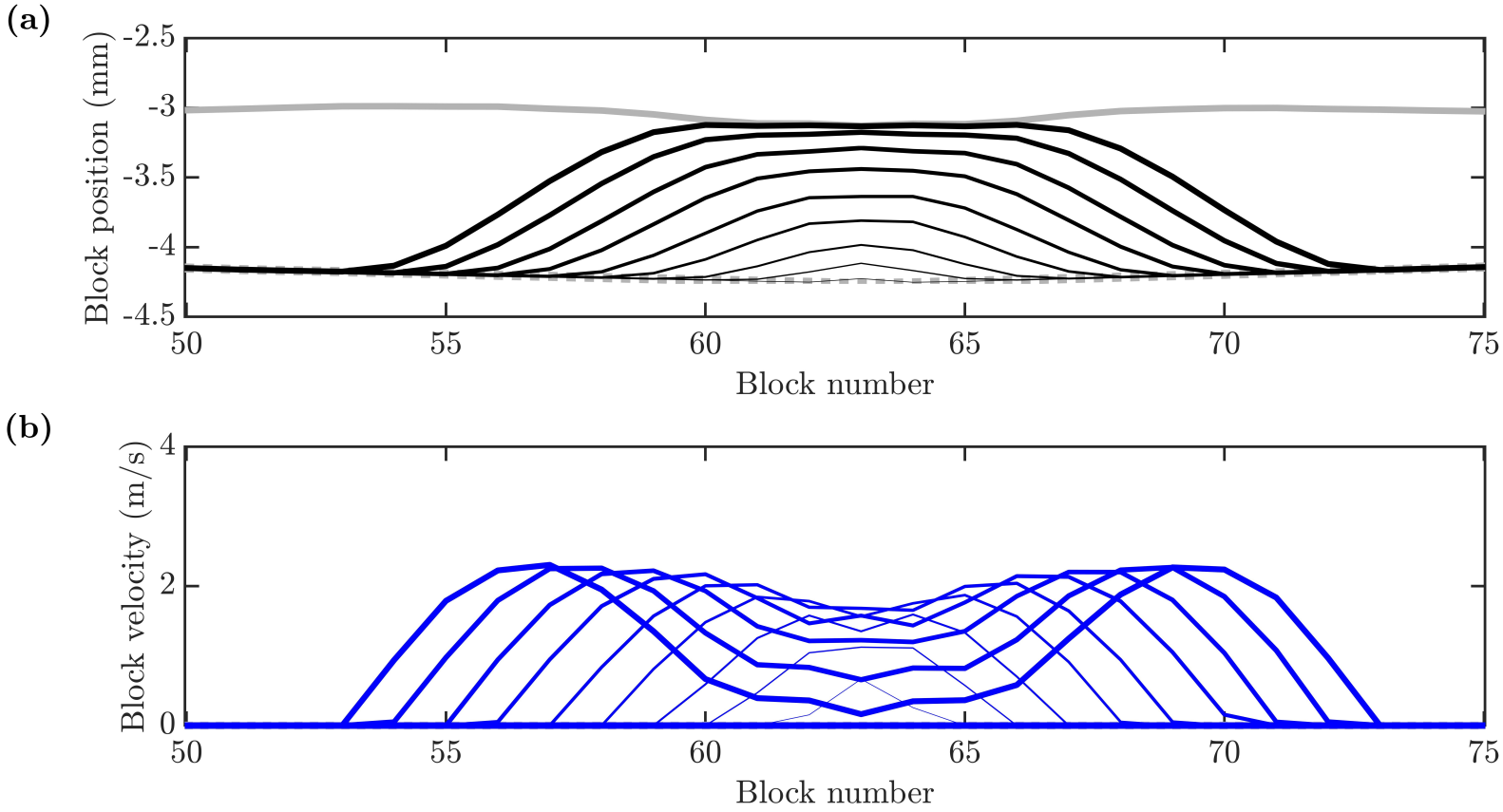

Figure 6.56: A zoomed view of Figure 6.55

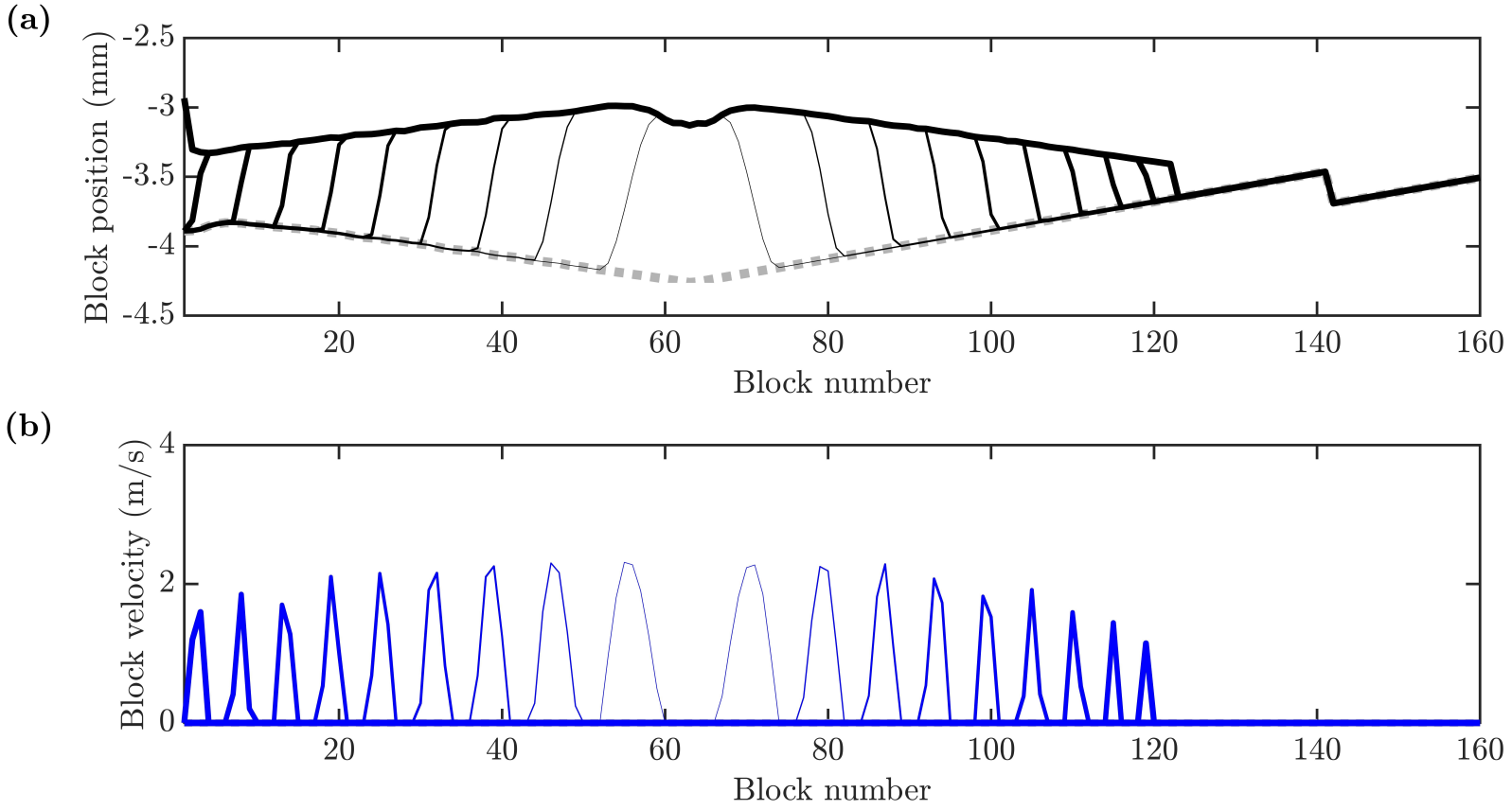

Figure 6.57: The position and velocity of the blocks during the time interval $(0.1t_{prop},\ t_{prop})$ for the pulse propagation that is shown in Figure 6.52, i.e. case two, zone number 2. The total duration of the propagation, t_{prop} is equal to $11.28\ ms$.

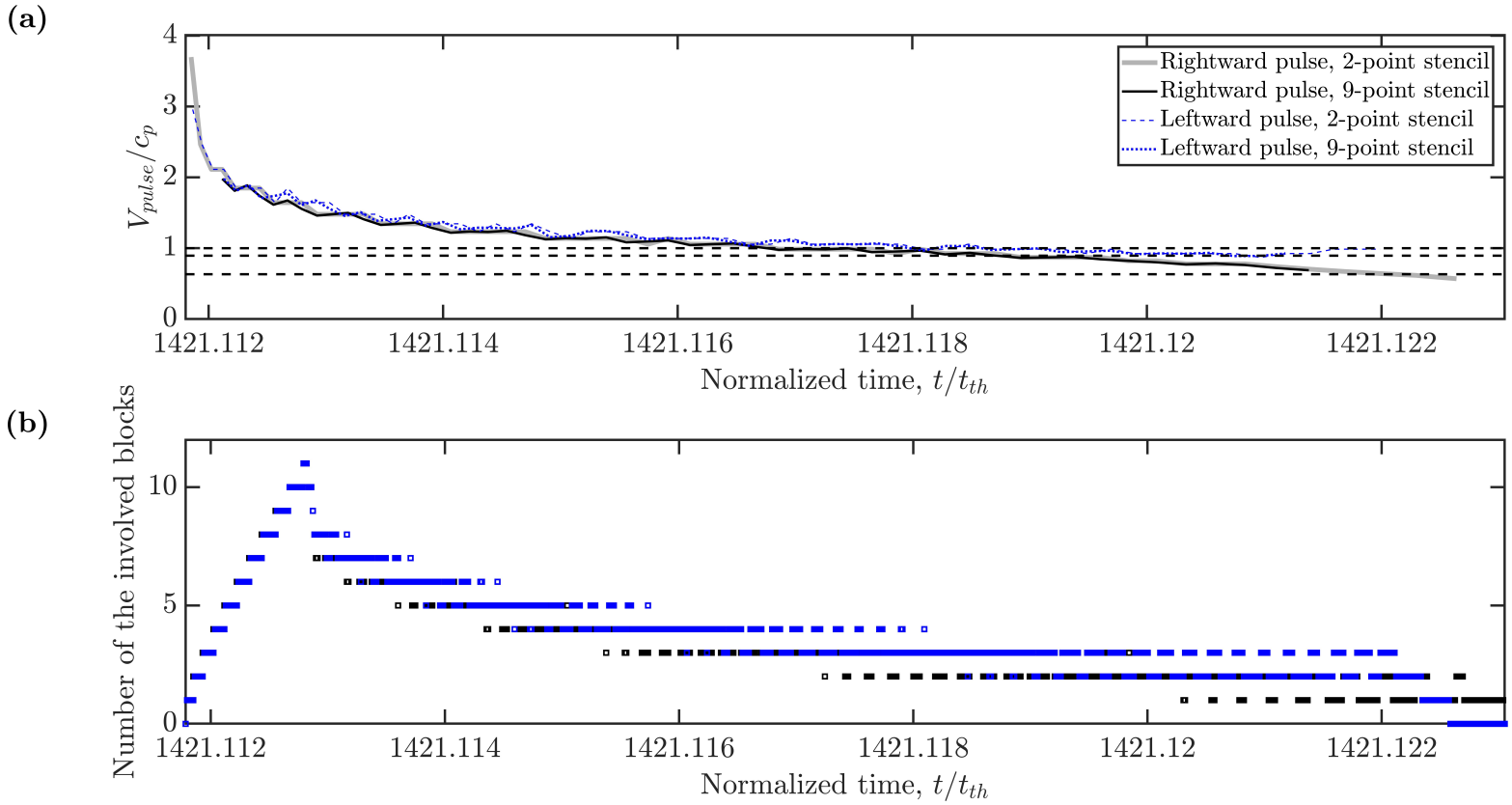

Figure 6.58: The pulse velocity and the number of involved (slipping) blocks during the propagation that is shown in Figure 6.52, i.e. case two, zone number 2. The threshold (normalization) parameter, t_{th}, is equal to $5714.3\ s$. The total duration of the propagation, t_{prop} is equal to $11.28\ ms$.

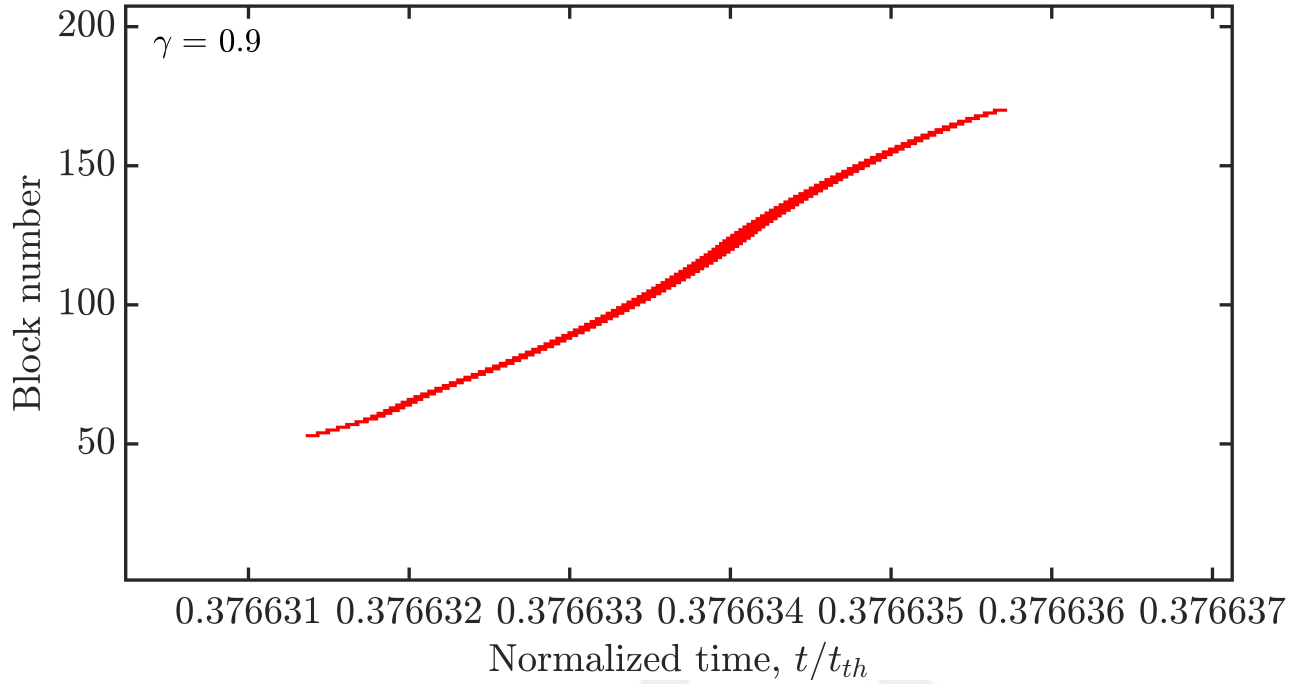

Figure 6.59: The zoomed view of zone number 3 (marked in Figure 6.44-(b)) of case two shows propagation of a slip pulse on the interface. The threshold (normalization) parameter, t_{th}, is equal to $5714.3\ s$. The total duration of the propagation, t_{prop} is equal to $24.88\ ms$.

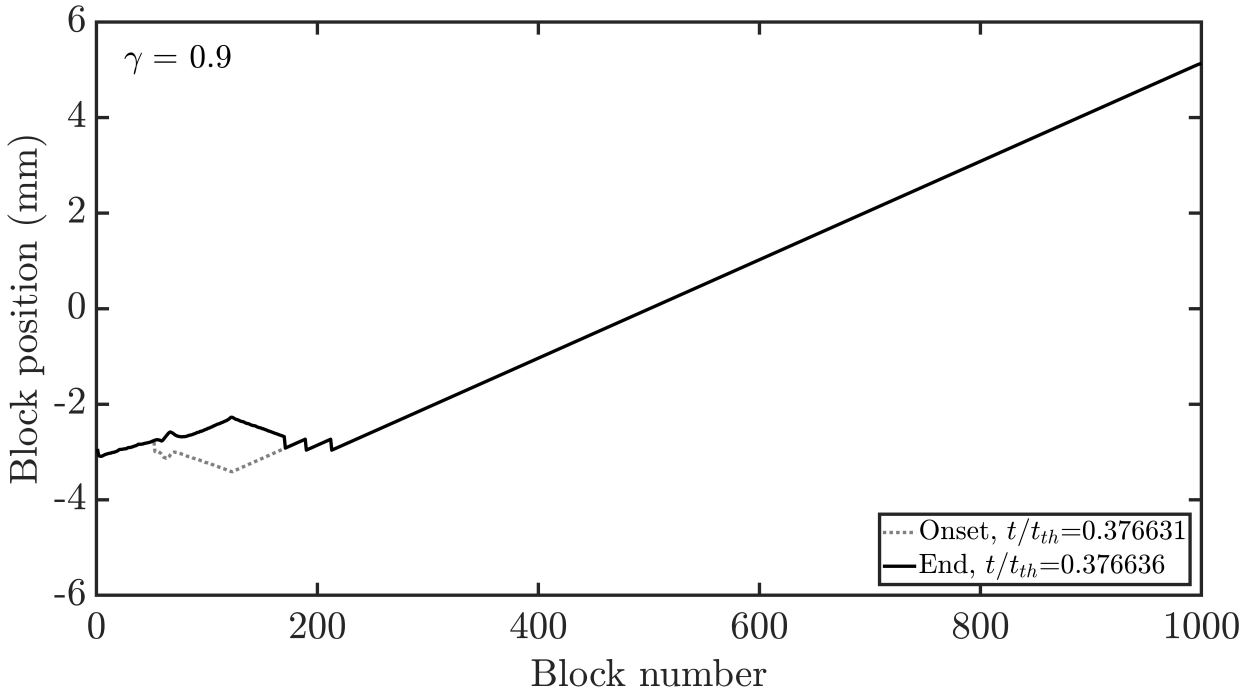

Figure 6.60: The position of the blocks just before and just after the event which is shown in Figure 6.59, i.e. case two, zone number 3. The driver position, x_d is 2.15 mm.

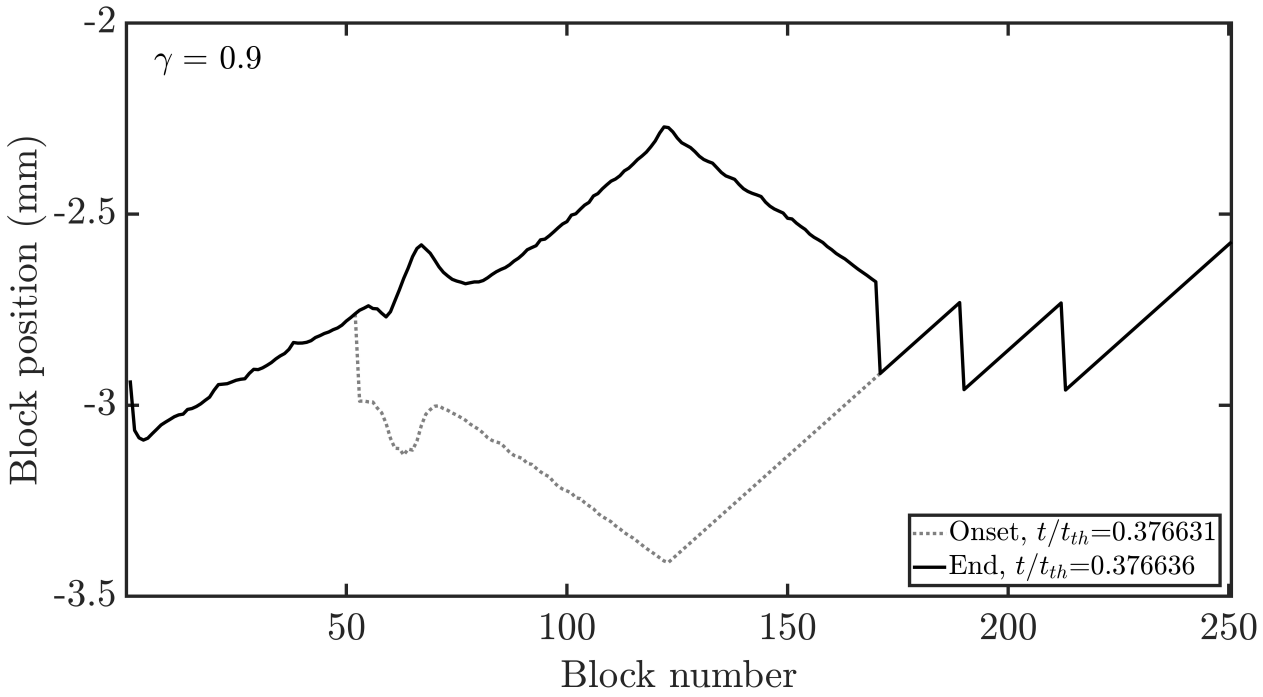

Figure 6.61: A zoomed view of Figure 6.60

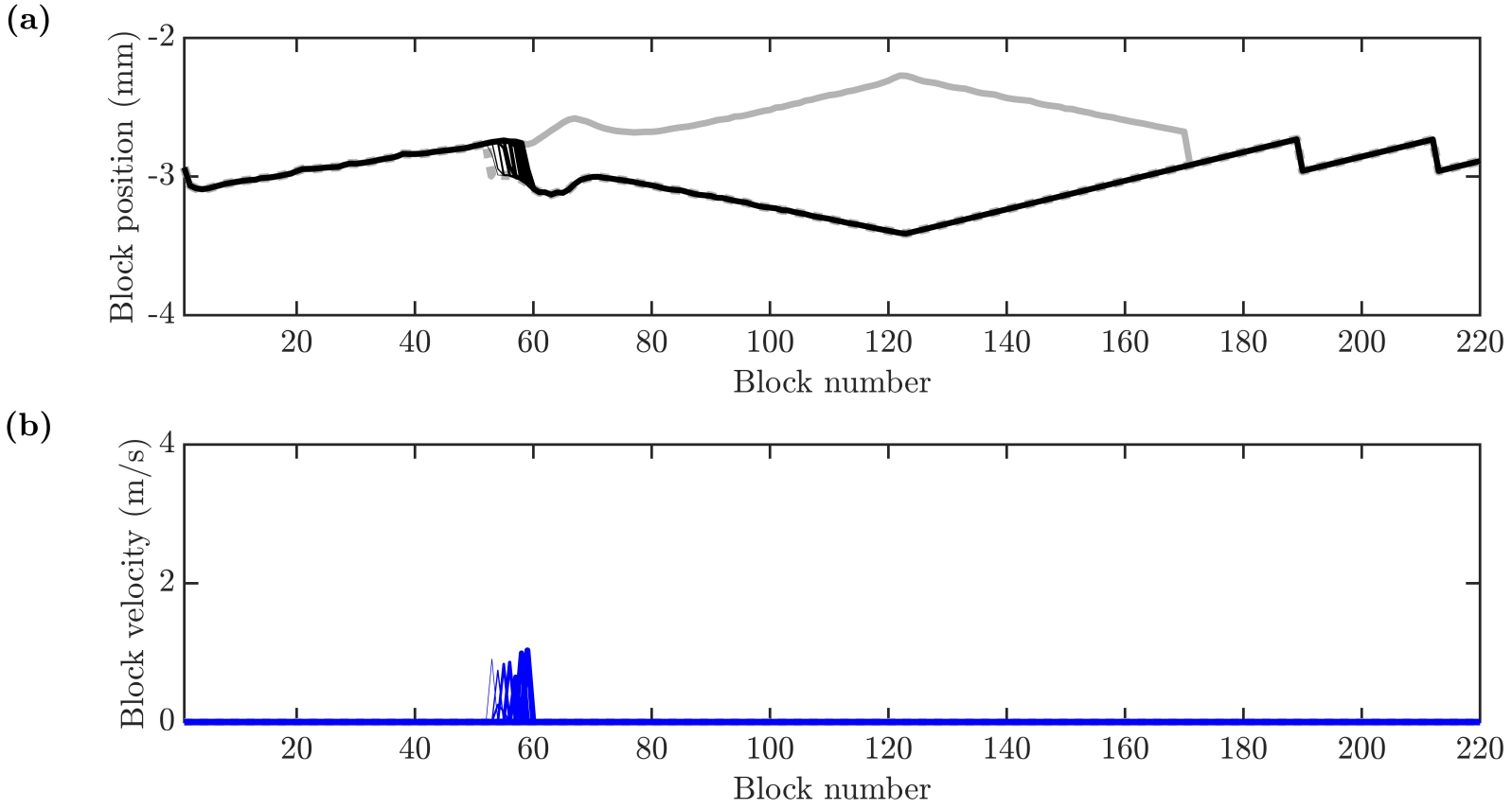

Figure 6.62: The position and velocity of the blocks during the time interval $(0,\ 0.09t_{prop})$ for the pulse propagation that is shown in Figure 6.59, i.e. case two, zone number 3. The total duration of the propagation, t_{prop} is equal to $24.88\ ms$.

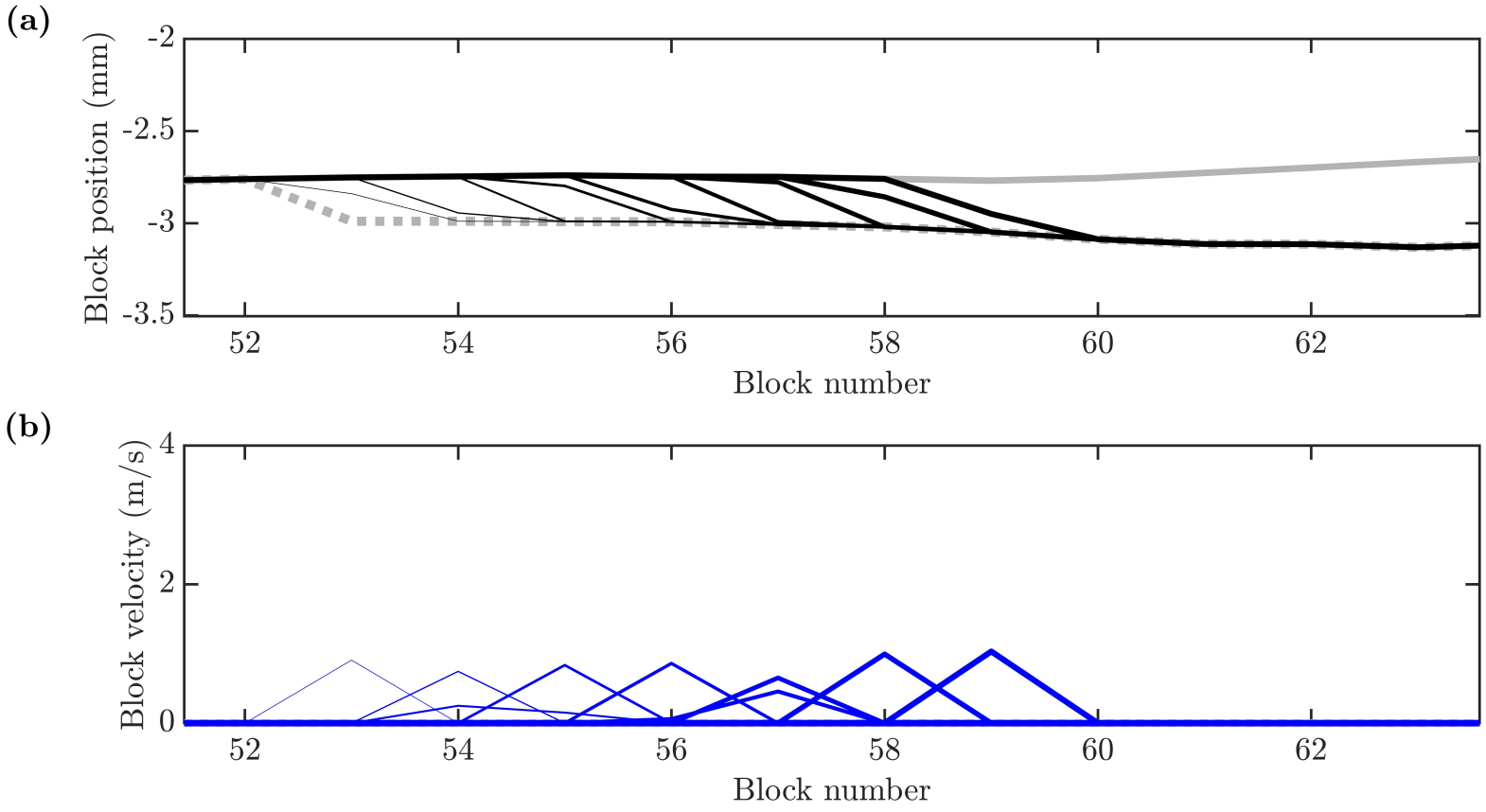

Figure 6.63: A zoomed view of Figure 6.62

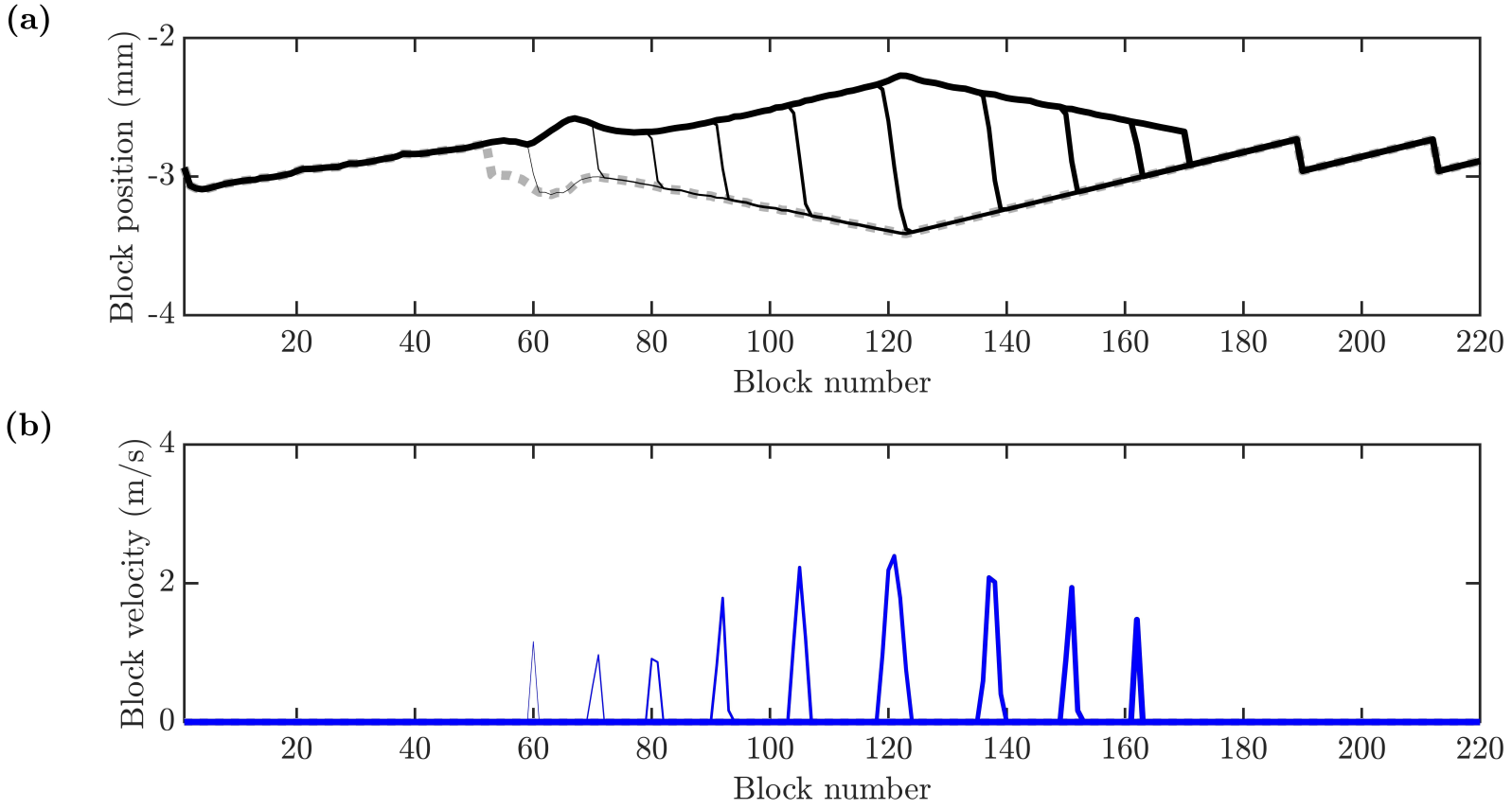

Figure 6.64: The position and velocity of the blocks during the time interval $(0.1t_{prop},\ t_{prop})$ for the pulse propagation that is shown in Figure 6.59, i.e. case two, zone number 3. The total duration of the propagation, t_{prop} is equal to $24.88\ ms$.

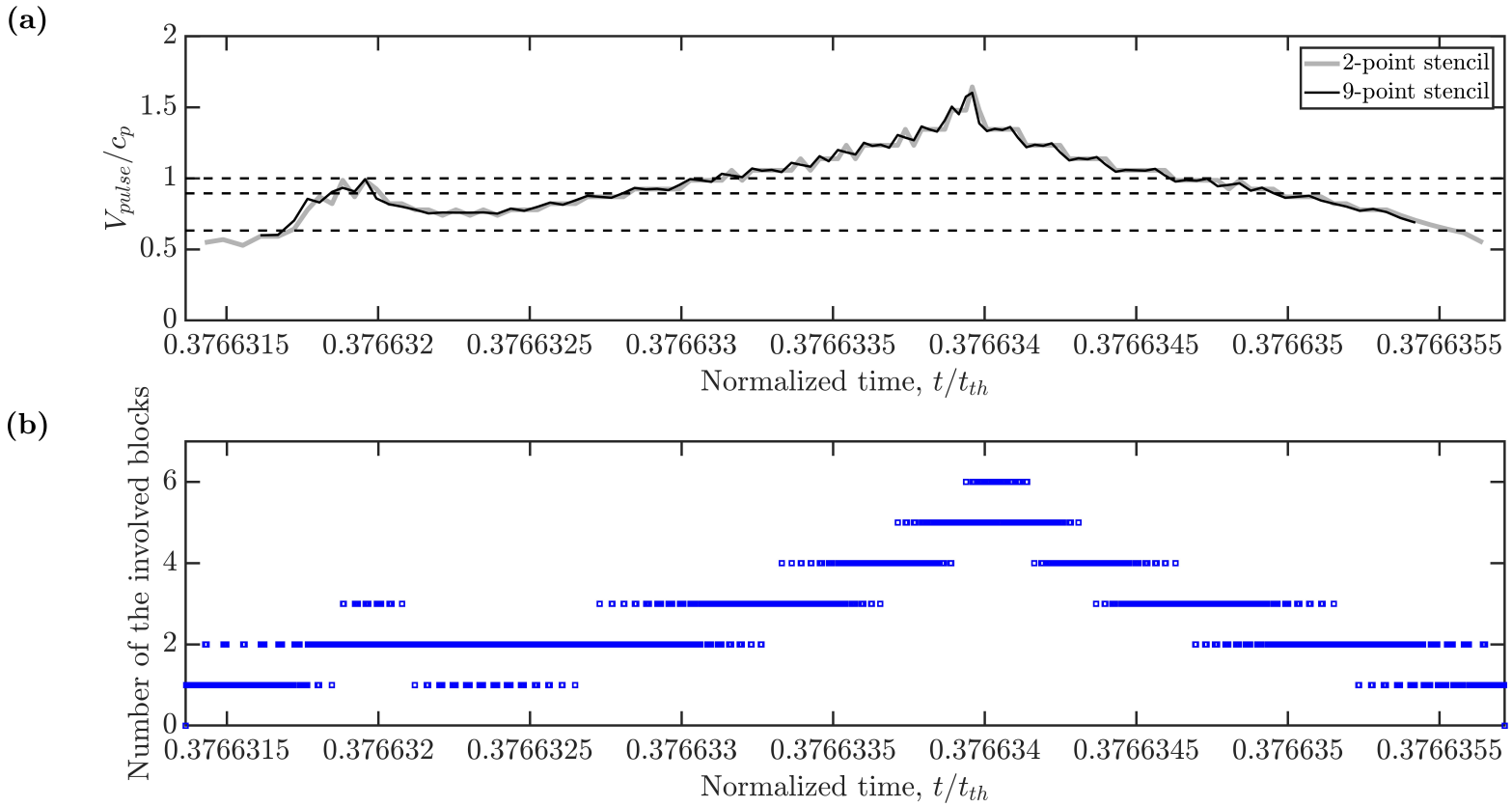

Figure 6.65: The pulse velocity and the number of involved (slipping) blocks during the propagation that is shown in Figure 6.59, i.e. case two, zone number 3. The threshold (normalization) parameter, t_{th}, is equal to 5714.3 s. The total duration of the propagation, t_{prop} is equal to 24.88 ms.

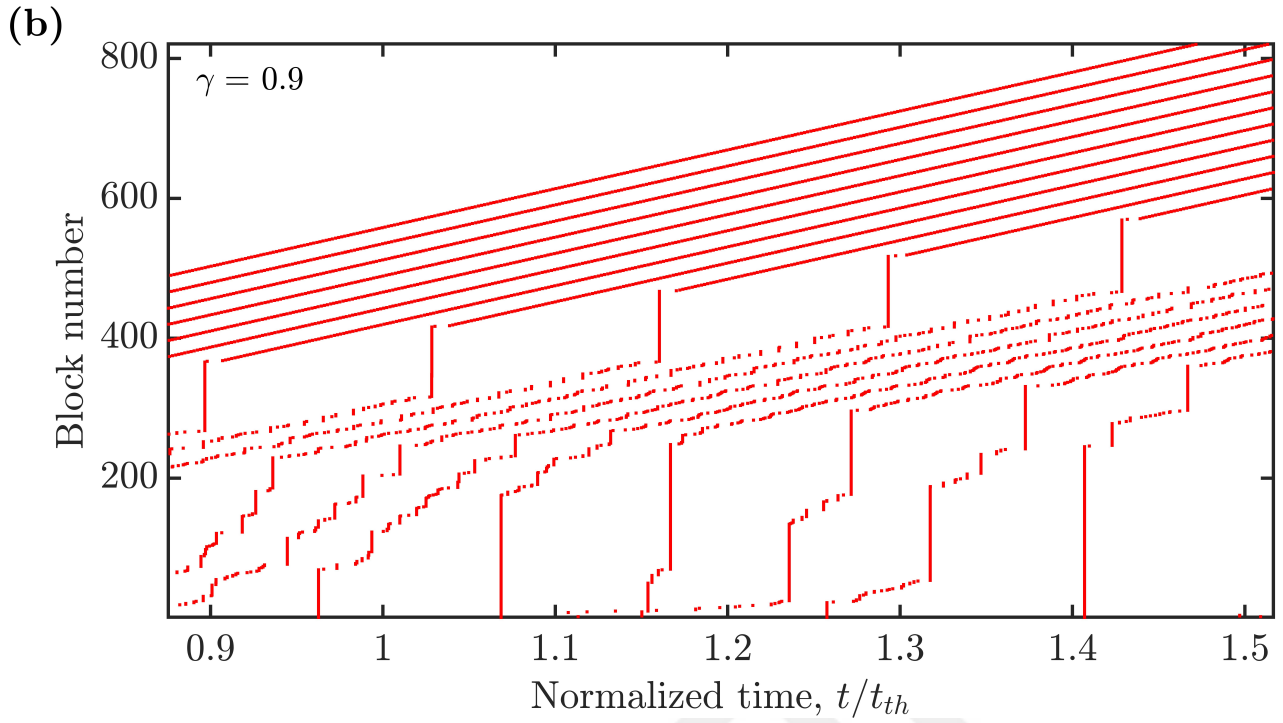

Figure 6.66: The zoomed view of zone number 4 (marked in Figure 6.44-(b)) of case two contains what seems to be a set of paralell lines, however, each line is constructed by a series isolated block slippages. The threshold (normalization) parameter, t_{th}, is equal to $5714.3\ s$. The speed of propagation is almost equal to $0.1\ m/s$.

6.4 Summary

A numerical scheme that was proposed by Dieterich at 1972 in [270] to deal with the BK model is investigated and explained by providing flowcharts and a pseudocode. The algorithm is then used to solve the equations of motion of the Burridge-Knopoff model with two different initial initial block positions. The block positions are obtained by assigning total spring force values that is applied to the blocks. The results show that the process of slippage of the blocks mainly starts in a crack-like mode and later converts to pulse-like mode.

6.5 Future work

- Does the BK model self-organize itself with time such that the rupture velocities drop below the pressure wave speed irrespective of the initial block positions?
- Can a linear slip-weakening friction law (Figure 6.2) keep the rupture velocities below the pressure wave speed?
- Can a linear slip-weakening friction law (Figure 6.2) affect the scaling law?
- Is the crack nucleation length a system characteristic?
- Viscosity can be incorporated into the BK model by inserting dampers.
- Is it possible to exert Dieterich's numerical scheme on the model shown in Figure 1.27?
- Is it possible to extend Dieterich's numerical scheme to the 2-D version of the BK model [300–303]? A 2-D model will be especially beneficial because width-dependent behavior (as opposed to the length-dependent behavior) of the crust rupture is still far from understood [304].

CHAPTER 7

DISCUSSION

The objective of this chapter is to critically discuss the results of the applied methods comparatively to highlight (dis)similarities. Such a comparison can show the coherence of the results that are generated by different approaches, assumptions, and limitations. The similarity in results, e.g., indifference to a variable, offers some insights about the used models and theories and can indicate a potential for further research. The provided big picture aims to frame the set of unconnected outputs in the previous chapters coherently and memorably.

7.1 General remarks

This section summarizes the assumptions and limitations of the methods applied in the previous chapters. Chapter 2 is an attempt to model surface roughness, i.e., the standard deviation of the asperity heights, into the Maxwell-slip model. The assumption is that a random initial lateral extension of the block-spring units can represent the effect of the random distribution of the asperity heights on friction. However, drawing such an analogy between the heights and lateral extensions seems unnecessary since a random distribution of heights can be directly assumed and modeled. Another drawback of this analogy is that the spring extensions lose their initial distribution, while roughness is not expected to change with time. The other problem is that compression is absent in this analogy.

All these handicaps are caused by trying to model roughness (measured in the vertical direction) with lateral spring extension; and are the artifacts of the indirect modeling and analogy. Whereas the approach can be easily revised such that during a normal

contact phase (which is absent in Chapter 2), asperities of random heights come into contact with the rigid flat. In such a case, the normal loads on the units would be a random variable too. Then, in the sliding contact phase, the units would be pulled under a compression value. Friction force would be the summation of the spring forces.

The above revised (proposed) approach may assume identical vertical stiffness for all units in the normal contact phase. This assumption and the notion of modeling heights as heights (and not as lateral extensions) will make the revised approach a rough draft of the asperity-based approaches used in Chapters 3 and 4.

In Chapters 3 and 4, the Maxwell-slip model block-spring units are characterized based on asperity-based (physically-based) theories. In Chapter 3, Nayak's PDFs generate the asperity heights and tip curvatures. The position of the asperities is not provided. In Chapter 4, the asperity heights and tip curvatures are obtained from a numerically generated fractal surface. The asperity positions are known. On the other hand, Chapters 5 and 6 deal with dynamic effects and do not concern with incorporating the effect of surface geometry into the models.

Nayak's PDFs have their roots in the random process theory and need Nayak's parameter as input in Equation (3.4). Yastrebov's formulas (Appendix B), which are based on the spectral analysis of the surface, can be used to express Nayak's parameter in terms of the standard deviation of heights, the PSD wavenumber cutoff values and the *fractal dimension* of the surface. Then, a set of random asperities (pairs of height-radius) can be produced by successive use of Nayak height PDF and Nayak joint PDF of heights and tip curvatures.

On the other hand, the fractal surface is generated by using the RMD method. The input parameters are the Hurst exponent, H, initial standard deviation, σ_0, and the grid size. The role of the grid size should be similar to that of the PSD wavelength cutoffs in Chapter 3. After the numerical generation of the surface, the tip curvatures are obtained by two methods: (i) paraboloid fitting and (ii) surface derivatives. This way, a set of height-radii pairs describing the surface asperities is produced.

The RMD method is criticized by Mandelbrot because of its problematic behavior

when the Hurst exponent is close to one [248]. He even suggested avoiding the RMD method since its output is neither stationary nor self-affine! The values of m_0 and m_2 are calculated by any of the schemes proposed in Subsection 4.2.2. These values alter dramatically in each execution of the algorithm (generation of the surface). Despite the non-stationary nature of the surfaces generated by the RMD method, Figures 4.3 and 4.4 indicate the possibility of calculating a reasonable m_2 value. For further references regarding non-stationary behavior of the surfaces generated by the RMD method, see Subsection 4.2.1. Another difficulty in using the RMD method is a lack of direct control over the surface standard deviation, $\sigma = \sqrt{m_0}$ which can considerably differ from the specified *initial* standard deviation, σ_0.

In Chapters 3 and 4, the generated set of rigid asperities, which are assumed to be circular paraboloids, is first pressed against an elastic half-space. Hertzian formulas (Appendix E) are used for the normal contact of each asperity contact. The development of overall real (elastic/plastic) contact area and normal load is monitored and checked against the available analytical solutions, i.e., those given by Greenwood [27] and [21], respectively. The average radius of the numerical schemes is used in the analytical solutions when needed. In the sliding phase, the stiffness of the asperity-substrate system is approximated by assuming a linear relationship between the asperity's tangential displacement over the flat and the amount of experienced tangential force. The tangential stiffness is calculated using Equation (3.6). At every compression value, every contacting asperity is replaced by an equivalent block-spring unit with known normal load and tangential stiffness. In contrast to Chapter 2, the initial extension of the units is assumed to be zero. The friction force (which is obtained from the superposition of the spring forces) is in the form of a nonlinear rise to the plateau of steady-sliding and seems not sensitive to the Hurst exponent in the generated case studies. On the other hand, the compression has a quite distinct effect; a relatively large compression causes a relatively late reach of the overall COF to the plateau. For further discussion, see Section 7.2.

In Chapter 5, as in Chapter 2, the stiffness and normal load of the Maxwell-slip model units are identical. In contrast to Chapter 2, instead of a random distribution, a linear distribution of the lateral initial spring extension is assigned. Furthermore, the block's inertial force is considered during its slippage. The inertial force causes the traction

force to differ from friction. In Chapter 2, the block moved to its destination in no time. A range of different frictional responses can be obtained by changing the driver velocity and the amount of spring extension.

At low driver velocities, the inertial force effect is negligible. A transition from the stick-slip behavior to steady sliding is observed depending on the amount of the spring extension. This transition resembles that of Chapter 2. When the maximum spring extension value is small, stick-slip occurs and is accompanied by a collective slippage of the blocks along the interface (a crack-like rupture). This behavior is similar to the Chapter 2 result for large shape parameters. On the other hand, when the maximum spring extension value is large, steady sliding occurs and is accompanied by a sequential slippage of the blocks which manifests as the propagation of a single (or multiple) slip region(s) along the interface. This behavior resembles the Chapter 2 result for small shape parameters The pulse-like slip regime neutralizes the effect of the inertial force.

A high driver velocity can intensify the inertial effects, which manifest as the oscillation of the traction force about the dynamic friction force. The traction force can even drop below zero periodically. This phenomenon is not observed at the macroscopic level; however, it is reported in a FEM simulation [174].

Chapter 6 uses the BK model with two initial linear lateral force distributions to study the friction variation and slip along the interface. The fundamental difference with the previous chapters is that each block is connected to its immediate neighbors on its left and right. Similar to Chapter 5, the effect of inertial force is taken into account, and the initial spring extension distribution is almost linear.

The results show that when the initial force (and consequently spring extension) has not a wide distribution, i.e., when the maximum spring extension is small, the response is apt to irregular stick-slip about the dynamic friction force, which is preceded by a linear rise. However, when the initial force is widely distributed, i.e., when the maximum spring extension is large, the friction force rises non-linearly to the plateau of dynamic friction force. Since the assumed driver velocity is low, the traction and friction forces are almost identical.

The results of the BK model include pulse-like propagation of slip along the interface during the friction force-drops. The observed slip events consist of (i) a single pulse propagation in one direction or (ii) the nucleation of a crack that grows on both sides and is later divided into two slip regions (pulses) that move in opposite directions along the interface. The second type of propagation was not observed in the Maxwell-slip model results of Chapter 5.

Since the blocks are connected in the BK model, the propagation speed can be calculated. Note that the calculation of the slip propagation speed for the Maxwell-slip model is not physically meaningful. The results of Chapter 6 show that at the beginning, the slip pulses propagate (or nucleate) very fast (multiples of the longitudinal wave speed) and then decelerate during the event. The obtained high speed can be the result of the Coulomb law. The question of supersonic propagation of rupture in discretized interface models is addressed by Knopoff himself, as mentioned in Section 6.1 [279, 280].

7.2 On asperity-based results

The results of Chapter 4 were obtained by assuming the initial standard deviation, σ_0 equal to $1\ \mu m$; however, the final height standard deviation of the generated fractal surface was $0.24\ \mu m$. Furthermore, Chapter 4 results included only the compression values $\delta = 0.5, 1, 1.5$. On the other hand, the results of Chapter 3 were obtained by assuming $\sigma = 1\ \mu m$ and $\delta = 1, 2, 3$. This incompatibility between the input values made drawing a comparison hardly possible.

In this subsection, some additional results of the asperity-based approaches (proposed in Chapters 3 and 4) are provided to make a meaningful comparison possible. The results include only the overall COF variation with the driver motion (or "time"). Figures 7.1 - 7.4 belong to the approach that is based on Nayak's surface model (Chapter 3). In these figures, $\tilde{k}_l = 256$. Figures 7.5 and 7.6 belong to the approach that is based on the fractal surface model (Chapter 4). In all of the above case studies, the height standard deviation, σ, is $0.24\ \mu m$, and the compression values are $\delta = 1, 2, 3$. The Hurst exponent values are $H = 0.75$ and $H = 0.95$. Note that the

Hurst exponent, as a parameter, is present in the procedure of calculating the Nayak parameter (Equation (B.7)) and is not specific to the fractal model.

By comparing the Figure 7.1 with Figure 7.2 and also Figure 7.3 with 7.4, one can deduce that the Hurst exponent value by itself hardly affects the nonlinear rise of COF to the plateau. Note that the shape of the curves and the points at which the plateau is reached in these pairs remain almost the same whether the Hurst exponent is equal to 0.75 or 0.95. In each of the pair of figures, Nayak's parameter is only slightly different. According to Equation (B.7), Nayak's parameter is a function of the Hurst exponent and the wavenumber ratio, ζ. It seems reasonable to claim that Nayak's parameter can be the factor that determines the shape of the nonlinear COF curve. With the increase of Nayak's parameter from below 6 in the first pair to over 11 in the second pair, the COF curves of $\delta = 1$ and $\delta = 3$ approach that of $\delta = 2$. However, the points at which the plateau is reached do not change much with the change in Nayak's parameter. The COF curves of $\delta = 2$ remain almost the same in Figures 7.1 to 7.4.

By comparing the results of the fractal-based approach, i.e., Figures 7.5 and 7.6 with each other, a slight change of the initial slope of the COF curves of $\delta = 2$ and $\delta = 3$ is observed with the increase of the Hurst exponent from 0.75 to 0.95. However, the curves of $\delta = 1$ differ significantly. Although the shape of this curve ($\delta = 1$) is different for $H = 0.75$ and $H = 0.95$, its reach point is almost the same as in the curves of $\delta = 2$ and $\delta = 3$.

To compare the Figures 7.5 and 7.6 with their counterparts in Figures 7.1 - 7.4, it is necessary to calculate the Nayak parameter for the fractal-based results. However, to use Equation (3.4), one must first calculate the fractal surface's fourth spectral moment, m_4. A possible way to perform this task is indicated in Section 4.5. Even after calculating the Nayak parameter, the value may differ from that of Nayak's approach. In other words, there is a lack of control over the Nayak parameter obtained from the fractal-based approach. Despite these handicaps in comparing the shape of the COF curves that are obtained by the asperity-based approaches at this stage, it is interesting to note that (whatever the Nayak parameter of the fractal surfaces would be) the reach points stay practically the same.

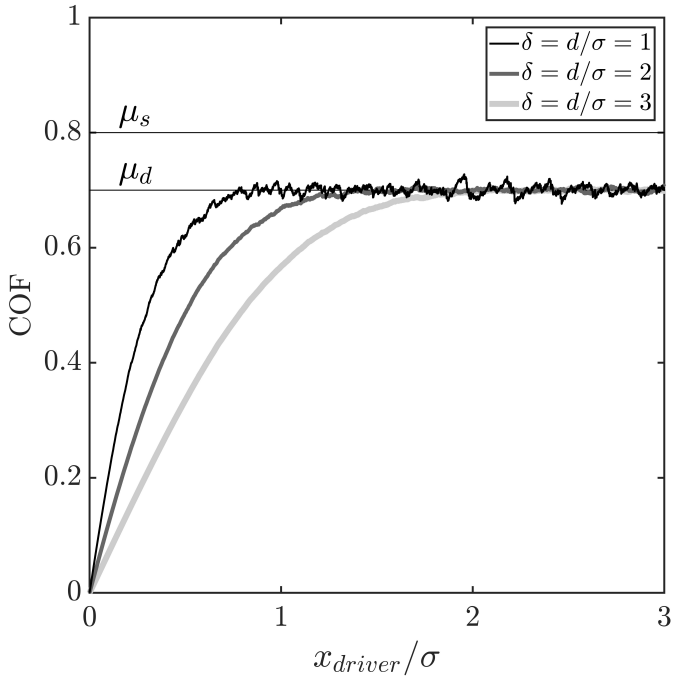

Figure 7.1: The numerical results for sliding under different compression values, for Nayak's model with $\alpha = 5.15$ ($H = 0.75$ and $\zeta = 8$)

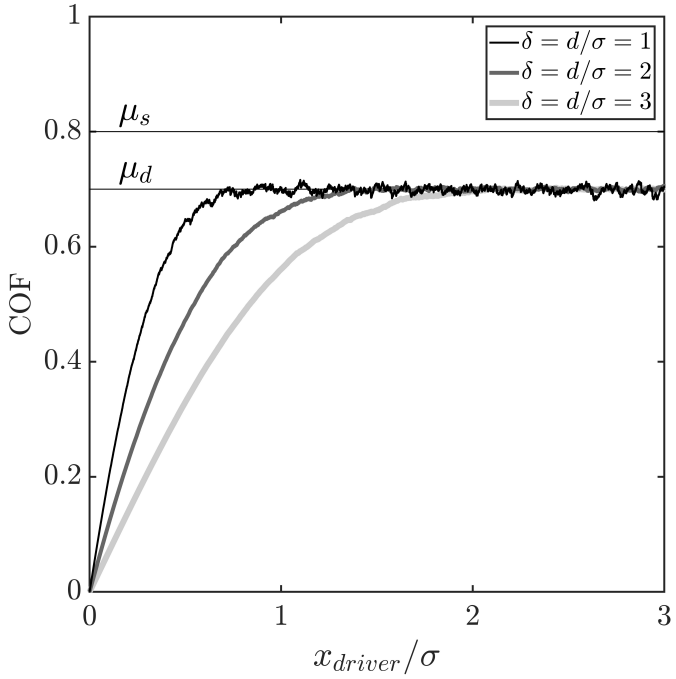

Figure 7.2: The numerical results for sliding under different compression values, for Nayak model with $\alpha = 5.37$ ($H = 0.95$ and $\zeta = 8$)

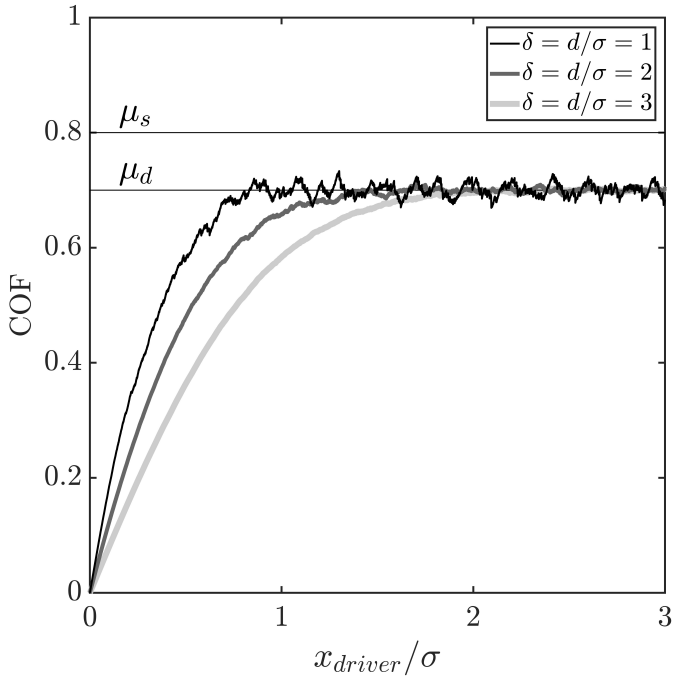

Figure 7.3: The numerical results for sliding under different compression values, for Nayak model with $\alpha = 11.19$ ($H = 0.75$ and $\zeta = 16$)

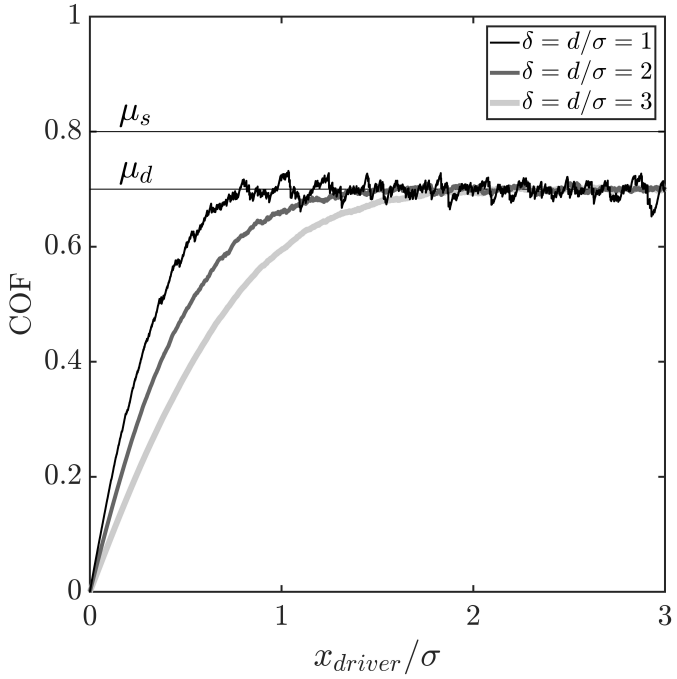

Figure 7.4: The numerical results for sliding under different compression values, for Nayak model with $\alpha = 12.34$ ($H = 0.95$ and $\zeta = 16$)

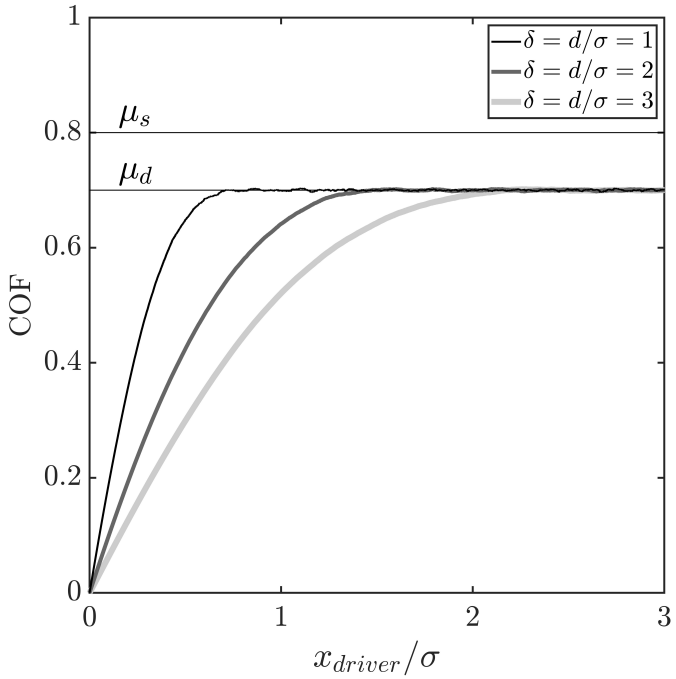

Figure 7.5: The numerical results for sliding under different compression values, for the fractal model with $H = 0.75$

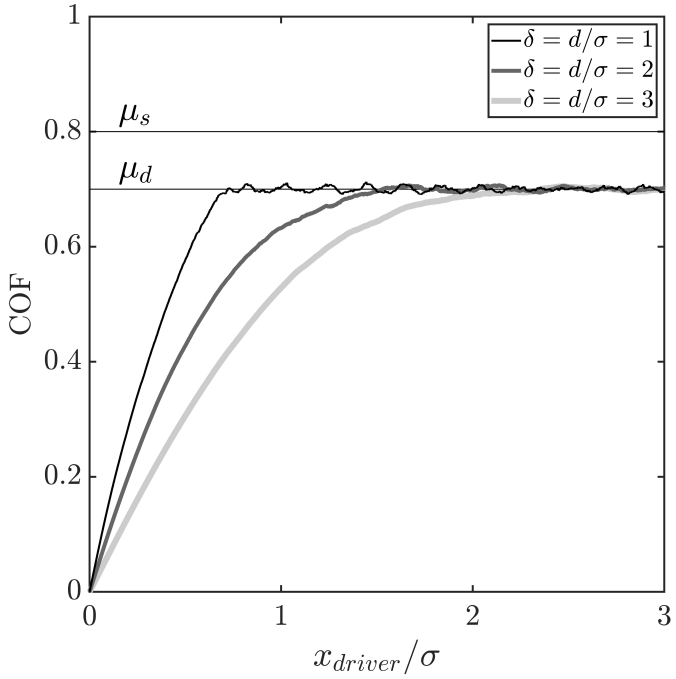

Figure 7.6: The numerical results for sliding under different compression values, for the fractal model with $H = 0.95$

REFERENCES

[1] C. M. Mate and R. W. Carpick, *Tribology on the Small Scale: A Modern Textbook on Friction, Lubrication, and Wear*. Oxford University Press, 2019.

[2] B. Feeny, A. Guran, N. Hinrichs, and K. Popp, "A historical review on dry friction and stick-slip phenomena," *Applied Mechanics Reviews*, vol. 51, no. 5, pp. 321–341, 1998.

[3] A. Fall, B. Weber, M. Pakpour, N. Lenoir, N. Shahidzadeh, J. Fiscina, C. Wagner, and D. Bonn, "Sliding friction on wet and dry sand," *Physical Review Letters*, vol. 112, no. 17, pp. 3–6, 2014.

[4] C. S. C. Davison, "Transporting sixty-ton statues in early Assyria and Egypt," *Technology and Culture*, vol. 2, no. 1, pp. 11–16, 1961.

[5] I. M. Hutchings, "Leonardo da Vinci's studies of friction," *Wear*, vol. 360-361, pp. 51–66, 2016.

[6] A. A. Pitenis, D. Dowson, and W. Gregory Sawyer, "Leonardo da Vinci's friction experiments: An old story acknowledged and repeated," *Tribology Letters*, vol. 56, no. 3, pp. 509–515, 2014.

[7] M. Paggi and M. Ciavarella, "The coefficient of proportionality κ between real contact area and load, with new asperity models," *Wear*, vol. 268, no. 7-8, pp. 1020–1029, 2010.

[8] Q. J. Wang and Y.-W. Chung, *Encyclopedia of Tribology*. Springer, 2013.

[9] V. L. Popov, *Contact Mechanics and Friction*. Springer, 2010.

[10] B. N. J. Persson, *History of Tribology*, pp. 791–797. Springer, 2014.

[11] J. Gao, W. D. Luedtke, D. Gourdon, M. Ruths, J. N. Israelachvili, and U. Landman, "Frictional forces and Amontons' law: from the molecular to the macro-

scopic scale," *The Journal of Physical Chemistry B*, vol. 108, no. 11, pp. 3410–3425, 2004.

[12] F. P. Bowden and D. Tabor, *The friction and lubrication of solids*. Oxford University Press, 1986.

[13] B. Bhushan, *Micro/Nanotribology and Materials Characterization Studies Using Scanning Probe Microscopy*, pp. 497–541. Berlin, Heidelberg: Springer, 2004.

[14] O. Braun and A. Naumovets, "Nanotribology: Microscopic mechanisms of friction," *Surface Science Reports*, vol. 60, no. 6, pp. 79–158, 2006.

[15] V. L. Popov and J. A. T. Gray, "Prandtl-Tomlinson model: History and applications in friction, plasticity, and nanotechnologies," *ZAMM - Journal of Applied Mathematics and Mechanics / Zeitschrift für Angewandte Mathematik und Mechanik*, vol. 92, no. 9, pp. 683–708, 2012.

[16] D. Tabor, *The Hardness of Metals*. Monographs on the physics and chemistry of materials, Oxford University Press, 1951.

[17] J. H. Dieterich and B. D. Kilgore, "Direct observation of frictional contacts: New insights for state-dependent properties," *Pure and Applied Geophysics (PAGEOPH)*, vol. 143, no. 1, pp. 283–302, 1994.

[18] J. F. Archard, "Elastic deformation and the laws of friction," *Proceedings of the Royal Society of London. Series A. Mathematical and Physical Sciences*, vol. 243, p. 190–205, 1975.

[19] B. B. Mandelbrot, "How long is the coast of Britain? Statistical self-similarity and fractional dimension," *Science*, vol. 156, pp. 636–638, 1967.

[20] M. F. Barnsley, R. L. Devaney, B. B. Mandelbrot, H.-O. Peitgen, D. Saupe, and R. F. Voss, *The Science of Fractal Images*. New York: Springer-Verlag, 1 ed., 1988.

[21] J. A. Greenwood and J. B. P. Williamson, "Contact of nominally flat surfaces," *Proceedings of the Royal Society of London. Series A. Mathematical and Physical Sciences*, vol. 295, no. 1442, pp. 300–319, 1966.

[22] J. A. Greenwood and J. J. Wu, "Surface roughness and contact: An apology," *Maccanica*, vol. 36, pp. 617–630, 2001.

[23] P. L. Menezes, I. S. P., M. Nosonovsky, S. V. Kailas, and M. R. Lovell, *Tribology for Scientists and Engineers*. Springer, 2013.

[24] P. R. Nayak, "Random process model of rough surfaces," *Journal of Lubrication Technology*, vol. 93, no. 3, pp. 398–407, 1971.

[25] V. A. Yastrebov, G. Anciaux, and J.-F. Molinari, "The role of the roughness spectral breadth in elastic contact of rough surfaces," *Journal of the Mechanics and Physics of Solids*, vol. 107, pp. 469–493, 2017.

[26] A. Bush, R. Gibson, and T. Thomas, "The elastic contact of a rough surface," *Wear*, vol. 35, no. 1, pp. 87–111, 1975.

[27] J. A. Greenwood, "A simplified elliptic model of rough surface contact," *Wear*, vol. 261, no. 2, pp. 191–200, 2006.

[28] B. N. J. Persson, "Contact mechanics for randomly rough surfaces," *Surface science reports*, vol. 61, no. 4, pp. 201–227, 2006.

[29] W. Manners and J. A. Greenwood, "Some observations on Persson's diffusion theory of elastic contact," *Wear*, vol. 261, no. 5, pp. 600–610, 2006.

[30] E. Rabinowicz, "The intrinsic variables affecting the stick-slip process," *Proceedings of the Physical Society*, vol. 71, no. 4, p. 668, 1958.

[31] J. H. Dieterich, "Time-dependent friction and the mechanics of stick-slip," *Pure and Applied Geophysics (PAGEOPH)*, vol. 116, pp. 790–806, 1978.

[32] J. H. Dieterich, "Modeling of rock friction: 1. Experimental results and constitutive equations," *Journal of Geophysical Research: Solid Earth*, vol. 84, no. B5, pp. 2161–2168, 1979.

[33] J. H. Dieterich, "Modeling of rock friction: 2. Simulation of preseismic slip," *Journal of Geophysical Research*, vol. 84, pp. 2169–2175, 1979.

[34] O. Vingsbo and S. Söderberg, "On fretting maps," *Wear*, vol. 126, no. 2, pp. 131–147, 1988.

[35] D. A. Hills, "Mechanics of fretting fatigue," *Wear*, vol. 175, no. 1-2, pp. 107–113, 1994.

[36] EJ. Berger, "Friction modeling for dynamic system simulation," *Applied Mechanics Reviews*, vol. 55, pp. 535–577, 10 2002.

[37] W. F. Brace and J. D. Byerlee, "Stick-slip as a mechanism for earthquakes," *Science*, vol. 153, no. 3739, pp. 990–992, 1966.

[38] R. Burridge and L. Knopoff, "Model and theoretical seismicity," *Bulletin of the seismological society of America*, vol. 57, no. 3, pp. 341–371, 1967.

[39] P. Bak, K. Christensen, L. Danon, and T. Scanlon, "Unified scaling law for earthquakes," *Physical Review Letters*, vol. 88, no. 17, p. 178501, 2002.

[40] P. R. Dahl, "A solid friction model," tech. rep., The Aerospace Corporation, 1968.

[41] D. Karnopp, "Computer simulation of stick-slip friction in mechanical dynamic systems," *Journal of Dynamic Systems, Measurement, and Control*, vol. 107, no. 1, pp. 100–103, 1985.

[42] D. C. Karnopp, D. L. Margolis, and R. C. Rosenberg, *System dynamics: modeling, simulation, and control of mechatronic systems*. Wiley, 2012.

[43] D. A. Haessig and B. Friedland, "On the modeling and simulation of friction," *Journal of Dynamic Systems, Measurement, and Control*, vol. 113, no. 3, pp. 354–362, 1991.

[44] C. Canudas de Wit, H. Olsson, K. J. Åström, and P. Lischinsky, "A new model for control of systems with friction," *IEEE Transactions on Automatic Control*, vol. 40, no. 3, pp. 419–425, 1995.

[45] N. B. Do, A. A. Ferri, and O. A. Bauchau, "Efficient simulation of a dynamic system with LuGre friction," *Journal of Computational and Nonlinear Dynamics*, vol. 2, no. 4, pp. 281–289, 2007.

[46] H. Dankowicz, "On the modeling of dynamic friction phenomena," *ZAMM - Journal of Applied Mathematics and Mechanics, /Zeitschrift für Angewandte Mathematik und Mechanik*, vol. 79, no. 6, pp. 399–409, 1999.

[47] N. P. Hoffmann, “Linear stability of steady sliding in point contacts with velocity dependent and LuGre type friction,” *Journal of Sound and Vibration*, vol. 301, no. 3-5, pp. 1023–1034, 2007.

[48] P. Gdaniec, C. Weiß, and N. Hoffmann, “On chaotic friction induced vibration due to rate dependent friction,” *Mechanics Research Communications*, vol. 37, no. 1, pp. 92–95, 2010.

[49] L. Freidovich, A. Robertsson, A. Shiriaev, and R. Johansson, “LuGre-model-based friction compensation,” *IEEE Transactions on Control Systems Technology*, vol. 18, no. 1, pp. 194–200, 2010.

[50] S. M. R. Sobczyk, E. A. Perondi, and M. A. B. Cunha, “A continuous approximation of the LuGre friction model,” in *ABCM Symposium Series in Mechatronics*, vol. 4, pp. 218–228, ABCM Ouro Preto, 2010.

[51] J. Swevers, F. Al-Bender, C. G. Ganseman, and T. Projogo, “An integrated friction model structure with improved presliding behavior for accurate friction compensation,” *IEEE Transactions on automatic control*, vol. 45, no. 4, pp. 675–686, 2000.

[52] M. Goldfarb and N. Celanovic, “A lumped parameter electromechanical model for describing the nonlinear behavior of piezoelectric actuators,” *Journal of Dynamic Systems, Measurement, and Control*, vol. 119, no. 3, pp. 478–485, 1997.

[53] B. J. Lazan, *Damping of materials and members in structural mechanics*. Pergamon Press, 1968.

[54] J. Wojewoda, A. Stefański, M. Wiercigroch, and T. Kapitaniak, “Hysteretic effects of dry friction: modelling and experimental studies,” *Philosophical Transactions of the Royal Society A: Mathematical, Physical and Engineering Sciences*, vol. 366, no. 1866, pp. 747–765, 2008.

[55] S. Biswas and A. Chatterjee, “A two-state hysteresis model from high-dimensional friction,” *Royal Society Open Science*, vol. 2, no. 7, p. 150188, 2015.

[56] T. H. Chiew, Z. Jamaludin, B. Hashim, R. A. Y., A. N. A., and L., "Identification of friction models for precise positioning system in machine tools," *Procedia Engineering*, vol. 53, pp. 569–578, 2013.

[57] T. Vo-Minh, T. Tjahjowidodo, H. Ramon, and H. Van Brussel, "A new approach to modeling hysteresis in a pneumatic artificial muscle using the maxwell-slip model," *IEEE/ASME Transactions on Mechatronics*, vol. 16, no. 1, pp. 177–186, 2011.

[58] A. K. Padthe, J. Oh, and D. S. Bernstein, "On the lugre model and friction-induced hysteresis," in *2006 American Control Conference*, pp. 3247–3252, IEEE, 2006.

[59] U. Parlitz, A. Hornstein, D. Engster, F. Al-Bender, V. Lampaert, T. Tjahjowidodo, S. D. Fassois, D. Rizos, C. X. Wong, K. Worden, and G. Manson, "Identification of pre-sliding friction dynamics," *Chaos: An Interdisciplinary Journal of Nonlinear Science*, vol. 14, no. 2, pp. 420–430, 2004.

[60] V. Lampaert, J. Swevers, and F. Al-Bender, "Modification of the Leuven integrated friction model structure," *IEEE Transactions on automatic control*, vol. 47, no. 4, pp. 683–687, 2002.

[61] K. De Moerlooze, F. Al-Bender, and H. Van Brussel, "A generalised asperity-based friction model," *Tribology Letters*, vol. 40, no. 1, pp. 113–130, 2010.

[62] D. A. Hills and D. Nowell, *Mechanics of Fretting Fatigue*. Solid Mechanics and Its Applications, Springer, 1994.

[63] S. Fouvry, Ph. Kapsa, and L. Vincent, "Developments of fretting sliding criteria to quantify the local friction coefficient evolution under partial slip condition," in *Tribology Series*, vol. 34, pp. 161–172, Elsevier, 1998.

[64] A. Rossmann, "Aeroengine safety." Available online at: `https://aeroenginesafety.tugraz.at/doku.php`, last accessed on 28.11.2022.

[65] Q. Yang, W. Zhou, P. Gai, X. Zhang, X. Fu, G. Chen, and Z. Li, "Investigation on the fretting fatigue behaviors of Ti-6Al-4V dovetail joint specimens treated with shot-peening," *Wear*, vol. 372-373, pp. 81–90, 2017.

[66] S. J. Lainé, K. M. Knowles, P. J. Doorbar, R. D. Cutts, and D. Rugg, "Microstructural characterisation of metallic shot peened and laser shock peened Ti-6Al-4V," *Acta Materialia*, vol. 123, pp. 350–361, 2017.

[67] K. K. Liu and M. R. Hill, "The effects of laser peening and shot peening on fretting fatigue in Ti-6Al-4V coupons," *Tribology International*, vol. 42, no. 9, pp. 1250–1262, 2009.

[68] B. P. Conner and T. Nicholas, "Using a dovetail fixture to study fretting fatigue and fretting palliatives," *Journal of Engineering Materials and Technology*, vol. 128, no. 2, pp. 133–141, 2003.

[69] C. Li, Z. Chen, Z. Shen, and H. She, "Analysis on vibration reduction of a rotating dovetailed blade with underplatform damper and installation preload," *Mechanics Based Design of Structures and Machines*, vol. 50, no. 3, pp. 877–896, 2022.

[70] L. Panning, "Symmetric and asymmetric underplatform dampers for turbine blades," in *PAMM: Proceedings in Applied Mathematics and Mechanics*, vol. 6, pp. 251–252, Wiley Online Library, 2006.

[71] N. Lapusta, J. R. Rice, Y. Ben-Zion, and G. Zheng, "Elastodynamic analysis for slow tectonic loading with spontaneous rupture episodes on faults with rate- and state-dependent friction," *Journal of Geophysical Research: Solid Earth*, vol. 105, no. B10, pp. 23765–23789, 2000.

[72] J. R. Rice, N. Lapusta, and K. Ranjith, "Rate and state dependent friction and the stability of sliding between elastically deformable solids," *Journal of the Mechanics and Physics of Solids*, vol. 49, no. 9, pp. 1865–1898, 2001.

[73] K. Ranjith and J. R. Rice, "Slip dynamics at an interface between dissimilar materials," *Journal of the Mechanics and Physics of Solids*, vol. 49, no. 2, pp. 341–361, 2001.

[74] D. Coker and A. J. Rosakis, "Experimental observations of intersonic crack growth in asymmetrically loaded unidirectional composite plates," *Philosophical Magazine A*, vol. 81, no. 3, pp. 571–595, 2001.

[75] D. Coker, G. Lykotrafitis, A. Needleman, and A. J. Rosakis, "Frictional sliding modes along an interface between identical elastic plates subject to shear impact loading," *Journal of the Mechanics and Physics of Solids*, vol. 53, no. 4, pp. 884–922, 2005.

[76] Y. Boneh and Z. Reches, "Geotribology - Friction, wear, and lubrication of faults," *Tectonophysics*, vol. 733, pp. 171–181, 2018.

[77] K. Johnson, *Contact Mechanics*. Cambridge University Press, 1987.

[78] D. A. Hills, D. Nowell, and B. J. R., "KL Johnson and contact mechanics," *Proceedings of the Institution of Mechanical Engineers, Part C: Journal of Mechanical Engineering Science*, vol. 231, no. 13, pp. 2451–2458, 2017.

[79] G. M. L. Gladwell, *Contact problems in the classical theory of elasticity*. Springer, 1980.

[80] D. A. Hills, D. Nowell, and A. Sackfield, *Mechanics of elastic contacts*. Butterworth-Heinemann, 1993.

[81] I. G. Goryacheva, *Contact mechanics in tribology*. Springer, 1998.

[82] V. Popov, M. Heß, and E. Willert, *Handbook of Contact Mechanics: Exact Solutions of Axisymmetric Contact Problems*. Springer, 2019.

[83] V. Popov and M. Heß, *Method of Dimensionality Reduction in Contact Mechanics and Friction*. Springer, 2014.

[84] J. J. Kalker, *Three-dimensional elastic bodies in rolling contact*. Springer Science, 1990.

[85] J. A. Greenwood, H. Minshall, and D. Tabor, "Hysteresis losses in rolling and sliding friction," *Proceedings of the Royal Society of London. Series A. Mathematical and Physical Sciences*, vol. 259, no. 1299, pp. 480–507, 1961.

[86] T. A. Laursen, *Computational contact and impact mechanics: fundamentals of modeling interfacial phenomena in nonlinear finite element analysis*. Springer, 2003.

[87] P. Wriggers, *Computational contact mechanics*. Springer, 2006.

[88] L. De Lorenzis, P. Wriggers, and C. Weißenfels, *Computational Contact Mechanics with the Finite Element Method*, pp. 1–45. Wiley, 2017.

[89] J. T. Oden and J. A. C. Martins, "Models and computational methods for dynamic friction phenomena," *Computer methods in applied mechanics and engineering*, vol. 52, no. 1-3, pp. 527–634, 1985.

[90] I. G. Goryacheva, M. Paggi, and V. L. Popov, "Contact mechanics perspective of tribology," *Frontiers in Mechanical Engineering*, p. 14, 2021.

[91] Q. J. Wang, L. Sun, X. Zhang, S. Liu, and D. Zhu, "Fft-based methods for computational contact mechanics," *Frontiers in Mechanical Engineering*, vol. 6, p. 61, 2020.

[92] M. Nosonovsky, "Entropy in tribology: in the search for applications," *Entropy*, vol. 12, no. 6, pp. 1345–1390, 2010.

[93] L. Makkonen, "A thermodynamic model of sliding friction," *AIP Advances*, vol. 2, no. 1, p. 012179, 2012.

[94] E. Cigeroglu, W. Lu, and C.-H. Menq, "One-dimensional dynamic microslip friction model," *Journal of Sound and Vibration*, vol. 292, no. 3-5, pp. 881–898, 2006.

[95] J. H. Wang and W. K. Chen, "Investigation of the Vibration of a Blade With Friction Damper by HBM," *Journal of Engineering for Gas Turbines and Power*, vol. 115, no. 2, pp. 294–299, 1993.

[96] G. Csaba, "Forced response analysis in time and frequency domains of a tuned bladed disk with friction dampers," *Journal of Sound and Vibration*, vol. 214, no. 3, pp. 395–412, 1998.

[97] N. Hinrichs, M. Oestreich, and K. Popp, "On the modelling of friction oscillators," *Journal of sound and Vibration*, vol. 216, no. 3, pp. 435–459, 1998.

[98] M. Bernardo, C. Budd, A. R. Champneys, and P. Kowalczyk, *Piecewise-smooth dynamical systems: theory and applications*, vol. 163. Springer, 2008.

[99] J. Bastien, F. Bernardin, and C.-H. Lamarque, *Non-smooth Deterministic Or Stochastic Discrete Dynamical Systems: Applications to Models with Friction Or Impact*. Wiley, 2013.

[100] N. M. Kinkaid, O. M. O'Reilly, and P. Papadopoulos, "Automotive disc brake squeal," *Journal of Sound and Vibration*, vol. 267, no. 1, pp. 105–166, 2003.

[101] T. Butlin and J. Woodhouse, "Friction-induced vibration: Model development and comparison with large-scale experimental tests," *Journal of Sound and Vibration*, vol. 332, no. 21, pp. 5302–5321, 2013.

[102] K. Ranjith and J. R. Rice, "Stability of quasi-static slip in a single degree of freedom elastic system with rate and state dependent friction," *Journal of the Mechanics and Physics of Solids*, vol. 47, no. 6, pp. 1207–1218, 1999.

[103] U. Galvanetto, "Some discontinuous bifurcations in a two-block stick-slip system," *Journal of Sound and vibration*, vol. 248, no. 4, pp. 653–669, 2001.

[104] U. Galvanetto and S. R. Bishop, "Computational techniques for nonlinear dynamics in multiple friction oscillators," *Computer methods in applied mechanics and engineering*, vol. 163, no. 1-4, pp. 373–382, 1998.

[105] A. R. Champneys and P. L. Várkonyi, "The Painlevé paradox in contact mechanics," *IMA Journal of Applied Mathematics*, vol. 81, no. 3, pp. 538–588, 2016.

[106] O. Makarenkov and J. S. W. Lamb, "Dynamics and bifurcations of nonsmooth systems: A survey," *Physica D: Nonlinear Phenomena*, vol. 241, no. 22, pp. 1826–1844, 2012.

[107] M. Jean, "The non-smooth contact dynamics method," *Computer methods in applied mechanics and engineering*, vol. 177, no. 3-4, pp. 235–257, 1999.

[108] P. Olejnik, J. Awrejcewicz, and M. Fečkan, *Modeling, Analysis and Control of Dynamical Systems with Friction and Impacts*. World Scientific, 2018.

[109] H. Olsson, *Control Systems with Friction*. PhD thesis, 1996.

[110] Y. Wang, D. Wang, and T. Chai, "Extraction and adaptation of fuzzy rules for friction modeling and control compensation," *IEEE Transactions on Fuzzy Systems*, vol. 19, no. 4, pp. 682–693, 2011.

[111] A. K. Geim and K. S. Novoselov, "The rise of graphene," *Nature materials*, vol. 6, no. 3, pp. 183–191, 2007.

[112] H. Zhang, Z. Guo, H. Gao, and T. Chang, "Stiffness-dependent interlayer friction of graphene," *Carbon*, vol. 94, pp. 60–66, 2015.

[113] Y. Liu, F. Grey, and Q. Zheng, "The high-speed sliding friction of graphene and novel routes to persistent superlubricity," *Scientific reports*, vol. 4, no. 1, pp. 1–7, 2014.

[114] F. Bonelli, N. Manini, E. Cadelano, and L. Colombo, "Atomistic simulations of the sliding friction of graphene flakes," *The European Physical Journal B*, vol. 70, no. 4, pp. 449–459, 2009.

[115] S. Li, Q. Li, R. W. Carpick, P. Gumbsch, X. Z. Liu, X. Ding, J. Sun, and J. Li, "The evolving quality of frictional contact with graphene," *Nature*, vol. 539, no. 7630, pp. 541–545, 2016.

[116] D. Mandelli, I. Leven, O. Hod, and M. Urbakh, "Sliding friction of graphene/hexagonal–boron nitride heterojunctions: a route to robust superlubricity," *Scientific reports*, vol. 7, no. 1, pp. 1–10, 2017.

[117] K. Obara, "Nonvolcanic deep tremor associated with subduction in southwest Japan," *Science*, vol. 296, no. 5573, pp. 1679–1681, 2002.

[118] G. Rogers and H. Dragert, "Episodic tremor and slip on the Cascadia subduction zone: The chatter of silent slip," *Science*, vol. 300, no. 5627, pp. 1942–1943, 2003.

[119] M. R. Brudzinski, "Episodic tremor and slip: potential clues to the earthquake process and how faults slip," *The Earth Scientist*, vol. 27, no. 1, pp. 7–11, 2011.

[120] J. R. Leeman, D. M. Saffer, M. M. Scuderi, and C. Marone, "Laboratory observations of slow earthquakes and the spectrum of tectonic fault slip modes," *Nature communications*, vol. 7, no. 1, p. 11104, 2016.

[121] K. Im, D. Saffer, C. Marone, and J.-P. Avouac, "Slip-rate-dependent friction as a universal mechanism for slow slip events," *Nature Geoscience*, vol. 13, no. 10, pp. 705–710, 2020.

[122] L. Dal Zilio, N. Lapusta, and J.-P. Avouac, "Unraveling scaling properties of slow-slip events," *Geophysical Research Letters*, vol. 47, no. 10, p. e2020GL087477, 2020.

[123] Y. Luo and Z. Liu, "Fault zone heterogeneities explain depth-dependent pattern and evolution of slow earthquakes in Cascadia," *Nature communications*, vol. 12, no. 1, p. 1959, 2021.

[124] D. M. Veedu and S. Barbot, "The Parkfield tremors reveal slow and fast ruptures on the same asperity," *Nature*, vol. 532, no. 7599, pp. 361–365, 2016.

[125] B. Rousset, R. Bürgmann, and M. Campillo, "Slow slip events in the roots of the San Andreas fault," *Science advances*, vol. 5, no. 2, p. eaav3274, 2019.

[126] M. J. Ikari and A. J. Kopf, "Seismic potential of weak, near-surface faults revealed at plate tectonic slip rates," *Science Advances*, vol. 3, no. 11, p. e1701269, 2017.

[127] C. Hulbert, B. Rouet-Leduc, P. A. Johnson, C. X. Ren, J. Rivière, D. C. Bolton, and C. Marone, "Similarity of fast and slow earthquakes illuminated by machine learning," *Nature Geoscience*, vol. 12, no. 1, pp. 69–74, 2019.

[128] K. Wang, C. W. Johnson, K. C. Bennett, and P. A. Johnson, "Predicting fault slip via transfer learning," *Nature Communications*, vol. 12, no. 1, p. 7319, 2021.

[129] D. S. Kammer, I. Svetlizky, G. Cohen, and J. Fineberg, "The equation of motion for supershear frictional rupture fronts," *Science advances*, vol. 4, no. 7, p. eaat5622, 2018.

[130] D. S. Kammer, V. A. Yastrebov, G. Anciaux, and J.-F. Molinari, "The existence of a critical length scale in regularised friction," *Journal of the Mechanics and Physics of Solids*, vol. 63, pp. 40–50, 2014.

[131] G. Petrillo, E. Lippiello, F. P. Landes, and A. Rosso, "The influence of the brittle-ductile transition zone on aftershock and foreshock occurrence," *Nature Communications*, vol. 11, no. 1, p. 3010, 2020.

[132] M. Heimpel, "Earthquake scaling: the effect of a viscoelastic asthenosphere," *Geophysical Journal International*, vol. 166, no. 1, pp. 170–178, 2006.

[133] F. Giacco, M. P. Ciamarra, L. Saggese, L. de Arcangelis, and E. Lippiello, "Non-monotonic dependence of the friction coefficient on heterogeneous stiffness," *Scientific Reports*, vol. 4, no. 1, pp. 1–4, 2014.

[134] T. A. L. Burgo and A. Erdemir, "Bipolar tribocharging signal during friction force fluctuations at metal-insulator interfaces," *Angewandte Chemie*, vol. 126, no. 45, pp. 12297–12301, 2014.

[135] K. Sayfidinov, S. D. Cezan, B. Baytekin, and H. T. Baytekin, "Minimizing friction, wear, and energy losses by eliminating contact charging," *Science advances*, vol. 4, no. 11, p. eaau3808, 2018.

[136] H. Sakuma, K. Kawai, I. Katayama, and S. Suehara, "What is the origin of macroscopic friction?," *Science Advances*, vol. 4, no. 12, p. eaav2268, 2018.

[137] J. Williams, *Engineering Tribology*. Cambridge University Press, 2005.

[138] K. Gurung, "Fractal dimension in architecture: An exploration of spatial dimension," Master's thesis, 2017.

[139] B. Persson, "On the fractal dimension of rough surfaces," *Tribology Letters*, vol. 54, no. 1, pp. 99–106, 2014.

[140] Y. Wang, A. Azam, M. C. T. Wilson, A. Neville, and A. Morina, "Generating fractal rough surfaces with the spectral representation method," *Proceedings of the Institution of Mechanical Engineers, Part J: Journal of Engineering Tribology*, vol. 235, no. 12, pp. 2640–2653, 2021.

[141] T. Jacobs, T. Junge, and L. Pastewka, "Quantitative characterization of surface topography using spectral analysis," *Surface Topography: Metrology and Properties*, vol. 5, no. 1, 2017.

[142] A. Majumdar and B. Bhushan, "Role of fractal geometry in roughness characterization and contact mechanics of surfaces," *ASME Journal of Tribology*, vol. 12, p. 205–216, 1990.

[143] A. Majumdar and B. Bhushan, "Fractal model of elastic-plastic contact between rough surfaces," *ASME Journal of Tribology*, vol. 113, pp. 1–11, 1991.

[144] A. Majumdar and B. Bhushan, "Contact mechanics of rough surfaces in tribology: multiple asperity contact," *Tribology Letters*, vol. 4, pp. 1–35, 1998.

[145] L. Afferrante, G. Carbone, and G. Demelio, "Interacting and coalescing Hertzian asperities: A new multiasperity contact model," *Wear*, vol. 278-279, pp. 28–33, 2012.

[146] V. A. Yastrebov, G. Anciaux, and J.-F. Molinari, "On the accurate computation of the true contact-area in mechanical contact of random rough surfaces," *Tribology International*, vol. 114, pp. 161–171, 2017.

[147] J. M. Monti, L. Pastewka, and M. O. Robbins, "Fractal geometry of contacting patches in rough elastic contacts," *Journal of the Mechanics and Physics of Solids*, vol. 160, p. 104797, 2022.

[148] J. Gao, Y. Cao, W.-w. Tung, and J. Hu, *Multiscale analysis of complex time series: integration of chaos and random fractal theory, and beyond*. Wiley, 2007.

[149] K. Popp and P. Stelter, "Stick-slip vibrations and chaos," *Philosophical Transactions: Physical Sciences and Engineering*, vol. 332, no. 12, pp. 89–105, 1990.

[150] B. Bona and M. Indri, "Friction compensation in robotics: An overview," in *Proceedings of the 44th IEEE Conference on Decision and Control* (S. Seville, ed.), 2005.

[151] S. Zschäck, S. Bichner, A. Amthor, and C. Ament, "Maxwell slip based adaptive friction compensation in high precision applications," in *IECON 2012*, (Montreal, QC, Canada), 38th Annual Conference on IEEE Industrial Electronics Society, 2012.

[152] C. H. Scholz, "Earthquakes and friction laws," *Nature*, vol. 391, no. 6662, pp. 37–42, 1998.

[153] C. H. Scholz, "Paradigms or small change in earthquake mechanics," *International Geophysics*, vol. 51, pp. 505–517, 1992.

[154] R. A. Harris, "Large earthquakes and creeping faults," *Reviews of Geophysics*, vol. 55, pp. 169–198, 2017.

[155] S. M. Lee, M. W. Shin, W. K. Lee, and H. Jang, "The correlation between contact stiffness and stick-slip of brake friction materials," *Wear*, vol. 302, no. 1-2, pp. 1414–1420, 2013.

[156] S. Maegawa, A. Suzuki, and K. Nakano, "Precursors of global slip in a longitudinal line contact under non-uniform normal loading," *Tribology Letters*, vol. 38, pp. 313–323, 2010.

[157] C. Gao, D. Kuhlmann-Wilsdorf, and D. D. Makel, "The dynamic analysis of stick-slip motion," *Wear*, vol. 173, no. 1-2, pp. 1–12, 1994.

[158] R. L. Biegel, W. Wang, C. H. Scholz, G. N. Boitnott, and N. Yoshioka, "Micromechanics of rock friction 1. effects of surface roughness on initial friction and slip hardening in westerly granite," *Journal of Geophysical Research*, vol. 97, pp. 8951–8964, 1992.

[159] A. Prevost, J. Scheibert, and G. Debrégeas, "Probing the micromechanics of a multi-contact interface at the onset of frictional sliding," *The European Physical Journal E*, vol. 36, p. 17, 2013.

[160] J. M. Carlson and J. S. Langer, "Properties of earthquakes generated by fault dynamics," *Physical Review Letters*, vol. 62, no. 22, pp. 2632–2635, 1989.

[161] H. Nakanishi, "Cellular-automaton model of earthquakes with deterministic dynamics," *Physical Review A*, vol. 41, no. 12, pp. 7086–7089, 1990.

[162] H. Nakanishi, "Statistical properties of the cellular-automaton model for earthquakes," *Physical Review A*, vol. 43, no. 12, pp. 6613–6621, 1991.

[163] J. Schmittbuhl, J.-P. Vilotte, and S. Roux, "Propagative macrodislocation modes in an earthquake fault model," *Europhysics Letters*, vol. 21, no. 3, pp. 375–380, 1993.

[164] Z. Olami, H. J. S. Feder, and K. Christensen, "Self-organized criticality in a continuous, nonconservative cellular automaton modeling earthquakes," *Physical Review Letters*, vol. 68, no. 8, pp. 1244–1248, 1992.

[165] P. G. Akishin, M. V. Altaisky, I. Antoniou, A. D. Budnik, and V. V. Ivanov, "Simulation of earthquakes with cellular automata," *Discrete Dynamics in Nature and Society*, vol. 2, no. 4, pp. 267–279, 1998.

[166] D. D. Rizos and S. D. Fassois, "Presliding friction identification based upon the maxwell slip model structure," *Chaos*, vol. 14, no. 2, pp. 431–445, 2004.

[167] F. Al-Bender, V. Lampaert, and J. Swevers, "The generalized Maxwell-slip model: A novel model for friction simulation and compensation," *IEEE Transactions on Automatic Control*, vol. 50, no. 11, pp. 1883–1887, 2005.

[168] I. Nilkhamhang and A. Sano, "Model-based adaptive friction compensation for accurate position control," in *Proceedings of the 47th IEEE Conference on Decision and Control* (M. Cancun, ed.), 2008.

[169] Y. Kligerman and M. Varenberg, "Elimination of stick-slip motion in sliding of split or rough surface," *Tribology Letters*, vol. 53, no. 2, pp. 395–399, 2014.

[170] O. Ben-David, S. M. Rubinstein, and J. Fineberg, "Slip-stick and the evolution of frictional strength," *Nature*, vol. 463, no. 7277, pp. 76–79, 2010.

[171] A. I. Vakis, V. A. Yastrebov, J. Scheibert, L. Nicola, D. Dini, C. Minfray, A. Almqvist, M. Paggi, S. Lee, G. Limbert, J.-F. Molinari, G. Anciaux, R. Aghababaei, S. Echeverri Restrepo, A. Papangelo, A. Cammarata, P. Nicolini, C. Putignano, G. Carbone, S. Stupkiewicz, J. Lengiewicz, G. Costagliola, F. Bosia, R. Guarino, N. M. Pugno, M. H. Müser, and M. Ciavarella, "Modeling and simulation in tribology across scales: An overview," *Tribology International*, vol. 125, pp. 169–199, 2018.

[172] P. L. Menezes, K. Kishore, L. S. V., and M. R., "Role of surface texture roughness, and hardness on friction during unidirectional sliding," *Tribology Letters*, vol. 41, no. 1, pp. 1–15, 2011.

[173] J. D. Byerlee, "Static and kinetic friction of granite at high normal stress," *International Journal of Rock Mechanics and Mining Sciences and Geomechanics Abstracts*, vol. 7, no. 6, pp. 577–582, 1970.

[174] V. A. Yastrebov, "Sliding without slipping under Coulomb friction: Opening waves and inversion of frictional force," *Tribology Letters*, vol. 62, p. 1, 2016.

[175] M. You, "Strength criterion for rocks under compressive-tensile stresses and its application," *Journal of Rock Mechanics and Geotechnical Engineering*, vol. 7, no. 4, pp. 434–439, 2015.

[176] B. Lorenz and B. N. J. Persson, "On the origin of why static or breakloose friction is larger than kinetic friction, and how to reduce it: the role of aging, elasticity and sequential interfacial slip," *Journal of Physics: Condensed Matter*, vol. 24, no. 22, p. 225008, 2012.

[177] A. Heuret, S. Lallemand, F. Funiciello, C. Piromallo, and C. Faccenna, "Physical characteristics of subduction interface type seismogenic zones revisited," *Geochemistry, Geophysics, Geosystems*, vol. 12, 2011.

[178] S. Lallemand, M. Peyret, E. van Rijsingen, D. Arcay, and H. A., "Roughness characteristics of oceanic seafloor prior to subduction in relation to the seismogenic potential of subduction zones," *Geochemistry, Geophysics, Geosystems*, vol. 19, pp. 2121–2146, 2018.

[179] E. van Rijsingen, S. Lallemand, M. Peyret, D. Arcay, A. Heuret, F. Funiciello, and C. F., "How subduction interface roughness influences the occurrence of large interplate earthquakes," *Geochemistry, Geophysics, Geosystems*, vol. 19, pp. 2342–2370, 2018.

[180] K. Wang and S. L. I. r. p. Bilek, "Fault creep caused by subduction of rough seafloor relief," *Tectonophysics*, vol. 610, pp. 1–24, 2014.

[181] O. Zielke, M. Galis, and P. M. Mai, "Fault roughness and strength heterogeneity control earthquake size and stress drop," *Geophysical Research Letters*, vol. 44, pp. 777–783, 2017.

[182] C. W. A. Harbord, S. B. Nielsen, N. De Paola, and R. E. Holdsworth, "Earthquake nucleation on rough faults," *Geology*, vol. 45, no. 10, pp. 931–934, 2017.

[183] Y. Tal, B. H. Hager, and J. P. Ampuero, "The effects of fault roughness on the earthquake nucleation process," *Journal of Geophysical Research: Solid Earth*, vol. 123, no. 1, pp. 437–456, 2018.

[184] G. C. McLaskey, "Earthquake initiation from laboratory observations and implications for foreshocks," *Journal of Geophysical Research: Solid Earth*, vol. 124, no. 12, pp. 12882–12904, 2019.

[185] E. R. Heimisson, "Crack to pulse transition and magnitude statistics during earthquake cycles on a self-similar rough fault," *Earth and Planetary Science Letters*, vol. 537, p. 116202, 2020.

[186] D. Lange, H. Kopp, J.-Y. Royer, P. S. Henry, S. Ergintav, L. Géli, Z. Çakır, F. Petersen, P. Sakic, V. Ballu, J. Bialas, and M. Özeren, "Interseismic strain build-up on the submarine North Anatolian Fault offshore Istanbul," *Nature Communications*, vol. 10, p. 3006, 2019.

[187] J. Schmittbuhl, H. Karabulut, O. Lengliné, and M. Bouchon, "Seismicity distribution and locking depth along the main marmara fault, turkey," *Geochemistry, Geophysics, Geosystems*, vol. 17, pp. 954–965, 2015.

[188] M. Bohnhoff, F. Bulut, G. Dresen, P. E. Malin, T. Eken, and M. Aktar, "An earthquake gap south of Istanbul," *Nature Communications*, vol. 4, p. 1999, 2013.

[189] S. W. Smith and M. Wyss, "Displacement on the San Andreas Fault subsequent to the 1966 Parkfield earthquake," *Bulletin of the seismological society of America*, vol. 58, no. 6, pp. 1955–1973, 1968.

[190] K. V. Steinbrugge, E. G. Zacher, D. Tocher, C. A. Whitten, and C. N. Claire, "Creep on the San Andreas Fault," *Bulletin of the seismological society of America*, vol. 50, no. 3, pp. 389–415, 1960.

[191] R. A. Harris and N. A. Abrahamson, "Strong ground motions generated by earthquakes on creeping faults," *Geophysical Research Letters*, vol. 41, pp. 3870–3875, 2014.

[192] R. Bürgmann, "The geophysics, geology and mechanics of slow fault slip," *Earth and Planetary Science Letters*, vol. 495, pp. 112–134, 2018.

[193] C. H. Scholz, *The mechanics of earthquakes and faulting*. Cambridge University Press, 2012.

[194] R. L. Wesson, "Dynamics of fault creep," *Journal of Geophysical Research*, vol. 93, pp. 8929–8951, 1988.

[195] P. Sakic, H. Piété, V. Ballu, J.-Y. Royer, H. Kopp, D. Lange, F. Petersen, M. S. Özeren, S. Ergintav, L. Geli, P. Henry, and A. Deschamps, "No significant steady state surface creep along the North Anatolian Fault offshore Istanbul: Results of 6 months of seafloor acoustic ranging," *Geophysical Research Letters*, vol. 43, pp. 6817–6825, 2016.

[196] R. Yamamoto, M. Kido, Y. Ohta, N. Takahashi, Y. Yamamoto, A. Pınar, D. Kalafat, H. Özener, and Y. Kaneda, "Seafloor geodesy revealed partial creep of the North Anatolian Fault submerged in the sea of Marmara," *Geophysical Research Letters*, vol. 46, pp. 1268–1275, 2019.

[197] J. R. Rice, "Fault stress states, pore pressure distributions, and the weakness of the San Andreas Fault," *International Geophysics*, vol. 51, pp. 475–503, 1992.

[198] A. H. Lachenbruch and J. H. Sass, "Heat flow and energetics of the San Andreas fault zone," *Journal of Geophysical Research*, vol. 85, pp. 6185–6222, 1980.

[199] T. H. Heaton, "Evidence for and implications of self-healing pulses of slip in earthquake rupture," *Physics of the Earth and Planetary Interiors*, vol. 64, pp. 1–20, 1990.

[200] B. M. Carpenter, C. Marone, and D. M. Saffer, "Weakness of the San Andreas Fault revealed by samples from the active fault zone," *Nature Geoscience*, vol. 4, pp. 251–254, 2011.

[201] O. Ben-David and J. Fineberg, “Static friction coefficient is not a material constant,” *Physical Review Letters*, vol. 106, p. 25430, 2011.

[202] M. S. Longuet-Higgins, “The statistical analysis of a random, moving surface,” *Philosophical Transactions of the Royal Society of London. Series A, Mathematical and Physical Sciences*, vol. 249, no. 966, pp. 321–387, 1957.

[203] M. S. Longuet-Higgins, “Statistical properties of an isotropic random surface,” *Philosophical Transactions of the Royal Society of London. Series A, Mathematical and Physical Sciences*, vol. 250, no. 975, pp. 157–174, 1957.

[204] M. Ciavarella, V. Delfine, and G. Demelio, “A "re-vitalized" Greenwood and Williamson model of elastic contact between fractal surfaces,” *Journal of the Mechanics and Physics of Solids*, vol. 54, no. 12, pp. 2569–2591, 2006.

[205] B. N. J. Persson, “Theory of rubber friction and contact mechanics,” *The Journal of Chemical Physics*, vol. 115, no. 8, pp. 3840–3861, 2001.

[206] B. N. J. Persson, F. Bucher, and B. Chiaia, “Elastic contact between randomly rough surfaces: Comparison of theory with numerical results,” *Physical Review B - Condensed Matter and Materials Physics*, vol. 65, no. 18, pp. 1841061–1841067, 2002.

[207] B. N. J. Persson, O. Albohr, U. Tartaglino, A. I. Volokitin, and E. Tosatti, “On the nature of surface roughness with application to contact mechanics, sealing, rubber friction and adhesion,” *Journal of Physics: Condensed Matter*, vol. 17, no. 1, pp. R1–R62, 2004.

[208] S. Björklund, “A random model for micro-slip between nominally flat surfaces,” *Journal of Tribology*, vol. 119, no. 4, pp. 726–732, 1997.

[209] J. B. Walsh, “A theoretical analysis of sliding of rough surfaces,” *Journal of Geophysical Research: Solid Earth*, vol. 108, no. B8, 2003.

[210] M. Eriten, A. A. Polycarpou, and L. A. Bergman, “Physics-based modeling for fretting behavior of nominally flat rough surfaces,” *International Journal of Solids and Structures*, vol. 48, no. 10, pp. 1436–1450, 2011.

[211] M. Eriten, A. A. Polycarpou, and L. A. Bergman, "A physics-based friction model and integration to a simple dynamical system," *Journal of Vibration and Acoustics*, vol. 134, no. 5, 2012.

[212] J. Armand, L. Salles, C. W. Schwingshackl, D. Süß, and K. Willner, "On the effects of roughness on the nonlinear dynamics of a bolted joint: a multiscale analysis," *European Journal of Mechanics-A/Solids*, vol. 70, pp. 44–57, 2018.

[213] K. Jankowski, A. Saha, and A. Stefański, "Introduction of novel model of friction and analysis of presliding domain of friction with non-local memory effect based upon Maxwell slip model structures," *Tribology International*, vol. 102, pp. 378–391, 2016.

[214] S. Medina, D. Nowell, and D. Dini, "Analytical and numerical models for tangential stiffness of rough elastic contacts," *Tribology Letters*, vol. 49, no. 1, pp. 103–115, 2013.

[215] C. Campañá, B. N. J. Persson, and M. H. Müser, "Transverse and normal interfacial stiffness of solids with randomly rough surfaces," *Journal of Physics: Condensed Matter*, vol. 23, no. 8, p. 085001, 2011.

[216] M. A. Yaqoob, A. Winogrodzka, H. R. Fischer, E. R. M. Gelinck, M. B. de Rooij, and D. J. Schipper, "Pre-sliding Behaviour of Single Asperity Contact," *Tribology Letters*, vol. 49, no. 3, pp. 553–562, 2013.

[217] W. R. Chang, I. Etsion, and D. B. Bogy, "Static friction coefficient model for metallic rough surfaces," *Journal of Tribology*, vol. 110, no. 1, pp. 57–63, 1988.

[218] N. I. Gershenzon and G. Bambakidis, "Transition from static to dynamic macroscopic friction in the framework of the Frenkel–Kontorova model," *Tribology International*, vol. 61, pp. 11–18, 2013.

[219] J. Y. Yoon and D. L. Trumper, "Friction microdynamics in the time and frequency domains: Tutorial on frictional hysteresis and resonance in precision motion systems," *Precision Engineering*, vol. 55, pp. 101–109, 2019.

[220] F. Al-Bender and K. De Moerlooze, "On the relationship between normal load and friction force in pre-sliding frictional contacts. Part 1: Theoretical analysis," *Wear*, vol. 269, no. 3, pp. 174–182, 2010.

[221] L. Kogut and I. Etsion, "A static friction model for elastic-plastic contacting rough surfaces," *Journal of Tribology*, vol. 126, no. 1, pp. 34–40, 2004.

[222] K. De Moerlooze and F. Al-Bender, "On the relationship between normal load and friction force in pre-sliding frictional contacts. Part 2: Experimental investigation," *Wear*, vol. 269, no. 3, pp. 183–189, 2010.

[223] F. Marques, P. Flores, J. C. Pimenta Claro, and H. M. Lankarani, "A survey and comparison of several friction force models for dynamic analysis of multibody mechanical systems," *Nonlinear Dynamics*, vol. 86, no. 3, pp. 1407–1443, 2016.

[224] H. Olsson, K. J. Åström, C. Canudas de Wit, M. Gäfvert, and L. P., "Friction models and friction compensation," *European Journal of Control*, vol. 4, no. 3, pp. 176–195, 1998.

[225] B. Armstrong-Hélouvry, P. Dupont, and C. Canudas de Wit, "A survey of models, analysis tools and compensation methods for the control of machines with friction," *Automatica*, vol. 30, no. 7, pp. 1083–1138, 1994.

[226] K. Worden, C. X. Wong, U. Parlitz, A. Hornstein, D. Engster, T. Tjahjowidodo, F. Al-Bender, D. D. Rizos, and S. Fassois, "Identification of pre-sliding and sliding friction dynamics: Grey box and black-box models," *Mechanical Systems and Signal Processing*, vol. 21, no. 1, pp. 514–534, 2007.

[227] V. A. Yastrebov, G. Anciaux, and J.-F. Molinari, "From infinitesimal to full contact between rough surfaces: Evolution of the contact area," *International Journal of Solids and Structures*, vol. 52, pp. 83–102, 2015.

[228] G. Carbone and F. Bottiglione, "Asperity contact theories: Do they predict linearity between contact area and load?," *Journal of the Mechanics and Physics of Solids*, vol. 56, no. 8, pp. 2555–2572, 2008.

[229] B. B. Mandelbrot and J. W. Van Ness, "Fractional Brownian motions, fractional noises and applications," *SIAM Review*, vol. 10, p. 422–437, 1968.

[230] H.-O. Peitgen, H. Jürgens, and D. Saupe, *Fractals for the classroom, part one: introduction to fractals and chaos*. Springer, 1992.

[231] H.-O. Peitgen, H. Jürgens, and D. Saupe, *Fractals for the classroom, part two: complex systems and Mandelbrot set*. Springer, 1992.

[232] G. Zavarise, M. Borri-Brunetto, and M. Paggi, "On the resolution dependence of micromechanical contact models," *Wear*, vol. 262, no. 1-2, pp. 42–54, 2007.

[233] B. B. Mandelbrot, "Self-affine fractals and fractal dimension," *Physica Scripta*, vol. 32, pp. 257–260, 1985.

[234] G. Shevchenko, "Fractional Brownian motion in a nutshell," *International Journal of Modern Physics: Conference Series*, vol. 36, p. 1560002, 2015.

[235] G. Zavarise, M. Borri-Brunetto, and M. Paggi, "On the reliability of microscopical contact models," *Wear*, vol. 257, no. 3-4, pp. 229–245, 2004.

[236] M. Paggi and J. R. Barber, "Contact conductance of rough surfaces composed of modified RMD patches," *International Journal of Heat and Mass Transfer*, vol. 54, pp. 4664–4672, 2011.

[237] H.-D. J. Jeong, J.-S. R. Lee, D. McNickle, and K. Pawlikowski, "Suggestions of efficient self-similar generators," *Simulation Modelling Practice and Theory*, vol. 15, no. 3, pp. 328–353, 2007.

[238] Y. Hu and K. Tonder, "Simulation of 3-D random rough surface by 2-D digital filter and Fourier analysis," *International Journal of Machine Tools and Manufacture*, vol. 32, no. 1, pp. 83–90, 1992.

[239] C. Putignano, L. Afferrante, G. Carbone, and G. Demelio, "A new efficient numerical method for contact mechanics of rough surfaces," *International Journal of Solids and Structures*, vol. 49, no. 2, pp. 338–343, 2012.

[240] B. Claudia and P. M., "Topology simulation and contact mechanics of bifractal rough surfaces," *Proceedings of the Institution of Mechanical Engineers, Part J: Journal of Engineering Tribology*, vol. 230, p. 1345–58, 2016.

[241] A. B. Dieker and M. Mandjes, "On spectral simulation of fractional Brownian motion," *Probability in the Engineering and Informational Sciences*, vol. 17, no. 3, pp. 417–434, 2003.

[242] O. Banna, Y. Mishura, K. Ralchenko, and S. Shklyar, *Fractional Brownian Motion: Approximations and Projections*. Wiley, 2019.

[243] M. H. Müser and A. Wang, "Contact-patch-size distribution and limits of self-affinity in contacts between randomly rough surfaces," *Lubricants*, vol. 6, 2018.

[244] J. H. Dieterich and B. D. Kilgore, "Imaging surface contacts: power law contact distributions and contact stresses in quartz, calcite, glass and acrylic plastic," *Tectonophysics*, vol. 256, no. 1, pp. 219–239, 1996.

[245] C. Campañá, "Using Green's function molecular dynamics to rationalize the success of asperity models when describing the contact between self-affine surfaces," *Physical Review E*, vol. 78, p. 026110, 2008.

[246] A. A. Polycarpou and I. Etsion, "Analytical approximations in modeling contacting rough surfaces," *Journal of Tribology*, vol. 121, no. 2, pp. 234–239, 1999.

[247] P. Lu and S. J. O'Shea, "Mechanical contact between rough surfaces at low load," *Journal of Physics D: Applied Physics*, vol. 45, no. 47, p. 475303, 2012.

[248] B. Mandelbrot, *The fractal geometry of nature*, vol. 1. W. H. Freeman and Company, 1982.

[249] T. R. Thomas, *Rough Surfaces*. Imperial College Press, 2nd ed., 1998.

[250] T. D. B. Jacobs, L. Pastewka, and Guest Editors, "Surface topography as a material parameter," *MRS Bulletin*, pp. 1–6, 2023.

[251] R. Capozza and M. Urbakh, "Static friction and the dynamics of interfacial rupture," *Physical Review B*, vol. 86, p. 085430, 2012.

[252] J. Trømborg, J. Scheibert, D. S. Amundsen, K. Thøgersen, and A. Malthe-Sørenssen, "Transition from static to kinetic friction: insights from a 2d model," *Physical review letters*, vol. 107, no. 7, p. 074301, 2011.

[253] D. S. Amundsen, J. Scheibert, K. Thøgersen, J. Trømborg, and A. Malthe-Sørenssen, "1D model of precursors to frictional stick-slip motion allowing for robust comparison with experiments," *Tribology Letters*, vol. 45, pp. 357–369, 2012.

[254] M. Radiguet, D. S. Kammer, P. Gillet, and J.-F. Molinari, "Survival of heterogeneous stress distributions created by precursory slip at frictional interfaces," *Physical review letters*, vol. 111, no. 16, p. 164302, 2013.

[255] K. Thøgersen, "Modeling the onset of dynamic friction: contact mechanics," Master's thesis, 2011.

[256] G. C. McLaskey and B. D. Kilgore, "Foreshocks during the nucleation of stick-slip instability," *Journal of Geophysical Research: Solid Earth*, vol. 118, no. 6, pp. 2982–2997, 2013.

[257] P. A. Selvadurai, S. D. Glaser, and J. M. Parker, "On factors controlling precursor slip fronts in the laboratory and their relation to slow slip events in nature," *Geophysical Research Letters*, vol. 44, no. 6, pp. 2743–2754, 2017.

[258] X. Zhou, W. Ma, L. Yang, J. Bi, and H. Cheng, "Experimental study of stick-slip failure processes and effect of physical properties on stick-slip behavior," *Journal of Geophysical Research: Solid Earth*, vol. 123, no. 1, pp. 653–673, 2018.

[259] R. Capozza, S. M. Rubinstein, I. Barel, M. Urbakh, and J. Fineberg, "Stabilizing stick-slip friction," *Physical review letters*, vol. 107, no. 2, p. 024301, 2011.

[260] G. C. McLaskey and S. D. Glaser, "Micromechanics of asperity rupture during laboratory stick slip experiments," *Geophysical Research Letters*, vol. 38, no. 12, 2011.

[261] O. Ben-David, G. Cohen, and J. Fineberg, "The dynamics of the onset of frictional slip," *Science*, vol. 330, no. 6001, pp. 211–214, 2010.

[262] E. Bayart, I. Svetlizky, and J. Fineberg, "Fracture mechanics determine the lengths of interface ruptures that mediate frictional motion," *Nature Physics*, vol. 12, no. 2, pp. 166–170, 2016.

[263] I. Svetlizky, E. Bayart, and J. Fineberg, "Brittle fracture theory describes the onset of frictional motion," *Annual Review of Condensed Matter Physics*, vol. 10, pp. 253–273, 2019.

[264] Y. Ben-Zion and G. Dresen, "A synthesis of fracture, friction and damage processes in earthquake rupture zones," *Pure and Applied Geophysics*, pp. 1–17, 2022.

[265] K. Nakano and S. Maegawa, "Stick-slip in sliding systems with tangential contact compliance," *Tribology International*, vol. 42, no. 11-12, pp. 1771–1780, 2009.

[266] J. R. Rice and A. L. Ruina, "Stability of steady frictional slipping," *Journal of Applied Mechanics*, vol. 50, no. 2, pp. 343–349, 1983.

[267] B. Erickson, B. Birnir, and D. Lavallée, "A model for aperiodicity in earthquakes," *Nonlinear processes in geophysics*, vol. 15, no. 1, pp. 1–12, 2008.

[268] F. Al-Bender and J. Swevers, "Characterization of friction force dynamics," *IEEE Control Systems Magazine*, vol. 28, no. 6, pp. 64–81, 2008.

[269] W. D. Iwan, "A distributed-element model for hysteresis and its steady-state dynamic response," *Journal of Applied Mechanics*, vol. 33, no. 4, pp. 893–900, 1966.

[270] J. H. Dieterich, "Time-dependent friction as a possible mechanism for aftershocks," *Journal of Geophysical Research*, vol. 77, no. 20, pp. 3771–3781, 1972.

[271] J. M. Carlson and J. S. Langer, "Mechanical model of an earthquake fault," *Physical Review A*, vol. 40, no. 11, p. 6470, 1989.

[272] J. M. Carlson, J. S. Langer, B. E. Shaw, and C. Tang, "Intrinsic properties of a Burridge-Knopoff model of an earthquake fault," *Physical Review A*, vol. 44, no. 2, p. 884, 1991.

[273] I. Clancy and D. Corcoran, "Criticality in the Burridge-Knopoff model," *Physical Review E*, vol. 71, no. 4, p. 046124, 2005.

[274] I. Clancy and D. Corcoran, "State-variable friction for the Burridge-Knopoff model," *Physical Review E*, vol. 80, no. 1, p. 016113, 2009.

[275] H. Kawamura, Y. Ueda, S. Kakui, S. Morimoto, and T. Yamamoto, "Statistical properties of the one-dimensional Burridge-Knopoff model of earthquakes obeying the rate-and state-dependent friction law," *Physical Review E*, vol. 95, no. 4, p. 042122, 2017.

[276] M. Renardy, "Ill-posedness at the boundary for elastic solids sliding under coulomb friction," *Journal of Elasticity*, vol. 27, no. 3, pp. 281–287, 1992.

[277] F. M. F. Simões and J. A. C. Martins, "Instability and ill-posedness in some friction problems," *International Journal of Engineering Science*, vol. 36, no. 11, pp. 1265–1293, 1998.

[278] E. A. Brener, M. Weikamp, R. Spatschek, Y. Bar-Sinai, and E. Bouchbinder, "Dynamic instabilities of frictional sliding at a bimaterial interface," *Journal of the Mechanics and Physics of Solids*, vol. 89, pp. 149–173, 2016.

[279] L. Knopoff, "Noncausality of numerical models of dynamic fracture growth," *Annali Di Geofisica*, vol. XL, no. 5, 1997.

[280] L. Knopoff and X. X. Ni, "Numerical instability at the edge of a dynamic fracture," *Geophysical Journal International*, vol. 147, no. 3, pp. F1–F6, 2001.

[281] R. Burridge, "Admissible speeds for plane-strain self-similar shear cracks with friction but lacking cohesion," *Geophysical Journal International*, vol. 35, no. 4, pp. 439–455, 1973.

[282] D. J. Andrews, "Rupture velocity of plane strain shear cracks," *Journal of Geophysical Research*, vol. 81, no. 32, pp. 5679–5687, 1976.

[283] M. Ohnaka and T. Yamashita, "A cohesive zone model for dynamic shear faulting based on experimentally inferred constitutive relation and strong motion source parameters," *Journal of Geophysical Research: Solid Earth*, vol. 94, no. B4, pp. 4089–4104, 1989.

[284] R. Burridge, G. Conn, and L. B. Freund, "The stability of a rapid mode II

shear crack with finite cohesive traction," *Journal of Geophysical Research: Solid Earth*, vol. 84, no. B5, pp. 2210–2222, 1979.

[285] C. Liu, Y. Huang, and A. J. Rosakis, "Shear dominated transonic interfacial crack growth in a bimaterial-II. Asymptotic fields and favorable velocity regimes," *Journal of the Mechanics and Physics of Solids*, vol. 43, no. 2, pp. 189–206, 1995.

[286] A. J. Rosakis, O. Samudrala, and D. Coker, "Cracks faster than the shear wave speed," *Science*, vol. 284, no. 5418, pp. 1337–1340, 1999.

[287] M. Bouchon, M.-P. Bouin, H. Karabulut, M. N. Toksöz, M. Dietrich, and A. J. Rosakis, "How fast is rupture during an earthquake? New insights from the 1999 Turkey Earthquakes," *Geophysical Research Letters*, vol. 28, no. 14, pp. 2723–2726, 2001.

[288] M. Bouchon and M. Vallée, "Observation of long supershear rupture during the magnitude 8.1 Kunlunshan earthquake," *Science*, vol. 301, no. 5634, pp. 824–826, 2003.

[289] T. H. Heaton, "Evidence for and implications of self-healing pulses of slip in earthquake rupture," *Physics of the Earth and Planetary Interiors*, vol. 64, no. 1, pp. 1–20, 1990.

[290] A. E. Elbanna and T. H. Heaton, "A new paradigm for simulating pulse-like ruptures: the pulse energy equation," *Geophysical Journal International*, vol. 189, no. 3, pp. 1797–1806, 2012.

[291] A. E. Elbanna, *Pulselike Ruptures on Strong Velocity-Weakening Frictional Interfaces: Dynamics and Implications*. PhD thesis, California Institute of Technology, 2011.

[292] X. Lu, N. Lapusta, and A. J. Rosakis, "Pulse-like and crack-like dynamic shear ruptures on frictional interfaces: experimental evidence, numerical modeling, and implications," *International Journal of Fracture*, vol. 163, no. 1, pp. 27–39, 2010.

[293] H. Shlomai and J. Fineberg, "The structure of slip-pulses and supershear ruptures driving slip in bimaterial friction," *Nature communications*, vol. 7, no. 1, p. 11787, 2016.

[294] Y. Ueda, S. Morimoto, S. Kakui, T. Yamamoto, and H. Kawamura, "Nucleation process in the burridge-knopoff model of earthquakes," *Europhysics Letters (EPL)*, vol. 106, no. 6, p. 69001, 2014.

[295] J. Schmittbuhl, J.-P. Vilotte, and S. Roux, "Propagative macrodislocation modes in an earthquake fault model," *Europhysics Letters (EPL)*, vol. 21, no. 3, p. 375, 1993.

[296] K. Thøgersen, E. Aharonov, F. Barras, and F. Renard, "Minimal model for the onset of slip pulses in frictional rupture," *Physical Review E*, vol. 103, no. 5, p. 052802, 2021.

[297] J. P. Ampuero and X. Mao, *Upper Limit on Damage Zone Thickness Controlled by Seismogenic Depth*, ch. 13, pp. 243–253. American Geophysical Union (AGU), 2017.

[298] J. H. Dieterich, "Time-dependent friction in rocks," *Journal of Geophysical Research*, vol. 77, pp. 3690–3697, 1972.

[299] G. C. McLaskey, A. M. Thomas, S. D. Glaser, and R. M. Nadeau, "Fault healing promotes high-frequency earthquakes in laboratory experiments and on natural faults," *Nature*, vol. 491, no. 7422, pp. 101–104, 2012.

[300] H. Kawamura, K. Yoshimura, and S. Kakui, "Nature of the high-speed rupture of the two-dimensional Burridge-Knopoff model of earthquakes," *Philosophical Transactions of the Royal Society A*, vol. 377, no. 2136, p. 20170391, 2019.

[301] T. Mori and H. Kawamura, "Simulation study of the two-dimensional Burridge-Knopoff model of earthquakes," *Journal of Geophysical Research: Solid Earth*, vol. 113, no. B6, 2008.

[302] T. Hasumi, T. Akimoto, and Y. Aizawa, "The Weibull-log Weibull transition of the interoccurrence time statistics in the two-dimensional Burridge-Knopoff earthquake model," *Physica A: Statistical Mechanics and its Applications*, vol. 388, no. 4, pp. 483–490, 2009.

[303] T. Hasumi, "Interoccurrence time statistics in the two-dimensional Burridge-Knopoff earthquake model," *Physical Review E*, vol. 76, no. 2, p. 026117, 2007.

[304] H. Weng and J.-P. Ampuero, "The dynamics of elongated earthquake ruptures," *Journal of Geophysical Research: Solid Earth*, vol. 124, no. 8, pp. 8584–8610, 2019.

[305] P. Abry and F. Sellan, "The wavelet-based synthesis for fractional Brownian motion proposed by F. Sellan and Y. Meyer: Remarks and fast implementation," *Applied and computational harmonic analysis*, vol. 3, no. 4, pp. 377–383, 1996.

[306] J.-M. Bardet, G. Lang, G. Oppenheim, A. Philippe, and M. S. Taqqu, "Generators of long-range dependent processes: a survey," *Theory and applications of long-range dependence*, vol. 1, pp. 579–623, 2003.

[307] K. Sigman, "Acceptance-Rejection Method." Available online at: `http://www.columbia.edu/~ks20/4703-Sigman/4703-07-Notes-ARM.pdf`, last accessed on 19.02.2023.

[308] R. D. Mindlin and H. Deresiewicz, "Elastic spheres in contact under varying oblique forces," *Journal of Applied Mechanics*, vol. 20, no. 3, pp. 327–344, 1952.

[309] V. L. Popov, *Contact Mechanics and Friction*, pp. 56–60. Springer, 2010.

[310] S. Yamagishi and S. Morishita, "Friction vibration modeling with detachment and adhesion by Cellular Automata," *Journal of Computational Science*, vol. 11, pp. 226–232, 2015.

Appendix A

FRACTIONAL BROWNIAN MOTION

The random path traveled by a microscopic particle in a solution was first observed by a botanist, Robert Brown, in 1827. The phenomenon and its mathematical model are named after him as Brownian motion. The stochastic process is widely studied in the theory of probability. The earliest studies of Brownian motion were performed by Louis Bachelier (1900) for modeling price fluctuations. Later, Einstein (1905) derived a mathematical model for Brownian motion by applying the laws of physics to the irregular motion of colloidal particles "without knowing that anyone had already observed anything of the kind" (as he wrote in 1948) [248]. Norbert Wiener developed a detailed mathematical formulation for Brownian motion in his 1918 dissertation. Due to Wiener's contributions, the Brownian motion is sometimes called the Weiner process. In 1968, Mandelbrot and Van Ness [229] extended the ordinary Brownian motion (oBm) to *fractional* Brownian motion (fBm) by incorporating the concept of fractal dimension. Since oBm is a special case of fBm, only the latter is studied in this appendix.

A.1 Definition

Fractional Brownian motion, $B_H(t)$, is a centered (zero-mean) Gaussian process whose covaraince function is:

$$\mathrm{Cov}\big[B_H(t), B_H(s)\big] = \mathrm{E}\big[B_H(t)B_H(s)\big] = \frac{1}{2}(t^{2H} + s^{2H} - |t-s|^{2H}) \qquad \text{(A.1)}$$

where $H \in (0,1)$ is called Hurst exponent [234]. This definition uniquely determines $B_H(t)$ since any Gaussian process is fully specified by its mean and covariance func-

tion. When $H = \frac{1}{2}$ the process is called oBm. A relation between Hurst exponent and the fractal dimension can be derived.

In the following subsections, some essential properties of fBm would be derived by using definition (A.1). In the last subsection the effect of Hurst exponent on the behavior of fBm would be explained in the light of the properties.

A.2 Statistical self-affinity

Self-affinity is defined as preservation of the statistical characteristics of the process under the specific transformation which scales the time, t, by a factor λ and the position, $B_H(t)$, by the factor λ^{-H}. This statistical scale-invariance under the above transformation (with the unequal scaling factors for time and position) is named statistically self-affinity and the fBm is therefore called statistically self-affine [233]. In this section the preservation of statistical properties of fBm under the above transformation is proved. In Subsection A.3.2 it will be explained why the scaling factors of the transformation are chosen as such.

The covariance function of two random processes X and Y is defined as:

$$\begin{aligned}
\mathrm{Cov}\big[X,Y\big] &= \mathrm{E}\big[(X-\mu_X)(Y-\mu_Y)\big] \\
&= \mathrm{E}\big[XY + \mu_Y X - \mu_X Y + \mu_X\mu_Y\big] \\
&= \mathrm{E}\big[XY\big] - \mu_Y\mathrm{E}\big[X\big] - \mu_X\mathrm{E}\big[Y\big] + \mathrm{E}\big[\mu_X\mu_Y\big] \\
&= \mathrm{E}\big[XY\big] - \mu_Y\mu_X - \mu_X\mu_Y + \mu_X\mu_Y \\
&= \mathrm{E}\big[XY\big] - \mu_X\mu_Y \\
&= \mathrm{E}\big[XY\big] - \mathrm{E}\big[X\big]\mathrm{E}\big[Y\big]
\end{aligned} \tag{A.2}$$

Then:

$$\mathrm{Cov}\big[X(t_i),X(t_j)\big] = \mathrm{E}\big[X(t_i)X(t_j)\big] - \mathrm{E}\big[X(t_i)\big]\mathrm{E}\big[X(t_j)\big] \tag{A.3}$$

Since the fBm has a zero-mean distribution the covariance function of the scaled process $\lambda^{-H}B_H(\lambda t)$ is:

$$\begin{aligned}\mathrm{Cov}\big[\lambda^{-H}B_H(\lambda t),\lambda^{-H}B_H(\lambda s)\big] &= \mathrm{E}\big[\lambda^{-H}B_H(\lambda t)\lambda^{-H}B_H(\lambda s)\big]\\ &= \lambda^{-2H}\mathrm{E}\big[B_H(\lambda t)B_H(\lambda s)\big]\end{aligned} \tag{A.4}$$

Then, by using definition (A.1):

$$\begin{aligned}\mathrm{Cov}\big[\lambda^{-H}B_H(\lambda t),\lambda^{-H}B_H(\lambda s)\big] &= \frac{\lambda^{-2H}}{2}\big[(\lambda t)^{2H}+(\lambda s)^{2H}-|\lambda t-\lambda s|^{2H}\big]\\ &= \frac{1}{2}(t^{2H}+s^{2H}-|t-s|^{2H})\\ &= \mathrm{Cov}\big[B_H(t),B_H(s)\big]\end{aligned} \tag{A.5}$$

Equivalence of the covariance functions of $\lambda^{-H}B_H(\lambda t)$ and $B_H(t)$ means that these processes have the same centered Gaussian probability distribution function. Then, the standard deviations have to be equal:

$$\sigma\big[\lambda^{-H}B_H(\lambda t)\big]=\sigma\big[B_H(t)\big]\Rightarrow\sigma\big[B_H(\lambda t)\big]=\lambda^{H}\sigma\big[B_H(t)\big] \tag{A.6}$$

The standard deviation is a measure of random fluctuation intensity. According to the above equation, when λ is decreased the standard deviation of $B_H(\lambda t)$ has to decrease compared to $B_H(t)$. In other words, in order to generate points at lower scales (e.g. $\lambda = 0.1$) the standard deviation of $B_H(t)$ has to be re-scaled by a factor λ^H. For a fixed value of Hurst exponent, a smaller the scaling factor λ leads to a smaller $\sigma[B_H(\lambda t)]$ with respect to $\sigma[B_H(t)]$. Thus, one expects a lower fluctuation intensity at lower scales. For a fixed value of λ, a higher Hurt exponent causes a faster decrease in the standard deviation of $B_H(\lambda t)$. This means that the higher the Hurt exponent is, the faster the expected low intensity of fluctuation at lower scales is reached. In other words, with a high Hurst exponent local smoothness is reached before λ become too small.

A.3 The variance of increments

The variance of the increments of a random process is called its variogram:

$$\mathrm{Var}\big[X(t_j) - X(t_i)\big] = \mathrm{Var}\big[X(t_j)\big] + \mathrm{Var}\big[X(t_i)\big] - 2\mathrm{Cov}\big[X(t_j), X(t_i)\big] \quad \text{(A.7)}$$

By substituting definition (A.3):

$$\begin{aligned}\mathrm{Var}\big[X(t_j) - X(t_i)\big] = \mathrm{Var}\big[X(t_j)\big] + \mathrm{Var}\big[X(t_i)\big] - \ldots \\ 2(\mathrm{E}\big[X(t_j)X(t_i)\big] - \mathrm{E}\big[X(t_j)\big]\mathrm{E}\big[X(t_i)\big])\end{aligned} \quad \text{(A.8)}$$

Then, by changing the notation the variogram of the fBm is:

$$\mathrm{Var}\big[B_H(t) - B_H(s)\big] = \mathrm{Var}\big[B_H(t)\big] + \mathrm{Var}\big[B_H(s)\big] - 2\mathrm{E}\big[B_H(t)B_H(s)\big] \quad \text{(A.9)}$$

Note that $\mathrm{Var}\big[B_H(t)\big] = \mathrm{E}\big[\big(B_H(t)\big)^2\big]$. Rewriting the right hand side terms by using definition (A.1):

$$\mathrm{Var}\big[B_H(t) - B_H(s)\big] = t^{2H} + s^{2H} - 2\{\frac{1}{2}(t^{2H} + s^{2H} - |t-s|^{2H})\} \quad \text{(A.10)}$$

Then, the variogram is:

$$\mathrm{Var}\big[B_H(t) - B_H(s)\big] = |t-s|^{2H} \quad \text{(A.11)}$$

Therefore, the standard deviation of the increments of fBm is:

$$\sigma\big[B_H(t) - B_H(s)\big] = |t-s|^{H} \quad \text{(A.12)}$$

The above relation expresses that variation in increment of $B_H(t)$ within a time interval is proportional to the length of the interval. For the fixed length of interval $|t-s| < 1$, a higher Hurst exponent means a lower $\sigma\big[B_H(t) - B_H(s)\big]$. This means that a $B_H(t)$ with a higher Hurst exponent is expected to be locally smoother compared to its low Hurst exponent counterparts (which are expected to be locally

rougher). However, for the fixed length of interval $|t-s|>1$, a higher Hurst exponent means a higher $\sigma\big[B_H(t)-B_H(s)\big]$. This means that a $B_H(t)$ with a higher Hurst exponent is expected to be globally "bumpier" compared to its low Hurst exponent counterparts (which are expected to be globally less "bumpy").

A.3.1 An inappropriate way for generating fBm

The literature provides a rich collection of exact and approximate methods for generating fBm. See [148, 241] for a list of the methods. The Hosking and Cholesky methods are among the exact methods. The spectral simulation, the RMD method, and wavelet-based simulation [305] are among the approximate methods. In [306], a review of long-range dependence process generators is provided. It may be thought that there is an easy way to generate fBm, as explained below. It will be explained why the easy way is not the proper way.

The fBm always starts from $B_H(t=0)=0$. It may seem easy to generate fBm by using the distribution of increments since the standard deviation of the increments of $B_H(t)$ is given by Equation (A.12). The half-baked idea is to start from $B_H(t=0)=0$ and generate $B_H(t)$ points by successively adding the randomly generated Gaussian increments. The technique is to multiply the known standard deviation value of ΔB_H, i.e., ΔT^H, with the set of random variables generated by the standard Gaussian probability distribution function, $\mathcal{N}(0,1)$. In other words, the set of Gaussian increments is obtained by applying the linear transformation law for random variables: $\mathcal{N}(\mu,\sigma)=\sigma\mathcal{N}(0,1)+\mu$, or in our case: $\mathcal{N}(0,\sigma)=\sigma\mathcal{N}(0,1)$.

Although ΔB_H is proportional to ΔT^H according to Equation (A.12), the above idea is not an appropriate way for generating the fBm since Equation (A.12) holds for *all* of the time intervals of the same length and not *just* for successive time intervals of a certain (minimum) size. Mandelbrot and Van Ness regard this property of fBm as *strong interdependence between distant samples* and call it the basic feature of fBm [229]. The infinite span of interdependence is emphasized in [229] in contrast to the processes in which the sufficiently distant samples are independent or nearly so. According to [229] the long-term interdependence is observed in economics and hydrology. The evidence for the latter [229] recorded in an empirical study conducted

by Harold Edwin Hurst (1880-1978) [248] who undertook an intensive study on the records of water flows through the Nile [229].

A.3.2 Self-affine transformation as a function

Here it is explained how the specific form of the process $\lambda^{-H}B_H(\lambda t)$ (as proposed in Section A.2) is selected as the self-affine transformation of $B_H(t)$. Putting $s = 0$ in Equation (A.12), since $B_H(s = 0) = 0$:

$$\sigma\big[B_H(t)\big] = t^H \tag{A.13}$$

Then:

$$\sigma\big[B_H(\lambda t)\big] = (\lambda t)^H \tag{A.14}$$

Note that (A.14) can also be obtained by substituting Equation (A.13) into Equation (A.6). Equation (A.14) is the mathematical expression of the resolution dependence of $B_H(t)$. As λ decreases the standard deviation of the lower scales decreases.

In Section A.2 it is claimed and proved that $\lambda^{-H}B_H(\lambda t)$ is statistically *affine* to $B_H(t)$. The statistical invariance of $\lambda^{-H}B_H(\lambda t)$ can be expressed explicitly by re-arranging and combining Equations (A.13) and (A.14) to:

$$\sigma\big[\lambda^{-H}B_H(\lambda t)\big] = \sigma\big[B_H(t)\big] = t^H \tag{A.15}$$

A conventional measure of surface roughness is the standard deviation of heights. However, the standard deviation is known to be strongly resolution dependent [13], i.e., the measure changes with scale of sampling (resolution of the data) or the resolution of the stylus profiler (resolution of the roughness measuring instrument).

A.4 The covariance of increments

As can be seen in Figure A.1, when $H \in (0, 0.5)$ the fBm fluctuate frequently. This pattern of behavior is named anti-persistence (or counter-persistence). On the other hand, when $H \in (0.5, 1)$ the fBm tends to persevere its rising or falling trend. This

pattern of behavior is called persistence. The fBm signals are generated using MATLAB command: `wfbm(H,N)`, where H is the Hurst exponent and N is the number of points. The black fBm is generated with $H = 0.1$ and fluctuates and fails to persist in rise or fall. The grey fBm is generated with $H = 0.9$ and persist in rise (or fall). In this section the switch in the behavior of $B_H(t)$ which occurs at $H = 0.5$ is explained.

The covariance of the increments of $B_H(t)$ discloses valuable information about behavior of the fBm. The definition (A.3) for $X(s_1, t_1) = B_H(t_1) - B_H(s_1)$ and $X(s_2, t_2) = B_H(t_2) - B_H(s_2)$ leads to:

$$\begin{aligned}
\mathrm{Cov}\big[X(s_1,t_1), X(s_2,t_2)\big] &= \mathrm{E}\big[\big(B_H(t_1) - B_H(s_1)\big)\big(B_H(t_2) - B_H(s_2)\big)\big] \\
&= \mathrm{E}\big[\big(B_H(t_1)B_H(t_2) - B_H(t_1)B_H(s_2) - \dots \\
&\qquad B_H(s_1)B_H(t_2) + B_H(s_1)B_H(s_2)\big)\big] \\
&= \mathrm{E}\big[B_H(t_1)B_H(t_2)\big] - \mathrm{E}\big[B_H(t_1)B_H(s_2)\big] - \dots \\
&\qquad \mathrm{E}\big[B_H(s_1)B_H(t_2)\big)] + \mathrm{E}\big[B_H(s_1)B_H(s_2)\big)]
\end{aligned}$$

Now, using the definition (A.1) for each of the terms on the right hand side and eliminating terms:

$$\begin{aligned}
&\mathrm{E}\big[\big(B_H(t_1) - B_H(s_1)\big)\big(B_H(t_2) - B_H(s_2)\big)\big] = \\
&\qquad \frac{1}{2}\big(|t_1 - s_2|^{2H} + |t_2 - s_1|^{2H} - |t_2 - t_1|^{2H} - |s_2 - s_1|^{2H}\big)
\end{aligned} \tag{A.16}$$

It is assumed that $s_2 = t_1$ and $s_1 < t_1 < t_2$ to produce neighbor intervals. Then, the above equation can be written as:

$$\begin{aligned}
&\mathrm{E}\big[\big(B_H(t_1) - B_H(s_1)\big)\big(B_H(t_2) - B_H(t_1)\big)\big] = \\
&\qquad \frac{1}{2}\big(|t_2 - s_1|^{2H} - |t_2 - t_1|^{2H} - |t_1 - s_1|^{2H}\big)
\end{aligned} \tag{A.17}$$

In addition it is assumed that the neighbor intervals are of the same length. Then, if $a = t_2 - s_1$, $t_2 - t_1 = a/2$ and $t_1 - s_1 = a/2$. Therefore, for the neighbor intervals of the same length equation (A.16) can be written as:

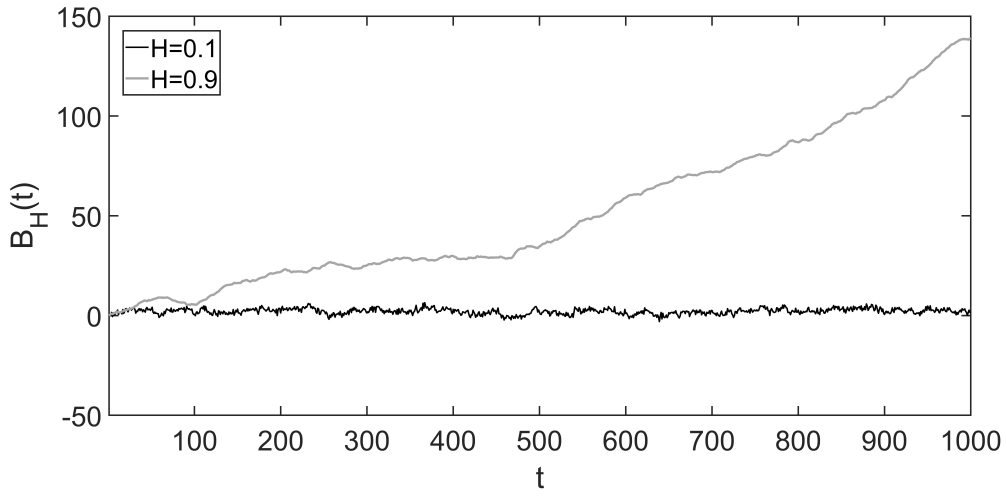

Figure A.1: The anti-persistence and persistence of the fBm

$$\begin{aligned} \mathrm{E}\big[\big(B_H(t_1)-B_H(s_1)\big)\big(B_H(t_2)-B_H(t_1)\big)\big] &= \frac{1}{2}\big(a^{2H}-(\frac{a}{2})^{2H}-(\frac{a}{2})^{2H}\big) \\ &= \frac{1}{2}a^{2H}(1-2^{1-2H}) \end{aligned} \tag{A.18}$$

The right hand side expression is: (i) negative when $H \in (0, 0.5)$ (ii) zero when $H = 0.5$ and (iii) positive when $H \in (0.5, 1)$. The left hand side expresses the average value of the multiplication of $B_H(t)$ increments. Therefore, when $H \in (0, 0.5)$ the sign of increments in the neighbor intervals are expected to be opposite, i.e., an increase in $B_H(t)$ is likely to be followed by a decrease and vice versa. This is why an fBm with $H \in (0, 0.5)$ is named anti-persistent (or counter-persistent); since the next increment will presumably be a reverse of the current one. On the other hand, when $H \in (0.5, 1)$ the sign of increments in the neighbor intervals are expected to remain the same, i.e., an increase in $B_H(t)$ is likely to be followed by another increase and vice versa. This is why an fBm with $H \in (0.5, 1)$ is called persistent; since the next increment will presumably be a continuation of the current one.

When $H = 0.5$, $B_H(t)$ is neither persistence nor anti-persistence, i.e., the oBm behaves with no memory of rising and falling its neighbor intervals and acts independently in this sense. Note that persistent or anti-persistent behavior would be the same over all of the length scales as no specific interval size is chosen in our reasoning. The covariance function of the random process depends solely on Hurst exponent [234].

It can be shown that the relation between Hurst exponent and the fractal dimension, i.e., $D = 2 - H$, is deduced from proportionality of ΔB_H to ΔT^H. One may find the explanations in [148] and Appendix B of [207] useful.

Assume that $B_H(t)$ is an stationary (time-shift invariant) stochastic process with a Hurst exponent $0 < H < 1$. Also assume that for any scaling factor $r > 0$, the finite joint distribution functions of $B_H(t)$ and $\lambda^{-H} B_H(\lambda t)$ are the same. This transformation is an affinity and $B_H(t)$ is named statistically self-affine random process. Contrary to *similarity*, in the above transformation the dimensions of the process, i.e., time, t, and displacement, $B_H(t)$, are scaled differently, namely by λ and λ^{-H} respectively. Statistical self-affinity of $B_H(t)$ leads to the proportionality relation:

$$\sigma(B_H(t+T) - B_H(t)) \propto T^H \tag{A.19}$$

The exact equality is given in [229]. For a fixed Hurst exponent, the more distant the time points are, i.e., the greater the T, the greater would be the possibility of a higher increment in $B_H(t)$ and vice versa. On the other hand, for a fixed T value, the higher the Hurts exponent is, the *lower* is the possibility of a the increments to remain about mean. In other words a high Hurst exponent encourages extreme fluctuations and a low Hurst exponent tends to keep fluctuations about a mean value.

In contrast to an oBm, an fBm renders a strong interdependence among the outcomes which is desired as empirical observations in finance and nature [20] require such an interdependence. While for the ordinary Brownian motion interpolation is linear and depends only on the endpoints, for fBm, interpolation is nonlinear and depends on all of the points [20]. Both oBm and fBm are statistically self-affine fractals [233].

Appendix B

YASTREBOV'S FORMULATIONS

In this appendix, the analytical formulation for rough surface characterization [25, 227] is summarized. Closed-form expressions for the density of the asperities, and the spectral moments of the surface (and consequently, Nayak parameter) are given. It is assumed that the upper and lower wavelength cutoff values and Hurst exponent are given. The algorithm applied in Chapter 3 to generate the set of asperities is provided.

B.1 Analytical formulas

Yastrebov assumes the rough surface PSD function to be a power function of the magnitude of the wave vector [25, 227]. The log-log plot of the function is a straight line with lower and upper wavenumber cutoffs, k_l and k_s respectively, as the end points:

$$\phi(K) = \begin{cases} \phi_0 (K/k_l)^{-2(1+H)}, & \text{if } 1 \leq K/k_l \leq \zeta. \\ 0, & \text{otherwise.} \end{cases} \tag{B.1}$$

where ϕ_0 is called *scaling factor*, $K = \sqrt{k_x^2 + k_y^2}$, and H, is Hurst exponent. For 3-D surfaces $H = 3 - D$, where D is the fractal dimension. According to [139], the Hurst exponent, H, of real surfaces is between 0.7 and 1. Therefore, the fractal dimension of 3-D realistic surfaces is between 2 and 2.3.

Based on Equation (4.1), by performing a double integral on the PDS function, a closed-form formula for the spectral moments of the surface is derived:

$$m_p = \phi_0 k_l^{p+2} \frac{\zeta^{p-2H} - 1}{p - 2H} T(p) \tag{B.2}$$

where:

$$T(p) = \begin{cases} 2\pi, & \text{if } p = 0. \\ \pi, & \text{if } p = 2. \\ 3\pi/4, & \text{if } p = 4. \end{cases} \tag{B.3}$$

and the wavenumber ratio is defined as $\zeta = k_s/k_l$.

Here, I assume that the zeroth spectral moment of the surface, $m_0 = \sigma^2$ is given. Then a closed-form expression for the scaling factor can be found:

$$\phi_0 = \frac{H}{\pi k_l^2 (1 - \zeta^{-2H})} m_0 \tag{B.4}$$

By substituting the above expression into Equation (B.2), closed-form expressions for the second and fourth spectral moments are obtained as:

$$m_2 = \frac{H(\zeta^{2-2H} - 1)}{(2 - 2H)(1 - \zeta^{-2H})} m_0 k_l^2 \tag{B.5}$$

$$m_4 = \frac{3H(\zeta^{4-2H} - 1)}{(16 - 8H)(1 - \zeta^{-2H})} m_0 k_l^4 \tag{B.6}$$

The above equations are important because m_2 is used in Equation (F.8) to calculate the plasticity index, and m_4 is the variance of the asperity tip curvatures, i.e., $m_4 = \sigma_\kappa^2$ and determines the values generated by the joint PDF (see Appendix C). Furthermore, by substituting Equations (B.5) and (B.6) into Equation (3.4), it can be seen that Nayak parameter is not only independent from m_0 (and consequently the RMS roughness) but also from k_l. In other words, the Nayak parameter is a function of the Hurst exponent and the wavenumber ratio, ζ:

$$\alpha = \alpha(H, \zeta) = \frac{3(1 - H)^2}{2H(H - 2)} \frac{(\zeta^{-2H} - 1)(\zeta^{4-2H} - 1)}{(\zeta^{2-2H} - 1)^2} \tag{B.7}$$

The Nayak parameter is plotted according to Equation (B.7) in Figure B.1 and tabulated in Table B.1. The Hurst exponent hardly affects the Nayak parameter only when the wavenumber ratio, ζ, is below 32. The Nayak parameter increases with increase in ζ.

According to [24], *the spatial density of summits*, i.e., the number of asperities per unit area of the surface, D, is calculated by:

$$D = \frac{\sqrt{3}}{18\pi}\frac{m_4}{m_2} \tag{B.8}$$

By substituting Equations (B.5) and (B.6) into Equation (B.8), m_0 is eliminated. Therefore, D is a function of H, ζ and k_l^2. The closed-form expression for D is given in [227]:

$$D = D(H, \zeta, k_l) = \frac{\sqrt{3}}{24\pi}\frac{1-H}{2-H}\frac{\zeta^{4-2H}-1}{\zeta^{2-2H}-1}k_l^2 \tag{B.9}$$

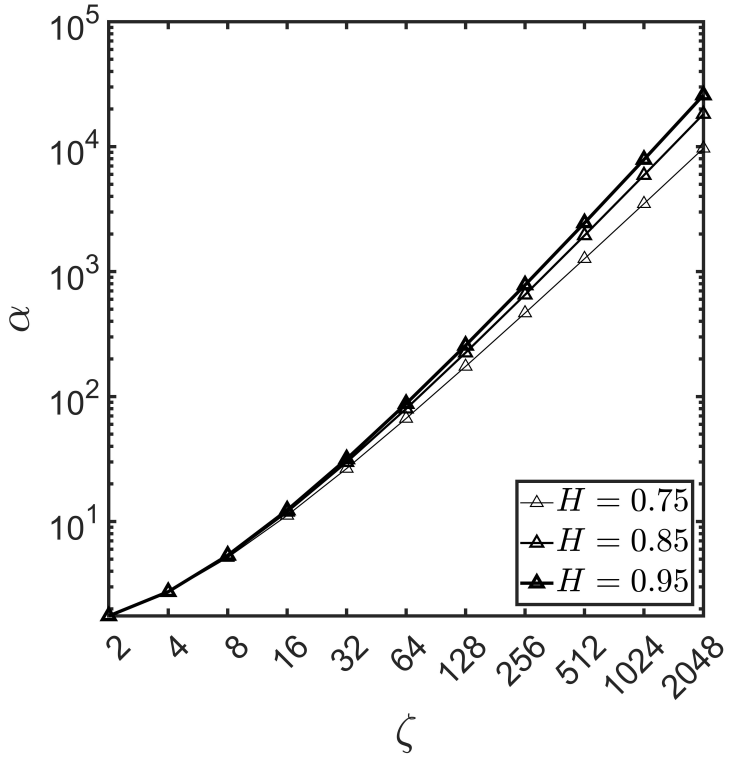

Figure B.1: Nayak parameter, α, against $\zeta = \tilde{k}_s/\tilde{k}_l$ for $H = \{0.75, 0.85, 0.95\}$ according to Equation (B.7).

Table B.1: Nayak parameter, α, against ζ values with $H = \{0.75, 0.85, 0.95\}$ according to Equation (B.7).

ζ \ H	0.75	0.85	0.95
2	1.75	1.76	1.76
4	2.71	2.73	2.74
8	5.15	5.29	5.37
16	11.19	11.94	12.34
32	26.56	29.82	31.67
64	66.74	79.85	87.71
128	174.14	224.39	256.52
256	465.92	652.51	781.00
512	1,268.03	1,945.60	2,451.77
1024	3,491.51	5,910.82	7,884.01
2084	9,691.67	18,214.25	25,846.58

B.2 Input

The algorithm input includes: length of the edge of the simulated surface area boundary (that is a square), L; the grid size, i.e., the number of points that are considered on each of the edges, N; Hurst exponent, H, which for a self-affine surface is related to the fractal dimension of the surface by $D = 3 - H$; the standard deviation of the heights of the surface points, σ, which directly gives the zeroth spectral moment of the surface ($m_0 = \sigma^2$) that is equal to the variance of the point heights; and the static and dynamic COF, μ_s and μ_d.

The dimensionless lower and upper cutoff wavenumbers of the PSD function are represented by $\tilde{k}_l$ and $\tilde{k}_s$ respectively:

$$\tilde{k}_l = \frac{L}{\lambda_l} = \frac{L}{2\pi} k_l \tag{B.10}$$

and similarly:

$$\tilde{k}_s = \frac{L}{\lambda_s} = \frac{L}{2\pi} k_s \tag{B.11}$$

where λ stands for wavelength.

The maximum meaningful value for λ_l is L. Thus, $\lambda_l \leq L$. Then, it would be reasonable to assume $\tilde{k}_l = L/\lambda_l \gg 2$. Therefore, a possible criterion can be $\tilde{k}_l \geq 8$. According to [227], in order to have a meaningful discretization, $\lambda_s \gg \Delta x$, where $\Delta x = L/N$. The criterion is then expressed as $\lambda_s = M\Delta x$, where $M \geq 8$. M can be called the wavelength discretization parameter. Substituting into Equation (B.11):

$$\tilde{k}_s = \frac{L}{\lambda_s} = \frac{N\Delta x}{M\Delta x} = \frac{N}{M},\ M \geq 8 \tag{B.12}$$

Note that M can be assigned such that for a various discretizations, namely different grid sizes (N values), $\tilde{k}_s$ values are kept the same. Table B.1 shows sets of the pairs of considered N and M values (in line with the values given in [25] for which $\tilde{k}_s$ values remain the same and also $M \geq 8$.

B.3 Pseudocode

The algorithm for obtaining the set of asperities in Chapter 3 can be summarized in the four steps:

1. Input the following parameters:
    (a) Hurst exponent: H
    (b) The grid size: N in $N_{points} = N^2$
    (c) The dimensionless cutoff wavenumbers: $\tilde{k}_l$ and $\tilde{k}_s$
    (d) The zeroth spectral moment: $m_0 = \sigma^2$
    (e) The side length of the simulation square: L
    (f) The static and dynamic COF: μ_s and μ_d
2. Calculate the following parameters:
    (a) The cutoff wavenumbers: k_l and k_s, by Equations (B.10) and (B.11)
    (b) The PSD function coefficient: ϕ_0, by Equation (B.4)
    (c) The surface spectral moments: m_2 and m_4, by Equations (B.5) and (B.6)
    (d) Nayak parameter: α, by Equation (B.7)

(e) The spatial density of asperities: D, by Equation (B.9)

(f) The number of the asperities: $N_{asp} = DL^2$

3. Use the acceptance-rejection method (Appendix D) to generate a set of N_{asp} random asperity heights according to the asperity height PDF, Equation (C.2).

4. Use the acceptance-rejection method (Appendix D) to generate a random asperity tip curvature according to the joint PDF, Equation (C.2), for each of the asperity heights that are produced in the preceding step.

Appendix C

GREENWOOD'S PROBABILITY DISTRIBUTION FUNCTIONS

In this appendix, the PDF of height and the joint PDF of heights and curvatures proposed by Greenwood in 2006 are presented [27]. These functions are plotted for a range of Nayak parameters to show how the generated asperity heights and curvatures are affected. In order to use the joint PDF of the asperity heights and curvatures, firstly, the set of asperity heights has to be generated using the corresponding PDF for heights as given in [235], and Appendix A of [27] (the expression given in [24] needs some corrections):

$$\begin{aligned} P(\xi) \;=\; & \frac{3}{2\pi}\frac{\sqrt{2\alpha-3}}{\alpha}\xi\exp(-C_1\xi^2) + \\ & \frac{3\sqrt{3}}{2\sqrt{2\pi}}\frac{1}{\alpha}(\xi^2-1)\exp(-\frac{1}{2}\xi^2)(1+\operatorname{erf}(\beta\xi)) + \\ & \sqrt{\frac{\alpha}{2\pi(\alpha-1)}}\exp(\frac{-\alpha\xi^2}{2(\alpha-1)})(1+\operatorname{erf}(\gamma\xi)) \end{aligned} \tag{C.1}$$

where $C_1 = \frac{\alpha}{2\alpha-3}$, $\beta = \sqrt{\frac{3}{2(2\alpha-3)}}$ and $\gamma = \sqrt{\frac{\alpha}{2(\alpha-1)(2\alpha-3)}}$.

The asperity height PDF is completely defined by Nayak parameter, $\alpha = \frac{m_0 m_4}{{m_2}^2}$, where m_0, m_2 and m_4 are the variances of heights, slopes and curvatures of the surface as defined in Equations (3.1)-(3.3). The random height values, $\xi = z/\sigma$, are generated by applying the accaptance-rejection method as explained in Appendix D. The asperity heights can be obtained from $z = \xi\sigma = \xi\sqrt{m_0}$. The asperity height PDFs for a range of Nayak parameter values are shown in Figure C.1.

The asperity heights are measured with respect to the mean of the *surface*. Figure C.1 shows that as Nayak parameter increases from 2 to 1000, the mean asperity height

approaches the surface mean, i.e., zero. Therefore, a low enough Nayak parameter means that the asperities tend to reach greater heights with respect to the surface mean. Conversely, a high enough Nayak parameter means that the asperity heights are distributed evenly about the surface mean.

In order to generate the corresponding asperity tip radii, the ξ values are substituted into the joint PDF to construct the curvature PDF from the joint PDF for each specific asperity height:

$$P(\xi,\hat{g}) = \frac{9}{2\sqrt{2\pi}}\sqrt{\frac{\alpha}{\alpha-1}}\hat{g}^3 \operatorname{erfc}\left[\mu\left(3\hat{g}-\frac{\sqrt{\alpha}}{\alpha-1}\right)\right]\exp\left(\frac{-\alpha\xi^2}{2(\alpha-1)}+\frac{3\hat{g}^2}{2}\right) \tag{C.2}$$

where $\mu = \sqrt{\frac{\alpha-1}{2(2\alpha-3)}}$

The curvature PDF is also completely defined by Nayak parameter, α. The random variable, $\hat{g}$, is generated by applying the accaptance-rejection method as explained in Appendix D. The asperity tip curvatures can be obtained from $g = \hat{g}\sigma_\kappa = \hat{g}\sqrt{m_4}$. The asperity curvature PDFs for a set of asperity heights and a range of Nayak parameter values are shown in Figures C.2 to C.6.

In each of Figures C.2 to C.6, a section of the joint probability distribution function is shown for $\alpha = \{2, 3, 5, 10, 50, 100, 1000\}$. Each figure corresponds to a specific asperity height, which is selected from $\xi = \{1, 1.5, 2, 2.5, 3\}$. Indeed, the curvature PDF is plotted by fixing the asperity height value.

In Figures C.2 to C.6, if one considers the PDFs with $\alpha = 2$, the higher the asperity height for which the is sought, the mean curvature becomes larger. In Figure C.2, for $\alpha = 2$ and $\xi = 1$, the mean curvature is the lowest among all of the plotted PDFs. On the other hand, in Figure C.6, for $\alpha = 2$ and $\xi = 3$, the mean curvature is the highest. This trend of greater mean curvature for higher asperities occurs for all of the considered Nayak parameters. However, when the Nayak parameter is lower, the increase in the mean curvature occurs faster, i.e., the curvature PDF shifts to the right faster. This can be interpreted as the tendency of the PDF to produce smaller radii values (sharper tips) for *higher* asperities. A low Nayak parameter reinforces this tendency, i.e., it not only encourage sharper asperity tips when an asperity tip is high

enough but also blunter asperity tips when the tip height is low enough. On the other hand, a high enough Nayak parameter, e.g., $\alpha = 50$, would hardly allow the asperity tip curvature to change with the asperity height.

In both [27] and [25] closed-form expressions for the total normal load and the real area are derived as a function of the compression, $\delta = d/\sigma$. These expressions include a double integral of the joint PDF given in Equation (C.2). However, the expressions need to include factor $1/\sqrt{3}$. Here the corrected form of the expressions are given:

$$A_{real} = \frac{\sqrt{\alpha}}{6\sqrt{3}} \int_{\hat{g}=0}^{\infty} \int_{\xi=\delta}^{\infty} P(\xi, \hat{g}) \frac{\xi - \delta}{\hat{g}} \, d\xi \, d\hat{g} \tag{C.3}$$

$$P_{total} = \frac{2}{9\pi\sqrt{3}} E^* \alpha^{3/4} \sqrt{m_2} \int_{\hat{g}=0}^{\infty} \int_{\xi=\delta}^{\infty} P(\xi, \hat{g}) \frac{(\xi - \delta)^{3/2}}{\sqrt{\hat{g}}} \, d\xi \, d\hat{g} \tag{C.4}$$

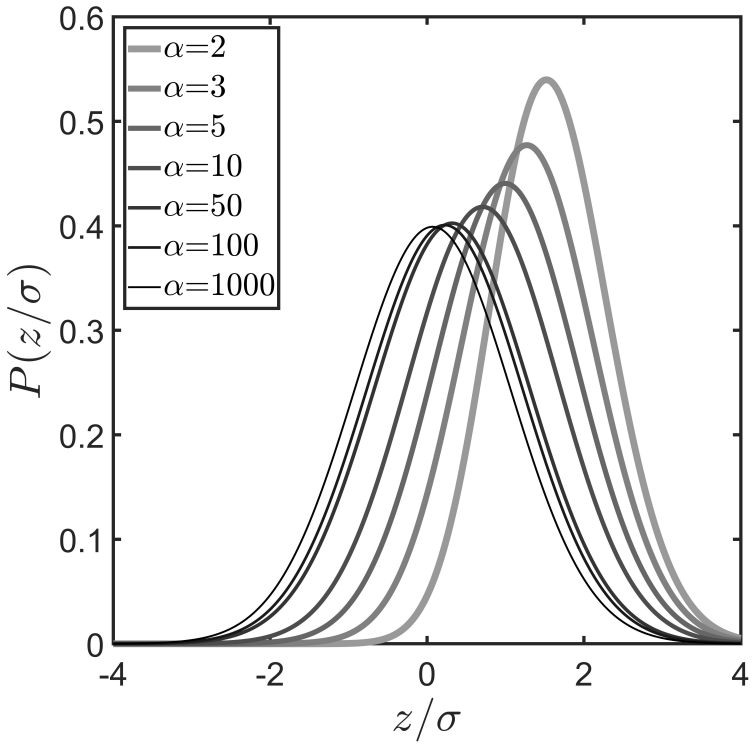

Figure C.1: The asperity height probability distribution functions for $\alpha = \{2, 3, 5, 10, 50, 100, 1000\}$ according to Greenwood's simplified elliptic model.

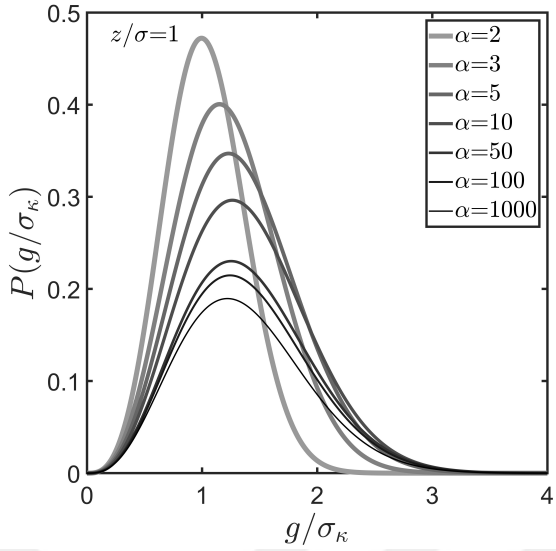

Figure C.2: The asperity tip curvature probability distribution functions for $\xi = 1$ and $\alpha = \{2, 3, 5, 10, 50, 100, 1000\}$ according to Greenwood's simplified elliptic model.

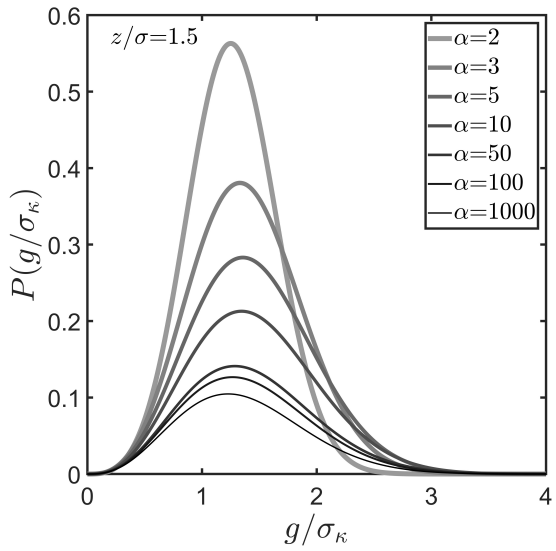

Figure C.3: The asperity tip curvature probability distribution functions for $\xi = 1.5$ and $\alpha = \{2, 3, 5, 10, 50, 100, 1000\}$ according to Greenwood's simplified elliptic model.

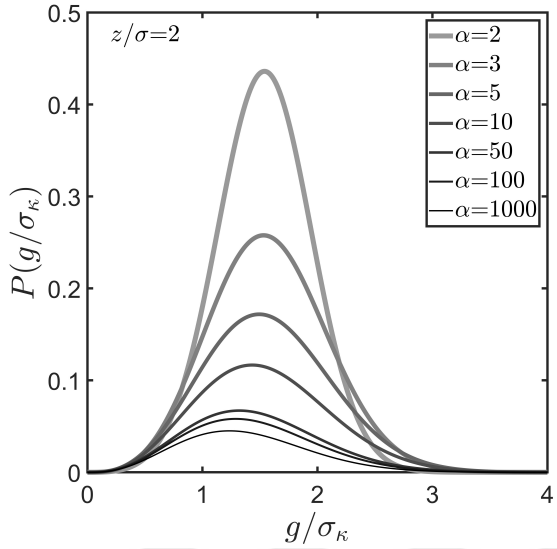

Figure C.4: The asperity tip curvature probability distribution functions for $\xi = 2$ and $\alpha = \{2, 3, 5, 10, 50, 100, 1000\}$ according to Greenwood's simplified elliptic model.

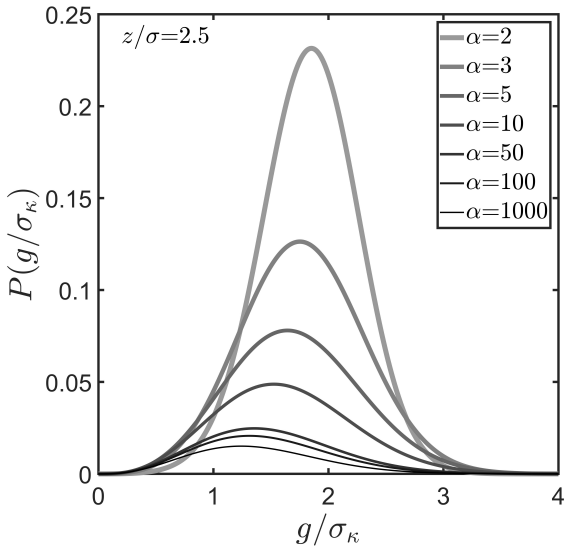

Figure C.5: The asperity tip curvature probability distribution functions for $\xi = 2.5$ and $\alpha = \{2, 3, 5, 10, 50, 100, 1000\}$ according to Greenwood's simplified elliptic model.

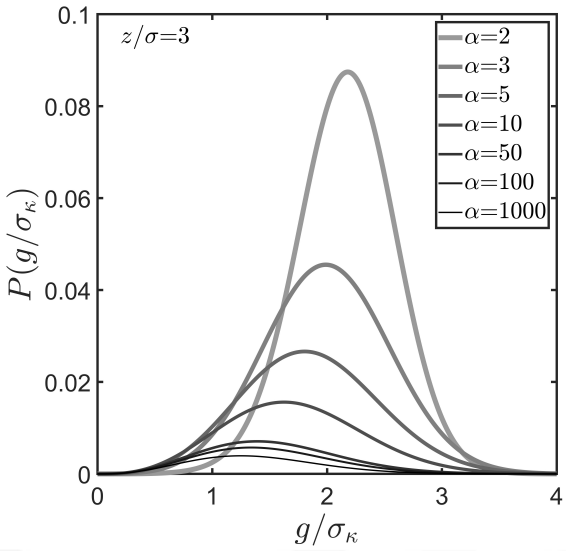

Figure C.6: The asperity tip curvature probability distribution functions for $\xi = 3$ and $\alpha = \{2, 3, 5, 10, 50, 100, 1000\}$ according to Greenwood's simplified elliptic model.

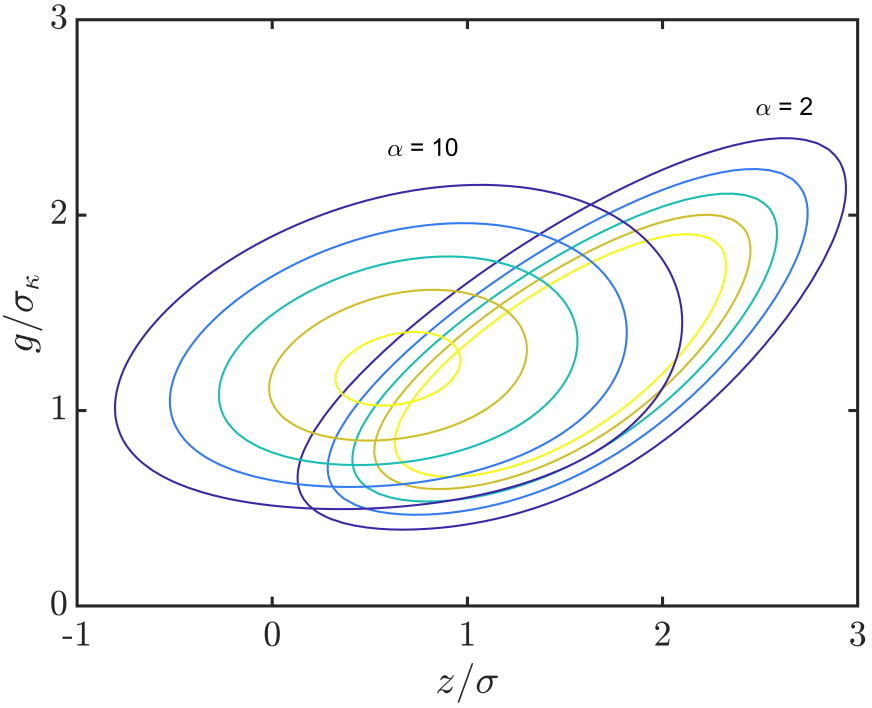

Figure C.7: Contours of Greenwood's joint PDF for heights and curvatures for $\alpha = 2$ and $\alpha = 10$

Appendix D

ACCEPTANCE-REJECTION METHOD

A common way of generating a set of random variables, X, governed by a probability distribution function (PDF), $f(X)$, is to use the inverse cumulative distribution function (CDF), $F^{-1}(x)$. According to the *inverse transform method*, if U is a uniformly random variable in $[0, 1]$, then $X = F^{-1}(U)$. Graphically, the method claims that if you shoot the inverse CDF from a uniformly random set of values that are placed on the vertical axis (i.e. U values) then the abscissas of the shot points will be the desired set of random variables that are governed by $f(X)$. Although the inverse transform method is quite straightforward, there are some cases in which it is impractical to find a closed form $F^{-1}(x)$ or even $F(x)$ [307].

An alternative way of generating a set of random variables, which bypasses the need for the closed form $F^{-1}(x)$, is called the *acceptance-rejection method* or simply the *accept-reject method*. In contrast to the aforementioned approach this method requires only the desired *probability distribution function*.

The basic idea is to envelop the desired PDF by a well-known PDF (e.g. the uniform distribution) and to shoot the envelope by shot marks which have uniformly random abscissas and ordinates. The claim is that *if* a shot mark is below the PDF its abscissa is governed by the desired PDF and is therefore accepted (otherwise, the abscissa is rejected). The mathematical proof of the claim is given in [307].

Assume that an arbitrary PDF, $P(X)$, is given and the question is to generate a set of random variables according to the PDF. In order to use the accceptance-rejection method, the PDF has to have a finite range, $[a, b]$. Otherwise, the PDF has to be reasonably confined to a finite interval. Then, the ordinates of the PDF are divided by the maximum value of the PDF, Y_m, to define the normalized function:

$$f(X) = P(X)/Y_m \tag{D.1}$$

Now, in order to generate an X from $P(X)$ the following steps have to be taken:

1. Generate a uniformly random number, X_p, within $[a, b]$. This can be done by calculating $X_p = a + (b - a)u$ where u is a uniformly random number in $[0, 1]$.
2. Generate another uniformly random number, Y_p, within $[0, 1]$.
3. If $Y_p < f(X_p)$, then X_p is accepted as a member of the desired set. Otherwise, X_p is rejected (ignored).

The first and second steps produce the abscissa, X_p, and the ordinate, Y_p of a point (or a shot mark) respectively. The third step check if the shot mark is below $f(X_p)$ (which leads to acceptance of X_p) or not (which causes rejection of X_p).

Appendix E

HERTZIAN CONTACT

The closed-form solution of the normal contact between elastic solids was proposed by Hertz in 1882. He assumed: (i) frictionless surfaces and (ii) small contact area. The assumptions simplify the problem of normal contact between the elastic bodies with parabolic profiles. Assumption (i) ignores the tangential stress distribution in the contact area (later investigated by Mindlin [308]). Assumption (ii) allows using the available boundary value solutions of elastic half-space deformation in the linear theory of elasticity. Hertz used the known body profile as the normal displacement distribution of the elastic half-space and calculated the corresponding pressure distribution (that would give rise to such a displacement). Hertzian contact solutions are valid when the amount of compression is small compared to the radius of the contact area, and also, the radius of the contact area is small compared to the radii of curvature of the contacting bodies [77].

Hertz's original solution was for the general case of elliptical contact area [82]. A quick way to derive Hertzian solution for the normal contact of a rigid *circular* paraboloid indenter (a paraboloid of revolution) with the elastic half-space is shown in [309]. The configuration of the problem is shown in Figure E.1.

Hertz provides solutions for: (1) the radius of the contact area, a, and immediately the contact area, A, (2) the normal load, P, and (3) maximum normal pressure, σ_{max}. The solutions are expressed as functions of the indentation depth, w, the radius of curvature of the circular paraboloid, R, and the elastic properties of the contacting bodies as shown below:

$$a = \sqrt{Rw} \Rightarrow A = \pi R w \tag{E.1}$$

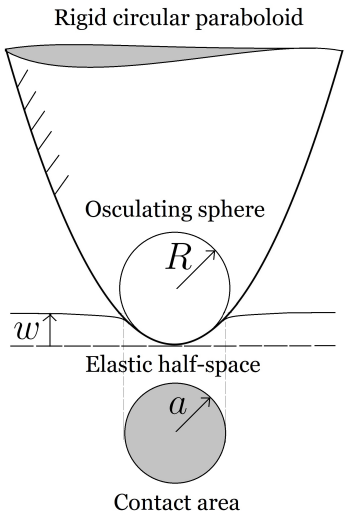

Figure E.1: A rigid circular paraboloid is pressed against the elastic half-space.

$$P = \frac{4}{3} E^* \sqrt{R w^3} \tag{E.2}$$

$$\sigma_{max} = \frac{2}{\pi} E^* \sqrt{\frac{w}{R}} \tag{E.3}$$

where E^* is called the composite Young modulus and is defined as $\frac{1}{E^*} = \frac{1-{\nu_1}^2}{E_1} + \frac{1-{\nu_2}^2}{E_2}$. For a rigid indenter ($E_1 = \infty$) and an elastic body with $E_2 = E$ and $\nu_2 = \nu$:

$$E^* = \frac{E}{1-\nu^2} \tag{E.4}$$

These formulas are used in [21]. As long as the indentation depth is small enough, it can be said that the given solution is also an approximate solution for the normal contact of a *sphere* too. However, to be exact, in [21] the asprities are assumed to be circular paraboloids since the above formulas belong to normal contact of circular paraboloids. In a loose sense it can be said that in the GW model, the asperities are assumed to have *spherical caps* since every circular paraboloids have and osculating sphere at its tip.

Appendix F

PLASTICITY INDEX

Since the Hertzian solution is obtained based on the theory of elasticity, it is important to define a measure to monitor the deformation regime quantitatively. The deformation (compression) has to be small *enough* in order to use Hertz formulas in Appendix E. But how small is small enough? To answer this question, a criterion is needed. Such a criterion should be based on the initiation and development of plasticity during contact. The measure of the surface deformation regime is called the plasticity index and is defined using two different methods in the [21], and [27]. Both of the studies relate the inception of plastic flow to material hardness. The definition in the [21] is based on the maximum Hertzian pressure on a paraboloid, while the definition in [27] is based on the average Hertzian pressure on a paraboloid. The definition given in [21] is:

$$\psi = \sqrt{\frac{\sigma}{w_p}} \tag{F.1}$$

where w_p is the amount of compression at which plasticity is incepted when a sphere is pressed upon an elastic half-space and σ is the standard deviation of the rough surface. The maximum contact pressure on a paraboloid [9] is:

$$p_0 = \frac{2}{\pi} E^* \sqrt{\frac{w}{R}} \tag{F.2}$$

where E^* is the composite Young modulus (as defined in Appendix E), w is elastic compression and R is the radius of the osculating sphere. Then:

$$w = \frac{\pi^2 p_0^2}{4E^{*2}} R \tag{F.3}$$

According to Tabor's hardness test with a spherical indenter [16] the plasticity emerges when the maximum Hertzian pressure, p_0, which occurs at the asperity tip (the center of the contact area) reaches 60% of the material hardness. Therefore, an expression for the limit of elastic deformation (inception of plasticity) is obtained by substituting $p_0 = 0.6H$ into Equation (F.3):

$$w_p = R \left(\frac{H}{E^*} \right)^2 \tag{F.4}$$

The above expression is then substituted into Equation (F.1) to rewrite the first definition of the plasticity index:

$$\psi \equiv \frac{E^*}{H} \sqrt{\frac{\sigma}{R}} \tag{F.5}$$

As stated in [21], if $\psi < 0.6$, then plastic deformation can hardly happen. If $0.6 < \psi < 1$ deformation can be either elastic or plastic and if $1 < \psi$ the deformation would be most probably largely plastic. But why $\psi = 0.6$ is a critical value? The answer is related to the question of how Equation (F.1) is derived in the first place. It is assumed [21] that when the ratio of the plastically deformed area to the real contact area, $A_{plastic}/A_{real}$ exceeds 2%, the elastic deformation limit is violated, i.e., the elastic analysis is no longer valid because the plastically deformed area is large *enough*.

By using the law of unconscious statistician and assuming an *exponential* PDF for the asperity heights the closed-form expressions of the real and plastic areas can be obtained [21]. The ratio of the obtained expressions will be:

$$\frac{A_{plastic}}{A_{real}} = \exp\left(-w_p/\sigma\right) \tag{F.6}$$

Therefore, for $A_{plastic}/A_{real}$ to be smaller than 2%, σ/w_p has to be smaller than 0.26, or, by considering Equation (F.1), $\psi \equiv \sqrt{\sigma/w_p}$ has to be smaller than 0.51. In [21]

the criterion for negligible plasticity is $\psi < 0.6$ because it is supposed that initially the plastic flow occurs internally and does not affect the behavior of the contact area much.

To answer why $\psi = 1$ is a critical value, the *average* real (actual) contact pressure, $\bar{p}_{real}/A_{real}$ formula that is derived by William in his book on tribology [137] is used in [27]. It should be noted that the formula, assumes an exponential PDF form that is different from that of the GW model [21]. Therefore, the closed-form expression that is obtained for the average real contact pressure in [137] is slightly different from $\bar{p}_{real} = 0.56E^*\sqrt{\sigma/R}$ (that can be obtained according to the derivations in [21]):

$$\bar{p}_{real} \approx 0.39E^*\sqrt{\sigma/R} \tag{F.7}$$

In [27] it is claimed that when $\bar{p}_{real}$ is smaller than $0.3H$, the contact remains primarily elastic. Afterwards, by replacing the factor in Equation (F.7) with 0.3, it is deduced that when the RHS of Equation (F.1) becomes unity, i.e., when $\psi = 1$, the plasticity has become dominant.

The above reasoning for $\psi = 1$ as a criterion for onset of plasticity is somehow unreliable. For developing a better understanding of derivations related to plasticity in GW model [217] and [221] are suggested. In [246], the exponential approximation of the Gaussian tail is shown to be inadequate for most practical cases.

The second definition of plasticity index is given in [27] as:

$$\psi_M \equiv \frac{E^*}{H}\sqrt{m_2} \tag{F.8}$$

This definition is directly obtained from the theoretical value that is proposed by the BGT model for the slope of load-real area function. By substituting the constant of proportionality that is proposed by the BGT model, i.e., $\kappa = \sqrt{2\pi}$, into Equation (3.5) and taking the nominal pressure, σ_0, to the LHS:

$$\sigma_0 \equiv \frac{P}{A_0} = E^*\sqrt{\frac{m_2}{\pi}}\frac{A_{real}}{A_0} \tag{F.9}$$

Note that the real average pressure, $\bar{p}_{real}$, is defined as division of the normal load, P, by A_{real}. In other words, $\bar{p}_{real}$ is the slope of the σ_0 when plotted against A_{real}/A_0. The BGT model predicts a linear relation. Hence, it follows from Equation (F.9) that:

$$\bar{p}_{real} \equiv \frac{P}{A_{real}} = E^* \sqrt{\frac{m_2}{\pi}} \tag{F.10}$$

The criterion that is proposed in [27] is when $1.1\bar{p}_{real} < 0.3H$, i.e., as long as the average real pressure (over the asperities) remains below 33% of the hardness, the contact area majorly deforms elastically. By rearranging the above criterion, the origin of the definition in Equation (F.8) is revealed:

$$\bar{p}_{real} < 0.33H \Rightarrow \frac{E^*}{H}\sqrt{m_2} < 0.58 \Rightarrow \psi_M < 0.58 \tag{F.11}$$

According to [27], when $\psi_M < 0.5$ plastic deformation is not expected, i.e., a conservative value is proposed.

Appendix G

STICK-SLIP OF THE EQUIVALENT BLOCK-SPRING UNIT

In this appendix, the stick-slip of the equivalent block-spring is investigated by incorporating the expression for the block slippage length according to Equation (2.2). The stick-slip of the equivalent block-spring unit is related to the compression, radius, and mechanical characteristics of a circular paraboloid asperity that contacts an elastic half-space. Furthermore, a fast algorithm for calculating force is proposed for the Maxwell-slip model.

Suppose that at the beginning, the block is right below the spring-driver attachment point (Figure G.1-(1)). Then, The driver moves horizontally and extends the spring. The spring force rises linearly. The block would slide when the spring force reaches the static friction threshold. The distance that the driver has to travel to trigger the first sliding of the block, x_{th}, can be immediately obtained by noting that (Figure G.1-(2)):

$$f_{spring} = kx \Rightarrow F_{th} = kx_{th} \Rightarrow \mu_s N = kx_{th} \tag{G.1}$$

Therefore, the required driver displacement for triggering the first block slippage is:

$$\Delta x_{d_1} = x_{th} = \mu_s \frac{N}{k} \tag{G.2}$$

It is assumed that the driver remains fixed during the block slippage. Therefore, at the end of its slippage, the block approaches the spring-driver attachment point by δx (Figure G.1-(3)). The block slippage length, δx, is obtained from Equation (2.2) and is not a function of the mass of the block. The load-drop in the spring due to the slippage is simply equal to:

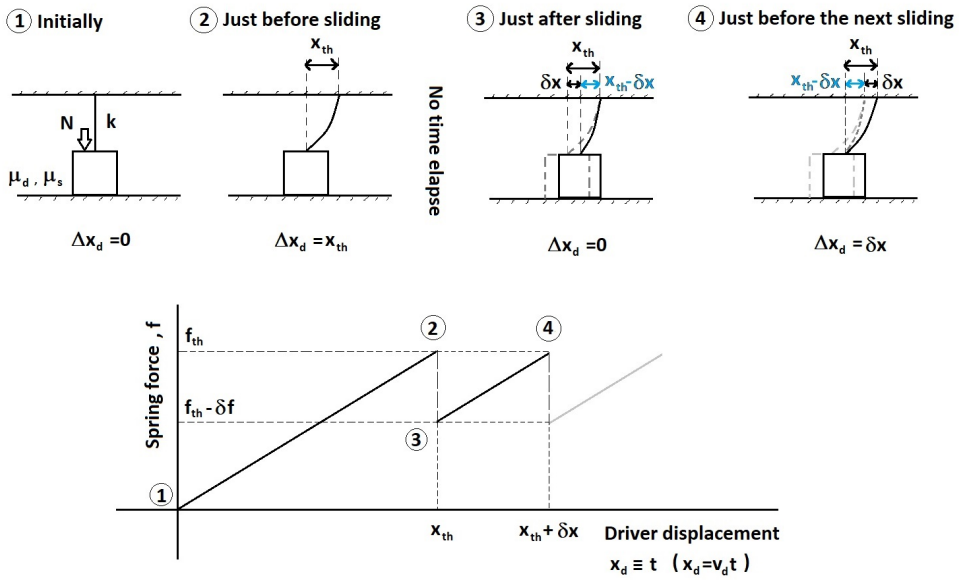

Figure G.1: The stick-slip of the block-spring unit

$$\delta f = k\delta x = 2(\mu_s - \mu_d)N \tag{G.3}$$

It can be deduced that the *driver* now has to move by δx forward to trigger the subsequent block slippage (Figure G.1-(4)). Till that point, the spring force will rise linearly. Therefore, the required driver displacement for triggering the subsequent block slippage is:

$$\Delta x_{d_2} = \delta x = 2(\mu_s - \mu_d)\frac{N}{k} \tag{G.4}$$

After the first load-drop the load-displacement behavior between Figures G.1-(3) and G.1-(4) repeats periodically and the slipping (load-drop) intervals follow the sticking (linear load rise) intervals. The stick-slip of the single block-spring unit is a known function of the driver position (time), normal load, spring stiffness, and the static/dynamic COF.

In Chapters 2 and 3, the surface asperities are modeled as block-spring units with different (leaf spring) stiffness and normal load values. The asperities are assumed to be circular paraboloids. The normal load and tangential stiffness of the equivalent

block-spring units are assigned according to Equations (E.2) and (3.6), respectively. Therefore, the normal load, N, and the tangential stiffness, k, are known functions of the mechanical and geometrical parameters of the asperity contact. By substituting N and k using Equations (E.2) and (3.6), respectively, into the fraction N/k:

$$\frac{N}{k} = \frac{2-\nu}{2(1-\nu)}w \tag{G.5}$$

where w is the amount of compression applied by the rigid circular paraboloid asperity on the elastic half-space. Then, by substituting N/k into Equations (G.2) and (G.4):

$$\Delta x_{d_1} = \frac{\mu_s}{2}\frac{2-\nu}{1-\nu}w \tag{G.6}$$

$$\Delta x_{d_2} = (\mu_s - \mu_d)\frac{2-\nu}{1-\nu}w \tag{G.7}$$

These result is interesting since the asperity tip radius and the mechanical properties are absent in the expressions. In other words, for identical material and COF values, only the amount of compression determines the intervals of the block slippages. On the other hand, since according to Equation (E.2), $N = \frac{4}{3}E^*\sqrt{Rw^3}$, besides N itself, the expression for δf in Equation (G.3) depends on the asperity tip radius as well as the compression.

The stick-slip function (force) of the single block-spring unit is a known function of the driver motion (displacement). The (spring) force - (driver) displacement function is composed of the straight lines with slope k, which breaks at $\Delta x_{d_1} + (j-1)\Delta x_{d_2}$, where $j = \{1, 2, 3, ...\}$ counts the load-drops (Figure G.1). The function can be written by considering the y-intercept of the sticking intervals as:

$$f_{spring} = \begin{cases} kx_d, & \text{if } x_d < x_{th}. \\ kx_d - j\delta f, & \text{if } x_{th} + (j-1)\delta x < x_d < x_{th} + j\delta x. \end{cases} \tag{G.8}$$

Based on the above function, a fast algorithm for calculating the total force in the

Maxwell-slip model is developed. The driver position, x_d, is given as a set of equally-spaced numbers. The intervals have to be small such that the smallest Δx_{d_2} (which would belong to the block which represents the asperity with the smallest compression) becomes appropriately divided.

For each block-spring unit, the algorithm will determine which interval the members of the x_d set belong. In other words, the algorithm will look for the sticking interval of each x_d set member for every unit. The chunks of x_d values are then used according to Equation (G.8) to calculate the spring force of each unit. Finally, the spring forces are superimposed to find the total friction.

Appendix H

SPRING STIFFNESS IN THE BURRIDGE-KNOPOFF MODEL

By a direct use of elasticity definitions and physical reasoning, a pair of expressions for the stiffness of equivalent coil and leaf springs can be derived for an elastic block under tension/compression or shear load:

$$\begin{cases} k_c = EWH/L \\ k_p = GWL/H \end{cases} \tag{H.1}$$

where E is Young modulus, G is shear modulus, and W, L, and H are the block's width, length, and height, respectively. In this appendix, the spring stiffness values of a BK mode unit are obtained using a global stiffness constructed by the linear triangular elements of FEM. It is shown that the leaf spring stiffness (the stiffness of the spring that attaches the block to the driver) is exactly the same as above. However, the stiffness of the block-coupling coil spring is different. This difference manifests itself as a multiplier of ETH/L which is a function of Poisson ratio only. The multiplier expression has different forms in plane stress and plane strain cases. For a Poisson ratio of $\nu = 0.33$, the multiplier is nearly 1.1 if the plane stress assumption is made in the FEM formulation. This means that according to the FEM formulation, the coil spring stiffness has to be $1.1 * ETH/L$. In the case of plane strain assumption, the multiplier is close to $0.75 * ETH/L$ when the Poisson ratio is equal to 0.33.

An isolated unit of the BK model is shown in Figure H.1-(a). Inspired by [310], in which a 2-D BK model's unit cell is assumed to be equivalent to an assemblage of tetrahedral elements, here it is assumed that the finite element model in Figure H.1-(b), composed of two linear triangular elements can be used to determine the stiffness values of the leaf and coil springs (i.e. k_p and k_c) in terms of the mechanical char-

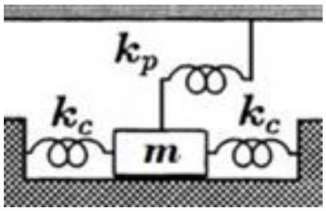

(a)

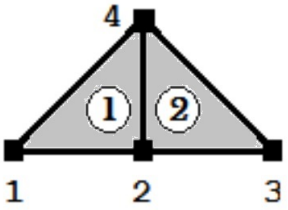

(b)

Figure H.1: (a) The isolated unit of the BK model and (b) Two triangular elements that model the unit

acteristics of the elastic body. It is assumed that node number 2 in Figure H.1-(b) represents the block in Figure H.1-(a); node number 4 represents the (fixed) driver and nodes 1 and 3 represent the (stuck) neighbors. The global stiffness matrix of the 2-element model in Figure H.1-(b) can be constructed by assembling the stiffness matrices of elements 1 and 2. The force developed on the nodes is related to displacement of the nodes by the global stiffness matrix:

$$\overrightarrow{F}_{8*1} = \mathbf{K_{8*8}}\,\overrightarrow{u}_{8*1} \tag{H.2}$$

$$\begin{bmatrix} X_1 \\ Y_1 \\ X_2 \\ Y_2 \\ X_3 \\ Y_3 \\ X_4 \\ Y_4 \end{bmatrix} = \mathbf{K_{8*8}} \begin{bmatrix} u_1 \\ v_1 \\ u_2 \\ v_2 \\ u_3 \\ v_3 \\ u_4 \\ v_4 \end{bmatrix}$$

Out of all displacement components only the horizontal displacement of node 2 (the block) is nonzero and only those matrix elements that correspond to the horizontal components of the force vector, $\overrightarrow{F}$, i.e. the horizontal force components of nodes 1, 3 and 4, specify the stiffness of the corresponding springs:

$$\begin{cases} X_1 = k_{11}u_1 \\ X_3 = k_{51}u_1 \\ X_4 = k_{71}u_1 \end{cases}$$

Hence,

$$\begin{cases} k_c \equiv k_{11} = k_{51} \\ k_p \equiv k_{71} \end{cases}$$

For plane stress:

$$k_c = \frac{ETH}{L} * \frac{1}{2(1-\vartheta^2)} \tag{H.3}$$

For plane strain:

$$k_c = \frac{ETH}{L} * \frac{1-\vartheta}{2(1-2\vartheta)(1+\vartheta)} \tag{H.4}$$

and for both plane stress and plane strain cases:

$$k_p = \frac{GTL}{H} \tag{H.5}$$

Figure H.2 shows the variation of the multiplier, k_{cFEM}/k_c with Poisson ratio. For the range of reasonable Poisson ratios values the former approximations of the spring stiffness values are acceptable. For example, for a rock with a Poisson ratio of 0.25, the multiplier in the plane stress case is about 1.07. Note that the multiplier is 0.6 for the plane strain case.

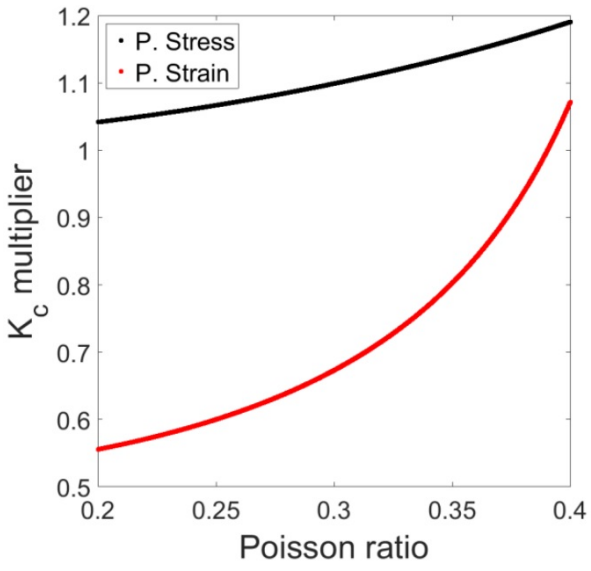

Figure H.2: Variation of the ratio of the FEM-predicted coil spring stiffness to that which is obtained by simple reasoning, $k_c = ETH/L$, with Poisson ratio for plane stress and plane strain cases

CURRICULUM VITAE

PERSONAL INFORMATION

Surname, Name: Amireghbali, Aydın

EDUCATION

Degree	Institution	Year of Graduation
M.Sc.	Middle East Technical University (METU)	2013
B.Sc.	Islamic Azad University (SRBIAU)	2007

PUBLICATIONS

1- A. Amireghbali and D. Coker, 2014, "Elastic analysis of a circumferential crack in an isotropic curved beam using the modified mapping-collocation method", Journal of Computational and Applied Mathematics, 264, 131–138.

2- I. T. Özcan, A. Amireghbali and D. Coker, "Quasi-static modeling of frictional sliding using Maxwell-slip model", Friction and Wear across Scales 2022, The international conference center of ETH Zürich, Switzerland, August 15-18, 2022.

3- A. Amireghbali and D. Coker, "Frictional dynamics using Maxwell-Slip model", 14th Virtual Congress WCCM ECCOMAS 2020, organized in virtual format from January 11th to 15th , 2021.

4- A. Amireghbali and D. Coker, “Parametric study of interface dynamics for sliding contact of elastic body on a rigid surface using Burridge-Knoppoff model”, 13th National Congress on Theoretical and Applied Mechanics (13th NCTAM), Sofia, Bulgaria, September 6-10, 2017.

5- A. Amireghbali and D. Coker, “Onset of sliding contact on the interface of elastic body and rigid surface using Burridge-Knopoff model”, 9th International Conference on Tribology (BALKANTRIB’17), Cappadocia, Turkey, September 13-15, 2017.

6- A. Amireghbali, “Stress field symmetry and Muskhelishvili potential series expansion”, 10th International Conference on Mathematical Problems in Engineering, Aerospace and Sciences (ICNPAA), Narvik University, Norway, July 15-18, 2014.

7- A. Amireghbali and D. Coker, “Tikhonov regularization for the modified mapping-collocation method applied to circumferentıal crack in a curved beam”, 11th World Congress on Computational Mechanics (WCCM XI), Barcelona, Spain, July 20-25, 2014.